

Do animals, including invertebrates,
have emotions? p. 1351

A better polymer for sensing
strain pp. 1353 & 1418

Convergent selection
affects grain yield p. 1372

Science

\$15
25 MARCH 2022
SPECIAL ISSUE
science.org

AAAS

SOCIAL MEDIA STORM

How science
gets swept up p. 1332



CALL FOR PAPERS



OLAR

Ocean-Land-Atmosphere Research (OLAR) is an online-only, Open Access journal published in affiliation with **Southern Marine Science and Engineering Guangdong Laboratory (Zhuhai) (SML-ZHUHAI)** and distributed by the **American Association for the Advancement of Science (AAAS)**. With an emphasis on ocean-related sciences, *OLAR* provides an international platform for researchers engaged in marine, terrestrial, and atmospheric studies and the interactions among them. The journal welcomes relevant fundamental research in physics, chemistry, biology and geology as well as emerging applied research in ocean observation, environment protection, and resources utilization. Manuscripts featuring cutting-edge science, innovative technology, and interdisciplinary studies within the journal's scope are particularly welcome.

Submit your research to *OLAR* today!

Learn more at spj.sciencemag.org/OLAR

The Science Partner Journal (SPJ) program was established by the American Association for the Advancement of Science (AAAS), the nonprofit publisher of the Science family of journals. The SPJ program features high-quality, online-only, Open Access publications produced in collaboration with international research institutions, foundations, funders, and societies. Through these collaborations, AAAS furthers its mission to communicate science broadly and for the benefit of all people by providing top-tier international research organizations with the technology, visibility, and publishing expertise that AAAS is uniquely positioned to offer as the world's largest general science membership society. Visit us at spj.sciencemag.org



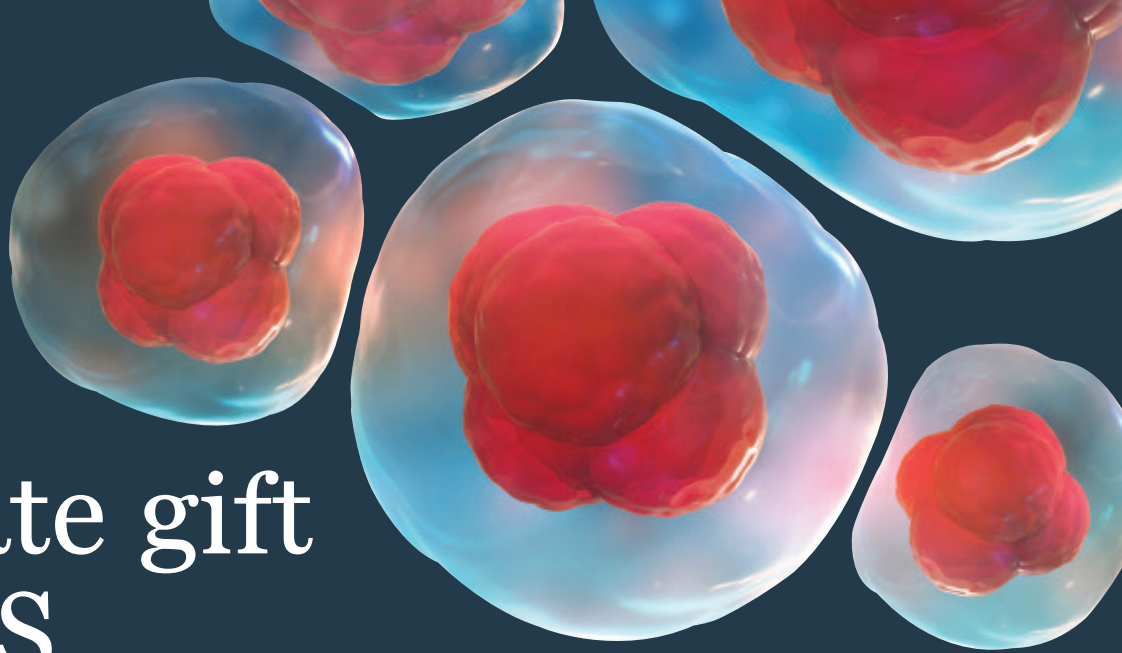
@SPJournals



@SPJournals

 OPEN ACCESS

ARTICLE PROCESSING CHARGES WAIVED UNTIL 2025



An estate gift to AAAS

Going all the way back to 1848, our founding year, the American Association for the Advancement of Science (AAAS) has been deeply committed to advancing science, engineering and innovation around the world for the benefit of all people.

Today, we are dedicated to advocating for science and scientific evidence to be fully and positively integrated into public policy and for the community to speak with one voice to advance science and engineering in the United States and around the world.

By making AAAS a beneficiary of your will, trust, retirement plan or life insurance policy, you will become a member of our 1848 Society and will help fuel our work on behalf of science and society – including publishing the world’s most promising, innovative research in the *Science* family of journals and engaging in the issues that matter locally, nationally and around the world.

“As a teacher and instructor, I bear responsibility for the younger generations. If you have extra resources, concentrate them on organizations, like AAAS, that are doing work for all.”

—Prof. Elisabeth Ervin-Blankenheim, 1848 Society member

If you intend to include AAAS in your estate plans, provide this information to your lawyer or financial adviser:

Legal Name: American Association for the Advancement of Science

Federal Tax ID Number: 53-0196568

Address: 1200 New York Avenue, NW, Washington, DC 20005

If you would like more information on making an estate gift to AAAS, cut out and return the form below or send an email to philanthropy@aaas.org. Additional details are also available online at www.aaas.org/1848Society.

AMERICAN ASSOCIATION FOR THE ADVANCEMENT OF SCIENCE

cut here

Yes, I would like more information about joining the AAAS 1848 Society.

PLEASE CONTACT ME AT:

Name: _____

Address: _____

City: _____ State: _____ Zip code: _____ Country: _____

Email: _____ Phone: _____

RETURN THIS FORM TO:

AAAS Office of Philanthropy and Strategic Partnerships • 1200 New York Avenue, NW • Washington, DC 20005 USA





Diversity is the focus

Female researchers at Saga University

With few institutions being models for diversity in Japan, Saga University seeks to become a leader with its Office for Equality, Diversity, and Inclusion.

The numbers are not flattering. While efforts have been made to improve the situation, as of 2018, Japan ranked at the bottom of 29 Organisation for Economic Co-operation and Development countries for its percentage of female university faculty (1). The future does not look bright either, with the number of female students enrolling in the sciences ranking no better (2).

One reason, according to Saga University president Hiroaki Kodama, is the lack of role models. "Our gender ratios depend on the field. We have almost one-to-one representation in the Departments of Medicine and Agriculture, but our ratio is very skewed toward men in engineering," he says. Unfortunately, he adds, these numbers are not unique and reflect trends across the country.

Moreover, girls and boys perform equally well on science test scores through high school, which suggests that the problem begins at the university level (3).

Ironically, these conditions have also created an exceptional opportunity. While research funding in Japan is predominately given to select universities in the biggest cities, the national government has been more generous in distributing its money when it comes to solving the gender gap. One of these beneficiaries has been Saga University, located in Saga, Japan, and its Office for Equality, Diversity, and Inclusion (OEDI).

"We feel that a more diverse campus will attract more female and overseas students, which in turn will lead to more innovative research," explains Kodama. In reference to the long hours that Japanese employees are reputed to work, he adds, "a more diverse workforce will lead to a broader range of working styles, which will

create a better working environment." Saga University officially declared a new commitment to diversity in 2017 with the launch of OEDI, and the timing could hardly have been better. OEDI saw a major increase in its budget in 2019, when it was awarded new funding from the national government. Its staff more than doubled, and the team made plans to implement a number of new programs.

However, the funding came with clear rules, says Kodama. "The funding is in 3-year cycles. It is a short time to make an impact, but, even if the funding is not renewed, we can still build a framework for the university to promote diversity," he explains.

One of the original plans was to give female researchers more opportunity to travel overseas for research collaborations, with the intention of boosting their careers and enhancing the university's reputation by showcasing the talent and diversity of its faculty. "For many reasons, female faculty have fewer opportunities to build international networks, which gives them fewer opportunities to travel abroad. We want to help them build joint research projects," explains Kaoru Araki, deputy manager of OEDI.

Those plans were upended, however, when the unexpected happened: COVID-19. "The restricted travel really disrupted our plans to promote and advance the research done by our female faculty. We had to conceive new ways [to accomplish this]," she continues.

The pandemic as a positive

"Before the COVID-19 pandemic, opportunities for international collaborative research and study abroad may have been limited to universities in large cities with access to lots of information and male researchers with fewer roles in the home, but that perception has changed dramatically with the pandemic," says Araki. "People are now

getting information more through the internet and collaborating with overseas researchers." University faculty see this as a time of transition, she adds, and an opportunity to promote the activities and achievements of Saga's excellent cadre of female researchers, particularly via digital media channels.

One way this is being done is through the website *Musubime* ("connection" in Japanese), which features female faculty members at Saga University (4). The site highlights the broad range of representative research disciplines—from software engineering to water sustainability—with an emphasis on diversity and multinationalism.

Aya Shiraki, a professor in the Faculty of Medicine, sees the website as a clear positive. "I want to inspire the next generation of female students. *Musubime* has increased my visibility inside and outside the university," she says. Others, like Mie Ishii, an associate professor of the Faculty of Art and Regional Design, who researches the conservation of textiles, are already seeing a great benefit to joining the site. "It has increased my exposure and the number of international students expressing interest in my work," she says.

Musubime also focuses attention on the extraordinary research done at Saga University, which boasts of some of the country's best semiconductor and energy research institutes, including its Institute of Ocean Energy, a leader in developing new forms of power generation and extracting remote resources from the ocean. "By showing the diversity of our faculty and our research," says Kodama, "we want to appeal to researchers and students who will join us to solve some of society's greatest challenges."

Cultural challenges

Despite OEDI's best efforts, there remain persistent cultural factors that discourage women from entering underrepresented fields. In Japan, regardless of their careers, women do most of the housework. OEDI has therefore allocated funding for researchers—women and men—with young children or older parents who need special care to allow them to hire additional laboratory staff, providing more family time. In addition, funds are available for academic writing services with the aim of reducing the workload for those overwhelmed with personal responsibilities.

Furthermore, because diversity is not limited to just gender, OEDI is taking many steps to make the university friendly to the lesbian, gay, bisexual, transexual,



Top left: President Hiroaki Kodama, Top right: Saga University campus, Bottom Right: Kaoru Araki, deputy manager of OEDI

and questioning (LGBTQ) community and to people with disabilities. "The gender gap is our biggest concern right now," says Araki. "But diversity includes many more groups, and it is our responsibility to create an environment that allows all of them to flourish." For example, staff are being trained about gender pronouns and the campus is being equipped with facilities that make it accessible to all.

Another initiative at OEDI is to educate staff and students about unconscious bias. To counteract possible misconceptions that the university's diversity initiative is some form of reverse discrimination, it is

important to acknowledge extraneous factors that are holding back talented female researchers. OEDI is therefore organizing workshops on this topic. "Unconscious gender bias is particularly prevalent in Japan. We believe this is a major factor in the underrepresentation of women at Japanese universities," says Araki.

For Kodama, enhancing diversity is a partial solution to another problem. Saga University sits in one of the least populated and most rural prefectures of Japan. With these programs, he hopes to reverse the brain drain happening in all rural areas in the country. "One of my biggest missions as university president is to show rural areas how they can effectively develop their human resources."

References

1. J. Lau, "Can Women Break Through Asian Universities' 'Net Ceiling'?" *Times Higher Education* (2020), available at <https://www.timeshighereducation.com/features/can-women-break-through-asian-universities-net-ceiling>.
2. "Japan Has Lowest Share of Women Studying Science," *Kyodo News* (2021), available at <https://english.kyodonews.net/news/2021/10/36d43f3b208d-japan-has-lowest-share-of-women-studying-science-oecd-report.html>.
3. N. Osumi, "Japan's Woman Problem," *Nature Index* (2018), available at <https://www.natureindex.com/news-blog/japans-woman-problem>.
4. *Musubime*, Saga University, <https://musubime.saga-u.ac.jp/en/>.

Sponsored by



SAGA UNIVERSITY



It's prime time!

Introducing LyoPrime™ Luna Probe One-Step RT-qPCR Mix with UDG – Lyophilized for increased flexibility, same optimized performance

Supplied as a lyophilized cake, the LyoPrime Luna Probe One-Step RT-qPCR Mix with UDG enables sensitive detection of targeted RNA sequences in a room temperature-stable format, and contains the same versatile features and strong performance as the liquid version. This is the first in a series of lyophilized products developed jointly by New England Biolabs and Fluorogenics™ Limited, which is now a subsidiary of New England Biolabs, Inc.

- Simply add nuclease-free water for rapid rehydration
- Store at room temperature for up to 2 years prior to rehydration
- Eliminate cold chain shipping requirements
- Multiplex up to 5 targets to increase throughput
- Increase reaction specificity and robustness with our unique pairing of Luna WarmStart® RT and Hot Start Taq
- Prevent carryover contamination with Thermolabile UDG and dUTP included in optimized mix
- Maintain RNA integrity with Murine RNase Inhibitor included in optimized mix
- Eliminate pipetting errors with non-interfering, visible blue tracking dye



By simply adding water, the cake can be rehydrated and is ready for use.

Learn more at
www.neb.com/L4001

One or more of these products are covered by patents, trademarks and/or copyrights owned or controlled by New England Biolabs, Inc. For more information, please email us at busdev@neb.com. The use of these products may require you to obtain additional third party intellectual property rights for certain applications.

© Copyright 2022, New England Biolabs, Inc.; all rights reserved.



be INSPIRED
drive DISCOVERY
stay GENUINE

CONTENTS

25 MARCH 2022 • VOLUME 375 • ISSUE 6587

SPECIAL SECTION

Social media storm

INTRODUCTION

1332 Inside the vortex *M. Enserink*

NEWS

1334 On the trail of bullshit
K. Kupferschmidt

1338 In the line of fire *C. O'Grady*
PODCAST

1344 Riding the Twitter wave
J. Brainard

ON THE COVER

Science, like the rest of society, has been swept up in the storms caused by social media. This special News section looks at how scientists study and fight mis- and disinformation, how harassment and intimidation have spiked during the COVID-19 pandemic, and how researchers use Twitter to inform the public and share their findings with colleagues. See page 1332. *Illustration: Davide Bonazzi/Salzmanart*



ILLUSTRATION: DAVIDE BONAZZI/SALZMANART

NEWS

IN BRIEF

1322 News at a glance

IN DEPTH

1324 Undersea mountains help stir up oceans

Seafloor topography plays outside role in currents that sequester carbon and heat
By P. Voosen

1325 Southern roots for the Maya—and the maize that fed them

Migrants from the south may have helped spread early farming in Central America, ancient DNA suggests
By A. Gibbons

1326 War halts animal tracking project

As space station antenna goes silent, ICARUS seeks new ways to collect animal GPS data
By E. Pennisi

1327 Brain implant enables man in locked-in state to communicate

Despite complete paralysis from amyotrophic lateral sclerosis, person used neural signals to spell out thoughts
By K. Servick

1328 Where does embryo editing stand now?

He Jiankui's expected release finds a field still wrestling with scientific and ethical challenges
By J. Cohen

1330 Ukrainian bat study spun into tale of bioweapons

Russian disinformation campaign targets routine research on bat parasites
By A. Curry

INSIGHTS

PERSPECTIVES

1348 Volcano-tectonic control of Cumbre Vieja

Unexpected features from the 2021 eruption might help forecast giant flank collapses
By P. J. González

1349 Effective surveillance of variants

Community testing studies can provide insights as SARS-CoV-2 evolves
By A. J. Kucharski and C. Cohen
REPORT p. 1406

1351 The question of animal emotions

Do animals, including invertebrates, have felt emotions and does this morally matter?
By F. B. M. de Waal and K. Andrews



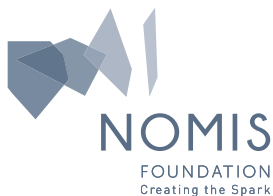
Research at the intersection of the social and life sciences

Unconventional. Interdisciplinary. Bold.

The **NOMIS & Science Young Explorer Award** recognizes and rewards early-career M.D., Ph.D., or M.D./Ph.D. scientists that perform research at the intersection of the social and life sciences. Essays written by these bold researchers on their recent work are judged for clarity, scientific quality, creativity, and demonstration of cross-disciplinary approaches to address fundamental questions.

A cash prize of up to 15 000 USD will be awarded to essay winners, and their engaging essays will be published in *Science*. Winners will also be invited to share their work and forward-looking perspective with leading scientists in their respective fields at an award ceremony as well as a meeting of the NOMIS Board of Directors to consider future funding.

Apply by May 15, 2022
at www.science.org/nomis



1353 Giant electromechanical effects in polymers

A four-ingredient polymer chain has record-breaking piezoelectric capability

By Z.-X. Wang and W.-Q. Liao

REPORT p. 1418

1354 Sieving gases with twisty polymers

Ladder polymers in three dimensions show promise as gas-separation membranes

By P. M. Budd

REPORT p. 1390

1355 Photons think inside the box

Light confined to a sheet offers a glimpse into low-dimensional quantum gases

By R. J. Fletcher and M. Zwiernik

REPORT p. 1403

POLICY FORUM**1357 Will the European Health Data Space change data sharing rules?**

Questions of consent and public interest research loom large

By M. Shabani

BOOKS ET AL.**1360 Escaping a planet in peril**

A tech company bankrolls a space-based retreat for Earth's elite. What could go wrong?

By E. P. S. Baumer

1361 Unlocking the mysteries of the written word

A philologist presents a lively tour of the world's foundational and undeciphered scripts

By A. Robinson

LETTERS**1362 Ethical drawbacks of sustainable meat choices**

By M. B. Mathur

1362 Self-spreading vaccines: Base policy on evidence

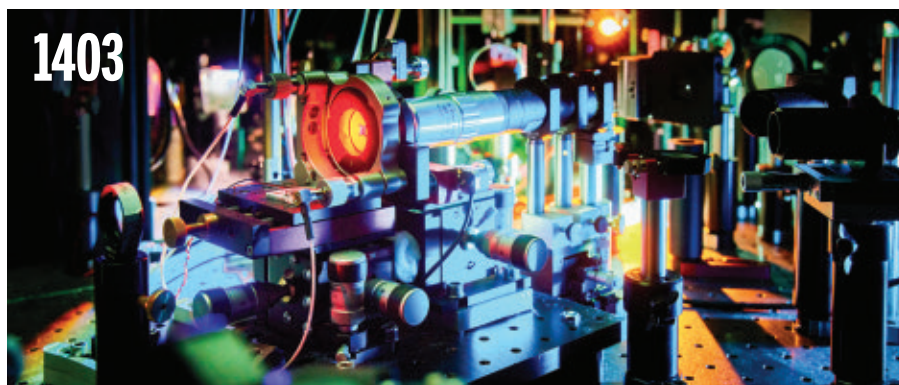
By D. G. Streicker et al.

1363 Response

By F. Lentzos et al.

1363 Technical Comment abstracts**RESEARCH****IN BRIEF**

1368 From *Science* and other journals



An optical microcavity setup is used to trap and compress a photon gas.

RESEARCH ARTICLES**1371 Structural biology**

A structural basis for amylin receptor phenotype

J. Cao et al.

RESEARCH ARTICLE SUMMARY; FOR FULL TEXT: DOI.ORG/10.1126/SCIENCE.ABM9609

1372 Crop genomics

Convergent selection of a WD40 protein that enhances grain yield in maize and rice

W. Chen et al.

RESEARCH ARTICLE SUMMARY; FOR FULL TEXT: DOI.ORG/10.1126/SCIENCE.ABG7985

1373 Virology

Architecture and antigenicity of the Nipah virus attachment glycoprotein

Z. Wang et al.

1378 Neuroscience

An action potential initiation mechanism in distal axons for the control of dopamine release

C. Liu et al.

REPORTS**1385 Thermoelectrics**

High thermoelectric performance realized through manipulating layered phonon-electron decoupling

L. Su et al.

1390 Membranes

Hydrocarbon ladder polymers with ultrahigh permselectivity for membrane gas separations

H. W. H. Lai et al.

PERSPECTIVE p. 1354

1393 Inorganic chemistry

Side-on coordination of diphosphorus to a mononuclear iron center

S. Wang et al.

1398 Valleytronics

Tunable and giant valley-selective Hall effect in gapped bilayer graphene

J. Yin et al.

1403 Quantum optics

Compressibility and the equation of state of an optical quantum gas in a box

E. Busley et al.

PERSPECTIVE p. 1355

1406 Coronavirus

Rapid increase in Omicron infections in England during December 2021: REACT-1 study

P. Elliott et al.

PERSPECTIVE p. 1349

1411 Biomaterials

Topological supramolecular network enabled high-conductivity, stretchable organic bioelectronics

Y. Jiang et al.

1418 Piezoelectrics

Relaxor ferroelectric polymer exhibits ultrahigh electromechanical coupling at low electric field

X. Chen et al.

PERSPECTIVE p. 1353

1422 Nanomaterials

Self-assembly of nanocrystals into strongly electronically coupled all-inorganic supercrystals

I. Coropceanu et al.

DEPARTMENTS**1321 Editorial**

Redo college intro science

By D. Asai et al.

1430 Working Life

No shame in my pain

By A. C. H. Jaeger

Science Staff1318

Science Careers 1427

SCIENCE (ISSN 0036-8075) is published weekly on Friday, except last week in December, by the American Association for the Advancement of Science, 1200 New York Avenue, NW, Washington, DC 20005. Periodicals mail postage (publication No. 484460) paid at Washington, DC, and additional mailing offices. Copyright © 2022 by the American Association for the Advancement of Science. The title SCIENCE is a registered trademark of the AAAS. Domestic individual membership, including subscription (12 months): \$165 (\$74 allocated to subscription). Domestic institutional subscription (51 issues): \$2212; Foreign postage extra: Air assist delivery: \$98. First class, airmail, student, and emeritus rates on request. Canadian rates with GST available upon request. GST #125488122. Publications Mail Agreement Number 1069624. Printed in the U.S.A.

Change of address: Allow 4 weeks, giving old and new addresses and 8-digit account number. Postmaster: Send change of address to AAAS, P.O. Box 96178, Washington, DC 20090-6178. Single-copy sales: \$15 each plus shipping and handling available from backissues.science.org; bulk rate on request. Authorization to reproduce material for internal or personal use under circumstances not falling within the fair use provisions of the Copyright Act can be obtained through the Copyright Clearance Center (CCC), www.copyright.com. The identification code for Science is 0036-8075. Science is indexed in the Reader's Guide to Periodical Literature and in several specialized indexes.

Editor-in-Chief Holden Thorp, hthorp@aaas.org

Executive Editor Monica M. Bradford

Editors, Research Valda Vinson, Jake S. Yeston Editor, Insights Lisa D. Chong

DEPUTY EDITORS Stella M. Hurlley (UK), Phillip D. Szoromi, Sacha Vignieri **SR. EDITORIAL FELLOW** Andrew M. Sugden (UK) **SR. EDITORS** Gemma Alderton (UK), Caroline Ash (UK), Brent Grocholski, Pamela J. Hines, Di Jiang, Priscilla N. Kelly, Marc S. Lavine (Canada), Yevgeniya Nusinovich, Ian S. Osborne (UK), Beverly A. Purnell, L. Bryan Ray, H. Jesse Smith, Keith T. Smith (UK), Jelena Stajic, Peter Stern (UK), Valerie B. Thompson, Brad Wible, Yuen Yiu **ASSOCIATE EDITORS** Michael A. Funk, Bianca Lopez, Seth Thomas Scanlon (UK), Yury V. Suleymanov, Ekeoma Uzogara **LETTERS EDITOR** Jennifer Hills **LEAD CONTENT PRODUCTION EDITORS** Harry Jach, Lauren Kmeč **CONTENT PRODUCTION EDITORS** Amelia Beyna, Jeffrey E. Cook, Chris Filiatreau, Julia Haber-Katris, Nida Masulis, Abigail Shashikamth, Suzanne M. White **SR. EDITORIAL COORDINATORS** Carolyn Kyle, Beverly Shields **EDITORIAL COORDINATORS** Aneera Dobbins, Joi S. Granger, Jeffrey Hearn, Lisa Johnson, Maryrose Madrid, Ope Martins, Shannon McMahon, Jerry Richardson, Hilary Stewart (UK), Alice Whaley (UK), Anita Wynn **PUBLICATIONS ASSISTANTS** Alexander Kief, Ronmel Navas, Isabel Schneidat, Brian White **EXECUTIVE ASSISTANT** Jessica Slater **ASI DIRECTOR, OPERATIONS** Janet Clements (UK) **ASI SR. OFFICE ADMINISTRATOR** Jessica Wallock (UK)

News Editor Tim Appenzeller

NEWS MANAGING EDITOR John Travis **INTERNATIONAL EDITOR** Martin Enserink **DEPUTY NEWS EDITORS** Elizabeth Culotta, Lila Guterman, David Grimm, Eric Hand (Europe), David Malakoff **SR. CORRESPONDENTS** Daniel Clery (UK), Jon Cohen, Jeffrey Mervis, Elizabeth Pennisi **ASSOCIATE EDITORS** Jeffrey Brainard, Kelly Servick, Catherine Maticic **NEWS REPORTERS** Adrian Cho, Jennifer Couzin-Frankel, Jocelyn Kaiser, Rodrigo Pérez Ortega (Mexico City), Robert F. Service, Erik Stokstad, Paul Voosen, Meredith Wadman **INTERN TESS JOOSE CONTRIBUTING CORRESPONDENTS** Warren Cornwall, Andrew Curry (Berlin), Ann Gibbons, Sam Kean, Eli Kintsich, Kai Kupferschmidt (Berlin), Andrew Lawler, Mitch Leslie, Eliot Marshall, Virginia Morell, Dennis Normile (Tokyo), Elisabeth Pain (Careers), Charles Pillar, Gabriel Popkin, Michael Price, Joshua Sokol, Richard Stone, Emily Underwood, Gretchen Vogel (Berlin), Lizzie Wade (Mexico City) **CAREERS** Rachel Bernstein (Editor), Katie Langin (Associate Editor) **COPY EDITORS** Julia Cole (Senior Copy Editor), Morgan Everett, Cyra Master (Copy Chief) **ADMINISTRATIVE SUPPORT** Meagan Weiland

Creative Director Beth Rakuskas

DESIGN MANAGING EDITOR Marcy Atarod **GRAPHICS MANAGING EDITOR** Chris Bickel **PHOTOGRAPHY MANAGING EDITOR** William Douthitt **WEB STRATEGY MANAGER** Kara Estelle-Powers **MULTIMEDIA MANAGING PRODUCER** Joel Goldberg **DESIGN EDITOR** Chrystal Smith **DESIGNER** Christina Aycock **GRAPHICS EDITOR** Nirja Desai **INTERACTIVE GRAPHICS EDITOR** Kelly Franklin **SENIOR GRAPHICS SPECIALISTS** Holly Bishop, Nathalie Caro **SENIOR SCIENTIFIC ILLUSTRATOR** Valerie Altounian **SCIENTIFIC ILLUSTRATOR** Ashley Mastin **SENIOR PHOTO EDITOR** Emily Petersen **CHART EDITOR** Kaitlyn Dolan **SOCIAL MEDIA STRATEGIST** Jessica Hubbard **SOCIAL MEDIA PRODUCER** Sabrina Jenkens **WEB DESIGNER** Jennie Pajeroski **SENIOR PODCAST PRODUCER** Sarah Crespi **VIDEO PRODUCER** Meagan Cantwell

Chief Executive Officer and Executive Publisher Sudip Parikh

Publisher, Science Family of Journals Bill Moran

DIRECTOR, BUSINESS SYSTEMS AND FINANCIAL ANALYSIS Randy Yi **DIRECTOR, BUSINESS OPERATIONS & ANALYSIS** Eric Knott **DIRECTOR OF ANALYTICS** Enrique Gonzales **BUSINESS OPERATIONS** Jessica Tierney **MANAGER, BUSINESS ANALYSIS** Cory Lipman **BUSINESS ANALYSTS** Kurt Ennis, Maggie Clark **FINANCIAL ANALYST** Isacco Fusi **DIGITAL/PRINT STRATEGY MANAGER** Jason Hillman **SENIOR MANAGER, PUBLISHING AND CONTENT SYSTEMS** Marcus Spiegler **ASSISTANT MANAGER** DIGITAL/PRINT Rebecca Doshi **SENIOR CONTENT & PUBLISHING SYSTEMS SPECIALIST** Jacob Hedrick **SENIOR CONTENT SPECIALISTS** Steve Forrester, Lori Murphy **PRODUCTION SPECIALIST** Kristin Wolk **DIGITAL PRODUCTION MANAGER** Lisa Stanford **CONTENT SPECIALIST** Kimberley Oster **ADVERTISING PRODUCTION OPERATIONS MANAGER** Deborah Tompkins **DESIGNER, CUSTOM PUBLISHING** Jeremy Huntsinger **SR. TRAFFIC ASSOCIATE** Christine Hall **SPECIAL PROJECTS ASSOCIATE** Sarah Dhene

ASSOCIATE DIRECTOR, BUSINESS DEVELOPMENT Justin Sawyers **GLOBAL MARKETING MANAGER** Allison Pritchard **DIGITAL MARKETING MANAGER** Aimee Aponte **JOURNALS MARKETING MANAGER** Shawana Arnold **MARKETING ASSOCIATES** Aaron Helmreich, Ashley Hylton, Mike Romano, Tori Velasquez, Jenna Voris **SENIOR DESIGNER** Kim Huynh

DIRECTOR AND SENIOR EDITOR, CUSTOM PUBLISHING Sean Sanders **ASSISTANT EDITOR, CUSTOM PUBLISHING** Jackie Oberst **PROJECT MANAGER** Melissa Collins

DIRECTOR, PRODUCT & PUBLISHING DEVELOPMENT Chris Reid **DIRECTOR, BUSINESS STRATEGY AND PORTFOLIO MANAGEMENT** Sarah Whalen **ASSOCIATE DIRECTOR, PRODUCT MANAGEMENT** Kris Bishop **PRODUCT DEVELOPMENT MANAGER** Scott Chernoff **PUBLISHING TECHNOLOGY MANAGER** Michael Di Natale **SR. PRODUCT ASSOCIATE** Robert Koepke **PRODUCT ASSOCIATE** Caroline Breul, Anne Mason **SPJ ASSOCIATE MANAGER** Samantha Bruno **Fuller SPJ ASSOCIATE** Casey Buchta

MARKETING MANAGER Kess Knight **BUSINESS DEVELOPMENT MANAGER** Rasmus Andersen **SENIOR INSTITUTIONAL LICENSING MANAGER** Ryan Rexroth **INSTITUTIONAL LICENSING MANAGER** Marco Castellano, Claudia Paulsen-Young **SENIOR MANAGER, INSTITUTIONAL LICENSING OPERATIONS** Judy Lillibridge **SENIOR OPERATIONS ANALYST** Lana Guz **SYSTEMS & OPERATIONS ANALYST** Ben Teincoff **FULFILLMENT ANALYST** Aminta Reyes

DIRECTOR, GLOBAL SALES Tracy Holmes **US EAST COAST AND MID WEST SALES** Stephanie O'Connor **US MID WEST, MID ATLANTIC AND SOUTH EAST SALES** Chris Hoag **US WEST COAST SALES** Lynne Stickrod **ASSOCIATE DIRECTOR, ROW** Roger Goncalves **SALES REP, ROW** Sarah LeIrage **SALES ADMIN ASSISTANT, ROW** Victoria Glasbey **DIRECTOR OF GLOBAL COLLABORATION AND ACADEMIC PUBLISHING RELATIONS, ASIA** Xiaoying Chu **ASSOCIATE DIRECTOR, INTERNATIONAL COLLABORATION** Grace Yao **SALES MANAGER** Danny Zhao **MARKETING MANAGER** Kilo Lan **ASCA CORPORATION, JAPAN** Yoshihito Toda (Tokyo), Miyuki Tani (Osaka)

DIRECTOR, COPYRIGHT, LICENSING AND SPECIAL PROJECTS Emilie David **RIGHTS AND PERMISSIONS ASSOCIATE** Elizabeth Sandler **LICENSING ASSOCIATE** Virginia Warren **CONTRACT SUPPORT SPECIALIST** Michael Wheeler

MAIN HEADQUARTERS

Science/AAAS
1200 New York Ave. NW
Washington, DC 20005

SCIENCE INTERNATIONAL

Clarendon House
Clarendon Road
Cambridge, CB2 8FH, UK

SCIENCE CHINA

Room 1004, Culture Square
No. 59 Zhongguancun St.
Haidian District, Beijing, 100872

SCIENCE JAPAN

ASCA Corporation
Sibaura TY Bldg. 4F, 1-14-5
Shibaura Minato-ku
Tokyo, 108-0073 Japan

EDITORIAL

science_editors@aaas.org

NEWS

science_news@aaas.org

INFORMATION FOR AUTHORS

science.org/authors/
science-information-authors

REPRINTS AND PERMISSIONS

science.org/help/
reprints-and-permissions

MEDIA CONTACTS

scipak@aaas.org

MULTIMEDIA CONTACTS

SciencePodcast@aaas.org
ScienceVideo@aaas.org

INSTITUTIONAL SALES AND SITE LICENSES

science.org/librarian

PRODUCT ADVERTISING

science_advertising@aaas.org

CLASSIFIED ADVERTISING

science-careers.org/
advertise@sciencecareers.org

JOB POSTING CUSTOMER SERVICE

empowers.sciencecareers.org
support@sciencecareers.org

MEMBERSHIP AND INDIVIDUAL SUBSCRIPTIONS

science.org/subscriptions

MEMBER BENEFITS

aaas.org/membership/benefits

AAAS BOARD OF DIRECTORS

CHAIR Claire M. Fraser
PRESIDENT Susan G. Amara
PRESIDENT-ELECT Gilda A. Barabino

TREASURER

Carolyn N. Ainslie
CHIEF EXECUTIVE OFFICER
Sudip Parikh

BOARD

Cynthia M. Beall
Rosina M. Bierbaum
Ann Bostrom
Janine Austin Clayton
Laura H. Greene
Kaye Husbands Fealing
Maria M. Klawe
Robert B. Millard
William D. Provine

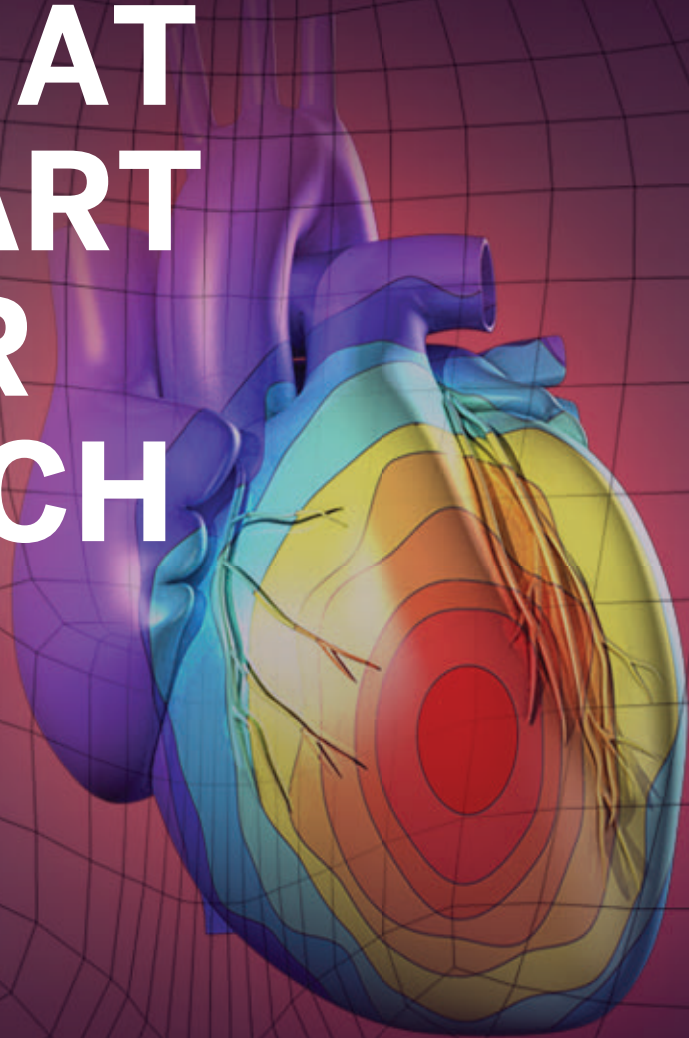
BOARD OF REVIEWING EDITORS (Statistics board members indicated with \$)

Erin Adams, U. of Chicago
Takuzo Aida, U. of Tokyo
Leslie Aiello, Wenner-Gren Fdn.
Deji Akinwande, UT Austin
Judith Allen, U. of Manchester
Marcella Alsan, Harvard U.
Sebastian Amigone, Inst. Curie
James Analytis, UC Berkeley
Trevor Archer, NIEHS, NIH
Paola Arlotta, Harvard U.
David Awschalom, U. of Chicago
Delia Baldassarri, NYU
Nenad Ban, ETH Zürich
Nandita Basu, U. of Waterloo
Franz Bauer, Pontificia U. Católica de Chile
Ray H. Baughman, UT Dallas
Carlo Beenakker, Leiden U.
Yasmine Bekkaid, NIAID, NIH
Philip Benfey, Duke U.
Kiros T. Berhane, Columbia U.
Joseph J. Berry, NREL
Alessandra Biffi, Harvard Med.
Chris Bowler, École Normale Supérieure
Ian Boyd, U. of St. Andrews
Malcolm Brenner, Baylor Coll. of Med.
Emily Brodsky, UC Santa Cruz
Ron Brookmeyer, UCLA (\$)
Christian Büchel, UIC Hamburg
Dennis Burton, Scripps Res.
Carter Tribble Butts, UC Irvine
György Buzsáki, NYU School of Med.
Mariana Byndloss, Vanderbilt U. Med. Ctr.
Annamarie Carlton, UC Irvine
Simon Cauchemez, Inst. Pasteur
Ling-Ling Chen, SIBCB, CAS
M. Keith Chen, UCLA
Zhijian Chen, UT Southwestern Med. Ctr.
Ib Chorkendorff, Denmark TU
Amander Clark, UCLA
James J. Collins, MIT
Robert Cook-Deegan, Arizona State U.
Virginia Cornish Columbia U.
Carolyn Coyne, Duke U.
Roberta Croce, VU Amsterdam
Christina Curtis, Stanford U.
Ismail Dabo, Penn State U.
Jeff L. Dangl, UNC
Chiara Daraio, Caltech
Nicolas Daughas, U. of Chicago
Christian Davenport, U. of Michigan
Frans de Waal, Emory U.
Claude Desplan, NYU
Sandra Diaz, U. Nacional de Córdoba
Samuel Díaz-Muñoz, UC Davis
Ulrike Diebold, TU Wien
Stefanie Dimmeler, Goethe-U. Frankfurt
Hong Ding, Inst. of Physics, CAS
Dennis Discher, UPenn
Jennifer A. Doudna, UC Berkeley
Ruth Drlja-Schutting, Med. U. Vienna
Raissa M. D'Souza, UC Davis
Bruce Dunn, UCLA
William Dunphy, Caltech
Scott Edwards, Harvard U.
Todd Ehlers, U. of Tübingen
Nader Engheta, UPenn
Karen Ersche, U. of Cambridge
Beate Escher, UFZ & U. of Tübingen
Barry Everitt, U. of Cambridge
Vanessa Ezenwa, U. of Georgia
Toren Finkel, U. of Pitt. Med. Ctr.
Gwynn Flowers, Simon Fraser U.
Peter Fratzl, Max Planck Inst. Potsdam
Elaine Fuchs, Rockefeller U.
Jay Gallagher, U. of Wisconsin
Daniel Geschwind, UCLA
Ramon Gonzalez, U. of South Florida
Sandra González-Bailón, UPenn
Nicolas Gruber, ETH Zürich
Hua Guo, U. of New Mexico
Taekjip Ha, Johns Hopkins U.
Daniel Haber, Mass. General Hos.
Sharon Hammersch-Schiffer, Yale U.
Wolf-Dietrich Hardt, ETH Zürich
Louise Harra, U. Coll. London
Carl-Philipp Heisenberg, IST Austria
Janet G. Hering, Eswag
Christoph Hess, U. of Basel & U. of Cambridge
Heather Hickman, NIAID, NIH
Hans Hilgenkamp, U. of Twente
Janneke Hille Ris Lambers, ETH Zürich
Kai-Uwe Hinrichs, U. of Bremen
Deirdre Hollingsworth, U. of Oxford
Randall Hulet, Rice U.
Auke Ijspeert, EPFL
Gwyneth Ingram, ENS Lyon
Darell Irvine, MIT
Akiko Iwasaki, Yale U.
Stephen Jackson, USGS & U. of Arizona
Erich Jarvis, Rockefeller U.
Peter Jonas, IST Austria
Matt Kaebelrinn, U. of Wash.
William Kaelin Jr., Dana-Farber Cancer Inst.
Dennis Kamm, UC Berkeley
Kisuk Kang, Seoul Nat. U.
Sabine Kastner, Princeton U.
Y. Narry Kim, Seoul Nat. U.
Robert Kingston, Harvard Med.
Nancy Knowlton, Smithsonian Institution
Etienne Koechlin, École Normale Supérieure
Alex L. Kolodkin, Johns Hopkins U.
Julija Krupic, U. of Cambridge
Paul Kubus, U. of Calgary
Gabriel Lander, Scripps Res. (\$)
Mitchell A. Lazar, UPenn
Luis Liz-Marzán, CIC bioMaGUNE
Omar Lizarola, UCLA
Jonathan Losos, Wash. U. in St. Louis
Ke Lu, Inst. of Metal Res., CAS
Christian Lüscher, U. of Geneva
Jean Lynch-Stieglitz, Georgia Inst. of Tech.
David Lyons, U. of Edinburgh
Fabienne Mackay, QIMR Berghofer
Anne Magurran, U. of St. Andrews
Ari Pekka Mähönen, U. of Helsinki
Afifa Majid, U. of York
Oscar Marín, King's Coll. London
Charles Marshall, UC Berkeley
Christopher Marx, U. of Idaho
David Masopust, U. of Minnesota
Geraldine Masson, CNRS
C. Robertson McClung, Dartmouth
Rodrigo Medellín, U. Nacional Autónoma de México
C. Jessica Metcalf, Princeton U.
Baoxia Mi, UC Berkeley
Tom Misteli, NCI, NIH
Alison Motsinger-Reif, NEHS, NIH (\$)
Suresh Naidu, Columbia U.
Danielle Navarro, U. of New South Wales
Daniel Nettle, Newcastle U.
Daniel Neumark, UC Berkeley
Beatriz Noheida, U. of Groningen
Helga Nowotny, Vienna Sci. & Tech. Fund
Rachel O'Reilly, U. of Birmingham
Pilar Ossorio, U. of Wisconsin
Andrew Oswald, U. of Warwick
Isabella Pagano, Istituto Nazionale di Astrofisica
Elizabeth Levy Paluck, Princeton U.
Jane Parker, Max Planck Inst. Cologne
Giannini Parmigiani, Dana-Farber Cancer Inst. (\$)
Daniel Pauly, U. of British Columbia
Ana Pêgo, U. do Porto
Samuel Pfaff, Salk Inst.
Julie Pfeiffer, UT Southwestern Med. Ctr.
Philip Phillips, UIUC
Matthieu Piel, Inst. Curie
Martin Plenio, Ulm U.
Katherine Pollard, UCSF
Elvira Poloczanska, Alfred-Wegener-Inst.
Julia Pongratz, Ludwig Maximilians U.
Philippe Poulin, CNRS
Jonathan Pritchard, Stanford U.
Lei Stanley Qj, Stanford U.
Trevor Robbins, U. of Cambridge
Joeri Rogelj, Imperial Coll. London
Amy Rosenzweig, Northwestern U.
Mike Ryan, UT Austin
Miquel Salmeron, Lawrence Berkeley Nat. Lab
Nitin Samarth, Penn State U.
Erica Ollmann Saphire, La Jolla Inst.
Joachim Saur, U. zu Köln
Alexander Schier, Harvard U.
Wolfram Schlenker, Columbia U.
Susannah Scott, UC Santa Barbara
Anuj Shah, U. of Chicago
Vladimir Shalae, Purdue U.
Jie Shan, Cornell U.
Beth Shapiro, UC Santa Cruz
Jay Shendure, U. of Wash.
Steve Sherwood, U. of New South Wales
Brian Shoichet, UCSF
Robert Siliciano, JHU School of Med.
Liu School of Med.
Lucia Silivotti, U. Coll. London
Richard Smith, UNC (\$)
John Speakman, U. of Aberdeen
Tara Spres-Jones, U. of Edinburgh
Allan C. Spradling, Carnegie Institution for Sci.
V. S. Subrahmanian, Northwestern U.
Ira Tabas, Columbia U.
Eriko Takano, U. of Manchester
Patrick Tan, Duke-NUS Med. School
Sarah Teichmann, Wellcome Sanger Inst.
Rocio Titianik, Princeton U.
Shubha Tole, Tata Inst. of Fundamental Res.
Maria-Elena Torres Padilla, Helmholtz Zentrum München
Kimani Toussaint, Brown U.
Barbara Treutlein, ETH Zürich
Susan Tylianakis, U. of Canterbury
Wim van der Putten, Netherlands Inst. of Ecology
Ivo Vankelecom, KU Leuven
Judith Varner, UC San Diego
Henrique Veiga-Fernandes, Champalimaud Fdn.
Reinhold Veugelers, KU Leuven
Berth Vogelstein, Johns Hopkins U.
Julia Von Blume, Yale School of Med.
David Wallach, Weizmann Inst.
Jane Ling Wang, UC Davis (\$)
Jessica Ware, Amer. Mus. of Natural Hist.
David Waxman, Fudan U.
Chris Wikle, U. of Missouri (\$)
Terrie Williams, UC Santa Cruz
Ian A. Wilson, Scripps Res. (\$)
Hao Wu, Harvard U.
Li Wu, Tsinghua U.
Wei Xie, Tsinghua U.
Benjamin Youngblood, St. Jude
Yu Xie, Princeton U.
Jan Zanen, Leiden U.
Kenneth Zaret, UPenn School of Med.
Bing Zhu, Inst. of Biophysics, CAS
Xiaowei Zhuang, Harvard U.
Maria Zuber, MIT


science.org/journal/stm

PUT HUMAN HEALTH AT THE HEART OF YOUR RESEARCH

Submit your research:
cts.Sciencemag.org



Science
Translational
Medicine

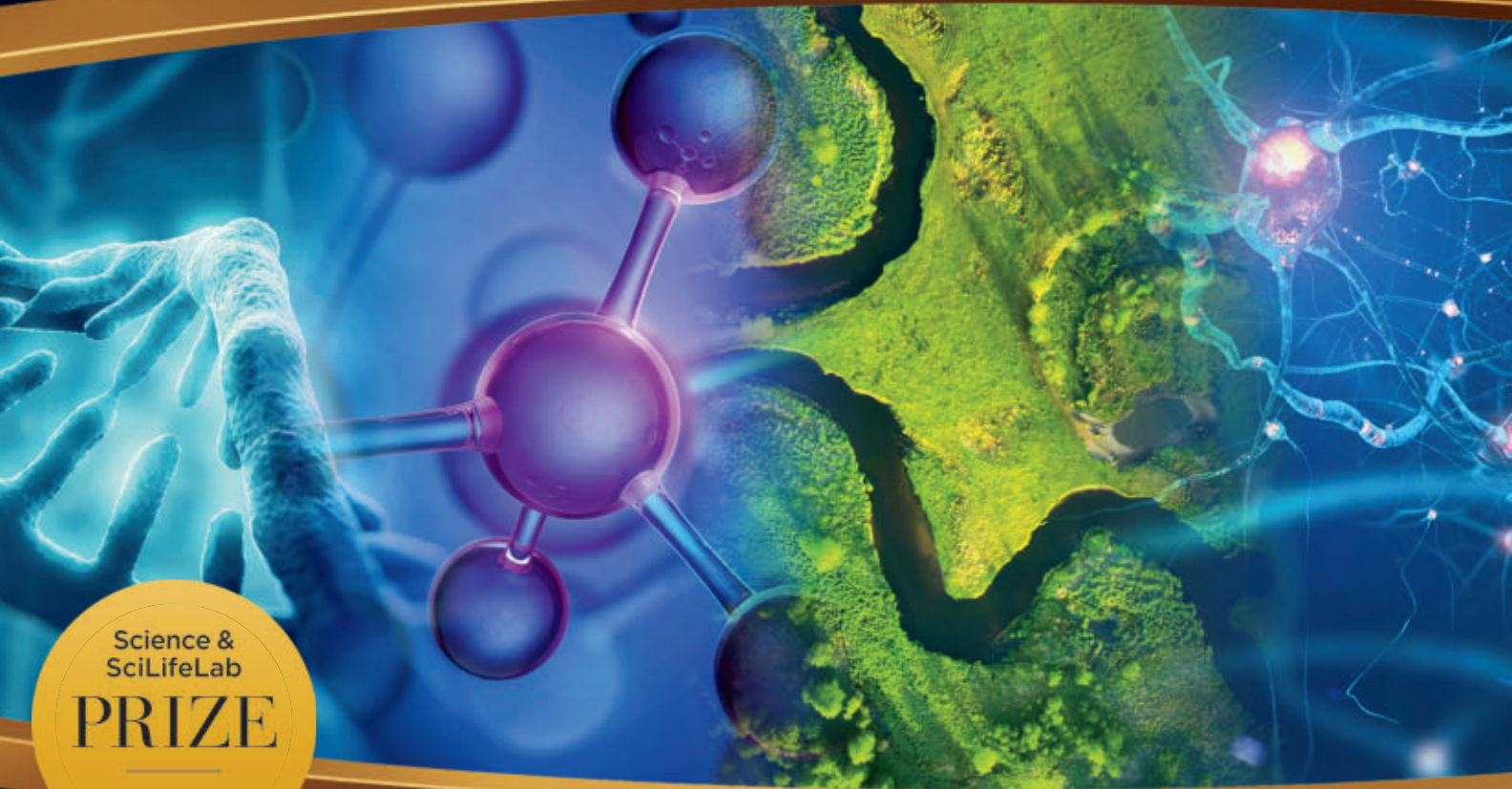

 Twitter: @ScienceTM

 Facebook: @ScienceTranslationalMedicine

Congratulations on your Ph.D.!

Ready for your next step?

Would you like to see your research published in *Science*, have the opportunity to receive USD 30,000, and get to travel to Sweden in December?



The *Science* & SciLifeLab Prize for Young Scientists is an annual prize awarded to early-career scientists. The prize is awarded in four research categories:

- Cell and Molecular Biology
- Ecology and Environment
- Molecular Medicine
- Genomics, Proteomics, and Systems Biology

Entrants for the 2022 prize must have received their Ph.D. between January 1, 2020 and December 31, 2021.

Applicants will submit a 1,000-word essay that is judged by an independent editorial team organized by the journal *Science*. Essays are assessed on the quality of research and the applicants' ability to articulate how their work would contribute to their scientific field.

Apply before July 15, 2022.

*Knut och Alice
Wallenbergs
Stiftelse*



Science
AAAS

scienceprize.scilifelab.se

Redo college intro science

The rapid development of highly effective vaccines against severe acute respiratory syndrome coronavirus 2 (SARS-CoV-2) was a monumental achievement, yet a large fraction of the public rejected this means of defense, resulting in far too many preventable deaths. This response reflects a shocking failure of science to produce citizens who understand and respect scientific evidence, and it demands a rethinking of science education goals.

Annually in the United States, nearly a million students enroll in an introductory college biology course. Whether to fulfill a general education requirement for nonscience majors or act as a gateway for students intending to pursue careers in science or health care, this course represents an enormous opportunity to develop scientific fluency.

An intro biology course designed to support student development through discovery and reasoning is far more inclusive than “weed out” courses that select for students who have memorized facts. Eliminating the second type of course offers a powerful way to nurture a widespread respect for science, as well as for diversifying the scientific profession. Far too often an introductory course asks students to merely repeat what they “know,” instead of to explain what they think. With so many facts and concepts to cover, faculty have little time to engage students in what should be the most important learning goal: to understand how the scientific process advances knowledge and arrives at evidence-based judgments on issues such as clean drinking water, climate change, and vaccination.

It is time for a major redo of introductory biology education, including the courses offered as preprofessional training for future scientists and physicians. All such courses should focus on preparing citizens to engage with evidence to make informed decisions. We urgently need to marshal resources to provide instructors with the tools and skills required to create such effective introductions to science. The restructured courses should empower students through active learning pedagogies and replace their standard “cookbook” laboratories with course-based research experiences—such as those from Tiny Earth, the Genomics Education Partnership, and Phage Hunters Advancing Genomics

and Evolutionary Science. We also must substantially expand the faculty training programs already in place, such as the National Institute on Scientific Teaching and the Partnership for Undergraduate Life Sciences Education, through alliances with scientific societies and other agencies.

How to begin? A good place to start is to challenge biologists to produce a syllabus that addresses the five foundational biological principles of the Vision and Change in Undergraduate Biology Education initiative. Groups of science colleagues should come together, with different perspectives and experiences, to develop a single-semester course for both majors and nonmajors that has no prerequisites beyond high school algebra.

This will require grappling with important design questions. For example, with the limited semester time available, how much detail do students need to know about parts of the cell or steps of a metabolic pathway? Is it more important to focus on how cells function as self-replicating chemical systems that communicate with each other and the environment? Likewise, what learning about ecosystems is really essential?

In creating such a syllabus, one key consideration is identifying a few biological systems that integrate multiple core concepts at different spatial and temporal scales, while also developing an understanding of how reliable scientific knowledge accumulates. Another is to devise ways to incorporate active learning and elements of student-driven discovery. Additionally, substantial time should be devoted to creating effective assessments of student learning.

Such a new syllabus will provide a comprehensive blueprint for the entire intro biology course. The desired changes can be accelerated by developing open-source “replacement units” for implementation in ongoing courses, where each unit would comprise approximately 2 weeks of activities, pedagogies, and assessments. By breaking up course changes into smaller parts, such replacement units can be effective vehicles for initiating change—not only in the United States, but across the globe. Through worldwide collaborations, we can overcome the inertia that has for too long caused science faculty to cling to the past instead of teaching to the future.

—David Asai, Bruce Alberts, Janet Coffey

“...inertia...
has...caused
science faculty to
cling to the past
instead of teaching
to the future.”

David Asai

is senior director of Science Education, Howard Hughes Medical Institute, Chevy Chase, MD, USA. asaid@hhmi.org

Bruce Alberts

is emeritus professor of Biochemistry and Biophysics, University of California, San Francisco, CA, USA. balberts@ucsf.edu

Janet Coffey

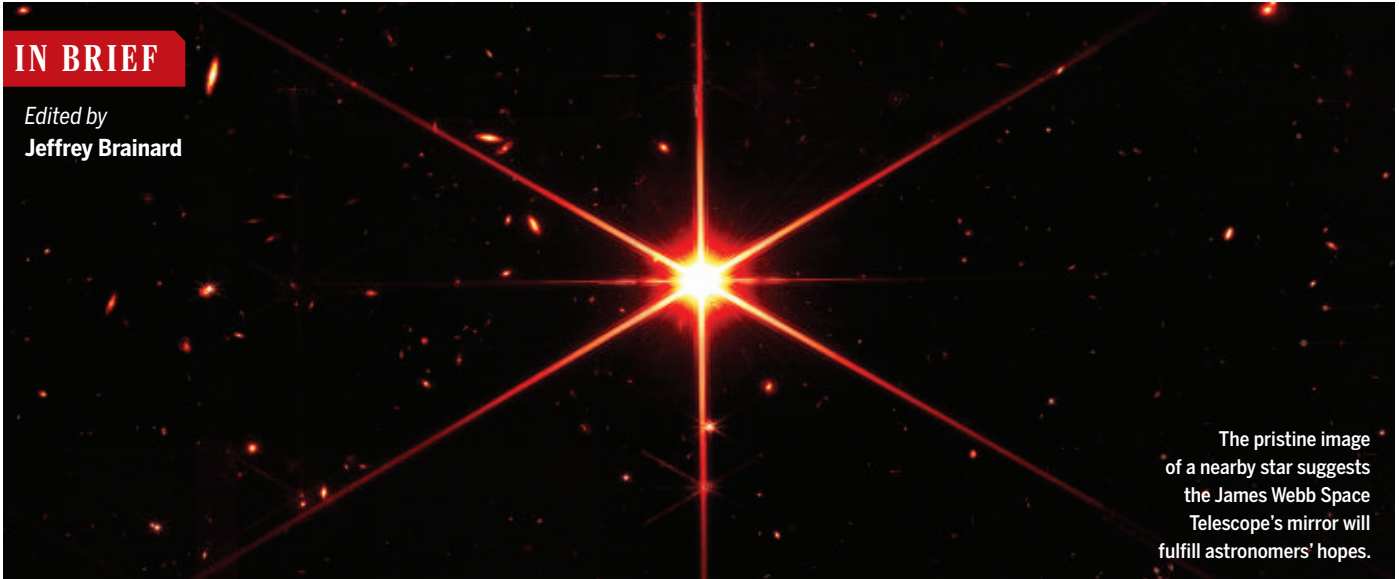
is program director, Science Learning, Gordon and Betty Moore Foundation, Palo Alto, CA, USA. janet.coffey@moore.org

“This event is completely unprecedented and upended our expectations about the Antarctic climate system.”

Polar meteorologist **Jonathan Wille**, in *The Washington Post*, about record-high temperatures in Antarctica last week. One, at Vostok Station, was more than 45°C warmer than average.

IN BRIEF

Edited by
Jeffrey Brainard



The pristine image of a nearby star suggests the James Webb Space Telescope's mirror will fulfill astronomers' hopes.

ASTRONOMY

In stellar test, Webb space telescope shows pin-sharp vision

A crisp image of a bright star shows the James Webb Space Telescope's complex, segmented mirror is functioning flawlessly, NASA announced last week. After launching the \$10 billion Webb in December 2021, engineers have spent weeks delicately tweaking the position and curvature of each of the mirror's 18 segments (which had been folded up during launch) until they behaved as a single, 6.5-meter reflector. Operators tested the mirror by

using Webb's Near Infrared Camera to observe a star in the Ursa Major constellation 2000 light-years away. "Performance is everything we dared hope," says Webb operations scientist Jane Rigby—and a sign that NASA's gamble on Webb's design, a first for any space telescope, is paying off. Operators will next test the mirror's alignment with the telescope's three other observational instruments. The science campaign is expected to begin in July after the instruments are calibrated.

U.S. shares 100,000 genomes

BIOMEDICINE | All of Us, the largest study by the U.S. National Institutes of Health (NIH) of links between genes, health, and the environment, last week gave U.S. researchers access to nearly 100,000 whole genome sequences, the first of many releases planned. The data will add to those gathered for similar studies by other DNA "biobanks," such as the 500,000-volunteer UK Biobank and the U.S. Million Veteran Program. But some researchers are disappointed that for now, only scientists at U.S. institutions can see the All of Us data; NIH is still working out policies for data sharing with

researchers in other countries. In most cases, the DNA data link to anonymized electronic health records, clinical exam details, and survey responses. Half the study's participants are from groups underrepresented in research, including people identifying as Black or African American (22%) and Hispanic or Latino (17%). The study has enrolled about 330,000 participants and hopes to reach 1 million by the end of 2026.

Russian space launches nixed

PLANETARY SCIENCE | The European Space Agency (ESA) formally suspended its ESA-Russian ExoMars mission last

week, citing Russia's invasion of Ukraine. The payload, a European-built rover and a Russian landing craft, was due to launch in September on a Russian Proton rocket; instead, ESA is considering the European Ariane 6, which is under development. Substituting a new lander could force ESA to skip the next launch window in 2024 in favor of one in 2026 or even 2028. ESA is also seeking alternatives for five other missions that had been slated for rides on Russian launchers, including the Euclid cosmology telescope and the EarthCARE atmospheric sensor. Options include ESA's smaller Vega-C, due for its inaugural flight in May.

Alzheimer's drug data out at last

DRUG DEVELOPMENT | Biogen last week published data from two pivotal clinical trials of its controversial Alzheimer's drug, Aduhelm, more than 2 years after it first announced their outcomes. The company faced criticism for both the long delay and its choice of outlet—the low-profile *Journal of Prevention of Alzheimer's Disease*. The journal's editor-in-chief, Paul Aisen, is also the second author on the study and has consulted for Biogen. (Aisen says he was not involved in the review of Biogen's manuscript or the publication decision, and the company is one among many he has consulted for.) The U.S. Food and Drug Administration (FDA) approved the drug against the recommendation of an independent advisory group. FDA cited evidence that the treatment removes Alzheimer's-associated protein plaques from the brain, even though only one of the two large trials showed clinical benefits from Aduhelm over a placebo.

Afghan scientists' limbo ends

REFUGEES | Seven months after Afghan agricultural scientists were whisked out of the country during the Taliban takeover, their limbo ended this week when they and their families received U.S. visas and flew to Washington, D.C. In August 2021, the scientists, affiliated with Michigan State University's Grain Research and Innovation project, and their relatives—75 people altogether—were flown to Tirana, Albania, only hours before the window for evacuations from Kabul's airport slammed shut. The move to the United States is “a big relief,” says an economist in the group who asked to be identified only by his family name, Halimi. But he adds that many other scientists still want to leave Afghanistan. “They've been begging us for help,” he says. “Life there is very, very difficult.”

Variant hits Black Americans hard

COVID-19 | Black adults in the United States were hospitalized for COVID-19 at a rate more than four times that of white adults during the Omicron variant's winter surge, the U.S. Centers for Disease Control and Prevention said last week. It noted differences between the two groups in receiving the primary series of two vaccinations (40% versus 47%) and a booster (44% versus 55% of those eligible). But among all adults, hospital stays for Omicron were shorter than when the Delta variant was common last year (5 days versus 4 days), and fewer patients needed intensive care.



DIVERSITY

Statues honoring female scientists throng Washington

Visitors to the U.S. National Mall in Washington, D.C., during March have encountered 120 statues of female trailblazers in science, technology, engineering, and math (STEM), displayed to help mark Women's History Month. *#IfThenSheCan—The Exhibit* includes, for example, the likeness of Jessica Esquivel (above, third from left), one of only 150 Black women in the United States with a physics Ph.D. The statues, 3D printed using acrylic by Amaze Design, were funded by Lyda Hill Philanthropies. Working with AAAS (which publishes *Science*), it selected the women depicted in the statues as part of a related project to encourage middle school girls to pursue studies and careers in STEM fields.

Statues honor (from left) science exhibit designer Olivia Castellini, computer scientist Gracie Ermi, particle physicist Jessica Esquivel, medical physicist Jessica Fagerstrom, and telescope specialist Miriam Fuchs.

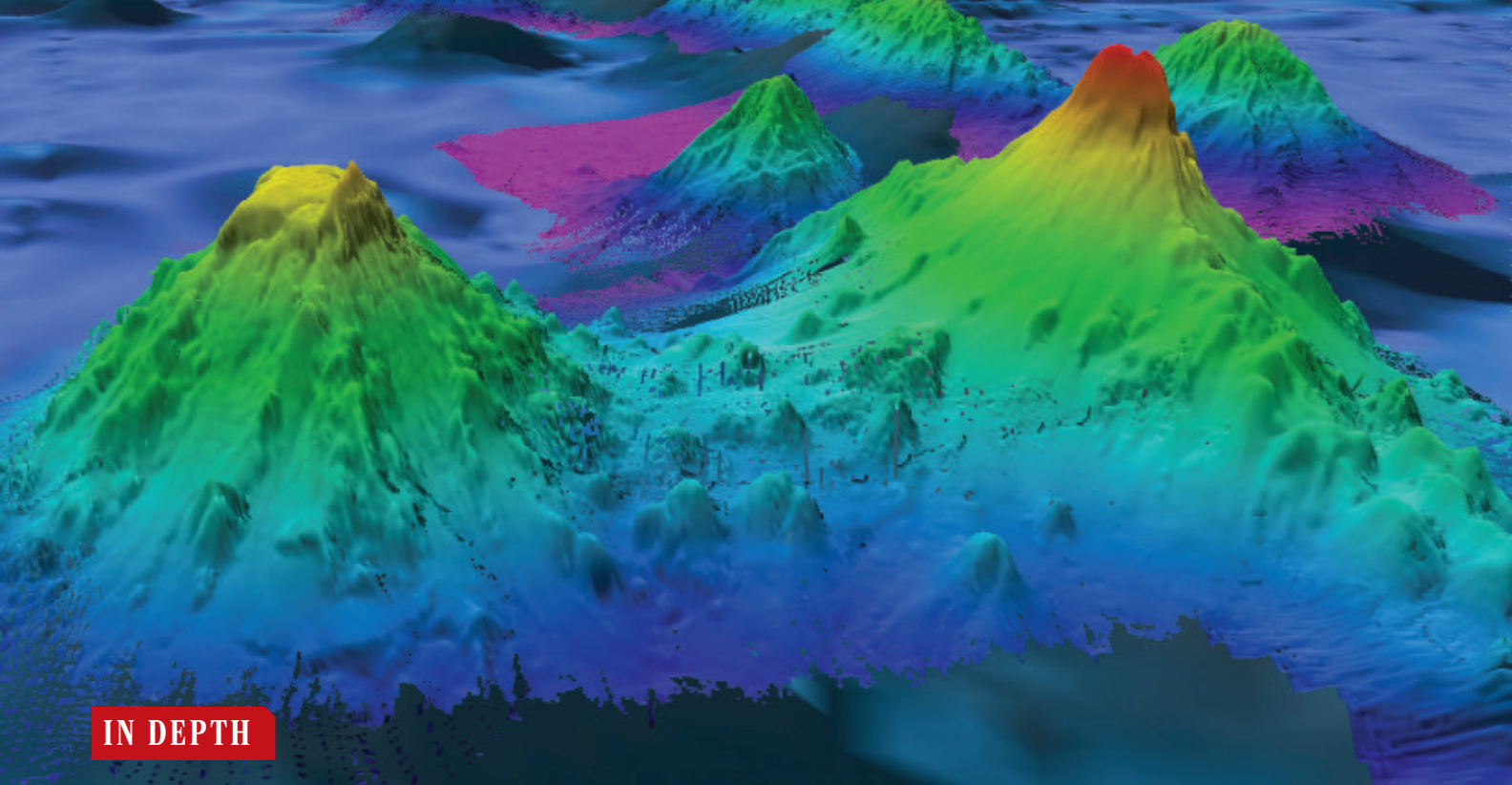
IN OTHER NEWS

LOSS FOR SOLAR PHYSICS Pioneering heliophysicist Eugene Parker died last week at the age of 94. In the mid-1950s, he predicted the existence of solar wind—soon proved by early space missions. He also thought myriad “nanoflares,” too small to see, heat the Sun's atmosphere, another idea that has gained credence. The Parker Solar Probe, now in close orbit around the Sun, is named in his honor, the first NASA spacecraft to be dedicated to a living person.

NEW COVID-19 COORDINATOR President Joe Biden has named Ashish Jha, a physician who has been dean of Brown University's School of Public Health, as his administration's pandemic response coordinator.

Jha, who has frequently commented about COVID-19 in media interviews and on social media, will bring experience in infectious disease research to a job that has been held for a year by Jeffrey Zients, who has a background in business and government.

CARBON'S SOCIAL COST In a rebuke to opponents of U.S. government action to curb climate change, a federal appeals court reversed a lower court ruling that blocked the Biden administration from putting a price on the damage caused by greenhouse gas emissions. The “social cost of carbon” is used to evaluate costs and benefits of new regulations. Fossil fuel producing states had claimed that the federal government lacks authority to set the cost figure.



IN DEPTH

Extinct volcanoes like the Pao Pao seamount (right) in the south Pacific Ocean may help deep waters rise, a function critical to ocean conveyor belts.

OCEANOGRAPHY

Undersea mountains help stir up oceans

Seafloor topography plays outsized role in currents that sequester carbon and heat

By **Paul Voosen**

Few forces are as fundamental to the climate as the overturning circulations in the world's oceans. These “conveyor belts,” as oceanographers call them, drag tropical surface waters toward the poles, where they warm the high latitudes before cooling and sinking to the abyss kilometers below, taking residual heat and dissolved carbon dioxide with them. But the last leg of the conveyor is mysterious. To keep the circulation going, those deep waters have to rise back to the surface—and oceanographers can't quite explain how it happens.

Now, results from a campaign by the *RRS Discovery*, a U.K. research ship, seem to confirm a radical new view for how deep-ocean water rises. Its measurements of tracers rising above rough seafloor topography suggest that deep water does not well up slowly across most of the ocean, as once thought. Instead, it is shunted upward in concentrated bursts by turbulence created by undersea mountains, including volcanic midocean ridges and seamounts. “The shape of the sea floor is intimately tied to the structure of the ocean,” says Trevor McDougall, an ocean physicist at the University of New South Wales who

helped lay the theoretical framework for the discovery. “This is a new way of looking at the deep ocean.”

The finding, reported earlier this month at the Ocean Sciences Meeting, could have broad implications. Deep waters, rather than remaining sequestered for hundreds or thousands of years, may return quickly—speeding climate change by releasing the carbon they store. The upwellings could also add to sea level rise in some locations. And the new picture could force oceanographers to rethink the behavior of past oceans, when the contours of the sea floor differed from today's.

Efforts to solve the puzzle of upwelling go back decades, to a seminal 1966 paper by famed oceanographer Walter Munk titled “Abyssal Recipes.” He proposed that internal waves forming along boundaries between ocean layers of different densities occasionally break, much like waves on a shore. This turbulence, if widely distributed, could slowly mix deep heavy waters and send them upward. Once they reached a level 2 kilometers below the surface, the waters would flow to the Southern Ocean, where fierce winds pull the waters to the surface.

When free-falling probes began to measure deep-ocean turbulence several de-

CADES ago, however, they found that much of the ocean was calm—too calm. “People went out and looked forever and ever and couldn't find [turbulence],” says Matthew Alford, a physical oceanographer at the Scripps Institution of Oceanography and co-investigator of the new campaign. The turbulence that was found tended to grow with depth. Like a spoon stirring milk into coffee, it was driving water down, not up, says Raffaele Ferrari, a physical oceanographer at the Massachusetts Institute of Technology and leader of the *Discovery* campaign. “The mixing was doing the opposite of what Walter Munk had predicted.” Water was sinking not only at the poles, but also throughout the ocean, twice as much as previously thought.

In 2016, two teams of researchers, including one led by Ferrari, pieced together a picture that could explain how the deep water rose in spite of the downward push. Close to the sea floor, they proposed, the breaking waves could no longer propel water downward. Instead, if there were any undersea mountains nearby, the turbulence would drive the waters up mountain slopes, mixing with lighter waters above. Water could surge all the way up to a depth of 2 kilo-

meters, where the pump of the Southern Ocean could take over.

The idea met skepticism—surely such large upwellings would have been detected before? But oceanographers had made few measurements near the sea floor to test the idea. “It’s a good way to break your instrument,” Ferrari says.

His team set out to fill the gap in two visits last year to the Rockall Trough, a rough terrain northwest of Ireland. The researchers released nontoxic tracers 1800 meters down, at the base of a jagged canyon wall, and monitored the water with moorings and free-falling turbulence profilers. One tracer will allow the researchers to document the long-term evolution of the water when they return on the *Discovery* in the summer. Another short-lived fluorescent dye could be followed in real time. It zipped upward 100 meters per day over 3 days. “That was quite exciting,” Alford says. “You could watch the water upwell.”

The initial results are “pretty cool,” says Sarah Purkey, a physical oceanographer at Scripps who is unaffiliated with the project. “It feels like we’ve been talking about this day for a long time.” The rate of upwelling seems to match the theory, she says. The question now is whether the processes at this one location can be extrapolated. “How do we scale this to the entire ocean?”

Soon-to-be-published measurements of upwelling and turbulence from a survey conducted 10 years ago in the Drake Passage, a bumpy seafloor channel between Chile and Antarctica, agree in principle, says Ali Mashayekhi, an environmental fluid dynamicist at Imperial College London. “So there is some indication that what they’re finding is of generic importance.”

The *Discovery* results also suggest the story won’t be as simple as Ferrari and others first indicated, says Sonya Legg, a physical oceanographer at Princeton University. Tides seem to influence the flows, not just turbulence. And the longer term fate of the upwelling water remains to be seen. It’s possible it was whisked away and dissipated by ocean eddies.

But Ferrari is emboldened by the results and says they help make sense of certain ocean idiosyncrasies. For example, the north Pacific Ocean lacks much of an overturning circulation. But it also has few volcanic seamounts or ridges—and without those enablers, the water can’t move upward. The findings also mean the currents of past oceans could have been fundamentally different depending on Earth’s volcanic activity—and how bumpy it made the sea floor. “It’s not just a matter of where the continents are,” he says. “You also need to know the structure of the sea floor.” ■

ARCHAEOLOGY

Southern roots for the Maya—and the maize that fed them

Migrants from the south may have helped spread early farming in Central America, ancient DNA suggests

By Ann Gibbons

In Maya creation myths, the gods created humans out of corn. Now, a new study from a site in Belize suggests corn really was important to the origin of the ancient Maya: More than half of their ancestry can be traced to migrants who arrived from the south sometime before 5600 years ago, likely bringing with them new cultivars of maize.

The previously unknown migrants “were the first pioneers who essentially planted the seeds of Maya civilization,” which emerged about 4000 years ago, says archaeologist and co-author Jaime Awe of Northern Arizona University, who is a native Belizean with Maya ancestry. “Without corn, there would have been no Mayans.”

The study also suggests that, as in Europe, farming in the Americas spread at least in part with people on the move, rather than being passed among cultures.

The paper is “groundbreaking ... a dramatic revelation,” says Maya archaeologist Mary Pohl of Florida State University.

At its height, Maya civilization spanned one-third of Central America and Mexico; today the Maya are an ethnolinguistic group of at least 7 million Indigenous peoples. Awe and others had long wondered how the ancient Maya were related to those who came before them. But the hot and humid climate had left few clues in bones and DNA.

The new study analyzes remains from two rock shelters in a rainforest in the Bladen Nature Reserve in southwestern Belize. There, archaeologist Keith Prufer of the University of New Mexico, Albuquerque, wildlife biologist Said Gutierrez of the Ya’axché Conservation Trust, and colleagues have unearthed more than 85 skeletons from shallow graves in the rock shelters’ dry dirt floors.

The archaeologists directly dated 50 individuals with radiocarbon to between 1000 to 9600 years ago. Then, population geneticist David Reich of Harvard University and his team extracted ancient DNA

from 20 individuals—“the oldest human DNA from a tropical rainforest,” Reich says. They analyzed 1.2 million nucleotide bases and compared them with DNA from ancient and living people from the Americas.

The DNA of people buried at the rock shelters from 9600 to 7300 years ago resembled that of ancient hunter-gatherers in the Americas. But after 5600 years ago, there was a major shift: All 15 individuals tested were most closely related to Indigenous people who today live from northern Colombia to Costa Rica and speak Chibchan languages.

The migration had a lasting impact: Living Maya have inherited more than half of their DNA from this influx from South

America and northern Central America, the team reported this week in *Nature Communications*. And it eventually led to a new diet. Researchers had previously analyzed carbon isotopes from the teeth of the people in the rock shelters, showing the kind of food they ate. As reported in *Science* in 2020, they found a steady increase in maize consumption over time. Maize was less than 10% of the diet of

the ancient hunter-gatherers. But between 5600 years ago and 4000 years ago, its proportion surged from 10% to 50%.

That shift happened hundreds of years after the migration, but the team says the results fit with the emerging story of maize cultivation. The plant was partially domesticated as early as 9000 years ago in southwestern Mexico, but it wasn’t fully domesticated there for thousands of years. Instead, farmers first developed larger, more nutritious cobs in South America, at 6500-year-old sites in Peru and Bolivia. Those improved plants were probably the maize the migrants brought to Belize by 5600 years ago, the team suggests.

The work tracing the origin of the Maya also illuminates the roots of one of the world’s great crops, says archaeobotanist Dolores Piperno of the Smithsonian Institution. “It really transforms our knowledge of how maize dispersed.” ■

**The study
“transforms
our knowledge
of how maize
dispersed.”**

Dolores Piperno,
Smithsonian Institution

ECOLOGY

War halts animal tracking project

As space station antenna goes silent, ICARUS seeks new ways to collect animal GPS data



By Elizabeth Pennisi

The past 2 weeks have been very good—and very bad—for Martin Wikelski and Walter Jetz. In a key proof of principle of their space-based wildlife tracking project, they published a paper tracing the travels of 15 species, including the meanderings of an endangered saiga antelope across Central Asia and the marathon flights of cuckoos from Japan to Papua New Guinea. But the very same week, their data stream from an antenna on the International Space Station (ISS) dried up, likely because data were relayed through a Russian ground station.

The war in Ukraine appears to have grounded their project, the International Cooperation for Animal Research Using Space (ICARUS), just as it was getting off the ground. “This will ruin all the efforts of a great many scientists,” says ecologist Nyambayar Batbayar, director of the Wildlife Science and Conservation Center of Mongolia, whose team has used ICARUS to track snipes and cuckoos. New studies of pinyon jays and robins are on hold because researchers don’t want to burden animals with tags whose data may not be retrievable.

Wikelski, an ornithologist at the University of Konstanz and the Max Planck Institute of Animal Behavior, and Jetz, a Yale University ecologist, say they are now fast-tracking planned efforts to put up other space-based receivers. But scientists who were already skeptical about ICARUS’s goals say its future is in doubt. “I’ve seen a lot of ambitious attempts, but ambition doesn’t always lead to

success,” says ecologist Greg Breed of the University of Alaska, Fairbanks.

To understand animal behavior and how humans are influencing it, researchers have increasingly put GPS tags on animals and tracked them with hand-held or ground-based receivers. But tagged animals often move out of range, and the tags were expensive, so few individuals could be tracked. ICARUS, founded in 2002, aimed to lift tracking into space and develop cheaper tags, affordable by researchers worldwide. By expanding the number—and sizes—of tagged animals, and tracing their complete journeys, Wikelski and his colleagues hoped to see how both the environment and human influences shape their survival.

It was such a grand vision that Breed and others were skeptical it would come to pass. NASA initially spurned Wikelski’s attempts to collaborate, so he partnered with the German and Russian space agencies; they and the

A space-based animal tracking project followed mountain plovers tagged in Colorado.

Max Planck Society have funded the project with €30 million to date. In 2019, a German-built antenna was unfurled on the Russian module of the ISS. By the end of last year, scientists had deployed tags on animals at 91 sites around the world, 21 in Russia.

Each time the space station passes over a tagged individual, its tag turns on and uploads stored data. Those data are transmitted to a ground station in Russia and automatically entered into Movebank, a public repository of animal movement information.

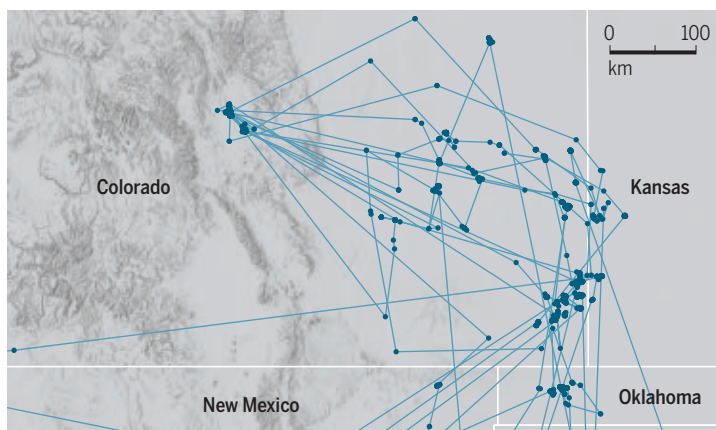
The tags have provided new and sometimes surprising insights, Jetz, Wikelski, and colleagues reported on 8 March in *Trends in Ecology & Evolution (TREE)*. The technology traced animals’ entire journeys, not just the end points, yielding clues about why some birds are declining.

Take the mountain plover, a short-grass prairie native about the size of a bluejay, which has declined by 80% since the 1960s. ICARUS data on 17 birds tagged last year showed that when the plovers left their breeding grounds in Colorado, “they all went to different places,” mostly in eastern Colorado, Kansas, and Oklahoma, says co-author Roland Kays, an ecologist at the North Carolina Museum of Natural Sciences. Then they moved on to diverse wintering grounds farther south and into Mexico (see map, left). The finding adds to evidence that migrators don’t always head back and forth between two fixed points, but instead follow food and avoid floods, fires, and other disturbances. Data like these are “changing

Flight risks

A space-based project tracked the migration of 17 tagged mountain plovers and found they may be vulnerable during midpoint stopovers in eastern Colorado, Kansas, and Oklahoma.

● Stopovers — Migratory path



the whole picture of [the] animal migration phenomenon as we know it,” Batbayar says.

The tags revealed some plovers are dying at the midpoint stopovers, says the project's director, Michael Wunder, a quantitative ecologist at the University of Colorado, Denver. “Once you get [this] ‘where’ you can try to figure out what’s contributing to the mortality” says Georgetown University ecologist Peter Marra.

Ecologists are also enthusiastic about the project's GPS tags, developed with a company, which at 4 grams and \$300 apiece are far lighter and cheaper than most. ICARUS “is making technology available to researchers in countries where we don’t have the means to buy other types of tags” says behavioral ecologist Adriana Maldonado-Chaparro of Del Rosario University in Bogotá, Colombia.

In the *TREE* paper, Jetz and colleagues propose expanding ICARUS to 100,000 animals that could act as Earth’s “sentinels” in the same way that smartphone data on the movements and speeds of individual cars have revolutionized traffic prediction. Tracking data on seabirds, for example, have shown they alter their courses in anticipation of brewing typhoons.

But shortly after the war in Ukraine began last month, all data downloads from the space station stopped. No one knows exactly why, although Wikelski presumes it’s because the German and Russian space agencies no longer collaborate.

Still, he, Kays, and Jetz remain upbeat. They say the ISS antenna was always intended as a temporary measure and they had already planned to expand the number of space-based receivers by flying them on microsatellites called CubeSats (*Science*, 14 July 2017, p. 118) or by piggybacking them on other satellites. Their efforts have yielded tentative promises from space agencies and satellite companies to get receivers back in space by the end of the year, and more by 2024. And in 2027, a joint NASA and German space agency mission to measure gravity variations, the Gravity Recovery and Climate Experiment, may carry ICARUS receivers.

For the near term, however, Breed and others think ecologists might do better to pin their hopes on more proven technologies. He and Sara Maxwell, a marine sustainability ecologist at the University of Washington, Bothell, suggest the 20,000 animals around the world now wearing GPS tags retrieved locally or, rarely, with private satellites, can already serve as environmental sentinels. Movebank is developing software to pool those data in the future, Kays says.

Wikelski thinks ICARUS has proved itself. He’s not giving up on getting the big picture of animal movement from space—and vows his project will take flight again. ■

NEUROSCIENCE

Brain implant enables man in locked-in state to communicate

Despite complete paralysis from amyotrophic lateral sclerosis, person used neural signals to spell out thoughts

By **Kelly Servick**

In its final stages, the neurological disease amyotrophic lateral sclerosis (ALS) can bring extreme isolation. People lose control of their muscles, and communication may become impossible. But with the help of an implanted device that reads his brain signals, a man in this “complete” locked-in state could select letters and form sentences, researchers report this week.

“People have really doubted whether this was even feasible,” says Mariska Vansteensel, a brain-computer interface researcher at the University Medical Center Utrecht who was not involved in the study, published in *Nature Communications*. If the new spelling system proves reliable for all people who are completely locked in—and if it can be made more efficient and affordable—it might allow thousands of people reconnect to their families and care teams, says Reinhold Scherer, a neural engineer at the University of Essex.

ALS destroys the nerves that control movement, and most patients die within 5 years of diagnosis. When a person with ALS can no longer speak, they can use an eye-tracking camera to select letters on a screen. Later in the disease’s progression, they can answer yes-or-no questions with subtle eye movements. But if a person chooses to prolong their life with a ventilator, they may spend months or years able to hear but not communicate.

In 2016, Vansteensel’s team reported that a woman with ALS could spell out sentences with a brain implant that detected attempts to move her hand. But this person still had minimal control of some eye and mouth muscles. It wasn’t clear whether a brain that has lost all control over the body can signal intended movements consistently enough to allow meaningful communication.

The participant in the new study, a man with ALS who is now 36, started to work with a research team at the University of Tübingen in 2018, when he could still move his eyes. He told the team he wanted an invasive implant to try to maintain com-

munication with his family, including his young son. His wife and sister provided written consent for the surgery.

Researchers inserted two square electrode arrays, 3.2 millimeters wide, into a part of the brain that controls movement. When they asked the man to try to move his hands, feet, head, and eyes, the neural signals weren’t consistent enough to answer yes-or-no questions, says Ujwal Chaudhary, a biomedical engineer and neurotechnologist at the German non-profit ALS Voice.

After nearly 3 months of unsuccessful efforts, the team tried neurofeedback, in which a person attempts to modify their brain signals while getting a real-time measure of whether they are succeeding. An audible tone got higher in pitch as the electrical firing of neurons near the implant sped up, lower as it slowed. Researchers asked the participant to change that pitch using any strategy. On the first day, he could move the tone, and by day 12, he could match it to a target pitch. “It was like music to the ear,” Chaudhary recalls. The researchers tuned the system by searching for the most responsive neurons and determining how each changed with the participant’s efforts.

By holding the tone high or low, the man could then indicate “yes” and “no” to groups of letters, and then individual letters. After about 3 weeks with the system, he produced an intelligible sentence: a request for caregivers to reposition him. In the year that followed, he made dozens of sentences at a painstaking rate of about one character per minute: “Goulash soup and sweet pea soup.” “I would like to listen to the album by Tool loud.” “I love my cool son.”

He eventually explained to the team that he modulated the tone by trying to move his eyes. But he did not always succeed. Only on 107 of 135 days reported in the study could he match a series of target tones with 80% accuracy, and only on 44 of those 107 could he produce an intelligible sentence.

“We can only speculate” about what happened on the other days, Vansteensel says. The participant may have been asleep or simply not in the mood. Maybe the brain



A man with amyotrophic lateral sclerosis breathes through a ventilator and communicates using a brain implant.

signal was too weak or variable to optimally set the computer's decoding system, which required daily calibration. Relevant neurons may have drifted in and out of range of the electrodes, notes co-author Jonas Zimmermann, a neuroscientist at the Wyss Center for Bio and Neuroengineering.

Still, the study shows it's possible to maintain communication with a person as they become locked in by adapting an interface to their abilities, says Melanie Fried-Oken, who studies brain-computer interface at Oregon Health & Science University. "It's so cool." But hundreds of hours went into designing, testing, and maintaining the personalized system, she notes. "We're nowhere near getting this into an assistive technology state that could be purchased by a family."

The demonstration also raises ethical questions, says Eran Klein, a neurologist and neuroethicist at the University of Washington, Seattle. Discussing end-of-life care preferences is difficult enough for people who can speak, he notes. "Can you have one of those really complicated conversations with one of these devices that only allows you to say three sentences a day? You certainly don't want to misinterpret a word here or a word there." Zimmermann says the research team stipulated the participant's medical care shouldn't depend on the interface. "If the speller output were, 'unplug my ventilator,' we wouldn't." But, he adds, it's up to family members to interpret a patient's wishes as they see fit.

Chaudhary's foundation is seeking funding to give similar implants to several more people with ALS. He estimates the system would cost close to \$500,000

over the first 2 years. Zimmermann and colleagues, meanwhile, are developing a signal processing device that attaches to the head via magnets rather than anchoring through the skin, which carries a risk of infection.

So far, devices that read signals from outside the skull haven't allowed spelling. In 2017, a team said it could classify with 70% accuracy yes-or-no answers from the brain of a completely locked-in participant using a noninvasive technology called functional near-infrared spectroscopy (fNIRS). Two co-authors on the new study, Chaudhary and University of Tübingen neuroscientist Niels Birbaumer, were part of that team. But other researchers have voiced concerns about the study's statistical analysis. Two investigations found misconduct in 2019, and two papers were retracted. The authors sued to challenge the misconduct findings, Chaudhary says. Scherer, who was skeptical of the fNIRS study, says the results with the invasive device are "definitely sounder."

Wyss Center researchers continue to work with this study participant, but his ability to spell has decreased, and he now mostly answers yes-or-no questions, Zimmermann says. Scar tissue around the implant is partly to blame because it obscures neural signals, he says. Cognitive factors could play a role, too: The participant's brain may be losing the ability to control the device after years of being unable to affect its environment. But the research team has committed to maintaining the device as long as he continues to use it, Zimmermann says. "There's this huge responsibility. We're quite aware of that." ■

BIOMEDICINE

Where does embryo editing stand now?

He Jiankui's expected release finds a field still wrestling with scientific and ethical challenges

By Jon Cohen

Biophysicist He Jiankui, having served a 3-year sentence for creating the world's first genetically engineered babies, may be released from a Chinese prison this week, *Science* has learned. He's largely secret use of the genome editor CRISPR to alter the DNA of human embryos and implant them into two women led to three births, sparking ethical outrage and fears for the babies' health (about which little is known). It did not, however, bring an end to basic research on human embryo editing.

The response to He's November 2018 announcement was "severe and vibrant," says Fyodor Urnov, who studies CRISPR-based genome editing at the University of California, Berkeley. For now, Urnov sees no circumstance that would justify efforts to genetically modify babies. But he strongly supports using CRISPR to fix disease-causing mutations after birth, without causing heritable changes to a human genome, and regrets that "we have poured a jar of tar on gene editing." And Urnov and others believe that, used responsibly and safely, embryo editing could eventually prove a powerful tool against disease in rare circumstances. In laboratory studies, they continue to explore possible avenues—and the many hurdles.

The work has proceeded with little notice. "The pandemic has pushed this topic out of people's primary attention," says Alta Charo, an emeritus bioethicist and lawyer at the University of Wisconsin, Madison, who notes that oversight measures intended to stop rogue experiments like He's have stalled, including a proposed global registry of pre-clinical heritable genome-editing research.

This type of registry might have noted a study reported last week in which a research team working with surplus human embryos from in vitro fertilization (IVF) clinics showed how CRISPR could rid a newly fertilized egg

of an extra copy of a chromosome—a problem that can lead to Down syndrome and other medical conditions. Other groups are exploring how to introduce heritable genetic changes via human sperm or eggs. There are “quite a lot of people pushing boundaries” in that regard, says Robin Lovell-Badge, a developmental geneticist at the Francis Crick Institute—although few if any think the work is ready for the clinic. “We’re still waiting for some better tools,” says developmental biologist Shoukhrat Mitalipov of Oregon Health & Science University.

The original concerns about designer babies centered on CRISPR’s sloppiness. The DNA-cutting enzyme that is one of its two components occasionally slices unintended spots, and even if the cut is on target, the cell’s gene repair equipment may scramble adjacent DNA by inserting or deleting bases, potentially creating new harm. Indeed, a study of CRISPR-altered human embryos found 16% had these “unintended editing outcomes” at the targeted DNA, a group led by Kathy Niakan of the Crick reported last year in the *Proceedings of the National Academy of Sciences*.

Genetic screening of edited IVF embryos might not catch these errors. Although CRISPR is introduced right after fertilization, at the single-cell stage, its action is not necessarily immediate. “The edit may occur at the two-cell or four-cell stage, so not all the cells are identical,” Lovell-Badge says—a phenomenon called mosaicism. Both incorrectly altered and unaltered cells can easily go undetected because an embryo is screened by taking a sample of its cells at the 5-day stage, when it contains about 100 cells. “If you have any mosaicism, then you don’t know what you’ve got in the rest of the embryo,” Lovell-Badge says.

Stem cell researcher Dietrich Egli at Columbia University hopes to find a way to start and stop CRISPR at the embryo’s single-cell stage, preventing mosaicism. In the meantime, his group has found a specific kind of CRISPR edit for an embryo that vastly reduces the risk of unintended DNA changes.

One of the most common abnormalities found when IVF clinics screen embryos, especially those made with eggs of older people, is the presence of either one or three copies of certain chromosomes rather than the normal two. In a preprint posted on bioRxiv on 10 March, Egli’s group demonstrated a strategy for trisomy, an errant third chromosome. The scientists showed they could target an extra paternal or ma-

ternal chromosome copy with a CRISPR cut at or near its centromere, the DNA-protein structure that holds the different arms of a chromosome together. The extra chromosome then falls apart during cell division. Unintended on- or off-target edits theoretically wouldn’t matter because CRISPR would, in effect, destroy the entire DNA sequence.

Mosaicism might still be a problem if CRISPR does not correct the trisomy in all of the cells in an early embryo, but Egli notes that when such embryos have a mix of cells with normal and abnormal chromosomes, a natural “rescue mechanism” usually seems to eliminate the abnormal cells. “There are still multiple obstacles,” he stresses. “We could have given this a different title, ‘Correction of Trisomy 16 in Hu-



At a Hong Kong meeting in 2018, He Jiankui revealed he had secretly created genetically engineered babies. He has now served a 3-year sentence in a Chinese prison and may soon be released.

man Embryo,’ and we might have created more buzz and news articles, but we didn’t think it was appropriate because it conveys that you’re going to do this clinically tomorrow, which is absolutely not the case.”

Researchers studying CRISPR in human embryos face obstacles beyond the science. In the United States, Congress forbids government funding of research with human embryos, forcing Egli, Mitalipov, and others to rely on foundations, academic institutions, or companies. Legislation also prevents the U.S. Food and Drug Administration from even evaluating therapies that edit human embryos.

Editing the DNA of egg or sperm precursor cells may avoid some of these hurdles. It also gets around what Kyle Orwig, a reproductive biologist at the University of Pittsburgh, calls “a numbers problem.” Even under the best circumstances, IVF clinics could only create, edit, and test a small number of embryos for a given couple, giving them few chances to get it right.

Editing the cells that give rise to sperm could improve the odds. Researchers have already removed these spermatogonial stem cells from mice and grown millions in culture. This allows for a rigorous quality control of CRISPR edits: Scientists can screen for the stem cells that have the correct edit, with no unintended DNA changes, and clone them en masse, again checking for errors. Then, they can transplant those cells into the testes where they should produce mature sperm, Orwig says. Indeed, rodents with edited sperm stem cells have been used to create offspring with a desired DNA edit.

Turning that basic research into a way to help potential parents won’t be easy. “The barrier is that we don’t yet know how to maintain human spermatogonial stem cells in culture,” Orwig says. His team is exploring a different

route to creating edited sperm stem cells: “reprogramming” adult human cells into a stem cell state and trying to coax them partly down the pathway that creates sperm. Other groups are hoping that reprogrammed adult cells could one day produce human eggs, which could then be altered in large numbers.

Discouragingly, in mice, spermatogonial stem cells only survive when placed into newborn animals, which isn’t a realistic option for humans. As a first step to exploring whether the scheme could work in people, Orwig’s team is now recruiting men who became infertile because of cancer treatment and had testicular tissue or cells frozen before chemotherapy or radiation. The team plans to isolate spermatogonial stem cells from the thawed tissue and then inject them, unedited, into the owner’s testis to see whether that produces viable sperm.

The 3 years since He went to prison have seen glimmers of progress in heritable human genome editing, but many scientists say the increased awareness of CRISPR’s shortcomings has underscored the recklessness of making babies from edited embryos with the technology available today. An exception is Russian geneticist Denis Rebrikov, one of the few scientists after the He scandal to openly advocate implanting edited embryos into people. “We’ve done a lot of validation experiments, and now we’re confident that we can move on to real clinical use,” Rebrikov says.

Lovell-Badge speaks for most researchers when he says such confidence is unwarranted. Stick to lab work on embryo editing for now, he advises. “People should do as much preclinical research as they can, and let’s find out whether it’s feasible.” ■

EUROPE

Ukrainian bat study spun into tale of bioweapons

Russian disinformation campaign targets routine research on bat parasites

By Andrew Curry

In 2020, German researchers began to collaborate with Ukrainian colleagues to survey bat parasites, mostly bloodsuckers such as ticks and fleas. They wanted to know what kinds of bacteria the bats in Ukraine harbored—a first step in identifying any potential threats to human health. Researchers at the Institute of Experimental and Clinical Veterinary Medicine in Kharkiv collected 140 fleas, ticks, and flies, plucked from captured bats in eastern Ukraine. They drowned the parasites in ethanol and shipped them to the Friedrich Loeffler Institute (FLI) near Greifswald, Germany.

There, DNA from the parasites revealed the identity of pathogens such as *Rickettsia*, a common tick-borne bacterium. Results were presented at a German Veterinary Society conference in 2021. “It was very basic epidemiological research,” says FLI veterinary parasitologist Cornelia Silaghi, a leader of the collaboration.

So she was shocked and baffled when, on 10 March, an official with the Russian Ministry of Defense claimed the research was part of a secret, Western-funded bioweapons effort. Russian state TV and news sites cited the Ministry of Defense report and said the work was a Ukrainian plot, aided by the United States, to send disease-ridden birds, bats, and reptiles over the border to infect Russians. Last week, Russian President Vladimir Putin spoke about “Pentagon-funded bioweapons labs in Ukraine” on state-owned TV channel Russia 24.

Silaghi’s straightforward collaboration swiftly became the eye of a disinformation storm: A few facts were spun into false accusations that were quickly amplified and spread via social media, repeated on Fox News, and discussed in QAnon forums. As supposed evidence, Russian authorities posted a grainy image of the sample transfer agreement between Silaghi’s lab and the Kharkiv veterinary institute.

“This is what makes disinformation work—you have to have these little kernels of truth,” says King’s College London biosecurity expert Filippa Lentzos. “If you’re able to plant enough doubt, people start to question.”

Russia has kept up its efforts to spread

innuendo about the basic research. On 11 March, at a meeting of the U.N. Security Council called by Russian representatives to discuss alleged Ukrainian “biological warfare” research, diplomat Vassily Nebenzia claimed “bats were considered as carriers of potential bioweapon agents,” and offered the sample transfer agreement as proof. “We do not know anything about the fate of those dangerous biomaterials and the consequences that may occur once they ‘dissipate,’” Nebenzia told the Security Council. “Risks are high that they may be stolen for terrorist purposes or to be sold at the black market.”

“Rubbish,” Silaghi says. “I know their fate—they are in my freezer.” She adds that there are no pathogens that could be spread. The ethanol used to kill and preserve the para-

The Kharkiv veterinary institute is part of a larger network of research institutions that receives funding from the U.S. Department of Defense (DOD) through its Biological Threat Reduction Program (BTRP). That decades-old effort aimed to secure the remnants of Soviet-era biological, chemical, and nuclear weapons research by dismantling labs and finding alternate work for Soviet weapons scientists. Later, the program—which included Russian labs until 2014—morphed into a public health and disease monitoring effort across the former Soviet Union, working with the World Health Organization and the U.S. Centers for Disease Control and Prevention. “That’s been turned into a narrative from Russia about a ring of American-funded labs on the Russian border,” Lentzos says.

According to DOD, the BTRP has provided \$200 million in funding to Ukrainian scientists since 2005. Labs with even the thinnest connections to the program have been targeted as part of the disinformation effort. For example, Russian reports describe research on the gut microbiome of vipers by Oleksandr Zinenko, a herpetologist at V. N. Karazin Kharkiv National University who has collaborated with the Kharkiv veterinary institute in the past, as “bioweapons research,” even though the viper study was an independent project. “None of the microorganisms in a viper’s gut is especially dangerous,” Zinenko says, adding that all the research is

publicly available, not secret.

To Vlaschenko, who runs the Ukrainian Bat Rehabilitation Center in Kharkiv, the efforts to turn their survey work into something menacing seem laughable—for now. “We don’t have such genetic laboratories that we would need for biological weapons,” he says. “It’s very funny to hear it from the Russians that we are doing this kind of research.” But if the city is occupied, Vlaschenko says he fears being captured and tortured into “some kind of confession.”

For Silaghi, who’s been getting disturbing emails from anonymous accounts, including one insinuating that she was acting like a Nazi, the experience has been deeply unsettling. “It’s very strange to be blamed for an almost absurd thing,” she says. “The Russians must know it’s a lie.” ■



Russia’s ambassador to the United Nations, Vassily Nebenzia, discussed alleged bioweapons in Ukraine at a U.N. Security Council meeting in March.

sites destroys the pathogens, leaving only genetic material intact for sequencing. The project received no U.S. funding. “Yes, we did work on ectoparasites and receive samples,” Silaghi says. “But what’s been made of it—this bioweapon stuff—is completely crazy.”

Silaghi still doesn’t know how the Russian Ministry of Defense obtained the routine sample transfer agreement. Anton Vlaschenko, a Kharkiv-based biologist and collaborator on the project, suspects one of the team’s email accounts was hacked by Russians.

Lentzos says focusing on bats might be a way to tap into hazy fears about COVID-19’s origins. “People ... start to think, ‘what else don’t I know about?’” she says. “All of it gets tangled together and causes a lot of unease.”

Other Ukrainian researchers have been swept up in the disinformation campaign.

2021 Winner
Amber L. Alhadeff, Ph.D.
Monell Chemical Senses Center, USA
For research on the gut-brain control
of hunger circuits



Tell the World About Your Work!

Application Deadline
June 15, 2022

Eppendorf & Science Prize for Neurobiology

The annual Eppendorf & Science Prize for Neurobiology is an international prize which honors young scientists for their outstanding contributions to neurobiological research based on methods of molecular and cell biology. The winner and finalists are selected by a committee of independent scientists, chaired by *Science's* Senior Editor, Dr. Peter Stern. If you are 35 years of age or younger and doing great research, now is the time to apply for this prize.

As the Grand Prize Winner, you could be next to receive

- > Prize money of US\$25,000
- > Publication of your work in *Science*
- > Full support to attend the Prize Ceremony held in conjunction with the Annual Meeting of the Society for Neuroscience in the USA
- > 10-year AAAS membership and online subscription to *Science*
- > Complimentary products worth US\$1,000 from Eppendorf
- > An invitation to visit Eppendorf in Hamburg, Germany

It's easy to apply! Write a 1,000-word essay and tell the world about your work. Learn more at:

eppendorf.com/prize

FEATURES



INSIDE THE VORTEX

By **Martin Enserink**; Illustrations by **Davide Bonazzi**

“**W**hen you give everyone a voice and give people power, the system usually ends up in a really good place,” Mark Zuckerberg, founder and CEO of Facebook, said in 2010. Twelve years later, the world is not in such a great place. Facebook, Twitter, and other platforms may have given everyone a voice, but they’ve also unleashed a storm of negative effects—spreading disinformation, inciting hate, and endangering democracy.

In this issue, *Science* explores how scientists are grappling with the radically altered information landscape. Social media has given them a voice and power, too—to communicate directly with the public, spread the word about exciting findings, criticize each other’s data, and fight disinformation with information. The COVID-19 pandemic has turned some into trusted beacons in an ocean of confusion.

But as reporter Jeffrey Brainard shows in his story about scientists’ use of Twitter, many have trouble overcoming the cacophony of lies and half-truths—some of them spread by other scientists. (Communication researchers Dominique Brossard and Dietram Scheufele of the University of Wisconsin, Madison, also explored some of these challenges [scim.ag/3ipcdNy]

in a commentary in *Science* on 10 February.) And for too many, speaking out publicly turns into a nightmare. In a survey conducted by reporter Cathleen O’Grady, 38% of COVID-19 scientists reported some sort of harassment, from online abuse to death threats.

It’s not a new phenomenon—“We feel your pain,” climate researcher Michael Mann says to the new victims—but the pandemic and today’s hyperpolarized climate have made things worse. And although an individual troll may be easy to block, the tsunami of abuse triggered by organized campaigns can take a serious toll.

For some researchers, the spread of mis- and disinformation has become a study subject in itself. Evolutionary biologist Carl Bergstrom believes our brains are maladapted for the daily diet of factoids and titillation that social media algorithms serve us, the same way our bodies can’t cope with an abundance of sugars and fat. As reporter Kai Kupferschmidt explains in his story, Bergstrom is convinced that “bullshit” spread online is one the biggest threats facing humanity in the 21st century—and that studying it is as important as climate science.

The social media storm isn’t calming down. How we cope with it in the years ahead may determine whether we end up in a better place—or one that’s far worse.

ON THE TRAIL OF BULLSHIT

Studying misinformation should become a top scientific priority, says biologist Carl Bergstrom By Kai Kupferschmidt



When Carl Bergstrom worked on plans to prepare the United States for a hypothetical pandemic, in the early 2000s, he and his colleagues were worried vaccines might not get to those who needed them most. “We thought the problem would be to keep people from putting up barricades and stopping the truck and taking all the vaccines off it, giving them to each other,” he recalls.

When COVID-19 arrived, things played out quite differently. One-quarter of U.S. adults remain unvaccinated against a virus that has killed more than 1 million Americans. “Our ability to convince people that this was a vaccine that was going to save a lot of lives and that everyone needed to take was much, much worse than most of us imagined,” Bergstrom says.

He is convinced this catastrophic failure can be traced to social media networks and

their power to spread false information—in this case about vaccines—far and fast. “Bullshit” is Bergstrom’s umbrella term for the falsehoods that propagate online—both misinformation, which is spread inadvertently, and disinformation, designed to spread falsehoods deliberately.

An evolutionary biologist at the University of Washington (UW), Seattle, Bergstrom has studied the evolution of cooperation and communication in animals, influenza pandemics, and the best ways to rank scientific journals. But over the past 5 years, he has become more and more interested in how “bullshit” spreads through our information ecosystem. He started fighting it before COVID-19 emerged—through a popular book, a course he gives at UW’s Center for an Informed Public, and, ironically, a vigorous presence on social media—but the pandemic underscored how persuasive and powerful misinformation is, he says.

“Misinformation has reached crisis proportions,” Bergstrom and his UW colleague Jevin West wrote in a 2021 paper in the *Proceedings of the National Academy of Sciences (PNAS)*. “It poses a risk to international peace, interferes with democratic decision-making, endangers the well-being of the planet, and threatens public health.” In another *PNAS* paper, Bergstrom and others issued a call to arms for researchers to study misinformation and learn how to stop it.

That research field is now taking off. “You have scholars from so many different disciplines coming together around this common theme”—including biology, physics, sociology, and psychology—says Philipp Lorenz-Spreen, a physicist who studies social media networks at the Max Planck Institute for Human Development.

But the influx has yet to coalesce into a coherent field, says Michael Bang Petersen, a political scientist at Aarhus University. “It’s still spread out in different disci-

plines and we are not really talking that much together.” There’s also disagreement about how best to study the phenomenon, and how significant its effects are. “The field is really in its infancy,” Lorenz-Spreen says.

BERGSTROM GREW UP in Michigan, but as a child twice spent almost a year in Australia, where his father, an economist, was on a sabbatical. “That’s where I fell in love with birds,” he says. In his bedroom he had a poster of all the parrots of Australia: “It’s like you handed an 8-year-old a bunch of crayons and a bunch of outlines of parrots and just said, ‘Make them pretty.’” Corvids are his favorite birds because of their cognitive abilities. On Twitter, his avatar is a crow.

As a biology student at Stanford University, Bergstrom grew fascinated by communication—an evolutionary puzzle because of the potential for deception. “If I listen to you, I give you a handle over my behavior,” Bergstrom says. “I might do the things you want, even if they’re not in my interest.” In his Ph.D. thesis, he tackled the question of how communication can stay useful when there is so much to be gained from misusing it.

In nature, he concluded the answer is often that lies are costly. Begging for food makes baby birds vulnerable, for example, so they have an incentive to do it only when necessary. “If you’re just a defenseless ball of meat sitting in a nest and can’t go anywhere, yelling at the top of your lungs is amazingly stupid,” Bergstrom says. “If they’re not really hungry, they’ll just shut up.” On social media, such repercussions barely exist, he says: Liars have little incentive to shut up.

In the early 2000s, while a postdoc in the lab of population biologist Bruce Levin at Emory University, Bergstrom awoke to the threat of infectious disease. He collaborated with a fellow postdoc, Marc Lipsitch—now an epidemiologist at the Harvard T.H. Chan School of Public Health—on papers about pandemic preparedness. Then he delved into network theory, which aims to mathematically describe the properties of networks, including those that spread disease. “It appealed to multiple aspects of my intellectual interests,” he says.

Network theory in turn led Bergstrom to the spread of information. Together with Martin Rosvall, a physicist at Umeå Uni-



Carl Bergstrom, a birding enthusiast who in the past studied animal communication, looks at social media through an evolutionary lens.

versity, he found a way to use citation data to create “maps” of the scientific enterprise that showed, for example, how fields cluster and which scientists are most influential. “The algorithms we came up with turned out to work much, much better than I expected,” Bergstrom says. “I still don’t really understand why they are so good.”

Bergstrom’s path through different disciplines is a testament to his curiosity and creativity, West says: “You’d be hard-pressed to find someone that really has moved around in such disparate fields and had impacts in all these different areas.”

Around 2017, Bergstrom’s interests started to coalesce around the topic of misinformation. The debate about Russian misinformation and the role it played in the 2016 election of Donald Trump as U.S. president, and an inspiring 2017 meeting about misinformation organized by biologist Joe Bak-Coleman, then at Princeton University, made him realize “this is actu-

ally a huge problem and one that’s going to take all these different approaches to deal with it, many of which I personally found very interesting,” he says.

BERGSTROM SEES social media, like many other things in life, through an evolutionary lens. The popular platforms exploit humanity’s need for social validation and constant chatter, a product of our evolution, he says. He compares it to our craving for sugar, which was beneficial in an environment where sweetness was rare and signaled nutritious food, but can make us sick in a world where sugar is everywhere. Facebook exploits humans’ thirst for contact, in his view, like a Coca-Cola for the mind, allowing people to connect with others in larger numbers during a single day than they might have over a lifetime in humanity’s past.

And whereas Coca-Cola cannot tweak its formula on a weekly basis, social media platforms can constantly change their algorithms and test out new strategies to keep us engaged. “The social media companies are able to run the largest scale psychological experiments in history by many orders of magnitude, and they’re running them in real time on all of us,” Bergstrom says.

Often, engagement comes from crass conflict: “In a schoolyard people cluster around fights, and the same thing happens on Twitter,” he says. Zeynep Tufekci, a sociologist at Columbia University, agrees. “Social connection is ingroup/outgroup,” Tufekci says. That promotes polarization and tribalism as well as exaggeration and misinformation, she says.

Online networks also undermine traditional rules of thumb about communication. Before the advent of the internet, for example, hearing the same information from multiple people made it more trustworthy. “In the physical world, it would be almost impossible to meet anyone else who thinks the world is flat,” Stephan Lewandowsky, a psychologist at the University of Bristol, wrote in an email. “But online, I can connect with the other .000001% of people who hold that belief, and may gather the (false) impression that it is widely shared.”

Social media companies have little incentive to change their practices because they make money selling ads. “The network structures along which we share informa-

tion have changed radically in the last 20 years, and they've changed without any kind of stewardship," Bergstrom says. "They've changed basically just to help some tech startups sell ads."

Seeing the problem does not mean he is immune to it. Bergstrom admits sometimes waking up at 4 a.m. and checking his Twitter mentions. "That's the stupidest thing I could possibly do. Because an hour and a half later, I'm pissed off and can't sleep," he says. "It works on all of us, even those of us who know what they're doing."

In a perspective published in *PNAS* last year, Bergstrom and 16 other scientists from various fields argued that the study of how the information ecosystem influences human collective behavior needed to become a "crisis discipline," much like climate science, that could also suggest ways to tackle the issue. "That paper was just pointing out that the building is on fire," says Bak-Coleman, the lead author, who's now also at UW's Center for the Informed Public. The problem is we don't know how to quench the fire, he says.

ONE KEY PROBLEM is that the way information spreads on social media is determined by the platforms' proprietary algorithms, which scientists have not been able to study. "Even if there was a crisis discipline like Carl wants it, we simply do not have the data," says Dietram Scheufele of the University of Wisconsin, Madison, who studies science communication. "The only way in which we can create that discipline is by policymakers forcing tech companies to provide data access," Petersen adds.

Researchers have tried to understand the flow of mis- and disinformation in other ways, but the results are often not clear-cut. Last year, a report by the Center for Countering Digital Hate claimed that just 12 people—which it dubbed the "disinformation dozen"—were the source of 73% of misinformation about COVID-19 on Facebook. Banning these "superspreaders" could reduce the amount of misinformation significantly, the authors suggested. But Meta, Facebook's parent company, pushed back against what it called "a faulty narrative" in a blog post. The report was based on just 483 pieces of content from only 30 groups and "in no way representative of the hundreds of millions of posts that people have shared about COVID-19 vaccines in the past months on Facebook," Meta said.

In 2018, researchers from the Massachusetts Institute of Technology's Media Lab published a study in *Science* showing false news spreads "farther, faster, deeper, and more broadly than the truth." The reason is that people like novelty, and false sto-

ries are likely to be more novel, the authors suggested. If true, this might allow false news to be identified automatically, simply through the way it spreads.

But a reanalysis of the data published late last year suggests the picture is more complicated. The *Science* paper used data on misinformation that had been fact-checked by independent organizations such as Snopes, which meant it was biased toward misinformation that had already spread wide enough to merit that kind of attention. When researchers factored in this bias, the difference between the speed and reach of false news and true news disappeared.

Bak-Coleman, who has studied how schools of fish suppress false alarms from fish in the periphery of the swarm, believes the density of connections on social media make it harder to filter out bad information. Bergstrom agrees. "If we actually cared



Carl T. Bergstrom
@CT_Bergstrom

We in the infectious disease epidemiology world spent decades preparing for a crisis like this, but were never imagining that we'd be fighting on two fronts, the virus on one and this sort of hyper-partisan disinformation on the other.

2:49 PM · Mar 26, 2020

On Twitter, Carl Bergstrom has battled against—and reflected on—the rise of disinformation.

about resisting disinformation, Twitter and Facebook might be better off if they said, "Look, you can have 300 friends and that's it," he says.

But that, too, needs study, he says, as do strategic questions: "What would agents do if they wanted to try to inject misinformation into a network? Where would they want to be? And then the flip side: How do you try to counter that?"

TO MAKE PROGRESS, some researchers say, the budding field needs to focus less on the network's properties and more on its human nodes. Like viruses, misinformation needs people to spread, Tufekci says. "So what you want to really do is study the people end of it," including people's reasons for clicking Like or Retweet, and whether misinformation changes their behavior and beliefs.

That's also difficult to study, however. At UW's Center for an Informed Public, billions of online conversations are captured every

year. If a certain piece of misinformation is identified, "you can go about measuring how it's amplified, how fast it grows, who's amplifying it," says West, who directs the center. "But it is very difficult to see whether that translates into behavior, and not just behavior, but beliefs."

A review of 45 studies on misinformation about COVID-19 vaccines, recently published as a preprint by researchers in Norway, concluded that—although misinformation was rampant—there were few high-quality studies of its effects. "There is a need for more robust designs to become more certain regarding the actual effect of social media misinformation on vaccine hesitancy," the authors concluded.

Scientists have tried to study the issue by isolating a very small part of the problem. A recent paper in *Nature Human Behaviour*, for example, reported the results of an experiment conducted in September 2020, before COVID-19 vaccines became available. Researchers asked 4000 people in both the United Kingdom and the United States whether they planned to get vaccinated, exposed them to either facts or false information about the vaccines in development, then measured their intent again. In both countries, exposure to misinformation led to a decline of six percentage points in the share of people saying they would "definitely" accept a vaccine.

Tufekci has no doubt social media has a major impact on society: "Just look around. It's a complete shift in how the information ecology works at a social level. How can you not expect it to have an impact?" But small-scale lab studies simply can't properly measure the problem, she says. "An ecological shift of this nature doesn't lend itself to that kind of study." People in the real world are likely exposed not to one piece of misinformation, but to a lot of it over time, often coming to them through friends, family, or other people they trust. And online misinformation cascades through the information ecosystem, pushing more traditional media to spread it as well. "Fox News is kind of competing with that stuff on Facebook," Tufekci says. "Fox News doesn't operate in a vacuum."

But Scheufele isn't so sure misinformation has a big impact. "There is a correlation of course between all this misinformation and the decision by so many people not to get vaccinated, but correlation does not mean causation," he says. He believes people choose information to conform to their world view, not the other way around. In his view, misinformation is a symptom, but the real disease is polarization and a political system and societal climate that rewards it. Given the deep political polarization in the United States and Trump's "unusual" presi-



gency, the pandemic “was always going to be a shitshow” there, Scheufele says.

A recent review in *Nature*, however, argued that people do not fall for misinformation because of polarization. The authors cited studies suggesting true information is more likely to be believed than false information, even if it doesn’t align with one’s political views. “Politics does not trump truth,” they concluded. The real problem is people sharing information with little attention to whether it is true, the authors wrote. “Rather than being bamboozled by partisanship, people often fail to discern truth from fiction because they fail to stop and reflect about the accuracy of what they see on social media.”

Reining in such thoughtless sharing is the goal of two approaches to tackling misinformation. One, known in the field as “nudging,” includes anything from flagging suspicious information—for example because it’s based on few or anonymous sources—to making it harder to share something. A platform might force users to copy and paste material before sharing it, or put a limit on how often a post can be reshared. “It’s being shown again and again that it has some benefits when you give people a little time to think about their decision to share something,” Lorenz-Spreen says.

The other approach, “boosting,” is designed to improve users’ critical skills. This

includes “prebunking”—teaching people how to spot misinformation—and “lateral reading,” verifying new information while you are reading it by looking for outside information. Those skills are what Bergstrom has tried to teach in a course he taught with West and in their book, *Calling Bullshit: The Art of Skepticism in a Data-Driven World*.

WHEN THE PANDEMIC started in early 2020, Bergstrom initially thought it would be a great opportunity to study the spread of misinformation, drawing on his background in network theory. “I thought when this has all gone away in March, then I can go through these data sets and figure out what were the spread patterns that we were seeing.” But the pandemic did not go away and Bergstrom was sucked into the practical work of explaining the science and calling out misinformation. He does so primarily in long threads on Twitter, where he now has more than 150,000 followers.

In early 2020, for example, he took on Eric Feigl-Ding, a nutritional epidemiologist then at Harvard Medical School who amassed a huge following with what many scientists felt were alarmist tweets. When Feigl-Ding tweeted about a preprint claiming that SARS-CoV-2 contained sequences from HIV and was likely engineered, Bergstrom called him an “alarmist attention-seeker.”

(The preprint was withdrawn within days.)

But the spat showed that defining misinformation is difficult. Feigl-Ding rang the alarm many times—he is “very, very concerned” about every new variant, Bergstrom says, and “will tweet about how it’s gonna come kill us all”—but turned out to be right on some things. “It’s misinformation if you present these things as certainties and don’t adequately reflect the degree of uncertainty that we have,” Bergstrom says.

Feigl-Ding says using Twitter early in the pandemic was “a big learning curve” for most scientists and that Bergstrom and he “have long made amends and got along well since mid 2020.” Indeed, Bergstrom worries that his tone stoked unnecessary division and helped spread the sense that scientists are just fighting over their egos. “The overall lesson, whether it’s dealing with Eric or others, is that I would have done better to be a bit drier, a bit more dispassionate.”

Bergstrom realizes his battle against misinformation is a Sisyphean task. He likes to quote Brandolini’s law, which says “the amount of energy needed to refute bullshit is an order of magnitude larger than is needed to produce it.” Tufekci concurs. “I like Carl’s stuff. I benefit from following him and I’m sure the people who follow him benefit from following him,” she says. “But the societal solution is not to need Carl.” ■



IN THE LINE OF FIRE

Scientists have been harassed for years. But a *Science* survey shows the pandemic has made things far worse for some

By **Cathleen O'Grady**; Graphics by **Kelly Franklin**

When Marion Koopmans, a virologist at Erasmus University Medical Center, visited a museum in Amsterdam with her family last year, she was spotted by the wrong crowd: people who hate Koopmans because of her work on COVID-19. “They started re-

ally yelling, banging,” she says. “Security locked the doors.”

Since early in the pandemic, Koopmans has found herself targeted by people who believe the pandemic is a hoax, the virus was created intentionally to cause harm, or vaccines are dangerous. She has received death threats, been accused of belonging to an elite network of pedophiles—a belief

held by devotees of the QAnon conspiracy theory—and told she should be tried for crimes against humanity.

Now, Koopmans no longer makes public appearances without first alerting the police. As a frequent guest on Dutch TV, “I cannot go out on the street anonymously,” she says. Her family is not comfortable walking outside with her, and they worry about her ever

traveling to the United States, where much of the vitriol originates.

She's not alone. When, in March 2020, a science story became the biggest news story in the world, scientists became household names overnight, even celebrities. But many also became the targets of new and extreme levels of harassment, intimidation, and threats. U.K. Chief Medical Advisor Chris Whitty was accosted by two men in a London park; disease ecologist Peter Daszak of the EcoHealth Alliance received a letter containing white powder that resembled anthrax; Belgian virologist Marc Van Ranst and his family were moved to a safe house after he was threatened by a former soldier who was later found dead in a national park.

To better understand the level of intimidation, its effects, and the ways scientists cope with it, *Science* asked 9585 researchers who have published on COVID-19 to fill out an online survey about their experiences. Of 510 who responded, 38% reported at least one type of attack, ranging from insults to death threats, delivered on social media, by email or phone, or sometimes even in person. Those who were harassed described a range of effects on their lives, including workplace problems and mental health issues. (For more details on the survey, see sidebar, p. 1340.)

The findings broadly align with other indications that harassment is hitting science and related fields. The Geneva-based nonprofit Insecurity Insight reports 517 instances of physical violence related to COVID-19, including 10 health workers killed, 24 kidnapped, and 89 injured. A study published in the *American Journal of Public Health* this month found harassment experiences at 57% of 583 U.S. local health departments and 80 departures by officials who reported harassment.

But the *Science* survey paints a nuanced picture of what researchers have experienced. A *Nature* survey published in October 2021 gave a startling figure: Eighty-one percent of 321 scientists who had frequently discussed COVID-19 in the media reported receiving at least occasional personal attacks, with 25% saying these attacks were common or constant. In contrast, *Science* surveyed COVID-19 researchers both with and without media exposure

and found the majority reported no harassment and only a small minority experienced intense levels. The most extreme forms of harassment, such as threats of violence, suspicious packages or letters, and unwanted visits—although terrible for those who experience them—were reported relatively rarely.

Harassment was more prevalent in a separate survey of 44,468 members of AAAS, publisher of *Science*, which asked not about harassment during the past 2 years, but over scientists' entire careers. In that survey, which yielded 1281 responses from scientists in a wide range of fields, more than half (51%) of respondents reported receiving at least one kind of harassment, sometimes continuing for decades.

Although the results are impossible to compare directly with the COVID-19 survey—which only looked at the past 2 years—they indicate harassment is not new or limited to COVID-19. To those in fields like climate science and animal research, the stories of COVID-19 scientists are depressingly fa-

miliar. "We're here; we feel your pain," says Michael Mann, a climatologist at Pennsylvania State University, University Park, who has faced decades of attacks. "Talk to us. We've got some lessons that we've learned."

The pandemic has nonetheless made things far worse for some researchers. More than half of the COVID-19 researchers who reported harassment said it was a new experience for them, and a further 31% said the pandemic had increased the problem. One reason is greater exposure: These researchers grew their audiences during the pandemic or entered the public sphere for the first time. The pandemic also struck at a time when polarization was already on the rise. Many other people working in the public interest—from election officials to school board members—are under attack as well, says Sarah Sobieraj, a sociologist at Tufts University who studies digital abuse and harassment. The widespread vitriol, she says, "impacts not just those people who are attacked, but all of us who rely on these kinds of professionals to do the work to keep societies functioning in a healthy way."

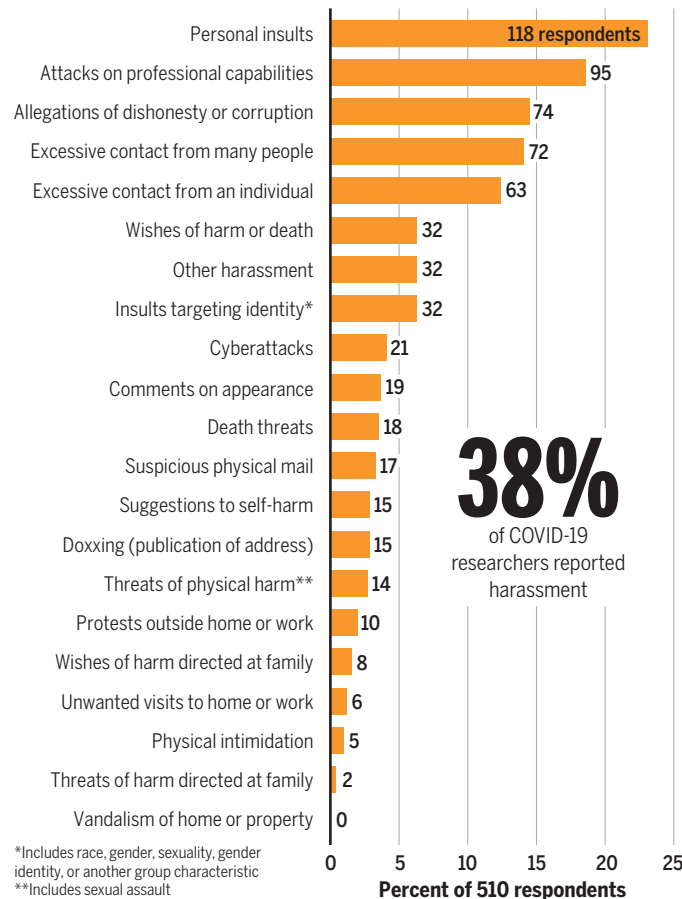
Some commentators say increased attention to the new victims and the shocking experiences they describe may be the catalyst for research institutions to finally pay some attention to the issue, rather than treating it as a problem for researchers to solve on their own—or, worse, blaming and even punishing them for the abuse they experience.

THE PANDEMIC WAS NOT Tara Smith's first brush with public hostility. Smith, an epidemiologist at Kent State University's main campus, has spoken out about politicized topics, including evolution and HIV denial, for many years. But since 2020, "frustration and hatred" have come pouring out at a higher volume and with more extreme content, she says, including death threats. When prominent Twitter accounts mention her, Smith is swarmed by multitudes tweeting abuse. "You just get overwhelmed by the hate," she says.

Several researchers have been exploring the dynamics behind such attacks. What Smith is experiencing, for example, is "networked harassment" by swarms of people who share social media networks, says

An outbreak of harassment

Out of 510 COVID-19 researchers surveyed by *Science*, 38% reported at least one kind of harassment. Personal insults and attacks on people's competence or integrity were most often reported. Threats of violence, "doxing," and unwanted visits were far less common.



ABOUT THIS SURVEY

To survey researchers who published on COVID-19, *Science's* News team extracted a list of corresponding author email addresses from the Web of Science, drawing from all research articles, editorials, and review papers that mentioned COVID as a keyword. We then limited the pool to 35,830 email addresses that appeared more than once, indicating multiple publications, and emailed a random selection of 9585 researchers. The survey asked respondents about their field of research, experiences with publicity and harassment, any institutional support they received, and how they coped with harassment.

We received 511 responses and removed one we questioned because it had identical answers across multiple questions. More than one-third (170) of respondents lived in the United States, followed by Germany (40 respondents) and Italy (26). A similar survey was sent to 59,653 members of AAAS, *Science's* publisher,

representing a wide range of disciplines; 1281 responded.

Science applied for ethical review of the survey through an independent review board. We worked with a methodological and statistical adviser to design the survey and process the results.

As with any survey, it is very likely that certain kinds of people responded more than others. Targets of abuse may have been more likely to respond, but they could also be more worried about maintaining anonymity or less willing to discuss their experiences. Either way, the results do not necessarily represent scientists more widely and should be interpreted with caution.

Because of the number of different questions and because we did not have specific hypotheses about our results, we have treated this as an exploratory data set. We have not used significance testing, which could lend undue weight to tentative findings. For full methods, data, and analyses, visit osf.io/3bn9u. —C.O.

Alice Marwick, a communication researcher at the University of North Carolina, Chapel Hill. Swarms are often not coordinated: Participants following similar prominent social media accounts may act independently but in the same way.

A driving force behind networked harassment is a perception that the target of the abuse has violated a moral norm, says Marwick, who has interviewed harassment victims and employees of social media companies to better understand the phenomenon. In the case of COVID-19, an important moral norm for people in a range of communities—from “wellness” fans to conspiracy theorists—is the belief that Big Pharma is evil. The conviction that researchers who, for example, promote vaccination are hiding conflicts of interest “allows people to feel like they’re on a high horse, and it triggers moral outrage,” Marwick says. They may come to see scientists as “bad people who must be stopped for the good of the world.” Morally motivated harassment occurs across the political spectrum, she adds; it is often directed at those perceived as racist or sexist.

Science's survey asked COVID-19 researchers about specific pandemic-related stances they had publicly supported, and found that positions in a few highly polarized debates were more strongly correlated with intense harassment than others. Arguing against the use of the antiparasitic medicine ivermectin to treat COVID-19 (for which it appears to be ineffective), and for the likelihood that the virus originated naturally rather

than in a lab accident, had the strongest links to harassment.

Even if the attacking swarms aren't coordinated, outside groups often inflame them, says Imran Ahmed, CEO of the Center for Countering Digital Hate, a U.S. nonprofit. Antivaccination groups, for instance, spread the message that vaccine advocates cannot be trusted, Ahmed says. They rely on social media companies' algorithms, built to monetize and prioritize attention, which in turn is driven by outrage. A controversial tweet is likely to accumulate interactions, as people leap into the fray to amplify the message or voice their disagreement (see story, p. 1344).

Some of these actors are “economically motivated,” Ahmed says. Expanding their reach means more revenue through donations and sales of products such as books and supplements. By driving networked harassment, such individuals can intimidate scientists into silence: “If you're a scientist—which has a lot of epistemic weight in society—and you decide not to post as a result: job done!”

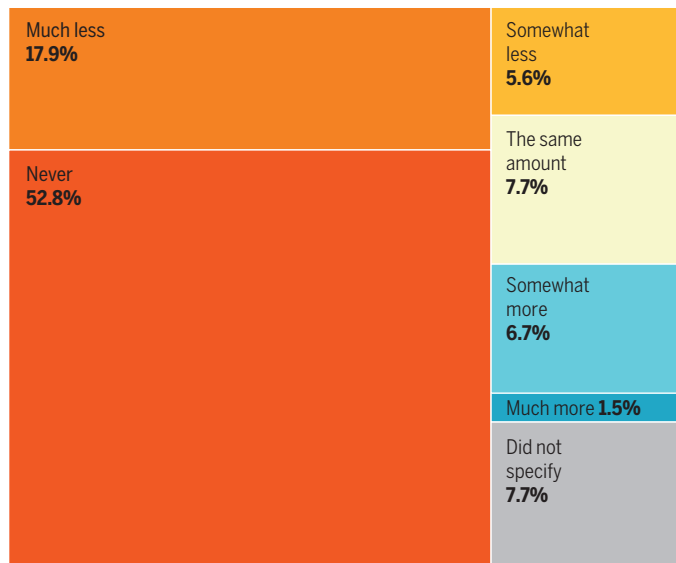
Another group of people driving the attacks are “essentially parasitic,” Ahmed says: pundits, politicians, and commentators who purposefully court conflict on social media, knowing that fights drive visibility and, in turn, lead to more followers and greater impact. Fox News host Tucker Carlson has called Anthony Fauci, a top U.S. government scientist, “an even shorter version of Benito Mussolini” and said Baylor University vaccine researcher Peter Hotez is a “nut-case” and a “charlatan.”

Hotez was also criticized by Florida Governor Ron DeSantis (R)—in a Fox News segment that referred to Hotez as a “medical cartel member”—which unleashed torrents of abuse. “Antiscience has become institutionalized,” Hotez says. “It's now firmly ensconced in Europe. It's a major element of the far right and the Republican Party, and it's working to portray scientists as the enemy of the state.” Mann and his fellow climatologist Ben Santer, formerly at Lawrence Livermore National Laboratory, have come under political fire as well. “You speak publicly about the science ... it conflicts with powerful politicians, you get hammered,” Santer says.

A new wave of abuse

Among COVID-19 researchers who reported being harassed, 71% said they experienced far less abuse or none at all before the pandemic began.

“Before the COVID-19 pandemic, had you ever experienced unwanted behaviors, harassment, bullying, intimidation, stalking, or threats as a result of your work?”



Ruth Ben-Ghiat, a historian at New York University, sees the attacks on science and scientists—and on the press—as a feature of the rise of authoritarianism. Russian President Vladimir Putin, Hungarian Prime Minister Viktor Orbán, and the U.S. Republican Party all use common tactics, she says. “Authoritarians and extremists want to intimidate you and get you to shut up,” she says. “They want you to say it’s not worth it, I’ll stay in my laboratory, I won’t speak out.”

Scientists and public health officials have sometimes inadvertently fanned the flames. Muddled communication about scientific uncertainty—like the World Health Organization’s original position that ordinary people should not wear masks, which was soon overturned—may have undermined trust in science, says Kolina Koltai, a misinformation researcher at the University of Washington, Seattle. “You feel like your life is being ruined because of these scientists,” she says. “You want to direct that hate to someone.”

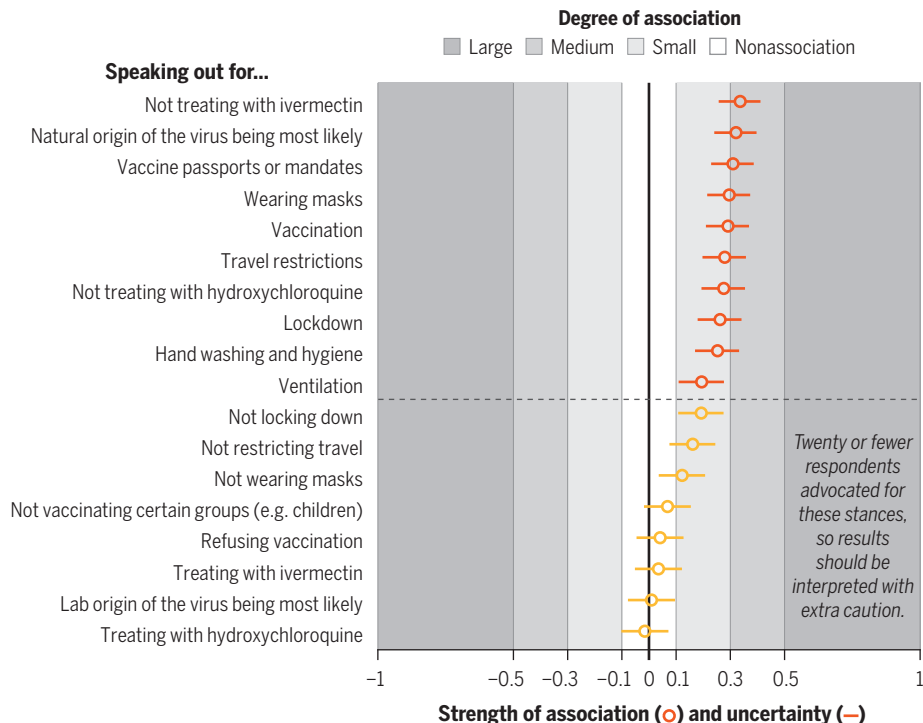
IN SCIENCE’S SURVEY of COVID-19 researchers, the most common types of harassment reported were insults, attacks on professional capabilities, and accusations of dishonesty or corruption. But for some, the attacks were more extreme: Six percent reported receiving wishes of harm or death, and 3% reported death threats. Among AAAS members, representing a broader range of scientific disciplines, these numbers were higher, with 14% reporting death wishes. (People with particularly terrible experiences may have been more likely to answer the survey, driving up those numbers.)

For Fatima Tokhmafshan, a geneticist at McGill University who came to Canada as a refugee from Iran at the age of 17, much of the vitriol has been Islamophobic or xenophobic. Before COVID-19, “I never experienced anybody calling me a filthy immigrant, telling me I deserve to be raped and have my head on a spike because I want to vaccinate kids,” says Tokhmafshan, who has tried to counter misinformation on social media. Hotez says much of the abuse he receives is antisemitic. For epidemiologist Saskia Popescu of the University of Arizona, it’s a “quiet week” if she doesn’t receive at least two or three sexualized messages, ranging from creepy men demanding attention to rape threats.

The survey had too few members of racial and sexual minorities to explore how these identities affected harassment. There was no correlation between gender and the level of harassment, but that result may be specific to the survey population and does not mean gender plays no role in abuse. “Any kind of person can be harassed,” Marwick says, but attackers are likely to seize on any weapon they can, including personal

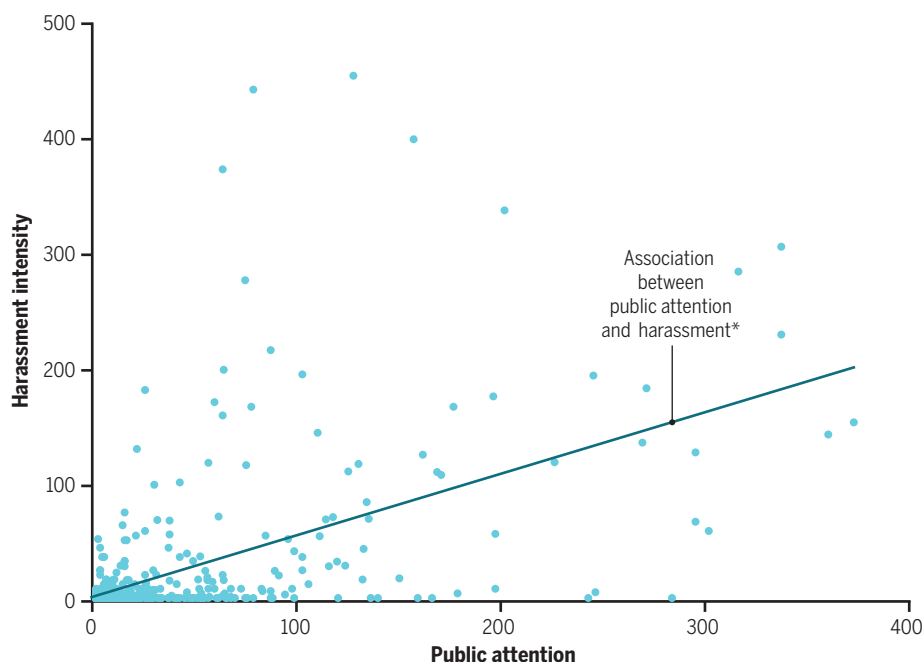
Views that draw vitriol

Scientists who publicly advocated hotly debated positions on COVID-19 received more harassment, the survey suggests. These correlations could have different explanations. The stances themselves could drive the abuse, for example, or prominent scientists may both receive more abuse and advocate for certain positions more often.



The effect of exposure

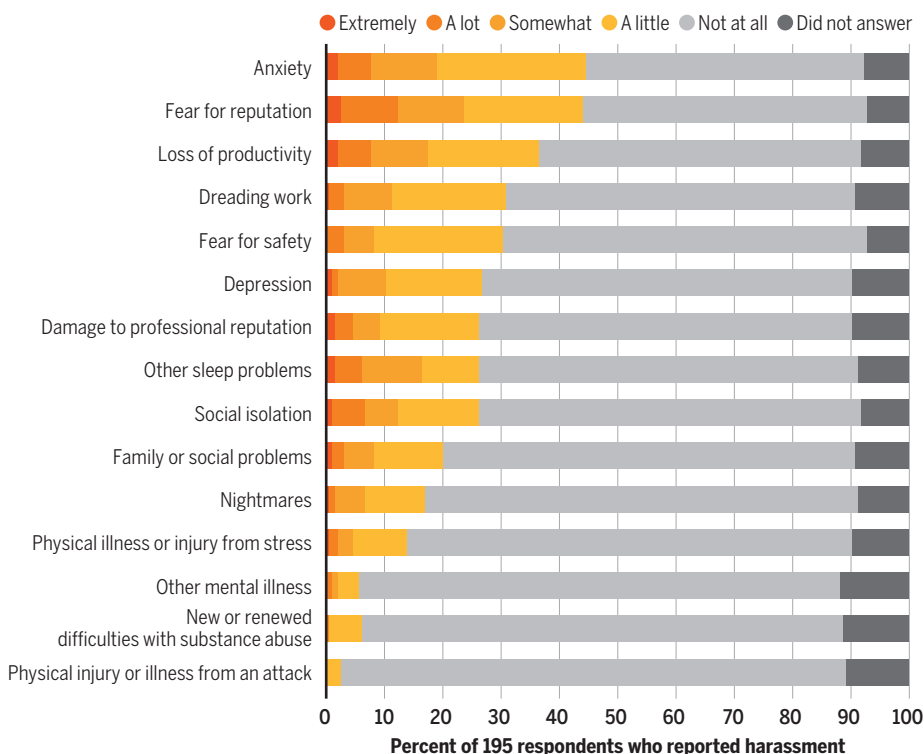
The attention COVID-19 scientists receive on social media, in news stories, and as policy advisers was correlated with the amount of harassment they experienced. (Both exposure and harassment are expressed as scores that factor in type and frequency of harassment and attention.) Exposure may directly drive abuse, or prominence or some other factor may drive both exposure and abuse. Some scientists had a great deal of exposure but suffered little harassment, and vice versa.



*The correlation coefficient (a measurement of how strong the association is) is 0.56, with an uncertainty range of 0.50 to 0.62.

A serious toll

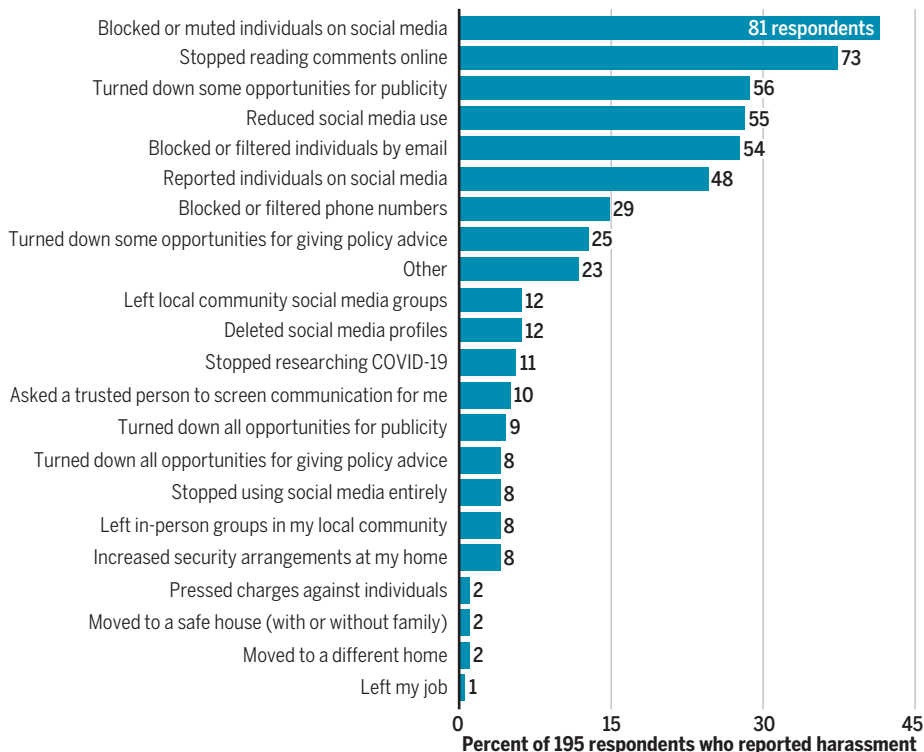
Researchers who were harassed reported a range of effects on both their professional and private lives, including workplace problems and mental health issues.



Coping mechanisms

Many of the COVID-19 researchers surveyed sought to avoid or suppress harassment by muting or blocking people on social media. Others took more drastic steps to withdraw from public communication, such as deleting accounts or turning down publicity opportunities.

“What measures have you taken to protect yourself from harassment and/or intimidation?”



characteristics and group identities. These are “attack vectors,” Marwick says: assumed vulnerabilities that attackers can exploit. Because people who are harassed and abused are more likely to self-censor—or withdraw from public appearances altogether—attacks on people from underrepresented groups could mean losing their voices at a higher rate, Sobieraj says.

Most researchers who spoke to *Science* for this story declined to comment on the impacts of the abuse on their lives, worried that doing so could fuel further sadism. But our survey shows researchers who were harassed most commonly reported anxiety, fear for their reputation, and loss of productivity as a result of the abuse. Other, more extreme effects included substance abuse and stress-related illness or injury.

One animal researcher who spoke on condition of anonymity said the threats affected their family as well. Their young daughter found a box of hate mail postcards—including death threats—in their office, for example. Santer says his son felt unsafe at home after someone left a dead rat on his doorstep. The attacks he faced “had catastrophic implications for my family,” he says. “It was, in a sense, a loss of innocence for me.” In the surveys, 22% of COVID-19 researchers and 20% of AAAS members reported that harassment had caused at least some family or social problems.

Accusations of immorality are particularly bruising, some researchers say. Ellie Murray, an epidemiologist at Boston University, has been vocal about the need to protect children from infections, but her message has been twisted into accusations of being “pro-school closure,” she says, and then to “people claiming that I encourage child suicide.” Theresa Chapple, who directs a local health department in the United States, has been accused of being “anti-children,” she says, “which is really hard to hear ... because my Ph.D. is in maternal and child health.”

The toll of online harassment is often too easily dismissed, says criminologist Matthew Williams of Cardiff University. “It’s akin to having your house burgled, in terms of the psychological impact,” he says. And there’s no escape, Sobieraj says: Online harassment is not constrained to a time or place, and can pop up in the middle of everyday activities, like texting a friend. Even nonviolent insults can be traumatic when they come in swarms, Marwick says: “On a day-to-day basis, there’s very few situations in which you’re going to have a roomful of people yelling at you.”

The impact has not stopped researchers like Mann and Santer from speaking publicly about climate science for many years. Others may not want to pay that price; ev-

Many researchers who spoke out about COVID-19 experienced abuse for the first time in their careers, according to *Science's* survey. A majority of harassed researchers did not receive institutional support. But there are organizations that offer help and resources for victims of online harassment.

- Crash Override, a resource center for people facing online abuse, has an automated cybersecurity helper (bit.ly/3Juw9KG) that offers a step-by-step guide to improving basic security and “self-defense.”
- Feminist website Feminist Frequency has a guide to securing personal information online (bit.ly/3D2Ai6i), with the aim of reducing risks like doxxing and threatening or suspicious physical mail.
- Free speech advocacy organization PEN America’s online harassment field manual (bit.ly/3NiRdGq) explains how to prepare for and respond to abuse, get law enforcement involved, and more.
- Front Line Defenders, a nonprofit that supports human rights activists, offers workbooks on creating security plans (bit.ly/36dfb4Y), both online and offline.
- CyberSmile.org and iHeartMob.org offer emotional and practical support.
- Communication researcher Alice Marwick of the University of North Carolina, Chapel Hill, and colleagues have written an in-depth guide for researchers (bit.ly/3CYINDW) facing online harassment that covers protective measures, external resources, and guidelines for institutions and supervisors. They have also produced a separate information sheet (bit.ly/3lmuV2R) for institutions. —C.O.

ery researcher should decide on their own comfort level, Santer says, but “if you do enter that public arena, then put on your battle armor.”

That should start with a thorough assessment of the threat of harassment before you enter the fray, says Cornell University computational social scientist J. Nathan Matias. Researchers should ask themselves what needs protection—like personal details, or family members—who wants to cause harm, what tactics they might use, and what can be done to minimize risks. Researchers should not underestimate the threat—or overestimate it, which can make them stay silent unnecessarily, Matias says.

Researchers reported a range of tactics to cope with abuse. Blocking or muting trolls on social media, or not reading comments on news articles or social media posts, were among the most widely used, *Science's* survey shows. (Some sources find blocking just fuels the hatred, however, as the blocked individuals create new accounts and swarm from them.) Smaller numbers of respondents reported far more drastic measures, such as deleting their social media accounts, refraining from giving policy advice, or beefing up home security.

Some scientists also use email filters to remove messages with certain keywords; others have assistants who screen their mailboxes. Simple steps like Googling one’s own address or phone number can help identify where personal details might need to be scrubbed so they can’t be revealed online, Marwick says. (For resources to help with online abuse, see sidebar, above.)

It’s imperative not to reply to abusive individuals on social media, Ahmed says, because this just fuels the algorithm. “Ignore, block, take a timeout, and then go and find some good content, and engage with that instead.” Engaging with politicians and pundits is

particularly risky, he adds: “A good political operative can wipe the floor on social media with someone who doesn’t know what fight they’re in. ... They’re thinking that we’re arguing about the truth. The political actor is just thinking, I’m arguing.”

Whitney Robinson, an epidemiologist at Duke University, has found an unusual outlet that avoids abuse. In the past, she studied and worked at a public university in a conservative state where retaliation against outspoken faculty is not uncommon, she says. That, and the vitriol she knows she would attract as a Black woman, has made her cautious on social media. But a newsletter in her historically Black neighborhood has welcomed her expertise on COVID-19. She feels fortunate to be part of a community not torn apart by politics: “There are people who live in places that are super-polarized. It’s so hard.”

THE PROBLEM of online hate can’t be solved by individuals, Sobieraj says. “We tend to misrecognize this as a personal problem, when it is absolutely a social problem or a public issue.” Universities that encourage public communication need to recognize that they are exposing researchers to a hostile environment, and that the impact of this may fall disproportionately on people from more marginalized groups, she says. All too often, institutions fail to support researchers who are experiencing abuse, Marwick adds.

Instead, administrators sometimes assume the abuse has some merit, particularly when they are receiving direct complaints about a researcher—which is a common abuse tactic. One researcher who spoke to *Science* on condition of anonymity says their university hauled them over the coals after they tweeted about attacks from a senior and eminent researcher. Another has been warned their promotion would be in

doubt if they did not stop their activity on social media.

Science's survey found that fewer than 10% of harassed COVID-19 researchers received legal (7%), technological (8%), security (5%), or mental health (6%) support from their employers. Respondents said they hoped for—but did not receive—help from university press offices and assistance with screening communication. Many also said they wanted emotional support: assurance that they were not at fault and that their public communication work was valuable. “Institutions haven’t invested the resources to protect people who are at the heart of the scientific endeavor,” Matias says.

Social media platforms could also do far more, Sobieraj says. A huge amount of abuse violates the terms of service of companies like Facebook and Twitter: “It is very reasonable that, as a society, we would expect these platforms to uphold their own policies.” Companies need to improve their moderation strategies, says Sarita Schoenebeck, a computer scientist at the University of Michigan, Ann Arbor, who studies online abuse. Moderating individual pieces of abusive content is like playing whack-a-mole, she says; focusing on entire communities and organized networks would be more effective.

But ultimately, the abuse stems from deep societal problems, Koltai says. When the pandemic hit, huge numbers of people had already lost faith in health care systems and governments. “Without addressing those big societal issues that make people feel like they’re unheard, or they’re dismissed, or feeling like they’re wronged in some particular way ... we’re never going to get rid of the harassment that scientists face.” ■

Science thanks Tim Errington for valuable advice on the survey. This story was supported by the *Science* Fund for Investigative Reporting.



RIDING THE TWITTER WAVE

Enthusiasm for the social media platform changed science communication during the pandemic—but will it last?

By Jeffrey Brainard

ILLUSTRATION: DAVIDE BONAZZI/SALZMANART

In January 2020, some 2 months before the World Health Organization declared the coronavirus pandemic a global emergency, a tweet appeared on virologist Benhur Lee's smartphone. It linked to a website, virological.org, where scientists had just posted the genetic sequence of SARS-CoV-2. Lee, at the Icahn School of Medicine at Mount Sinai, quickly shared the tweet with his followers, along with the words "Here we go" and an animation of planes taking off. Within days, the pharmaceutical firm Moderna and the U.S. National Institutes of Health had announced plans to develop what just 10 months later proved to be an effective vaccine, based on the sequence that codes for the virus' spike protein.

In an earlier age, it might have taken days or longer for such useful DNA data to reach interested scientists via a Table of Contents alert from a journal. But the rise of Twitter and other social media platforms enabled users like Lee to spread the word about the SARS-CoV-2 sequence within hours, sparking global conversations and accelerating efforts to develop vaccines and treatments.

It was an early sign of how the pandemic prompted many scientists—and the public—to turn to social media to share and learn about hot new findings. COVID-19 "changed the game" because the threat "immediately connects with the public, [so] there's a much bigger natural audience" for information about pandemic science than for most areas of research, says Michael Thelwall, a data scientist at the University of Wolverhampton, City Campus, who studies social media. In particular, Twitter has become a go-to resource for anyone trying to make sense of the torrent of pandemic studies—and for those intent on quickly pushing back against misinformation.

"I like that there's a low bar to entry [on Twitter]—I can put something out and see how other scientists are thinking of a problem, people who have a different skill set than mine," says biostatistician Natalie Dean of Emory University, whose Twitter account has some 138,000 followers.

But the pandemic has also helped demonstrate the limitations of social media. It can be difficult, for example, for scientists to be heard over the cacophony of messages on Twitter—some 500 million each day. And although some scientists have used the platform to elevate their online presence,

that has rarely translated into concrete professional rewards. Eventually the sizable Twitter followings some have built during the pandemic may fade. And in the meantime, some have suffered from their digital fame, attracting harsh personal attacks and threats of violence (see story, p. 1338). Despite such challenges, many researchers believe that—like it or not—the pandemic has forever altered how certain scientists communicate with each other and the public.

THE MARRIAGE OF TWITTER and science came later than researchers who study scholarly communication expected. A decade ago, many predicted that scientists would flock to social media as a complement to tradi-

Researchers have been even more skeptical of the social media giant Facebook, which has a greater reach than Twitter among the general public. Instead, they gravitated toward online platforms geared to scientists, such as the citations manager Mendeley, which gives users details about how often a paper is bookmarked by other users.

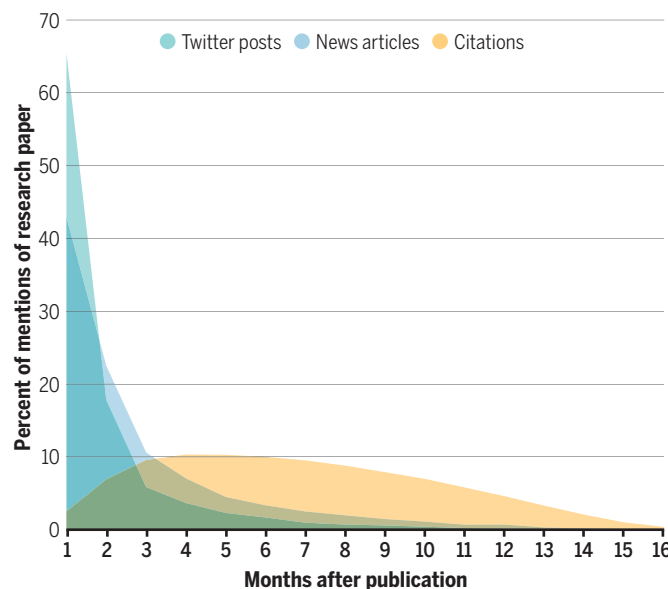
But as the pandemic exploded and researchers sought to pump out information to each other and an eager public, many saw advantages to Twitter. Its vast reach became a draw: more than 200 million active daily users, including an estimated one-quarter of U.S. adults, according to the Pew Research Center. This allows scientists to use a single platform to share research

findings with both peers and the public and to foster open discussions. Twitter's interactivity and viral features added to its appeal—for example, users can amplify others' tweets by "liking" them or retweeting them to their own followers.

One result is that the platform has carried posts about a majority of the total COVID-19 literature—about 51% of journal articles on pandemic research had been mentioned in at least one tweet through May 2021, according to a report by the Research on Research Institute (RoRI). That exceeds the number cited in scholarly articles or mentioned in several other communications venues, including news stories, Facebook, YouTube, Wikipedia, blogs, and policy documents. And it's well above the level before the pandemic, when studies found that just 10% to 30% of papers on any scientific topic got a mention on Twitter.

Rapid responses

Conversations about new research papers on Twitter happen quickly—then soon tail off, like mentions in news stories. Citations in other journal articles, the more traditional channel for scholarly attention, are spread out over many more months.



tional channels such as email alerts, Google searches, and scientific meetings. But at first many researchers expressed apathy or disdain for Twitter, which debuted in 2006. Some saw little value in the platform's large, nonscientific audience. Others bridled at the initially tight limits on message length—just 140 characters per tweet (now 280). As a result, studies before the pandemic suggested as few as 2% of published scientists, and no more than one in five researchers in the United States and Europe, had Twitter accounts. (The disparate results reflect differences in the studies' methods, the authors say.) Researchers working in the health and social sciences were more likely to have an account. And scientists who did tweet typically drew little engagement.

ONE SCIENTIST WHO jumped headlong into tweeting about COVID-19 is Muge Cevik of the University of St. Andrews. Before the pandemic, her tweets about tuberculosis and HIV had attracted only about 2000 followers to her Twitter account. Now, she has more than 170,000, among them members of the U.K. Parliament, scientists, and journalists. "I never thought that I would get this much engagement," she says. But she realized the "privilege ... comes with a lot of responsibility"—for communicating respectfully and "distinguishing opinion versus facts based on data," she says.

Cevik's approach to tweeting is to synthesize the findings of several scientific papers in a way that researchers can use and nonscientists can understand. She

does this by posting long threads—a linked series of tweets, often 20 or more, which Twitter has allowed since 2017. In early 2020, for example, Cevik posted a thread about how poorly ventilated rooms increased the risk of transmitting the pandemic coronavirus, highlighting research that was driving government calls to pause many kinds of gatherings.

“I mainly want people to understand that there’s a scientific basis to the [public health] decisions being made,” Cevik says. “There are so many published data, I think no one is able to follow them.” Cevik’s approach has proved popular: Other Twitter users have retweeted her more than 200 posts about COVID-19 research papers at least 12,000 times, placing her Twitter account in the top 50 on that measure, according to unpublished data provided to *Science* by Zhichao Fang of Leiden University (which he developed for RoRI’s report).

Beyond that, it’s difficult to quantify the impact of her tweets, Cevik says. But several readers told Cevik the threads helped persuade them to get inoculated. Cevik says she works to build such trust by spelling out what scientists don’t yet know about COVID-19 and answering questions from readers. “We can’t really deal with misinformation just by sharing facts,” she says. “We just need to use facts as the foundation for a strategic conversation.”

EVEN AS SOME USERS have turned to Twitter to promote clarity, however, others have flooded the platform with misleading or false information, including tweets deliberately intended to confuse readers (see story, p. 1334). Tweeters, including some scientists, have also helped elevate questionable findings, by linking to studies that were done quickly, had problematic designs, or were first published online with no peer review.

TIPS FOR TWITTER NOVICES

As more researchers turn to Twitter to communicate with colleagues and the public, academic studies and other analyses have identified tweeting practices that tend to draw readers. Here are some tips:

- Tweet regularly. Users who tweet more tend to attract more followers.
- Include images from a paper’s charts or tables.
- Tweet about conferences you’re attending, using the conference’s hashtag.
- To reach nonscientists, avoid or explain jargon. Respond to questions asked in good faith. And aim for at least 1000 followers—a study of ecologists showed that threshold enabled them to reach people other than scientists.
- Sprinkle in humor. Biologist Eric Topol, who runs the Twitter account with the most retweets about COVID-19 scientific papers, also tweets cartoons about the pandemic.
- Don’t tweet links to scientific articles without commenting on them. Comments can add value.
- Encourage university departments to provide training in using Twitter effectively and to set up departmental guidelines on Twitter use. Many universities lack such guidance.

Other researchers are less enamored with Twitter’s threading capability. Dean, for instance, finds the process cumbersome and says it is difficult to embed scientific charts. She’s experimenting with posting longer essays on Substack, a newsletter platform. “It’s more readable and writable,” she says—but the content appears to reach fewer people.

For Cevik, however, Twitter threads have paid off. She expanded her thread on poor ventilation into a paper published in *Clinical Infectious Diseases*. Her posts were also retweeted by Harvard University’s Marc Lipsitch, who then invited her to collaborate, leading to three co-authored papers about COVID-19. That partnership “would have never happened prior to social media,” says Cevik, who also became a pandemic adviser to Scotland’s chief medical officer.

This double-edged sword can be seen in Fang’s list of the top 50 accounts whose posts about COVID-19 papers have drawn the most retweets. Besides Cevik’s account, the list includes others run by scientists who have tried to highlight the best available research, including those of Eric Topol, director of the Scripps Research Translational Institute, and several leading scientific journals, such as *Science* and the *Nature* family of journals.

But the same list also includes Didier Raoult, the controversial French microbiologist at the Hospital Institute of Marseille Mediterranean Infection who has authored a blizzard of tweets urging the use of hydroxychloroquine to treat COVID-19, despite little evidence that the drug is efficacious.

Some scientists have repeatedly taken to Twitter to challenge Raoult’s views in a bid

to curb the viral spread of misinformation in real time—a tactic some call “Twitter peer review.” These watchdogs say such rapid response is necessary because some manuscripts published only as preprints never get formally reviewed at all, and journals often take months to publish letters critiquing peer-reviewed papers. “Obviously, in a pandemic that’s far, far too long” to wait, says Gideon Meyerowitz-Katz, a Ph.D. candidate in epidemiology at the University of Wollongong. He has used Twitter to rapidly challenge scientific claims he believes are backed by little evidence.

In March 2021, for example, Meyerowitz-Katz used his “Health Nerd” account to challenge a paper that, contradicting the weight of scientific evidence, found no proof that lockdowns reduced COVID-19 deaths. Critics of lockdowns had ballyhooed the article, which was published by *Scientific Reports*. In a long thread published only 3 days after the paper appeared, Meyerowitz-Katz took issue with its mathematical assumptions. Soon after, *Scientific Reports* invited him to submit the critique for publication—but it didn’t appear until December 2021, 9 months after the original paper. A week later, after the journal published the critique, it retracted the lockdown study, which has been accessed online by nearly 400,000 people.

Meyerowitz-Katz says data from his Twitter account indicate his March thread was available immediately to tens of thousands of readers, vastly more than later accessed his journal letter. “There’s an immediacy to Twitter I don’t see in traditional academic formats,” he says.

Other COVID-19 papers that might have influenced public policy also drew critical peer review on Twitter before they were retracted. One wrongly claimed that the antiparasitic drug ivermectin could treat the disease; another drew the conclusion, contested by many scientists, that cotton face masks did not prevent transmission of the pre-Omicron variants of the virus.

Such instances remain rare. The Retraction Watch blog, for example, lists more than 200 COVID-19 papers and preprints that have been retracted or withdrawn. But *Science* found that only about a dozen of those had received Twitter peer review. And among 673 scientists who posted preprints about COVID-19, more than twice as many (65%) reported receiving colleagues’ comments about them via emails than via social media posts (30%), according to a 2021 RoRI survey.

Meyerowitz-Katz says such numbers might reflect the lack of professional rewards for scientists who use social media to critique papers, rather than taking a

more traditional route by serving as a journal peer reviewer. Many scientists list their journal service, but not their tweeting, on CVs. Those who publicly challenge findings may also run career risks. Journal peer reviewers typically remain anonymous, he notes, but many academic tweeters list their names on their accounts. “You may be calling into question the results of people who make hiring and firing decisions in your field,” he says.

THAT KIND OF ATTENTION could harm a career. But an emerging body of research about tweeting suggests that, overall, scientists often struggle to be heard on social media. One study, for example, found tweets containing links to scholarly papers typically get little engagement. Of 1.1 million such tweets about papers published before the pandemic, half drew no clicks, and an additional 22% attracted just one or two, according to a 2021 paper in the *Journal of the Association for Information Science and Technology*.

Other research suggests scientists need to attract a critical mass of Twitter followers before their tweets will reach many nonscientists. A 2018 study in *Facets* that examined the Twitter accounts of 110 academic ecologists and evolutionary biologists found those with fewer than 1000 followers were read mostly by colleagues. But above that tipping point, policymakers, journalists, and other nonscientists made up a majority of followers. And scientists might have more success reaching nonscientists on Twitter if they tweet about news articles that mention a scientific paper, rather than the paper itself, according to forthcoming research by information scientist Stefanie Haustein of the University of Ottawa and colleagues.

Such studies are in the vanguard of nascent scholarly efforts to examine Twitter’s role in science communication. For now, Haustein says, “We are really not at the point where we want to get, which is, ideally, seeing the impact of research on the greater good of society.”



Eddie Holmes
@edwardcholmes

All, an initial genome sequence of the coronavirus associated with the Wuhan outbreak is now available at <http://Virological.org> here:

<https://virological.org/t/novel-2019-coronavirus-genome/319>

8:08 PM · Jan 10, 2020

A tweet by Edward Holmes of the University of Sydney at the pandemic’s outset helped kick off a global response by scientists.



Muge Cevik
@mugecevik

Over the last 6 months, we’ve learned a lot about how SARS-CoV-2 spreads

What does the evidence so far tell us about SARS-CoV-2 transmission dynamics, high-risk activities and environments? Thread (1/n)

https://papers.ssrn.com/sol3/papers.cfm?abstract_id=3692807

12:26 PM · Sep 21, 2020



Muge Cevik @mugecevik · Sep 21, 2020

The risk of transmission is complex and multi-dimensional. It depends on many factors: contact pattern (duration, proximity, activity), individual factors, environment (i.e. outdoor, indoor) & socioeconomic factors (i.e. crowded housing, job insecurity). (2/n)



Muge Cevik @mugecevik · Sep 21, 2020

Contact pattern:

We now know that sustained close contact drives the majority of infections and clusters. For instance, close family/friend contacts and gatherings are a higher risk for transmission than market shopping or brief community encounters. (3/n)

Tweet threads, such as this one from Muge Cevik, an infectious diseases researcher at the University of St. Andrews, allow scientists to expand on ideas beyond the 280-character limit for a single tweet.

Still, studies of Twitter use have revealed some intriguing trends. In a study published in *Scientometrics* in 2020, for example, Leiden University data scientist Rodrigo Costas Comesana and colleagues found that some Twitter accounts that spread antivaccine messages also tweet about the same, legitimate scientific papers as pro-vaccine accounts. Better understanding the behavior of these “bridging” tweeters could inform scientists’ strategies to engage with them and address their mis-

representation of facts, and help understand why their posts draw attention, the authors concluded.

As the pandemic wanes, scientists on Twitter may wonder whether the platform can also advance their own research or careers. The evidence is mixed. Before and during the pandemic, studies by Costas Comesana and others found little correlation between the attention a publication gets on social media and its number of citations—the usual measure of scholarly impact.

Many universities today consider scientists’ public service activities in professional evaluations as well, but there is no consensus about the role metrics involving social media should play in this. The Altmetric Attention Score debuted in 2012 as a way to summarize the attention drawn by a research paper across a variety of communication venues; in a single, weighted number, it amalgamates counts of Twitter retweets and likes and mentions in news stories and policy documents, for example. But university tenure and promotion committees haven’t considered the scores—nor should they, say scholars of social media metrics. The Altmetric score covers venues too disparate to be meaningful for tenure decisions, Haustein says. And attention does not always translate into social impact: A scientist with lots of Twitter followers may be ignored by policymakers.

Haustein suggests, though, that scientists consider strategically presenting metrics from Twitter or other social media to highlight papers that mattered to audiences outside of academe. And Dean notes that Twitter can

offer researchers a way to build their professional reputations “by letting people know who you are and what you think.”

Even if social media metrics cannot replace citations and peer review to measure scholarly quality, Costas Comesana says, the new measures can serve as a complement and help researchers better understand how the public is perceiving, ignoring, or misunderstanding their work. “And that,” he says, “is where the thing gets more interesting.” ■

INSIGHTS

PERSPECTIVES

VOLCANOLOGY

Volcano-tectonic control of Cumbre Vieja

Unexpected features from the 2021 eruption might help forecast giant flank collapses

By **Pablo J. González**^{1,2}

The 2021 Cumbre Vieja volcano eruption started on 19 September 2021 and ended after 85 days and 8 hours, becoming La Palma's longest and most voluminous (more than 200 million m³) eruption in historical times. Because of the good monitoring effort, this eruption will allow the testing of a wide range of scientific ideas, from the importance of a possible 436-year-long supercycle of duration-decreasing eruptions to using the geophysical observations to understand how magma is stored and migrates within a vertically extended upper mantle and crustal magmatic system (1). These types of magmatic and volcanological information will transform volcano eruption hazard assessment and long-term planning (2). Moreover, a key research question remains as to why this eruption did not create a catastrophic volcano flank collapse as perhaps expected (3). The answer may be tied to its distinct volcano-tectonic features and, in particular, an unexpected fissure system

that opened during the eruption's last phase.

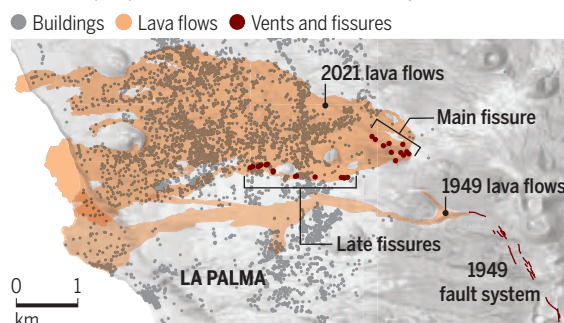
Many ocean island volcanoes grow at formidable rates over short geological periods, collapsing catastrophically to form many-kilometers-wide amphitheater-shaped valleys and causing tsunamis. The low recurrence rate of these events obscured the origin of the valleys until the identification of debris avalanche deposits around Hawai'i (4) and less-well-known studies of underground ge-

ology in the Canary Islands (5). Moreover, it was the catastrophic collapse accompanying the 1980 Mount St. Helens eruption (6) that revealed the sheer scale of this volcanic hazard. Among worldwide volcanoes, Cumbre Vieja has long been identified as a candidate tsunamigenic source, with models supporting variable transoceanic potential (3, 7). Since the 1980s, progress has been made, but flank collapse-triggering mechanisms and feedbacks with active magmatic systems remain elusive.

Cumbre Vieja is a volcano with a major 2000-m-above-sea-level-high topographic ridge elongated in a north-south direction—a pattern largely interpreted as the consequence of repeated intrusions and eruptions along the ridge. Over the past 150 to 125 thousand years (kyr), the volcano has rapidly grown, resulting in steep-sided volcano flanks. Two decades ago, Day *et al.* (8) presented a detailed volcano-structural map of the volcano. The picture was clear—during the past 7 kyr, its western flank has started to show signs of incipient volcano instability. The key elements were a well-developed pattern

Volcano-tectonic features of Cumbre Vieja

The main lava-erupting fissure is in a different direction than the later formation of fissures. These may be key to understanding flank collapse processes in this sort of volcanic system.



Unexpected effusive vents and fractures opened during the late phase of the 2021 Cumbre Vieja volcano eruption in La Palma, Canary Islands.

of recent northwest-southeast and east-west fractures and eruptive fissure systems and the reinterpretation of an unusual 3-km-long normal faulting system with a maximum 4-m throw movement that developed during the last summit eruption in 1949.

The 2021 eruption bursted along a north-west-southeast fissure because of the emplacement of a largely westerly dipping magmatic feeding dike, revealed by satellite radar interferometry and precise relocated seismicity (9). Notably, the 2021 eruptive fissure occurred along the northwestern continuation of the unusual 1949 normal faulting system and at the location of a previous eruptive site (Hoya de Tajogaite) with the same orientation (see the figure). Therefore, the 2021 magmatic pathways must be added to existing evidence for instability from geological structural studies (8); deformation during the intereruptive period (10); detailed gravity and electrical resistivity surveys (11, 12); and the reappearance of erupted oceanic sediment xenoliths, which indicate the role of a rheologically layered crust (13). Moreover, the Cumbre Vieja western volcano flank, luckily, seems to have not yet reached runaway conditions.

But, like a blockbuster thriller movie, this Cumbre Vieja eruption left the biggest surprise for its last act. In mid- to late November, coinciding with an increase in the number of earthquakes, a complex set of fractures and slumps broke apart the northeastern flank of the 2-month-long active cone developed at the eruptive site. A north-northeast-south-southwest (NNE-SSW) fissure at the summit rapidly grew a large 100-m-high cone in less than 2 days. Almost simultaneously, short-lived vents opened along a roughly east-west trending direction downslope within 2 km of the summit active cone. Over the next week, multiple small vents and en-echelon fissures appeared at 1- to 3-km distance from the main fissure site and along that “late fissure” system. The spatial-temporal relationship will have to be carefully analyzed, but notably on 4 December, a well-developed graben opened near the summit of the active cone, and several more eruptive sites opened at the far west end of the late fissure system, feeding a more voluminous lava flow.

The puzzling aspect of this set of later events is twofold—that there is an appar-

ent lack of large-magnitude and wide-area geodetic signals associated with such strong ground fracturing events and that this late fissure system has an unexpected orientation with respect to the focused NNW-SSE activity of the previous 2 months of eruptive activity. The late fissure system is roughly 100 m wide and hosts eruptive fissures with variable orientations. Those multiple fissures must have opened and erupted lava at low magmatic pressures because some fissures developed extremely short—10- to 20-m-long—lava flows. Those volcano-tectonic structural changes should be critically assessed as to whether they released magmatic and/or gravitational volcano flank stresses.

Although it is still too early to provide a completed set of interpretations for all of the volcano-tectonic observations for the 2021 Cumbre Vieja eruption, exploring complex volcano-tectonic stress fields should be a possible venue for understanding the timing, occurrence, and character of this eruption. Taking it further, the volcano-tectonic control of this eruption will certainly help advance our knowledge of elusive magmatic and tectonic feedbacks that influence eruptive activity. Particularly revealing should be the sequence of events that resulted in there being no catastrophic collapse, as it should inform how to assess the likelihood of these for other systems. Finally, the detailed study of this eruption should contribute to answering the open question of what physical mechanism triggers giant catastrophic volcano flank collapses, such as those that are up to orders of magnitude larger than the recent and deadly 2018 Anak Krakatau volcano flank collapse (14). ■

REFERENCES AND NOTES

1. A. Klügel *et al.*, *Earth Planet. Sci. Lett.* **236**, 211 (2005).
2. M.-A. Longpré, *Science* **374**, 1197 (2021).
3. S. N. Ward, S. Day, *Geophys. Res. Lett.* **28**, 3397 (2001).
4. J. G. Moore, US Geological Survey Professional Paper 501-D, D95 (1964).
5. T. Bravo, *Bol. R. Soc. Esp. Hist. Nat.* **60**, 93 (1962).
6. P. W. Lipman, D. R. Mullineaux, US Geological Survey Professional Paper 1250 (1981).
7. S. M. Abadie, J. C. Harris, S. T. Grilli, R. Fabre, *J. Geophys. Res. Oceans* **117**, C05030 (2012).
8. S. J. Day, J. C. Carracedo, H. Guillou, P. Gravestock, *J. Volcanol. Geotherm. Res.* **94**, 135 (1999).
9. S. Atzori, A. Lomax, “InSAR and relocated seismicity analysis” (2021); <https://twitter.com/SimoneAtzori73/status/1441037469466640389>.
10. P. J. González, K. F. Tiampo, A. G. Camacho, J. Fernández, *Earth Planet. Sci. Lett.* **297**, 545 (2010).
11. A. G. Camacho *et al.*, *J. Geophys. Res.* **114**, B05411 (2009).
12. X. Garcia, A. G. Jones, *J. Geophys. Res.* **115**, B07104 (2010).
13. J. S. Collier, A. B. Watts, *Geophys. J. Int.* **147**, 660 (2001).
14. L. Ye *et al.*, *Sci. Adv.* **6**, eaaz1377 (2020).

ACKNOWLEDGMENTS

This work was supported by the Spanish Ministerio de Ciencia e Innovación research project COMPACT (proyecto PID2019-104571RA-I00 de investigación financiado por MCIN/AEI/10.13039/501100011033) and a 2020 Leonardo Fellowship Grant for Researchers and Cultural Creators, BBVA Foundation.

¹Volcanological Research Group, Department of Life and Earth Sciences, Instituto de Productos Naturales y Agrobiología, Consejo Superior de Investigaciones Científicas, La Laguna, Canary Islands, Spain. ²COMET, Department of Earth, Ocean and Ecological Sciences, School of Environmental Sciences, University of Liverpool, Liverpool, UK. Email: pabloj.gonzalez@csic.es

CORONAVIRUS

Effective surveillance of variants

Community testing studies can provide insights as SARS-CoV-2 evolves

By Adam J. Kucharski¹ and Cheryl Cohen²

As countries move into a third year of the COVID-19 pandemic, they continue to face the threat of novel variants and the challenge of monitoring them. In England, the Real-time Assessment of Community Transmission (REACT-1) study has been tracking community infection levels since May 2020, routinely collecting samples from hundreds of thousands of randomly selected individuals and testing for the presence of severe acute respiratory syndrome coronavirus 2 (SARS-CoV-2). On page 1406 of this issue, Elliott *et al.* (1) show a rapid increase of the Omicron variant in REACT-1 data during December 2021, estimating that this variant grew from comprising 10% of all infections to 90% in just over a week. By contrast, it took around a month for Delta to reach such prevalence. The REACT-1 program demonstrates the value of community surveillance programs as immunity builds and new variants emerge.

Whereas the emergence of the Delta variant of SARS-CoV-2 was accompanied by scenes of overwhelmed hospitals in India, the initial identification of Omicron in South Africa was not followed by the same severe impact of earlier waves. Faced with a new variant, it is crucial to understand its ability to spread and cause disease. Early analysis of clinical data in South Africa suggested that Omicron was associated with a lower risk of hospitalization than other circulating SARS-CoV-2 variants, using a surveillance system that links case and hospital records with genome data (2). Even so, it is increasingly hard to extrapolate conclusions about emerging variants because of variations in population immunity through natural infection and vaccination across different countries.

¹Centre for Epidemic Preparedness and Response, London School of Hygiene and Tropical Medicine, London, UK.

²Centre for Respiratory Diseases and Meningitis, National Institute for Communicable Diseases of the National Health Laboratory Service, Johannesburg, South Africa. Email: adam.kucharski@lshtm.ac.uk

Four major variants have now circulated in South Africa, causing large epidemics (3), which means that there are multiple different combinations of prior infection and vaccination that individuals may have had. By contrast, a larger proportion of immunity in Europe and the United States has been derived from vaccination (4), further complicating the extent to which researchers can obtain generalizable insights. Moreover, symptom-based surveillance systems, like the ones used to analyze early trends in South Africa, may not reflect mild or asymptomatic infections in the community. Throughout the pandemic, additional data have been required to understand the true relationship between observed disease and background levels of infection.

Elliott *et al.* highlight the value of systematic repeated community testing that samples individuals regardless of symptoms. Their framework of prospective surveys of similar structure allowed comparison to age-specific trends observed in previous waves and before the availability of vaccination in these age groups. They show that as vaccination coverage increased among adolescents aged 12 to 17 years, the burden of infection for Delta shifted to unvaccinated younger age groups. Moreover, the drive to ensure that older age groups received booster doses was also followed by reduced infection levels among older people. The approach of random community sampling is resource intensive; Elliott *et al.* invited more than 800,000 individuals to participate during late November and early December 2021, with ~97,000 samples collected and analyzed, of which 1192 were positive. However, these efforts allow quantification of community transmission dynamics, including among asymptotically infected individuals. These data are critically important to properly understand the underlying dynamics of SARS-CoV-2, particularly during periods of sudden epidemic growth or decline. Such studies will become yet more valuable as the relationship between infection and disease continues to change: Countries with growing levels of immunity against SARS-CoV-2 will have an increasing proportion of infections that are vaccine breakthrough or reinfections, with a decreasing fraction of infections having symptoms or severe illness.

Since 2020, there have been several examples of routine testing regardless of symptoms in specific populations, including the SIREN and SAFER studies of UK health care workers (5, 6) and the National Basketball Association testing program in the United States (7). Such studies can provide valuable epidemiological insights, including viral shedding dynamics and the characteristics of reinfection. However, it is increasingly

challenging to generalize results from these subpopulations. The exposure and immunity history of groups such as health care workers can be substantially different to that of the wider community (6), and in the United Kingdom, SARS-CoV-2 transmission has become increasingly focused in unvaccinated younger age groups, which are not included in workplace cohorts. Community testing studies therefore provide an important complement to other data collection efforts.

Although Elliott *et al.* provide an overview of early Omicron dynamics, much of the value of REACT-1 lies in its continuous nature, allowing it to proactively collect monthly data on emerging variants. Relying on reactively implemented research to understand epidemics can lead to delayed—and less useful—insights, as has happened during previous health emergencies (8). Given the potential

“...it is increasingly hard to extrapolate conclusions about emerging variants because of variations in population immunity...”

for the emergence of further variants with greater immune escape in the future, routine community surveillance will be important to provide insight into the causes of changing infection dynamics. The population growth rate of a new variant can be influenced by multiple factors: the ability of the virus to spread between hosts, the social interactions of the groups within which it is spreading, and the extent to which prior vaccination or infection protects against the new variant. Untangling these factors will continue to be essential in developing effective policies to protect against SARS-CoV-2 variants.

Uncertainty about the future evolutionary path of SARS-CoV-2 means that it will be crucial to use triangulation of multiple lines of evidence when analyzing variant characteristics (9). In addition to the REACT-1 infection testing study and the accompanying REACT-2 study that tracks antibody concentrations, the UK Office for National Statistics runs a community testing survey and antibody study. There is also routine testing data from symptomatic and hospitalized cases, plus data from contact tracing studies (10). Triangulation using combinations of these data can help make sense of epidemiological patterns in real time. For example, in early May 2021, there was an apparent discrepancy between estimated growth in Delta cases, which suggested substantial spread in the community (11), and initial transmission es-

timates from contact tracing data (10), which did not show Delta having a transmission advantage over Alpha. In REACT-1, however, it was observed that two of three sequenced samples in London during early May 2021 were Delta, supporting the hypothesis of extensive community spread (12). Although there will always be a data gap for the early phase of the pandemic, community studies have provided a valuable resource for our understanding of SARS-CoV-2 since.

There is also potential for better triangulation with international data sources. Traveler screening has been another example of routine testing regardless of symptoms (13). Both for Omicron and earlier variants, such data provided early insights into the geographic distribution of spread, in some instances with imported infections coming from countries yet to report the variant domestically (14). However, logistical and privacy challenges have, to date, limited the sharing and combination of these datasets, reducing the potential for real-time estimation of variant distribution and prevalence globally.

As well as supporting the response to COVID-19 and future pandemics, carefully designed community studies can also help us rethink familiar infections. For example, research involving routine testing has revealed the role of asymptomatic and undetected infections during influenza epidemics (15). As SARS-CoV-2 restrictions are lifted, many countries could see increased circulation of previously suppressed seasonal respiratory viruses such as influenza virus and respiratory syncytial virus. Expanding testing in platforms such as REACT to include these seasonal viruses would provide a better view of the underlying dynamics of viral transmission, as well as proof of concept for similar potential surveillance programs in the future. ■

REFERENCES AND NOTES

1. P. Elliott *et al.*, *Science* **375**, 1406 (2022).
2. N. Wolter *et al.*, *Lancet* **399**, 437 (2022).
3. J. Kleynhans *et al.*, *Emerg. Infect. Dis.* **27**, 3020 (2021).
4. L. A. C. Chapman *et al.*, *Euro Surveill.* **27**, 2101038 (2022).
5. V. J. Hall *et al.*, *Lancet* **397**, 1459 (2021).
6. C. F. Houlihan *et al.*, *Lancet* **396**, e6 (2020).
7. S. M. Kissler *et al.*, *N. Engl. J. Med.* **385**, 2489 (2021).
8. M. Koopmans *et al.*, *Lancet Infect. Dis.* **19**, e59 (2019).
9. M. R. Munafò, G. Davey Smith, *Nature* **553**, 399 (2018).
10. Public Health England, Investigation of SARS-CoV-2 variants: Technical briefings, Technical briefing 11; <https://bit.ly/3pPsb7F>.
11. A. J. Kucharski, N. Davies, R. Eggo, S. Funk, “CMMD COVID-19 Working Group: Modelling importations and local transmission of B.1.617.2 in the UK, 12 May 2021” (Scientific Advisory Group for Emergencies, 2021).
12. S. Riley *et al.*, “REACT-1 round 11 report: Low prevalence of SARS-CoV-2 infection in the community prior to the third step of the English roadmap out of lockdown.” Working paper, Imperial College London (2021).
13. Radio New Zealand (RNZ), “Covid-19 update: 19 new imported cases in past three days,” *RNZ*, 3 January 2021.
14. European Centre for Disease Prevention and Control (ECDC), “Threat Assessment Brief: Implications of the emergence and spread of the SARS-CoV-2 B.1.1.529 variant of concern (Omicron) for the EU/EEA” (ECDC, 2021).
15. C. Cohen *et al.*, *Lancet Glob. Health* **9**, e863 (2021).

10.1126/science.abo4257



HYPOTHESIS

The question of animal emotions

Do animals, including invertebrates, have felt emotions and does this morally matter?

By **Frans B. M. de Waal¹** and **Kristin Andrews²**

If the UK joins a handful of other nations to recognize the sentience of invertebrates, such as cephalopod mollusks and decapod crustaceans, by, for example, prohibiting the boiling of live lobsters, this will be based on evidence that emotions and felt experiences (i.e., sentience) are not limited to animals close to humans, such as the mammals. This topic has been heavily debated in both affective neuroscience (how to define an emotion?) and philosophy (what is the moral relevance of animal experiences?), but a consensus on the criteria for and implications of recognizing animal sentience seems to be emerging (1).

Over a decade ago, the same debate revolved around fish. Do fish feel pain? It was thought that these animals only had nociception—i.e., unconscious reactions to noxious stimuli mediated by the peripheral nervous system, such as when humans reflexively withdraw a hand from a hot stove before they are aware of the burn. Fish may react to pain, it was thought, but without any associated feelings. Because nociception does not necessarily reach the central nervous system and consciousness, it does

not amount to sentience. Sentience in this case requires valenced experiences—i.e., experiences judged by the organism as either attractive/positive or aversive/negative. This debate was settled when fish were found to learn from encounters with negative stimuli by avoiding dangerous locations. The best explanation is that fish remember these locations because they felt and neuronally processed aversive experiences (2).

The same logic has been followed for arthropods, such as crabs, which in experiments learn to avoid locations where they have been shocked. Nociception cannot explain associative learning because there is no motivation to avoid the stimulus if it does not feel bad at the time. The negative experiences underlying their behavior may even be integrated with other evaluations, because hermit crabs need stronger shocks to evacuate a high-quality shell that protects their abdomen than a poor-quality shell (3). If valenced experiences guide behavior in complex ways, the central nervous system must be involved. In vertebrates, the typical pathway to do so is through the emotions. Emotions are temporary physical and mental states that prepare the organism for adaptive action. The suggestion from studies on crabs, then, is that arthropods have felt emotions, hence they are sentient.

After a long period of Cartesian denials of animal emotions owing to doubts about what they feel, or even skepticism that they feel at

There is increasing evidence that some invertebrates, such as lobster, are sentient and experience emotions. This means they should be killed ethically, rather than being boiled.

all, most affective scientists have settled on a distinction between feelings and emotions. Feelings are private conscious states that are not publicly observable and hence are inaccessible to science, whereas the emotions are measurable physiological and/or neural states that are often reflected in behavior. Affective science concentrates on the emotions of animals while generally staying neutral on their associated feelings (4).

The distinction between emotions and feelings is less relevant in our species because humans communicate feelings by means of language. Humans accept verbal statements about internal states as evidence of those states, and conversely sometimes equate the absence of language with the absence of those states. Until well into the 1980s, this argument was even extended to members of our own species. Skeptical that preverbal human babies felt anything, the medical profession freely subjected them to surgery without anesthesia (5). Verbal reports of private states are not the same as the states themselves, however, but rather they are a source of evidence. In relation to human babies, the linguistic focus has since been abandoned and their pain is taken into account. We think it is time for the same step in relation to nonhuman animals. To deny them felt emotions does not seem a reasonable position given the fundamental similarity between the nervous systems of humans and other animal species and the shared evolutionary history that has promoted similar emotionally mediated reactions to the environment and social partners.

Affective neuroscience relies on animals to study which brain areas and neural circuits are activated during specific emotional reactions, such as fear, anger, disgust, and attraction. These findings are often extended to humans. This work began with observations of animal behavior suggestive of emotional states. For example, the face—the proverbial window on human emotions—expresses emotions through similar muscular contractions to those in other primates owing to a homologous facial musculature, which is nearly indistinguishable between humans and chimpanzees (6). Obviously, increasingly distant species have increasingly different expressions of the emotions, but research has found that, for example, physiological changes, lowered temperature of the extremities, and activation of the amygdala during fear are notably similar in fearful

¹Psychology Department, Emory University, Atlanta, GA, USA. ²Philosophy Department, York University, Toronto, ON, Canada. Email: dewaal@emory.edu; andrewsk@yorku.ca

rats and fearful humans. Even outside of the mammals, continuities in the expression and underlying physiology of the emotions are observed. Research in comparative endocrinology, for example, finds a role for glucocorticoids (stress) and an oxytocin-/vasopressin-type peptide system (reproduction, bonding) across a wide range of animals that includes invertebrates (7).

Behavioral tools to evaluate emotional responses have been sharpened, too, such as the cognitive bias test. In this paradigm, investigators first manipulate the animals' environment, making it rich versus impoverished, or calm versus disturbing. Then they train subjects on two different stimuli, such as a high versus a low tone, which triggers either positive or negative reinforcement. By subsequently presenting the animals with an ambiguous stimulus, such as an intermediate tone, they can gauge their optimism (approach) or pessimism (avoidance) about the stimulus. The typical outcome in mammals and birds has been that a poor environment negatively affects their expectations about the world (8).

This innovative testing paradigm, which offers an index of the animals' felt emotions, was recently extended to honey bees. Bees subjected to vigorous physical agitation (shaking) to simulate a predatory attack proved less willing to explore new tastes, and hence were negatively biased by their experience. They also showed reduced amounts of hemolymph dopamine, octopamine, and serotonin. Changes in these neurotransmitters mark anxiety or depression in humans. In any mammal, a pessimistic behavioral response associated with physiological indications of stress would be taken as a sign of negative emotions. The same logic should be applied to insects (9).

Animals are exquisitely sensitive to signs of emotion in conspecifics, resulting in empathic reactions, such as consolation of distressed individuals by means of body contact, and synchronized behavior, such as when the fear and alarm of one individual arouses fear and alarm in nearby conspecifics (10). When humans show empathy, be it through a hug or verbally with "I feel your pain," this is perceived as them also experiencing the other's emotion—and if they do not show the appropriate emotional reactions, the empathy is not judged to be genuine. In a recent study of prairie voles, the stress of another individual increased its mate's circulating corticosterone concentrations and led to a comforting response that could be blocked by an oxytocin receptor antagonist injected into the anterior cingulate cortex. This suggests an empathy response regulated by neural mechanisms that are conserved between rodents and humans (11).

Even though feelings can (as yet) not be directly demonstrated in other animals, these findings strongly hint at their existence. Recognizing that there is only indirect evidence of human feelings as well—humans do not directly experience what other people feel—it seems appropriate to adopt a stance of consistency and evolutionary parsimony such that similar emotional expressions and processes in related species call for similar psychological descriptions when it comes to sentience. The frequent exhortation to avoid anthropomorphic language is often misguided, especially for species that are evolutionarily close to humans, because it forces us into linguistic distinctions between their behavior and ours that remain unsupported by evidence for an actual distinction. Warnings of anthropomorphism assume that there are stark differences between humans and animals, an assumption that is questionable given that humans are animals (12, 13). Although every animal species is distinct, science recognizes fundamental similarities when it comes to neurophysiology, cognition, emotions, and sentience.

It is not hard to see that the denial of animal emotions, and by extension animal feelings, has been morally convenient during human's history of animal exploitation. Conversely, their recognition is bound to shake up our moral decision-making. This is because sentience is widely taken to be sufficient for what ethicists call moral standing, or the status of having one's interests morally matter. What this means in practice is that to act morally, a person must take into account those individuals with moral standing. Although we are used to thinking about how our actions affect other humans, recognizing widespread animal sentience requires us to also notice—and consider—our impact on other species. This way, animal sentience is bound to complicate an already complex moral world.

If crabs experience emotional states, then they have an interest in these states being positively valenced. Current research indicates that a wide range of animals have interests in avoiding felt pain, and that they would not consent to painful procedures if given the opportunity. This makes pain a harm to them, and thus places a moral obligation on humans to recognize that harm and to avoid causing it if possible.

With an increasing number of species whose emotional states have moral standing, what follows about how exactly we should treat them? Here there remain more questions than answers. To make progress requires knowing the range and variety of animal emotions and feelings. It is not much of a stretch to presume that for many

species, avoidance of pain is just one interest among many. For example, animal empathy research may find that cows are distressed by seeing their calf in pain, an additional interest that goes beyond the desire to avoid their own pain. These added interests also need to be considered when making decisions about good husbandry and agricultural practices (14). With more interests among more species come more pronounced and numerous conflicts of interest between humans and other animals.

Philosophical ethics offers theories and tools for managing conflicts of interests, although without understanding the wide range of features that may be morally relevant, the tools are only of limited help. For this reason, we think that greater integration between ethics and affective science by ethologists, comparative psychologists, and neuroscientists is needed to reach moral conclusions. This integration cannot come from ethicists alone but requires students of animal behavior to engage with the ethical implications of their work, which until now most have been reluctant to do (15).

When the medical community recognized infant pain in the 1980s, it was because the evidence was so overwhelming that physicians could no longer act as if infants are immune to pain. A similar point is being reached where invertebrates can no longer be treated as if they only have a nociceptive response to harmful stimuli. If they can no longer be considered immune to felt pain, invertebrate experiences will need to become part of our species' moral landscape. ■

REFERENCES AND NOTES

1. J. Birch *et al.*, *Review of the Evidence of Sentience in Cephalopod Molluscs and Decapod Crustaceans* (London School of Economics and Political Science, 2021).
2. V.A. Braithwaite, F.A. Huntingford, *Anim. Welf.* **13**, S87 (2004).
3. M. Appel, R. W. Elwood, *Appl. Anim. Behav. Sci.* **119**, 120 (2009).
4. D.J. Anderson, R. Adolphs, *Cell* **157**, 187 (2014).
5. E. N. Rodkey, R. Pillai Riddell, *J. Pain* **14**, 338 (2013).
6. A. M. Burrows, B. M. Waller, L. A. Parr, C. J. Bonar, *J. Anat.* **208**, 153 (2006).
7. H. Ando, K. Ukena, S. Nagata, Eds., *Handbook of Hormones Comparative Endocrinology for Basic and Clinical Research* (Elsevier, ed. 2, 2021).
8. M. Mendl, O. H. P. Burman, R. M. A. Parker, E. S. Paul, *Appl. Anim. Behav. Sci.* **118**, 161 (2009).
9. M. Bateson, S. Desire, S. E. Gartside, G. A. Wright, *Curr. Biol.* **21**, 1070 (2011).
10. F. B. M. de Waal, S. D. Preston, *Nat. Rev. Neurosci.* **18**, 498 (2017).
11. J. P. Burkett *et al.*, *Science* **351**, 375 (2016).
12. F. B. M. de Waal, *Philos. Top.* **27**, 255 (1999).
13. K. Andrews, *How to Study Animal Minds* (Cambridge Univ. Press, 2020).
14. S. Monsó, J. Benz-Schwarzburg, A. Bremhorst, *J. Ethics* **22**, 283 (2018).
15. C. E. Webb, P. Woodford, E. Huchard, *BioEssays* **42**, 2000030 (2020).

Giant electromechanical effects in polymers

A four-ingredient polymer chain has record-breaking piezoelectric capability

By Zhong-Xia Wang and Wei-Qiang Liao

Polymers can be found everywhere from natural cellulose to synthetic plastics. They are known for being pliable and chemically stable. Ferroelectric polymers, one of the classical functional polymers, are considered an important branch of piezoelectric materials, which can produce electric energy in response to mechanical stress. Achieving simultaneously a large electromechanical coupling factor (k_{33}) and a large piezoelectric coefficient (d_{33}) in such materials is desirable for electromechanical devices (1) such as medical imaging ultrasonic probes, which require high image resolution and large penetration depth. However, ferroelectric polymers tend to exhibit less-than-desirable k_{33} and d_{33} values, far behind those of widely used ferroelectric ceramics and crystals. On page 1418 of this issue, Chen *et al.* (2) describe a poly(vinylidene fluoride) (PVDF)-based tetrapolymer whose electromechanical performance is superior to that of the best piezoelectric $\text{Pb}(\text{ZrTi})\text{O}_3$ (PZT) ceramics.

PVDF is the semicrystalline homopolymer of vinylidene fluoride (VDF), whose piezoelectric and ferroelectric properties were discovered around 1970 (3). PVDF has five different crystalline phases: α , β , γ , δ , and ϵ . It also has three different types of polymer chain conformations: TTTT, TG^+TG^- , and $\text{T}_3\text{G}^+\text{T}_3\text{G}^-$, where T stands for “trans” (the substituents of two adjacent carbon atoms are 180° apart) and G^\pm stands for “gauche” (the substituents are $\pm 60^\circ$ apart) (4). A ferroelectric form of PVDF in the β phase with the TTTT chain conformation is known to have the highest piezoelectric performance. Certain processing conditions such as mechanical stretching are usually needed to obtain the β phase, which can show a k_{33} of 27% and d_{33} of -28 pm/V (5). These electromechanical performances, however, are much lower than those of PZT ceramics, which can show a k_{33} up to 80% and a d_{33} up to 800 pm/V (6).

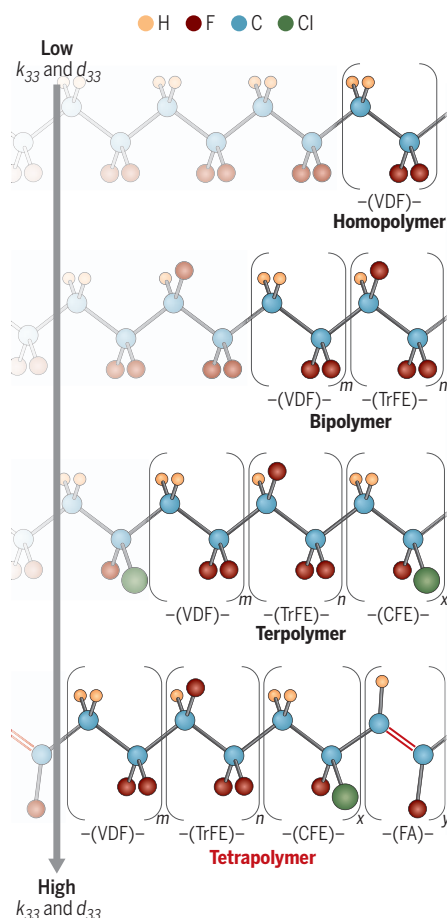
Although PZT ceramics are the most commonly used piezoelectric material, they contain lead, which limits their application in implantable biomedical devices such as energy harvesters on heart pacemakers. In com-

parison, PVDF is lead-free and has the inherent advantages of mechanical flexibility, light weight, low acoustic impedance, and easy processing over its inorganic counterparts. However, its low electromechanical performance substantially limits its applications.

To improve electromechanical performance, various PVDF-based copolymers have been developed (see the figure). PVDFs copolymerized with trifluoroethylene (TrFE)

Tetrapolymer achieves high piezoelectricity

Different random copolymers of ferroelectric poly(vinylidene fluoride) (PVDF) have been developed to progressively improve the piezoelectric performance. A substantial enhancement of electromechanical coupling factor k_{33} and piezoelectric coefficient d_{33} was achieved in poly(vinylidene fluoride-trifluoroethylene-chlorofluoroethylene-fluorinated alkyne) tetrapolymer, here written as P(VDF-TrFE-CFE-FA).



represent the most well-explored option. The TrFE unit has a larger size than the VDF, which restricts the formation of G conformation and imposes the TTTT chain conformation required for the β phase, regardless of the processing conditions (4). Moreover, a P(VDF-TrFE) chain shows a higher crystallinity (the proportion of crystalline regions in the polymer) than PVDF, resulting in a modest improvement of k_{33} and d_{33} to 37% and -38 pm/V (5). Recently, the morphotropic phase boundary, a phenomenon to enhance piezoelectricity, was reported in P(VDF-TrFE) with 49 to 55 mol % VDF and a d_{33} of -63.5 pm/V (7).

Among inorganic ferroelectrics, relaxor ferroelectrics such as $\text{Pb}(\text{Mg}_{1/3}\text{Nb}_{2/3})\text{O}_3$ - PbTiO_3 are characterized by frequency dispersion of the dielectric response resulting from the presence of local structural heterogeneity at the nanoscale. These relaxor materials have been found to exhibit stronger electromechanical responses than conventional ferroelectrics such as PZT ceramics (8). Modifying P(VDF-TrFE) by introducing a third bulky monomer can result in relaxor ferroelectric terpolymers, as seen in P(VDF-TrFE-CFE), where CFE stands for chlorofluoroethylene (9). The incorporated CFE increases the distance between polymer chains and modulates some TTTT chain conformations into TG^+TG^- and $\text{T}_3\text{G}^+\text{T}_3\text{G}^-$. With the application of electric fields, the changes between different conformations induce a high k_{33} of 55% (9) and an exceptional d_{33} of -400 pm/V (10), which are larger than those of the pristine P(VDF-TrFE), albeit still lower than those of high-end PZT ceramics. Moreover, a very high electric field (> 100 MV/m) is required, severely hindering their practical applications.

Chen *et al.* take this approach one step further by including a fourth monomer to boost the electromechanical performance of P(VDF-TrFE-CFE). They engineered a small amount of fluorinated alkyne (FA) monomer into P(VDF-TrFE-CFE) to achieve a relaxor ferroelectric tetrapolymer—P(VDF-TrFE-CFE-FA). The FA was incorporated from the dehydrochlorination of CFE unit in the terpolymer and offers a way to tune the chemical composition of the tetrapolymer, in contrast to the conventional direct polymerization of monomers. Through compositional optimization, they found that P(VDF-TrFE-CFE-FA), with a mol % share of 63 to 29.7 to 5.4 to 1.9, shows giant

electromechanical performances, with a k_{33} of 88% and a d_{33} of -1050 pm/V, while only under a low electric field of 40 MV/m. This result greatly outperforms those of state-of-the-art PVDF-based polymers and even the best PZT ceramics.

Unlike the commonly added bulkier monomer in PVDF copolymers, Chen *et al.* used an FA with a smaller size than VDF. They found that the small FA unit can be partially incorporated in the crystalline region of P(VDF-TrFE-CFE-FA). This is distinct from the case of P(VDF-TrFE-CFE), where the bulky CFE is absent in the crystalline phase. Additionally, the smaller size of FA markedly decreases the barrier for the transformation among the TTTT, TG⁺TG⁻, and T₃G⁺T₃G⁻ chain conformations. This leads to a large electromechanical performance at low electric fields. Taking advantage of the distinctive features of polymers, the outstanding electromechanical performance suggests great potential for P(VDF-TrFE-CFE-FA) in applications that would be difficult for inorganic piezoelectrics to achieve. This includes functioning as low-field actuators for artificial muscles and soft robots (11) and as wearable force sensors for health care (12).

Chen *et al.* have demonstrated a major improvement of electromechanical performance achieved in a P(VDF-TrFE-CFE-FA) tetrapolymer, a breakthrough finding for ferroelectric polymers. An important task ahead is to explore its practical applications. Apart from FA, it is unclear whether other monomers can be incorporated into this ternary system to improve performance or impart other exotic properties. For example, chiral monomers, which are not superimposable on their mirror images, are good building units to construct ferroelectrics with intriguing optical properties (13). ■

REFERENCES AND NOTES

1. S. Zhang *et al.*, *Prog. Mater. Sci.* **68**, 1 (2015).
2. X. Chen *et al.*, *Science* **375**, 1418 (2022).
3. A. J. Lovinger, *Science* **220**, 1115 (1983).
4. P. Martins, A. C. Lopes, S. Lanceros-Mendez, *Prog. Polym. Sci.* **39**, 683 (2014).
5. K. S. Ramadan, D. Sameoto, S. Evoy, *Smart Mater. Struct.* **23**, 033001 (2014).
6. T. R. Shrout, S. J. Zhang, *J. Electroceram.* **19**, 113 (2007).
7. Y. Liu *et al.*, *Nature* **562**, 96 (2018).
8. F. Li *et al.*, *Science* **364**, 264 (2019).
9. F. Xia *et al.*, *Adv. Mater.* **14**, 1574 (2002).
10. S. Bauer, F. Bauer, in *Piezoelectricity Evolution and Future of a Technology*, W. Heywang, K. Lubitz, W. Wersing, Eds. (Springer, 2008), pp. 157–177.
11. L. Hines, K. Petersen, G. Z. Lum, M. Sitti, *Adv. Mater.* **29**, 1603483 (2017).
12. B. Stadlober, M. Zirkl, M. Irimia-Vladu, *Chem. Soc. Rev.* **48**, 1787 (2019).
13. H.-Y. Liu, H.-Y. Zhang, X.-G. Chen, R.-G. Xiong, *J. Am. Chem. Soc.* **142**, 15205 (2020).

ACKNOWLEDGMENTS

The authors acknowledge support from the Natural Science Foundation of China (grant nos. 21991141 and 91856114).

10.1126/science.abn7440

POLYMER MEMBRANES

Sieving gases with twisty polymers

Ladder polymers in three dimensions show promise as gas-separation membranes

By Peter M. Budd

Whether the goal is to capture carbon dioxide (CO₂), recover gas from an industrial process, or separate air into its components, there is a need for energy-efficient gas separations. An attractive option is the use of thin films, or membranes, that allow some gases to flow through more easily than others. Polymers are often used to fabricate these membranes because of their processability, but it has been a struggle to create something that can satisfy the levels of performance required for practical and large-scale operations. On page 1390 of this issue, Lai *et al.* (1) report how exceptional selectivity for one gas over another can be achieved in polymer membranes while allowing very easy passage of the chosen gas. The authors offer a way to improve and tune the selectivity of polymer membranes by simply “aging” them under ambient temperature and pressure over a long period of time (see the figure).

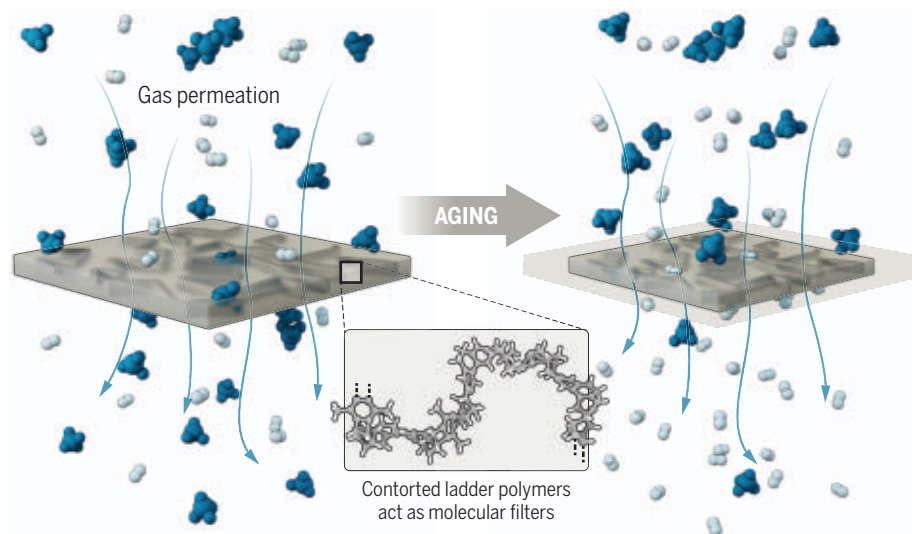
Different pairs of gases are of interest for distinct applications. The hydrogen (H₂)-ni-

trogen (N₂) gas pair is relevant, for example, to the recovery of hydrogen from ammonia purge gases and was the first large-scale commercial application of membrane gas separation. The H₂-methane (CH₄) and CO₂-CH₄ gas pairs are important in gas processing. The CO₂-N₂ gas pair is pertinent to carbon dioxide capture from industrial exhaust gases, and potentially from the air, to help mitigate global warming. The oxygen (O₂)-N₂ gas pair relates to air separation, either to throw away the oxygen and generate an inert gas for safety in potentially explosive situations or to enrich the oxygen for medical or other applications. Of course, real-world applications, in general, do not deal with just two gases, and there are also other gases present that may affect the functionality.

If gas molecules are to travel through a membrane, they first must enter the material, either by dissolution or by sorption. Then, the molecules must diffuse through the membrane, traveling along the little bits of space within the membrane material. In recent decades, chemists have designed polymers with an exceptionally large amount of

Aging a polymer membrane can shrink its pores

The rigid, twisty structure of certain polymers means that they cannot easily pack together. Lai *et al.* found that these irregularly shaped chains become more densely packed together as a result of thermal vibrations over time, similar to how one can more tightly pack a box of irregularly shaped toys by gently jiggling them. This aging process can be used to control the filtering efficiency of polymer membranes.



space around the macromolecules, sometimes referred to as free volume, which leads to higher gas permeabilities. In 2005 (2), the first gas permeation data were reported for a new class of polymers called polymers of intrinsic microporosity (PIMs), which were not only more permeable than the vast majority of other polymers but also reasonably selective. This discovery, alongside others, has since prompted membrane technologists to reevaluate the upper bounds of performance that are achievable with polymeric membranes for a range of gas pairs (3). Subsequent developments of PIMs have led to fresh updates of the upper bounds for some gas pairs in 2015 (4) and separations involving carbon dioxide in 2019 (5).

The high free volume of a PIM arises from two features of the main chain of the polymer that discourages it from filling space (6). A PIM has, at least predominantly, a ladder structure with limited ability to change conformation. A PIM also incorporates units that force the backbone into a contorted shape. The first PIMs, prepared using aromatic nucleophilic substitution reactions, used spiro-centers as “sites of contortion.” Subsequently, other types of chemistry have been explored, and a variety of motifs, including what is known as Tröger’s base and triptycene, have been used to create twisty polymer chains.

Recently, catalytic arene-norbornene annulation (CANAL) polymerization was introduced to generate contorted ladder polymers (7). In early examples, the contortions are essentially in two dimensions, leading to ribbon-like structures (8). Building on previous work, Lai *et al.* created dinorbornene monomers with an extra bend as the main ingredient for CANAL polymerizations alongside *p*-dibromo-*p*-xylene, which gave rise to three-dimensionally contorted polymers with high internal surface areas.

Chemical ingenuity enables polymers to be fashioned that trap free volume when formed into a membrane. But nature does all it can to squeeze out free volume over time, a process referred to as physical aging. Such aging usually leads to a reduction in gas permeability. However, this decrease in performance can be counteracted if the membrane can improve its selectivity as it physically ages. Thus, like a fine wine, the aging of a well-designed membrane can attain a better balance of properties over time. The three-dimensional (3D) CANAL polymer membranes prepared by Lai *et al.* show particularly good aging behavior such that over time, performances are achieved that surpass the state-of-the-art upper bounds for important gas separations such as hydrogen from methane. For exam-

ple, over 158 days, the H₂-CH₄ selectivity for one of the CANAL polymers increased from just seven—allowing seven H₂ molecules to pass through for every CH₄ molecule—to an impressive 621.

Permeation studies often focus on single gases, with the selectivity for a pair of gases calculated simply as a ratio of the pure-gas permeabilities. This may not reflect what happens with a mixture of gases, where one gas can affect the transport of another, either because it competes for space within the polymer or because it influences the properties of the polymer itself. For example, in the separation of carbon dioxide from methane, the selectivities obtained with mixed gases are generally lower than those predicted from single-gas measurements. In 2008, a CO₂-CH₄ mixed-gas upper bound was established (9), based on data then available in the literature. This limit is surpassed by the aged 3D CANAL polymers of Lai *et al.* Mixed-gas selectivities of nearly 50 were achieved for one of the CANAL polymers after being aged at ambient temperature and pressure for 190 days, with another CANAL polymer offering even higher selectivities, albeit with lower permeabilities. The mixed-gas limit can also be surpassed for previous PIMs if the polymerization conditions are controlled to optimize the range of topologies present in the polymer, which may include looped, branched, and network structures (10).

PIMs that exhibit beneficial aging provide a route to enhanced membrane performance. This research brings closer the prospect of much more efficient polymeric membranes for hydrogen and carbon dioxide separations. However, the behavior of high free-volume polymers in films with thicknesses greater than 40 μm, as used in studies of material properties, does not necessarily translate into the performance of films less than 2 μm thick that are commonly found in commercial membranes (11). The next phase of research is to optimize and control the performance of these types of polymers in very thin films, as well as to extend the permeation studies to more complex, commercially relevant gas mixtures. ■

REFERENCES AND NOTES

1. H. W. H. Lai *et al.*, *Science* **375**, 1390 (2022).
2. P. M. Budd *et al.*, *J. Membr. Sci.* **251**, 263 (2005).
3. L. M. Robeson, *J. Membr. Sci.* **320**, 390 (2008).
4. R. Swaidan, B. Ghanem, I. Pinnau, *ACS Macro Lett.* **4**, 947 (2015).
5. B. Comesaña-Gándara *et al.*, *Energy Environ. Sci.* **12**, 2733 (2019).
6. S. Bandehali *et al.*, *Separ. Purif. Tech.* **278**, 119513 (2022).
7. S. Liu, Z. Jin, Y. C. Teo, Y. Xia, *J. Am. Chem. Soc.* **136**, 17434 (2014).
8. H. W. H. Lai *et al.*, *Macromolecules* **52**, 6294 (2019).
9. Y. Wang *et al.*, *Mater. Today Nano* **3**, 69 (2018).
10. A. B. Foster *et al.*, *Macromolecules* **53**, 569 (2020).
11. A. B. Foster *et al.*, *J. Mater. Chem. A Mater. Energy Sustain.* **9**, 21807 (2021).

QUANTUM GASES

Photons think inside the box

Light confined to a sheet offers a glimpse into low-dimensional quantum gases

By Richard J. Fletcher^{1,2} and Martin Zwiernik^{1,2}

When the light from distant stars streams across the Universe, it remains unperturbed by other light rays going about their own business. Despite their reluctance to interact with each other, photons are nevertheless particles, carrying energy and momentum just like molecules, atoms, and electrons do. This raises the possibility of creating exotic new types of matter, made not from those familiar massive particles but from light itself. On page 1403 of this issue, Busley *et al.* (1) report creating a quantum gas made from photons and confining it to a flat two-dimensional space. Just like a gas made from atoms, this photonic gas undergoes Bose-Einstein conden-

“Busley *et al.* bring these advantages to quantum gases of light and explore a textbook scenario: a two-dimensional, spatially uniform gas of bosons.”

sation (BEC) and adjusts its shape to that of its container.

Busley *et al.* use two closely spaced mirrors, between which photons reflect back and forth. Most of each photon’s energy is devoted to its back-and-forth motion, leaving only a small amount of energy for its motion parallel to the mirrors. This restriction imbues each photon with an effective mass, meaning that it behaves like a conventional particle—albeit a very light one, with a mass only 10 millionths that of one electron. Crucially, in between the mirrors is a “dye,” which contains molecules whose role is to continually absorb and emit photons. Because this dye is held at room temperature, the photon gas settles into thermodynamic equilibrium at a balmy 300 K.

In previous experiments that used this setup, the light was confined in the

transverse direction by using curved mirrors (2). This enforced an energy cost for the photons to move away from the center, trapping them like marbles rolling in a bowl. In comparison, Busley *et al.* use special mirrors that are flat aside from a square raised ridge, along which the gap between the two mirrors is reduced. From a photon's perspective, this results in a confining wall, creating a box inside which the photons are trapped. In the context of ultracold atomic quantum gases, in the past decade box traps have emerged as a powerful tool (3). This is because the confined gas in a box trap has a uniform density, meaning that one may probe its properties much more cleanly than in inhomogeneous systems. Busley *et al.* bring these advantages to quantum gases of light and explore a textbook scenario: a two-dimensional, spatially uniform gas of bosons (see the figure).

The physics of bosons in two dimensions has a fascinating history. In 1967, Pierre Hohenberg (4) showed that thermal excitations in two-dimensional quantum gases destroy long-range order at any nonzero temperature. This destruction of long-range order typically precludes BEC, which requires all the particles in a gas to share the same quantum state. Similarly, one may naively expect superfluidity, in which the gas flows without friction, to also be impossible. Superfluidity may nevertheless emerge in two-dimensional gases through the Berezinskii-Kosterlitz-Thouless (BKT) transition (5, 6). This mechanism requires interactions between the particles, meaning that in the limit of vanishing interactions, the BKT transition occurs at absolute zero, which coincides with the temperature for BEC. This convergence of the BEC and BKT transitions was previously seen by using ultracold gases of atoms (7). However, experiments were not able to directly access the noninteracting regime because atomic gases rely on scattering between particles to mediate equilibration. By contrast, in the experiment by Busley *et al.* thermalization occurs indirectly through the dye, whereas the photons themselves do not interact with each other. This setup provides an almost perfect experimental realization of a noninteracting gas.

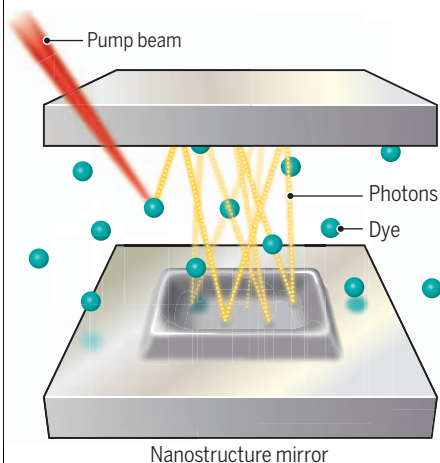
The question is which, if any, transition will occur in the two-dimensional photonic gas created by Busley *et al.*? The answer relies on two facts: The distance over which the particles' quantum states become

scrambled grows as the temperature falls, and any real experimental system is finite in size. This means that upon cooling, eventually, the distance required for the quantum states to scramble exceeds the system size. This restores the possibility for all photons to share the same state and BEC to occur.

Busley *et al.* directly observe the formation of a BEC of light as the number of photons in the box is increased. At first, the photons occupy many different energy states, according to the same Maxwell-Boltzmann distribution that governs more "ordinary" gases, such as the air around us. However, when the total number of photons reaches a critical value, the population of the thermally excited states satu-

Photons form a 2D quantum gas

Researchers have created a gas of photons confined to a two-dimensional space. A laser injects photons between two mirrors that restrict the photons' motion along the vertical direction but leave them free to explore the horizontal plane within the square wells. In between the mirrors, "dye" molecules continually absorb and emit the photons, which keeps the gas at a thermal equilibrium.



rates, and additional photons start to pile up in macroscopic numbers in the quantum mechanical ground state. In previous work that used photons (2), BEC occurred because of the harmonic trap providing confinement (8). Here, a BEC is formed in the uniform box trap solely because of the presence of confining walls, whereas it would never occur in the case of an unconfined, infinitely extended gas.

Given this newly created form of photonic matter, a natural question to ask is how it responds to applied forces. For example, can it be compressed? In contrast to an ordinary gas, a quantum degenerate gas should become more compressible as its density is increased. This unexpected effect occurs because as the gas approaches BEC,

the population of higher-energy states saturates first. This means that any further added particles predominantly populate low-energy states. These only contribute weakly to the pressure of the gas, which therefore remains approximately constant despite the increasing gas density. Busley *et al.* measure the compressibility of their photon gas by tilting one of the confining mirrors, which caused the photons to accumulate on one side like water in a tilted bowl. Initially, as more photons are added, the gas becomes harder to compress. However, this behavior changes dramatically as the photonic gas becomes quantum degenerate, and the compressibility is seen to sharply increase. This effect is purely a consequence of quantum statistics and is cleanly demonstrated here by using noninteracting photons.

This work heralds the advent of quantum gases of light trapped in uniform box potentials. The ability to probe a homogeneous system at constant density is invaluable for studying its transport properties, excitations, and behavior near phase transitions. The experiments of Busley *et al.* reproduce several paradigmatic textbook results for a noninteracting but thermalized quantum gas in two dimensions—a regime that is difficult to explore otherwise. Looking ahead, the most interesting phases of matter arise once the constituents of a system begin interacting with each other, meaning that an important goal for future experiments is to persuade the trapped photons to react to the presence of their neighbors. In other systems, this has been achieved by allowing different photons to interact with cotrapped atoms (9, 10). Alternatively, the authors suggest using a cavity medium whose properties presented to one photon are modified by the presence of a second. These developments in the ability to summon matter out of light offer exciting new perspectives, approaches, and surprises in the study of quantum gases. ■

REFERENCES AND NOTES

1. E. Busley *et al.*, *Science* **375**, 1403 (2022).
2. J. Klaers *et al.*, *Nature* **468**, 545 (2010).
3. N. Navon *et al.*, *Nat. Phys.* **17**, 1334 (2021).
4. P. C. Hohenberg, *Phys. Rev.* **158**, 383 (1967).
5. V. L. Berezinskii, *Sov. Phys. JETP* **34**, 610 (1971).
6. J. M. Kosterlitz, D. J. Thouless, *J. Phys. C Solid State Phys.* **6**, 1181 (1973).
7. R. J. Fletcher *et al.*, *Phys. Rev. Lett.* **114**, 255302 (2015).
8. V. Bagnato, D. Kleppner, *Phys. Rev. A* **44**, 7439 (1991).
9. L. W. Clark *et al.*, *Nature* **582**, 41 (2020).
10. T. Peyronel *et al.*, *Nature* **488**, 57 (2012).

ACKNOWLEDGMENTS

The authors acknowledge support from the National Science Foundation through the Center for Ultracold Atoms, Air Force Office of Scientific Research, and M.Z. acknowledges support through the Vannevar Bush Faculty Fellowship.

¹MIT-Harvard Center for Ultracold Atoms, Research Laboratory of Electronics, Massachusetts Institute of Technology, Cambridge, MA 02139, USA. ²Department of Physics, Massachusetts Institute of Technology, Cambridge, MA 02139, USA. Email: rlfletch@mit.edu



POLICY FORUM

DATA AND REGULATION

Will the European Health Data Space change data sharing rules?

Questions of consent and public interest research loom large

By **Mahsa Shabani**

In early 2020, the European Commission (EC) announced an ambitious plan for a common European Health Data Space (EHDS)—a legal, governance, data quality, and operability framework—to facilitate access to and reuse of health data to improve health care delivery, research, and policy-making. Preparatory work and research around the EHDS have identified challenges that negatively affect access to and reuse of health data, including limited data interoperability, fragmented rules for access to data for research, and barriers on individuals to exercise access to and control of their own health data. In response, the EC has embarked on adopting a new legislative proposal in early 2022, establishing a new health data access governance model that may become a model for other jurisdictions. This new regulatory landscape will affect data-driven biomedical research on the European Union (EU) and global level; hence, it is essential to shed light on regulatory complexities and discuss the path forward.

This plan to construct a common space to facilitate health data access and reuse has been promoted in light of the growing availability of health data and the clear benefits of broad access to existing health databases for research, clinical, and public health purposes. The importance of accessing data from the EHDS for training, validation, and testing of high-risk artificial intelligence systems has also been emphasized in the upcoming EU Artificial Intelligence Act. The benefits of facilitating data sharing in health have been further clarified during COVID-19, and efforts have been made to coordinate data sharing on the European level. However, the current data sharing ecosystem falls behind the needs of health care systems, which demand easy exchange of and access to various types of health data to improve quality of delivery of care and facilitate data-driven biomedical research.

The roadmap of the EHDS legislative proposal, published in 2021 for feedback and public consultation (1), recognized the negative impact of regulatory complexities on easy access to and reuse of health data and stressed the importance of examining

the coherence and complementarity of the health sector-specific EHDS with existing health sector-nonspecific data protection and data governance frameworks—namely, the EU General Data Protection Regulation (GDPR) and the proposed Data Governance Act (DGA).

The GDPR provides specific legal bases for the processing of data for various purposes, including for scientific research. Recent investigations into the implementation of the GDPR have shown that the rules related to consent requirements, the research exemption, and permissibility of international transfer of data have been far from clear or too restrictive at times, hindering collaborative international research (2). More recently, the proposal for the DGA set forth additional requirements for sharing data and making data available for reuse, including by individuals and on altruistic grounds. The proposal for the DGA also includes a new model of consent—namely, “data altruism” consent—raising questions about its relationship with the existing consent requirements under the GDPR (3). The European Council and European Parliament reached agreement in December 2021 on the proposal for the DGA. The next step is that this proposal should be approved by the Council, after which it will be turned to a regulation.

SPECIFIC CONSENT

The GDPR hinges on the principle of purpose limitation as one of the main principles of data protection, which requires controllers to limit collection and use of

Key elements in regulation of data sharing and the relevant provisions/guidance

	CONSENT	PUBLIC/GENERAL INTEREST	SCIENTIFIC RESEARCH
The General Data Protection Regulation (GDPR)	<ul style="list-style-type: none"> • Definition [Article 4 (11)] • Conditions for valid consent (Article 7) (“Free/freely given, specific, informed”) • Consent as a legal basis [Article 6 (1)(a), Article 9 (2)(a)] 	<ul style="list-style-type: none"> • Public interest as a legal basis for processing data [Article 6 (e) and Article 9 (2)(j)] • Leaving it to the member states to define the purposes of public interest (Recital 45) 	<ul style="list-style-type: none"> • “...the processing of personal data for scientific research purposes should be interpreted in a broad manner” (Recital 159)
Data Governance Act (proposal)	<ul style="list-style-type: none"> • Data altruism consent definition and conditions [Recital 38 and 39 proposal, Article 2 (10), chapter IV] 	<ul style="list-style-type: none"> • Nonexhaustive list of purposes of general interest including for healthcare and scientific research provided (Recital 35) 	<ul style="list-style-type: none"> • The examples of research falling under the general interest provided: “...including for example technological development and demonstration, fundamental research, applied research and privately funded research...” (Recital 35, first draft proposal)
Further guidance issued by the EU Data Protection Authorities [European Data Protection Board (EDPB) and European Data Protection Supervisor (EDPS)]	<ul style="list-style-type: none"> • Consent as a legal basis in the context of clinical trials not favored (EDPB opinion 3/2019) • Permissibility of consent for observational studies (EDPB 3/2020 guidelines related to COVID-19) • Not-permissibility of nonspecified consent in the context of research reiterated (EDPB 5/2020 guidelines on consent) • Importance of compatibility of data altruism consent by the consent requirement under the GDPR has been stressed (EDPS-EDPB 3/2021 joint opinion on DGA) 	<ul style="list-style-type: none"> • Referring to the case law: “necessity and the public interest imply a ‘pressing social need’, as opposed to largely private or commercial advantages.” (EDPS preliminary opinion on Scientific Research, 2020) 	<ul style="list-style-type: none"> • “The notion may not be stretched beyond its common meaning” and understands that “‘scientific research’ in this context means a research project set up in accordance with relevant sector-related methodological and ethical standards, in conformity with good practice” (EDPB 5/2020 guidelines on consent)

data to specific purposes (4). By contrast, the reality of building a health data space entails facilitating reuse and sharing of data collected from diverse sources for diverse purposes, while respecting the rights of individuals (5). Currently adopted data protection approaches have proven to be far from optimal, overemphasizing the role of individual consent as a legal basis for reuse of data (4). The GDPR requires consent, as a legal basis for data processing, to be specific to be considered valid, a condition that has proven to be difficult to meet when there are plans to share data for various and yet unknown purposes. The guidance provided by European data protection authorities so far has reiterated time and time again that so-called broad consent, meaning consent for any kind of unspecified future research purposes, cannot fulfill the consent requirement under the GDPR, even for data sharing related to COVID-19 research (see the table).

Furthermore, although there are some indications that further processing of data for research would be permissible, including one mentioned in Recital 50 of the GDPR, a broad interpretation of those rules to allow data sharing has not been considered suitable by the same authorities. This means that data sharing for research purposes may fall on a legal basis that is recognized under the GDPR other than consent, including those related to public interest and the

research exemption regime, which allow a broader use and sharing of data for scientific research purposes.

DATA SHARING FOR THE COMMON GOOD

Both the GDPR and the proposal for the DGA distinguish between data processing for the public and general interest and data processing for other purposes. In principle, it seems that regulators see scientific research as falling within the scope of public interest, allowing for a potentially more relaxed approach toward relevant data sharing requirements or some exemptions from data subjects rights, such as the right to restriction of processing, right to object to processing, and right to rectification (an individual can request that a company fix inaccuracies in personal information it holds about them) (6).

In practice, however, use of the so-called research exemption rules has generated uncertainties for data controllers. First, there has been little guidance on how scientific research for public interest and general interest must be defined under the GDPR and the proposal for the DGA, particularly when commercial entities are involved (7). Although according to the preamble of the GDPR “privately funded research” has been included as an example of scientific research, questions remain regarding implications for for-profit versus nonprofit privately funded research and how to determine the primacy of public interest to private and commercial interests. Besides the nature of funding, other aspects of research—such as the importance of research questions to the population under study,

models of benefit sharing, and equitable access to research databases—are yet to be considered when defining research in the public interest under the regulation.

Second, the implementation of the rules related to “research exemption” has been mainly left to the member states under the GDPR. This has led to the adoption of multiple approaches toward the use of public interest as a legal basis for processing data for research purposes, leaving a fragmented landscape across the European Union. According to a recent survey, 18 countries so far have developed specific national regulations related to scientific research and public interest, with only nine countries adopting specific provisions regarding research conducted by private sector organizations (8).

DATA ALTRUISM CONSENT

The proposal for the DGA has introduced a new consent model for so-called data altruism. Under this concept, data can be made voluntarily available by individuals or companies for reuse on altruistic grounds, without compensation, for purposes such as scientific research or improving public services. Although the concept of data altruism was just recently introduced in a legislation, broader ethical and sociological discussions around it have been around for some time.

The term “health-information altruists” was used to propose an approach in which individuals who have access to their health data can share them directly for research purposes with lower levels of privacy guar-

Metamedica, Faculty of Law and Criminology,
Ghent University, Campus Aula, Ghent, Belgium.
Email: mahsa.shabani@ugent.be

antees (9). Under this approach, the process of sharing data should still be fully transparent, and individuals must have an option to decide which subset of information they want to share. In addition, measures must be in place to punish users who attempt to re-identify individuals.

To date, such use of data altruism as a framework for data sharing has been limited to a very few examples, including in the context of Personal Genome Project(s), which pursue a citizen science approach in which individuals directly make their genomic and health-related data available for research (10). This is mainly because a higher threshold was set in terms of the familiarity of the participants with the relevant privacy concerns and their willingness to (partly) forfeit their privacy rights, through required entrance tests and signing open consent, respectively (11). These measures cannot be easily achieved at a population level (11).

Although the proposal for the DGA aims to codify data altruism, there is little evidence as to whether the concept as proposed partly or fully aligns with how data altruism or similar concepts such as data donation have been previously conceptualized in the literature. Looking at the proposal for the DGA, it seems that the concept of general interest or common good plays a pivotal role in how the proposal defines data use on altruistic grounds. In addition, the “data altruism consent” has been introduced as an extra measure to enhance transparency and consolidate the agency of individuals when their data are being shared for data altruism purposes. Although the relationship between data altruism consent and other consent requirements under the GDPR and research with human subjects has not been fully explained in the proposal for the DGA, the importance of their compatibility—through the existing rights of the individuals recognized under other regulations and the respecting of transparency requirements—has been stressed.

However, the successful implementation of this concept requires taking at least two extra steps that are currently missing from the proposal for the DGA: First, to define what constitutes general interest or common good and whether this should take into account the proposed research agenda, funding sources, or the type of distribution of the research outcomes; second, to clarify what privacy rights individuals will maintain upon signing data altruism consent and how this will be justified under the existing regulations regarding data protection and research with human subjects. In doing that, special attention needs to be paid to fairness in data sharing toward the individuals.

ARE RULES FAIR ENOUGH?

In recent years, considerable attention has been paid by researchers to adhere to FAIR principles, which aim to make data findable, accessible, interoperable, and reusable through responsible data sharing (12). Missing from this discourse are approaches that also make data sharing fair toward the individuals whose data are being shared and used for downstream purposes.

Individuals have had limited effective involvement in data sharing governance thus far. Consent has been used as a tool to allow individuals to exercise a degree of control over their health data, but the insufficiency of various consent models has been discussed extensively in scholarly literature and policy reports (13). Data altruism consent, as an extra consent requirement, can allow individuals to decide whether they agree with sharing their data for the purpose of the general interest. However, it offers very little to enhance their negotiating power when it comes to how their data are to be shared, under what conditions, and how the final outcomes of the data use are to be distributed.

Establishing this type of collective data governance can be particularly challenging because there is still a lack of clarity over what constitutes “fair” data sharing from the perspective of citizens. This is not least because perception of “fairness” among individuals varies, with some directly linking it to the level of control they can exercise over their data, whereas others also demand clear benefit sharing models and equitable distribution of the research outcomes (14). To this end, some private entities have recently initiated innovative models for sharing the financial benefits of data sharing with individuals, but public research entities and regulators have mainly stayed away from this type of approach (15).

A DIFFICULT TASK AHEAD

The drafters of the EHDS regulation have a difficult task ahead, navigating the existing legal complexities related to consent requirements and uncertainties regarding the concept of scientific research for the public interest. To date, the consent mechanisms that enable individuals to exercise individual agency over personal data have played a pivotal role in data protection and research ethics. Current data sharing demands in health research are inconsistent with requirements to obtain specific consent and use it as a legal basis for processing data. Newly proposed data altruism consent, on the other hand, integrates the element of multiple secondary uses of data. The upcoming EHDS regulation should clarify how these consent models

will interplay in the context of secondary uses of data in the framework of the EHDS. If not, there are risks of further confusion that will affect the future of data sharing in health.

Furthermore, the legislator has an opportunity to clearly define what constitutes research for public interest by stressing the importance of fair distribution of research outcomes and clear benefit for the population under study. This approach can assist to achieve a level of fairness in the data sharing ecosystem that has not been adequately developed in the existing regulatory frameworks. Concurrently, because the notion of fairness may vary among various communities and individuals, special attention should be paid to how fairness has been conceived by citizens, and appropriate approaches should be adopted that reflect those notions in the upcoming EHDS.

Considering the limitations of individual control on data sharing, controllers should adopt adequate safeguards, both organizational and technical, to ensure that the privacy rights of the individuals have been respected, regardless of the relevant consent requirements or research exemption rules. In that sense, organizational safeguards, such as robust oversight by designated data access committees and ethical boards, could provide an extra layer of privacy protection to ensure that the reuse of data aligns with ethical standards and serves public interest. With the legislative proposal of EHDS on the horizon, there will be opportunity to assess how the identified legal complexities regarding sharing health data have been addressed in the new initiative and what should be further taken into consideration in the next legislative steps. ■

REFERENCES AND NOTES

1. https://ec.europa.eu/info/law/better-regulation/have-your-say/initiatives/12663-Digital-health-data-and-services-the-European-health-data-space_en
2. H. B. Bentzen *et al.*, *Nat. Med.* **17**, 1329 (2021).
3. M. Shabani, *Mol. Syst. Biol.* **17**, e10229 (2021).
4. J. Bovenberg, D. Pelloquin, B. Bierer, M. Barnes, B. M. Knoppers, *Science* **370**, 40 (2020).
5. D. Mascalzoni *et al.*, *Ann. Intern. Med.* **170**, 332 (2019).
6. D. Pelloquin, M. DiMaio, B. Bierer, M. Barnes, *Eur. J. Hum. Genet.* **28**, 697 (2020).
7. K. C. O'Doherty *et al.*, *Nat. Genet.* **53**, 2 (2021).
8. European Commission, “Assessment of the EU Member States’ rules on health data in the light of GDPR” (2021); https://ec.europa.eu/health/sites/default/files/ehealth/docs/ms_rules_health_data_en.pdf.
9. I. S. Kohane, R. B. Altman, *N. Engl. J. Med.* **353**, 2074 (2005).
10. PGP-UK Consortium, *BMC Med. Genomics* **11**, 108 (2018).
11. J. E. Lunshof, R. Chadwick, D. B. Vorhaus, G. M. Church, *Nat. Rev. Genet.* **9**, 406 (2008).
12. M. Boeckhout, G. A. Zielhuis, A. L. Bredenoord, *Eur. J. Hum. Genet.* **26**, 931 (2018).
13. D. Nicol *et al.*, *Science* **364**, 445 (2019).
14. M. Murtagh *et al.*, *Wellcome Open Res.* **6**, 311 (2021).
15. E. Ahmed, M. Shabani, *Front. Genet.* **10**, 1107 (2019).

10.1126/science.abn4874

FICTION

Escaping a planet in peril

A tech company bankrolls a space-based retreat for Earth's elite. What could go wrong?

By Eric P. S. Baumer



Deadly heat blocks. City-destroying megastorms. Unbreathable outdoor air quality. Ceaseless wildfires. This is the future in which Rebecca Scherm sets *A House Between Earth and the Moon*. The eponymous house is a space station constructed and inhabited by a team of scientists and engineers who are attempting to balance the competing goals of making scientific advances to save a planet in peril and completing a viable space-based retreat for Earth's elite.

One of the book's central characters is biologist Alex Welch-Peters, who is working to create a new species of algae that can capture enough carbon dioxide to offset global warming (his hope) or at least sustain life in the space station (his employers' hope). Alex's obsessive pursuit of this goal strains his marriage, his relationship with his daughter Mary Agnes, and ultimately his scientific integrity.

In addition to climate catastrophe, the book also anticipates a future in which so-called phones—the technical details of which are left to the reader's imagination—are implanted in one's ear, allowing users access to messages; timely predictions about disaster-triggered evacuations; biometric data about his or her physiological state; and a personal, searchable audiovisual archive of everything the individual has experienced.

The personal archive feature is key. The reader learns that in 2028—a time that has passed in the book—the US Supreme Court ruled that privacy is not a right afforded to every citizen but rather a privilege that is bought and sold. Indeed, only the wealthy

can afford to be “privatized,” with increasing levels of privacy costing increasing sums of money. Everyone else's daily choices and actions can be, and are, scraped as data. (The book's US-centric viewpoint eschews questions of international regulation.)

The data collected by these devices, however, is interesting only in so far as the analysis they enable. Sensus—the tech company that makes the phones and is bankrolling the space station—is working on an algorithm that leverages the data from a user's archives to predict behavior. To do so, Katherine Son, the more enigmatic of Sensus's co-owners, recruits computational social scientist Tess Littlefield to train the algorithm using data collected from Alex and the rest of the space station crew, all of whom are using Sensus phones but are unaware they are being observed. When Mary Agnes secretly begins using the device intended for her mother, she too becomes an unwitting participant in the study.

Scherm offers a compelling metaphor-driven idea here: Seeing the world quite literally through someone else's eyes can help you, and perhaps even an algorithm, understand them. “The Algo” thus serves not as a technical marvel but as a dramatic force, both driving and anticipating tensions among the numerous characters.

The book simultaneously embraces and questions this seeing-through-their-eyes metaphor. The narration is never omniscient, always focusing on a single character's perspective at a time. On one hand, the Algo exhibits increasing accuracy in predicting how interactions will play out among the test subjects—from power grabs, to confiding in one

An artistic rendering of Earth as seen from space mimics the protagonists' perspective.

another, to sexual encounters, to betrayals. On the other, Scherm repeatedly highlights the limitations of the book's seemingly all-knowing algorithm. For instance, when Tess observes Esther, the crew's psychiatrist, viewing recordings of her son back on Earth, the Algo can only predict what she will do next, not what she is thinking or feeling.

A House touches on several themes that will be of particular interest to scientists: the idea of the lone genius toiling in isolation, as contrasted with collaborative interdisciplinary team-based research; the ethics of intervening (or not intervening) in human subjects research; and the tensions that arise between corporate research and those who conduct it and academic research and researchers, to name a few. More broadly, the book repeatedly engages with competing ideas about the most effective way to make the world a better place.

Which is more important, for example, working on grand challenges, such as reversing climate change, or caring for those in our midst who are in peril now? Scherm's characters seem unsatisfied with the ways they themselves answer such questions, an interpretive ambiguity that is one of the book's strengths.

A House Between Earth and the Moon does not offer prescriptive answers to the various problems it identifies, leaving the reader room to consider their own views. In doing so, the reader may learn something about themselves. In the end, what more can one ask of a book? ■



A House Between Earth and the Moon
Rebecca Scherm
Viking, 2022. 400 pp.

The reviewer is at the Department of Computer Science and Engineering, Lehigh University, Bethlehem, PA 18015, USA. Email: ericpsb@lehigh.edu

PHILOLOGY

Unlocking the mysteries of the written word

A philologist presents a lively tour of the world's foundational and undeciphered scripts

By Andrew Robinson

An expert on the undeciphered ancient Cypro-Minoan script, philologist Silvia Ferrara is the founder of a research group focused on the invention of writing, known by the acronym "INSCRIBE" (Invention of Scripts and Their Beginnings). The group organizes scholarly lectures on writing that ranges from the four crucial ancient scripts widely accepted to be of independent origin (Chinese characters, Egyptian hieroglyphs, Mayan glyphs, and Mesopotamian cuneiform) to undeciphered scripts such as the Indus script of Pakistan and India, the Isthmian script of Mesoamerica, Linear A of the eastern Mediterranean, Rongorongo of Rapa Nui (Easter Island), and the notoriously singular Phaistos Disk of Crete. All these scripts receive attention in Ferrara's newly translated book, *The Greatest Invention: A History of the World in Nine Mysterious Scripts*—an intellectually stimulating, deliberately chatty, remarkably diverse survey of the invention and significance of writing in both the ancient and modern worlds.

As Ferrara notes, not everyone agrees with the academic verdict that writing constitutes one of humanity's greatest inventions. Asked to rank the 100 most important inventions in history, adult visitors to the Swedish National Museum of Science and Technology voted for the wheel, followed by electricity, the telephone, and the computer, with the printing press at position 18. Writing was relegated to position 30. "Writing sits just beneath the zipper, and well beneath—wait for it—the stove," observes Ferrara. "At least it beat the vacuum cleaner."

Socrates, perhaps surprisingly, was one of those who doubted the wisdom of writing. He authored no texts, unlike his student Plato, who nevertheless shared his teacher's ambivalence toward writing, as discussed by Ferrara. According to Plato,

Socrates spoke of the Egyptian god Thoth, the supposed inventor of writing, who came to the king seeking a royal blessing for his hieroglyphic invention. However, the king admonished Thoth, replying, "You have invented an elixir not of memory, but of reminding; and you offer your pupils the appearance of wisdom, not true wisdom, for they will read many things without instruction and will therefore seem to know many things, when they are for the most part ignorant." These words, spoken in antiquity, have a distinctly contemporary ring.



This Linear B tablet contains records from the Kingdom of Pylos.

Ferrara sympathizes with this perspective, to an extent. "True list-o-holics," such as herself, "write exclusively by hand—making lists on the computer is like studying on Wikipedia: nothing sticks. It's all gone by the morning," she notes. "Plus, what about that triumphant satisfaction you feel when you press your pen to the page and cross out an item with a nice fat line?"

The book's strongest section is probably its discussion of decipherment. Here,

The Greatest Invention: A History of the World in Nine Mysterious Scripts
Silvia Ferrara
Translated by Todd Portnowitz
Picador, 2022. 304 pp.



Ferrara deals in some depth with Mycenaean Linear B, the earliest attested form of Greek, dating to circa 1450 BCE. She describes classicist Alice Kober's pioneering 1940s analysis of the script before her premature death in 1950, architect Michael Ventris's decipherment breakthrough in 1952, and Ventris's subsequent close collaboration with classicist John Chadwick. Enough Linear B script extracts are illustrated that the uninformed reader can easily follow the decipherment in detail—unlike some other scripts, which lack sufficient extracts.

Moreover, Ferrara's discussion of some key Linear B scholars by name is a departure from most of the other chapters, where many leading modern scholars are left unaccountably uncredited. The Egyptian archaeologist Günter Dreyer, discoverer of the earliest known Egyptian scripts (circa 3200 BCE), for example, and Indus philologist Asko Parpola, author of the classic 1994 study *Deciphering the Indus Script*, receive no mention. Nor, for that matter, do the author's fellow INSCRIBE researchers in Cypro-Minoan.

Such omissions perhaps reflect Ferrara's deeply held—and no doubt valid—belief that future decipherments will depend on broad-based teamwork rather than on solitary scholarship. "These days, the study of writing, and of decipherment, is vastly different," she remarks. "The mantra today is synergy. Not only of group action but of thought: epigraphists, archaeologists, anthropologists, geomatics engineers, historians, cognitivists, semiologists, and computer scientists. And linguists. Perhaps linguists above all. But that hardly matters. What matters is their united effort." ■

The reviewer is the author of *Lost Languages: The Enigma of the World's Undeciphered Scripts* (Thames & Hudson, 2009). Email: andrew@andrew-robinson.org

10.1126/science.abo7807



LETTERS

Replacing beef consumption with poultry overlooks the ethical issues raised by inhumane animal treatment.

Edited by Jennifer Sills

Ethical drawbacks of sustainable meat choices

Major restaurant chains, food suppliers, and university consortia are introducing nudges, such as “climate-friendly” labels, to encourage sustainable food choices (1). Many nudges encourage replacing foods from ruminants (such as beef and dairy) with foods from nonruminants (such as chicken, eggs, and fish). Such changes could reduce environmental impacts (2). However, food from nonruminant animals—albeit more sustainable—has serious ethical drawbacks when we consider animal welfare. To optimize holistic ethical decision-making, such nudges should instead encourage replacing meats and animal products with plant-based foods, which can be sustainable, humane, and healthy (2).

Almost all land animals raised for consumption in the United States (99%) live in intensive farms with poor animal welfare (3). Because chickens and fish are smaller than cows, they require vastly more animals to produce the same food yield. Compared with beef, consuming a given amount of calories from chicken or eggs requires about 18 to 40 times as many days of animals living in intensive farms (4). Consuming fish requires even greater increases in animal-days (4). Scaling species’ moral weights proportional to public judgments of their relative moral statuses (5), or by proxies for sentience such as neuron counts (6), supports the conclusion that shifting to

chicken, eggs, and fish has overwhelmingly negative animal welfare impacts.

Balancing the ethical considerations of sustainability versus animal welfare is challenging. But with more than 70 billion terrestrial animals slaughtered annually for consumption (7), assigning even a miniscule moral weight to each animal suggests an exigent ethical problem. Polls indicate considerable public concern (4, 8, 9). Raising animals in nonintensive pastures could improve welfare but requires more emissions and land than hyperefficient, crowded systems (10). With wild fish populations severely depleted, intensive aquaculture is rapidly replacing wild capture (2).

Sustainable food nudges are still nascent. There is a time-sensitive opportunity to design them using holistic ethical considerations. Instead of encouraging shifts to chicken, eggs, and fish, effective and noncoercive nudges should encourage consuming plant-based foods by providing additional plant-based options (11) or making such options the default (12).

Maya B. Mathur

Quantitative Sciences Unit and Department of Pediatrics, Stanford University, Stanford, CA 94304, USA. Email: mmathur@stanford.edu

REFERENCES AND NOTES

1. J. Wolfrom, “Companies bet carbon labels can help the climate. Will consumers catch on?” *The Washington Post* (2021).
2. W. Willett *et al.*, *Lancet* **393**, 447 (2019).
3. J. Anthis, “U.S. Factory Farming Estimates,” Sentience Institute (2019); <https://sentienceinstitute.org/us-factory-farming-estimates>.
4. J. Reese, *The End of Animal Farming* (Beacon Press, Boston, MA, 2018), p. 60.
5. C. Possidónio *et al.*, *Animals* **9**, E475 (2019).

6. L. Scherer *et al.*, *One Earth* **1**, 349 (2019).
7. Food and Agriculture Organization of the United Nations, “Crops and livestock products” (2021); www.fao.org/faostat/en/#data/QCL.
8. A. Cornish *et al.*, *Animals* **6**, E74 (2016).
9. Gallup, Inc., “In U.S., more say animals should have same rights as people” (2015); <https://news.gallup.com/poll/183275/say-animals-rights-people.aspx>.
10. D. Nijdam *et al.*, *Food Pol.* **37**, 760 (2012).
11. E. E. Garnett *et al.*, *Proc. Natl. Acad. Sci. U.S.A.* **116**, 20923 (2019).
12. P. G. Hansen *et al.*, *J. Public Health* **43**, 392 (2021).

COMPETING INTERESTS

M.M. is a member of the research advisory boards of Sentience Institute and Greener by Default.

10.1126/science.abo2535

Self-spreading vaccines: Base policy on evidence

In their Policy Forum “Eroding norms over release of self-spreading viruses” (7 January, p. 31), F. Lentzos *et al.* caution that the risks of introducing viruses to a population to act as vaccines (“self-spreading vaccines”) outweigh the benefits and argue for tighter regulation of research in this area. Although we echo the authors’ call to modernize regulatory frameworks, their misrepresentations of the risks, benefits, and challenges of developing self-spreading vaccines undermine rational policy and erode public trust in science at a pivotal moment of rising vaccine hesitancy.

To emphasize the dangers of self-spreading vaccines, Lentzos *et al.* reference the unintended escape of rabbit hemorrhagic disease virus (RHDV) and the well-studied reversion of the oral polio vaccine (OPV) to virulence (1, 2). However, neither example portrays relevant risks for developing self-spreading vaccine viruses. RHDV is a natural pathogen of rabbits that was being tested to see if it could selectively kill European rabbits in Australia; it is neither a self-spreading vaccine nor genetically modified. OPV was developed from pathogenic poliovirus through classical attenuation and was not designed to transmit (i.e., spread). Modern self-spreading vaccine development rejects platforms that use attenuated forms of pathogenic viruses; instead, the approach involves inserting a small piece of pathogen genome into intrinsically benign and host-restricted viruses (i.e., vectors) that already circulate in target host populations (3). Here, the likely evolutionary outcome is a return to the benign wild type (4).

Lentzos *et al.* also describe a Spanish vaccine created to protect wild rabbits from RHDV and myxoma virus and suggest that efforts were abandoned due to

PHOTO: EDWIN REMSBURG/VW PICS/GETTY IMAGES

biosafety concerns. In fact, the vaccine was demonstrated to be safe and effective in field trials in an island population (5, 6). However, poor spread in a mainland rabbit population led to the withdrawal of private funding, and pharmaceutical companies considered the vaccine unprofitable due to its potential to self-spread (7, 8). These decisions underscore the scientific challenges that remain to be resolved for self-spreading vaccines to be effective in natural populations and the need for funding of this research through public and nonprofit organizations.

Lentzos *et al.* dismiss the benefits of self-spreading vaccines by focusing on the challenges inherent in preventing spillover from animals to humans of zoonoses that have not yet been identified. However, this application is an unlikely first step. Lentzos *et al.* do not mention the potential for managing neglected zoonoses with known animal reservoirs, such as rabies and Lassa fever, or the possibility of combating disease threats to wildlife conservation (9–11). Self-spreading vaccines could be an inexpensive way to reduce the chronic and predictable burden of such pathogens on human and animal health.

Lentzos *et al.* speculate that self-spreading vaccines can now be made easily and have not been adopted because of widespread concerns. We disagree. Despite substantial technical advances, a vaccine capable of transmitting and immunizing has yet to be developed using a naturally occurring and benign viral vector (3). Meeting this challenge requires investment and scientifically informed policy that adopts a balanced view of the risks and benefits.

Daniel G. Streicker^{1,2*}, James J. Bull³, Scott L. Nuismer³

¹Institute of Biodiversity, Animal Health and Comparative Medicine, College of Medical, Veterinary, and Life Sciences, University of Glasgow, Glasgow, UK. ²Medical Research Council-University of Glasgow Centre for Virus Research, Glasgow, UK. ³Department of Biological Sciences, University of Idaho, Moscow, ID 83844, USA. *Corresponding author. Email: daniel.streicker@glasgow.ac.uk

REFERENCES AND NOTES

- J. Kovaliski, *J. Wildl. Dis.* **34**, 421 (1998).
- O. M. Kew *et al.*, *Annu. Rev. Microbiol.* **59**, 587 (2005).
- A. A. Murphy, A. J. Redwood, M. A. Jarvis, *Expert Rev. Vaccines* **15**, 31 (2016).
- A. Willemsen, M. P. Zwart, *Virus Evol.* **5**, vez045 (2019).
- J. Bárcena *et al.*, *J. Virol.* **74**, 1114 (2000).
- J. M. Torres *et al.*, *Vaccine* **19**, 4536 (2001).
- C. Doyle, "Self-propagating vaccines—on a silent mission in the jungle," *Deutschlandfunk* (2020); www.deutschlandfunk.de/selbstausbreitende-impfstoffe-auf-stiller-mission-im-urwald-100.html [in German].
- R. P. Ortega, "Can vaccines for wildlife prevent human pandemics?" *Quanta Magazine* (2020); www.quantamagazine.org/can-vaccines-for-wildlife-prevent-human-pandemics-20200824/.
- M. E. Griffiths *et al.*, *Nat. Commun.* **11**, 1 (2020).
- S. L. Nuismer *et al.*, *PLoS Negl. Trop. Dis.* **14**, e0007920 (2020).
- A. Marzi *et al.*, *Sci. Rep.* **6**, 21674 (2016).

10.1126/science.abo0238

Response

Our Policy Forum is not a risk-benefit analysis; it does not, as Streicker *et al.* assert, caution that the risks of self-spreading vaccines outweigh the benefits, and we do not call for "tighter regulation." We are calling for engagement and evidence-based debate in appropriate technical and political forums.

Although we agree with Streicker *et al.* that vaccine hesitancy is an important concern in the current pandemic, we disagree that the timing of our call for discussion is problematic. Rather, it is the lack of ethical discussion and public engagement on the far-reaching implications of self-spreading vaccines that is likely to reduce public trust. This is particularly pressing due to ongoing development in the absence of debate.

Streicker *et al.* argue that preventing zoonotic spillover "is an unlikely first step" for self-spreading vaccines. Yet it is clearly a goal. For example, the ongoing PREEMPT program, funded by the US Defense Advanced Research Projects Agency (DARPA), aims to target animal pathogens before they are "adapted to become capable of infecting humans" (1). Our view is that all proposed applications should be part of the debate.

Streicker *et al.* present reduced cost as a benefit of self-spreading vaccines. However, all human and veterinary vaccines must complete rigorous licensing processes, which represent a substantial proportion of the cost of vaccine development. Self-spreading vaccines would be subject to these standards, and therefore costs, as well. Despite ongoing development, as we explain in our Policy Forum, there are no articulated proposals for regulatory pathways to establish self-spreading vaccines as safe, effective, useful, and publicly trusted.

According to Streicker *et al.*, more investment should be directed to the development of self-spreading vaccines. If this is to be the case, we urge funders and developers who choose to work on self-spreading vaccines to publicly commit to use them to address needs within their own borders. Currently, applications in other nations are used to motivate development activities, and field trials are being proposed in overseas countries. Keeping applications and

initial field trials within the borders of where the research originates will maximize the chances of sufficiently robust debate among fellow citizens and nations about the wisdom of self-spreading viral approaches in the environment.

Filippa Lentzos^{1*}, Edward P. Rybicki², Margret Engelhard³, Pauline Paterson⁴, Wayne Arthur Sandholtz⁵, R. Guy Reeves⁶

¹Departments of Global Health and Social Medicine and of War Studies, King's College London, London, UK. ²Biopharming Research Unit, Department of Molecular and Cell Biology, University of Cape Town, Cape Town, South Africa. ³Federal Agency for Nature Conservation (BfN), Bonn, Germany. ⁴Department of Infectious Disease Epidemiology, London School of Hygiene and Tropical Medicine, London, UK. ⁵Department of Political Science and International Relations, University of Southern California, Los Angeles, CA 90089, USA. ⁶Department of Evolutionary Genetics, Max Planck Institute for Evolutionary Biology, Plön, Germany. *Corresponding author. Email: filippa.lentzos@kcl.ac.uk

REFERENCES AND NOTES

- DARPA Biological Technologies Office, "Broad Agency Announcement PREempting EMerging Pathogenic Threats (PREEMPT), HR001118S0017" (2018), pp. 4–5; https://assets.ctfassets.net/syq3snmxc9/6K3RxBIDVf6ZhvXQLSjzxl/6be5c276bc8af7921ce6b23f0975a6c3A_preempt-background-hr001118s0017.pdf.

10.1126/science.abo1980

TECHNICAL COMMENT ABSTRACTS

Comment on "Reversible disorder-order transitions in atomic crystal nucleation"

Cheng-Long Yu, Hang Cheng, Yong Qi, Jie Song, Chen-Guang Yang, Yu Wen, Xiu-Feng Wang Jeon *et al.* (Reports, 29 January 2021, p. 498) reported reversible fluctuations between disordered and crystalline states during nucleation. We argue that the adoption of "magic numbers" for separation of the size range into three parts is misleading when using the sigmoid functions and that their figure 3B was wrongly illustrated. The crystal shape effect was neglected during theoretical analysis.

Full text: [dx.doi.org/10.1126/science.abj1711](https://doi.org/10.1126/science.abj1711)

Response to Comment on "Reversible disorder-order transitions in atomic crystal nucleation"

Sungho Jeon, Sang-Yeon Hwang, Jim Ciston, Karen C. Bustillo, Bryan W. Reed, Sukjoon Hong, Alex Zettl, Woo Youn Kim, Peter Ercius, Jungwon Park, Won Chul Lee Yu *et al.* suggested calculating precisely the size ranges of the three parts of our figure 3A, adjusting the free-energy levels in figure 3B, and considering the shape effect in the first-principles calculation. The first and second suggestions raise strong concerns for misinterpretation and overinterpretation of our experiments. The original calculation is sufficient to support our claim about crystalline-to-disordered transformations.

Full text: [dx.doi.org/10.1126/science.abj3683](https://doi.org/10.1126/science.abj3683)



2022 AAAS Student E-poster Competition Winners

The AAAS Student E-poster competition recognizes the individual efforts of students who are actively working toward an undergraduate, graduate or doctoral-level degree. The winners' presentations displayed originality and understanding that set them apart from their peers. Eligible students can apply to present at the 2023 E-poster Competition starting in July 2022.



BIOCHEMISTRY AND MOLECULAR BIOLOGY

Graduate Student First Place:

Reiko Uenoyama, Iwate University, *The Response to Plants Containing Iridoids Allows Cats to Repel Mosquitoes*

Graduate Student Honorable

Mention: Edna Chiang, University of Wisconsin-Madison, *The Hibernating Squirrel Microbiome Exhibits Seasonal Shifts in Genomic Composition*

Undergraduate First Place:

Marisa Arthur, Biola University, *Killing Viruses (Bacteriophages) by Molecular Nanomachines*

Undergraduate Honorable Mention:

Sarah Batarseh, University of California, Irvine, *Caspase-8 Cleavage in Human Monocytes Infected with Toxoplasma Gondii*

BRAIN AND BEHAVIOR

Graduate Student First Place:

Gregory Boyek, University of Pennsylvania, *Quantitation of TDP-43 Localization for Genetic Targeting of Future ALS Therapeutics*

Graduate Student Honorable

Mention: Danalaxshmi Shanen Ganapathie, Duke University/ University of Edinburgh, *Conjuring The Dead: Using Ancient DNA Analysis to Understand Human Artistic Endeavors*

Undergraduate First Place:

Olivia Siu, Embry-Riddle Aeronautical University, *Effect of Simulated Cosmic Radiation on Male and Female Mice Behavior and Cognition*

Undergraduate Honorable Mention:

Sandra Sandria, University of California, Irvine, *A Kainic Acid Model of Juvenile Status Epilepticus and Exercise Intervention in Mice*

CELL BIOLOGY

Graduate Student First Place:

Joselyn Landazuri Vinueza, University of Washington, *Elucidating Mechanisms of Transformation by Merkel Cell Polyomavirus Tumor Antigens*

Graduate Honorable Mention:

Benjamin Robinson, Drexel University, *Immature MVBs are Immobilized on a Subset of Septin-Associated Microtubules*

Undergraduate First Place:

Yashvi Shah, Drexel University, *Astrocyte to Neuron Reprogramming for Spinal Cord Repair*

Undergraduate Honorable Mention:

Lizeth Gutierrez, University of California, Irvine, *Novel Multidrug Resistance IS1 Composite Transposon in Escherichia Coli IncX Plasmid*

DEVELOPMENTAL BIOLOGY GENETICS AND IMMUNOLOGY

Graduate Student First Place:

Shreya Soni, Drexel University, *Identification and Targeted Delivery of Macrophage-Polarizing Drugs for Tissue Injury*

Graduate Student Honorable

Mention: James Nassur, Drexel University, *THBS2 as a Genetic Modifier of Liver Disease Severity in Alagille Syndrome*

Undergraduate First Place:

Sarah van Dijk, Arizona State University, *P2RX7 Promotes CD8+ T Cell Memory Through Zeb2 Negative Regulation*

Undergraduate Honorable Mention:

Iris Irby, University of Florida, *Genetic Determinants of Microbial Survival on the International Space Station*

meetings.aaas.org/e-posters



ENVIRONMENT AND ECOLOGY

Graduate Student First Place:

Ghazal Shabestanipour, Tufts University, *A Basin Level Robust Decision-Support Tool in Response to Hydrologic Changes*

Graduate Student Honorable

Mention: Takaaki Ogura, The University of Tokyo, *Radioimaging and Ion Flux Analysis Identify Sodium Ion Efflux Sites in Plant Roots*

Undergraduate First Place:

Kelsey O'Brien, Iowa State University, *RNA Sequencing for The Masses*

Undergraduate Honorable Mention:

Maggie Burdell, The University of Georgia, *Population Distribution and Mortality of the Antarctic Scallop*

MEDICINE AND PUBLIC HEALTH

Graduate Student First Place:

Janelle Edwards, Drexel University Associations, *Between Greenspace Utilization, Proximity, and Changes in Loneliness*

Graduate Student Honorable Mention:

Rim Saab, Drexel University, *Muscle Strength Treatment for Chronic Cough—A Four-Week Single Exercise Program*

Undergraduate First Place:

Camryn Zurita, University of California, Irvine, *Multidrug Resistance Region Is Globally Disseminated Across Diverse Bacterial Species*

Undergraduate Honorable Mention:

Katy Trampel, The George Washington University, *Chamber Specific Metabolic Profile of Adult Human Hearts*

PHYSICAL SCIENCES

Graduate Student First Place:

James Malloy, Georgetown University, *Efficient And Robust Metal Nanowire Foams for Deep Submicron Particulate Filtration*

Graduate Student Honorable

Mention: Louis Mueller, Drexel University, *Direct Oxazole Synthesis from Asmic, Alkyl Halides, and Acid Chlorides*

Undergraduate First Place:

Emily Saulino, Moravian University, *Synthesis and Cytotoxicity Study of Novel Dirhodium Complexes*

Undergraduate Honorable Mention:

Sky A Harper, Drexel University, *In Situ Bulk Polymerization of Acrylic Acid Using DBD Plasma in Mesoporous Materials*

SCIENCE IN SOCIETY

Graduate Student First Place:

Katherine Jordan, Carnegie Mellon University, *Zero-Emission Vehicles? Not Without Climate Policy*

Graduate Student Honorable

Mention: Gabriela Reznik, Federal University of Rio de Janeiro, *Gender Equity and Inclusion in Brazilian Informal STEM Education*

Undergraduate First Place:

Samantha Maas, Arizona State University, *Navigating Academic Biology as an LGBTQ+ Ph.D. Student*

Undergraduate Honorable Mention:

Mariana de Araujo Bryan, Middle Tennessee State University, *Undergraduate Biology Students' Attitude and Communication About COVID-19 and Vaccines*

SOCIAL SCIENCES

Graduate Student First Place:

Carly Busch, Arizona State University, *Coming Out to The Class: Students Benefit When Instructor Reveals Her LGBTQ+ Identity*

Graduate Student Honorable

Mention: Virginia Katherine Blackwell, Massachusetts Institute of Technology, *AstroAmpSeq: Microbial Bioinformatics Education with NASA GeneLab's Amplicon Pipeline*

Undergraduate First Place:

Swetha Rao, Drexel University, *Music Therapy's Impact on Chronic Pain Management and Opioid Use in Cancer Survivors*

Undergraduate Honorable Mention:

Chloe Bowen, Middle Tennessee State University, *Experiences of Black Christian Students in Biology Graduate Programs*

TECHNOLOGY, ENGINEERING AND MATH

Graduate Student First Place:

Sandhya Sharma, Florida Atlantic University, *Pandemic Screening with a Low-Cost COVID-19 Diagnostic Chip*

Graduate Student Honorable

Mention: Chenqi Fu, Pennsylvania State University, *Evidence Synthesis with Reconstructed Survival Data*

Undergraduate First Place:

Jessica Rosendorf, Harvard University, *Pressure Plate for Quantifying Balance and Plantar Perfusion*

Undergraduate Honorable Mention:

Siddhanth Agrawal, Drexel University, *Seirv Model of SARS-CoV-2 with Global Sensitivity Analysis*

meetings.aas.org/e-posters



We appreciate the time and commitment from the judges and reviewers of the 2022 AAAS E-posters

STUDENT E-POSTER COMPETITION JUDGES

Adria Schwarber, University of Maryland/
Joint Global Change Research Institute

Adriana Bankston, Future of Research

Amrita A Iyer, Baylor College of Medicine

Anna Drangowska-Way, Federation of
American Societies for Experimental
Biology

Annissa Furr, Purdue University Global

Annwesa Dasgupta, University of
Mississippi

Barbara Kramer, Truman State University

Catherine Takizawa, Quinnipiac University

Cecily Steppe, USNA Oceanography
Department

Celine Hall, Purdue University Global

Chiungwei Huang, University of
North Carolina

Christopher Marcum, National Institutes
of Health

Debanjana Das, George Mason University

Eleftheria Kontou, University of Illinois at
Urbana-Champaign

Erdogan Memili, Mississippi State
University

Georgette Briggs, Arizona State University

Hamid Ghaednia, Massachusetts General
Hospital, Harvard Medical School

Ismail Odetokun, University of Ilorin

Jaswinder Sharma, Oak Ridge National
Laboratory

John Hughes, Independent Consultant

Julie Stahlhut, National Science Foundation

Kapil Dave, University of Illinois
Urbana-Champaign

Katharina Fellnhofer, Harvard University/
ETH Zürich

Kathleen Victoir, Institut Pasteur

Keegan Sawyer, US Dept of Energy,
Office of Science

Kiki Ikossi, National Science Foundation

Laura Schramm, St. John's University

Lauren Ragle, George Washington
University

Linda Lara-jacobo, The University of
Ontario Institute of Technology

Luis A. Guevara, Universidad Peruana
De Ciencias Aplicadas

Mary Ann Ottinger, University of Houston

Melissa Davis, Millersville University
of Pennsylvania

Mingde Zheng, Nokia Bell Labs

Naseer Kutchy, St. George's University

Olanrewaju Morenikeji, University of
Pittsburgh at Bradford

Peggy Hohensee, Purdue University Global

Priyanka Mishra, University of Texas
at San Antonio

Riley St Clair, Quest University

Seena Mathew, University of Mary
Hardin-Baylor

Sesha Lakshmi Arathi Paluri, Michigan
State University

Shangying Wang, IBM Research

Soheil Ashkani-Esfahani, Massachusetts
General Hospital, Harvard Medical School

Srijon Banerjee, University of Pittsburgh

Stephanie Del Tufo, University of Delaware

Stewart Fast, Natural Resources Canada


Surbhi Sharma, Stanford University

Surya Banerjee, Arkansas Tech University

Valeria Visconte, Cleveland Clinic

Woi Sok Oh, Princeton University

Yu-Chien (Alice) Chien, University of
California, Irvine



The AAAS team appreciates the help of reviewers, who evaluated general E-posters and scientific sessions of the 2022 Annual Meeting. Full list of reviewers can be seen here:

meetings.aaas.org/2022-reviewers

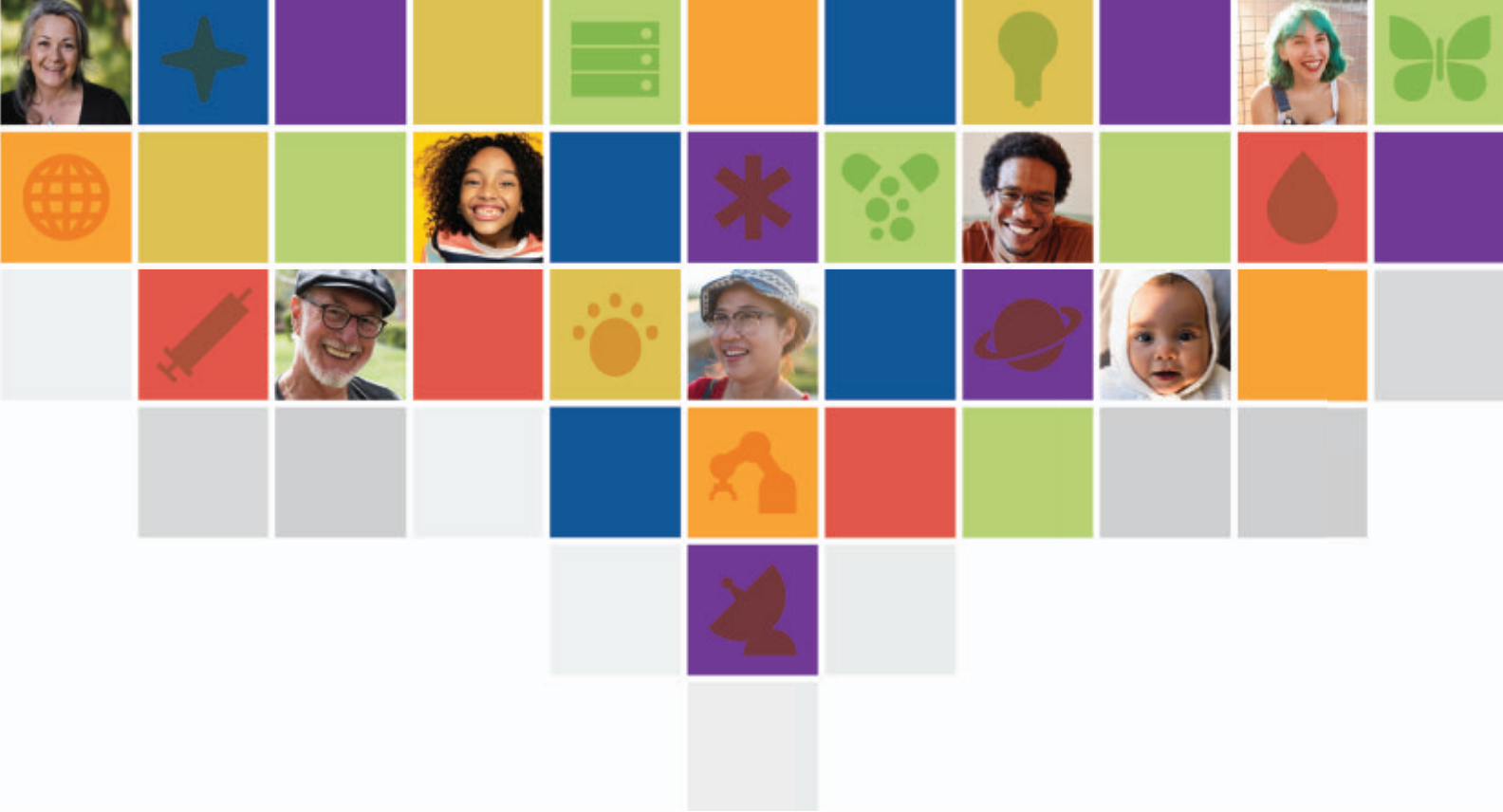


CONNECT WITH US:

[aaas.org/meetings](https://meetings.aaas.org) | [#AAASmtg](https://twitter.com/AAASmtg)



meetings.aaas.org/e-posters



SCIENCE FOR HUMANITY

 AAAS | ANNUAL MEETING

**SUBMIT A SCIENTIFIC SESSION OR WORKSHOP PROPOSAL
FOR THE 2023 AAAS ANNUAL MEETING!**

Highlighting the importance and just integration of our multiplicity, the 2023 AAAS Annual Meeting will feature groundbreaking multi-disciplinary research—research that advances knowledge and responds to the needs of humanity.

CONNECT WITH US:

aaas.org/meetings | [#AAASmtg](https://twitter.com/AAASmtg)

RESEARCH

IN SCIENCE JOURNALS

Edited by Michael Funk

VIROLOGY

Targeting Nipah virus

The zoonotic Nipah virus (NiV) was discovered in 1999, and since then outbreaks in humans have been recorded almost annually in parts of Asia. This virus causes encephalitis and respiratory symptoms that can be serious and often fatal. Viral entry into host cells requires the attachment glycoprotein (G) and the fusion glycoprotein (F), and these proteins are targeted by the immune system. Z. Wang *et al.* determined the structure of the tetrameric ectodomain of the NiV G protein in complex with a broadly neutralizing antibody. Vaccinating macaques with the ectodomain tetramer elicited antibodies against the G protein head domain, resulting in potent neutralizing activity against NiV. The structure provides a blueprint for engineering next-generation vaccine candidates. —VV

Science, abm5561, this issue p. 1373

NANOMATERIALS

Conducting colloidal nanocrystals

Organic capping ligands on nanocrystals can promote ordering of films and crystals but tend to block electronic conduction. Smaller inorganic ligands, such as diindium tetraselenide anions, promote conduction for semiconductors such as cadmium selenide but tend to form gels rather than crystals. Coropceanu *et al.* show that these inorganic anions can form electronically coupled superlattices of nanocrystals of metals such as gold and nickel and semiconductors with high dielectric constants such as lead sulfide. In these cases, the multivalent

anions bind in a dense but reversible manner to the nanocrystal surface and enable rearrangements that lead to the formation of crystals rather than amorphous gels. —PDS

Science, abm6753, this issue p. 1422

BIOMATERIALS

Designing the right polymer blend

Approaches to making soft electronics can involve putting rigid objects onto a soft substrate or finding ways to improve the conductivity and mechanical strength of inherently soft materials. Jiang *et al.* considered the systematic introduction of polyrotaxanes into soft conductive

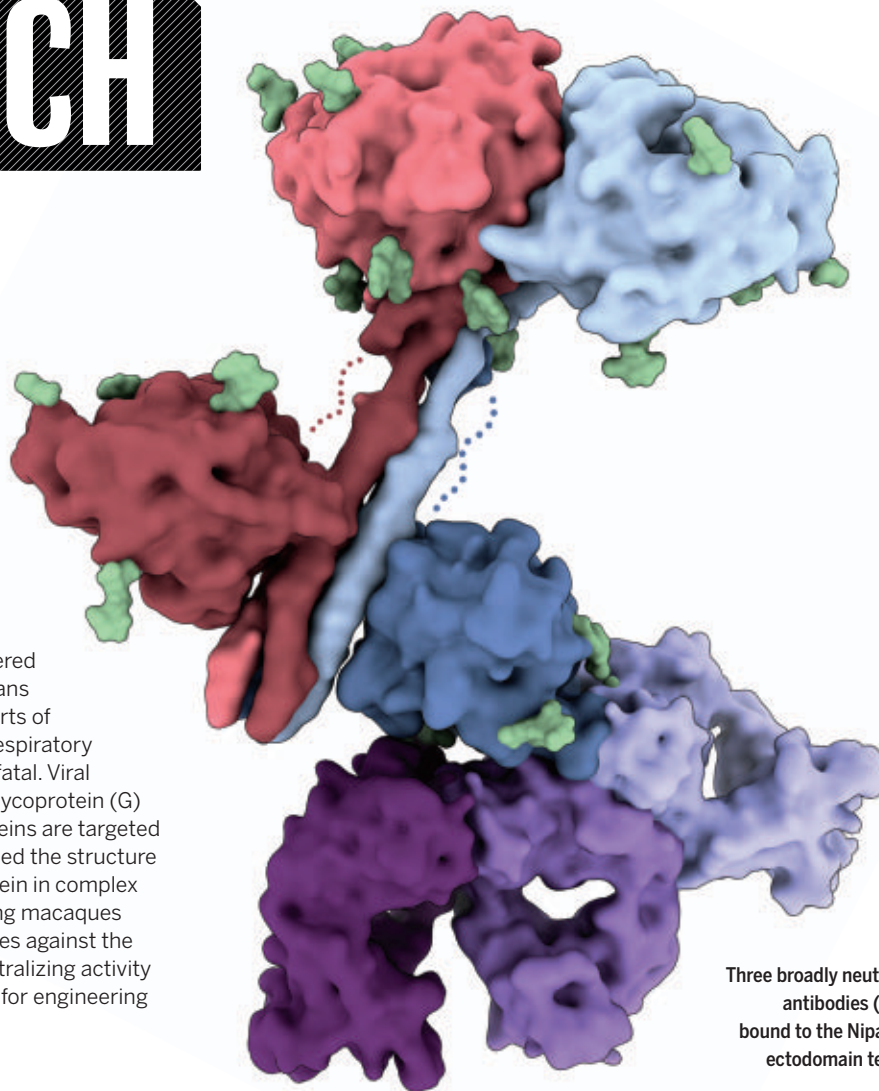
membranes made of the conductive polymer poly(3,4-ethylenedioxythiophene):poly(styrene sulfonate) (PEDOT:PSS). The polyrotaxane consisted of a poly(ethylene glycol) (PEG) backbone with cyclodextrins attached using PEG-methacrylate side chains. The cyclodextrins can slide back and forth along the chains, thus preventing crystallization of the PEG and providing better stretchability. The blended polymers could be photopatterned down to two-micrometer feature sizes and exhibited enhanced conductivity, making them suitable for surface-mounted and implanted bioelectronic devices. —MSL

Science, abj7564, this issue p. 1411

ALLERGY

Gasping over IL-9-expressing CD4s

Interleukin-9 (IL-9) is involved in asthma, but which cells produce it and what its role is in seasonally induced asthma (recall immune responses) are unclear. Ulrich *et al.* used an allergen rechallenge mouse model to study the impact of IL-9-producing immune cells on lung inflammation and recall responses. The authors found that IL-9 primarily came from multifunctional CD4⁺ T cell resident memory (Trm) populations present in the lungs of mice. These cells secreted IL-9 in an antigen-specific manner, had a distinct transcriptomic and epigenetic profile, and



Three broadly neutralizing antibodies (purple) bound to the Nipah virus ectodomain tetramer

largely depended on IL-33 for IL-9 up-regulation. Together, these data suggest that targeting IL-9⁺ Trm cells in the lungs during seasonal allergies might abrogate lung inflammation. —DAE

Sci. Immunol. **7**, eabg9296 (2022).

VALLEYTRONICS Gapped, twisted, and curved

Two-dimensional Dirac materials such as graphene and transition metal dichalcogenides are attractive materials with which to realize a host of new topological and quantum geometrical effects. The multiple extrema, or valleys, in the electronic band structure of these materials provide an additional valley degree of freedom that allows charge carriers to effectively perform exotic electronic dance routines as they navigate their way through the material. In bilayer graphene with a tunable bandgap, Yin *et al.* show that the dance routine can be choreographed, providing a route to developing topological opto-electronic devices such as robust switches and detectors. —ISO

Science, ab14266, this issue p. 1398

ENERGETIC MATERIALS A new energy peak for organic explosives

Explosive organic chemicals typically contain a relatively high ratio of nitrogen to carbon. Trinitrotoluene is a familiar example, and hexanitrobenzene has long been the energy peak benchmark. Pang *et al.* disclose a route to synthesis of 1,3,5-trinitro-2,4,6-trinitroaminobenzene (TNTNB), which they performed on one-millimole scale. Although its thermal stability is modest (decomposition at 65°C), two of its salts are stable at temperatures over 150°C and have higher heat of detonation than trinitrotoluene, making this family of

energetic materials promising for commercial use. —SRC

Sci. Adv. **10**.1126/
sciadv.abn3176 (2022).

NEUROSCIENCE Axon firing without signal integration

The standard model of information flow in the nervous system states that neurons receive input through their dendrites and send output through their axons. Liu *et al.* used functional imaging, superresolution microscopy, axonal whole-cell electrophysiology, amperometry, and *in vivo* photometry to identify a previously unknown form of action potential initiation in dopaminergic axons in the striatum. Unlike the conventional form of action potential initiation near the soma, followed by propagation along the axon to synaptic terminals, in this case, activity starts near the synaptic terminals. Axonal action potentials are promoted by the activation of nicotinic acetylcholine receptors on the dopaminergic axons. —PRS

Science, abn0532, this issue p. 1378

INORGANIC CHEMISTRY Sideways diphosphorus

Elemental phosphorus tends to form single-bonded clusters, in contrast to the triple-bonded diatomic of its periodic tablemate, nitrogen. It is nonetheless possible to synthesize and trap diphosphorus in certain circumstances, and S. Wang *et al.* now report a complex in which this species coordinates sideways to an iron center. The metal-ligand bonding motif, which was analyzed crystallographically, spectroscopically, and computationally, resembles coordination by triple-bonded carbons in alkynes. This similarity highlights the diagonal relationship between phosphorus and carbon in the periodic table. —JSY

Science, abn7100, this issue p. 1393

IN OTHER JOURNALS

Edited by **Caroline Ash**
and **Jesse Smith**

PLANT SCIENCE

Seagrass cell walls

Seagrasses, which evolved from terrestrial origins, help to stabilize the sediment of coastal aquatic environments. Turtles, sea horses, and many other marine organisms find homes and food among the seagrasses. The adaptations that these angiosperm plants needed to succeed while submerged would be different from adjustments evolved in their dry-land grass cousins. Pfeifer *et al.* analyzed the composition of cell walls from a variety of globally sourced seagrasses, with particular attention to polysaccharide composition and lignin content. Shifts in pectin structure may carry hints about osmoregulation. Other shifts in cell wall chemistry might be in response to the salty environment. Those seagrasses with particularly low lignin content might be useful in the production of sustainable biofuels. —PJH *BMC Plant Biol.* **22**, 63 (2022).

Seagrasses evolved from terrestrial flowering plants to live in saltwater, where they provide important marine habitats.



MATERIALS SCIENCE

Putting a spotlight on sintering

Sintering is a key step in the production of parts from metal or ceramic particles to ensure a dense, well-fused structure, although it can be undesirable

when working with nanoscale catalysts. Fiuza *et al.* used high-resolution transmission electron microscopy to study the final sintering stage in freestanding films of nanometer-scale monoclinic zirconium dioxide particles. A key finding was the role of anisotropy in the surface



Dogs associated with fishing communities have become an important reservoir for a human parasite, the Guinea worm.

PARASITOLOGY

Power of the dog

Guinea worms (*Dracunculus medinensis*) are very long (70 to 120 cm), parasitic nematodes that cause disabling subcutaneous infections in humans. The female worms cause skin ulcers, and when an infected person's ulcerated feet contact water, eggs are released. The worm's larvae are consumed by copepods that in turn are consumed by people drinking untreated water. Huge efforts have been made to eradicate Guinea worm from humans in central Africa under sometimes terrible conditions but with a great deal of success. Goodwin *et al.* show that these control efforts have been undermined by an unexpected aspect of the parasite's biology. Domestic dogs are a known host, and the authors discovered that infections occur when dogs scavenge fish waste produced by seasonal fisheries. Most Guinea worm infections are now found in dogs in these fishing communities, supplying a reservoir of potential infections that threaten eradication efforts in humans. —CA *Curr. Biol.* **32**, 775 (2022).

energy that drives the mobility of surface atoms from the rougher regions into a gas phase and subsequent reattachment onto a faceted surface. The authors also observed how pores pin grain boundaries. Based on these findings, they suggest how current models should be modified to account for these two driving forces. —MSL

Nano Lett. **22**, 1978 (2022).

LIFE CYCLE

Cold, starved, and male

In most mammals, starvation and other adverse environmental conditions stunt sexual maturation. Thirteen-lined ground squirrels spend

7 months in hibernation at 4°C without access to food and water and in total darkness. Males will mate whenever they rouse from hibernation, so their offspring have as much time as possible in warm months to build up fat reserves before the cold weather returns to northern America. Dai Pra *et al.* show that juvenile males interrupt their long sleep about 27 times, waking for 24 to 48 hours when their body temperature rises to 37°C. During these brief arousals, the hypothalamic reproductive axis activates, and the testes grow. Although this makes sense for the life cycle of the squirrel, how they activate when other animals suppress

sexual maturation under harsh conditions with no access to food is an intriguing question. —DJ

Curr. Biol. 10.1016/j.cub.2022.02.032 (2022).

NEUROSCIENCE

Movement control

The generation of locomotion is an intensively studied but incompletely understood function of the central nervous system. Chalif *et al.* found that in mice, ventral spinocerebellar tract neurons receive input from both sensory nerve fibers and motor neurons. In addition to projecting to the cerebellum, these cells

directly contact motor neurons and interneurons in different spinal segments. Ventral spinocerebellar tract neurons act as pacemaker neurons. Optogenetic and chemogenetic activation or inhibition showed that they are the only presently known type of spinal neurons that are necessary and sufficient to induce locomotion in neonatal and adult mice. —PRS
Cell **185**, 328 (2022).

PHYSICS

Dynamics in a box

Unitary Fermi gases can serve as a model for strongly interacting quantum many-body systems, which are ubiquitous in physics. Studying their dynamical properties is especially challenging. Wang *et al.* placed an ultracold gas of ⁶Li atoms in a box potential and monitored its dynamics after the quench of an additional periodic potential. By analyzing the Fourier transform of the perturbation of the gas density, the researchers were able to measure both the thermal conductivity and the shear viscosity of this system. —JSt

Phys. Rev. Lett. **128**, 090402 (2022).

CHEMICAL BIOLOGY

Hitting hidden electrophiles

Proteins do not typically contain highly electrophilic functional groups, but cofactors and post-translational modifications in enzymes can add to the chemical repertoire and enable various catalytic transformations. Extending prior work on reverse-polarity activity-based protein profiling, Wang *et al.* developed an expanded nucleophilic probe library to label proteins with pyruvyl or glyoxylal modifications. Using hydrazine-based probes, the authors established efficient and selective labeling of known electrophilic targets and inhibition of a target enzyme. Such probes may serve as effective lead compounds in drug discovery. —MAF

J. Am. Chem. Soc. 10.1021/jacs.1c12748 (2022).

ALSO IN SCIENCE JOURNALS

Edited by Michael Funk

STRUCTURAL BIOLOGY
Complex responses of an obesity target

Amylin receptors (AMyRs), which respond to the peptide hormones amylin and calcitonin, are targets for treating obesity and metabolic disorders. They are heterodimers comprising the calcitonin receptor, which is a G protein-coupled receptor, and one of three receptor-modifying proteins. An impediment to functional studies is that it is difficult to separate AMyR phenotypes from calcitonin receptor phenotypes. Cao *et al.* present six cryo-electron microscopy structures of active AMyRs bound to amylin or calcitonin. The structures reveal that the two peptide hormones activate AMyRs by distinct mechanisms. The structural and mechanistic insights will be valuable in designing both specific agonists and antagonists with dual action. —VV

Science, abm9609, this issue p. 1371

QUANTUM OPTICS
Putting light under pressure

The equation of state of a material system describes the various phases of the material under a set of physical conditions (pressure, volume, temperature, etc.). The same is true for quantum materials, in which exotic quantum phases can emerge. Busley *et al.* examined the mechanical properties of a quantum gas of light (see the Perspective by Fletcher and Zwerlein). Using light confined to a two-dimensional cavity with a box potential, the authors measured the compressibility of a photon gas in a regime around the phase transition to quantum degeneracy and determined its equation of state. The results hint at the formation of a highly compressible Bose-Einstein condensate, and this work provides a platform with which to

study exotic quantum phases at room temperature. —ISO

Science, abm2543, this issue p. 1403;
see also abo2856, p. 1355

CROP GENOMICS
Amazing grains

Maize and rice are important sources of human calories and have been, mostly independently, subject to human selection for thousands of years, often for similar traits such as grain yield. W. Chen *et al.* examined the genomes of accessions of domestic maize and its wild relative, teosinte, for evolutionary signals of selection. From these sequences, the authors identified a quantitative trait locus in maize that increased kernel row number. Fine mapping determined that this locus contains a candidate gene, *KRN2*. Gene-editing experiments of *KRN2* and its homolog in rice determined that a similar phenotype increasing grain number per plant could be recapitulated. Thus, identifying genes under selection in one cereal provides useful fodder for crop improvements. —LMZ

Science, abg7985, this issue p. 1372

PIEZOELECTRICS
Polymer piezo

The best-performing piezoelectric materials are oxide ceramics, which are widely used for sensors and actuators. X. Chen *et al.* added two additional components to poly(vinylidene difluoride) trifluoroethylene to improve the electromechanical coupling (see the Perspective by Wang and Liao). The resulting tetrapolymer has piezoelectric properties that are dramatically improved and appears to be competitive with traditional oxides. The pliability and relative ease of fabrication of this tetrapolymer piezoelectric makes it attractive for a range of interesting applications. —BG

Science, abn0936, this issue p. 1418;
see also abn7440, p. 1353

ANIMAL BEHAVIOR
Do animals have emotions?

Whether animals are sentient beings with emotions and feelings has been debated for some time. Although it might be easier to find evidence of mammals, especially those most similar to humans, that have emotional responses such as fear, pleasure, and empathy, increasing evidence suggests that other animals, such as some invertebrates (crustaceans, mollusks, and honeybees), also exhibit emotions. In a Perspective, de Waal and Andrews discuss the evidence that a wide variety of animals exhibit positive and negative emotions. Recognizing their emotions raises ethical questions about our moral obligations to avoid causing harm to animals by ensuring good husbandry and agricultural practices. —GKA

Science, abo2378, this issue p. 1351

CORONAVIRUS
REACTing to SARS-CoV-2 Omicron

The Omicron variant of severe acute respiratory syndrome coronavirus 2 (SARS-CoV-2) swept the world in the last months of 2021. This new wave occurred despite very high levels of vaccine coverage in some countries and the prevalence of the highly transmissible Delta variant. Elliott *et al.* tracked the course of the Omicron takeover in England from the first case report on 27 November 2021 using data gathered from a community transmission study called REACT-1 (see the Perspective by Kucharski and Cohen). The data indicated a steep increase in prevalence among younger adults in London, reaching more than 6% in mid-December. Most participants reported classical symptoms of loss of sense of taste and smell, fever, and cough. An excess of Omicron infections

occurred in Black and Asian groups, those with two vaccine shots (although none in those who received three shots), and those living in less affluent communities. By 17 December, 75% of infections were estimated to be caused by Omicron. —CA

Science, abn8347, this issue p. 1406;
see also abo4257, p. 1349

METABOLISM
Liver inflammation: Not so sweet

Interferon regulatory factor 3 (IRF3) has been linked to metabolic dysregulation in obesity and nonalcoholic fatty liver disease (NAFLD), but its exact role in this context is unclear. Patel *et al.* report that hepatic IRF3 induces transcription of a gene encoding for a component of serine/threonine phosphatase PP2A, with downstream effects on glucose homeostasis through AMP-activated protein kinase. Hepatocyte-specific deletion of IRF3 in mice fed a high-fat diet affected glycemic control only, uncoupled from steatosis. Antisense targeting of *Irf3* improved insulin-mediated metabolic responses in obese mice, demonstrating a proof-of-principle therapeutic strategy. Enhanced hepatic activation of IRF3 in patients with NAFLD and obesity decreased after bariatric surgery, suggesting relevance to humans. —CAC

Sci. Transl. Med. **14**, eabh3831 (2022).

CELL BIOLOGY
Blocking proliferation without ligand

The glucocorticoid receptor (GR) has a cytoplasmic localization in the absence of activating ligands. Caratti *et al.* found that cytoplasmic GR interacted with the small GTPase RAS and the RAS-activating kinase RAF1. GR deficiency or ligand-induced nuclear translocation of GR increased RAS-dependent

mitogenic signaling and promoted the growth of xenografts formed by A549 human lung cancer cells in mice. Thus, glucocorticoids may block the ability of GR to limit tumor growth, which has potential implications for the use of this class of drugs in cancer patients. —AMV

Sci. Signal. **15**, eabm4452 (2022).

MEMBRANES

When aging is an asset

Separations achieved using membrane processes offer the prospect of reducing the energy costs of industrial-scale chemical separations, but innovative membrane materials are required to achieve the combinations of flux and selectivity. Lai *et al.* developed a set of ladder polymers prepared using catalytic arene-norbornene annulation polymerization that incorporate fluorene and dihydrophenanthrene units (see the Perspective by Budd). Upon physical aging, these polymers contort in a way that enhances their size-sieving capabilities, as demonstrated for separation between methane and carbon dioxide mixes and hydrogen and methane. —MSL

Science, ab17163, this issue p. 1390;
see also abm5103, p. 1354

THERMOELECTRICS

A material with high potential

Thermoelectric materials convert heat to electricity and are attractive for energy generation or solid-state cooling. Su *et al.* found that doping tin selenide with chlorine and lead substantially improved the thermoelectric figure of merit over a wide temperature range. This effect was mostly due to an improvement in the material's deformation potential related to mass and strain fluctuations introduced into the n-type material. Improving the figure of merit in this way is challenging because properties are often intertwined, and trying to improve one will often degrade others. —BG

Science, abn8997, this issue p. 1385

RESEARCH ARTICLE SUMMARY

STRUCTURAL BIOLOGY

A structural basis for amylin receptor phenotype

Jianjun Cao, Matthew J. Belousoff, Yi-Lynn Liang[†], Rachel M. Johnson, Tracy M. Josephs, Madeleine M. Fletcher[‡], Arthur Christopoulos, Debbie L. Hay, Radostin Danev, Denise Wootten*, Patrick M. Sexton*

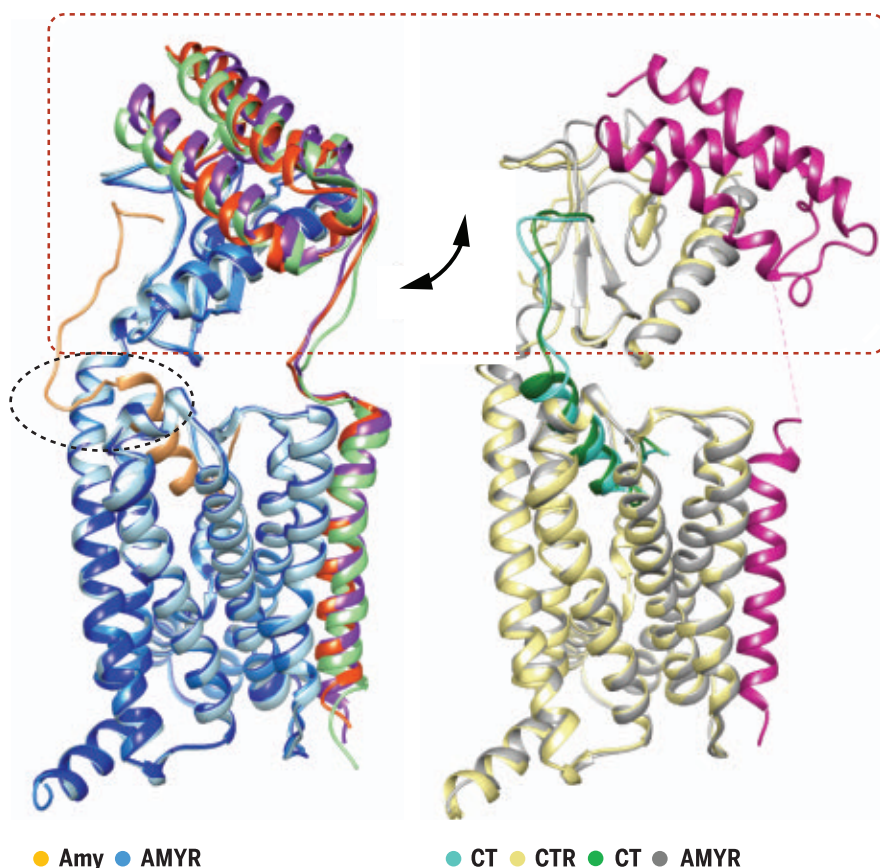
INTRODUCTION: Amylin receptors (AMYRs) are heterodimers of the calcitonin (CT) receptor (CTR) and one of three receptor activity-modifying proteins (RAMPs), AMY₁R, AMY₂R, and AMY₃R. AMYRs have emerged as important potential disease targets, and selective AMYR agonists and dual AMYR/CTR agonists (DACRAs) are being developed as obesity treatments. However, it is unclear whether DACRAs based on amylin-template peptides versus calcitonin-template peptides activate target receptors by similar or distinct molecular mechanisms. Understanding the structural basis for the binding and selectivity of peptides to CTRs and AMYRs is important for future drug discovery and development.

RATIONALE: Currently, no structural information exists on any of the AMYRs. To address this gap, we applied cryo-electron microscopy (cryo-EM) to determine structures of AMY₁R, AMY₂R, AMY₃R bound to rat amylin (rAmy), AMY₁R and AMY₂R bound to salmon CT (sCT), AMY₂R with human CT (hCT), and the CTR bound to rAmy, hCT, or sCT, all in complex with Gs.

RESULTS: Purified samples for each complex were vitrified and imaged by cryo-EM to yield consensus maps at gold standard Fourier shell correlation 0.143 of 2.2 Å (rAmy-AMY₁R), 2.6 Å (rAmy-AMY₂R), 2.4 Å (rAmy-AMY₃R), 3.0 Å (sCT-AMY₁R), 3.0 Å (sCT-AMY₂R), 3.3 Å (hCT-

AMY₂R), 3.3 Å (rAmy-CTR), 2.6 Å (sCT-CTR), or 2.7 Å (hCT-CTR). The CT-CTR co-complexes had similar backbone conformations, and, similarly, the rAmy-bound AMY₁R, AMY₂R, and AMY₃R complex structures exhibited almost identical backbone conformations. However, the ECD of the CTR subunit in rAmy-bound AMYRs undergoes an ~12-Å rigid-body translation relative to CT-CTR complexes. Although there was a high degree of overlap in the location of the N-terminal loop and midregion helical extension of both rAmy and CT peptides within the transmembrane domain (TMD), the peptides diverge as they exit the receptor core. The CT peptides have an unstructured C-terminal region that extends in the same vertical plane as the helix. By contrast, the α -helix of the rAmy peptide terminates half a turn earlier, extending in the plane of the membrane toward the top of the transmembrane helix 1 (TMI) (bypass motif) before forming a tight turn that extends to interact with the ECD. In the sCT-AMY₁R and sCT- or hCT-bound AMY₂R complexes, the backbone structure and orientation of the CTR protomer, including the ECD, and CT peptides were effectively equivalent to those in the CT-CTR complexes, with a consequent reorientation of the RAMP ECD compared with rAmy occupied receptors. RAMP2 has a weaker TMD interface than the other two RAMPs, and this becomes destabilized, allowing repositioning of the RAMP ECD in CT-bound complexes. By contrast, the tighter TMD interface for RAMP1 and CTR leads to only partial disengagement of the top of the RAMP TMD helix with greater mobility of the RAMP ECD to accommodate the position of the CTR ECD. The tighter TMD constraint for this RAMP likely contributes to lower potency of hCT at AMY₁R and AMY₃R. The rAmy-bound CTR complex could be resolved into two major classes, CT-like and rAmy bypass-like, differing in the ECD orientations and peptide conformations.

CONCLUSION: Our data provide details of the molecular basis for activation of AMYRs and reveal that CT peptides activate AMYRs by distinct mechanisms compared with activation by Amy peptides. Our work provides a template for the future development of selective and nonselective agonists of CTR and AMY receptors. ■



CT and Amy peptides have distinct modes of amylin receptor activation. Left: overlay of the rAmy-AMY₁R, rAmy-AMY₂R, and rAmy-AMY₃R complexes. rAmy, gold; CTR, blue; RAMP1, purple; RAMP2, green; RAMP3, orange. Right: overlay of the hCT (cyan)-CTR (yellow) and sCT (green)-AMY₂R (CTR, gray; RAMP2, dark pink) complexes. Amylin peptides display a midregion “bypass” motif (black dashed oval) that reorients the extracellular domains of CTR and RAMP relative to CT-bound receptor (red dashed rectangle).

The list of author affiliations is available in the full article online.

*Corresponding author. Email: patrick.sexton@monash.edu (P.M.S.); denise.wootten@monash.edu (D.W.)

[†]Present address: Confo Therapeutics, 9052 Ghent (Zwijnaarde), Belgium.

[‡]Present address: GlaxoSmithKline, Abbotsford 3067, Victoria, Australia.

Cite this article as J. Cao *et al.*, *Science* **375**, eabm9609 (2022). DOI: 10.1126/science.abm9609

S READ THE FULL ARTICLE AT
<https://doi.org/10.1126/science.abm9609>

RESEARCH ARTICLE

STRUCTURAL BIOLOGY

A structural basis for amylin receptor phenotype

Jianjun Cao^{1,2}, Matthew J. Belousoff^{1,2}, Yi-Lynn Liang^{1,†}, Rachel M. Johnson^{1,2}, Tracy M. Josephs^{1,2}, Madeleine M. Fletcher^{1,†}, Arthur Christopoulos^{1,2}, Debbie L. Hay³, Radostin Danev⁴, Denise Wootten^{1,2,*}, Patrick M. Sexton^{1,2,*}

Amylin receptors (AMYRs) are heterodimers of the calcitonin (CT) receptor (CTR) and one of three receptor activity-modifying proteins (RAMPs), AMY₁R, AMY₂R, and AMY₃R. Selective AMYR agonists and dual AMYR/CTR agonists are being developed as obesity treatments; however, the molecular basis for peptide binding and selectivity is unknown. We determined the structure and dynamics of active AMYRs with amylin, AMY₁R with salmon CT (sCT), AMY₂R with sCT or human CT (hCT), and CTR with amylin, sCT, or hCT. The conformation of amylin-bound complexes was similar for all AMYRs, constrained by the RAMP, and an ordered midpeptide motif that we call the bypass motif. The CT-bound AMYR complexes were distinct, overlapping the CT-bound CTR complexes. Our findings indicate that activation of AMYRs by CT-based peptides is distinct from their activation by amylin-based peptides. This has important implications for the development of AMYR therapeutics.

Amylin receptors (AMYRs) have emerged as important potential targets for the treatment of obesity and related metabolic disorders. These receptors respond to the 37-amino-acid peptide hormone amylin (Amy) (fig. S1), which plays an important role in the regulation of energy homeostasis through a range of actions including acting as a satiation signal, reducing food intake, and decreasing adiposity while increasing energy expenditure (1, 2).

AMYRs are heterodimers of the calcitonin (CT) receptor (CTR), a class B1 G protein-coupled receptor (GPCR), and one of three receptor activity-modifying proteins (RAMPs) to yield AMY₁Rs (CTR-RAMP1), AMY₂Rs (CTR-RAMP2), or AMY₃Rs (CTR-RAMP3) (3). These receptors each respond to amylin but have phenotypes that are distinct from each other and from CTR in the absence of RAMPs (3–5). AMYRs have high affinity for, and are potentially activated by, Amy but have lower affinity for human CT (hCT) (fig. S1) relative to CTR, with CTR exhibiting the reverse phenotype with higher relative affinity for hCT. By contrast, salmon CT (sCT) (fig. S1) has high affinity for both CTR and AMYRs (6–10). The related peptide, calcitonin gene-related peptide (CGRP),

is a selective agonist of the human AMY₁R relative to AMY₃R, whereas the AMY₂R is not well characterized because of the relative limited phenotypic expression of AMY₂R in most recombinant systems (3, 4).

Pramlintide, a peptide analog of human Amy (fig. S1) that is FDA approved for treatment of insulin-requiring diabetes, induces small but significant weight loss in diabetic patients, despite having a short plasma half-life (11, 12), and numerous preclinical studies support targeting of AMYRs as an effective intervention for obesity (13–16). By contrast, selective activation of CTRs by human CT does not elicit weight loss (17). Nonetheless, recent data has suggested that parallel activation of both CTR and AMYRs can enhance weight loss compared with selective activation of AMYRs (17–22). The dual amylin and calcitonin receptor agonist (DACRA), cagrilintide (fig. S1) (5, 23), demonstrated high efficacy as a monotherapy in a phase 2 trial for obesity, as well as additive benefit in combination with the glucagon-like peptide-1 receptor agonist, semaglutide (24), indicative of a distinct mechanism of action from other obesity therapies. Despite this, sCT, also a DACRA, has only a limited effect on weight in patients treated with sCT for osteoporosis (25). This suggests that there may be distinct modes of receptor activation by sCT, compared with Amy peptides. A major impediment to drug discovery for AMYRs is that it has not been possible to develop a CTR-RAMP coexpression system that generates AMYRs without a background CTR alone phenotype. As such, the functional pharmacology of AMYRs has relied on inference from differences between behavior of CTRs in the presence and absence of RAMPs (3, 4, 6–10). Thus, understanding the structural basis for binding, and selectivity, of peptides to CTR and AMYRs

is important for future drug discovery and development.

The active, Gs-coupled CTR was the first GPCR structure to be determined using cryo-electron microscopy (cryo-EM). This structure was solved in complex with sCT and the heterotrimeric Gs protein, the primary signaling transducer for class B1 GPCRs (26); however, no structural information exists on any of the AMYRs or on the structure of CTR bound to its endogenous, selective agonist, hCT. We present structures of each of AMY₁R; AMY₂R; AMY₃R bound to Amy; AMY₁R and AMY₂R bound to sCT; and AMY₂R with hCT and the CTR bound to Amy, hCT, or sCT, all in complex with Gs. The latter was used to provide a higher-resolution comparator for the new structures. Comparison of the high-resolution structures and the intrinsic dynamics of each of the receptor complexes reveals key features of the binding and selectivity of peptide agonists of this receptor family.

Results and Discussion

Structure determination

Active heterodimers of AMY₁R, AMY₂R, or AMY₃R were formed by simultaneously expressing CTR and individual RAMPs in *Trichoplusia ni* insect cells, along with a stabilized form of heterotrimeric Gs (DNGs). The complexes were assembled in the presence of excess rat Amy (rAmy) (1 μM or 10 μM) for all AMYRs and further stabilized by the addition of nanobody 35 (Nb35) and removal of nucleotides with the enzyme apyrase. rAmy was used because it has high sequence identity to hAmy but is less prone to aggregation. sCT is considered a high-affinity agonist of both CTR and AMYRs. However, although we could robustly generate stable, Gs-coupled complexes of sCT with AMY₂R, the yield for AMY₁R was low. Moreover, the AMY₃R complex was not sufficiently stable to support structure determination, suggesting that sCT may have a distinct interaction mode in the formation and stabilization of the ternary complex relative to rAmy, at least for AMY₁R and AMY₃R. The limited pharmacological data for AMY₂R indicates that hCT is more potent for cAMP production at this subtype compared with AMY₁R and AMY₃R (7), and we could indeed also form hCT-AMY₂R-DNGs complexes.

Purified samples for each complex were vitrified and imaged by cryo-EM to yield consensus maps at gold standard Fourier shell correlation (FSC) 0.143 of 2.2 Å (rAmy-AMY₁R), 2.6 Å (rAmy-AMY₂R), 2.4 Å (rAmy-AMY₃R), 3.0 Å (sCT-AMY₁R), 3.0 Å (sCT-AMY₂R), and 3.3 Å (hCT-AMY₂R) (fig. S2, D to I). Additional focused refinement, masking around the heterodimeric receptor, yielded receptor focused maps with global resolutions of 2.3 Å (AMY₁R), 2.8 Å (AMY₂R), 2.5 Å (AMY₃R), 3.3 Å (sCT-AMY₁R), 3.1 Å (sCT-AMY₂R), and 3.4 Å (hCT-AMY₂R)

¹Drug Discovery Biology Theme, Monash Institute of Pharmaceutical Sciences, Monash University, Parkville 3052, Victoria, Australia. ²ARC Centre for Cryo-Electron Microscopy of Membrane Proteins, Monash Institute of Pharmaceutical Sciences, Monash University, Parkville 3052, Victoria, Australia. ³Department of Pharmacology and Toxicology, University of Otago, Dunedin 9054, New Zealand. ⁴Graduate School of Medicine, University of Tokyo, N415, 7-3-1 Hongo, Bunkyo-ku, 113-0033 Tokyo, Japan.

*Corresponding author. Email: patrick.sexton@monash.edu (P.M.S.); denise.wootten@monash.edu (D.W.)

†Present address: Confo Therapeutics, 9052 Ghent (Zwijnaarde), Belgium.

‡Present address: GlaxoSmithKline, Abbotsford 3067, Victoria, Australia.

(fig. S2, D to I). New structures of CTR-DNGs complexes with rAmy (3.3 Å), sCT (2.6 Å), or hCT (2.7 Å) bound were also determined using previously established expression and purification protocols (26) (fig. S2, A to C).

High-resolution features were observed for the CTR-RAMP transmembrane cores, the first 23 amino acids of rAmy, and the heterotrimeric G protein, except for the α -helical domains (AHDs) (Fig. 1, A to I, and fig. S3). Lower density was observed for the CTR-RAMP extracellular domains (ECDs) and associated peptide C termini. For these regions, most side chain rotamers could be modeled using focused refined maps (fig. S3). Where these could not be modeled robustly, the side chains were stubbed in the final models. Limited density was observed for the ECD-transmembrane domain (TMD) linker region and C termini of RAMPs, and the C termini of CTR beyond F409^{8,61} [superscript numbers are the Wootten *et al.* (27) class B numbering scheme] was not detected. The Gas AHD was poorly resolved in

all maps and was masked out in the final three-dimensional (3D) refinement. In postprocessed consensus maps and local refinement maps of AMY₁R and AMY₃R, stable waters could be modeled ab initio (fig. S4), whereas density for ordered annular lipids was observed around the receptor TMD in all higher-resolution maps (Fig. 1). The sCT-AMY₁R complex map displayed reduced density at the top of the RAMP1 TMD and for the RAMP1 ECD, whereas no robust density was observed for the linker. The sCT- and hCT-bound AMY₂R maps exhibited robust resolution for CTR and peptide and low resolution for the RAMP2 TMD and membrane proximal linker region, whereas the relative resolution of the RAMP ECD was improved (Fig. 1 and figs. S2 and S3).

The N-terminal and midregions of the peptide (residues 1 to 23), the transmembrane receptor core, intracellular loops (ICLs) and extracellular loops (ECLs), G α_s -Ras domain, and G $\beta\gamma$ were all well resolved in the maps for the two calcitonin-bound CTR structures,

allowing robust modeling of side chain rotamers for these regions (Fig. 1 and figs. S2 and S3). There was lower density for the ECDs in the consensus maps; however, local refined maps enabled modeling of side chain rotamers to visualize the full-length receptor and peptide (figs. S2 and S3). The rAmy-CTR complex exhibited two distinct conformational classes, accounting for 45 or 55% of the particles, respectively (fig. S2C).

Global structural features of active AMY₁R, AMY₂R, AMY₃R, and CTR structures

The sCT and hCT co-complexes of the CTR exhibited very similar backbone conformation for the receptor core and loops (Fig. 2A). The structures of the CT-bound complexes are consistent with the previously published lower-resolution model for sCT-CTR-Gs [Protein Data Bank (PDB) ID: 6NIY (28)] but substantially extend the map resolution and thus modeling of the full-length receptor (Fig. 1 and fig. S3). Both CT peptides exhibited equivalent N-terminal disulfide-bonded loops, α -helical secondary structure between residues 8 and 19, and disordered C terminus (Fig. 2A and fig. S5A).

Overall, the AMY₁R, AMY₂R, and AMY₃R complex consensus structures exhibited almost identical backbone conformations of the rAmy peptide, heterotrimeric Gs, and CTR subunit, with exception of ICL2 that adopts different conformations linked to differential interaction with individual RAMP C-terminal tail residues (Fig. 2B and fig. S5B).

Within the AMYRs, the location and orientation of the ECDs is very similar, with only subtle differences in the orientation of the RAMP ECD relative to the CTR ECD for individual receptor complexes (Fig. 2B). This differs from the observations with the related calcitonin receptor-like receptor (CLR)-RAMP, CGRP, and adrenomedullin (AM) receptors, where diversity in the ECD location and relative orientation of RAMP and CLR ECDs occurred (29, 30). This may reflect differences in the relative specificity of individual CLR-RAMP complexes for CGRP and AM peptide binding and activation (30), whereas amylin is an agonist for all three AMYRs.

Compared with CT-bound CTR structures (without RAMP), the ECD of the CTR subunit in rAmy-bound AMYRs undergoes an ~12-Å rigid-body translation, measured at C α of E123^{ECD, loop5}, which facilitates packing of the CTR ECD with the antiparallel triple helix conformation of the RAMP ECD (Fig. 2C) and relocates the ECD N-terminal helix away from ECL2 (Fig. 2C). Although there is a high degree of overlap in the location of the N-terminal loop and midregion helical extension of both rAmy and CT peptides within the TM domain, the peptides diverge as they exit the receptor core. The CT peptides have an unstructured

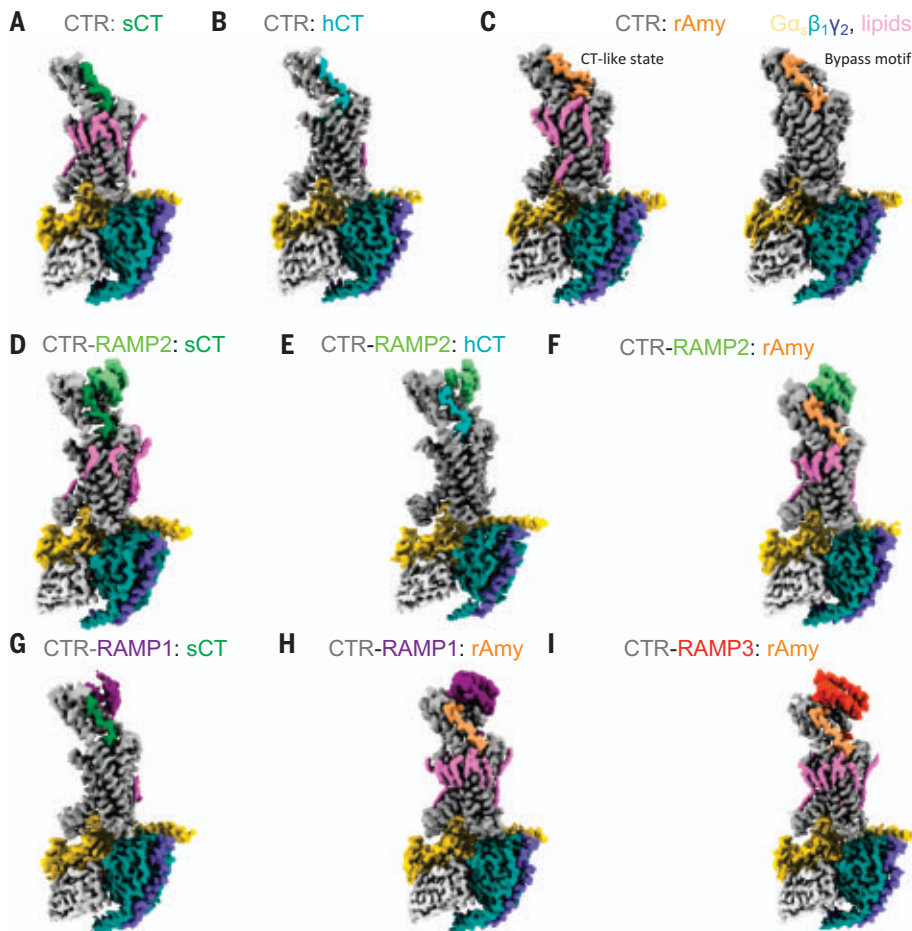


Fig. 1. Cryo-EM structures of active, Gs-coupled complexes of AMYRs and CTRs with peptide agonists.

Shown are orthogonal views of the cryo-EM maps (surface representation). (A to C) CTR-Gs in complex with sCT (A), hCT (B), or rAmy (C). (D to F) AMY₂R-Gs in complex with sCT (D), hCT (E), or rAmy (F). (G and H) AMY₁R-Gs in complex with sCT (G) or rAmy (H). (I) AMY₃R-Gs in complex with rAmy. Protein chains are colored according to the labeling on the figure. Lipids are colored in pink and Nb35 is colored in light gray.

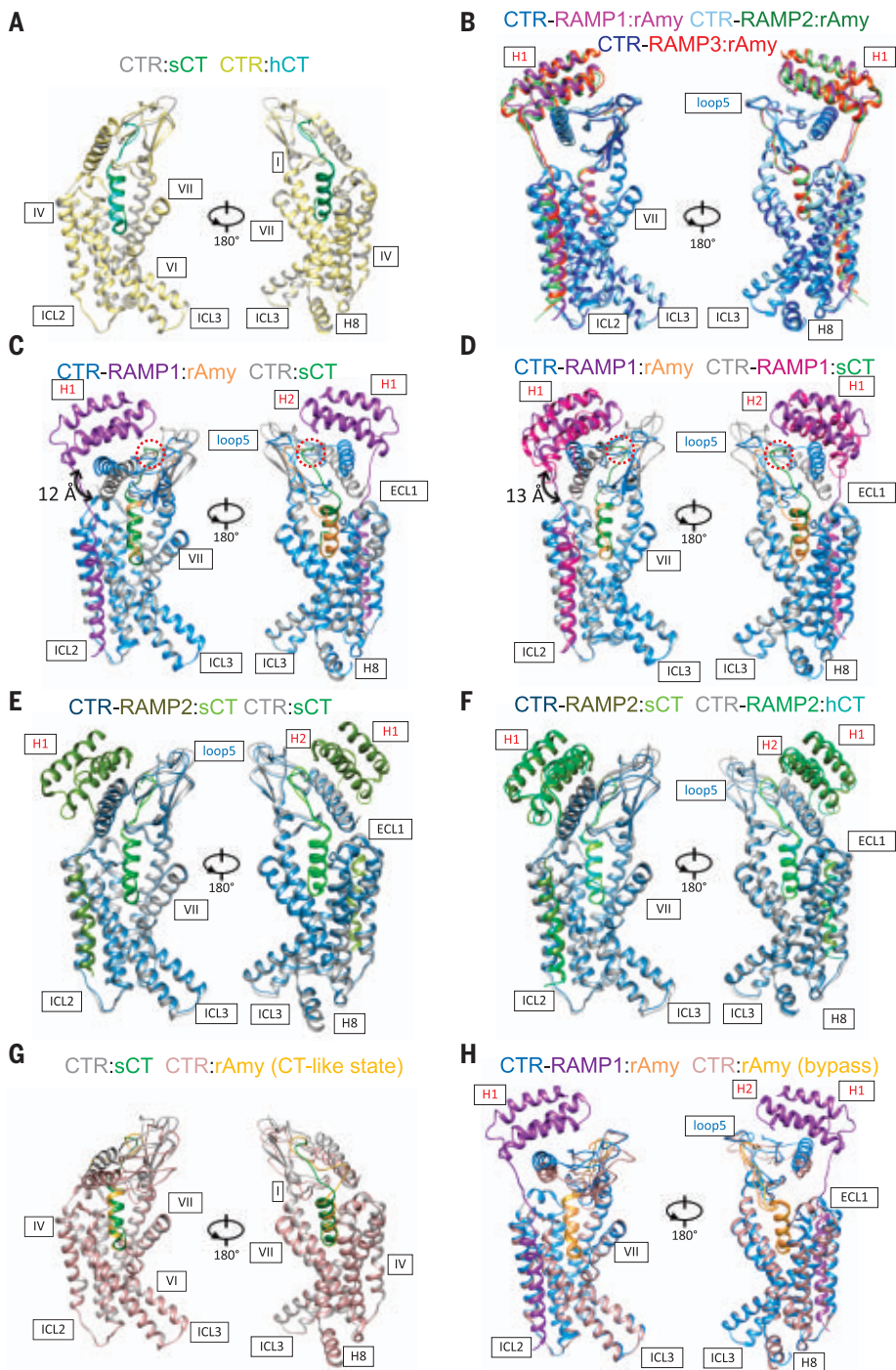


Fig. 2. Comparison of the structures of active, CTR, and AMYR complexes bound to peptide agonists. Structures were aligned on the CTR protomer with protein backbones displayed in ribbon format. **(A)** hCT-CTR versus sCT-CTR. **(B)** AMYRs bound to rAmy. **(C)** sCT-CTR versus rAmy-AMY₁R. **(D)** sCT-AMY₁R versus rAmy-AMY₁R. **(E)** sCT-CTR versus sCT-AMY₂R. **(F)** hCT-AMY₂R versus sCT-AMY₂R. **(G)** sCT-CTR versus rAmy-CTR in the CT-like CTR conformation. **(H)** rAmy-AMY₁R versus rAmy-CTR in the bypass conformation. Protein chains are colored according to the labeling on the panels. The dashed red circles in (C) and (D) highlight the location of the far C-terminal residues of the peptides.

C-terminal region that extends in the same vertical plane as the helix. By contrast, the α -helix of the rAmy peptide terminates half a turn earlier, extending in the plane of the membrane toward the top of the transmembrane

helix 1 (TM1) before forming a tight turn that extends to interact with the ECD (Fig. 2 and fig S5A). Although CT peptides are five amino acids shorter than Amy peptides (32 versus 37 amino acids), the conformational differences in the

“hinge” region of the peptides between the ECD and core-binding domains results in the C-terminal residue of both CT and rAmy peptides occupying a similar location across the structures, although they form distinct interactions with the ECD (Fig. 2, C and D).

Despite the distinctions in ECD engagement, the lateral interaction of the RAMP TMD segment with the CTR had little effect on the backbone conformation of the rAmy-bound CTR core, which exhibits an equivalent conformation to that of the CTR bound to either sCT or hCT (Fig. 2). This included highly similar conformations of each of the ECLs and identical locations of the intracellular ends of the TMD helices that support binding of Gs, including an equivalent degree of kinking of TM6 (Fig. 2). Although the backbone conformations of ICL1 and ICL3 were also identical, subtle differences in the conformation of ICL2 occurred between the CTR complexes and each of the AMYRs (fig. S5), which might be attributed to the nature of the interaction between ICL2 and the RAMP C-terminal tail, as noted above for individual RAMP-CTR complexes.

In the sCT-AMY₁R and sCT- or hCT-bound AMY₂R complexes, the backbone structure and orientation of the CTR protomer, including the ECD, and sCT peptide were effectively equivalent to those in the sCT-CTR complex (Fig. 2, C to F). In the CT-bound AMYR complexes, the RAMP ECD and CTR ECD interface remained similar to that in other AMYR complexes (fig. S6, A to C) with a consequent reorientation of the RAMP ECD compared with rAmy-occupied receptors (Fig. 2, D to F). Whereas the RAMP ECD was generally of lower resolution compared with the CTR protomer ECD in rAmy-bound AMYRs, the RAMP2 ECD resolution in the CT-bound complexes was similar to that of the CTR ECD. By contrast, the RAMP2 TMD was poorly resolved in these latter structures (fig. S6, E and F). As discussed below, RAMP2 has a weaker TMD interaction interface with CTR than RAMP1 and RAMP3 that was also observed for the CLR-based CGRP and AM receptors (30), and this is likely a key factor in the stability of the CT-AMY₂R complex compared with those with AMY₁R and AMY₃R. For AMY₁R, the tighter TMD-TMD interaction is primarily maintained; however, interactions at the top of the RAMP1 TMD and those between the linker and CTR ECL2 are lost to accommodate the shift in the location of the RAMP ECD from that observed in the rAmy-AMY₁R complex. In contrast to the CT-AMY₂R complexes, the RAMP1 ECD is more dynamic along the interface with the CTR ECD because of the stronger TMD constraint (fig. S6D). The tighter TMD constraint is also likely to contribute to the lower potency of hCT at AMY₁R and AMY₃R.

The rAmy-bound CTR complex could be resolved into two major classes, differing in the

ECD orientations and peptide conformations. In the first class (~55%), rAmy displayed a “bypass” motif, and the CTR ECD was in a similar orientation to that seen in rAmy-bound AMYRs (Fig. 2H), whereas in the second class (45%), the receptor ECD was similar to that in CT-CTR complexes, with the midregion of rAmy becoming disordered to accommodate this conformation (Fig. 2G).

Peptide interactions with receptors

N-terminal peptide binding and the selective activation of CTR and AMYRs

Amy and CT follow the classical “two-domain model of binding” proposed for class B1 peptide hormone GPCRs with initial engagement of the peptide C terminus by the receptor ECD facilitating interaction of the peptide N terminus with the receptor TMD core to initiate receptor activation (31).

As reported for the CLR-RAMP structures (29, 30), there are no direct interactions between peptide N termini and the RAMPs. Furthermore, the RAMPs do not significantly modify the structure of the core and extracellular face of the CTR, resulting in a highly conserved binding pocket for the N-terminal sequences of the peptides (fig. S7A). Consequently, the overall patterns of peptide interaction for CTR and AMYRs are similar, with a bulky N-terminal loop (residues 1 to 7) and initial helical segment (residues 8 to 16) principally interacting with TM3/TM5/ECL2 and TM6/TM7/ECL3, with additional interactions of the distal helix (residues 16 to 18 for rAmy, residues 16 to 21 for CT) toward the top of TM1 and ECL1 (Figs. 3 and 4 and tables S1 and S2). There is also an extensive network of structural waters surrounding the peptide N terminus that was resolved in the higher-resolution maps for AMY₁R and AMY₃R that contribute to peptide-receptor engagement and extended from the base of the peptide to the conserved class B1 GPCR central polar network (27, 31) (Fig. 3, E to H, and fig. S4). Although density for waters was not resolved in the lower-resolution cryo-EM maps, the overlap in receptor side chain rotamers across the structures indicates that similar water networks are also likely to be present in these structures.

The N-terminal peptide loops, constrained by the disulphide bridge of either C2^{rAmy}-C7^{rAmy} or C1^{CT}-C7^{CT}, are critical for agonist activity and this is reflected in the loss of potency of N-terminal truncated peptides, including sCT (8-32) (6) and rAmy (8-37) (32). The N-terminal loops bind deeply within an open TMD cavity that is enabled by the splayed outward location of TM6/TM7/ECL3 (Fig. 3). Whereas the loop length differs between Amy and CT peptides, neither removal of Ser2^{sCT} nor the K1^{hAmy}A substitution analogs have altered peptide potency (32, 33). These residues are

solvent exposed in the structures consistent with tolerance of the shorter loop length. There are conserved H-bonds between the backbone of A5^{rAmy}/S5^{CT} and P360^{6.57} and between the conserved peptide T6 and H302^{5.40} (Fig. 3, A,

C, and E). The latter is the only conserved interaction residue within the N-terminal loop across all CT-family peptides, and it plays a vital role in agonist-dependent cAMP production. For example, T6^{hAmy}A substitution results in a loss

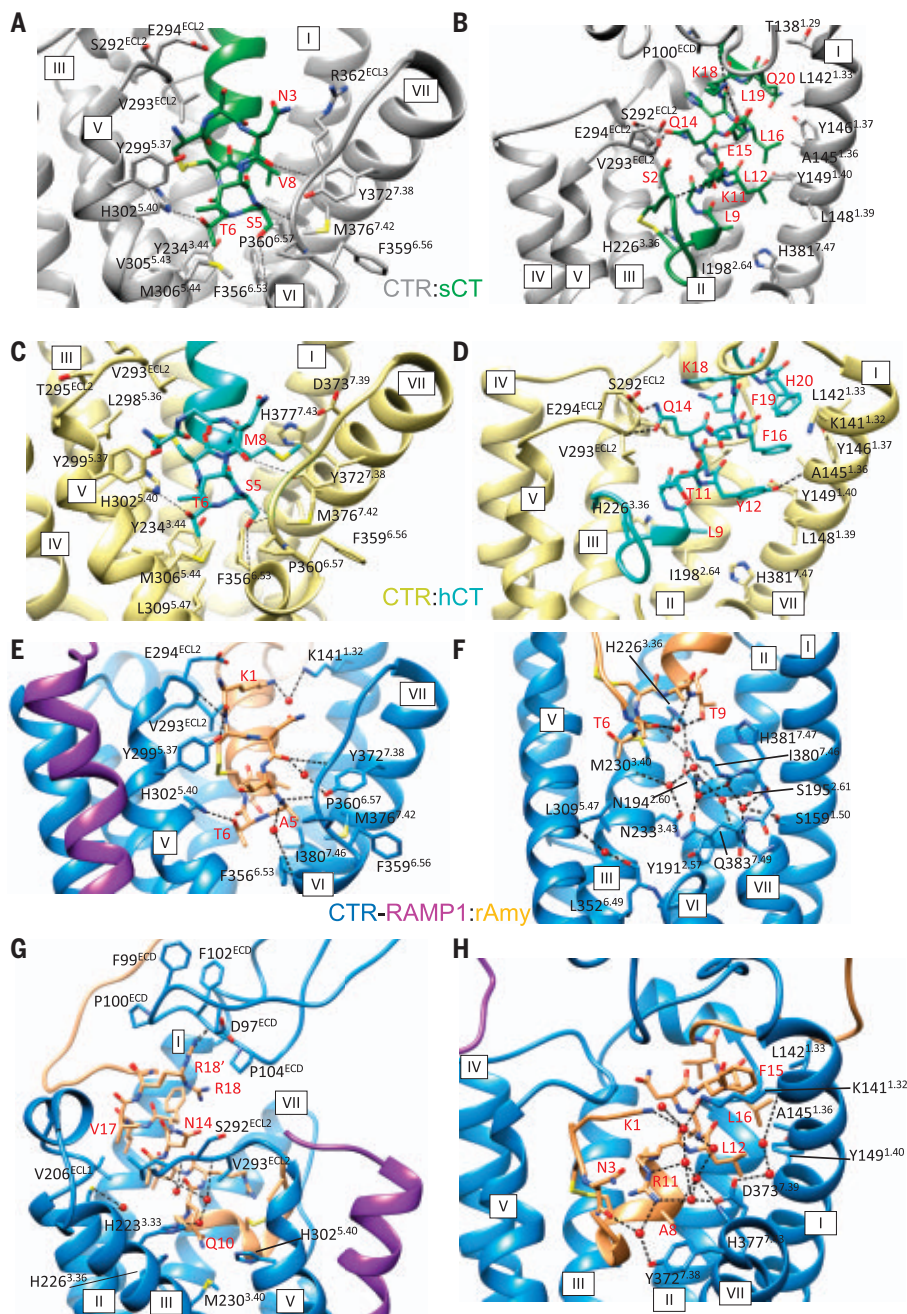


Fig. 3. The N-terminal activation domains of CT and Amy peptides bind to similar pockets in the CTR protomer of CTR and AMYRs. CTR residues that interact with peptides or waters (red balls) are displayed in stick format; multiple side views are depicted for clarity. (A, C, and E) TMD bundle viewed from the upper portion of TM5/TM6 with side chains of CTR (361-362) omitted for clarity. (B, D, and H) TMD bundle viewed from the upper portion of TM6/TM7 with CTR (359-380) omitted for clarity. (F) TMD bundle viewed from the middle portion of TM6/TM7 with CTR (353-379) omitted for clarity. (G) TMD bundle viewed from the upper portion of TM4/TM5 with CTR (274-303 and 38-61) omitted for clarity. Dashed lines depict hydrogen bonds as determined using UCSF Chimera. In addition, (A) and (B) show the sCT-CTR complex, (C) and (D) show the hCT-CTR complex, and (E) to (H) show the rAmy-AMY₁R complex. For clarity, only the side chain residues for the key interactions in each panel are displayed in stick format.

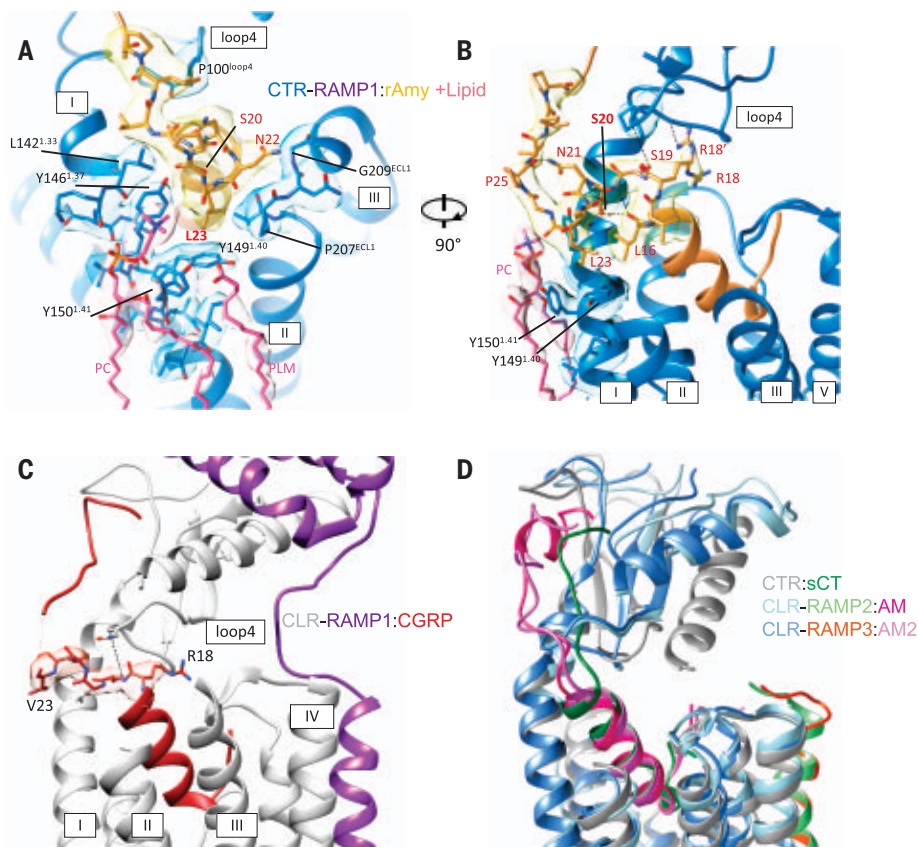


Fig. 4. The “bypass” conformation of the midregion of rAmy. (A and B) Map to model representation of the bypass motif of rAmy (residues 19 to 25) and the interactions with the CTR TM1 stalk, ECL1, and phospholipids. Receptor TM helices are numbered using roman numerals. H-bonds are shown as dashed lines in (B); CTR residues 201 to 218 are not displayed for figure clarity. (C) Map to model representation of the active CGRPR complex, illustrating a similar bypass conformation of hCGRP (residues 19 to 23); CLR residues 200 to 209 are not displayed for figure clarity. (D) AM peptides do not display a bypass conformation at AM₁R or AM₂R and exit the receptor core in the same plane as CT peptides. The RAMP ECDs, CTR residues 207 to 216, and CLR residues 35 to 40 and 200 to 209 are not displayed for figure clarity. Backbone protein and EM density are colored according to the labeling on the figures.

of ~60% in maximal response (E_{\max}) for CTR, AMY₁R, and AMY₃R and a substantial reduction in peptide potency at these receptors (32). Similarly, alanine substitution of Thr at this position in related CT-family peptides leads to large attenuation of signaling response; however, there is less effect on affinity (34–36). The hydroxyl of S5^{CT} forms a potential additional direct H-bond with F356^{6,53} (Fig. 3, A and C), whereas the equivalent A5^{rAmy} interacts with F356^{6,53} through a water-bridged H-bond (Fig. 3E). The serine substitution of A5^{hAmy} leads to an ~10-fold increase in the potency for CTR and AMY₃R (but a twofold increase for AMY₁R) (32), suggesting that the stability of bonds between the receptor and loop residues could contribute to the observed functional phenotype of individual receptors.

The hydroxyl of T9^{rAmy} engages an extensive H-bond network mediated by several structural waters that link to side chains of central polar residues (H226^{3,36}, N194^{2,60},

N233^{3,43}, Q383^{7,49}, S159^{1,50}, and S195^{2,61}), as well as backbone atoms (M230^{3,40}, Y191^{2,57}, I380^{7,46}, and H381^{7,47}) at the bottom of the binding pocket (Fig. 3F and fig. S4). This structural water network fills the space at the base of the peptide-binding site and likely contributes to stabilization of the active receptor conformation. Alanine substitution of T9^{hAmy} leads to an ~10-fold reduction in potency along with decreased affinity (32). The equivalent residue L9^{CT} forms hydrophobic contacts with H381^{7,47}, I198^{2,64}, and H226^{3,36} (Fig. 3, B and D). Unlike V8^{sCT} or A8^{rAmy}, the hydrophobic side chain of M8^{hCT} extends toward ECL3, interacting with M376^{7,42}, D373^{7,39}, and H377^{7,43} (Fig. 3C). Consistent with this observation, M376^{7,42}A mutation in CTR causes a selective reduction in the affinity and potency of hCT (37). In comparison with sparse interaction of G10^{CT} with the receptor, Q10^{rAmy} forms interactions with a cluster of residues including V293^{ECL2}, H226^{3,36}, M230^{3,40}, and H302^{5,40} (Fig. 3G and

table S2). Q10A substitution in either hAmy or pramlintide increases the maximal cAMP responses relative to the parent peptides, at CTR, AMY₁R, and AMY₃R (32), with varying effects on peptide potency, suggesting that Q10^{rAmy} interactions can influence signaling efficacy.

The triplet of residues from 11 to 13 in CT family peptides (R¹¹L¹²A¹³, rAmy; K¹¹L¹²S¹³, sCT; T¹¹Y¹²T¹³, hCT) have important roles in peptide selectivity and off-rate kinetics. Similar to CGRP (29), the side chain guanidine of R11^{rAmy} is packed toward the N-terminal peptide loop forming polar interactions with the backbones of C2^{rAmy} and T4^{rAmy} (Fig. 3H). The bulky charged surface of R11 stabilizes multiple structural waters, facilitating water-mediated bridges between rAmy and ECL3, including interactions between N3^{rAmy} and Y372^{7,38}, as well as H377^{7,43} and the backbone of A8^{rAmy} (Fig. 3H). R11^{hAmy}A substitution induces a sixfold loss of potency at AMY₁R and AMY₃R, but not CTR, in cAMP assays, indicating that this residue in Amy peptides contributes to the selective activation of AMYRs (32). The smaller positively charged K11^{sCT} occupies a distinct rotameric position to R11^{rAmy} in all sCT-CTR complexes, as illustrated for the sCT-CTR complex (Fig. 3B), and forms fewer and distinct interactions, including likely transient H-bonds with S2^{sCT} and N3^{sCT} (observed in a subset of structures) that could stabilize the N-terminal loop conformation and H-bonding of N3^{sCT} with R362^{ECL3}. However, K11^{sCT} is in a polar pocket that likely facilitates additional water-mediated interactions in addition to a weak salt bridge with D373^{7,39}. By contrast, T11^{hCT} does not H-bond with the N-terminal loop residues of the peptide and has only a weak hydrophobic interaction with V293^{ECL2} (Fig. 3D). Prior MD simulations of hCT modeled into the CTR were consistent with hCT forming weaker and less stable interactions within the binding pocket and particularly with ECL3 (28). In the absence of stabilization of the conformation of the N-terminal loop by intramolecular interaction, the C1^{hCT}-C7^{hCT} disulfide bond is required for high peptide potency, whereas removal of this bond by Acm1,7 substitution in sCT has limited effect (38).

Among the CT family peptides, sCT exhibits a very slow binding off-rate that is not seen for hCT, Amy, or the truncated antagonist analog sCT (8–32) (5, 39). The persistent binding of sCT requires formation of an active conformation and is associated with prolonged signaling, but the transition to pseudoirreversible binding occurs slowly at the population level (39), suggesting that this state is infrequently sampled. Using chimeras of sCT and hCT, a critical sequence for the distinct kinetics of sCT was resolved to residues 11 to 13 (39, 40). R11-substituted analogs of sCT have similar or

slower off-rates to the parent peptide, including the amylin mimetics davalintide and AM1784, which contain an R¹¹L¹²S¹³ motif (5, 41), whereas those peptides lacking a polar S13 have faster off-rates, including rAmy, cagrilintide, and AM1213 (5). These data suggest that the polar S13^{sCT} provides additional critical interactions. In the structures, S13^{sCT} has only limited direct interactions with the receptor but is within potential water-mediated H-bond distance to a series of His residues in TM2 and TM3, H201^{2.67}, H223^{3.33}, and H226^{3.36} (fig. S7B). Indeed, weak density consistent with a structural water can be observed in the sCT-AMYR structures (fig. S7B). Although speculative, it is possible that there is a critical geometry of residues that must be attained for a stable interaction network to form that can provide a second high-energy anchor to that enabled by K/R at position 11. The kinetics of peptide dissociation is potentially important in the design of clinical Amy/CT analogs because there is regulatory concern regarding long-term use of sCT-like, slow off-rate agonists based on a weak correlation between sCT use and cancer risk in a meta-analysis of clinical data (42). Nonetheless, off-rate kinetics do not appear to be important for receptor selectivity (5).

All CT-family peptides except hCT (Y12, F16) contain conserved Leu/Ile residues at positions 12 and 16 that contribute to the hydrophobic face of the short amphipathic α -helix and reside deep within a groove between TM1 and TM2 (Fig. 3, B, D, and H, and tables S1 and S2), as has been previously described for CTR, and the CLR-RAMP-based CGRPR and AMR complexes (26, 28–30). The hydrophobic packing enabled by these residues is important for peptide activity with Ala substitution, particularly at position 12, decreasing potency in cAMP assays (32, 34, 43), whereas L12 substitution in hCT increases potency (44).

N14^{rAmy} and Q14^{CT} form conserved hydrophobic contacts with L291^{ECL2}–E294^{ECL2} in an orientation that also provides solvent accessibility. Position 14 in CT peptides can be derivatized while maintaining affinity and potency, indicating that the polar head group is not required for peptide activity. In CT peptides, D15^{hCT}/E15^{sCT} constrain the position of K18^{CT} to differing extents through salt bridge/H-bond interactions, respectively, whereas E15^{sCT} can also support a salt bridge with K141^{1.32}. Both peptides form additional hydrophobic interactions with TM1; F19^{hCT}/L19^{sCT} with L142^{1.33} and K141^{1.32} (Fig. 3, B and D), consistent with moderate reductions in the affinity of hCT after alanine mutation of K141^{1.32}, L142^{1.33}, and K143^{1.34} (28). F15^{rAmy} forms hydrophobic interactions with a cluster of residues (K141^{1.32}, A145^{1.36}, and L142^{1.33}) in the TM1 stalk (Fig. 3H); however, F15A^{rAmy} substitution causes only weak effects on peptide-mediated cAMP

production at either CTR or AMYRs (32). The lack of constraint on the location of the positively charged R18^{rAmy} enables this residue to adopt two alternate rotamer conformations that are observed in all three AMYRs (Fig. 3G). The upward conformation of R18^{rAmy} enables extensive interactions with D97^{ECD}, F99^{ECD}, P100^{ECD}, and F102^{ECD} in loop 4 of the CTR ECD, including an H-bond with F102^{ECD}. By contrast, the constrained position of K18^{sCT} restricts interactions with the ECD that are limited to P100^{ECD} and D101^{ECD}. This dynamic interaction of R18^{rAmy} with the ECD could be influenced by allosteric modulation of the ECD orientation by RAMPs. It could also contribute to the termination of the peptide helix and the subsequent turn conformation of the middle region of rAmy.

The “bypass” motif of the midregion in rAmy contributes to selective interaction with AMYRs

The N-terminal helix of CT peptides terminates at residue 21, between the TM1 stalk and ECL1, and directly extends upward to the CTR ECD loop 4 region. By contrast, in rAmy, the helix terminates half a turn earlier at S19^{rAmy}, and the additional five amino acids of the Amy peptide sequence extend through the gap between TM1 and ECL1 before turning sharply at P25^{rAmy} and redirecting toward the ECD (Fig. 4, A and B, and fig. S5). This “bypass” conformation (S19^{rAmy}–P25^{rAmy}) was conserved across all rAmy-AMYR complex structures with robust density in the maps (Fig. 4, A and B), indicating that this may be an important feature of selective AMYR agonism. Within this short sequence, S19^{rAmy} can H-bond with the backbone of P100^{ECDloop4}, whereas the hydroxyl of S20^{rAmy} bridges the backbones of L16^{rAmy} and L23^{rAmy}, and N21^{rAmy} forms an H-bond with the backbone of P25^{rAmy} (Fig. 4B). These intramolecular polar interactions constrain the secondary structure of the motif that also forms extensive van der Waals interactions with a cluster of hydrophobic residues including L142^{1.33}, P207^{ECL1}, Y146^{1.37}, G209^{ECL1}, and Y149^{1.40} (Fig. 4A). In particular, the bulky nonpolar side chain of L23 inserts downwards to form a hydrophobic contact with Y149^{1.40}, anchoring the peptide segment to the outer surface of the CTR bundle. Additionally, there is a lipid head group in proximity to L23^{rAmy} and G24^{rAmy}, supported by well-resolved EM map density, which is tightly packed with Y146^{1.37} and Y150^{1.41} that likely further supports anchoring of L23^{rAmy}. Density for this lipid molecule is observed at an identical position across both the high-resolution AMYR maps and the lower-resolution CTR structures (Figs. 1 and 4). The conformation and interactions of the Amy bypass motif are likely critical to the selectivity of Amy peptides for AMYRs because they constrain the position of the pep-

ptide and the orientation of the receptor ECD, as discussed below in the context of 3D variance analysis (3DVA) of CTR and AMYRs. Moreover, the lipid interactions with TM1 might contribute to the strength of the anchoring of the bypass motif and thus to selective engagement of AMYRs by amylin.

In contrast to the well-resolved density for rAmy in the AMYRs, the equivalent midregion of CGRP was poorly resolved in the published active CGRPR (29). Nonetheless, CGRP also primarily exhibited a bypass-like conformation when bound to the CGRPR (Fig. 4C) (29), which is consistent with the overlap in orientation of the ECD of the CGRPR and those of the AMYRs and the ability of CGRP to act as a high-potency agonist of AMY₁R. However, whereas the bypass conformation of Amy peptides is preserved by multiple intramolecular interactions, the weaker secondary structure of CGRP may not support productive engagement with CTR complexes with RAMP2 or RAMP3, similar to the selectivity seen between CGRPR and AMRs. In this latter example, ECD dynamics that were dependent upon the RAMP linker sequence were critical for the observed peptide selectivity phenotype (30). It is likely that ECD dynamics are also important for AMYRs for peptides that cannot form a stable bypass conformation. Despite being of equivalent length to CGRP and Amy peptides, after the N-terminal loop, the AM peptides do not exhibit a bypass conformation but instead exit the receptor in the same plane as the CT peptides (Fig. 4D) in a manner that allows the AM₁R and AM₂R to adopt very distinct ECD orientations to the CTR or AMYRs (30).

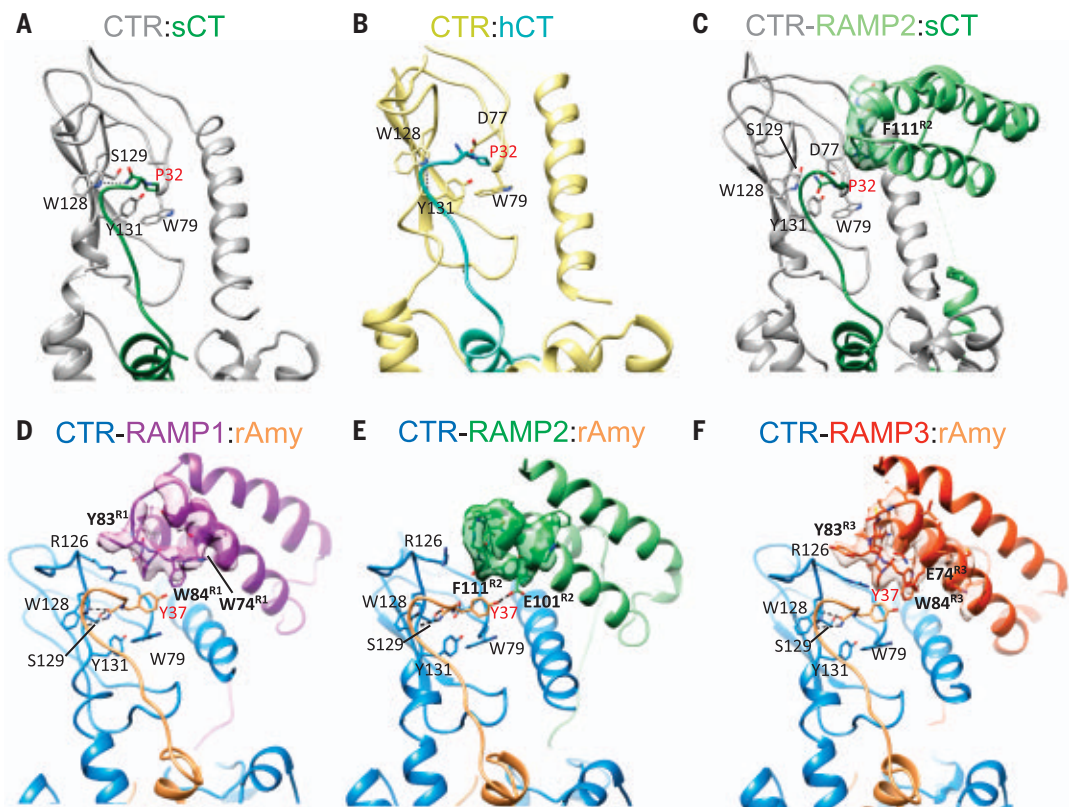
The binding initiator: C-terminal peptide interactions with the ECD

The C-terminal ~10 amino acids of CT-family peptides, including sCT, hCT and rAmy, are devoid of secondary structure and bind to a similar groove within the ECD of their cognate receptors. The binding of the peptide C terminus with the isolated ECD has been previously described for sCT and in models of Amy binding to AMYR ECDs (45–47).

Multiple crystal structures of the CTR ECD bound to sCT analogs (45, 47) have provided molecular details that underpin the high-affinity binding of sCT and have been used to model the low-affinity interaction of hCT to the isolated ECD (45). These key interactions were confirmed in our full-length, active-state CTR structures (Fig. 5A and table S1). CT residues 22 to 25 form extensive hydrophobic contacts with a cluster of residues in loop 4, including F99^{ECD}, P100^{ECD}, D101^{ECD}, and F102^{ECD}. In addition, the conserved T25^{CT} forms H-bonds with N135^{1.26} and D101^{ECDloop4}, contributing to the stability of peptide interactions (table S1). The type II β turn formed by residues 28 to 31 of CT peptides leads to

Fig. 5. The amidated peptide C terminus makes critical contacts with the receptor ECD.

(A to C) Interactions of the C-terminal Pro-NH₂ of CT peptides with the CTR ECD in complexes with CTR [hCT (A); sCT (B)] or AMY₂R [sCT (C)]. (D to F) Interactions of rAmy C-terminal Tyr-NH₂ with CTR and RAMP ECDs in AMY₁R (D), AMY₂R (E), or AMY₃R (F). The side chains of contact CTR residues, the α 2- α 3 loop of individual RAMPs, and the peptide C terminus are displayed in x-stick representation. H-bonds are shown as dashed lines. The cryo-EM density of RAMP residues proximal to the peptide C terminus are displayed as transparent surfaces.



shape complementarity that supports interactions with ECD loop 5. The C-terminal P32-NH₂ is packed over W79^{ECD}, and there are complementary H-bonds between the C-terminal amide and the backbone of S129^{ECD} (Fig. 5, A and B, and table S1). sCT can also form H-bonds with N135¹⁻²⁶ through R24^{sCT} and T27^{sCT}, whereas the side chain of T31^{sCT} provides an additional intramolecular H-bond to the backbone of G28^{sCT} to increase the stability of the β turn. S29^{sCT} likely also H-bonds to E123^{ECD}, as is seen in ECD crystal structures (47), albeit that side chain density for E123^{ECD} was not resolved in the map. hCT contains nonpolar substitutions (I27^{hCT}, V29^{hCT}, and A31^{hCT}) of these key sCT residues, and consequently Q24^{hCT} is oriented away from N135¹⁻²⁶. Collectively, these differences reduce direct interactions with the ECD and stability of the structurally important β turn, markedly reducing hCT affinity for the CTR ECD (table S1).

The interactions observed in the rAmy-bound ECD in the local refined EM maps are consistent with the past predictions (46) from homology models based on the ECD crystal structures of CLR-RAMP1 [CGRP analog-bound, PDB ID: 4RWG (48)] and sCT-bound CTR [PDB: 5II0 (45)]. The C-terminal peptide binding interface is formed by loops 2, 4, and 5 of the CTR ECD and the α 2- α 3 loop of RAMPs (Fig. 5, D to F, and table S2). The proposed binding-site residues within CTR ECD have been validated

by alanine mutations in AMY₁R (46). The bypass motif in the midregion of rAmy ends at P29^{rAmy}, in proximity to ECD loop4. T30^{rAmy}, equivalent to T25^{CT}, resides in an identical position and contributes highly conserved interactions with F99^{ECD}, D101^{ECD}, F102^{ECD}, and N135¹⁻²⁶. This Thr is conserved across CT, CGRP, and Amy peptides, providing a common, stable anchoring of the peptides as they transition from the TM domain to interact with the ECD. T30A^{rAmy} leads to substantial reduction in peptide-mediated cAMP potency for both CTR (5-fold) and AMYRs (>10-fold, AMY₁R and AMY₃R), whereas V32A^{rAmy} causes an ~10-fold loss of potency at AMY₁R and AMY₃R but not CTR alone (32). V32^{rAmy} forms extensive hydrophobic interactions with Y131^{ECD}, W128^{ECD}, and F102^{ECD}, facilitating the interactions of the adjacent type I β -turn (residues 33 to 36) within the complementary pocket formed by H121^{ECD}, E123^{ECD}, R126^{ECD}, and W128^{ECD} in loop 5. Ala substitution of the “turn inducer” G33^{rAmy} resulted in significant attenuation of potency for cAMP production at AMYRs but had no effect on CTR alone (32).

Critical interactions of the amidated C-terminal amino acids

The amidated Y37^{rAmy} H-bonds with the backbone of S129^{ECD}, and the carboxylate analog of hAmy has markedly reduced potency at AMYRs (32). Similar to F37^{CGRP} in the CGRPR, the aromatic side chain of Y37^{rAmy} exhibits

perpendicular π stacking with W79^{ECD} (Fig. 5, D to F) and direct hydrophobic interactions with W84^{R1,R3}, P85^{R1,R3}, or F111^{R2} that have been validated by the loss of peptide affinity with cognate alanine mutation of RAMPs (49, 50). The importance of the C-terminal residue in AMYR function has also been demonstrated in studies using C-terminal residue exchange peptides (among CT, CGRP, and Amy) on either intact receptors or isolated ECD (32, 45, 51). Regardless of peptide type, a proline amide increases affinity and potency at CTR in the presence or absence of RAMPs, whereas a bulky Tyr or Phe requires interaction with RAMPs to rescue their poor affinity on CTR alone. For example, the P32Y substitution in sCT(8-32) decreases affinity for CTR by 40-fold (45), whereas the incorporation of proline to replace Y37^{rAmy} increases potency at CTR to a greater extent than at AMYRs with a consequent reduction in selectivity (32). A role for the C-terminal Tyr in ligand affinity and specificity was illustrated with the antagonist AC187 [acetyl-(Asn30, Tyr32)-sCT(8-32)] (fig. S1), which is a more effective antagonist of peptide signaling at AMYRs than sCT compared with the parent antagonist sCT(8-32) (6).

We also observed specific structural differences in the ECD-binding interfaces between CTR and individual RAMPs. First, F83^{R1} and Y83^{R3} are oriented over ECD loop 5 residues N124^{ECD}-R126^{ECD} of CTR, which stabilizes the RAMP-CTR interface and likely influences

interactions of the loop 5 residues with the proximal N35^{rAmy}-T36^{rAmy} residues, (Fig. 5, D and F). By contrast, the lack of side chain in the equivalent G110^{R2} weakens the interface, and there is poorly defined side chain density for R126^{ECD} in the AMY₂R complex. Prior alanine mutagenesis of R126^{ECD} in AMY₁R or CTR indicates that this residue is important for Amy but not hCT potency, selectively for AMY₁R (46). Second, E101^{R2} and E74^{R3} are in close proximity to the hydroxyl of Y37^{rAmy} with the potential to form transient polar contacts, whereas the equivalent W74^{R1} is remote from Y37^{rAmy} (Fig. 5, D to F). Consistent with this, Ala or Lys mutation of W74^{R1} did not alter rAmy-induced cAMP production, whereas the W74E^{R1} mutant increased potency (52). Conversely, E74W^{R3} mutation decreased rAmy potency (52). The differential role of polar contacts in peptide potency between AMYRs likely contributes to the selectivity of CGRP for AMY₁R relative to the other AMYRs. This is supported by Y37F^{rAmy} substitution that selectively decreased potency for cAMP production at CTR and AMY₃R. However, although the reciprocal F37Y^{CGRP} displayed a higher E_{\max} than CGRP at AMY₃R, it had a lower potency at both AMY₁R and AMY₃R (32), indicating that peptide-receptor geometry and dynamics are also important.

The receptor–Gs protein interface

Regardless of the presence of RAMPs, the overall interfaces between the CTR and Gs protein were nearly identical for all six structures with overlapping positions of Gs proteins (fig. S10A). The exception to this was ICL2, which exhibited high flexibility and adopted a distinct conformation in each consensus structure (figs. S5B and S9).

The primary interactions of the CTR with the G protein occurred through the C-terminal Gs $\alpha 5$ helix ($\alpha H5$), where it engaged within the receptor cavity created by the outward movement of TM6 and TM5 that is a conserved feature of activated class B1 GPCRs, forming highly conserved hydrophobic and H-bonded interactions (E392 ^{$\alpha H5$} , N396^{S.48}, Q384 ^{$\alpha H5$} , I248^{S.58}, and R385 ^{$\alpha H5$} , K326^{S.64}) across all structures (fig. S10, A to C, and table S3). Within the higher-resolution structures of AMY₁R and AMY₃R that included density for structural waters, Y391 ^{$\alpha H5$} formed water-mediated H-bonds with the highly conserved E240^{S.50}, and a cluster of waters engaged in a polar interaction network linking R180^{S.46}, N395^{S.47}, and E392 ^{$\alpha H5$} (fig. S10, B and C). Because of the conserved position of the $G_{\alpha s}$ subunit, the $G\beta 1$ also exhibited conserved interactions with CTR through residues of helix 8 and ICL1.

Within the flexible conformation of ICL2, the F253^{ICL2} deeply inserted into the junction of the αN and $\alpha 5$ helices of $G_{\alpha s}$, and this conserved rotamer anchors the initial position

for the packing of ICL2. Nonetheless, the modeling accuracy of side chains is limited between T254^{ICL2} and R258^{ICL2} because of the low-resolution density. In particular, the density for ICL2 (T254–R256) was very poor and discontinuous in the hCT-bound CTR, so even the backbone position is ambiguous, suggesting that ICL2 interactions with Gs may be more dynamic in hCT- versus sCT-bound complexes (fig. S3). Distinctions in the conformational changes of Gs protein for sCT- and hCT-bound receptors have also previously been reported (40). Among the AMYRs, AMY₃R exhibited the greatest conformational dynamics in the side chain rotamer of F253^{ICL2} (movie S1).

The RAMP–CTR interface and allosteric modulation of receptor phenotype

RAMPs form extensive interactions with the ECD and TM domain of CTR, similar to that seen for CLR–RAMP structures (29, 30). Previous mutagenesis and modeling of the AMY₁R ECD has demonstrated that RAMP1 allosterically regulates the ligand-interactive residues in the CTR–ECD and validated the importance of the conserved RAMP–CTR ECD interface along the N-terminal CTR helix distal to the peptide-binding site in modulation of receptor selectivity (46). These predicted structural features were confirmed in our full-length CTR–RAMP structures, where key RAMP residues interacting with the far C terminus of the peptides and the N-terminal helix of CTR were robustly modeled despite the lower overall map resolution for the RAMP ECDs (Fig. 5).

As expected, the RAMP TM domain in rAmy-bound AMYRs interacts with CTR residues in TM3, TM4, and TM5, similar to the interaction of RAMPs with CLR observed in CLR–RAMP structures (29, 30) (fig. S8A), and then extends beyond the TM helix (residues I11–I14^{R1/R3}/138–141^{R2}) to make extensive, conserved, interactions with ECL2. This includes H-bonds between the conserved Asp (D113^{R1/R3}/D140^{R2}) and each of H296^{ECL2} and T295^{ECL2}, as well as sequential hydrophobic interactions (fig. S8B). Beyond this, the RAMPs have a disordered linker that connects to the RAMP ECD. This is distinct from the weaker engagement of the 138–141^{R2} segment that was observed in the AM₁R (CLR–RAMP2) cryo-EM structure (30) and likely reflects the stabilization of the RAMP ECD location that arises from the anchored bypass motif of rAmy.

Overall, the RAMP2 TM in the rAmy–AMY₂R consensus structure displayed looser packing with the CTR TMD than the corresponding RAMP1/RAMP3 domains and a 2.7 Å/3 Å downward shift from P158^{R2} (L131^{R1}/V131^{R3}) because of disruption of the midregion of the canonical α -helical backbone (fig. S8C). The C-terminal tail of RAMP2 unwound from R167^{R2} but was resolved to S171^{R2} supported

by H-bond interactions between the N-terminal helix (αN) of Gs, Q35 ^{αN} , and D170^{R2}/S171^{R2} in the consensus structure (fig. S9B). The C terminus of the RAMP3 helix also unwound from R140^{R3}, whereas there was a continuous helix to the last resolved residue in RAMP1 (R143^{R1}). This was distinct from CLR–RAMP1 and CLR–RAMP3 structures, in which the resolved C-terminal conformation was equivalent to that observed in the AMY₁R (fig. S9D). Nonetheless, 3DVA of the cryo-EM data for the complexes revealed that the receptor–G protein interface is conformationally dynamic. The RAMP3 C terminus transitions between helical and nonhelical conformations. The helical unwinding allows RAMP3 to maintain interactions with the G protein αN as the latter rocks away from ICL2. The interactions are similar to those between RAMP2 and αN , but are weaker and more dynamic interactions (movies S1B, S1C). By contrast, interactions between the RAMP1 C terminus and the Gs αN were only apparent when this domain was closer to ICL2 (movie S1A). These differences in the interaction of the RAMP C terminus and the G protein likely contribute to the increased potency of CGRP for Gs-mediated cAMP production seen with the RAMP2 chimera containing the RAMP1 C terminus (7) and the improvement in the expression of the AMY₂R phenotype with overexpression of G proteins (8). Furthermore, our previous studies demonstrated marked reductions in amylin binding for C-terminal deletion mutants of all three RAMPs that could be partially overcome by overexpression of Gs (8).

Although there are differences in the conformations of ICL2 and dynamic interactions of the RAMP C terminus with the Gs protein, overall, the orientation of the Gs heterotrimer with the receptors and the receptor–G protein interface is similar to that described previously for CTR and other class B1 GPCRs (26, 28, 31) (fig. S10 and table S3).

In recombinant systems, RAMP2 coexpression with CTR generates a weaker AMYR phenotype than is seen with coexpression of RAMP1 or RAMP3 (3, 6–8). This is likely due, at least in part, to the weaker TM interaction interface between CTR and RAMP2 because TM chimeras of RAMP1 and RAMP2 have demonstrated that this domain is the major determinant of the level of rAmy binding (7).

As discussed above, CTR ECD orientations were equivalent for active CT–AMYR and CT–CTR complexes and distinct from those in rAmy-bound AMYR structures. For the AMY₂R, this was enabled by the weaker TM interface of RAMP2 that has poorly resolved density in the CT-bound complexes, with additional loss of resolution for the RAMP linker that no longer forms stable interactions with ECL2 (fig. S8A). The C terminus of sCT has high relative affinity for the isolated CTR ECD (45, 47, 51)

independent of G protein binding and formation of the active-state conformation. Quantitative evaluation of the extent of conformational movement between the first and last frames from 3DVA principal components reveals that, although mobile, the length of the CT peptides constrains the conformational space explored by the ECD. The maximal deviations are 4 to 5 Å (measured from the C α of E123^{ECD} loop 5; Fig. 6A and movie S2, A and B) and ~3 to 5 Å (Fig. 6, A to C, and movie S2, C to E) in the CT-CTR and CT-AMYR complexes, respectively. The rAmy-AMY₁R and rAmy-AMY₃R complexes exhibit even more stable ECD orientations that are constrained by both the rAmy conformation that is anchored by the bypass domain and the robust TM interface between RAMP and CTR; <2 Å deviations in CTR ECD position across the extremes of the 3DVA principal components (Fig. 6E and movie S2, F and H). By contrast, the rAmy-AMY₂R ECD is much more dynamic, transitioning from the consensus conformation (Fig. 2B) through to the orientation observed in the CT-AMY₂R complexes (Fig. 6F and movie S2G). In this latter conformation, the rAmy bypass motif becomes disordered, with the peptide exiting the TMD bundle in the same plane as sCT, along with increased mobility of the RAMP TMD and linker domains that is evidenced by loss of density in the map, similar to that observed in the CT-AMY₂R complexes (Fig. 6, F and G, and figs. S6, E and F, and S8). In 3DVA analysis of the rAmy-CTR complex, the receptor transitions between the major conformations observed in the consensus maps (Fig. 6D and movie S2I). These data support pliancy in the bypass motif to transition between structured and unstructured states. Early nuclear magnetic resonance imaging studies have also demonstrated the presence of a short helix between S20 and L23 in detergent micelles but not in aqueous solution (53), suggesting that the conformation of the “bypass” motif may be facilitated by hydrophobic interactions, including potential interactions with lipid membranes.

A number of lines of evidence support a proposal that sCT signaling from AMY₁R and AMY₃R also requires the receptors to adopt a CTR-like ECD orientation. In recombinant CTR+RAMP1 coexpression systems, ¹²⁵I-sCT can cross-link to bands corresponding to both the AMY₁R and CTR, whereas ¹²⁵I-rAmy selectively cross-links to the higher-molecular-weight CTR-RAMP1 complex (3). Upon endoglycosidase F deglycosylation of the cross-linked complexes, only the deglycosylated CTR was labeled by ¹²⁵I-sCT, whereas ¹²⁵I-rAmy labeled both the free CTR and CTR-RAMP1 complex. These data suggest that CTR glycosylation helps to stabilize interactions with RAMP1, but the interface is weaker for sCT-bound versus Amy-bound receptors. The low yield of

complexes for active sCT-AMY₁R or sCT-AMY₃R complexes is consistent with a higher energy barrier for adoption of the active conformation arising from the more extensive TM interface of these RAMPs and CTR. The sCT-AMY₁R complex structure directly supports

this hypothesis with maintenance of strong TM-TM interactions between RAMP1 and CTR (fig. S8A). In contrast to sCT, hCT has relatively low affinity for the isolated CTR ECD (45, 51) that would be predicted to be insufficient to overcome the activation barrier of

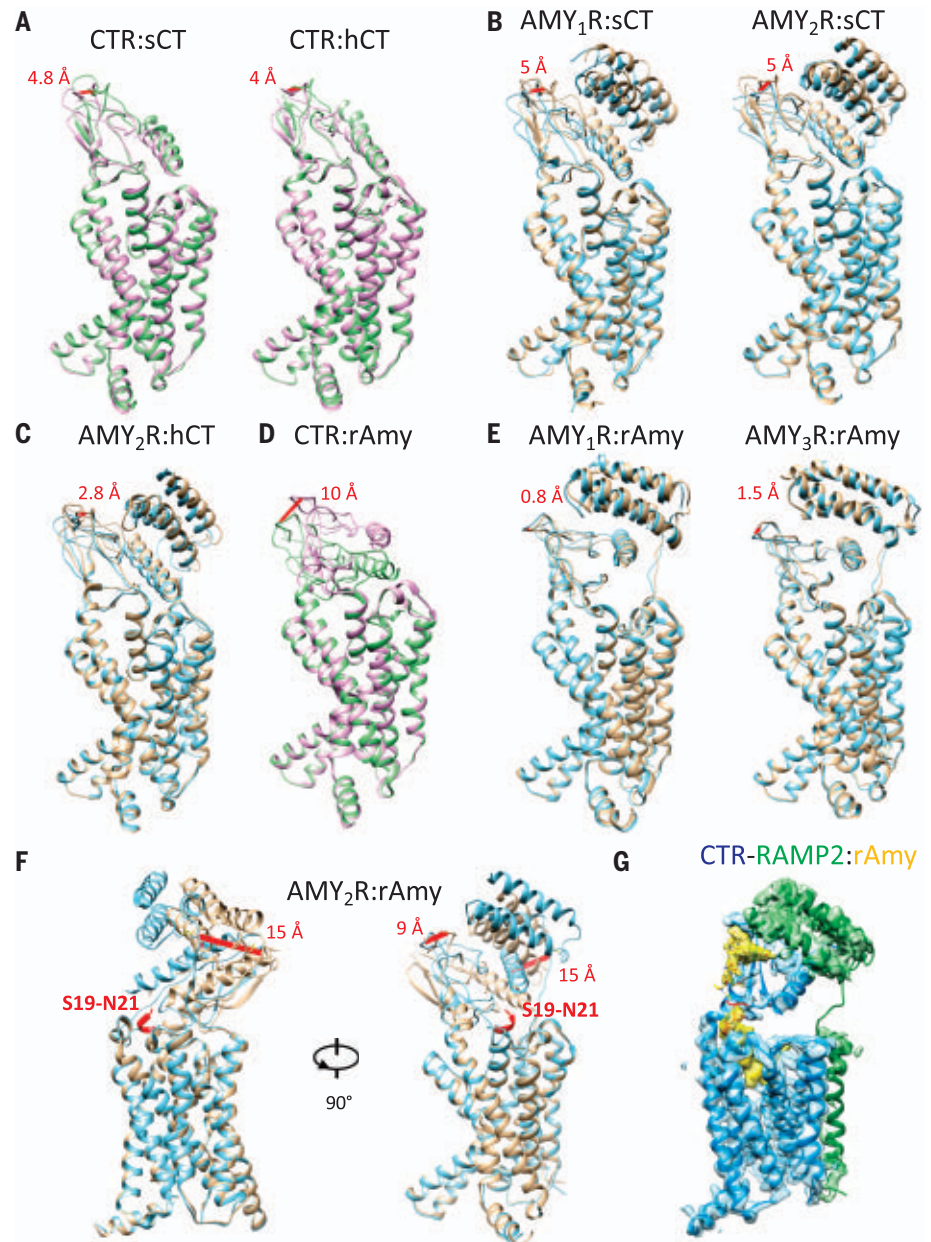


Fig. 6. 3D variability analysis of AMYR and CTR complexes with individual peptide agonists. (A to F) Overlay of backbone models of receptor and peptide rigid body fitted to the two extreme maps: frames 000 and 019 from the main principal component of the 3DVA. Measurement of the distance between the C α of E123^{CTR} revealed differential movement of the CTR ECD in all complexes. Compared with the ECD motions in CT-bound CTRs (A), sCT-AMYR (B), and hCT-AMY₂R (C) of 3 to 5 Å, AMY₁R and AMY₃R (E) restrained the ECD motion when bound to rAmy. (D) In the rAmy-CTR, larger scale motion is observed for the CTR ECD (~10 Å), with similar extensive translational motions in the rAmy-AMY₂R complex for the RAMP2 ECD (15-Å movement measured by the C α of C131^{RAMP2}), which is associated with rAmy (S19-N21) adopting a different conformation (highlighted in red) in frame 000 (F). (G) Map to model representation of frame 000 illustrating the density (yellow) for the extended helix in rAmy (S16-N21) and the poor density for the TM region of RAMP2 (green). Corresponding movies of the cryoSPARC 3DVA are shown in movie S2.

AMY₁R and AMY₃R, leading to the low affinity and potency of hCT at these receptors (3, 6). However, the higher intrinsic dynamics of the AMY₂R facilitate activation of this receptor (and higher affinity binding) by hCT. Indeed, although not extensively studied, the AMY₂R has higher affinity and higher cAMP potency for hCT than other AMYRs (7).

Collectively, the data support a model for CTR and AMYR selectivity that is a combination of the conformational dynamics of the receptors bound to peptide agonists and more subtle effects that arise from differential interactions of select amino acids. Amy is more selective for AMYR than CTR, at least in part through the formation of a structured bypass motif that enables binding to the energetically favorable ECD orientation observed for all rAmy-AMYR complexes that is supported by the robust TMD/linker interactions with CTR for each of the RAMPs (Fig. 7B). Although Amy can bind to conformations of the receptors that mimic the CTR alone conformation, this requires disordering of the bypass motif and likely accounts for the lower affinity and potency of Amy at CTRs (Fig. 7A). By contrast, the length of the CT peptides limits the ECD conformational sampling so that activation requires the receptors to adopt a CTR-like conformation for signaling (Fig. 7, C and D). Like hCT, which has limited affinity for the isolated ECD, CT peptides are selective for CTR over AMYRs, although the AMY₂R is less selective because of the weaker RAMP-CTR TMD interface (Fig. 7D). By contrast, CT-like peptides

that have high affinity for the ECD are able to act as nonselective agonists by constraining the position of the RAMP ECD that in turn destabilizes the RAMP-CTR interface allowing the peptide N terminus to activate the receptors through TMD/ECL interactions that are conserved across all receptors (Fig. 7D). Overall, the Amy and CT peptides activate the receptor through markedly different molecular mechanisms.

Although the greatest structural divergence between CTR and AMYRs occurred in the orientation of the ECD domain, 3DVA of the AMYRs revealed coordinated motions throughout the intact complexes, indicating that allosteric modulation of CTR by RAMPs links the ECDs to the receptor-G protein interface (movie S3), consistent with observations from RAMP1/RAMP2 chimeras of distinct roles for the ECD, TMD, and C-terminal segment (7). The RAMP TMD segment is a foundational determinant for prototypical amylin binding (7). Compared with RAMP1 and RAMP3, the loose packing of the TMD segment in RAMP2 relaxes the constraint on the ECD domain, allowing greater motion; however, the decreased stability of the interface also affects the efficiency of cell surface translocation of the AMY₂R and the strength of the observed AMYR phenotype (7). Moreover, all three RAMP C-terminal domains interact with ICL2 and the α N helix of Gs, which may be linked to Gs coupling efficiency.

With the increasing interest in DACRAs, there have been two approaches to the devel-

opment of new peptide agonists that are based on either an Amy template (37 amino acid peptides) or a sCT template (32 amino acid peptides). Our data suggest that these two approaches will yield peptides with very distinct modes of action for engagement and activation of AMYRs. Nonselective agonists based on Amy templates likely achieve this through greater flexibility in conformational transition of the bypass motif, from the structured motif that supports activation of AMYRs to more disordered conformations that support engagement of receptors in the CTR-alone active conformation. By contrast, nonselective agonists based on sCT templates likely achieve this through high affinity of the peptide C terminus for CTR and AMYRs that allow the receptors to signal from the “CTR active conformation.”

To try to improve clinical weight loss, a hybrid analog, davalintide, was developed that contained a shorter midpeptide [R^{11,18}sCT(8-22)] flanked by rAmy N- and C-terminal sequences (41). Although this peptide demonstrated a longer half-life and sustained weight loss in rodent models, phase 2 clinical trials indicated that it was not superior to pramlintide. By contrast, cagrilintide, a nonselective chimeric Amy-based peptide, provides highly efficacious weight loss in patients (24). Recent DACRAs based on the sCT template have demonstrated superior efficacy to davalintide in rodent obesity models (18–22); however, it remains to be seen whether this can translate to human efficacy. Most of these latter peptides also include an RLS motif for residues 11 to 13, and

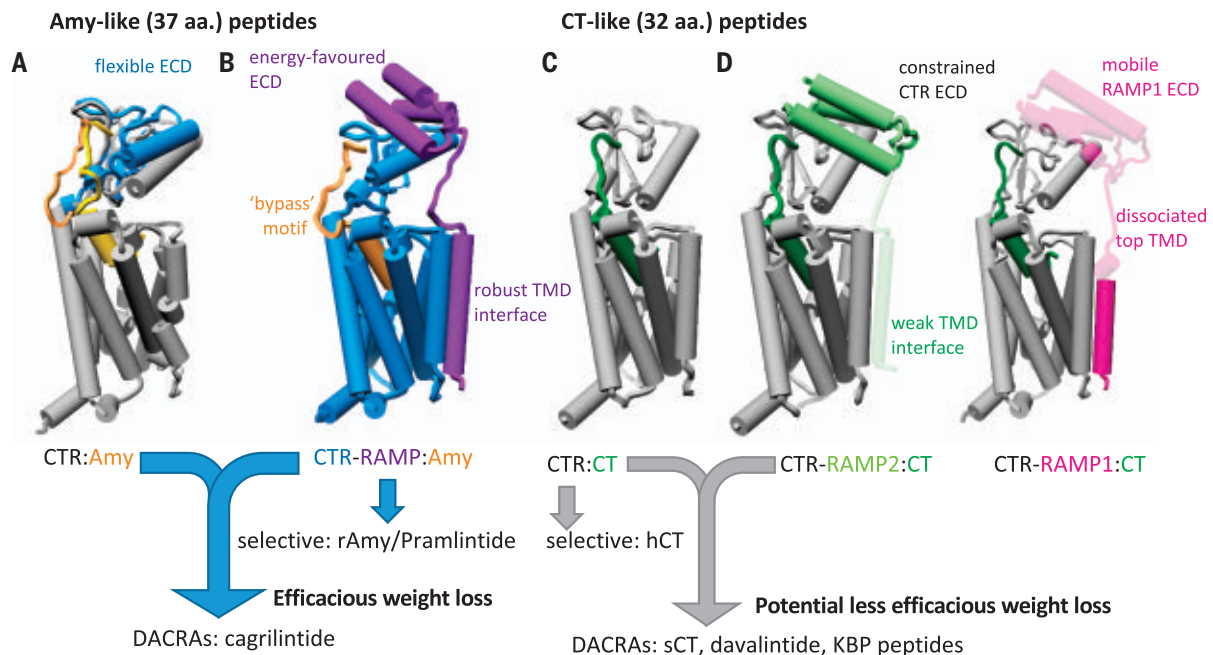


Fig. 7. Schematic illustrating key modes of AMYR and CTR selectivity and the distinct modes of activation of AMYRs by CT-based and Amy-based peptides.

(A) Activation of CTRs by Amy-template peptides. (B) Activation of AMYRs by Amy-template peptides. (C) Activation of CTR by CT-template peptides. (D) Activation of AMYRs by CT-template peptides.

consequently would be expected to have slow off-rate kinetics and persistent signaling. This is similar to sCT, which has been restricted by regulatory authorities to a maximum of 3 months use because of a potential link to cancer risk found in a meta-analysis of clinical data (42).

Conclusion

Through determination of active structures of each of the AMYR subtypes, we provide insight into the complex allosteric modulation of CTRs by RAMPs to generate AMYR phenotypes. Our data provide details of the molecular basis for activation of AMYRs and reveal that CT peptides likely activate AMYRs by distinct mechanisms compared with activation by Amy peptides. The work confirms the important role of conformational dynamics in the observed phenotype of heterodimers of CT family receptors and RAMPs that was previously reported to be important to selectivity of CGRP and AM receptors (30). Our work provides a template for the future development of selective and nonselective agonists of CT and AMY receptors with potential implications for translational application of DACRAs.

Materials and methods

Constructs

The CTR (26), RAMPs (29, 30), and DNGas protein (54) constructs used in the current study have been previously described. Wild-type human CTR was modified to contain an N-terminal Flag tag epitope and a C-terminal eight-histidine tag epitope, each flanked by an HRV 3C protease cleavage site. Human RAMP1-3 contained an N-terminal FLAG tag epitope. To improve expression, the native signal peptides were replaced by that of hemagglutinin in both the CTR and RAMP constructs. The constructs were generated in both an insect (pFastBac) and a mammalian (pcDNA3.1) cell expression vector. cAMP accumulation activation assay performed in transiently transfected COS-7 cells (5) validated the equivalent pharmacological profiles between the modified constructs and the untagged version (fig. S11).

Insect cell expression

CTR, RAMPs, DNGas, and G β 1 γ 2 were simultaneously expressed in *T. ni* cell lines (Expression Systems) (26, 29, 30). Cells were transfected at a density of 3 to 4 million cells/ml in ESF 921 serum-free medium (Expression Systems) with a combination of four separate baculoviruses. Cultures were harvested by centrifugation ~48 hours after infection, and cell pellets were stored at -80°C until use.

Complex purification

CTR-RAMP-DNG complex purification was conducted as described in Liang *et al.* (30). CTR, RAMP, and DNGs containing cell pellets

were thawed in 30 mM HEPES, pH 7.4, 50 mM NaCl, 5 mM CaCl₂, and 2 mM MgCl₂ supplemented with 3C protease (10 μ g/ml, to cleave tags from CTR), cOmplete Protease Inhibitor Cocktail tablets (Roche), and benzonase (37.5 U/ml, Merck Millipore). Complex formation was initiated by adding 1 μ M (rAmy-AMY₁R; sCT-CTR), 10 μ M (hCT-CTR; sCT-AMY₂R; hCT-AMY₂R, rAmy-AMY₂R; rAMY-AMY₃R), or 50 μ M (rAmy-CTR; sCT-AMY₁R) concentrations of peptide (China Peptides) and stabilized in the presence of Nb35 (10 μ g/ml) and apyrase (25 mU/ml, New England Biolabs). Subsequently, lauryl maltose neopentyl glycol (LMNG 1%, Anatrace) and cholesteryl hemisuccinate (CHS 0.06%, Anatrace) were added to solubilize complexes for 1 hour at 4°C, and the insoluble portion was removed by centrifugation. The supernatant was incubated with the Ni-NTA resin for 2 hours of batch binding. The resin was packed into a glass column and washed with 25 column volumes of 20 mM HEPES, pH 7.4, 100 mM NaCl, 2 mM MgCl₂, 0.01% (w/v) LMNG, 0.0006% (w/v) CHS, and 1 μ M peptide. The complexes eluted in the imidazole buffer were immobilized by batch binding to M1 anti-Flag affinity resin in the presence of 3 mM CaCl₂ for 2 hours at room temperature. The M1 resin was packed into a column and washed with 20 column volumes of 20 mM HEPES, pH 7.4, 100 mM NaCl, 2 mM MgCl₂, 3 mM CaCl₂, 0.01% (w/v) LMNG, 0.0006% (w/v) CHS, and 1 μ M peptide. The bound material was eluted using 20 mM HEPES, pH 7.4, 100 mM NaCl, 2 mM MgCl₂, 0.01% (w/v) LMNG, 0.0006% (w/v) CHS, 1 μ M peptide, 5 mM EGTA, and 0.1 mg/ml Flag peptide. The eluted product was concentrated using an Amicon Ultra Centrifugal Filter (MWCO 100 kDa) and subjected to size-exclusion chromatography on a Superdex 200 Increase 10/300 column pre-equilibrated with 20 mM HEPES, pH 7.4, 100 mM NaCl, 2 mM MgCl₂, 1 μ M peptide, 0.01% (w/v) LMNG, and 0.0006 (w/v) CHS. Eluted fractions consisting of complex were pooled, concentrated to ~4 mg/ml, flash frozen by liquid nitrogen as aliquots, and stored at -80°C until use. When complex formation was initiated using 50 μ M peptide, the peptide concentration was reduced to 10 μ M in subsequent purification steps. Similarly, the purification of CTR-DNGs complex was performed according to a previously described protocol (54).

Vitrified specimens and data collection

Acetone-pretreated EM grids (Ultrafoil R1.2/1.3 Au 300 gold foil grids, Quantifoil GmbH) were glow discharged. Three microliters of sample was applied to the grid, which was subsequently blotted and vitrified in liquid ethane using a Vitrobot Mark IV (Thermo Fisher Scientific) under 100% humidity at 4°C.

Optimal grids for six complexes were imaged by conventional cryo-transmission elec-

tron microscopy (cryo-TEM) on a Thermo Fisher Scientific Titan Krios microscope operated at an accelerating voltage of 300 kV with a 50 μ m C2 aperture at an indicated magnification of 105 k \times in nanoprobe EFTEM mode. A Gatan K3 direct electron camera equipped with a Gatan Quantum energy filter (Gatan, Pleasanton, CA, USA) was operated in a zero-energy-loss mode with a slit width of 25 eV to acquire dose-fractionated images. Movies were recorded as compressed TIFFs in normal-resolution mode at an indicated magnification of 105 k \times , yielding a magnified pixel size of 0.83 Å for sCT-CTR and rAmy-bound AMY₁R and AMY₂R samples. The movies of AMY₃R and hCT-CTR samples were collected at a magnification of 130 k \times , corresponding to a pixel size of 0.65 $\text{Å}/\text{pix}$, and with the Gatan K3 was operated in correlated double sampling (CDS) mode. Movies for sCT-bound AMY₂R were collected at 105 k \times , yielding a 0.82- Å pixel size with the Gatan K3 detector operated in CDS mode. Each movie comprises 62 to 83 subframes with a total dose of 53 to 71 e⁻ per Å^2 , and the exposure time was 3 to 5 s with a dose rate of 4.5 to 15.0 e⁻ pixel⁻¹ s⁻¹. To achieve a higher-throughput data collection, a nine-position beam-image shift acquisition pattern was used by custom scripts in SerialEM (see table S4 for data collection parameters).

Datasets for the three remaining complexes were collected using conventional cryo-TEM on a Thermo Fisher Scientific Glacios microscope operated at an accelerating voltage of 200 kV with a 50- μ m C2 aperture, a 100- μ m objective aperture, and at an indicated magnification of 120 k \times in nanoprobe TEM mode, yielding a physical pixel size of 0.856 $\text{Å}/\text{pix}$. A bottom-mounted Falcon 4 direct electron detector operated in Electron Event Representation (EER) mode was used to acquire images of the samples. Data were collected using aberration-free image shift implemented in EPU. Movies for rAmy-CTR were recorded with an exposure time of 7.33 s amounting to a total dose of 50 e⁻/ Å^2 at a dose rate of 5.27 e⁻/pixel/second, and movies for hCT-AMY₂R and sCT-AMY₁R were recorded with an exposure time of 8.29 s and a total dose of 50 e⁻/ Å^2 at a dose rate of 4.66 e⁻/pixel/second. Defocus range was set between -1.4 and -0.6 μ m using 0.1- μ m increments for all datasets (see table S4 for data collection parameters).

Cryo-EM data processing

Movies recorded in LZW-compressed TIFF mode from the Krios microscope were subjected to motion correction, dose weighted, and integrated using motion correction2 software (55). Contrast transfer function (CTF) estimation was conducted using GCTF software package (56). Particles were picked from the micrographs using a pretrained model in the crYOLO software package (57), followed by

particle extraction and reference-free 2D classification using RELION (version 3.1-beta for rAmy:AMY₂R and AMY₃R, version 3.1.2 for sCT:AMY₂R) (58). After a further 2D classification in cryoSPARC (59), the selected particles were used to generate an ab initio model that was used in RELION for 3D classification. After particle screening by 2D/3D classification on a binned dataset, a homogeneous subset of particles was re-extracted, subjected to cycles of Bayesian particle polishing, and another round of 2D classification was performed in RELION. The resulting particles were subjected to CTF refinement and 3D autorefinement, followed by a further classification into 3D classes with fine-grain angular sampling only allowing for local Euler angle searches. The particles belonging to the best-looking classes were used to generate the final resolved map from which the AHD of the Gas protein and the detergent micelle were masked out. Gold standard Fourier shell correlation was calculated to determine the global resolutions using the 0.143 criterion. Local resolution estimations were performed using RELION 3.1 with half maps as input (60). Additional focused refinements of “receptor region” were performed in RELION through separate masking of the receptor domain. Nonuniform refinement was also performed on the final particle selection using the cryoSPARC software package, as well as local angle refinement on both the receptor and G proteins, to obtain multiple high-resolution maps for atomic model building and refinement.

EER (61) data were collected from the 200-kV Glacios microscope (Thermo Scientific) and motion corrected using RELION (version 3.1.2). The resulting dose-weighted averaged micrographs were used for CTF estimation and then further processed using a similar image analysis workflow as described for the 300-kV datasets.

Atomic model refinement

The initial template for the rAmy:AMY₁R complex was generated by replacing the CLR in the CLR-RAMP1:hCGRP complex (PDB: 6E3Y) with the CTR from the sCT:CTR complex (PDB: 6NIY). The model was rigid body fitted into the consensus EM density map using UCSF Chimera (version 1.14) (62), followed by molecular dynamics flexible fitting simulation in nanoscale molecular dynamics (63). The fitted model was further refined by rounds of manual adjustment in Coot (version 0.9) (64) and real space refinement as implemented in PHENIX (65). The ECD region was modeled manually against the ECD- and receptor-focused maps. The final model was subjected to comprehensive validation in MolProbity (66). The resulting model of rAmy:AMY₁R complex was used to generate the initial templates for AMY₂R and AMY₃R complexes by

replacing the cognate RAMP component with RAMP2 or RAMP3 from the AM:AM₁R (PDB: 6UUN) and AM2:AM₂R (PDB: 6UVA) complexes, respectively. The model of sCT:CTR (PDB: 6NIY) was used as the initial template for the CTR complexes.

Water molecules were modeled manually into clear spherical density within reasonable H-bonding distance to amino acids or other waters. The positions of waters were further refined in Coot and PHENIX based on the consensus- and receptor-focused maps. Lipid molecules were modeled into the strips of density that were decorated tightly around the TM helices. Receptors used here were isolated from *T. ni* insect cells. Previous lipidomics studies of whole cells or isolated receptors have addressed the abundance of common phospholipids in insect cells, such as PE, PC, PI, etc. (67, 68). The relatively complete density was recognized as a PE or PC with consideration of density fitting to the phosphate group. Fragmented densities were simplified to palmitic acids. Although native cholesterol has been identified in insect cell lines, the clear density for the succinic acid tail in our maps confirmed the modeling of CHS that is present as an artifact of the solubilization buffer rather than endogenous cholesterol.

Model residue interaction analysis

Interactions of receptors with peptide ligands, RAMPs, and G proteins were analyzed using the “Dimplot” module within the Ligplot⁺ program (version 2.2) (69). H-bonds were additionally analyzed using the UCSF Chimera package, with relaxed distance and angle criteria (0.4 Å and 20° tolerance, respectively).

Cryo-EM dynamics analysis

Three-dimensional variability analysis implemented in cryoSPARC (version 3.2) (70) was performed to understand and visualize the dynamics of the CTR-based complexes, as previously described for the analysis of the dynamics of AMRs (30). The final particle stack from the RELION consensus refinement was imported into the cryoSPARC environment. Two-dimensional classification and selection were conducted to further ensure that only highly resolved particles were included in the analysis. These particles underwent a consensus 3D refinement using a low-pass-filtered RELION consensus map as an initial model. The resulting soft mask covered the detergent micelle and was used to ensure that any possible motions could be captured. Three-dimensional variability analysis was calculated across three principal components that accounted for the most common motions, and the 20 volume frame data in each motion was generated in cryoSPARC. Output files were visualized in UCSF ChimeraX (71) volume series and captured as movies.

REFERENCES AND NOTES

1. T. A. Lutz, The role of amylin in the control of energy homeostasis. *Am. J. Physiol. Regul. Integr. Comp. Physiol.* **298**, R1475–R1484 (2010). doi: [10.1152/ajpregu.00703.2009](https://doi.org/10.1152/ajpregu.00703.2009); pmid: 20357016
2. H. L. Zakariassen, L. M. John, T. A. Lutz, Central control of energy balance by amylin and calcitonin receptor agonists and their potential for treatment of metabolic diseases. *Basic Clin. Pharmacol. Toxicol.* **127**, 163–177 (2020). doi: [10.1111/bcpt.13427](https://doi.org/10.1111/bcpt.13427); pmid: 32363722
3. G. Christopoulos *et al.*, Multiple amylin receptors arise from receptor activity-modifying protein interaction with the calcitonin receptor gene product. *Mol. Pharmacol.* **56**, 235–242 (1999). doi: [10.1124/mol.56.1.235](https://doi.org/10.1124/mol.56.1.235); pmid: 10385705
4. D. L. Hay, S. Chen, T. A. Lutz, D. G. Parkes, J. D. Roth, Amylin: Pharmacology, physiology, and clinical potential. *Pharmacol. Rev.* **67**, 564–600 (2015). doi: [10.1124/pr.115.010629](https://doi.org/10.1124/pr.115.010629); pmid: 26071095
5. M. M. Fletcher *et al.*, AM833 is a novel agonist of calcitonin family G protein-coupled receptors: Pharmacological comparison to six selective and non-selective agonists. *J. Pharmacol. Exp. Ther.* **377**, 417–440 (2021). doi: [10.1124/jpet.121.000567](https://doi.org/10.1124/jpet.121.000567); pmid: 33727283
6. D. L. Hay, G. Christopoulos, A. Christopoulos, D. R. Poyner, P. M. Sexton, Pharmacological discrimination of calcitonin receptor: Receptor activity-modifying protein complexes. *Mol. Pharmacol.* **67**, 1655–1665 (2005). doi: [10.1124/mol.104.008615](https://doi.org/10.1124/mol.104.008615); pmid: 15692146
7. M. Udawela *et al.*, Distinct receptor activity-modifying protein domains differentially modulate interaction with calcitonin receptors. *Mol. Pharmacol.* **69**, 1984–1989 (2006). doi: [10.1124/mol.105.021915](https://doi.org/10.1124/mol.105.021915); pmid: 16531504
8. M. Udawela *et al.*, A critical role for the short intracellular C terminus in receptor activity-modifying protein function. *Mol. Pharmacol.* **70**, 1750–1760 (2006). doi: [10.1124/mol.106.024257](https://doi.org/10.1124/mol.106.024257); pmid: 16912219
9. M. Morfis *et al.*, Receptor activity-modifying proteins differentially modulate the G protein-coupling efficiency of amylin receptors. *Endocrinology* **149**, 5423–5431 (2008). doi: [10.1210/en.2007-1735](https://doi.org/10.1210/en.2007-1735); pmid: 18599553
10. J. J. Gingell, E. R. Burns, D. L. Hay, Activity of pramlintide, rat and human amylin but not Aβ1-42 at human amylin receptors. *Endocrinology* **155**, 21–26 (2014). doi: [10.1210/en.2013-1658](https://doi.org/10.1210/en.2013-1658); pmid: 24169554
11. L. Aronne *et al.*, Progressive reduction in body weight after treatment with the amylin analog pramlintide in obese subjects: A phase 2, randomized, placebo-controlled, dose-escalation study. *J. Clin. Endocrinol. Metab.* **92**, 2977–2983 (2007). doi: [10.1210/jc.2006-2003](https://doi.org/10.1210/jc.2006-2003); pmid: 17504894
12. L. J. Aronne, A. E. Halseth, C. M. Burns, S. Miller, L. Z. Shen, Enhanced weight loss following coadministration of pramlintide with sibutramine or phentermine in a multicenter trial. *Obesity (Silver Spring)* **18**, 1739–1746 (2010). doi: [10.1038/oby.2009.478](https://doi.org/10.1038/oby.2009.478); pmid: 20094043
13. T. A. Lutz, S. Tschudy, P. A. Rushing, E. Scharrer, Amylin receptors mediate the anorectic action of salmon calcitonin (sCT). *Peptides* **21**, 233–238 (2000). doi: [10.1016/S0196-9781\(99\)00208-9](https://doi.org/10.1016/S0196-9781(99)00208-9); pmid: 10764950
14. P. K. Chellikani, A. C. Haver, R. D. Reidelberger, Effects of intermittent intraperitoneal infusion of salmon calcitonin on food intake and adiposity in obese rats. *Am. J. Physiol. Regul. Integr. Comp. Physiol.* **293**, R1798–R1808 (2007). doi: [10.1152/ajpregu.00386.2007](https://doi.org/10.1152/ajpregu.00386.2007); pmid: 17761508
15. M. Feigh *et al.*, A novel oral form of salmon calcitonin improves glucose homeostasis and reduces body weight in diet-induced obese rats. *Diabetes Obes. Metab.* **13**, 911–920 (2011). doi: [10.1111/j.1463-1326.2011.01425.x](https://doi.org/10.1111/j.1463-1326.2011.01425.x); pmid: 21615667
16. D. S. Mathiesen, A. Lund, T. Vilsbøll, F. K. Knop, J. I. Bagger, Amylin and calcitonin: Potential therapeutic strategies to reduce body weight and liver fat. *Front. Endocrinol. (Lausanne)* **11**, 617400 (2021). doi: [10.3389/fendo.2020.617400](https://doi.org/10.3389/fendo.2020.617400); pmid: 33488526
17. A. T. Larsen, N. Sonne, K. V. Andreassen, M. A. Karsdal, K. Henriksen, The calcitonin receptor plays a major role in glucose regulation as a function of dual amylin and calcitonin receptor agonist therapy. *J. Pharmacol. Exp. Ther.* **374**, 74–83 (2020). doi: [10.1124/jpet.119.263392](https://doi.org/10.1124/jpet.119.263392); pmid: 32317372
18. K. V. Andreassen *et al.*, A novel oral dual amylin and calcitonin receptor agonist (KBP-042) exerts antiobesity and antidiabetic effects in rats. *Am. J. Physiol. Endocrinol. Metab.* **307**, E24–E33 (2014). doi: [10.1152/ajpendo.00121.2014](https://doi.org/10.1152/ajpendo.00121.2014); pmid: 24801386

19. S. Gydesen *et al.*, KBP-088, a novel DACRA with prolonged receptor activation, is superior to davalintide in terms of efficacy on body weight. *Am. J. Physiol. Endocrinol. Metab.* **310**, E821–E827 (2016). doi: [10.1152/ajpendo.00514.2015](https://doi.org/10.1152/ajpendo.00514.2015); pmid: [26908506](https://pubmed.ncbi.nlm.nih.gov/26908506/)
20. S. Gydesen *et al.*, Optimization of tolerability and efficacy of the novel dual amylin and calcitonin receptor agonist KBP-089 through dose escalation and combination with a GLP-1 analog. *Am. J. Physiol. Endocrinol. Metab.* **313**, E598–E607 (2017). doi: [10.1152/ajpendo.00419.2016](https://doi.org/10.1152/ajpendo.00419.2016); pmid: [28292761](https://pubmed.ncbi.nlm.nih.gov/28292761/)
21. A. T. Larsen *et al.*, The dual amylin and calcitonin receptor agonist KBP-088 induces weight loss and improves insulin sensitivity superior to chronic amylin therapy. *J. Pharmacol. Exp. Ther.* **370**, 35–43 (2019). doi: [10.1124/jpet.119.257576](https://doi.org/10.1124/jpet.119.257576); pmid: [31028106](https://pubmed.ncbi.nlm.nih.gov/31028106/)
22. A. T. Larsen, N. Sonne, K. V. Andreassen, M. A. Karsdal, K. Henriksen, Dose frequency optimization of the dual amylin and calcitonin receptor agonist KBP-088: Long-lasting improvement in food preference and body weight loss. *J. Pharmacol. Exp. Ther.* **373**, 269–278 (2020). doi: [10.1124/jpet.119.263400](https://doi.org/10.1124/jpet.119.263400); pmid: [32071103](https://pubmed.ncbi.nlm.nih.gov/32071103/)
23. T. Kruse *et al.*, Development of cagrilintide, a long-acting amylin analogue. *J. Med. Chem.* **64**, 11183–11194 (2021). doi: [10.1021/acs.jmedchem.1c00565](https://doi.org/10.1021/acs.jmedchem.1c00565); pmid: [34288673](https://pubmed.ncbi.nlm.nih.gov/34288673/)
24. L. B. Enebo *et al.*, Safety, tolerability, pharmacokinetics, and pharmacodynamics of concomitant administration of multiple doses of cagrilintide with semaglutide 2.4 mg for weight management: A randomised, controlled, phase 1b trial. *Lancet* **397**, 1736–1748 (2021). doi: [10.1016/S0140-6736\(21\)00845-X](https://doi.org/10.1016/S0140-6736(21)00845-X); pmid: [33894838](https://pubmed.ncbi.nlm.nih.gov/33894838/)
25. N. Binkley *et al.*, A phase 3 trial of the efficacy and safety of oral recombinant calcitonin: The Oral Calcitonin in Postmenopausal Osteoporosis (ORACAL) trial. *J. Bone Miner. Res.* **27**, 1821–1829 (2012). doi: [10.1002/jbmr.1602](https://doi.org/10.1002/jbmr.1602); pmid: [22437792](https://pubmed.ncbi.nlm.nih.gov/22437792/)
26. Y.-L. Liang *et al.*, Phase-plate cryo-EM structure of a class B GPCR-G-protein complex. *Nature* **546**, 118–123 (2017). doi: [10.1038/nature22327](https://doi.org/10.1038/nature22327); pmid: [28437792](https://pubmed.ncbi.nlm.nih.gov/28437792/)
27. D. Wootten, J. Simms, L. J. Miller, A. Christopoulos, P. M. Sexton, Polar transmembrane interactions drive formation of ligand-specific and signal pathway-biased family B G protein-coupled receptor conformations. *Proc. Natl. Acad. Sci. U.S.A.* **110**, 5211–5216 (2013). doi: [10.1073/pnas.1221585110](https://doi.org/10.1073/pnas.1221585110); pmid: [23479653](https://pubmed.ncbi.nlm.nih.gov/23479653/)
28. E. dal Maso *et al.*, The molecular control of calcitonin receptor signaling. *ACS Pharmacol. Transl. Sci.* **2**, 31–51 (2019). doi: [10.1021/acspstci.8b00056](https://doi.org/10.1021/acspstci.8b00056); pmid: [32219215](https://pubmed.ncbi.nlm.nih.gov/32219215/)
29. Y. L. Liang *et al.*, Cryo-EM structure of the active, G_s-protein complexed, human CGRP receptor. *Nature* **561**, 492–497 (2018). doi: [10.1038/s41586-018-0535-y](https://doi.org/10.1038/s41586-018-0535-y); pmid: [30209400](https://pubmed.ncbi.nlm.nih.gov/30209400/)
30. Y. L. Liang *et al.*, Structure and dynamics of adrenomedullin receptors AM1 and AM2 reveal key mechanisms in the control of receptor phenotype by receptor activity-modifying proteins. *ACS Pharmacol. Transl. Sci.* **3**, 263–284 (2020). doi: [10.1021/acspstci.9b00080](https://doi.org/10.1021/acspstci.9b00080); pmid: [32296767](https://pubmed.ncbi.nlm.nih.gov/32296767/)
31. Y. L. Liang *et al.*, Toward a structural understanding of class B GPCR peptide binding and activation. *Mol. Cell* **77**, 656–668.e5 (2020). doi: [10.1016/j.molcel.2020.01.012](https://doi.org/10.1016/j.molcel.2020.01.012); pmid: [32004469](https://pubmed.ncbi.nlm.nih.gov/32004469/)
32. R. L. Bower *et al.*, Molecular signature for receptor engagement in the metabolic peptide hormone amylin. *ACS Pharmacol. Transl. Sci.* **1**, 32–49 (2018). doi: [10.1021/acspstci.8b00002](https://doi.org/10.1021/acspstci.8b00002); pmid: [32219203](https://pubmed.ncbi.nlm.nih.gov/32219203/)
33. S. Houssami *et al.*, Divergent structural requirements exist for calcitonin receptor binding specificity and adenylate cyclase activation. *Mol. Pharmacol.* **47**, 798–809 (1995). pmid: [7723741](https://pubmed.ncbi.nlm.nih.gov/7723741/)
34. M. L. Garelja *et al.*, Molecular mechanisms of class B GPCR activation: Insights from adrenomedullin receptors. *ACS Pharmacol. Transl. Sci.* **3**, 246–262 (2020). doi: [10.1021/acspstci.9b00083](https://doi.org/10.1021/acspstci.9b00083); pmid: [32296766](https://pubmed.ncbi.nlm.nih.gov/32296766/)
35. D. L. Hay *et al.*, Structure-activity relationships of the N-terminus of calcitonin gene-related peptide: Key roles of alanine-5 and threonine-6 in receptor activation. *Br. J. Pharmacol.* **171**, 415–426 (2014). doi: [10.1111/bph.12464](https://doi.org/10.1111/bph.12464); pmid: [24125506](https://pubmed.ncbi.nlm.nih.gov/24125506/)
36. H. Musa *et al.*, Pharmacological characterization and investigation of N-terminal loop amino acids of adrenomedullin 2 that are important for receptor activation. *Biochemistry* **58**, 3468–3474 (2019). doi: [10.1021/acs.biochem.9b00571](https://doi.org/10.1021/acs.biochem.9b00571); pmid: [31328503](https://pubmed.ncbi.nlm.nih.gov/31328503/)
37. E. Dal Maso *et al.*, Extracellular loops 2 and 3 of the calcitonin receptor selectively modify agonist binding and efficacy. *Biochem. Pharmacol.* **150**, 214–244 (2018). doi: [10.1016/j.bcp.2018.02.005](https://doi.org/10.1016/j.bcp.2018.02.005); pmid: [29454620](https://pubmed.ncbi.nlm.nih.gov/29454620/)
38. R. C. Orłowski, R. M. Epanand, A. R. Stafford, Biologically potent analogues of salmon calcitonin which do not contain an N-terminal disulfide-bridged ring structure. *Eur. J. Biochem.* **162**, 399–402 (1987). doi: [10.1111/j.1432-1033.1987.tb10615.x](https://doi.org/10.1111/j.1432-1033.1987.tb10615.x); pmid: [3803393](https://pubmed.ncbi.nlm.nih.gov/3803393/)
39. J. M. Hilton, M. Dowton, S. Houssami, P. M. Sexton, Identification of key components in the irreversibility of salmon calcitonin binding to calcitonin receptors. *J. Endocrinol.* **166**, 213–226 (2000). doi: [10.1677/joe.0.1660213](https://doi.org/10.1677/joe.0.1660213); pmid: [10856900](https://pubmed.ncbi.nlm.nih.gov/10856900/)
40. S. G. B. Furness *et al.*, Ligand-dependent modulation of G protein conformation alters drug efficacy. *Cell* **167**, 739–749.e11 (2016). doi: [10.1016/j.cell.2016.09.021](https://doi.org/10.1016/j.cell.2016.09.021); pmid: [27720449](https://pubmed.ncbi.nlm.nih.gov/27720449/)
41. C. M. Mack *et al.*, Glucoregulatory effects and prolonged duration of action of davalintide: A novel amylinomimetic peptide. *Diabetes Obes. Metab.* **13**, 1105–1113 (2011). doi: [10.1111/j.1463-1326.2011.01465.x](https://doi.org/10.1111/j.1463-1326.2011.01465.x); pmid: [21733060](https://pubmed.ncbi.nlm.nih.gov/21733060/)
42. G. Wells, J. Chernoff, J. P. Gilligan, D. S. Krause, Does salmon calcitonin cause cancer? A review and meta-analysis. *Osteoporos. Int.* **27**, 13–19 (2016). doi: [10.1007/s00198-015-3339-z](https://doi.org/10.1007/s00198-015-3339-z); pmid: [26438308](https://pubmed.ncbi.nlm.nih.gov/26438308/)
43. R. M. Epanand, R. F. Epanand, R. C. Orłowski, Study of a series of analogs of salmon calcitonin in which alanine replaces leucine. *Eur. J. Biochem.* **188**, 633–635 (1990). doi: [10.1111/j.1432-1033.1990.tb15444.x](https://doi.org/10.1111/j.1432-1033.1990.tb15444.x); pmid: [2331988](https://pubmed.ncbi.nlm.nih.gov/2331988/)
44. R. Maier, B. Kamber, B. Riniker, W. Rittel, Analogues of human calcitonin. IV. Influence of leucine substitutions in positions 12, 16 and 19 on hypocalcaemic activity in the rat. *Clin. Endocrinol. (Oxf.)* **5** (Suppl), 327S–332S (1976). doi: [10.1111/j.1365-2265.1976.tb03841.x](https://doi.org/10.1111/j.1365-2265.1976.tb03841.x); pmid: [1052782](https://pubmed.ncbi.nlm.nih.gov/1052782/)
45. E. Johansson *et al.*, Type II turn of receptor-bound salmon calcitonin revealed by X-ray crystallography. *J. Biol. Chem.* **291**, 13689–13698 (2016). doi: [10.1074/jbc.M116.726034](https://doi.org/10.1074/jbc.M116.726034); pmid: [27189946](https://pubmed.ncbi.nlm.nih.gov/27189946/)
46. J. J. Gingell *et al.*, An allosteric role for receptor activity-modifying proteins in defining GPCR pharmacology. *Cell Discov.* **2**, 16012 (2016). doi: [10.1038/celldisc.2016.12](https://doi.org/10.1038/celldisc.2016.12); pmid: [27462459](https://pubmed.ncbi.nlm.nih.gov/27462459/)
47. S. M. Lee *et al.*, Calcitonin receptor N-glycosylation enhances peptide hormone affinity by controlling receptor dynamics. *J. Mol. Biol.* **432**, 1996–2014 (2020). doi: [10.1016/j.jmb.2020.01.028](https://doi.org/10.1016/j.jmb.2020.01.028); pmid: [32035902](https://pubmed.ncbi.nlm.nih.gov/32035902/)
48. J. M. Booe *et al.*, Structural basis for receptor activity-modifying protein-dependent selective peptide recognition by a G protein-coupled receptor. *Mol. Cell* **58**, 1040–1052 (2015). doi: [10.1016/j.molcel.2015.04.018](https://doi.org/10.1016/j.molcel.2015.04.018); pmid: [25982113](https://pubmed.ncbi.nlm.nih.gov/25982113/)
49. J. J. Gingell, T. Qi, R. J. Bailey, D. L. Hay, A key role for tryptophan 84 in receptor activity-modifying protein 1 in the amylin 1 receptor. *Peptides* **31**, 1400–1404 (2010). doi: [10.1016/j.peptides.2010.03.027](https://doi.org/10.1016/j.peptides.2010.03.027); pmid: [20347903](https://pubmed.ncbi.nlm.nih.gov/20347903/)
50. S. Lee, A. A. Pioszak, Molecular interaction of an antagonistic amylin analog with the extracellular domain of receptor activity-modifying protein 2 assessed by fluorescence polarization. *Biophys. Chem.* **267**, 106477 (2020). doi: [10.1016/j.bpc.2020.106477](https://doi.org/10.1016/j.bpc.2020.106477); pmid: [33137565](https://pubmed.ncbi.nlm.nih.gov/33137565/)
51. S. M. Lee, D. L. Hay, A. A. Pioszak, Calcitonin and amylin receptor peptide interaction mechanisms: Insights into peptide-binding modes and allosteric modulation of the calcitonin receptor by receptor activity-modifying proteins. *J. Biol. Chem.* **291**, 8686–8700 (2016). doi: [10.1074/jbc.M115.713628](https://doi.org/10.1074/jbc.M115.713628); pmid: [26895962](https://pubmed.ncbi.nlm.nih.gov/26895962/)
52. T. Qi *et al.*, Identification of N-terminal receptor activity-modifying protein residues important for calcitonin gene-related peptide, adrenomedullin, and amylin receptor function. *Mol. Pharmacol.* **74**, 1059–1071 (2008). doi: [10.1124/mol.108.047142](https://doi.org/10.1124/mol.108.047142); pmid: [18593822](https://pubmed.ncbi.nlm.nih.gov/18593822/)
53. S. M. Patil, S. Xu, S. R. Sheffia, A. T. Alexandrescu, Dynamic alpha-helix structure of micelle-bound human amylin. *J. Biol. Chem.* **284**, 11982–11991 (2009). doi: [10.1074/jbc.M809085200](https://doi.org/10.1074/jbc.M809085200); pmid: [19244249](https://pubmed.ncbi.nlm.nih.gov/19244249/)
54. Y.-L. Liang *et al.*, Dominant negative G proteins enhance formation and purification of agonist-GPCR-G protein complexes for structure determination. *ACS Pharmacol. Transl. Sci.* **1**, 12–20 (2018). doi: [10.1021/acspstci.8b00017](https://doi.org/10.1021/acspstci.8b00017); pmid: [32219201](https://pubmed.ncbi.nlm.nih.gov/32219201/)
55. S. Q. Zheng *et al.*, MotionCor2: Anisotropic correction of beam-induced motion for improved cryo-electron microscopy. *Nat. Methods* **14**, 331–332 (2017). doi: [10.1038/nmeth.4193](https://doi.org/10.1038/nmeth.4193); pmid: [28250466](https://pubmed.ncbi.nlm.nih.gov/28250466/)
56. K. Zhang, Gctf: Real-time CTF determination and correction. *J. Struct. Biol.* **193**, 1–12 (2016). doi: [10.1016/j.jsb.2015.11.003](https://doi.org/10.1016/j.jsb.2015.11.003); pmid: [26592709](https://pubmed.ncbi.nlm.nih.gov/26592709/)
57. T. Wagner *et al.*, SPHIRE-crYOLO is a fast and accurate fully automated particle picker for cryo-EM. *Commun. Biol.* **2**, 218 (2019). doi: [10.1038/s42003-019-0437-z](https://doi.org/10.1038/s42003-019-0437-z); pmid: [31240256](https://pubmed.ncbi.nlm.nih.gov/31240256/)
58. J. Zivanov *et al.*, New tools for automated high-resolution cryo-EM structure determination in RELION-3. *eLife* **7**, e42166 (2018). doi: [10.7554/eLife.42166](https://doi.org/10.7554/eLife.42166); pmid: [30412051](https://pubmed.ncbi.nlm.nih.gov/30412051/)
59. A. Punjani, J. L. Rubinstein, D. J. Fleet, M. A. Brubaker, cryoSPARC: Algorithms for rapid unsupervised cryo-EM structure determination. *Nat. Methods* **14**, 290–296 (2017). doi: [10.1038/nmeth.4169](https://doi.org/10.1038/nmeth.4169); pmid: [28165473](https://pubmed.ncbi.nlm.nih.gov/28165473/)
60. T. Nakane, D. Kimanius, E. Lindahl, S. H. W. Scheres, Characterisation of molecular motions in cryo-EM single-particle data by multi-body refinement in RELION. *eLife* **7**, e36861 (2018). doi: [10.7554/eLife.36861](https://doi.org/10.7554/eLife.36861); pmid: [29856314](https://pubmed.ncbi.nlm.nih.gov/29856314/)
61. H. Guo *et al.*, Electron-event representation data enable efficient cryoEM file storage with full preservation of spatial and temporal resolution. *IUCrJ* **7**, 860–869 (2020). doi: [10.1107/S205225252000929x](https://doi.org/10.1107/S205225252000929x); pmid: [32939278](https://pubmed.ncbi.nlm.nih.gov/32939278/)
62. E. F. Pettersen *et al.*, UCSF Chimera—A visualization system for exploratory research and analysis. *J. Comput. Chem.* **25**, 1605–1612 (2004). doi: [10.1002/jcc.20084](https://doi.org/10.1002/jcc.20084); pmid: [15264254](https://pubmed.ncbi.nlm.nih.gov/15264254/)
63. K.-Y. Chan, L. G. Trabuco, E. Schreiner, K. Schulten, Cryo-electron microscopy modeling by the molecular dynamics flexible fitting method. *Biopolymers* **97**, 678–686 (2012). doi: [10.1002/bip.22042](https://doi.org/10.1002/bip.22042); pmid: [22696404](https://pubmed.ncbi.nlm.nih.gov/22696404/)
64. P. Emsley, B. Lohkamp, W. G. Scott, K. Cowtan, Features and development of Coot. *Acta Crystallogr. D Biol. Crystallogr.* **66**, 486–501 (2010). doi: [10.1107/S0907444910007493](https://doi.org/10.1107/S0907444910007493); pmid: [20383002](https://pubmed.ncbi.nlm.nih.gov/20383002/)
65. P. D. Adams *et al.*, PHENIX: A comprehensive Python-based system for macromolecular structure solution. *Acta Crystallogr. D Biol. Crystallogr.* **66**, 213–221 (2010). doi: [10.1107/S0907444909052925](https://doi.org/10.1107/S0907444909052925); pmid: [20124702](https://pubmed.ncbi.nlm.nih.gov/20124702/)
66. C. J. Williams *et al.*, MolProbity: More and better reference data for improved all-atom structure validation. *Protein Sci.* **27**, 293–315 (2018). doi: [10.1002/pro.3330](https://doi.org/10.1002/pro.3330); pmid: [29067766](https://pubmed.ncbi.nlm.nih.gov/29067766/)
67. H. Y. Yen *et al.*, PtdIns(4,5)P₂ stabilizes active states of GPCRs and enhances selectivity of G-protein coupling. *Nature* **559**, 423–427 (2018). doi: [10.1038/s41586-018-0325-6](https://doi.org/10.1038/s41586-018-0325-6); pmid: [29995853](https://pubmed.ncbi.nlm.nih.gov/29995853/)
68. K. Marheineke, S. Grünwald, W. Christie, H. Reiländer, Lipid composition of *Spodoptera frugiperda* (Sf9) and *Trichoplusia ni* (Tn) insect cells used for baculovirus infection. *FEBS Lett.* **441**, 49–52 (1998). doi: [10.1016/S0014-5793\(98\)01523-3](https://doi.org/10.1016/S0014-5793(98)01523-3); pmid: [9877163](https://pubmed.ncbi.nlm.nih.gov/9877163/)
69. R. A. Laskowski, M. B. Swindells, LigPlot+: Multiple ligand-protein interaction diagrams for drug discovery. *J. Chem. Inf. Model.* **51**, 2778–2786 (2011). doi: [10.1021/ci200227u](https://doi.org/10.1021/ci200227u); pmid: [21919503](https://pubmed.ncbi.nlm.nih.gov/21919503/)
70. A. Punjani, D. J. Fleet, 3D variability analysis: Resolving continuous flexibility and discrete heterogeneity from single particle cryo-EM. *J. Struct. Biol.* **213**, 107702 (2021). doi: [10.1016/j.jsb.2021.107702](https://doi.org/10.1016/j.jsb.2021.107702); pmid: [33582281](https://pubmed.ncbi.nlm.nih.gov/33582281/)
71. E. F. Pettersen *et al.*, UCSF ChimeraX: Structure visualization for researchers, educators, and developers. *Protein Sci.* **30**, 70–82 (2021). doi: [10.1002/pro.3943](https://doi.org/10.1002/pro.3943); pmid: [32881101](https://pubmed.ncbi.nlm.nih.gov/32881101/)

ACKNOWLEDGMENTS

Funding: This work was supported by the Monash University Ramaciotti Centre for Cryo-Electron Microscopy and the Monash MASSIVE high-performance computing facility. Figures were created with UCSF ChimeraX, developed by the Resource for Biocomputing, Visualization, and Informatics at the University of California, San Francisco, with support from National Institutes of Health grant R01-GM129325 and the Office of Cyber Infrastructure and Computational Biology, National Institute of Allergy and Infectious Diseases. This work was also funded by the Australian Research Council (ARC Centre grant IC200100052 to P.M.S. and D.W.); the National Health and Medical Research Council of Australia (NHMRC project grant 1120919 to P.M.S.; NHMRC project grant 1159006 to D.W.; NHMRC program grant 1150083 to P.M.S. and A.C.; NHMRC senior principal research fellowship 1154434 to P.M.S.; and NHMRC senior research fellowship 1155302 to D.W.); the Victoria Endowment for Science Knowledge and Innovation (fellowship to T.M.J.); the Takeda Science Foundation (2019 Medical Research Grant to R.D.); and the Japan Science and Technology Agency (PRESTO grant 18069571 to R.D.). **Author contributions:** Conceptualization: A.C., D.W., P.M.S.; Funding acquisition: P.M.S., D.W., A.C., R.D.; Interpretation: J.C., R.M.J., T.M.J., A.C., D.L.H., D.W., P.M.S., R.D.; Investigation: J.C., R.M.J., Y.L.L., M.J.B., R.D., M.M.F.; Methodology: Y.L.L.; Project administration: P.M.S., D.W., M.J.B.; Supervision: P.M.S., D.W., M.J.B.; Visualization: J.C., M.J.B., R.M.J., R.D.; Writing – original

draft: J.C., D.W., P.M.S.; Writing – review and editing: J.C., M.J.B., Y.L.L., R.M.J., T.M.J., M.M.F., A.C., D.L.H., R.D., D.W., P.M.S.

Competing interests: P.M.S. and D.W. receive funding from Novo Nordisk to study the pharmacology of peptide agonists of AMYRs and CTR. This funding is unrelated to the current work. D.L.H. has acted as a consultant for Intarcia Therapeutics in the past 3 years. The remaining authors declare no competing interests. **Data and materials availability:** All materials are available upon reasonable request. All relevant data are available from the authors and/or are included in the manuscript or the supplementary materials. Atomic coordinates and the cryo-EM

density maps have been deposited in the Protein Data Bank (PDB) under accession numbers 7TYF (rAmy-AMY₁R), 7TYX (rAmy-AMY₂R), 7TZF (rAmy-AMY₃R), 7TYW (sCT-AMY₁R), 7TYY (sCT-AMY₂R), 7TYH (hCT-AMY₂R), 7TYI (rAmy-CTR, CT-like), 7TYL (rAmy-CTR, bypass motif), 7TYN (sCT-CTR), and 7TYO (hCT-CTR), and in the Electron Microscopy Data Bank (EMDB) under accession numbers EMD-26178 (rAmy-AMY₁R), EMD-26197 (rAmy-AMY₂R), EMD-26208 (rAmy-AMY₃R), EMD-26196 (sCT-AMY₁R), EMD-26199 (sCT-AMY₂R), EMD-26179 (hCT-AMY₂R), EMD-26180 (rAmy-CTR, CT-like), EMD-26184 (rAmy-CTR, bypass motif), EMD-26188 (sCT-CTR), and EMD-26190 (hCT-CTR).

SUPPLEMENTARY MATERIALS

[science.org/doi/10.1126/science.abm9609](https://doi.org/10.1126/science.abm9609)

Figs. S1 to S11

Tables S1 to S4

Movies S1 to S3

MDAR Reproducibility Checklist

25 October 2021; accepted 25 February 2022
10.1126/science.abm9609

RESEARCH ARTICLE SUMMARY

CROP GENOMICS

Convergent selection of a WD40 protein that enhances grain yield in maize and rice

Wenkang Chen[†], Lu Chen[†], Xuan Zhang[†], Ning Yang[†], Jianghua Guo, Min Wang, Shenghui Ji, Xiangyu Zhao, Pengfei Yin, Lichun Cai, Jing Xu, Lili Zhang, Yingjia Han, Yingni Xiao, Gen Xu, Yuebin Wang, Shuhui Wang, Sheng Wu, Fang Yang, David Jackson, Jinkui Cheng, Saihua Chen, Chuanqing Sun, Feng Qin, Feng Tian, Alisdair R. Fernie, Jiansheng Li*, Jianbing Yan*, Xiaohong Yang*

INTRODUCTION: During the independent process of cereal evolution, many trait shifts appear to have been under convergent selection to meet the specific needs of humans. Identification of convergently selected genes across cereals could help to clarify the evolution of crop species and to accelerate breeding programs. In the past several decades, researchers have debated whether convergent phenotypic selection in distinct lineages is driven by conserved molecular changes or by diverse molecular pathways. Two of the most economically important crops, maize and rice, display some conserved phenotypic shifts—including loss of seed dispersal, decreased seed dormancy, and increased grain number during evolution—even though they experienced independent selection. Hence, maize and rice can serve as an excellent system for understanding the extent of convergent selection among cereals.

RATIONALE: Despite the identification of a few convergently selected genes, our understanding of the extent of molecular convergence on a genome-wide scale between maize and rice is very limited. To learn how often selection acts on orthologous genes, we investigated the functions and molecular

evolution of the grain yield quantitative trait locus *KRN2* in maize and its rice ortholog *OsKRN2*. We also identified convergently selected genes on a genome-wide scale in maize and rice, using two large datasets.

RESULTS: We identified a selected gene, *KRN2* (*kernel row number 2*), that differs between domesticated maize and its wild ancestor, teosinte. This gene underlies a major quantitative trait locus for kernel row number in maize. Selection in the noncoding upstream regions resulted in a reduction of *KRN2* expression and an increased grain number through an increase in kernel rows. The rice ortholog, *OsKRN2*, also underwent selection and negatively regulates grain number via control of secondary panicle branches. These orthologs encode WD40 proteins and function synergistically with a gene of unknown function, DUF1644, which suggests that a conserved protein interaction controls grain number in maize and rice. Field tests show that knockout of *KRN2* in maize or *OsKRN2* in rice increased grain yield by ~10% and ~8%, respectively, with no apparent trade-off in other agronomic traits. This suggests potential applications of *KRN2* and its orthologs for crop improvement.

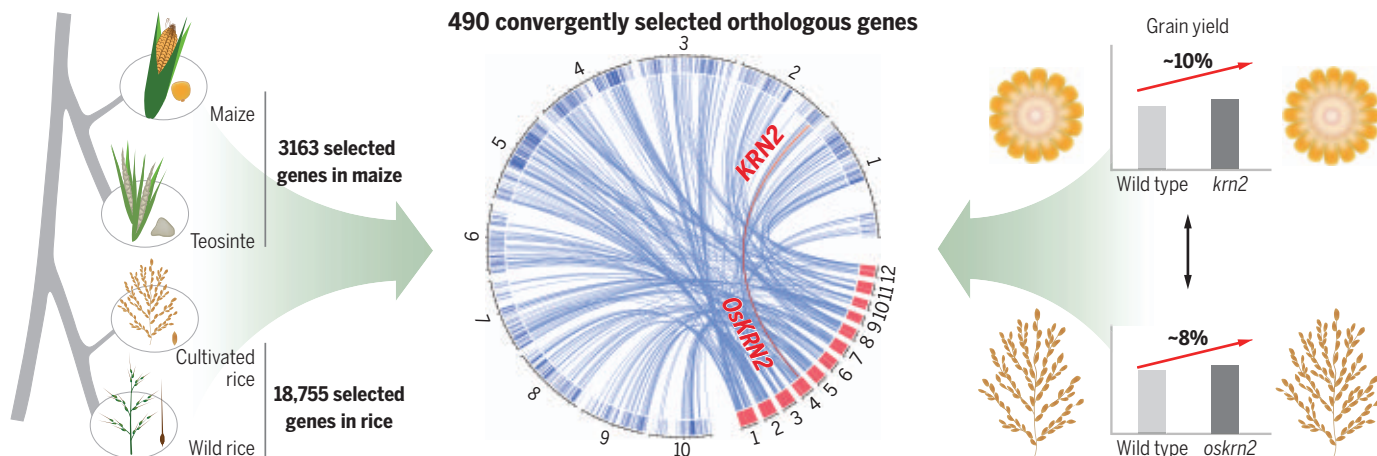
On a genome-wide scale, we identified a set of 490 orthologous genes that underwent convergent selection during maize and rice evolution, including *KRN2/OsKRN2*. We found that the convergently selected orthologous genes appear to be significantly enriched in two specific pathways in both maize and rice: starch and sucrose metabolism, and biosynthesis of cofactors. A deep analysis of convergently selected genes in the starch metabolic pathway indicates that the degree of genetic convergence via convergent selection is related to the conservation and complexity of the gene network for a given selection.

CONCLUSION: Our findings show that common phenotypic shifts during maize and rice evolution acting on conserved genes are driven at least in part by convergent selection, which in maize and rice likely occurred both during and after domestication. We provide evolutionary and functional evidence on the convergent selection of *KRN2/OsKRN2* for grain number between maize and rice. We further found that a complete loss-of-function allele of *KRN2/OsKRN2* increased grain yield without an apparent negative impact on other agronomic traits. Exploring the role of *KRN2/OsKRN2* and other convergently selected genes across the cereals could provide new opportunities to enhance the production of other global crops. ■

The list of author affiliations is available in the full article online.
*Corresponding author. Email: yxiaohong@cau.edu.cn (X.Y.); yjianbing@mail.hzau.edu.cn (J.Y.); lijiansheng@cau.edu.cn (J.L.)

†These authors contributed equally to this work.
Cite this article as W. Chen et al., *Science* 375, eabg7985 (2022). DOI: 10.1126/science.abg7985

S READ THE FULL ARTICLE AT
<https://doi.org/10.1126/science.abg7985>



Shared selected orthologous genes in maize and rice for convergent phenotypic shifts during domestication and improvement. By comparing 3163 selected genes in maize and 18,755 selected genes in rice, we identified 490 orthologous gene pairs, including *KRN2* and its rice ortholog *OsKRN2*, as having been convergently selected. Knockout of *KRN2* in maize or *OsKRN2* in rice increased grain yield by increasing kernel rows and secondary panicle branches, respectively.

RESEARCH ARTICLE

CROP GENOMICS

Convergent selection of a WD40 protein that enhances grain yield in maize and rice

Wenkang Chen^{1†}, Lu Chen^{2‡}, Xuan Zhang^{1†}, Ning Yang^{2,3†}, Jianghua Guo¹, Min Wang¹, Shenghui Ji¹, Xiangyu Zhao¹, Pengfei Yin¹, Lichun Cai¹, Jing Xu¹, Lili Zhang¹, Yingjia Han¹, Yingni Xiao¹, Gen Xu¹, Yuebin Wang², Shuhui Wang¹, Sheng Wu¹, Fang Yang^{2,3}, David Jackson^{2,4}, Jinkui Cheng^{1,5}, Saihua Chen⁶, Chuanqing Sun¹, Feng Qin^{1,5}, Feng Tian^{1,5}, Alisdair R. Fernie⁷, Jiansheng Li^{1,5*}, Jianbing Yan^{2,3*}, Xiaohong Yang^{1,5*}

A better understanding of the extent of convergent selection among crops could greatly improve breeding programs. We found that the quantitative trait locus *KRN2* in maize and its rice ortholog, *OsKRN2*, experienced convergent selection. These orthologs encode WD40 proteins and interact with a gene of unknown function, *DUF1644*, to negatively regulate grain number in both crops. Knockout of *KRN2* in maize or *OsKRN2* in rice increased grain yield by ~10% and ~8%, respectively, with no apparent trade-offs in other agronomic traits. Furthermore, genome-wide scans identified 490 pairs of orthologous genes that underwent convergent selection during maize and rice evolution, and these were enriched for two shared molecular pathways. *KRN2*, together with other convergently selected genes, provides an excellent target for future crop improvement.

The major cereals, including maize, rice, wheat, barley, and sorghum, were domesticated independently ~10,000 years ago and represent a primary source of human calories (1). Genome-wide analyses indicate that domestication and improvement in the cereals were complex and involved numerous genes associated with various biological traits (2–5). Although the cereals underwent independent domestication and improvement, many morphological and physiological or biochemical traits appear to have been under convergent selection, resulting in an ease of cultivation, high yield, and nutrient richness (1). Given the close phylogenetic relationships among cereals, a key question is whether convergent phenotypic selection in distinct lineages was driven by conserved molecular changes. In some cases, selection in independent lineages appears to have acted on conserved genetic loci that control convergent phenotypes (6–8), whereas in other cases the convergent phenotypic changes appear to have arisen by

diverse genetic routes due to homoplasy of selected genetic loci (9–11).

Two of the most economically important crops, maize (*Zea mays* L. ssp. *mays*) and rice (*Oryza sativa* L.), diverged >50 million years ago (12). Although the collinearity of cereal genomes has long been recognized (12–14), only a few genes—such as those involved in shattering resistance—have been identified as having been convergently selected during the evolution of maize and rice (7, 15). Hence, a genome-wide identification of the genes that have undergone convergent selection in maize and rice could help to clarify the evolution of crop species as well as to accelerate breeding programs.

KRN2 is a selected gene underlying kernel row number variation

We mapped eight quantitative trait loci (QTLs) for kernel row number (KRN) in a maize recombinant inbred line (RIL) population developed from a cross between an inbred line, B73, and an introgression line, MT-6, of which ~25% of its genome is derived from that of teosinte, the wild ancestor of maize (16) (Fig. 1A and table S1). *qKRN2*, the QTL with the largest effect, was located within a selective sweep on the short arm of chromosome 2 (2), and the maize allele increased KRN relative to the teosinte allele. To identify the gene(s) underlying *qKRN2*, we performed positional cloning using nine markers and 7056 individuals derived from a backcross of MT-6/B73 F₁ plants with B73 (fig. S1). We delimited this QTL to a 5799–base pair (bp) region that contained only one candidate gene (*Zm00001d00264t*), which we named *KRN2* (*kernel row number2*; Fig. 1, B and C). Comparisons of the maize and teosinte alleles indicated that the maize (B73) allele

increased KRN by ~1.4 rows relative to teosinte (Fig. 1, D and E). To confirm the function of *KRN2*, we identified a loss-of-function allele carrying a *Mutator* (*Mu*) transposon insertion in exon 1. Ears from plants homozygous for the *Mu* insertion produced ~1.8 more rows than wild-type segregants (fig. S2). These results suggest that *KRN2* is the causal gene for KRN variation in *qKRN2* and that loss-of-function alleles can increase KRN in maize.

Genomic sequencing identified 63 single-nucleotide polymorphisms (SNPs) and 37 insertions or deletions (indels) in the promoter and 5' untranslated region (UTR) of *KRN2*, as well as seven synonymous and seven non-synonymous SNPs in coding exons between the B73 and teosinte alleles (Fig. 1C and fig. S3). Real-time quantitative polymerase chain reaction (qPCR) showed that *KRN2* expression was lower in NIL-*KRN2*^{B73} relative to NIL-*KRN2*^{teosinte} in the early stage of maize inflorescence meristem (IM) development (Fig. 1F and fig. S4). To test whether the sequence polymorphisms in the promoter or 5'UTR might underlie these different expression levels, we performed transient expression assays in maize protoplasts, in which two fragments (~1.2 kb or ~2.0 kb) upstream of the start codon of *KRN2* from maize or teosinte were fused upstream of the luciferase (LUC) gene (Fig. 1G). Both teosinte fragments exhibited higher LUC activity than the maize fragments (Fig. 1H), which suggests that polymorphisms within the ~1.2-kb region of *KRN2* account for expression differences between maize and teosinte alleles. Furthermore, we overexpressed the coding sequences of *KRN2*^{B73} and of *KRN2*^{teosinte} alleles in a maize inbred line and confirmed enhanced expression of *KRN2* by qPCR (fig. S5, A to C). Relative to wild-type plants, all six independent overexpression lines consistently decreased KRN by ~2.0 rows, with no difference between *Ubi::KRN2*^{B73} and *Ubi::KRN2*^{teosinte} transgenic plants (fig. S5D). These findings indicate that KRN changes are mediated through changes in *KRN2* expression, most likely caused by polymorphisms within the ~1.2-kb promoter and 5'UTR region.

To ascertain whether *KRN2* underwent selection during maize evolution, we calculated nucleotide diversity across its promoter and coding regions. Similar diversity was observed between maize landraces and inbred lines (Fig. 1I). We observed a reduction in nucleotide diversity in maize relative to its ancestor, *Zea mays* ssp. *parviglumis* (hereafter, *parviglumis*; $\pi_{parviglumis} = 2.6 \times 10^{-2}$, $\pi_{landrace} = 6.1 \times 10^{-3}$, $\pi_{inbred} = 2.1 \times 10^{-3}$), and a negative Tajima's D-statistic in maize inbred lines and landraces for a ~700-bp region containing the 5'UTR of *KRN2* (Fig. 1I and fig. S6); these findings suggest that this region underwent selection. This result was further supported by a coalescence simulation (fig. S6). This severe loss of

¹State Key Laboratory of Plant Physiology and Biochemistry and National Maize Improvement Center of China, China Agricultural University, Beijing 100193, China. ²National Key Laboratory of Crop Genetic Improvement, Huazhong Agricultural University, Wuhan 430070, China. ³Hubei Hongshan Laboratory, Wuhan 430070, China. ⁴Cold Spring Harbor Laboratory, Cold Spring Harbor, NY 11724, USA. ⁵Center for Crop Functional Genomics and Molecular Breeding, China Agricultural University, Beijing 100193, China. ⁶Key Laboratory of Plant Functional Genomics of the Ministry of Education, Yangzhou University, Yangzhou, Jiangsu 225009, China. ⁷Department of Molecular Physiology, Max Planck Institute of Molecular Plant Physiology, 14476 Potsdam-Golm, Germany.

*Corresponding author. Email: yxiaohong@cau.edu.cn (X.Y.); yjianbing@mail.hzau.edu.cn (J.Y.); lijiansheng@cau.edu.cn (J.L.)

†These authors contributed equally to this work.

‡Present address: State Key Laboratory of Plant Genomics and National Center for Plant Gene Research, Institute of Genetics and Developmental Biology, Chinese Academy of Sciences, Beijing 100101, China.

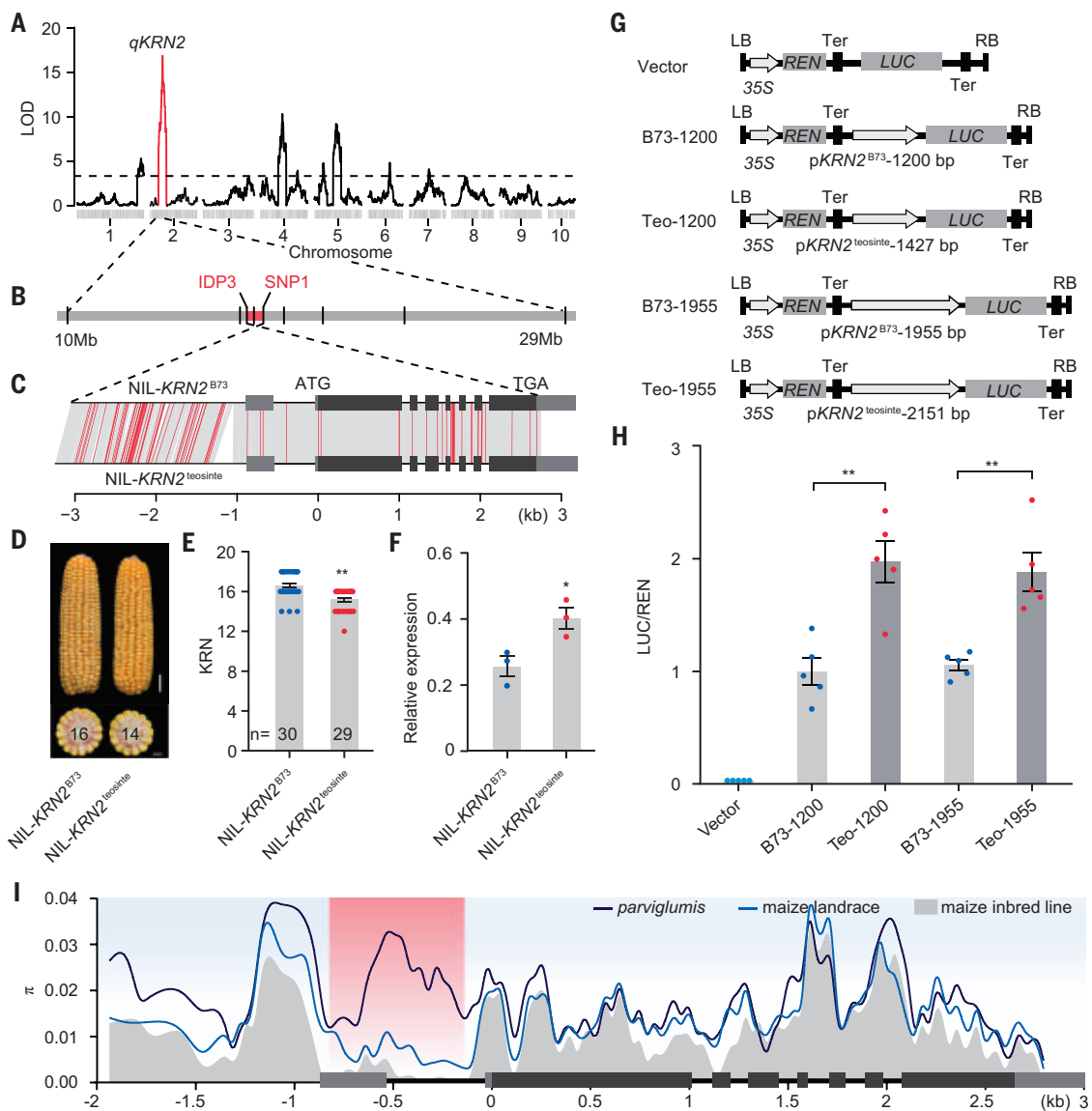


Fig. 1. *KRN2* affects kernel row number and underwent selection during maize domestication. (A) Logarithm of odds (LOD) profile of QTLs for KRN in the MT-6/B73 RIL population. The dashed line shows the threshold LOD value (3.3) for putative QTLs. (B) *qKRN2* was fine-mapped to a 5799-bp interval (red) flanked by the markers IDP3 and SNP1. (C) *KRN2* gene structure and sequence comparison of the target region between NIL-*KRN2*^{B73} and NIL-*KRN2*^{teosinte}. Black, exons; gray, UTRs. The red lines denote SNPs; the white spaces show indels. (D to F) Ear performance (D), KRN quantification (E), and *KRN2* expression in 0.5-mm IMs (F) of NIL-*KRN2*^{B73} and NIL-*KRN2*^{teosinte}. Scale bars in (D), 2 cm for the ear, 1 cm for ear transverse sections. The expression levels of *KRN2* in (F) were quantified using qPCR and normalized to that of maize

ACTIN. (G) Constructs used to test the effect of polymorphisms in the promoter and 5'UTR on *KRN2* expression in transient expression assays in maize leaf protoplasts. B73-1200, Teo-1200, B73-1955, and Teo-1955 constructs harbor the promoter and 5'UTR of different *KRN2* alleles, including 1200 bp from B73, 1427 bp from teosinte, 1955 bp from B73, and 2151 bp from teosinte. (H) The teosinte sequences drive increased LUC activity relative to the B73 alleles. The data were normalized with respect to the average values of the B73-1200 construct. (I) Nucleotide diversity across the *KRN2* locus. A 150-bp sliding window with a 35-bp step size was used to calculate nucleotide diversity (π). The selected region (-800 to -100 bp) is shaded in red. In (E), (F), and (H), data are means \pm SEM, $n = 3$ in (F) and $n = 5$ in (H). * $P < 0.05$, ** $P < 0.01$ (two-tailed Student's *t* test).

diversity could not be explained by a domestication bottleneck or modern improvement in maize alone. Our selection analyses seem to suggest that human selection was likely involved in the evolution of *KRN2* between initial domestication and modern improvement. Taken together, both our transgenic studies and surveys of nucleotide diversity suggest that selection in the noncoding upstream regions

resulted in a reduction in *KRN2* expression and, in turn, an increased KRN in maize.

***KRN2* negatively regulates KRN by interacting with DUF1644, a protein of unknown function**

Sequence analysis of *KRN2* predicted that it encodes a cytoplasmic WD40 protein containing seven WD40 repeats (figs. S7 and S8, A and B). Members of the WD40 family act as scaffolds

for protein-protein interactions (17, 18) and have diverse functions in plants, including in development, metabolite biosynthesis, and immune responses (19–21). To illuminate the molecular mechanism of *KRN2*, we identified six potential interaction partners using a yeast two-hybrid (Y2H) screen (table S2). Among them, we focused on the gene *DUF1644*, which encodes a DUF1644-containing protein that

localized to both the cytoplasm and the nucleus (fig. S8, A and C). We confirmed a direct interaction between KRN2 and DUF1644 by Y2H assays as well as split firefly LUC complementation assays (Fig. 2, A and B). Next, to further elucidate the relationship between *KRN2* and *DUF1644*, we generated *krn2* and *duf1644* null mutants by CRISPR-Cas9 technology as well as a *krn2 duf1644* double mutant (fig. S9). Neither of the two single *duf1644* mutants had an obvious phenotype, but the *krn2 duf1644* double mutant had a significantly higher KRN relative to the *krn2* single mutant (16.3 ± 1.2 versus 15.9 ± 1.1 ; unpaired *t* test, $t = 2.0$, $df = 124$, $P = 4.6 \times 10^{-2}$; Fig. 2C and fig. S9). This result suggests that DUF1644 acts with KRN2, although it remains unknown how this affects KRN and the underlying molecular function of DUF1644.

To better understand the cause of the increase in KRN, we measured IM size. The NIL-*KRN2*^{B73} IMs ($345.5 \pm 25.2 \mu\text{m}$) were wider

than those of NIL-*KRN2*^{teosinte} ($313.0 \pm 19.6 \mu\text{m}$), and *KRN2* overexpression decreased IM diameter by $\sim 56 \mu\text{m}$ (fig. S10). Consistently, both the *krn2* single mutant and *krn2 duf1644* double mutant significantly increased their IM size relative to the wild-type plants (unpaired *t* test; $446.3 \pm 33.0 \mu\text{m}$ versus $422.4 \pm 23.8 \mu\text{m}$, $t = 3.3$, $df = 61$, $P = 1.7 \times 10^{-3}$ for the single mutant; $465.9 \pm 27.4 \mu\text{m}$ versus $422.4 \pm 23.8 \mu\text{m}$, $t = 6.5$, $df = 56$, $P = 2.6 \times 10^{-8}$ for the double mutant; Fig. 2, D and E). We hypothesize that these increases in IM size provided additional space for initiation of spikelet pair meristems, and hence a higher KRN (Fig. 2F).

Convergent selection of the *KRN2* ortholog in rice

A single ortholog of *KRN2* containing conserved WD40 domains was identified in most major cereal crops (Fig. 3A and fig. S7). The rice *KRN2* ortholog, *Os04.g0568400* (hereafter, *OsKRN2*), mapped to a region that underwent

a selective sweep (27.5 to 29.0 Mb) on rice chromosome 4 (3) that is syntenic with the short arm of chromosome 2 in maize (Fig. 3B) and is within a QTL for rice grain number (22, 23). These observations suggest that *OsKRN2* may have also experienced selection on rice grain number. Consistent with this, nucleotide diversity was reduced in an ~ 1100 -bp region upstream of the *OsKRN2* start codon in cultivated rice (fig. S11). As expected, a minimum-spanning tree of 27 haplotypes in the ~ 1100 -bp region separated wild rice *Oryza rufipogon* (hereafter, *rufipogon*; 59 accessions) from cultivated rice (109 accessions) according to the sequenced accessions (Fig. 3C).

Like the *KRN2* expression profile in maize, *OsKRN2* was expressed in all rice tissues, with high levels in panicle primordia (fig. S12). Rice panicle branches are initiated by branch meristems, which are analogous to spikelet pair meristems in maize (24). We made *OsKRN2* null mutants using CRISPR-Cas9 technology,

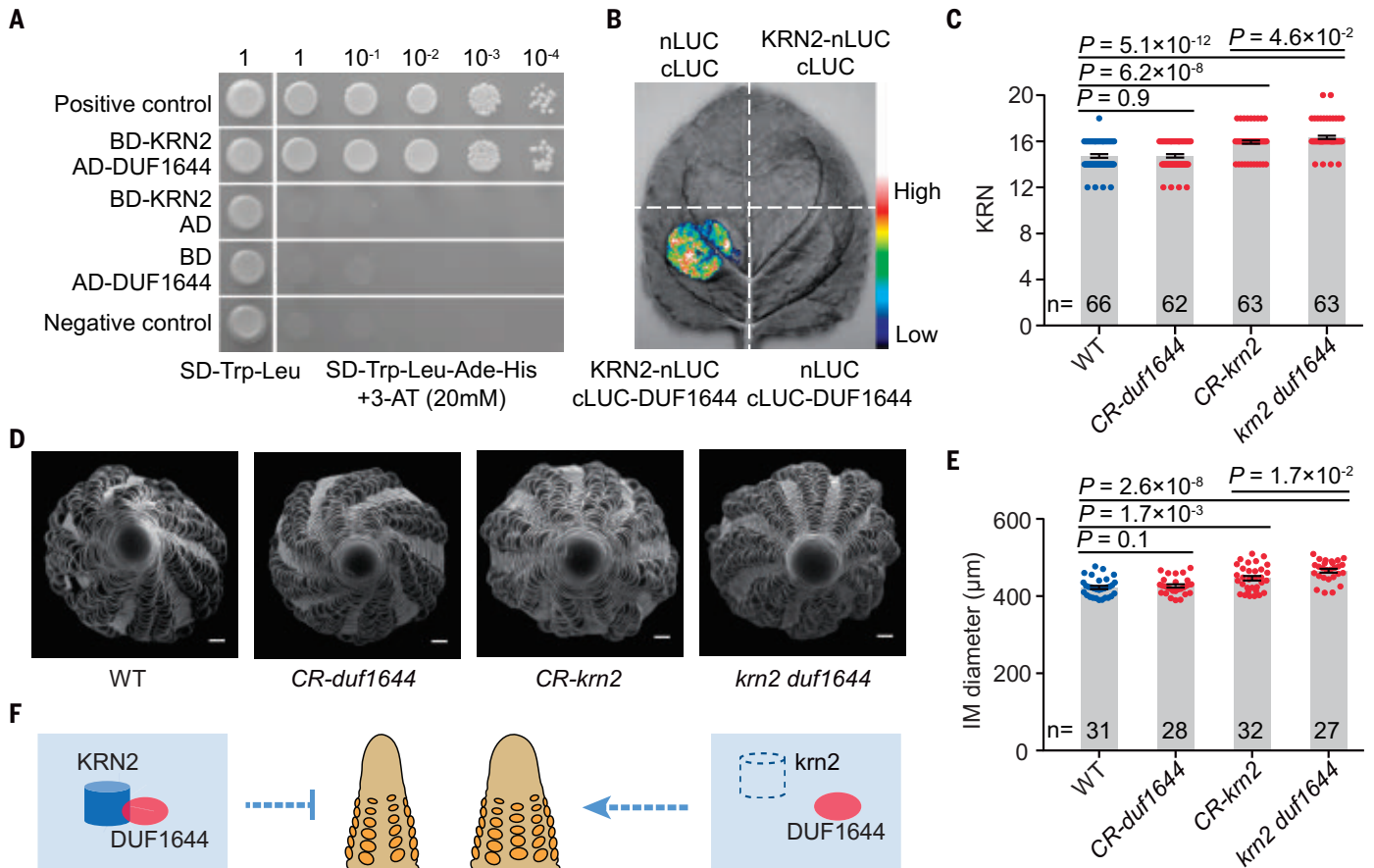


Fig. 2. *KRN2* and its interactor, DUF1644, regulate KRN in a synergistic pathway. (A and B) Interaction between *KRN2* and DUF1644 confirmed by Y2H assays (A) and the split firefly LUC complementation assay in tobacco (B). BD, binding domain; AD, activation domain; Ade, adenine; 3-AT, 3-aminotriazole. Fluorescence intensity represents the strength of the interaction. (C to E) KRN quantification (C), top-down scanning electron microscopy views of ear primordia (D), and IM diameter quantification (E) from wild type (WT) and single and double mutants of *krn2* and *duf1644*. In (C) and (E), data are means \pm SEM. *P* values were calculated from two-tailed Student's *t* test. Scale bars in (D), 100 μm . (F) A hypothetical working model for *KRN2* in controlling KRN in maize. When *KRN2* function is lost, DUF1644 cannot interact with it, resulting in an increase in IM diameter and, consequently, KRN. Otherwise, DUF1644 interacts with *KRN2* to synergistically and negatively regulate IM diameter and KRN.

and, similar to the results in maize, we observed an increase in secondary branches from an average of 16.0 (± 2.5) branches in the wild-type plants to as many as 18.9 (± 3.5) in the null mutants (Fig. 3, D and E, and fig. S13). Consequently,

an increase in grain number in the mutant panicles (up to 118.1 ± 11.9 grains) was observed relative to wild-type panicles (107.7 ± 9.5 grains) (Fig. 3F). In contrast, lines overexpressing *OsKRN2* had fewer secondary branches with

fewer grains (Fig. 3, G to I, and fig. S13). These findings indicate that *OsKRN2* likely controls grain production in rice by affecting the number of secondary branches. In addition, Y2H and split firefly LUC complementation assays

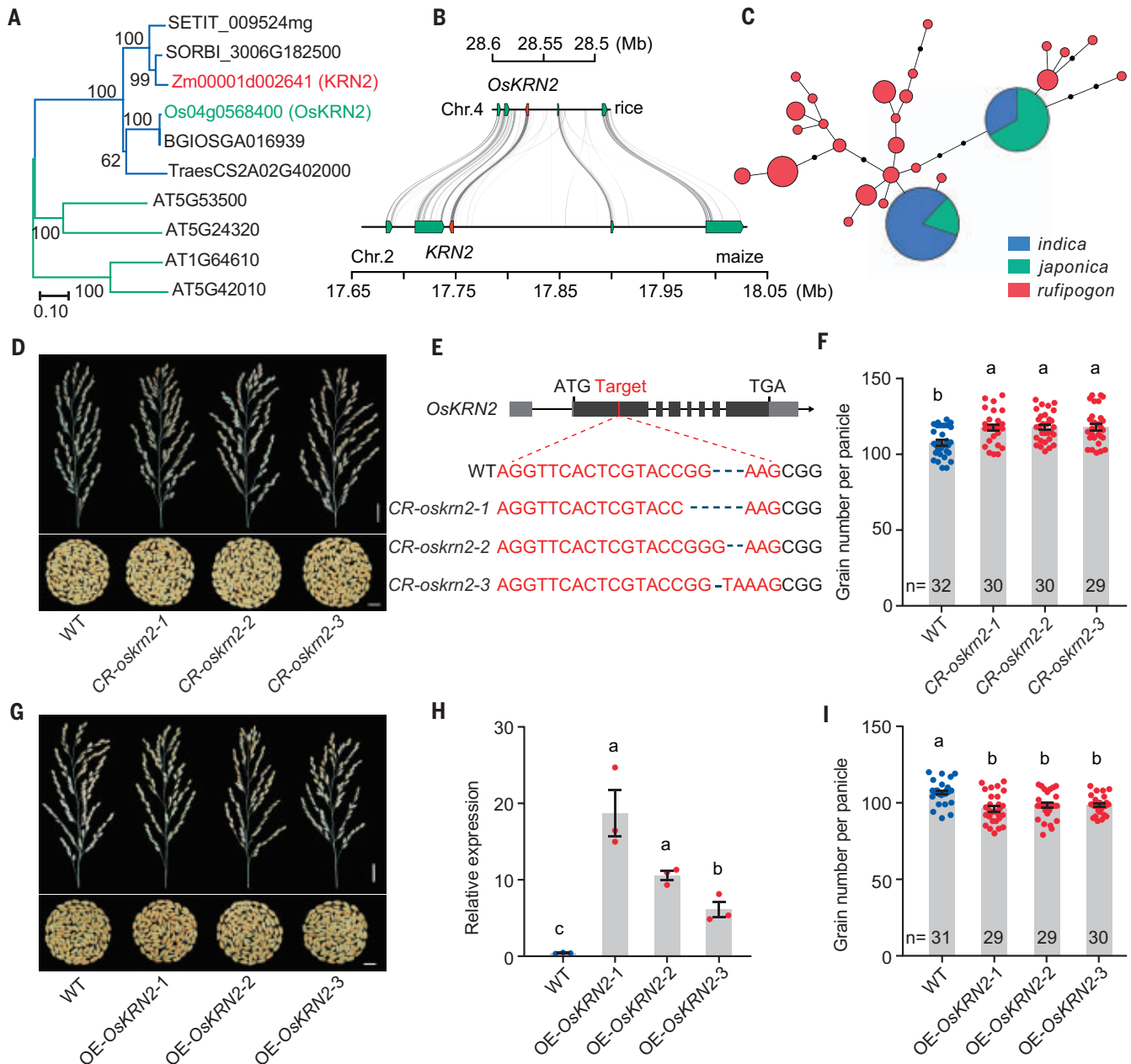


Fig. 3. *OsKRN2* is a selected gene in rice and contributes to grain number.

(A) The neighbor-joining phylogenetic tree of *KRN2* and its orthologs from major cereal crops and *Arabidopsis*. Bootstrap values from 1000 replicates are indicated at each node; the scale represents branch length. (B) Comparative genomic analysis of syntenic and conserved sequences in the 0.4/0.1-Mb region around *KRN2* (*OsKRN2*) (red) from maize (B73) and rice (Nipponbare). The aligned orthologs (from left to right, in green) are *Zm00001d002639*, *Zm00001d002640*, *Zm00001d002642*, and *Zm00001d002644* in maize and *Os04 g0568900*, *Os04 g0568800*, *Os04 g0567800*, and *Os04 g0566900* in rice. (C) A minimum-spanning tree for the ~1100-bp *OsKRN2* promoter and 5'UTR region. Each haplotype group is represented by a circle whose size is proportional to the individual number of the

haplotype. (D) *CR-oskrm2* mutants increase panicle branching and grain number. (E) Null coding sequences of *CR-oskrm2* mutants. Gene diagram is shown. Black, exons; gray, UTRs. The red line indicates the guide RNA site. (F) Quantification of grain number per panicle from WT and *CR-oskrm2* mutants. (G to I) Panicle morphologies and grains per panicle (G), *OsKRN2* expression level (H), and grain number per panicle (I) of WT and *OsKRN2*-overexpressing transgenic lines. The expression levels of *OsKRN2* in (H) were quantified using qPCR and normalized to that of rice *ACTIN*. Scale bars in (D) and (G), 2 cm for panicle morphologies, 1 cm for grains. In (F), (H), and (I), data are means \pm SEM, n = 3 in (H); different letters indicate significant differences at $P < 0.05$ (one-way analysis of variance followed by Tukey's multiple-comparison test).

confirmed a direct interaction between *OsKRN2* and *OsDUF1644* (fig. S14), suggesting that a conserved protein interaction controls KRN in maize and the number of secondary branches in rice.

Gene editing of *KRN2* and *OsKRN2* enhances grain yield in maize and rice field trials

We next asked whether gene editing of *KRN2/OsKRN2* could increase yield in the field, which serves as a proxy for applicability in breeding programs. Thus, we planted maize *KRN2* and rice *OsKRN2* gene-edited lines in multiple environments for yield testing (Fig. 4). For maize, field tests across three environments showed that two *KRN2*-edited lines (*CR-krn2-1* and *CR-krn2-2*) stably increased KRN by ~1.6 to 2.0 rows and kernel numbers per ear by ~27 to 53 kernels, resulting in an increase in grain yield of 9.0 to 10.5% (Fig. 4B, figs. S9B and S15, and table S3). Remarkably, these *krn2* knockouts did not alter plant architecture, flowering time, or ear length, although kernel width was slightly reduced (Fig. 4A and table S3). In rice, *OsKRN2*-edited lines (*CR-oskrn2-1* and *CR-oskrn2-2*) showed a similar increase in

the number of grains per panicle (average increase of 9.8 to 10.3 grains per panicle) and grain yield per plant (7.9 to 8.2%), again with no obvious changes in other agronomic traits (Fig. 4, C and D, and fig. S16). These findings indicate that a complete loss-of-function allele of *KRN2/OsKRN2* increased grain yield without an apparent negative impact on other agronomic traits in tested environments. Whether the performance is consistent in diverse environments remains to be resolved. We neither identified any natural loss-of-function mutations of *KRN2/OsKRN2* nor detected association signals for grain number-related traits in natural populations, including hundreds of diverse lines in maize (table S4) and rice (25); this suggests that gene editing of *KRN2/OsKRN2* could provide a unique way to modify grain number in breeding lines.

Genome-wide convergent selection between maize and rice

Morphologically, cultivated maize and rice differ substantially from their ancestors and display a “domestication syndrome”—a common

suite of traits that have changed in domesticated crops (26). These include loss of seed dispersal, decreased seed dormancy, and increased grain number, size, and weight (1) (Fig. 5A). In addition to *KRN2/OsKRN2* for grain number, two additional orthologous gene pairs—*ZmSh1/OsSh1* for seed shattering (7) and *ZmSWEET4c/OsSWEET4* for grain filling (27)—have also experienced convergent selection during maize and rice evolution. Hence, it is worth exploring the extent of molecular convergence on a genome-wide scale between maize and rice, which could reveal how often selection acts on orthologous gene pairs. We therefore reanalyzed selected genes using two large new datasets, including ~65 million SNPs in 507 maize inbred lines and 70 *parviglumis* accessions, as well as ~71 million SNPs in 461 cultivated rice and 257 wild rice accessions (fig. S17 and table S5). Using phylogenetic information (3, 28), we estimated cross-population composite likelihood ratios (XP-CLRs) (29) followed by cross-validation on the basis of permutation tests for nucleotide diversity in the regions with the top 10% of XP-CLR scores

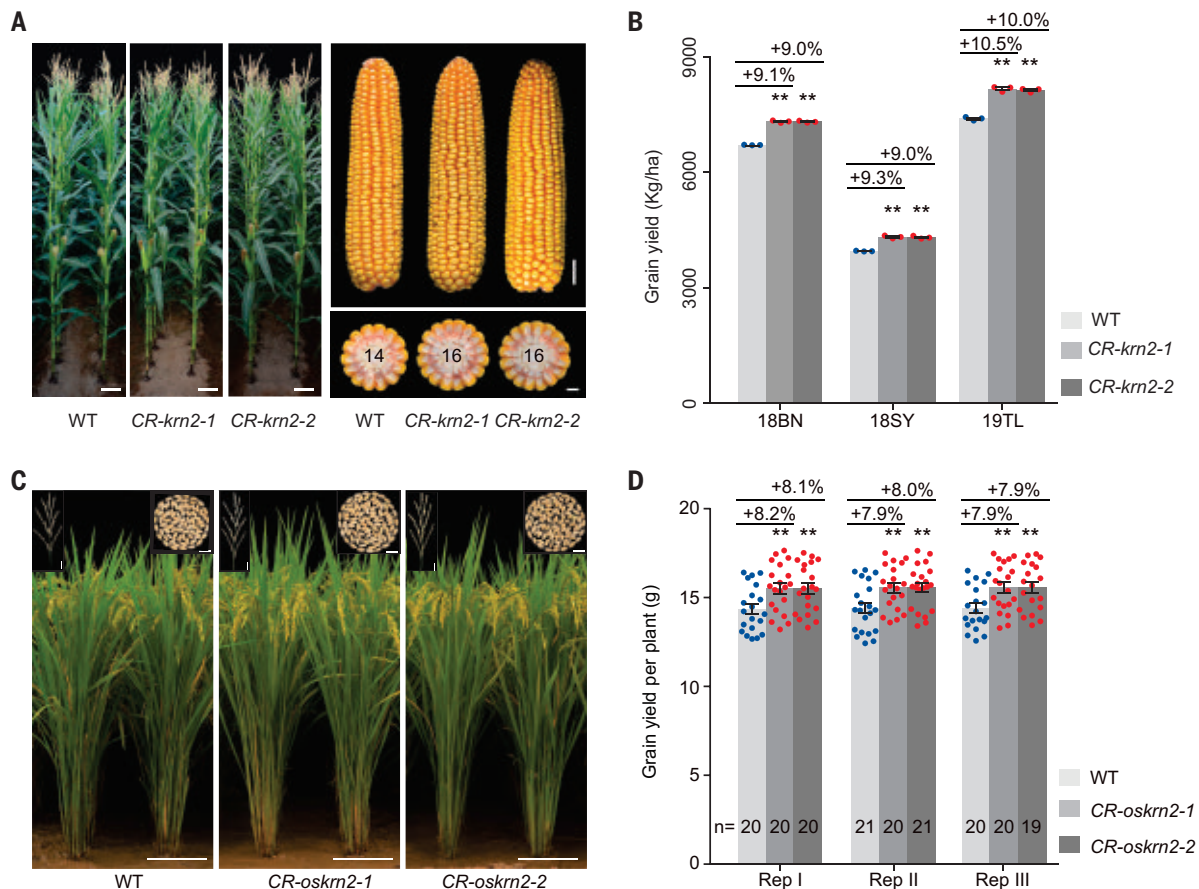


Fig. 4. Yield performance of *KRN2* and *OsKRN2* gene-edited lines under field conditions. (A) Plant and ear morphologies of WT, *CR-krn2-1*, and *CR-krn2-2*. **(B)** Grain yield of WT, *CR-krn2-1*, and *CR-krn2-2* in three locations. At each location, 26 to 38 ears for each replicate were quantified; data are means \pm SEM from three replicates (shown as dots) in each location. 18BN, 18SY, and 19TL indicates the field trials performed in Bayan Nur in 2018, Sanya in 2018, and Tieling

in 2019, respectively. **(C)** Plants, panicle, and grain morphologies of WT, *CR-oskrn2-1*, and *CR-oskrn2-2*. **(D)** Grain yield of WT, *CR-oskrn2-1*, and *CR-oskrn2-2* in one location with three replicates (Rep I to Rep III). For each replicate, 19 to 21 plants were quantified; data are means \pm SEM. Scale bars in (A) and (C), 20 cm for plants, 2 cm for ears and panicles, 1 cm for ear transections and grains. In (B) and (D), $**P < 0.01$ (two-tailed Student's *t* test).

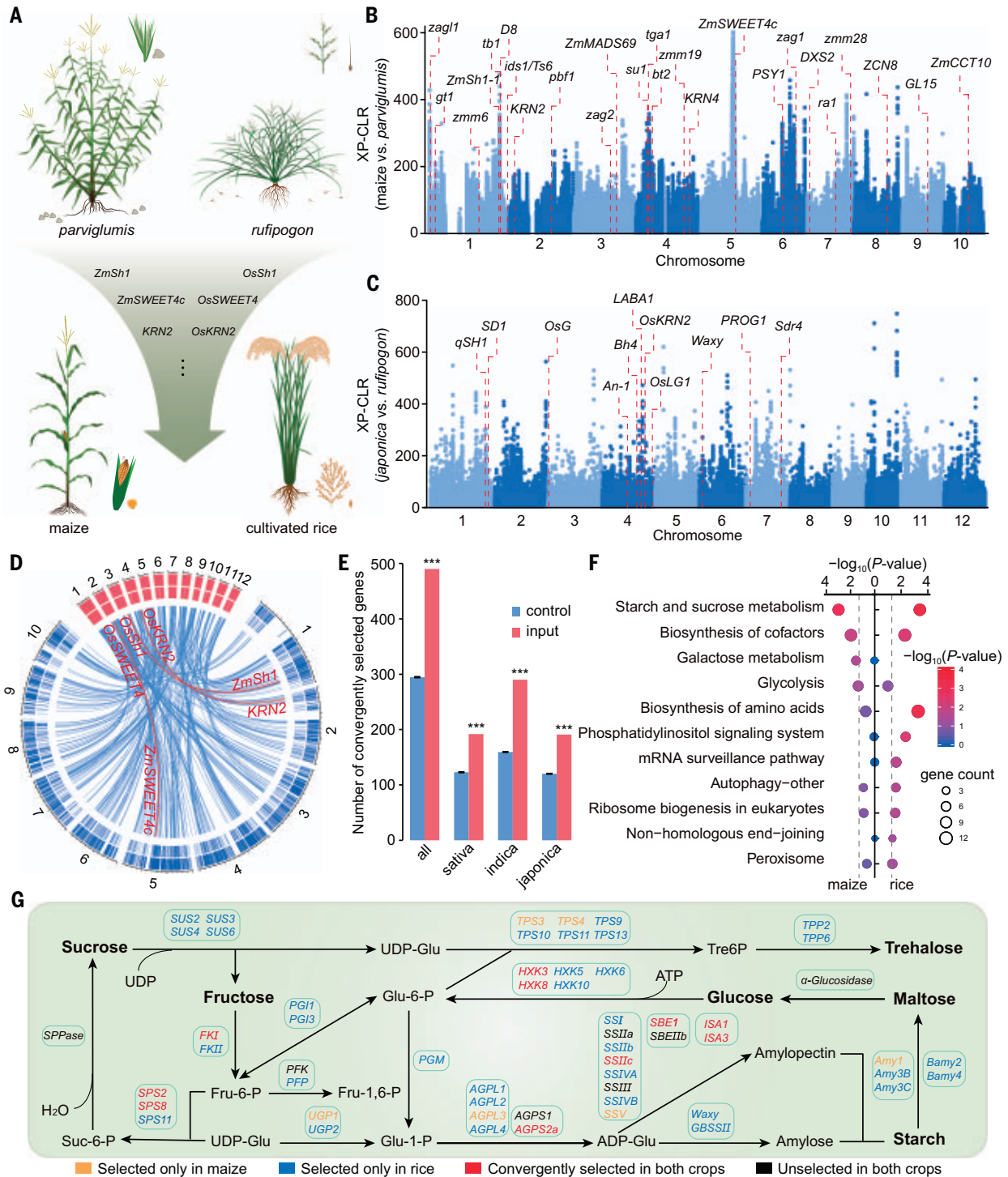


Fig. 5. Overview of convergent selection in maize and rice. (A) Convergence of traits in domesticated species versus wild ancestors, likely driven by genes with conserved functions. Three pairs of known orthologous genes under convergent selection are shown: *ZmSh1*/*OsSh1* for seed shattering (7), *ZmSWEET4c*/*OsSWEET4* for grain filling (27), and *KRN2*/*OsKRN2* for grain number. (B and C) Genome-wide XP-CLR values between maize and *parviglumis* (B) and between *japonica* and *rufipogon* (C). Regions of 1 kb and 300 bp were used to calculate the XP-CLR values for maize and rice, respectively; each point represents a value in a region. The red dashed lines indicate the positions of known selected genes detected in our study (table S7). (D) The distribution of selected regions (outer) and genes (inner) in maize (blue) and rice (red). The blue lines in the inner rings show the convergently selected genes that were syntenic in the maize and rice

genomes. The red lines highlight the positions of genes that are known to have undergone convergent selection. (E) Convergent selection acts on the identified orthologs more often than expected by chance between maize and different rice datasets. *** $P < 0.001$ (pairwise comparison via permutation test). (F) Enriched pathways in maize or rice identified using g:Profiler (adjusted $P < 0.05$, multiple-testing correction via the g:SCS algorithm) among the 490 orthologous gene pairs under convergent selection. Circle size indicates the number of genes from the common gene hit list included in each pathway; circle color and x-axis position indicate the $-\log_{10}$ -transformed P value. The vertical dashed lines indicate the significant threshold $P < 0.05$. (G) Detailed molecular representation of genes implicated in the starch and sucrose metabolism pathway during selection. Detailed information for these genes is listed in table S9.

(2). By comparing maize and *parviglumis*, we identified a total of 69.6 Mb of selected genomic regions that covered 3.3% of the maize B73 reference genome (30) and contained 3163 genes (Fig. 5B and tables S6 to S8). In this analysis, we identified two canonical domestication genes: *tb1*, which controls branching (31), and *tga1*, which controls the formation of the stony fruitcase (32) (Fig. 5B and table S7). In rice, we identified a total of 27.6, 25.8, and 26.3 Mb of selected genomic regions, including 7709, 10,196, and 7864 genes, respectively, by comparing *rufipogon* with *Oryza sativa* subsp. *japonica*, *O. sativa* subsp. *indica*, and *O. sativa*, respectively (hereafter, *japonica*, *indica*, and *sativa*; Fig. 5C, fig. S18, and tables S6 to S8). Collectively, these selected regions covered 17.2% (64.0 Mb) of the Nipponbare reference genome (33) and encompassed 18,755 genes (tables S6 to S8). Notably, 16 genes that are known to have undergone selection were detected, such as *PROG1* for growth habit (34, 35) and *OsLGI* for inflorescence architecture (36, 37) (Fig. 5C, fig. S18, and table S7).

By comparing these datasets, we identified 490 pairs of orthologous genes that had an apparent history of convergent selection in maize and rice (Fig. 5D and table S7), which is significantly greater than expected by chance (permutation test, $P < 0.001$; Fig. 5E), indicating that we observed an excess of shared selected genes in maize and rice on the basis of comparative genomics results. However, because the time period during which traits of common interest to humans were selected is far less than the time necessary for the evolutionary divergence between maize and rice (12), it is not surprising that only a limited number of selected genes in maize (15.5%) and rice (2.6%) experienced convergent selection during evolution. Of the 490 orthologous gene pairs, 67.8% were localized to syntenic blocks between the maize and rice genomes (Fig. 5D and table S7). In addition to the three known orthologous gene pairs that have undergone convergent selection mentioned above, the functions of an additional 13 orthologous gene pairs have been experimentally verified. These include *KNI/OSHI*, regulators of shoot meristem development (38, 39), and *SBE1*, which controls starch biosynthesis (40, 41) (table S7). The prevalence of shared selected genes with conserved functions supports the idea that common phenotypic shifts during maize and rice evolution acting on conserved genes are driven at least in part by convergent selection, which in maize and rice likely occurred both during and after domestication. Further characterization of these orthologs could provide insight into the processes driving human selection on cereal traits and, in turn, enhance knowledge-driven crop breeding.

Interestingly, the convergently selected orthologous genes appear to be significantly enriched

in specific pathways in maize and rice (multiple-testing correction via the g:Profiler g:SCS algorithm, adjusted $P < 0.05$), including two commonly enriched pathways (starch and sucrose metabolism, biosynthesis of cofactors; Fig. 5F). Starch is the main component of cereal seeds and contributes substantially to grain yield, so it is reasonable that starch and sucrose metabolism is a primary pathway of convergent selection when human selection targeted high cereal productivity. Of 25 maize and 93 rice selected genes that are known contributors to the starch metabolic pathway (42, 43), we found that 11 orthologous gene pairs showed convergence at the genic level (Fig. 5G and table S9). The types and functions of starch synthesis-related enzymes are highly conserved, although their copy number and isoenzyme number differ between maize and rice (43). Hence, different functionally redundant paralogs could be differentially selected. For example, *UGP1* was selected in maize, whereas its homolog, *UGP2*, was selected in rice (Fig. 5G). In addition to whether a gene contributes to selected traits, whether a gene is selected is also affected by the levels of genetic diversity and the frequency of the pre-existing desirable alleles in the ancestral population (1, 10, 44). For example, *TPS4* was selected in maize but not in rice (Fig. 5G). The various levels of genetic diversity in wild ancestors (e.g., there is less nucleotide diversity in maize than in its *parviglumis* ancestor, but there is more in cultivated rice than in its *rufipogon* ancestor; fig. S19) indicate that it may be difficult to target *TPS4* for selection in rice. These findings suggest that some orthologous genes function in the same metabolic or regulatory pathway for the same selected traits but have distinct selection routes among crops. Indeed, the degree of genetic convergence via convergent selection is related to the conservation and complexity of the gene network for a given selection (11).

Discussion

Collectively, we found a set of 490 orthologous genes that underwent convergent selection during maize and rice evolution, including *KRN2/OsKRN2*, which affect grain number. Because grain number is a common domestication syndrome trait as well as a key grain yield component in cereal crops, exploring the role of *KRN2/OsKRN2* across the cereals could provide new opportunities for enhancing production of other global crops, such as wheat. These findings suggest that the identification of genes that have undergone convergent selection could further inform breeding efforts of cereals. A deep understanding of the conservation of selection-driven genetic elements will not only enable more rapid innovation of the maize and rice germplasm but also inform knowledge-driven de novo domestication of

new crops to meet the diverse needs of food production worldwide (45).

Methods summary

QTL mapping for KRN in the MT-6/B73 RIL population was performed using composite interval mapping (46). *qKRN2* was positionally cloned using a recombinant-derived progeny testing strategy (47). The functions of *KRN2*, *DUF1644*, and *OsKRN2* were investigated via mutant analysis, transgenic overexpression or CRISPR-Cas9 gene editing. The constructed overexpression and gene-editing vectors were transformed into maize inbred line LH244 or rice cultivar Nipponbare through an *Agrobacterium*-mediated transformation system. *KRN2*-based association mapping was performed using a mixed linear model (48) in a subset of 379 maize inbred lines (49). The yield tests of *KRN2/OsKRN2* gene-edited lines were carried out in a randomized block design with three replicates.

The expression levels of *KRN2* and *OsKRN2* in tested samples were detected via qPCR. The expression differences caused by the sequence polymorphisms in *KRN2* promoter or 5'UTR were tested by transient expression assays in maize protoplasts (50). The candidate interaction partners of *KRN2* were identified using a Y2H screen by Hybrigenics Services. The interaction between *KRN2/OsKRN2* and *DUF1644/OsDUF1644* was validated by Y2H assays and split firefly LUC complementation assays in tobacco (51). The fresh IM was imaged with a scanning electron microscope, and then the IM diameter was measured with an EZ4 HD stereo microscope and corresponding LAS EZ software.

To determine the molecular evolution of the *KRN2* or *OsKRN2* locus, we sequenced their target regions in a set of cultivar or landrace, and wild relatives in maize or rice. Nucleotide diversity (π) and Tajima's D were calculated using DnaSP software (52). Coalescent simulations were performed for *KRN2* using the MS program (53). A minimum spanning tree was constructed for *OsKRN2* using Arlequin software (54).

To explore the extent of molecular convergence on a genome-wide scale between maize and rice, we collected or generated two high-depth SNP datasets in 507 maize inbred lines and 70 *parviglumis* accessions, and 461 cultivated rice and 257 wild rice accessions. The genetic relationship of rice accessions was estimated using ADMIXTURE software (55) and confirmed by principal components analysis using GCTA software (56). The SNP alignment (57) and phylogenetic tree construction in maize and rice were performed using SNPhylo software (58). The genome-wide scans for selection signals were performed via an XP-CLR method (29) followed by cross-validation on the basis of permutation tests for the nucleotide diversity ratio between wild and cultivar

accessions (2, 57). The genes that are located within the selected regions were regarded as having undergone selection. The maize and rice orthologs were identified by reciprocal blastp with protein sequence coverage of ≥ 0.7 . Collinearity was analyzed using MCScanX software (59). A permutation test was performed for the enrichment of the orthologous genes under convergent selection (57). Finally, the g:Profiler program (60) was used for KEGG pathway enrichment analysis of genes under convergent selection.

All details of the materials and methods, including those summarized above, are provided in the supplementary materials.

REFERENCES AND NOTES

- J. F. Doebley, B. S. Gaut, B. D. Smith, The molecular genetics of crop domestication. *Cell* **127**, 1309–1321 (2006). doi: 10.1016/j.cell.2006.12.006; pmid: 17190597
- M. B. Hufford et al., Comparative population genomics of maize domestication and improvement. *Nat. Genet.* **44**, 808–811 (2012). doi: 10.1038/ng.2309; pmid: 22660546
- X. Huang et al., A map of rice genome variation reveals the origin of cultivated rice. *Nature* **490**, 497–501 (2012). doi: 10.1038/nature11532; pmid: 23034647
- A. Pankin, M. von Korff, Co-evolution of methods and thoughts in cereal domestication studies: A tale of barley (*Hordeum vulgare*). *Curr. Opin. Plant Biol.* **36**, 15–21 (2017). doi: 10.1016/j.cpb.2016.12.001; pmid: 28011443
- Y. Liang, H. J. Liu, J. Yan, F. Tian, Natural variation in crops: Realized understanding, continuing promise. *Annu. Rev. Plant Biol.* **72**, 357–385 (2021). doi: 10.1146/annurev-arplant-080720-090632; pmid: 33481630
- A. H. Paterson et al., Convergent domestication of cereal crops by independent mutations at corresponding genetic loci. *Science* **269**, 1714–1718 (1995). doi: 10.1126/science.269.5231.1714; pmid: 17821643
- Z. Lin et al., Parallel domestication of the *Shattering1* genes in cereals. *Nat. Genet.* **44**, 720–724 (2012). doi: 10.1038/ng.2281; pmid: 22581231
- M. Wang et al., Parallel selection on a dormancy gene during domestication of crops from multiple families. *Nat. Genet.* **50**, 1435–1441 (2018). doi: 10.1038/s41588-018-0229-2; pmid: 30250128
- H. Tang et al., Seed shattering in a wild sorghum is conferred by a locus unrelated to domestication. *Proc. Natl. Acad. Sci. U.S.A.* **110**, 15824–15829 (2013). doi: 10.1073/pnas.1305213110; pmid: 24019506
- B. S. Gaut, Evolution is an experiment: Assessing parallelism in crop domestication and experimental evolution. *Mol. Biol. Evol.* **32**, 1661–1671 (2015). doi: 10.1093/molbev/msv105; pmid: 26012904
- Q. Chen, W. Li, L. Tan, F. Tian, Harnessing knowledge from maize and rice domestication for new crop breeding. *Mol. Plant* **14**, 9–26 (2021). doi: 10.1016/j.molp.2020.12.006; pmid: 33316465
- B. S. Gaut, Evolutionary dynamics of grass genomes. *New Phytol.* **154**, 15–28 (2002). doi: 10.1046/j.1469-8137.2002.00352.x
- M. D. Gale, K. M. Devos, Comparative genetics in the grasses. *Proc. Natl. Acad. Sci. U.S.A.* **95**, 1971–1974 (1998). doi: 10.1073/pnas.95.5.1971; pmid: 9482816
- A. H. Paterson, J. E. Bowers, B. A. Chapman, Ancient polyploidization predating divergence of the cereals, and its consequences for comparative genomics. *Proc. Natl. Acad. Sci. U.S.A.* **101**, 9903–9908 (2004). doi: 10.1073/pnas.0307901101; pmid: 15161969
- M. R. Woodhouse, M. B. Hufford, Parallelism and convergence in post-domestication adaptation in cereal grasses. *Philos. Trans. R. Soc. London Ser. B* **374**, 20180245 (2019). doi: 10.1098/rstb.2018.0245; pmid: 31154975
- L. Cai, K. Li, X. Yang, J. Li, Identification of large-effect QTL for kernel row number has potential for maize yield improvement. *Mol. Breed.* **34**, 1087–1096 (2014). doi: 10.1007/s11032-014-0101-8
- C. U. Stirnimann, E. Petsalaki, R. B. Russell, C. W. Müller, WD40 proteins propel cellular networks. *Trends Biochem. Sci.* **35**, 565–574 (2010). doi: 10.1016/j.tibs.2010.04.003; pmid: 20451393
- B. P. Jain, S. Pandey, WD40 repeat proteins: Signalling scaffold with diverse functions. *Protein J.* **37**, 391–406 (2018). doi: 10.1007/s10930-018-9785-7; pmid: 30069656
- K. A. Lease et al., A mutant Arabidopsis heterotrimeric G-protein β subunit affects leaf, flower, and fruit development. *Plant Cell* **13**, 2631–2641 (2001). doi: 10.1105/tpc.010315; pmid: 11752377
- Y. Wu et al., Presence of tannins in sorghum grains is conditioned by different natural alleles of *Tannin1*. *Proc. Natl. Acad. Sci. U.S.A.* **109**, 10281–10286 (2012). doi: 10.1073/pnas.1201700109; pmid: 22699509
- Q. Wu et al., The maize heterotrimeric G protein β subunit controls shoot meristem development and immune responses. *Proc. Natl. Acad. Sci. U.S.A.* **117**, 1799–1805 (2020). doi: 10.1073/pnas.1917577116; pmid: 31852823
- M. J. Thomson et al., Mapping quantitative trait loci for yield, yield components and morphological traits in an advanced backcross population between *Oryza rufipogon* and the *Oryza sativa* cultivar Jefferson. *Theor. Appl. Genet.* **107**, 479–493 (2003). doi: 10.1007/s00122-003-1270-8; pmid: 12736777
- C. Li, A. Zhou, T. Sang, Genetic analysis of rice domestication syndrome with the wild annual species, *Oryza nivara*. *New Phytol.* **170**, 185–193 (2006). doi: 10.1111/j.1469-8137.2005.01647.x; pmid: 16539615
- P. Bommert, N. Satoh-Nagasawa, D. Jackson, H. Y. Hirano, Genetics and evolution of inflorescence and flower development in grasses. *Plant Cell Physiol.* **46**, 69–78 (2005). doi: 10.1093/pcp/pci504; pmid: 15659432
- X. Bai et al., Genome-wide association analysis reveals identical genetic control in panicle architecture between *indica* and *japonica* rice. *Plant Genome* **9**, (2016). doi: 10.3835/plantgenome2015.11.0115
- K. Hammer, Das Domestikationssyndrom. *Kulturpflanze* **32**, 11–34 (1984). doi: 10.1007/BF02098682
- D. Sosso et al., Seed filling in domesticated maize and rice depends on SWEET-mediated hexose transport. *Nat. Genet.* **47**, 1489–1493 (2015). doi: 10.1038/ng.3422; pmid: 26523777
- Y. Matsuoka et al., A single domestication for maize shown by multilocus microsatellite genotyping. *Proc. Natl. Acad. Sci. U.S.A.* **99**, 6080–6084 (2002). doi: 10.1073/pnas.052125199; pmid: 11983901
- H. Chen, N. Patterson, D. Reich, Population differentiation as a test for selective sweeps. *Genome Res.* **20**, 393–402 (2010). doi: 10.1101/gr.100545.109; pmid: 20086244
- Y. Jiao et al., Improved maize reference genome with single-molecule technologies. *Nature* **546**, 524–527 (2017). doi: 10.1038/nature22971; pmid: 28605751
- A. Studer, Q. Zhao, J. Ross-Ibarra, J. Doebley, Identification of a functional transposon insertion in the maize domestication gene *tbt1*. *Nat. Genet.* **43**, 1160–1163 (2011). doi: 10.1038/ng.942; pmid: 21946354
- H. Wang et al., The origin of the naked grains of maize. *Nature* **436**, 714–719 (2005). doi: 10.1038/nature03863; pmid: 16079849
- S. A. Goff et al., A draft sequence of the rice genome (*Oryza sativa* L. ssp. *japonica*). *Science* **296**, 92–100 (2002). doi: 10.1126/science.1068275; pmid: 11935018
- L. Tan et al., Control of a key transition from prostrate to erect growth in rice domestication. *Nat. Genet.* **40**, 1360–1364 (2008). doi: 10.1038/ng.197; pmid: 18820699
- J. Jin et al., Genetic control of rice plant architecture under domestication. *Nat. Genet.* **40**, 1365–1369 (2008). doi: 10.1038/ng.247; pmid: 18820696
- T. Ishii et al., *OslG1* regulates a closed panicle trait in domesticated rice. *Nat. Genet.* **45**, 462–465 (2013). doi: 10.1038/ng.2567; pmid: 23435087
- Z. Zhu et al., Genetic control of inflorescence architecture during rice domestication. *Nat. Commun.* **4**, 2200 (2013). doi: 10.1038/ncomms3200; pmid: 23884108
- R. A. Kerstetter, D. Laudencia-Chinguanco, L. G. Smith, S. Hake, Loss-of-function mutations in the maize homeobox gene, *knot1d1*, are defective in shoot meristem maintenance. *Development* **124**, 3045–3054 (1997). doi: 10.1242/dev.124.16.3045; pmid: 9272946
- K. Tsuda, Y. Ito, Y. Sato, N. Kurata, Positive autoregulation of a *KNOX* gene is essential for shoot apical meristem maintenance in rice. *Plant Cell* **23**, 4368–4381 (2011). doi: 10.1105/tpc.111.090050; pmid: 22207572
- S. L. Blauth et al., Identification of *Mutator* insertional mutants of starch-branching enzyme 1 (*sbe1*) in *Zea mays* L. *Plant Mol. Biol.* **48**, 287–297 (2002). doi: 10.1023/A:1013335217744; pmid: 11855730
- H. Satoh et al., Starch-branching enzyme I-deficient mutation specifically affects the structure and properties of starch in rice endosperm. *Plant Physiol.* **133**, 1111–1121 (2003). doi: 10.1104/pp.103.021527; pmid: 14526120
- F. Fichtner, J. E. Lunn, The role of trehalose 6-phosphate (Tre6P) in plant metabolism and development. *Annu. Rev. Plant Biol.* **72**, 737–760 (2021). doi: 10.1146/annurev-arplant-050718-095929; pmid: 33428475
- L. Huang, H. Tan, C. Zhang, Q. Li, Q. Liu, Starch biosynthesis in cereal endosperms: An updated review over the last decade. *Plant Commun.* **2**, 100237 (2021). doi: 10.1016/j.xplc.2021.100237; pmid: 34746765
- L. Wang et al., Molecular parallelism underlies convergent highland adaptation of maize landraces. *Mol. Biol. Evol.* **38**, 3567–3580 (2021). doi: 10.1093/molbev/msab119; pmid: 33905497
- A. R. Fernie, J. Yan, *De novo* domestication: An alternative route toward new crops for the future. *Mol. Plant* **12**, 615–631 (2019). doi: 10.1016/j.molp.2019.03.016; pmid: 30999078
- Z. B. Zeng, Precision mapping of quantitative trait loci. *Genetics* **136**, 1457–1468 (1994). doi: 10.1093/genetics/136.4.1457; pmid: 8013918
- J. Tian et al., Teosinte ligule allele narrows plant architecture and enhances high-density maize yields. *Science* **365**, 658–664 (2019). doi: 10.1126/science.aax5482; pmid: 31416957
- J. Yu et al., A unified mixed-model method for association mapping that accounts for multiple levels of relatedness. *Nat. Genet.* **38**, 203–208 (2006). doi: 10.1038/ng1702; pmid: 16380716
- X. Yang et al., Characterization of a global germplasm collection and its potential utilization for analysis of complex quantitative traits in maize. *Mol. Breed.* **28**, 511–526 (2011). doi: 10.1007/s11032-010-9500-7
- C. Huang et al., *ZmCCT9* enhances maize adaptation to higher latitudes. *Proc. Natl. Acad. Sci. U.S.A.* **115**, E334–E341 (2018). doi: 10.1073/pnas.1718058115; pmid: 29279404
- Z. Zhang, J. Yang, Y. Wu, Transcriptional regulation of zein gene expression in maize through the additive and synergistic action of opaque2, prolamine-box binding factor, and O2 heterodimerizing proteins. *Plant Cell* **27**, 1162–1172 (2015). doi: 10.1105/tpc.15.00035; pmid: 25901087
- P. Librado, J. Rozas, DnaSP v5: A software for comprehensive analysis of DNA polymorphism data. *Bioinformatics* **25**, 1451–1452 (2009). doi: 10.1093/bioinformatics/btp187; pmid: 19346325
- R. R. Hudson, Generating samples under a Wright-Fisher neutral model of genetic variation. *Bioinformatics* **18**, 337–338 (2002). doi: 10.1093/bioinformatics/18.2.337; pmid: 11847089
- L. Excoffier, H. E. Lischer, Arlequin suite ver 3.5: A new series of programs to perform population genetics analyses under Linux and Windows. *Mol. Ecol. Resour.* **10**, 564–567 (2010). doi: 10.1111/j.1755-0998.2010.02847.x; pmid: 21565059
- D. H. Alexander, J. Novembre, K. Lange, Fast model-based estimation of ancestry in unrelated individuals. *Genome Res.* **19**, 1655–1664 (2009). doi: 10.1101/gr.094052.109; pmid: 19648217
- J. Yang, S. H. Lee, M. E. Goddard, P. M. Visscher, GCTA: A tool for genome-wide complex trait analysis. *Am. J. Hum. Genet.* **88**, 76–82 (2011). doi: 10.1016/j.ajhg.2010.11.011; pmid: 21167468
- W. Chen et al., Code and processed data for “Convergent selection of a WD40 protein that enhances grain yield in maize and rice.” Figshare (2022). doi: 10.6084/m9.figshare.18104336
- T. H. Lee, H. Guo, X. Wang, C. Kim, A. H. Paterson, SNPPhylo: A pipeline to construct a phylogenetic tree from huge SNP data. *BMC Genomics* **15**, 162 (2014). doi: 10.1186/1471-2164-15-162; pmid: 24571581
- Y. Wang et al., MCScanX: A toolkit for detection and evolutionary analysis of gene synteny and collinearity. *Nucleic Acids Res.* **40**, e94 (2012). doi: 10.1093/nar/gkr1293; pmid: 22217600

60. U. Raudvere *et al.*, g:Profiler: a web server for functional enrichment analysis and conversions of gene lists (2019 update). *Nucleic Acids Res.* **47**, W191–W198 (2019). doi: [10.1093/nar/gkz369](https://doi.org/10.1093/nar/gkz369); pmid: [31066453](https://pubmed.ncbi.nlm.nih.gov/31066453/)

ACKNOWLEDGMENTS

We thank L. Tan and H. Chen for help growing rice, G. Wang for sharing the wild rice leaves, and J. Ross-Ibarra for constructive suggestions on manuscript revision. **Funding:** Supported by the National Natural Science Foundation of China (91935302, 31421005, 31961133002, and 91435205), the National Key Research and Development Program of China (2020YFE0202300), Beijing Outstanding Young Scientist Program (BJJWZYJH01201910019026), Young Elite Scientists Sponsorship Program by CAST (2019QNR001), and NSF (IOS-2129189). **Author contributions:** X.Y., J.Y., and J.L.

conceived and designed this study. W.C., X.Z., J.G., S.J., X-Y.Z., L-C.C., J.X., L.Z., Y.H., Y.X., G.X., Y.W., S-H.W., S.W., J.C., and S.C. performed experiments. L.C., X.Z., W.C., N.Y., M.W., and P.Y. analyzed data. F.Y., D.J., C.S., F.Q., F.T., and A.R.F. contributed valuable suggestions on this study. W.C., L.C., X.Z., N.Y., J.Y., and X.Y. wrote the manuscript. All the authors edited and proofed the manuscript. **Competing interests:** D.J. serves as a consultant for Inari Agriculture, and the authors declare no competing interests. A patent with application no. PCT/CN2018/117844 is pending. **Data and materials availability:** All data are available in the main text, supplementary materials, public databases, or referenced permanent online repositories. Sequence data were deposited in NCBI GenBank under accession number MW238854-MW239029 for *KRN2*, MW219821-MW219975 and OK655843-OK655881 for *OsKRN2*, PRJNA771523 for all CRISPR knockouts in maize and rice, and PRJNA771230 for our resequenced rice data.

The alignments used for phylogenetic tree and all codes are provided online at Figshare ([57](#)).

SUPPLEMENTARY MATERIALS

science.org/doi/10.1126/science.abg7985

Materials and Methods

Figs. S1 to S19

Tables S1 to S12

References ([61–86](#))

MDAR Reproducibility Checklist

1 February 2021; resubmitted 27 November 2021

Accepted 24 February 2022

[10.1126/science.abg7985](https://doi.org/10.1126/science.abg7985)

Pushing the Boundaries of Knowledge

As AAAS's first multidisciplinary, open access journal, *Science Advances* publishes research that reflects the selectivity of high impact, innovative research you expect from the *Science* family of journals, published in an open access format to serve a vast and growing global audience. Check out the latest findings or learn how to submit your research: [ScienceAdvances.org](https://www.scienceadvances.org)

Science
Advances
AAAS

GOLD OPEN ACCESS, DIGITAL, AND FREE TO ALL READERS

RESEARCH ARTICLES

VIROLOGY

Architecture and antigenicity of the Nipah virus attachment glycoprotein

Zhaoqian Wang¹, Moushimi Amaya^{2,3}, Amin Addetia¹, Ha V. Dang¹, Gabriella Reggiano¹, Lianying Yan^{2,3}, Andrew C. Hickey^{2,4}, Frank DiMaio¹, Christopher C. Broder², David Velesler^{1,5*}

Nipah virus (NiV) and Hendra virus (HeV) are zoonotic henipaviruses (HNVs) responsible for outbreaks of encephalitis and respiratory illness. The entry of HNVs into host cells requires the attachment (G) and fusion (F) glycoproteins, which are the main targets of antibody responses. To understand viral infection and host immunity, we determined a cryo-electron microscopy structure of the NiV G homotetrameric ectodomain in complex with the nAHL3 broadly neutralizing antibody Fab fragment. We show that a cocktail of two nonoverlapping G-specific antibodies neutralizes NiV and HeV synergistically and limits the emergence of escape mutants. Analysis of polyclonal serum antibody responses elicited by vaccination of macaques with NiV G indicates that the receptor binding head domain is immunodominant. These results pave the way for implementing multipronged therapeutic strategies against these deadly pathogens.

Nipah virus (NiV) and Hendra virus (HeV) are bat-borne zoonotic pathogens of the *Henipavirus* (HNV) genus causing encephalitis and respiratory symptoms in humans, with fatality rates between 50 and 100% (1). Over the past two decades, NiV has spilled over into humans almost annually in Bangladesh (Bangladesh strain, NiV-B) (2) and has also caused outbreaks in India (NiV-B) and the Philippines (Malaysia strain, NiV-M) (3–5). The detection of cross-reactive HNV antibodies (Abs) in humans and *Pteropus* bats in Africa underscored that 2 billion people worldwide live in regions threatened by HNV spillovers (6). Moreover, the recent discovery of a previously unknown HeV genotype (7, 8) is an urgent reminder of the HNV zoonotic threat. To date, no approved vaccines or therapeutics for use in people exist against HNV infections (9).

HNV entry into host cells requires fusion of the viral membrane and the host plasma membrane through the concerted action of an attachment (G) glycoprotein and a fusion (F) glycoprotein. The NiV and HeV entry receptors at the surface of host cells are the transmembrane protein tyrosine kinases ephrin-B2 or ephrin-B3 (10–13). G and F have been proposed to undergo a cascade of conformational changes to promote membrane fusion upon receptor engagement (14, 15). HNV G and F are

the targets of the humoral immune response (16–19), and serum neutralizing Abs are a correlate of protection in animals experimentally infected with NiV or HeV (20–23). The cross-reactive NiV and HeV G-specific m102.4 monoclonal antibody (mAb) has been administered on an emergency compassionate use basis to 15 individuals with high-risk exposure to HeV or NiV infection and recently completed a phase 1 clinical trial in Australia (24).

A soluble HeV G tetrameric ectodomain immunogen (HeV sG) elicits high titers of cross-reactive neutralizing Abs and protects against both NiV and HeV challenge in pre-clinical studies (20, 25–30). A vaccine using HeV sG is commercially available for use in horses in Australia (Equivac HeV, Zoetis Inc.), and a formulation suitable for human use has recently entered phase 1 clinical trials (NCT04199169). Although crystal structures of the isolated NiV and HeV G head domains were previously determined (10, 13), no structural information is available for any HNV G tetramer, hindering both our understanding of immunity directed toward G and the rational design of improved vaccine candidates.

Results

Architecture of the NiV G tetramer

To unveil the three-dimensional (3D) organization of the HNV G protein and provide a blueprint for vaccine design, we determined a cryo-electron microscopy (cryo-EM) structure of the NiV G ectodomain homotetramer bound to the mouse nAHL3 neutralizing antibody Fab fragment (31) at 3.5-Å overall resolution (fig. S1). We used local refinement to account for the flexibility of the viral membrane proximal region relative to the distal region, yielding reconstructions at 3.5-Å and

3.2-Å resolution, respectively, allowing us to build a (composite) model of the NiV G ectodomain tetramer (Fig. 1, A to C; fig. S1; and table S1). The final model comprises nearly the entire NiV sG ectodomain from residues 96 to 602 along with the nAHL3 Fab variable domains. NiV G forms a 200-Å-long and 120-Å-wide intertwined homotetramer. At the core is an N-terminal four-helix bundle (the stalk) followed by an interlaced β sandwich (the neck) that connects to a C-terminal β propeller head domain on each protomer (Fig. 1, A to C). The NiV G tetramer is stabilized by interprotomer disulfide bonds formed in the neck and stalk (Fig. 1D).

NiV G residues 96 to 147 form a pseudo-two-fold symmetric helical bundle, which is presumably extended at its N-terminal end toward the viral membrane in which the tetramer is anchored (residues 70 to 95 are weakly resolved in the cryo-EM map and were not modeled) (Fig. 1, A to C). The interlaced β sandwich neck domain is formed by apposition of two four-stranded mixed β sheets, packed against each other through hydrophobic contacts, comprising residues 153 to 163 from each of the four protomers (Fig. 1D). The neck is covalently cross-linked through formation of two antiparallel interprotomer disulfide bonds between residues C158 and C162 of chains A and D and two antiparallel disulfide bonds between residues C158 and C162 of chains B and C. The neck is decorated with four N-linked glycans protruding from residue N159 on each protomer, partially shielding this domain on both sides of the β sandwich (Fig. 1D). Each of the four C-terminal head domains form a six-bladed β propeller decorated with five N-linked oligosaccharides at positions N306, N378, N417, N481, and N529, which are all resolved in the cryo-EM map (Fig. 1, A to C). Two head domains are connected to the neck through flexible linkers folding back toward the viral membrane, with the β propellers docked on either side of the stalk (Fig. 1, B and C). The other two head domains form a head-to-tail dimer positioned distal to the viral membrane and are connected to the neck through linkers that adopt distinct folds (Fig. 1, B and C). As a result, the NiV G tetramer is assembled from four identical polypeptides adopting three distinct folding patterns (Fig. 1E). Interactions between the two distal head domains maintain their approximately antiparallel orientation, whereas contacts between each proximal head and the NiV G stalk lead to their pseudo-two-fold symmetrical arrangement. Only one of the four head domains orients its receptor binding site toward the host cell surface, whereas the other three sites point toward the viral membrane (Fig. 1F), suggesting that conformational dynamics would allow reorienting the head domains for receptor engagement. Although the

¹Department of Biochemistry, University of Washington, Seattle, WA 98195, USA. ²Department of Microbiology and Immunology, Uniformed Services University, Bethesda, MD 20814, USA. ³Henry M. Jackson Foundation for the Advancement of Military Medicine, Bethesda, MD 20814, USA. ⁴U.S. Public Health Services Commissioned Corps, Rockville, MD 20852, USA. ⁵Howard Hughes Medical Institute, University of Washington, Seattle, WA 98195, USA. *Corresponding author. Email: dvelesler@uw.edu

cryo-EM map does not resolve the topology of the two stalk C146 disulfide bonds unambiguously, previous biochemical data suggest that they form across pairs of protomers that are not covalently cross-linked in the neck (25, 32). The overall NiV G architecture described here adopts a distinctive two-heads-up and two-heads-down conformation that is different from structures of any other paramyxovirus attachment glycoproteins. In comparison, Newcastle disease virus hemagglutinin-neuraminidase (HN) ectodomain adopts a four-heads-down conformation, whereas parainfluenza virus 5 HN exhibits a distinct two-heads-up and two-heads-down conformation with the receptor binding sites oriented differently than for NiV G (33, 34) (fig. S2).

nAH1.3-mediated broad neutralization of NiV and HeV

The nAH1.3 mAb was previously shown to potently neutralize NiV-M, NiV-B, and HeV in vitro (31). Using a green fluorescent protein (GFP)-encoding, replication-competent Cedar (henipa)virus (rCedV) chimeras in which the native glycoproteins are substituted with the NiV-B (rCedV-NiV-B-GFP) or the HeV (rCedV-HeV-GFP) F and G glycoproteins (35), we determined nAH1.3 half-maximum inhibitory concentrations (IC_{50}) of 33 and 32 ng/ml, respectively (fig. S3A). This neutralization potency is comparable to the human mAb m102.4, for which we determined IC_{50} values of 17 and 58 ng/ml against rCedV-NiV-B-GFP and rCedV-HeV-GFP, respectively (fig. S3B). Our cryo-EM structure reveals that one nAH1.3 Fab fragment is bound to each NiV G head domain (Figs. 1, B and C, and 2A). nAH1.3 heavy and light chains interact with an antigenic site located on the side of the β propeller that is opposite to the ephrin-B2 or ephrin-B3 binding site (Fig. 2A). As a result, nAH1.3 does not compete with receptor binding to the NiV G ectodomain (Fig. 2B), unlike m102.4, which forms interactions mimicking receptor interactions (18). nAH1.3 buries $\sim 1000 \text{ \AA}^2$ of its paratope upon binding through shape complementarity and hydrogen bonding involving complementarity-determining regions (CDRs) H1, H3, L1, and L2, explaining its high-affinity binding to NiV G (Fig. 2, C and D, and fig. S3C). nAH1.3 is conformation dependent and recognizes a discontinuous epitope, spanning residues 172, 182 to 191, 358, 448 to 451, 468 to 478, 515 to 518, and 570 and 571, which is in close proximity to the oligosaccharide at position N481 (Figs. 1A and 2A). Twenty-one out of 26 epitope residues are strictly conserved across NiV G and HeV G, and three residues are conservatively substituted from NiV G to HeV G [Asn¹⁸⁷→Gln (N187Q), N478Q, and I517L]. Only two residues are nonconservatively substituted (L470D and K571V), and these map to the periphery of the epitope (Fig. 2E). Our

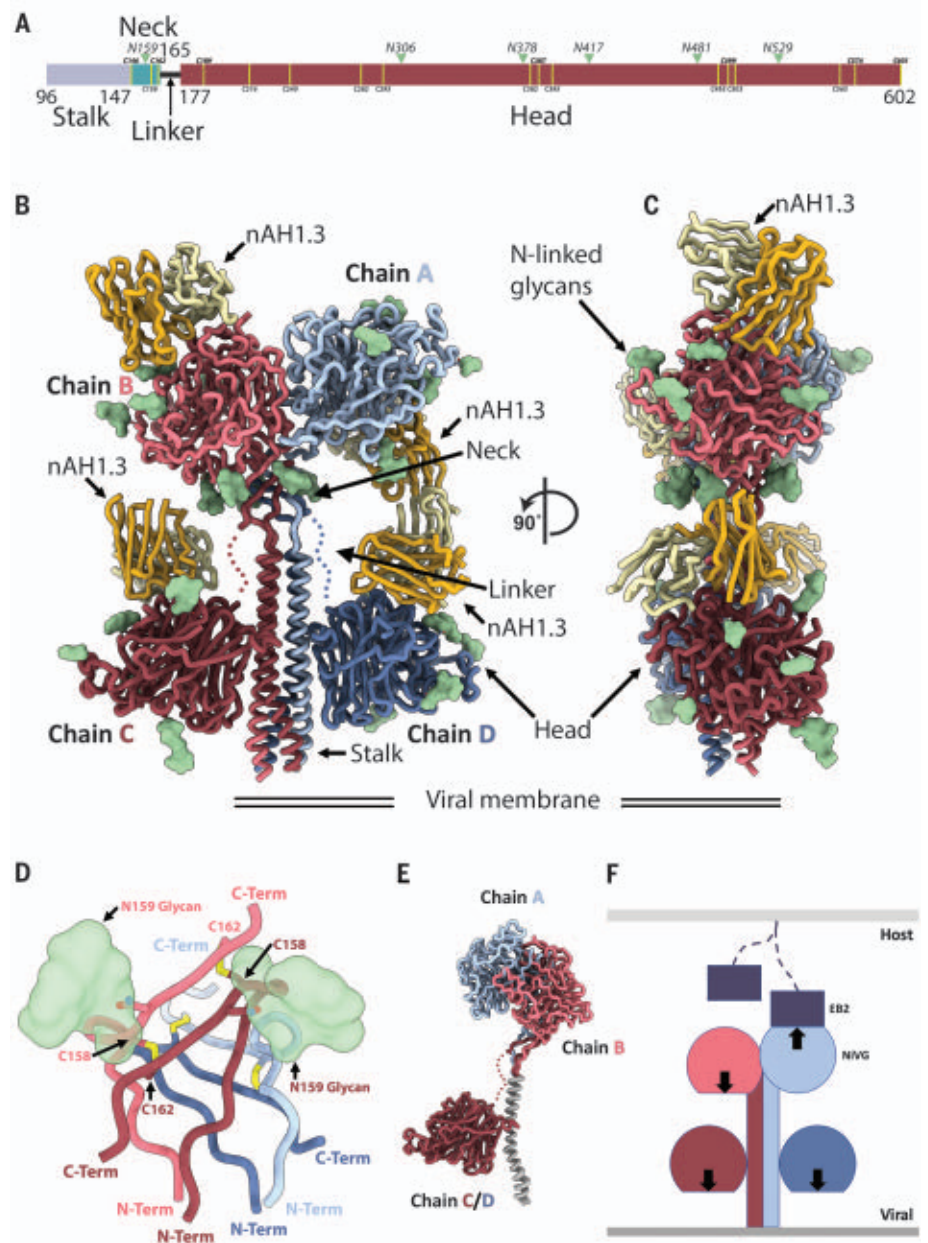


Fig. 1. Architecture of the NiV G homotetramer. (A) Linear representation of the NiV G ectodomain (as resolved in the cryo-EM map), which contains an N-terminal stalk (residues 96 to 147), a neck domain (residues 148 to 165), a linker region (residues 166 to 177), and a C-terminal head domain (residues 178 to 602). Green arrowheads indicate N-linked glycosylation sites. Yellow lines refer to cysteine residues. (B and C) Ribbon diagram of the NiV G ectodomain bound to the broadly neutralizing nAH1.3 Fab fragment in two orthogonal orientations. Each of the four NiV G protomers is shown in a different color, and resolved N-linked glycans are rendered as green surfaces. The nAH1.3 heavy and light chains are colored gold and yellow, respectively, and only the variable domains were modeled in density. The linkers connecting the neck to the two proximal head domains are shown as dotted lines owing to weaker density in the cryo-EM reconstruction. (D) Zoomed-in view of the interlaced β sandwich neck domain showing the four antiparallel interprotomer disulfide bonds between residues C158 and C162 and the glycan at position N159 protruding from the two chains shown in the foreground. (E) Superimposition of NiV G protomers along the stalk region, highlighting that the same polypeptide chain adopts three distinct folds in the homotetrameric assembly. (F) Schematic representation of the NiV G homotetramer showing that only one out of four head domains orients its receptor binding site (arrow) toward the host cell membrane (light gray), whereas the other three sites point toward the viral membrane (dark gray). EB2, ephrin-B2.

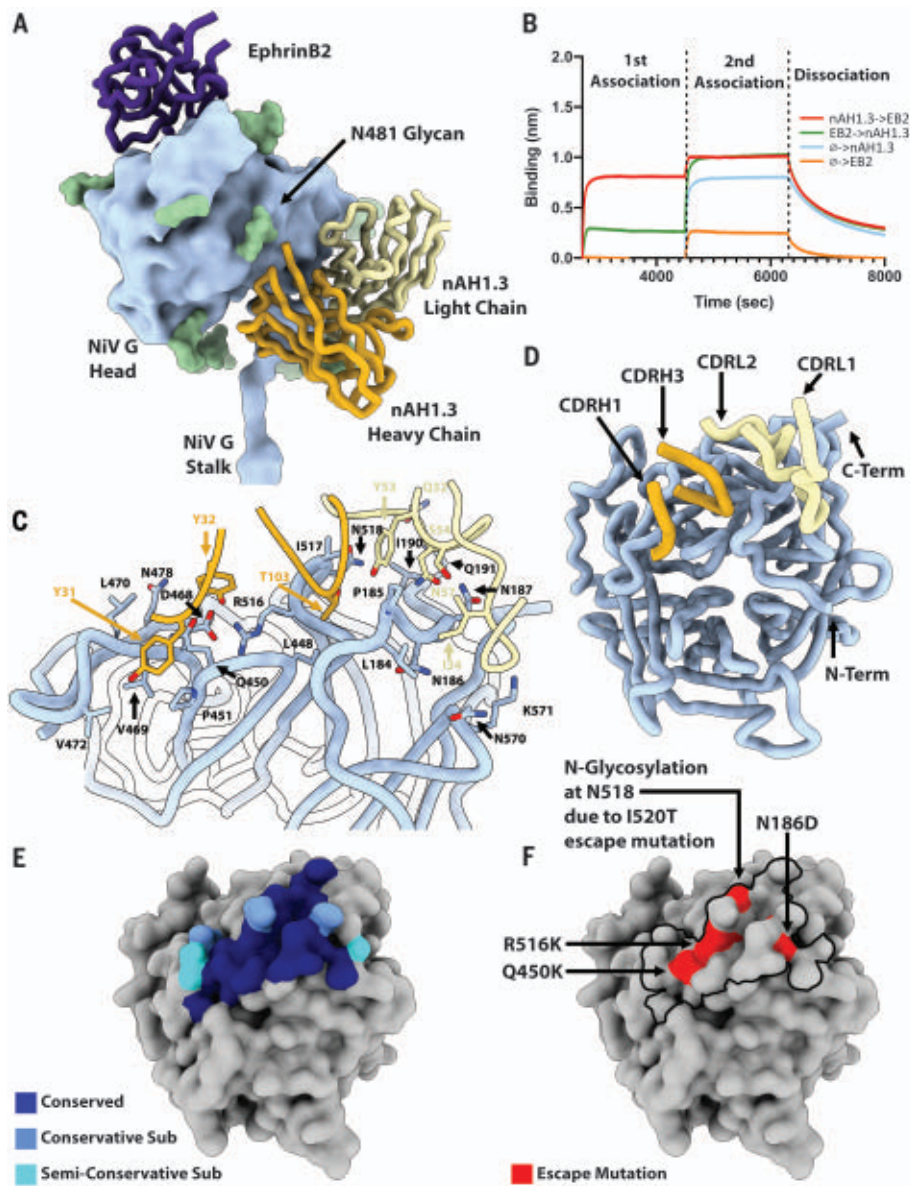


Fig. 2. Structural basis for nAH1.3-mediated broad neutralization of NiV and HeV. (A) Superimposition of the NiV G head domain (blue surface) bound to nAH1.3 (heavy and light chains, colored gold and yellow, respectively) or to ephrin-B2 [purple; Protein Data Bank (PDB) ID 2VSM] showing that they bind to opposite sides of the β propeller (13). (B) Biolayer interferometry analysis of binding of the nAH1.3 Fab and EB2 to immobilized NiV G ectodomain showing absence of competition irrespective of their order of addition. Each NiV G loaded anti-penta-His biosensor probe was sequentially dipped in a solution containing 25 nM nAH1.3 Fab (red) and then 50 nM EB2 plus 25 nM nAH1.3 Fab (red) or 50 nM EB2 and then 25 nM of nAH1.3 Fab plus 50 nM EB2 (green). Controls with only nAH1.3 Fab (blue) or EB2 (orange) are shown for comparison. (C) Zoomed-in view of the interface between NiV G and nAH1.3 with selected side chains shown as sticks. Single-letter abbreviations for the amino acid residues are as follows: A, Ala; C, Cys; D, Asp; E, Glu; F, Phe; G, Gly; H, His; I, Ile; K, Lys; L, Leu; M, Met; N, Asn; P, Pro; Q, Gln; R, Arg; S, Ser; T, Thr; V, Val; W, Trp; and Y, Tyr. (D) Ribbon diagram of a NiV G head domain (blue) with the interacting nAH1.3 heavy and light chains CDRs (CDRH and CDRL) rendered in gold and yellow, respectively. (E) Molecular surface representation of the NiV G head showing the nAH1.3 footprint colored by residue conservation between NiV G and HeV G. Conservative sub, conservative substitution; semi-conservative sub, semi-conservative substitution. (F) Molecular surface representation of the NiV G head showing the nAH1.3 escape mutations identified here (I520T introducing an N-linked glycosylation site at position N518; N186D comes from HeV G escape mutant) and Q450K and R516K [previously described (31)].

structural data suggest that none of the five substitutions would affect nAH1.3 recognition, as confirmed by the similar neutralization potencies determined against rCedV-NiV-B-GFP and rCedV-HeV-GFP (fig. S3A). However, no cross-reactivity was detected with more-divergent HNv sG ectodomain tetramers from CedV, Ghana virus (GhV), and Mojiang virus (MojV) (fig. S3, D and E). Given that mAb nAH1.3 does not appear to affect the overall NiV G conformation (36) or bind to the ephrin virus entry receptor binding site, we propose that the mAb inhibits HNv entry into cells by interfering with its F fusion triggering mechanism, as supported by membrane fusion assays (37).

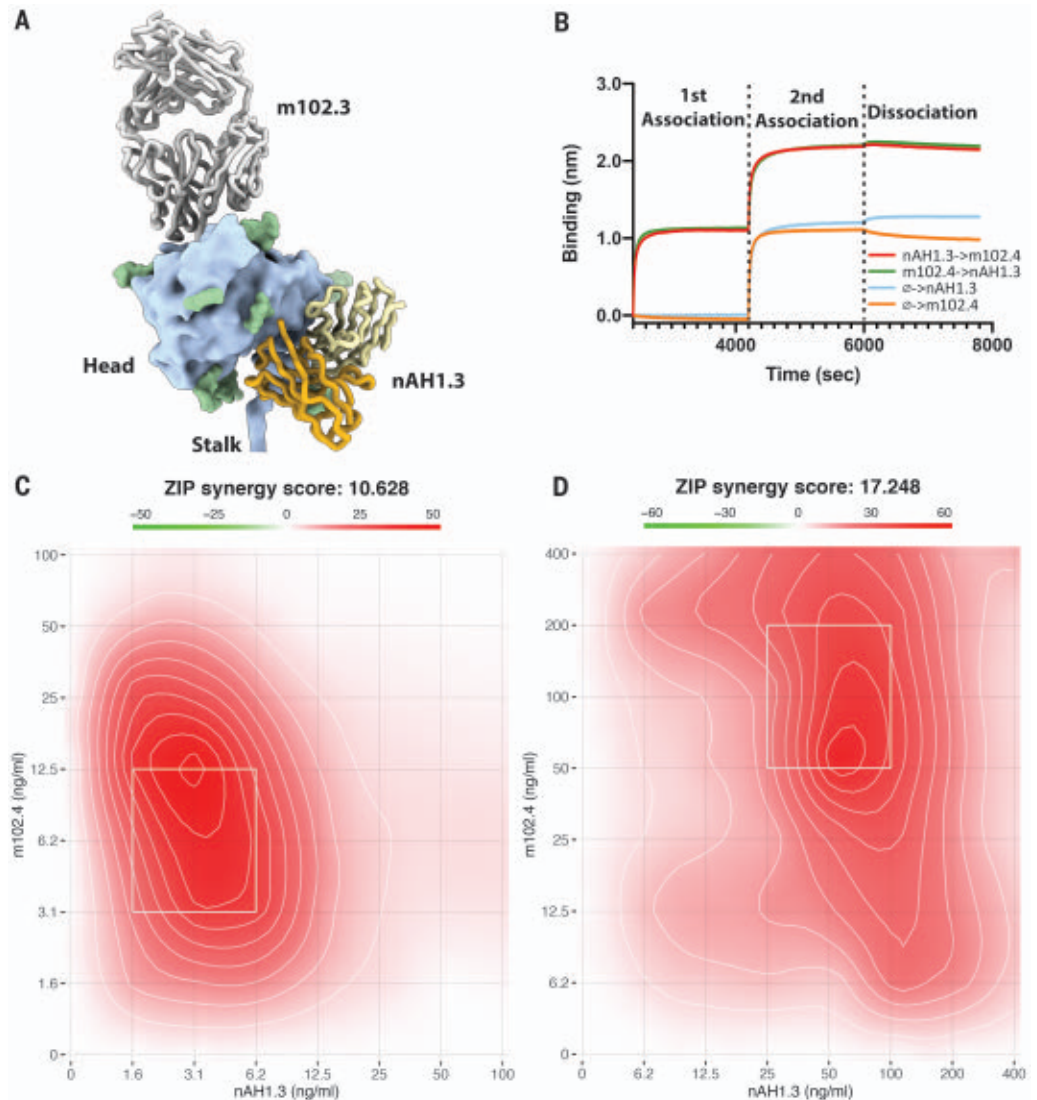
To validate our structural data, we passaged chimeric rCedV-NiV-B-GFP and rCedV-HeV-GFP in the presence of a subneutralizing concentration of nAH1.3. Deep sequencing revealed the selection of a clone harboring the I520T mutation (T1559C nucleotide substitution) introducing an N-linked glycosylation site at position N518 of NiV G. This is within the epitope recognized by nAH1.3 and likely abrogates mAb binding and neutralization via steric hindrance (Fig. 2F and fig. S4A). For HeV G, we identified an escape mutant harboring the T117A and N186D mutations. The latter substitution resides within the epitope and likely disrupts interactions with the nAH1.3 light chain (Fig. 2, D and F, fig. S4B). Previously identified Q450K and R516K nAH1.3 escape mutations (31) further validate our structure, as both residues form extensive interactions with the Fab heavy chain (Fig. 2F). Moreover, passaging of rCedV-HeV-GFP in the presence of m102.4 led to the emergence of a single amino acid mutation in HeV G (D582N) (fig. S4C), which is identical to the one previously identified using authentic HeV and NiV (31), validating the use of the chimeras as a surrogate system for pathogenic HNvs.

Synergistic neutralization of NiV and HeV by a mAb cocktail

mAb cocktails have successfully been used to prevent or treat infections with RNA viruses (38). For instance, although the individual Regeneron 10933 (casirivimab) and 10987 (imdevimab) mAbs against severe acute respiratory syndrome coronavirus 2 (SARS-CoV-2) are affected by a range of residue substitutions detected in clinical isolates, their combined cocktail proved more resilient to escape mutations (39, 40). Because experimental passaging of NiV and HeV with low concentrations of neutralizing mAbs can favor the emergence of neutralization escape mutants, we tested a cocktail of m102.4 and nAH1.3, which recognize epitopes located on opposite sides of the β propeller (Fig. 3A). Analysis of the negatively stained complex between NiV G and the nAH1.3 and m102.4 Fabs by single particle

Fig. 3. A HNv G head-directed mAb cocktail with synergistic neutralizing activity.

(A) Superimposition of the NiV G head domain (blue surface) bound to nAH1.3 (heavy and light chains colored gold and yellow, respectively) or to the m102.3 Fab (heavy and light chains colored dark and light gray, respectively; PDB ID 6CMI) showing that they bind to opposite sides of the β propeller. m102.3 is closely related to the m102.4 mAb. **(B)** Biolayer interferometry analysis of binding of the nAH1.3 and m102.4 IgGs to the immobilized NiV G ectodomain showing absence of competition irrespective of the order of addition. Each NiV G loaded anti-penta-His biosensor probe was sequentially dipped in a solution containing 100 nM nAH1.3 IgG (red) and then 100 nM m102.4 IgG plus 100 nM nAH1.3 IgG (red) or 100 nM m102.4 IgG and then 100 nM of nAH1.3 IgG plus 100 nM m102.4 IgG (green). Controls with only nAH1.3 IgG (blue) or m102.4 IgG (orange) are shown for comparison. **(C and D)** Synergy maps for neutralization of replication-competent rCedV-NiV-B-GFP (C) and rCedV-HeV-GFP (D) by varying concentrations of the m102.4 and nAH1.3 mAb cocktail analyzed with SynergyFinder (59). ZIP synergy score of >10 indicates a strong synergistic relationship. The white box indicates the most synergistic region on each plot.



analysis confirmed formation of a ternary complex (fig. S5, A to C), allowing the determination of a 3D reconstruction with three nAH1.3 and three m102.4 Fabs bound to a NiV G tetramer (fig. S5C). We subsequently used biolayer interferometry to confirm that both mAbs can recognize the NiV G ectodomain immobilized at the surface of biosensors irrespective of their order of addition (Fig. 3B). We then carried out virus neutralization assays using rCedV-NiV-B-GFP or rCedV-HeV-GFP to examine whether these mAbs had synergistic virus-neutralizing activity (35). Using a concentration matrix of each mAb, we found that combining m102.4 and nAH1.3 led to synergistic neutralization of the two rCedV chimeras (Fig. 3, C and D, and fig. S6, A and B). Passaging chimeric rCedV-HeV-GFP in the presence of the cocktail of nAH1.3 and m102.4 led to the emergence of the T117A, N186D, and T507I triple mutant, with T507I mapping to the m102.4 epitope and N186D to the nAH1.3 epitope, as described

above (Fig. 2, D and F, and fig. S4D). These findings support the potential use of a cocktail of these two noncompeting G glycoprotein-directed neutralizing mAbs as a therapeutic against these two deadly HNvs owing to their synergy and the higher barrier for resistance due to the requirement for multiple mutations to escape neutralization.

The NiV G head domain is the main target of vaccine-elicited serum neutralizing activity

We next investigated the nature and fine specificity of polyclonal Ab responses against the NiV G and HeV G glycoproteins using sera from two rhesus macaques that were immunized three times (4 weeks apart) with 200 μ g of an alum-adjuvanted equimolar mixture of the purified NiV-B and NiV-M sG tetramers (Fig. 4A). The two immunizations elicited potent serum neutralizing activity at day 84, with geometric mean neutralization titers of 1/8434 and 1/992 against rCedV-NiV-B-GFP and rCedV-

HeV-GFP, respectively (Fig. 4B). Using a competition enzyme-linked immunosorbent assay (ELISA) with the nAH1.3 (37), m102.4 (41), and HENV-32 (42) mAbs, we showed that vaccine-elicited Abs target at least three distinct antigenic sites at the surface of the NiV G head domain with comparable magnitudes, illustrating the diversity of polyclonal Ab responses elicited by vaccination (Fig. 4, C to E). To directly visualize the epitopes recognized by serum Abs, we used single particle electron microscopy analysis of negatively stained complexes formed between NiV G and purified polyclonal Fab fragments [obtained from immunoglobulin G (IgG) cleavage] after size-exclusion chromatography (43–45). 3D classification of the data led to the identification of at least three distinct classes of head-binding Abs and one class of stalk-specific Ab (Fig. 4, F to J, and fig. S5, D to F). Overall, Ab responses are almost exclusively directed to the NiV G head domain, despite using the full ectodomain

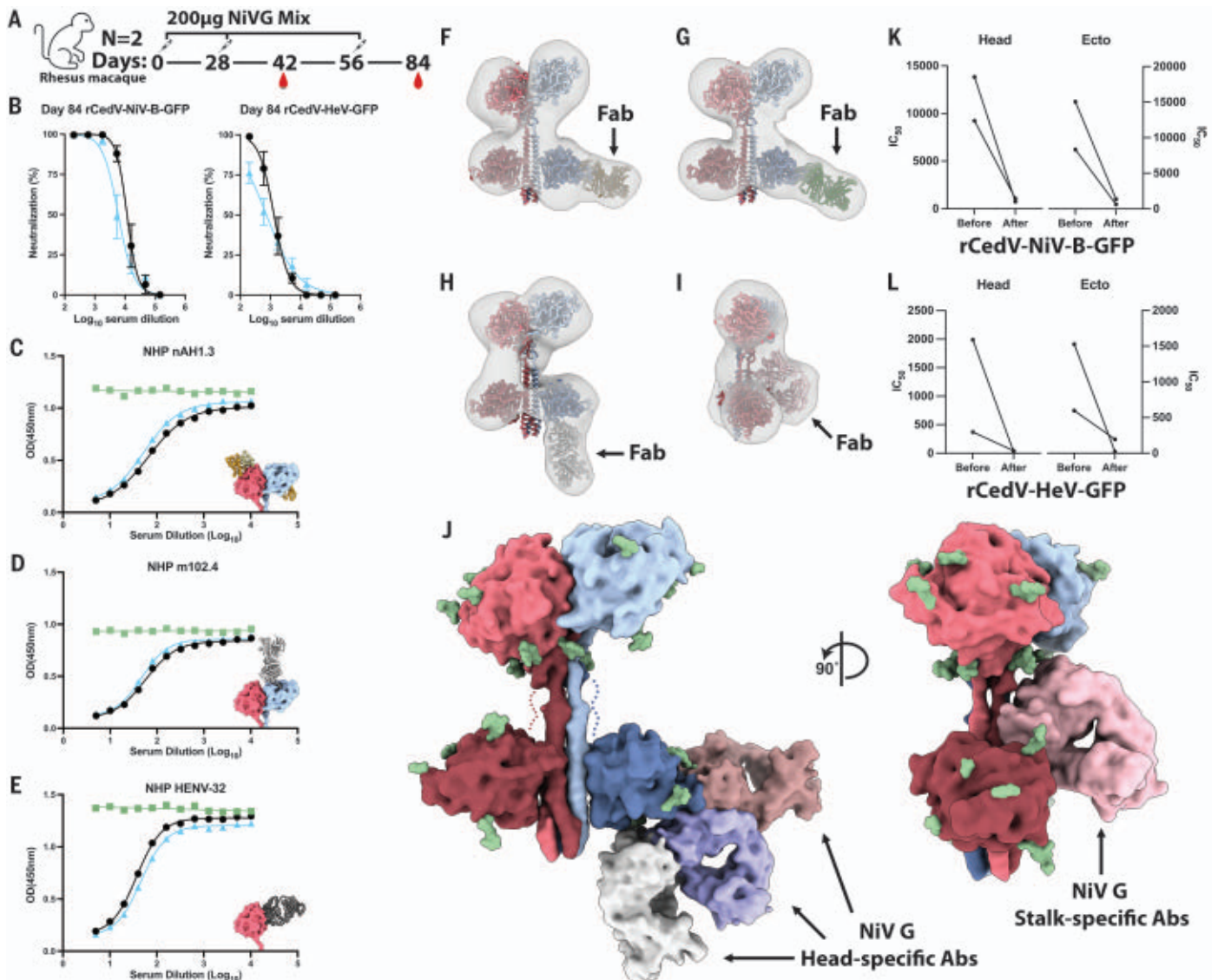


Fig. 4. The NiV G receptor binding head domain is immunodominant and accounts for most of the neutralizing activity elicited by vaccination.

(A) Study design for vaccination of rhesus macaques, where two rhesus macaques have been immunized three times (4 weeks apart) with 200 µg of an alum-adsorbed equimolar mixture of the purified NiV-B and NiV-M sG tetramers. Blood was collected on days 42 and 84 after immunization. (B) Serum neutralizing Ab titers against rCedV-NiV-B-GFP and rCedV-HeV-GFP measured on day 84. The curves for each animal are shown in black or blue. (C to E) Competition ELISAs showing binding of biotinylated nAH1.3 (C), m102.4 (D), and HENV-32 (E) mAbs to the immobilized NiV G ectodomain in the presence of various dilutions of vaccine-elicited rhesus

macaque sera (obtained on day 84). The curves for each animal are shown in black or blue, whereas binding of the mAb in the absence of sera is shown in green (control). (F to I) Representative electron microscopy reconstructions (gray surfaces) of negatively stained complexes formed between purified polyclonal serum Fab fragments and NiV G tetramers with atomic models for visualization of antigenic sites targeted. (J) Surface representation of the NiV G tetramer with three head domain-specific Fabs bound (left) and a stalk-directed Fab bound (right), highlighting antigenic sites detected in vaccine-elicited polyclonal serum Abs. (K and L) Neutralizing Ab titers against rCedV-NiV-B-GFP (K) and rCedV-HeV-GFP (L) before and after depletion with the NiV G head domain (Head) or the ectodomain tetramer (Ecto).

tetramer for immunization, underscoring an apparent focusing of Ab responses on the receptor binding domain (Fig. 4, F to J, and fig. S5, D to F).

To understand the quantitative contribution of the different NiV G domains to serum neutralizing activity induced by vaccination, we depleted polyclonal Abs using either the purified isolated NiV G head domain or the tetrameric NiV G ectodomain. Neutralizing Ab titers for each of the two rhesus macaques

were respectively reduced by a factor of 9 and 19 against rCedV-NiV-B-GFP (Fig. 4K and fig. S6, C to F) and by a factor of 9 and 93 against rCedV-HeV-GFP (Fig. 4L and fig. S6, G and H) after depletion of NiV G head-specific Abs. Serum Ab depletion using the NiV G ectodomain tetramer resulted in a respective dampening of neutralizing activity by a factor of 11 and 13 against rCedV-NiV-B-GFP (Fig. 4K and fig. S6, I to L) and by a factor of 69 and 2.5 against rCedV-HeV-GFP (Fig. 4L and fig. S6, M and N).

Collectively, these data indicate that the NiV G head domain is immunodominant and the target of most serum neutralizing activity elicited by NiV G vaccination in rhesus macaques.

Discussion

Our structure of the NiV G ectodomain tetramer reveals the ultrastructural organization of this key target of the immune system, informs the mechanism of HNV entry into host cells, and provides a blueprint for engineering

next-generation vaccine candidates with improved stability and immunogenicity, as was achieved for respiratory syncytial virus (46, 47) and SARS-CoV-2 (48–54). The discovery that the NiV and HeV G head domain is the target of most neutralizing activity in the serum of rhesus macaques vaccinated with tetrameric NiV G ectodomains motivates the development of vaccines focusing Ab responses on this domain of vulnerability. Presenting the head antigen as an ordered array through multivalent display holds the promise of enhancing immunogenicity, as recently described for SARS-CoV-2 (50, 55, 56), and would allow presentation of a mosaic of HNV head domains with the goal of inducing neutralizing Ab responses with maximal breadth (44, 56–58). Finally, the enhanced expression yield, stability, and homogeneity of the NiV G head domain compared with HeV sG (35) would improve scalability of the manufacturing process of such a vaccine.

REFERENCES AND NOTES

- B. T. Eaton, C. C. Broder, D. Middleton, L. F. Wang, *Nat. Rev. Microbiol.* **4**, 23–35 (2006).
- E. S. Gurtley et al., *Emerg. Infect. Dis.* **23**, 1446–1453 (2017).
- G. Arunkumar et al., *J. Infect. Dis.* **219**, 1867–1878 (2019).
- M. S. Chhadha et al., *Emerg. Infect. Dis.* **12**, 235–240 (2006).
- P. K. Ching et al., *Emerg. Infect. Dis.* **21**, 328–331 (2015).
- O. Pernet et al., *Nat. Commun.* **5**, 5342 (2014).
- E. J. Annand et al., *bioRxiv* 2021.07.16.452724 [Preprint] (2021). <https://doi.org/10.1101/2021.07.16.452724>.
- J. Wang et al., *Virology* **18**, 197 (2021).
- M. Amaya, C. C. Broder, *Annu. Rev. Virol.* **7**, 447–473 (2020).
- K. Xu et al., *Proc. Natl. Acad. Sci. U.S.A.* **105**, 9953–9958 (2008).
- M. I. Bonaparte et al., *Proc. Natl. Acad. Sci. U.S.A.* **102**, 10652–10657 (2005).
- O. A. Negrete et al., *Nature* **436**, 401–405 (2005).
- T. A. Bowden et al., *Nat. Struct. Mol. Biol.* **15**, 567–572 (2008).
- Q. Liu et al., *PLoS Pathog.* **9**, e1003770 (2013).
- Q. Liu et al., *J. Virol.* **89**, 1838–1850 (2015).
- H. V. Dang et al., *Nat. Struct. Mol. Biol.* **28**, 426–434 (2021).
- H. V. Dang et al., *Nat. Struct. Mol. Biol.* **26**, 980–987 (2019).
- K. Xu et al., *PLoS Pathog.* **9**, e1003684 (2013).
- V. A. Avanzato et al., *Proc. Natl. Acad. Sci. U.S.A.* **116**, 25057–25067 (2019).
- K. N. Bossart et al., *Sci. Transl. Med.* **4**, 146ra107 (2012).
- K. N. Bossart et al., *PLoS Pathog.* **5**, e1000642 (2009).
- T. W. Geisbert et al., *Sci. Transl. Med.* **6**, 242ra82 (2014).
- C. E. Mire et al., *J. Infect. Dis.* **221** (suppl. 4), S471–S479 (2020).
- E. G. Playford et al., *Lancet Infect. Dis.* **20**, 445–454 (2020).
- K. N. Bossart et al., *J. Virol.* **79**, 6690–6702 (2005).
- B. A. Mungall et al., *J. Virol.* **80**, 12293–12302 (2006).
- J. A. McEachern et al., *Vaccine* **26**, 3842–3852 (2008).
- Z. Pallister et al., *Vaccine* **29**, 5623–5630 (2011).
- C. E. Mire et al., *J. Virol.* **88**, 4624–4631 (2014).
- D. Middleton et al., *Emerg. Infect. Dis.* **20**, 372–379 (2014).
- V. Borisovich et al., *J. Infect. Dis.* **213**, 448–455 (2016).
- D. Maar et al., *J. Virol.* **86**, 6632–6642 (2012).
- B. D. Welch et al., *PLoS Pathog.* **9**, e1003534 (2013).
- P. Yuan et al., *Proc. Natl. Acad. Sci. U.S.A.* **108**, 14920–14925 (2011).
- M. P. Doyle et al., *Cell Rep.* **36**, 109628 (2021).
- J. W. Wong et al., *Nat. Commun.* **8**, 781 (2017).
- A. C. Hickey, thesis, Uniformed Services University of the Health Sciences, Bethesda, MD (2009).
- A. Patel, D. B. Weiner, *Cell Host Microbe* **25**, 10–12 (2019).
- A. Baum et al., *Science* **369**, 1014–1018 (2020).
- J. Hansen et al., *Science* **369**, 1010–1014 (2020).
- Z. Zhu et al., *J. Virol.* **80**, 891–899 (2006).
- J. Dong et al., *Cell* **183**, 1536–1550.e17 (2020).
- M. Bianchi et al., *Immunity* **49**, 288–300.e8 (2018).
- S. Boyoglu-Barnum et al., *Nature* **592**, 623–628 (2021).
- C. O. Barnes et al., *Cell* **182**, 828–842.e16 (2020).
- J. S. McLellan et al., *Science* **342**, 592–598 (2013).
- J. Marcandalli et al., *Cell* **176**, 1420–1431.e17 (2019).
- J. Pallesen et al., *Proc. Natl. Acad. Sci. U.S.A.* **114**, E7348–E7357 (2017).
- C. L. Hsieh et al., *Science* **369**, 1501–1505 (2020).
- P. S. Arunachalam et al., *Nature* **594**, 253–258 (2021).
- D. Wrapp et al., *Science* **367**, 1260–1263 (2020).
- A. C. Walls et al., *Cell* **181**, 281–292.e6 (2020).
- M. McCallum, A. C. Walls, J. E. Bowen, D. Corti, D. Velesler, *Nat. Struct. Mol. Biol.* **27**, 942–949 (2020).
- K. S. Corbett et al., *Nature* **586**, 567–571 (2020).
- A. C. Walls et al., *Cell* **183**, 1367–1382.e17 (2020).
- A. C. Walls et al., *Cell* **184**, 5432–5447.e16 (2021).
- A. A. Cohen et al., *Science* **371**, 735–741 (2021).
- M. Kanekyo et al., *Nat. Immunol.* **20**, 362–372 (2019).
- A. Ianevski, A. K. Giri, T. Aittokallio, *Nucleic Acids Res.* **48**, W488–W493 (2020).

ACKNOWLEDGMENTS

We thank Auro Vaccines, LLC, for providing the rhesus macaque NiV-M and NiV-B sG immune sera, and we also acknowledge the Coalition for Epidemic Preparedness Innovations (CEPI) for their support of the Nipah virus vaccine program. Molecular graphics and analyses were performed with UCSF ChimeraX, developed by the Resource for Biocomputing, Visualization, and Informatics at the University of California, San Francisco, with support from National Institutes of Health R01-GM129325 and the Office of Cyber Infrastructure and Computational Biology, National Institute of Allergy and Infectious Diseases. The opinions and assertions expressed herein are those of the authors and do not necessarily reflect the official policy or position of the Uniformed Services University, the US Department of Defense, or the Henry M. Jackson Foundation for the Advancement of Military Medicine, Inc. D.V. is an investigator of the Howard Hughes Medical Institute. **Funding:** This study was supported by the National Institute of Allergy and Infectious Diseases (DP1AI158186 and HHSN272201700059C to D.V., AI077995 to C.C.B., and U19AI142764 to C.C.B. and D.V.), a National Institutes of Health Cellular and Molecular Biology Training Grant (T32GM007270 to A.A.), a Pew Biomedical Scholars Award (D.V.), an Investigator in the Pathogenesis of Infectious Disease Award from the Burroughs Wellcome Fund (D.V.), the University of Washington Arnold and Mabel Beckman cryo-EM center, and National Institutes of Health grant S10DD032290 (D.V.). **Author contributions:** Z.W., M.A., A.A., H.V.D., C.C.B.,

and D.V. conceived of the study. Z.W. and H.V.D. designed NiV sG and head domain constructs and recombinantly expressed and purified them. L.Y. developed, characterized, and produced the other recombinant tetrameric henipavirus sG glycoproteins. A.C.H. developed and characterized mAb nAHL3. Z.W. and H.V.D. carried out biolayer interferometry binding assays. M.A. performed neutralization assays and viral antibody escape passaging. A.A. prepared libraries for deep sequencing and analyzed the data. Z.W. purified serum polyclonal antibodies and performed ELISA and depletion assays. Z.W. carried out cryo-EM and negative stain EM sample preparation and data collection. Z.W. and D.V. processed the cryo-EM data and built and refined atomic models. G.R. and F.D. assisted with model building. Z.W. and D.V. wrote the manuscript, with input from all the authors. C.C.B. and D.V. acquired funding to support this study. **Competing interests:** C.C.B. is a US federal employee and co-inventor on US and foreign patents pertaining to soluble forms of Nipah virus and Hendra virus G glycoproteins and human monoclonal antibodies against Hendra and Nipah viruses. C.C.B. and M.A. are co-inventors on US and foreign patents pertaining to Cedar virus and methods of use and recombinant Cedar virus chimeras, whose assignees are the US, as represented by the Henry M. Jackson Foundation for the Advancement of Military Medicine (Bethesda, MD, USA). **Data and materials availability:** The cryo-EM maps and coordinates have been deposited to the Electron Microscopy Data Bank (EMDB) and Protein Data Bank (PDB) under accession numbers EMD-26164, EMD-26162, EMD-26163, PDB ID 7TXZ, and PDB ID 7TYO. Materials generated in this study will be made available on request after signing a materials transfer agreement with the University of Washington (Uniform Biological MTA).

SUPPLEMENTARY MATERIALS

[science.org/doi/10.1126/science.abm5561](https://doi.org/10.1126/science.abm5561)

Materials and Methods

Figs. S1 to S6

Table S1

References (60–78)

MDAR Reproducibility Checklist

24 September 2021; accepted 18 February 2022

Published online 3 March 2022

[10.1126/science.abm5561](https://doi.org/10.1126/science.abm5561)

NEUROSCIENCE

An action potential initiation mechanism in distal axons for the control of dopamine release

Changliang Liu^{1*}, Xintong Cai¹, Andreas Ritzau-Jost², Paul F. Kramer³, Yulong Li⁴, Zayd M. Khaliq³, Stefan Hallermann², Pascal S. Kaeser^{1*}

Information flow in neurons proceeds by integrating inputs in dendrites, generating action potentials near the soma, and releasing neurotransmitters from nerve terminals in the axon. We found that in the striatum, acetylcholine-releasing neurons induce action potential firing in distal dopamine axons. Spontaneous activity of cholinergic neurons produced dopamine release that extended beyond acetylcholine-signaling domains, and traveling action potentials were readily recorded from dopamine axons in response to cholinergic activation. In freely moving mice, dopamine and acetylcholine covaried with movement direction. Local inhibition of nicotinic acetylcholine receptors impaired dopamine dynamics and affected movement. Our findings uncover an endogenous mechanism for action potential initiation independent of somatodendritic integration and establish that this mechanism segregates the control of dopamine signaling between axons and somata.

Neurons receive input through dendrites and send output through axons. Although axonal function is regulated locally, it is thought that distal axons are not equipped with endogenous, physiological mechanisms for action potential induction. Midbrain dopamine neurons innervate the striatum with extensively arborized axons

to regulate a wide variety of functions (1–4). Of striatal neurons, 1 to 3% are tonically active interneurons that release acetylcholine (ACh), and their axons intertwine with those of dopamine neurons (5, 6). Dopamine axons express high levels of nicotinic ACh receptors (nAChRs), and synchronous activation of these receptors can drive dopamine release directly

(6–12). Hence, distal dopamine axons are under local striatal control and can release dopamine independent of activity ascending from their midbrain somata. However, because the command for neurotransmitter release generally originates from the soma, fundamental questions remain as to how nAChR activation is translated into dopamine release and whether this process represents a bona fide regulation used by the dopamine system.

The striatal cholinergic system broadcasts dopamine release

We expressed GRAB_{DA2m} [abbreviated as GRAB_{DA}, a D2 receptor-based dopamine sensor (13); GRAB, G protein-coupled receptor (GPCR) activation-based] in midbrain dopamine neurons and monitored fluorescence changes in acute striatal slices (Fig. 1A). Restricting GRAB_{DA} expression to dopamine axons provides a widespread sensor network in the striatum and facilitates detection because the sensors are present in the immediate vicinity of dopamine release (Fig. 1B). Dopamine release was detected in both dorsal and ventral striatum without any stimulation, and this spontaneous release was sensitive to DHβE, a blocker of β2-containing nAChRs (Fig. 1, A to E; fig. S1A; and movie S1). Release occurred stochastically and exhibited all-or-none properties: Either an event covered a large area, estimated to contain 3 million to 15 million dopamine terminals (14), or no release was detected (Fig. 1C and fig. S1C). Because midbrain dopamine cell bodies are absent in this striatal slice preparation, the detected release is induced without involvement of dopamine neuron somata.

Using a corresponding strategy with GRAB_{ACh3.0} [abbreviated as GRAB_{ACh}, an M3-receptor-based ACh sensor (15)], we also detected spontaneous ACh release in both dorsal and ventral striatum, which is consistent with previous work on spontaneous ACh neuron activity (16). ACh release was sensitive to the sodium channel blocker tetrodotoxin (TTX) and exhibited an all-or-none pattern like that of dopamine (Fig. 1, F and G; fig. S1, A to C; and movie S2). The frequency of ACh release was approximately threefold higher than that of dopamine release, suggesting that not all ACh triggers dopamine release (Fig. 1, E and G). Although less frequent, areas covered by dopamine release were approximately three times larger compared with those of ACh (Fig. 1H). Adjusting event detection thresholds or enhancing

GRAB_{ACh} expression by injecting the respective adeno-associated virus (AAV) directly into the striatum slightly influenced the signals (fig. S1, D to G), but dopamine release continued to be less frequent and broader than ACh release. Increasing slice thickness enhanced dopamine release frequency, but blocking synaptic transmission only marginally influenced dopamine and ACh release (fig. S2).

Cholinergic interneurons exhibit multiple firing activities: They have spontaneous pacemaker activity and respond with pause-rebound firing *in vivo* to a variety of sensory stimuli (17–20). Because spontaneous cholinergic activity drives dopamine release stochastically (Fig. 1, C and D), we speculated that pause-rebound firing might induce time-locked dopamine release. We mimicked ACh pause-rebound activity in striatal slices and found that it induces a robust dopamine transient during rebound firing (fig. S3).

We next evoked dopamine and ACh release using electrical stimulation (Fig. 1, I to S). A large proportion of electrically evoked dopamine release was driven by activation of nAChRs (Fig. 1, I and J) (6, 10, 12, 14). Consistent with the findings from spontaneous release, evoked dopamine release covered an area three to four times larger than that of evoked ACh release, and nAChR blockade strongly reduced its area (Fig. 1, K and O). Similar results were obtained when ACh and dopamine release were measured simultaneously [with GRAB_{ACh} and rGRAB_{DA1h}, abbreviated as rGRAB_{DA}, a red-shifted dopamine sensor (13)], and the release areas were positively correlated with one another (Fig. 1, Q to S).

Dopamine release with nAChR activation depressed more strongly during repetitive stimulation than release evoked without it (Fig. 1 I to L) (12, 14). This is thought to be a result of rapid nAChR desensitization, but our data indicate that it is most likely caused by depression of ACh release after the first stimulus (Fig. 1, M to P). The depression of ACh release was attenuated by blocking nAChRs or D2 receptors, but not AMPA, *N*-methyl-D-aspartate (NMDA), or γ -aminobutyric acid type A (GABA_A) receptors (Fig. 1P and fig. S4, A to D), suggesting that it is due to feedback inhibition mediated by dopamine. Blocking nAChRs or D2 receptors also increased ACh release in response to the first stimulus (Fig. 1, M to O, and fig. S4, E to G), likely because ACh release is tonically inhibited by dopamine (18).

ACh- and action potential-induced dopamine secretion share release mechanisms

We next asked why dopamine release spreads beyond the area of ACh release (Fig. 1, Q to S). We first examined the organization of striatal ACh terminals and dopamine axons using super-resolution three-dimensional structured illumination microscopy (3D-SIM). Although

synaptophysin-tdTomato-labeled ACh terminals were intermingled with tyrosine hydroxylase (TH)-labeled dopamine axons, no prominent association was detected (8, 21), and their contact frequency was much lower than the density of release sites in dopamine axons (Fig. 2, A and B) (14).

Dopamine axons contain varicosities that are filled with vesicles, but only a small fraction of the vesicles are releasable, and only a subset of the varicosities contains active release sites to respond to action potentials (3, 14, 22). Thus, one way for ACh neurons to boost dopamine release could be by recruiting additional vesicles and/or release sites. To test this possibility, we performed cross-depletion experiments. We expressed the light-activated cation channel channelrhodopsin-2 (ChR2) in dopamine axons and evoked dopamine release with light (to specifically activate dopamine axons) followed by electrical stimulation (to activate dopamine axons and ACh neurons) (Fig. 2C). Electrical stimulation induces dopamine release with two phases (fig. S5), and the second phase is entirely mediated by ACh (12, 14). Preceding light stimulation nearly abolished the second phase (Fig. 2, D and E), indicating that vesicles and release sites are shared between the two release modes.

In principle, ACh may trigger dopamine release in three ways. First, because nAChRs [including the $\alpha 6$ - and $\alpha 4$ -containing nAChRs on dopamine axons (8)] are nonselective cation channels (23), Ca²⁺ entry through them might directly trigger dopamine vesicle fusion. Second, nAChR activation might depolarize the dopamine axon membrane and activate low-voltage-gated Ca²⁺ channels to induce dopamine release. Last, nAChR activation on dopamine axons might initiate ectopic action potentials followed by opening of low- and high-voltage-gated Ca²⁺ channels and release.

We started distinguishing between these possibilities by characterizing the Ca²⁺ sources for ACh-induced dopamine release. Double removal of Ca_v2.1 (P/Q-type) and Ca_v2.2 (N-type) channels in dopamine neurons similarly reduced ACh-induced release (the second phase in response to electrical stimulation) and action potential-induced release (by optogenetic activation of dopamine axons) (Fig. 2, F to I, and fig. S5A). Removing Ca_v2.3 (R-type) channels had no effect (fig. S5, B to D). Hence, both release modes rely on these voltage-gated Ca²⁺ channels to a similar extent, ruling out that nAChRs are the main source of Ca²⁺ influx. Because Ca_v2.1 and Ca_v2.2 are high-voltage activated and open efficiently at membrane potentials higher than typical action potential thresholds (24, 25), generating ectopic action potentials in dopamine axons is most likely necessary for ACh to induce dopamine release.

¹Department of Neurobiology, Harvard Medical School, Boston, MA, USA. ²Carl-Ludwig-Institute of Physiology, Faculty of Medicine, Leipzig University, Leipzig, Germany. ³Cellular Neurophysiology Section, National Institute of Neurological Disorders and Stroke, National Institutes of Health, Bethesda, MD, USA. ⁴State Key Laboratory of Membrane Biology, Peking University School of Life Sciences, Beijing, China.
*Corresponding author. Email: changliang_liu@hms.harvard.edu (C.L.); kaeser@hms.harvard.edu (P.S.K.)

Fig. 1. ACh-induced dopamine secretion expands beyond ACh release.

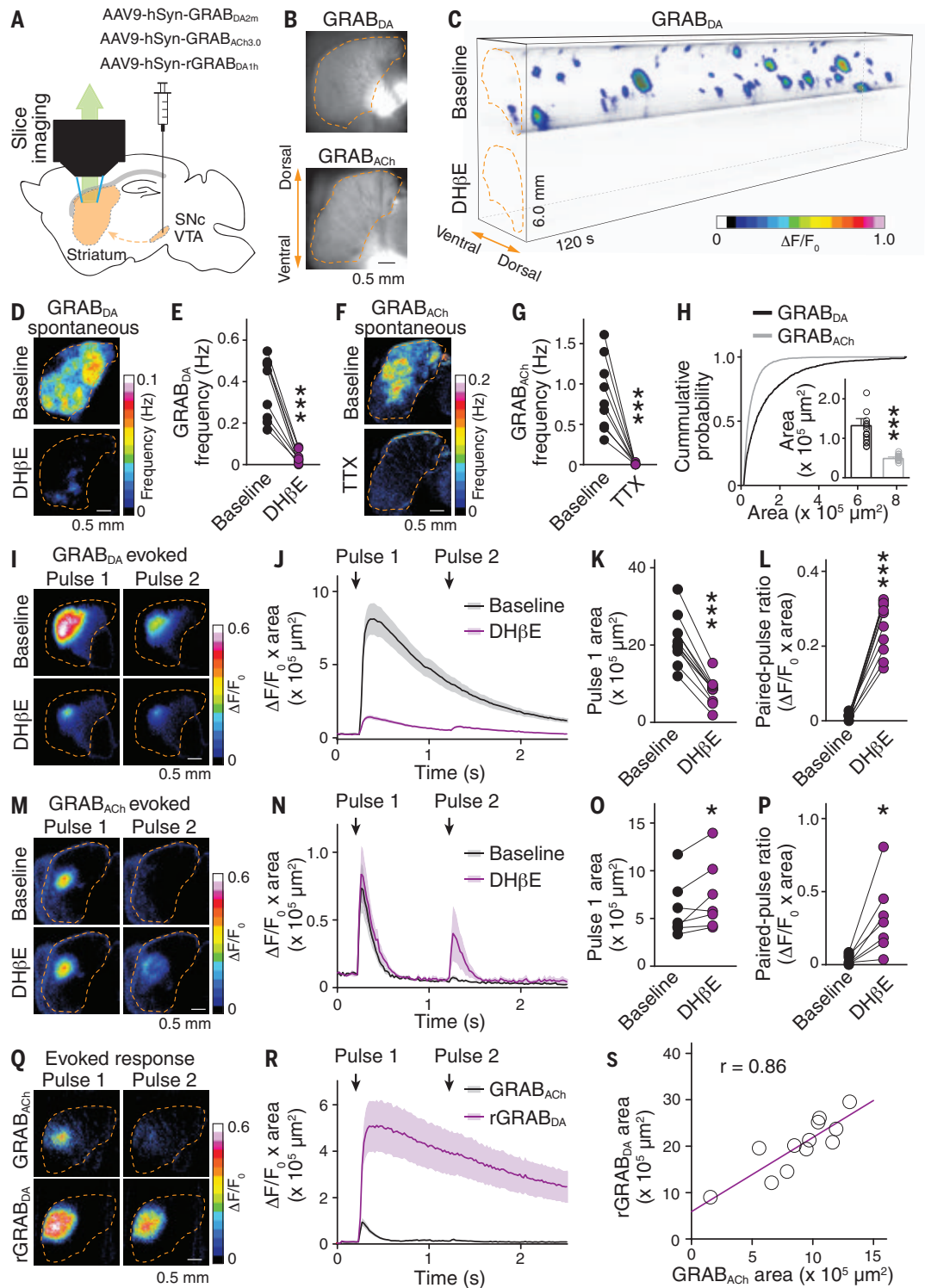
(A) Schematic of midbrain AAV injection for dopamine axonal expression of GRAB_{DA}, rGRAB_{DA}, or GRAB_{ACh} sensors followed by widefield fluorescence imaging in parasagittal striatal slices.

(B) GRAB_{DA} and GRAB_{ACh} expression in striatal slices. Dashed lines (orange) outline the striatum. (C) Volume-rendered time series of spontaneous GRAB_{DA} fluctuations (expressed as $\Delta F/F_0$, color-coded for magnitude) before (top) and after (bottom) application of DH β E (1 μ M). Areas with $\Delta F/F_0 < 0.02$ were made transparent for clarity.

(D) Example frequency maps and (E) quantification of spontaneous GRAB_{DA} events detected before and after 1 μ M DH β E; $n = 9$ slices from four mice. (F and G) As in (D) and (E) but for GRAB_{ACh} before and after 1 μ M TTX; $n = 9$ slices from three mice. (H) Comparison of the area covered by GRAB_{DA} and GRAB_{ACh} events;

$n = 1010$ events from 17 slices from four mice for GRAB_{DA}, $n = 2087$ events from 14 slices from four mice for GRAB_{ACh}. (I) Example images and (J to L) quantification of GRAB_{DA} fluorescence evoked by paired electrical stimuli (1-s interval) before and after 1 μ M Dh β E; $n = 11$ slices from four mice. (M to P) As I to L, but for GRAB_{ACh}; $n = 7$ slices from three mice. (Q and R) As in (I) and (J) but for simultaneous assessment of GRAB_{ACh} and rGRAB_{DA}; $n = 12$ slices from four mice.

(S) Correlation of areas in (R). Data are mean \pm SEM; * $P < 0.05$, *** $P < 0.001$; Wilcoxon signed-rank tests for (E), (G), (K), (L), (O), and (P); Mann-Whitney rank-sum test for (H).



Striatal cholinergic activation induces action potential firing in distal dopamine axons

To test whether ACh can induce dopamine axon firing, we expressed ChR2 in dopamine or ACh neurons and recorded evoked dopamine release and field potentials in striatal slices using a carbon fiber electrode (Fig. 3A

and fig. S6, A and B). Optogenetic activation of dopamine axons evoked robust dopamine release and a triphasic field potential that was abolished by TTX but insensitive to a range of neurotransmitter receptor blockers (Fig. 3B and fig. S7A). This indicates that the field potential represents dopamine axon pop-

ulation firing. Optogenetic activation of the cholinergic system produced a similar triphasic response that was disrupted by DH β E or by 6-hydroxydopamine (6-OHDA) lesion of dopamine axons (Fig. 3C and fig. S6C), demonstrating that it is evoked by nAChR activation and originates from dopamine axons.

Fig. 2. ACh triggers dopamine secretion through the same release mechanisms as dopamine neuron action potentials. (A) Example 3D-SIM images of dorsal striatal slices showing dopamine axons (labeled with TH antibodies) and ACh nerve terminals [labeled by crossing Cre-dependent Synpatophysin-tdTomato mice (SYP-tdTomato^{LSL}) with

ChAT^{IRES-Cre} mice]. Images were obtained by means of (left) volume rendering of an image stack, (middle) surface rendering of detected objects, and (right) surface rendering of ACh terminals that contact dopamine axons (>0 voxel overlap).

(B) Comparison of the minimal distance of ACh terminals from the nearest dopamine axons. Controls were generated by averaging 1000 rounds of local shuffling and distance calculation of each ACh terminal within 5 by 5 by 1 μm^3 ; $n = 5482$ objects from 33 images from four mice.

(C) Schematic of slice recordings. Chr2-EYFP was expressed in dopamine neurons (by crossing Chr2-EYFP^{LSL} with DAT^{IRES-Cre} mice), and dopamine release was measured by using amperometry in dorsal striatal slices in the area of light stimulation.

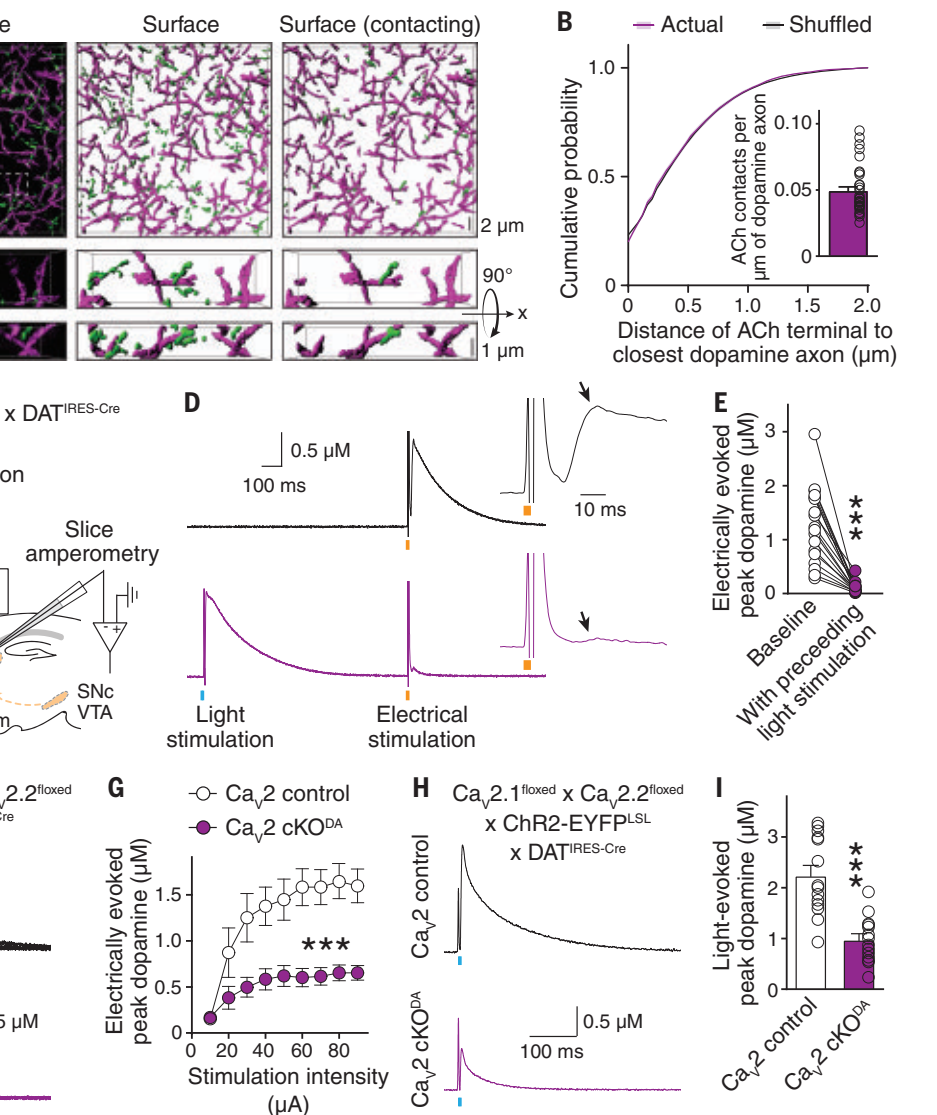
(D) Example traces and (E) quantification of peak amplitude of the second dopamine release phase (arrows) evoked by means of electrical stimulation (orange bar) with (bottom) or without (top) a preceding 1-ms light stimulus (blue bar; 1 s before); $n = 18$ slices from three mice.

(F) Example traces and (G) quantification of peak dopamine amplitude (second phase) evoked by means of electrical stimulation in Ca_v2 cKO^{DA} mice (Ca_v2.1 + 2.2 double floxed mice crossed to DAT^{IRES-Cre} mice)

and sibling Ca_v2 control mice; $n = 13$ slices from four mice each [$P < 0.001$ for genotype, stimulation intensity and interaction; two-way analysis of variance (ANOVA); genotype effect reported in the figure].

(H and I) Similar to (F) and (G) but with dopamine release evoked by means of light stimulation in mice expressing Chr2-EYFP transgenically in dopamine neurons; $n = 14$ slices from five mice each. Data are mean \pm SEM; *** $P < 0.001$; Kolmogorov-Smirnov test for (B); Wilcoxon signed-rank test for (E); and Mann-Whitney rank-sum test for (I).

The shape of the DH β E-sensitive component of cholinergic activation was similar to the TTX-sensitive component of dopamine axon stimulation (Fig. 3, D and E, and fig. S7, B and C), suggesting that ACh induces firing in dopamine axons. The potential induced through cholinergic activation lagged 5.1 ms behind that of dopamine axon stimulation, which is consistent with the timing of ACh-induced dopamine release (Fig. 3, D to F) (12, 14). Similar to evoked ACh release (fig. S4, E to H), the field potential induced by cholinergic activation exhibited a strong de-



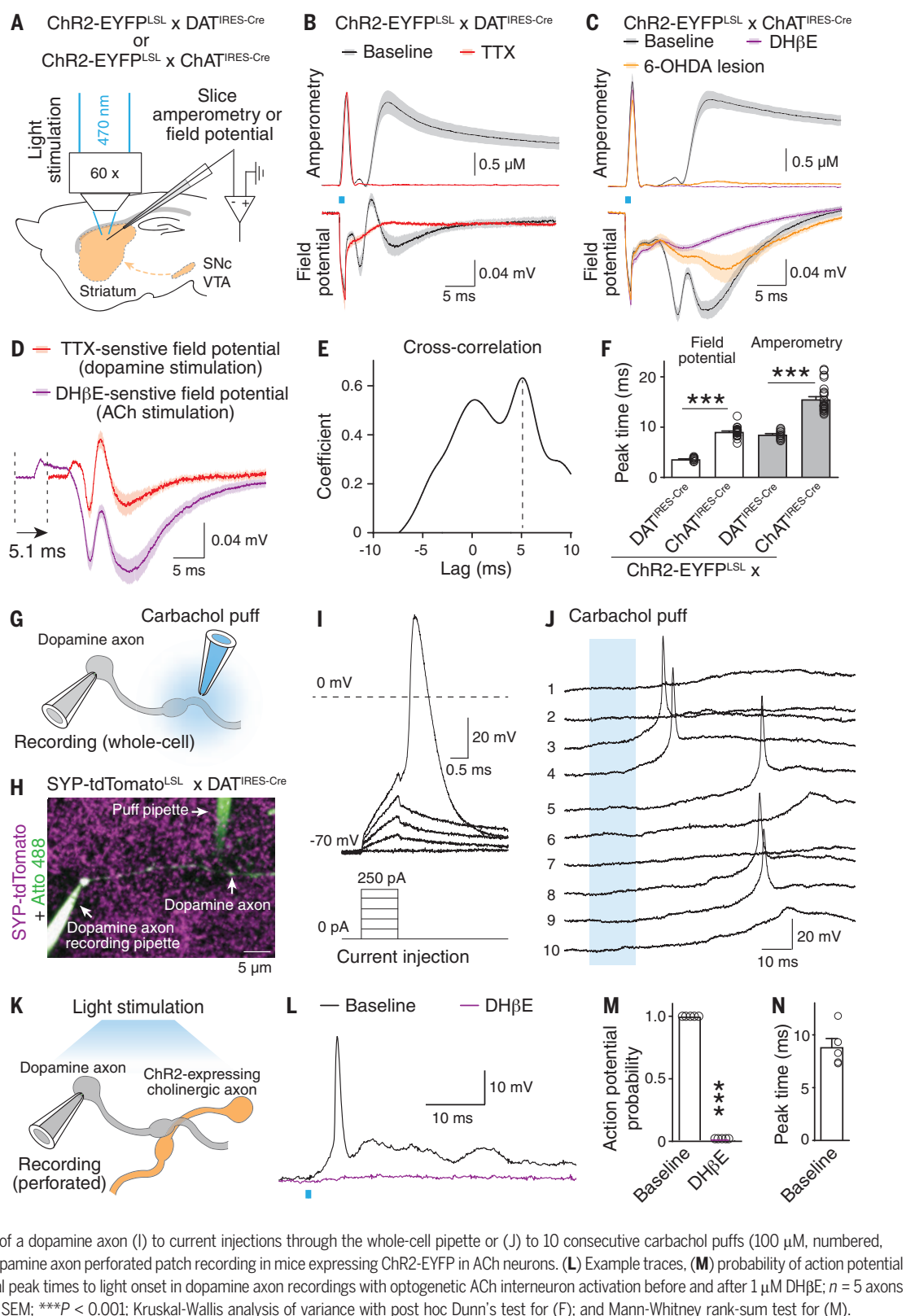
pression during repetitive stimulation that was partially relieved by blocking D2 receptors (fig. S7, D and E). To investigate the firing of individual axons, we performed direct recordings (26) from genetically labeled dopamine axons (Fig. 3, G and H). Current injection reliably induced large and brief action potentials (amplitude, 113 ± 2 mV; half-width, 0.64 ± 0.03 ms; $n = 24$ axons from nine mice) (Fig. 3I). Upon puffing of carbachol (an nAChR agonist) onto the axon 20 to 40 μm away from the recording site, 3 out of 14 axons exhibited action po-

tential firing (Fig. 3J and fig. S7F). To test whether action potentials can be induced by endogenous ACh release, we expressed Chr2 in cholinergic interneurons and performed perforated patch recordings from dopamine axons (Fig. 3K). Optogenetic activation of ACh neurons could be tuned to evoke action potentials in all five recorded dopamine axons, and nAChR blockade abolished firing (Fig. 3, L and M). Action potential peak times matched precisely with those of the potentials measured in the field recordings (Fig. 3, F and N).

25 MARCH 2022 • VOL 375 ISSUE 6587 1381

Fig. 3. Activation of nAChRs triggers action potentials in striatal dopamine axons.

(A) Schematic of recordings with carbon fiber electrodes in voltage-clamp (0.6 V, amperometric recordings) or current-clamp (no current injection, field potential recordings). (B and C) Average traces of (top) light-evoked dopamine release (amperometry) and (bottom) field potentials in brain slices of mice with ChR2-EYFP in (B) dopamine axons or (C) ACh neurons. Example traces are provided in fig. S7, B and C. Recordings were in ACSF (baseline), (B) in 1 μ M TTX, or (C) in 1 μ M DH β E or (C) after 6-OHDA injection. (B) $n = 12$ slices from three mice each; (C), $n = 25$ slices from six mice (each) for baseline, $n = 21$ slices from six mice (amperometry) and $n = 9$ slices from four mice (field potentials) for DH β E, and $n = 11$ slices from six mice each for 6-OHDA. (D) Comparison of TTX-sensitive and DH β E-sensitive field potentials (obtained through subtraction) (fig. S7, B and C). TTX-sensitive components are right-shifted by 5.1 ms [lag detected in (E)]; n is as in (B) and (C). (E) Cross-correlation of TTX- and DH β E-sensitive components shown in (D). (F) Lag of peak response from the start of the light stimulus; n is as in (B) and (C). (G) Schematic and (H) example two-photon image of direct recording from dopamine axons. Synaptophysin-tdTomato was expressed by using mouse genetics in dopamine axons, the recorded axon was filled with Atto 488 (green) through the recording pipette, and the puff pipette contained carbachol and Atto 488. (I and J) Example responses of a dopamine axon (I) to current injections through the whole-cell pipette or (J) to 10 consecutive carbachol puffs (100 μ M, numbered, 10-s intervals). (K) Schematic of dopamine axon perforated patch recording in mice expressing ChR2-EYFP in ACh neurons. (L) Example traces, (M) probability of action potential firing, and (N) lag of action potential peak times to light onset in dopamine axon recordings with optogenetic ACh interneuron activation before and after 1 μ M DH β E; $n = 5$ axons from three mice. Data are mean \pm SEM; *** $P < 0.001$; Kruskal-Wallis analysis of variance with post hoc Dunn's test for (F); and Mann-Whitney rank-sum test for (M).



Striatal ACh and dopamine covary with movement direction

To investigate the functional relevance of ACh-induced dopamine release, we expressed GRAB_{DA}

or GRAB_{ACh} together with tdTomato in the right dorsal striatum and monitored the dynamics of the corresponding transmitters by using dual-color fiber photometry in mice ex-

ploring an open field arena (Fig. 4A and fig. S8). Because striatal dopamine and ACh might play important roles in movement initiation (27–31), we aligned GRAB_{DA} or GRAB_{ACh}

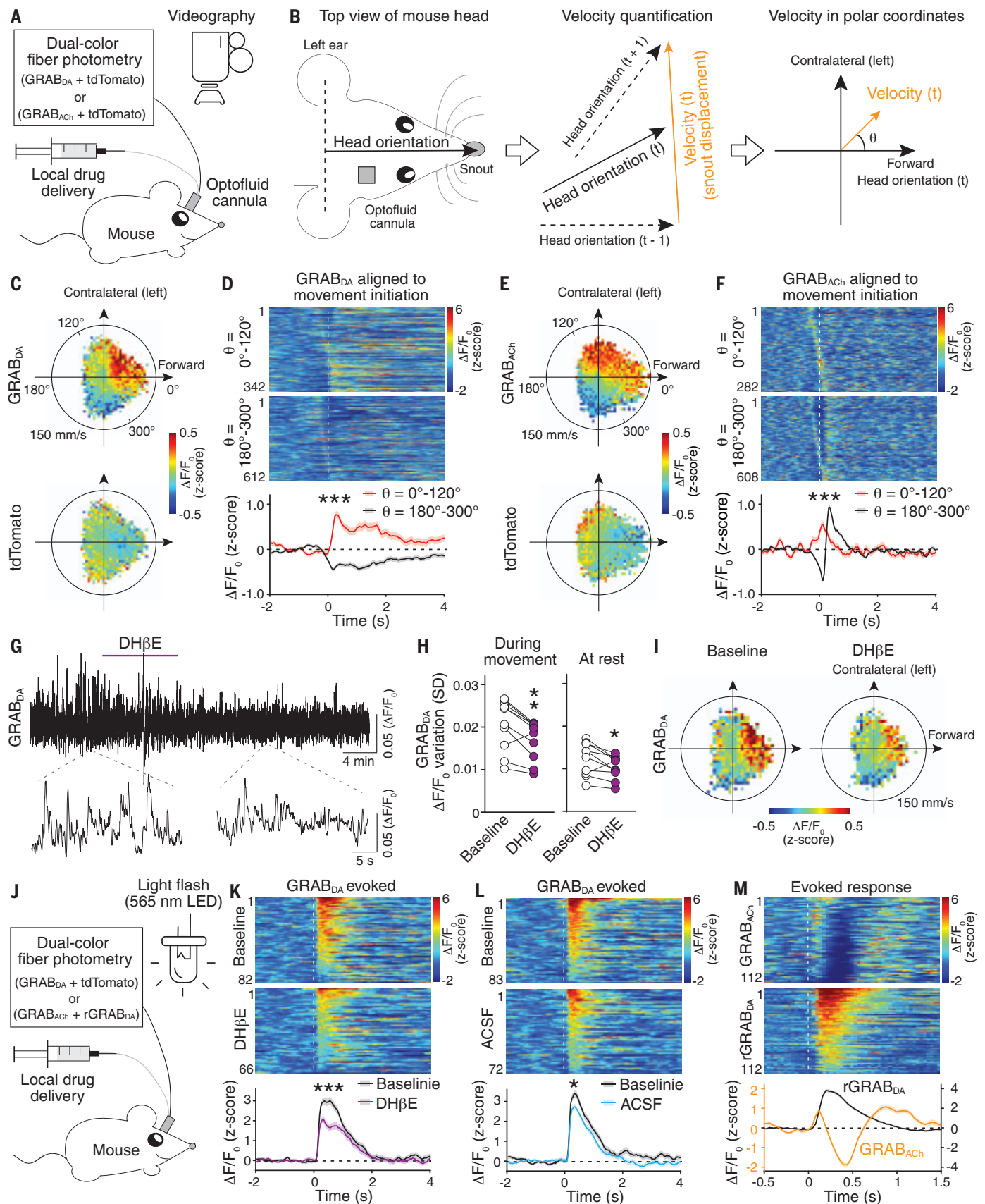


Fig. 4. Dopamine and ACh dynamics correlate with movement direction, and dopamine dynamics are attenuated after blocking nAChRs. (A) Strategy for simultaneous measurements of dopamine or ACh dynamics and behavior in freely moving mice. (B) Fiber photometry and drug delivery were in the right dorsal

striatum by using an optofluid cannula. Head orientation was defined as the direction from the center point between the ears to the snout. Instantaneous velocity at time point t was calculated from the displacement of the snout from $t - 1$ to $t + 1$ and plotted in polar coordinates with head orientation at t defined as $\theta = 0^\circ$. **(C)** Average GRAB_{DA} and tdTomato signals registered to their concurrent velocities in polar coordinates; $n = 10$ mice. **(D)** Individual (heatmap) and average GRAB_{DA} fluctuations aligned to movement initiation (dashed line) with (top) $\theta = 0^\circ$ to 120° or (bottom) 180° to 300° . Heatmaps were sorted by peak time; $n = 342$ events from 10 mice for $\theta = 0^\circ$ to 120° , $n = 612$ events from 10 mice for $\theta = 180^\circ$ to 300° . **(E and F)** As in (C) and (D) but for GRAB_{ACh}; $n = 282$ events from 11 mice for $\theta = 0^\circ$ to 120° ; $n = 608$ events from 11 mice for $\theta = 180^\circ$ to 300° . **(G)** Example trace and **(H)** quantification (standard deviation of $\Delta F/F_0$) of

GRAB_{DA} fluorescence before and after DH β E (50 μ M, 1 μ l) delivered through the optofluid canula; $n = 10$ mice. **(I)** Average GRAB_{DA} signals registered to concurrent velocities before and after DH β E; $n = 10$ mice. **(J)** Schematic for measurements of dopamine release induced by 200-ms light flashes in freely moving mice. **(K and L)** Individual (heatmap) and average GRAB_{DA} fluctuations aligned to the light flash (dashed line) before and after local infusion of (K) DH β E or (L) ACSF. (K), $n = 82$ responses from 10 mice for baseline, $n = 66$ responses from 10 mice for DH β E; (L) $n = 83$ responses from 10 mice for baseline, $n = 72$ responses from 10 mice for ACSF. **(M)** Similar to (K) but for simultaneous assessment of GRAB_{ACh} and rGRAB_{DA}; $n = 112$ responses from four mice. Data are mean \pm SEM; *** $P < 0.001$, ** $P < 0.01$, * $P < 0.05$; Mann-Whitney rank-sum tests for areas under the curve (0 to 400 ms) in (D), (F), (K), and (L). Wilcoxon signed-rank test for (H).

signals to movement onset. We found that both exhibited an increase on average, but there was strong heterogeneity in individual responses (fig. S9).

In previous studies, movement was often restricted to specific directions and/or treated as a scalar quantity (27–31). In our experiments, mice traveled freely in a large arena and constantly adjusted body posture and movement direction. If only the amplitude of velocity (speed) is considered, spatial information is lost. Hence, we treated velocity as a two-dimensional vector relative to the mouse's head orientation and registered photometry signals to the corresponding velocity plotted in polar coordinates (with angle θ defined as the direction of velocity) (Fig. 4B and fig. S10, A and D). Striatal dopamine and ACh levels were highly correlated with movement direction (Fig. 4, C and E); both exhibited an increase when the animal was turning to the contralateral side or moving forward ($\theta = 0^\circ$ to 120°) and a decrease when the animal was turning to the ipsilateral side or backward ($\theta = 180^\circ$ to 300°). This pattern became more evident when the time series of velocity was right-shifted (fig. S10, B and E), indicating that the velocity peak precedes that of the photometry signal.

When aligned to movement initiations with selected directions, dopamine responses diverged. There was an increase at $\theta = 0^\circ$ to 120° and a decrease at $\theta = 180^\circ$ to 300° ; and dopamine transients peaked ~ 150 ms after movement onset (Fig. 4, C and D, and fig. S10, A to C). ACh levels also diverged when aligned to movement onset with selected directions. However, instead of a monotonic decrease, ACh exhibited a decrease followed immediately by an increase for movement initiations with $\theta = 180^\circ$ to 300° (Fig. 4, E and F). This was also detected in the polar coordinates when the velocity time course was right-shifted (fig. S10, D to F).

Striatal ACh contributes to dopamine dynamics

Local inhibition of nAChRs by infusion of DH β E through the optofluid canula slightly decreased dopamine fluctuations (Fig. 4, G and H, and fig. S11, A and B). Dopamine cell bodies and

the striatal cholinergic system both drive firing in dopamine axons. The effect of nAChR blockade may be limited because firing of dopamine cell bodies might dominate the signal, and somatic firing could also compensate for the loss of dopamine release induced by blocking nAChRs.

The correlation between dopamine fluctuations and movement direction was largely preserved after unilateral nAChR block with DH β E (Fig. 4I and fig. S11C). However, unilateral DH β E infusion caused a robust reduction in both amplitude and frequency of movement initiations with $\theta = 0^\circ$ to 120° , but only a slight change in amplitude and no change in frequency of those with $\theta = 180^\circ$ to 300° (fig. S11, D to G).

Dopamine neurons respond to salient sensory stimuli (4). We evoked dopamine release by applying 200-ms flashes of light to the open field arena at random intervals (Fig. 4J). Local infusion of DH β E reduced the evoked GRAB_{DA} response (Fig. 4K). Artificial cerebrospinal fluid (ACSF) infusion also caused a reduction, likely owing to habituation of the mice to the repeated stimuli, that was smaller than the one induced by nAChR blockade (Fig. 4L and fig. S11H). When dopamine and ACh were monitored simultaneously with rGRAB_{DA} and GRAB_{ACh}, respectively, light stimulation evoked a triphasic ACh response, with the initial rise in ACh preceding that of dopamine (Fig. 4M and fig. S11I).

Discussion

Neurotransmitter release from nerve terminals is generally determined by action potentials initiated at the axon initial segment near the soma. Ectopic action potentials are less common, and their functional roles remain elusive (32, 33). Here, we show that ACh induces firing in distal dopamine axons as a physiological mechanism to regulate dopamine signaling. This explains how the striatal cholinergic system broadcasts dopamine release. Ectopic action potentials likely propagate through the axonal network and trigger release along the path. This firing mechanism also accounts for the all-or-none pattern of spontaneous dopamine release and answers

why coincident activity in multiple cholinergic neurons is necessary (6): ACh has to quickly depolarize dopamine axons to trigger action potentials before the opening of potassium channels and before ACh is degraded by acetylcholinesterase.

Axonal transmitter secretion is generally viewed to rely on the interplay between firing from the soma (which recruits the entire axon) and local regulation in single nerve terminals (which locally tunes release). We found that local ACh release not only triggers dopamine release (6, 9–12) but hijacks the dopamine axon network to expand signaling with high temporal precision. The exceptionally high levels of nAChRs on dopamine axons (7, 8) might serve to initiate axonal firing. Because presynaptic nAChRs enhance release in multiple types of neurons (34), this axonal firing mechanism might be important beyond the dopamine system.

Individual dopamine terminals are likely indifferent as to where an action potential is generated, and an immediate question is the functional relevance of initiating action potentials in two distinct brain areas. We propose that ACh-induced dopamine axon firing not only represents a distinct input but also sculpts a different dopamine signaling architecture compared with somatic firing. Both phasic somatic and axonal firing induction recruit groups of dopamine axons. Striatal ACh triggers action potentials in neighboring axons centered around the site of ACh release. By contrast, phasic firing in the midbrain recruits cell bodies that share excitatory input, and their axons may or may not be intermingled in the striatum (1, 35, 36). Hence, ACh-induced dopamine release might endow dopamine signaling with spatial control over striatal circuitry that is distinct from release induced by activating midbrain somata. Our work further suggests that information flow in dopamine neurons between the midbrain and striatum might be bidirectional. Axon→soma signaling could occur through action potential back-propagation (37, 38) upon striatal cholinergic activity to regulate somatodendritic dopamine release, dendritic excitability, or other midbrain processes.

Roles for striatal dopamine and ACh are under intense investigation, and both excitation and inhibition in the firing have been associated with spontaneous movement (27, 28, 30, 31). We demonstrate that striatal dopamine and ACh not only correlate with movement initiation but also with its direction, potentially explaining the heterogeneity of their responses at movement onset. The findings that ACh and dopamine covary with movement direction and that ACh enhances dopamine dynamics suggest that the two systems are coordinated for their roles in motor control (27). These findings fit well with classical observations that unilateral lesions of dopamine or ACh systems induce asymmetric behavior and support that dynamic transmitter balance between hemispheres is important for adjusting body posture (29, 39). Last, we observed that dopamine dynamics are regulated by nAChRs regardless of movement state, which indicates that ACh-induced dopamine release likely has additional physiological roles.

REFERENCES AND NOTES

- W. Matsuda et al., *J. Neurosci.* **29**, 444–453 (2009).
- J. D. Berke, *Nat. Neurosci.* **21**, 787–793 (2018).
- C. Liu, P. Goel, P. S. Kaeser, *Nat. Rev. Neurosci.* **22**, 345–358 (2021).
- E. S. Bromberg-Martin, M. Matsumoto, O. Hikosaka, *Neuron* **68**, 815–834 (2010).
- C. J. Wilson, *Neuron* **45**, 575–585 (2005).
- S. Threlfell et al., *Neuron* **75**, 58–64 (2012).
- N. Le Novère, M. Zoli, J.-P. Changeux, *Eur. J. Neurosci.* **8**, 2428–2439 (1996).
- I. W. Jones, J. P. Bolam, S. Wonnacott, *J. Comp. Neurol.* **439**, 235–247 (2001).
- M. F. Giurgiuieff, M. L. Le Floch, J. Glowinski, M. J. Besson, *J. Pharmacol. Exp. Ther.* **200**, 535–544 (1977).
- F.-M. Zhou, Y. Liang, J. A. Dani, *Nat. Neurosci.* **4**, 1224–1229 (2001).
- R. Cachope et al., *Cell Rep.* **2**, 33–41 (2012).
- L. Wang et al., *J. Physiol.* **592**, 3559–3576 (2014).
- F. Sun et al., *Nat. Methods* **17**, 1156–1166 (2020).
- C. Liu, L. Kershberg, J. Wang, S. Schneberger, P. S. Kaeser, *Cell* **172**, 706–718.e15 (2018).
- M. Jing et al., *Nat. Methods* **17**, 1139–1146 (2020).
- A. A. Mammaligas, C. P. Ford, *Neuron* **91**, 574–586 (2016).
- J. M. Schulz, M. J. Oswald, J. N. J. Reynolds, *J. Neurosci.* **31**, 11133–11143 (2011).
- G. Morris, D. Arkadir, A. Nevet, E. Vaadia, H. Bergman, *Neuron* **43**, 133–143 (2004).
- Y. Cai, C. P. Ford, *Cell Rep.* **25**, 3148–3157.e3 (2018).
- C. Straub, N. X. Tritsch, N. A. Hagan, C. Gu, B. L. Sabatini, *J. Neurosci.* **34**, 8557–8569 (2014).
- H. T. Chang, *Brain Res. Bull.* **21**, 295–304 (1988).
- D. W. Pereira et al., *Nat. Neurosci.* **19**, 578–586 (2016).
- E. R. Decker, J. A. Dani, *J. Neurosci.* **10**, 3413–3420 (1990).
- R. G. Held et al., *Neuron* **107**, 667–683.e9 (2020).
- Y. Yang et al., *Front. Cell. Neurosci.* **13**, 317 (2019).
- A. Ritzaue-Jost et al., *Cell Rep.* **34**, 108612 (2021).
- M. H. Howe et al., *eLife* **8**, e44903 (2019).
- P. D. Dodson et al., *Proc. Natl. Acad. Sci. U.S.A.* **113**, E2180–E2188 (2016).
- S. Kaneko et al., *Science* **289**, 633–637 (2000).
- M. H. Howe, D. A. Dornbeck, *Nature* **535**, 505–510 (2016).
- J. A. da Silva, F. Tecuapetla, V. Paixão, R. M. Costa, *Nature* **554**, 244–248 (2018).
- T. Dugladze, D. Schmitz, M. A. Whittington, I. Vida, T. Gloveli, *Science* **336**, 1458–1461 (2012).
- M. E. J. Sheffield, T. K. Best, B. D. Mensh, W. L. Kath, N. Spruston, *Nat. Neurosci.* **14**, 200–207 (2011).
- J. A. Dani, D. Bertrand, *Annu. Rev. Pharmacol. Toxicol.* **47**, 699–729 (2007).
- N. Eshel, J. Tian, M. Bukwich, N. Uchida, *Nat. Neurosci.* **19**, 479–486 (2016).
- J. G. Parker et al., *Proc. Natl. Acad. Sci. U.S.A.* **107**, 13491–13496 (2010).

- A. A. Grace, B. S. Bunney, *Science* **210**, 654–656 (1980).
- L. J. Gentet, S. R. Williams, *J. Neurosci.* **27**, 1892–1901 (2007).
- N. F. Parker et al., *Nat. Neurosci.* **19**, 845–854 (2016).
- C. Liu, Data table for an action potential initiation mechanism in distal axons for the control of dopamine release. Zenodo (2022); doi: 10.5281/zenodo.6342359.
- C. Liu, Matlab script for object recognition and analysis. Zenodo (2022); doi: 10.5281/zenodo.6342367.

ACKNOWLEDGMENTS

We thank C. Qiao, M. Han, and J. Wang for technical assistance; N. Uchida, M. Watabe-Uchida, and I. Tsutsui-Kimura for advice on setting up fiber photometry; A. van den Maagdenberg for $\text{Ca}_v2.1^{\text{loxex}}$ mice and T. Schneider for $\text{Ca}_v2.3^{\text{loxex}}$ mice; and C. Harvey, B. Sabatini, W. Regehr, N. Uchida, J. Williams, and R. Wise for discussions and comments on the manuscript. We acknowledge the Neurobiology Imaging Facility (supported by P30NS072030) and Cell Biology Microscopy Facility for microscope availability and advice. **Funding:** This work was supported by the NIH (R01NS103484 and R01NS083898 to P.S.K. and NINDS Intramural Research Program Grant NS003135 to Z.M.K.), the European Research Council (ERC CoG 865634 to S.H.), the German Research Foundation (DFG; HA6386/10-1 to S.H.), the Dean's Initiative Award for Innovation (to P.S.K.), a Harvard-MIT Joint Research Grant (to P.S.K.), and a

Gordon family fellowship (to C.L.). X.C. is a visiting graduate student and received a PhD Mobility National Grants fellowship from Xi'an Jiaotong University/China Scholarship Council. **Author contributions:** Conceptualization: C.L. and P.S.K. Methodology: C.L., X.C., A.R.-J., P.F.K., Z.M.K., S.H., and P.S.K. Investigation: C.L., X.C., A.R.-J., and P.F.K. Resources: Y.L. Visualization: C.L., A.R.-J., P.F.K., and P.S.K. Funding acquisition: P.S.K. Project administration: C.L. and P.S.K. Supervision: C.L. and P.S.K. Writing, original draft: C.L. and P.S.K. Writing, review and editing: C.L., X.C., A.R.-J., P.F.K., Y.L., Z.M.K., S.H., and P.S.K. **Competing interests:** Y.L. is listed as an inventor on a patent application (PCT/CN2018/107533) describing GRAB probes. The other authors declare no competing interests. **Data and material availability:** All data and code are available at Zenodo (40, 41).

SUPPLEMENTARY MATERIALS

science.org/doi/10.1126/science.abn0532
Materials and Methods
Figs. S1 to S11
References (42–48)
MDAR Reproducibility Checklist
Movies S1 to S2

31 October 2021; accepted 23 February 2022
10.1126/science.abn0532

REPORTS

THERMOELECTRICS

High thermoelectric performance realized through manipulating layered phonon-electron decoupling

Lizhong Su¹, Dongyang Wang¹, Sining Wang¹, Bingchao Qin¹, Yuping Wang¹, Yongxin Qin¹, Yang Jin¹, Cheng Chang^{2*}, Li-Dong Zhao^{1,3*}

Thermoelectric materials allow for direct conversion between heat and electricity, offering the potential for power generation. The average dimensionless figure of merit ZT_{ave} determines device efficiency. N-type tin selenide crystals exhibit outstanding three-dimensional charge and two-dimensional phonon transport along the out-of-plane direction, contributing to a high maximum figure of merit Z_{max} of $\sim 3.6 \times 10^{-3}$ per kelvin but a moderate ZT_{ave} of ~ 1.1 . We found an attractive high Z_{max} of $\sim 4.1 \times 10^{-3}$ per kelvin at 748 kelvin and a ZT_{ave} of ~ 1.7 at 300 to 773 kelvin in chlorine-doped and lead-alloyed tin selenide crystals by phonon-electron decoupling. The chlorine-induced low deformation potential improved the carrier mobility. The lead-induced mass and strain fluctuations reduced the lattice thermal conductivity. Phonon-electron decoupling plays a critical role to achieve high-performance thermoelectrics.

Thermoelectric materials have a huge potential for green energy generation because they can realize direct conversion between heat and electricity (1–4). The thermoelectric performance is determined by a dimensionless figure of merit $ZT = S^2\sigma T/\kappa_{\text{tot}}$, where S is the Seebeck coefficient; σ is the electrical conductivity; T is the temperature in kelvin; and κ_{tot} is the total thermal conductivity, which includes the lattice thermal conductivity κ_{lat} and the electronic thermal conductivity κ_{ele} (5). Although the complex interrelationships between these parameters pose a challenge for optimizing

thermoelectric performance (6, 7), after decades of effort, researchers have developed several strategies to resolve it, including band structure engineering to enhance electrical transport properties (8–10), designing multidimensional defects to suppress thermal conduction (11–13), and exploiting intrinsically low-thermal conductivity materials to focus on the optimization of electrical transport properties (14–17). Owing to these strategies, thermoelectric materials with ZT_{max} values beyond 2.0 are no longer as rare as they were decades ago. However, high ZT values may originate from the temperature factor. It is more intuitive to evaluate the electron and phonon transports at different temperatures using Z instead of ZT . With regard to the thermoelectric device setup, some state-of-the-art thermoelectric materials still fail to meet the necessary requirements

¹School of Materials Science and Engineering, Beihang University, Beijing 100191, China. ²Institute of Science and Technology Austria, 3400 Klosterneuburg, Austria.

*Corresponding author. Email: cheng.chang@ist.ac.at (C.C.); zhaolidong@buaa.edu.cn (L.-D.Z.)

because the practical thermoelectric device requires high ZT in a wide temperature range, namely high ZT_{ave} .

Wide-bandgap semiconductors have recently received much attention because of their characteristics of exhibiting high thermoelectric performance over a wide temperature range (18). SnSe, a layered semiconductor with a wide bandgap of $E_g \sim 33 k_B T$ (0.86 eV), exhibits notable thermoelectric performance in both p- and n-type crystals (19–21). The recent strategy of momentum and energy multiband alignment in p-type SnSe crystals has achieved a high ZT_{ave} of ~ 1.9 at 300 to 773 K along the in-plane direction (22). However, the thermoelectric performance of its n-type counterpart in the same temperature range requires further improvement. In contrast to p-type SnSe crystals, n-type SnSe crystals achieve higher thermoelectric performance in the out-of-plane direction than in the in-plane direction (23, 24). The different optimized crystallographic directions originate from the distinct layered lattice structures. The thermal transport in both p- and n-type SnSe crystals is nearly the same because the phonon dispersions are related to the lattice vibration and independent of the carrier type. Thus, all crystallographic directions have low κ_{lat} because of the strong anharmonicity, and the out-of-plane κ_{lat} is the lowest because of the extra interlayer phonon scattering [two-dimensional (2D) phonon] (15). However, the carrier transport varies in p- and n-type SnSe crystals because of the different band dispersions in the valence and conduction bands, respectively. The charge density in p-type SnSe tends to overlap within the in-plane direction but along the out-of-plane direction in n-type SnSe (3D charge). Therefore, the in-plane direction in p-type SnSe crystals presents the optimized thermoelectric performance owing to the ultrahigh in-plane charge transport and the low phonon transport, whereas the out-of-plane direction in n-type SnSe crystals presents the optimized thermoelectric performance because of the 3D charge transport and the lowest 2D phonon transport. Although the established 3D charge and 2D phonon transport of n-type SnSe facilitate high electrical transport properties while using the lowest κ_{lat} along the out-of-plane direction, the strong phonon-electron coupling along the out-of-plane direction prohibits the further improvement of the carrier mobility (μ_{H}) and the power factor ($PF = S^2\sigma$).

Improving μ_{H} is vital for achieving high ZT_{ave} in a wide temperature range (25, 26). Because of the absence of nanostructures and grain boundaries, μ_{H} in SnSe crystals is primarily determined by acoustic phonon scattering, which can be expressed as $\mu_{\text{H}} \sim AC_1/[m_1^*(m_b^*k_B T)^{1.5}\Xi^2]$, where C_1 is the longitudinal elastic modulus, m_1^* is the inertial ef-

fective mass, m_b^* is the effective mass of a single band, k_B is the Boltzmann constant, Ξ is the deformation potential, and A is a coefficient associated with the Fermi integral and other physical constants (27–29). Based on the equation, increasing C_1 or reducing effective mass (m^*) can result in a higher μ_{H} ; however, it can lead to a respective detrimental increase in κ_{lat} or decrease in S . By contrast, a lower deformation potential can improve μ_{H} without detrimentally affecting κ_{lat} and m^* . Deformation potential is an intrinsic material parameter correlated to the crystal structure that describes the energy change of the electronic band with the lattice elastic deformation, thereby providing the phonon-electron coupling (30–32). This motivated us to modify the crystal structure of n-type SnSe crystals to decrease the deformation potential and mitigate the phonon-electron coupling, thereby enhancing μ_{H} in the out-of-plane direction.

We investigated the effect of Cl doping and Pb alloying on the electrical and thermal transport of n-type SnSe crystals. First, we found that Cl-doped SnSe (SnSe-Cl) crystals exhibited $\sim 30\%$ higher μ_{H} than Br-doped SnSe

(SnSe-Br) crystals without deteriorating m^* . Additionally, SnSe-Cl displayed a notably higher crystal symmetry in the results of high-temperature synchrotron radiation x-ray diffraction (SR-XRD) (figs. S1 to S3). This prominent structural modification resulted in their lowered deformation potential, largely decoupling the electron and phonon transports and consequently enhancing μ_{H} (Fig. 1A). Combined with the unchanged m^* , we found a marked improvement in PF . Specifically, the room-temperature PF increased from $\sim 8.6 \mu\text{W cm}^{-1} \text{K}^{-2}$ in SnSe-Br to $\sim 12.8 \mu\text{W cm}^{-1} \text{K}^{-2}$ in SnSe-Cl crystals with the comparable Hall carrier concentration (n_{H}) (fig. S4), and ZT_{ave} at 300 to 773 K increased by $\sim 20\%$ to ~ 1.2 . These results indicate that improving μ_{H} can achieve a higher ZT_{ave} . Moreover, we introduced Pb in SnSe-Cl to further optimize ZT_{ave} . Pb alloying promotes charge and phonon transport in two aspects: It increases m^* through conduction band convergence (33) and reduces κ_{lat} through enhanced mass and strain fluctuations. We obtained a low κ_{tot} of $0.24 \text{ W m}^{-1} \text{K}^{-1}$ at 748 K in Pb-alloyed SnSe. Additionally, we investigated and reevaluated the κ_{tot} during the two-step

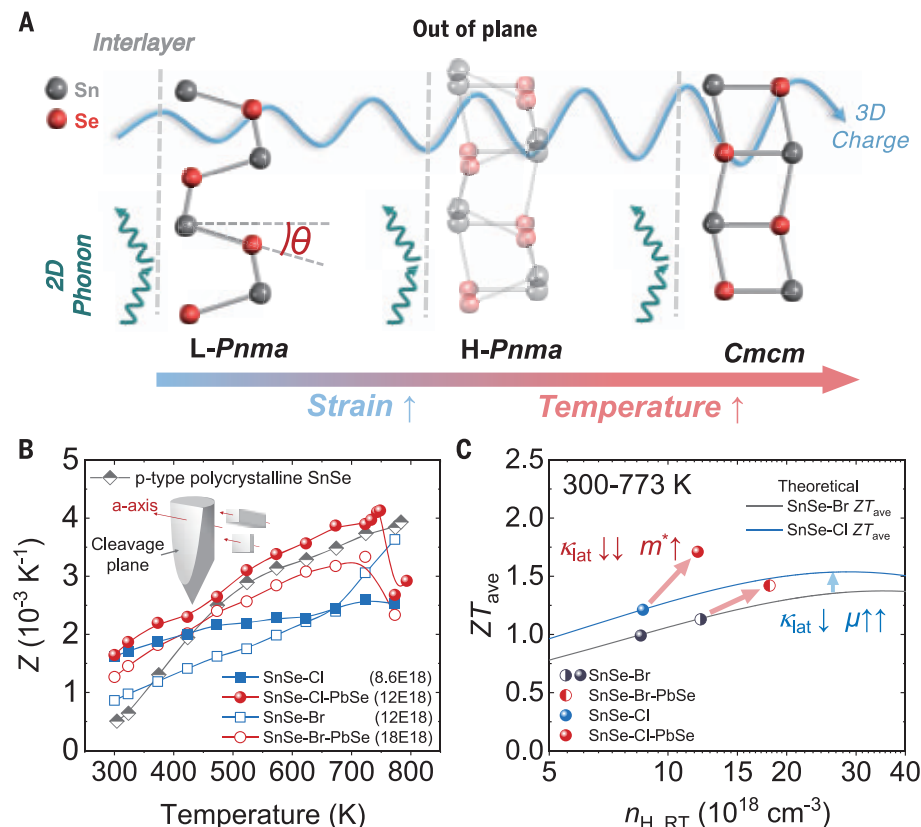


Fig. 1. Electron and phonon decoupling by intensifying 3D charge and 2D phonon transports. (A) Schematic of electron and phonon transports in SnSe crystal along the out-of-plane direction. (B) Z as a function of temperature. The inset illustrates the out-of-plane measurement direction (a axis). SnSe-Br, SnSe-Cl, SnSe-Br-PbSe, and SnSe-Cl-PbSe represent Br- or Cl-doped and Pb-alloyed SnSe crystals with the optimized thermoelectric performance (figs. S5 to S7). (C) ZT_{ave} as a function of carrier concentration at 300 to 773 K along the out-of-plane direction. The theoretical lines were calculated using the single-band model, assuming that κ_{lat} is independent of carrier concentration. SnSe-Br, SnSe-Br-PbSe, and p-type polycrystalline SnSe data are taken from (23, 33, 44). RT, room temperature.

continuous phase transition. We applied a phase transition rate model to eliminate the overestimating effect of latent heat (ΔH) on the real heat capacity (C_p) and κ_{tot} . Lastly, we achieved a Z_{max} of $\sim 4.1 \times 10^{-3} \text{ K}^{-1}$ at 748 K (Fig. 1B) and a ZT_{ave} of ~ 1.7 at 300 to 773 K (Fig. 1C) in n-type Cl-doped and Pb-alloyed SnSe crystals (SnSe-Cl-PbSe).

We synthesized a series of SnSe-Br and SnSe-Cl crystals with different n_{H} values (figs. S5 and S6). The maximum n_{H} obtained in SnSe-Cl was lower than that in SnSe-Br as a result of the lower solubility and higher electronegativity of Cl. We compared the electrical transport properties of SnSe-Cl ($8.6 \times 10^{18} \text{ cm}^{-3}$) and SnSe-Br ($1.2 \times 10^{19} \text{ cm}^{-3}$) in the out-of-plane direction with their respective optimized thermoelectric performances (Fig. 2). Both samples exhibited nearly identical electrical conductivity σ at different temperatures, which indicated higher μ_{H} in SnSe-Cl, according to $\sigma = n_{\text{H}}e\mu_{\text{H}}$ (where e is the electron charge) (Fig. 2A). We observed the same phenomenon in SnSe-Cl-PbSe and Pb-alloyed SnSe-Br (SnSe-Br-PbSe) with the optimized thermoelectric performance as well (Fig. 2A). However, S for SnSe-Cl was superior to that of SnSe-Br over the entire temperature range. Specifically, the absolute room-temperature S increased substantially from $\sim 182 \mu\text{V K}^{-1}$ in SnSe-Br to $\sim 236 \mu\text{V K}^{-1}$ in SnSe-Cl. Likewise, for similar σ , S for SnSe-Cl-PbSe was higher than that of SnSe-Br-PbSe. To investigate the origin of these high Seebeck coefficient values, we compared our experimental data with the Pisarenko line $S = \frac{8\pi^2 k_{\text{B}}^2}{3eh^2} m^* T \left(\frac{\pi}{3n_{\text{H}}}\right)^{\frac{2}{3}}$ (where h is the Planck constant) (23). For both SnSe-Br and SnSe-Cl, S was consistent with the single parabolic band model at room temperature, indicating identical m^* values of SnSe-Cl and SnSe-Br at $m^* = 0.47m_{\text{e}}$ (Fig. 2C), and the high S of SnSe-Cl was solely derived from the low n_{H} . Combining high μ_{H} with large S , we obtained a substantial improvement in PF from $\sim 7.7 \mu\text{W cm}^{-1} \text{ K}^{-2}$ in SnSe-Br to $\sim 12.8 \mu\text{W cm}^{-1} \text{ K}^{-2}$ in SnSe-Cl at 300 K (Fig. 2D). However, for SnSe-Br-PbSe and SnSe-Cl-PbSe, S deviated from the SnSe-based Pisarenko line, indicating conduction band convergence and enhanced m^* (33). Additionally, we synthesized SnSe-Cl and SnSe-Br with comparable n_{H} (fig. S4). Herein, although both samples had identical S values, SnSe-Cl revealed high σ and PF , confirming the superior electrical transport properties of SnSe-Cl.

We illustrated the room-temperature μ_{H} as a function of n_{H} (Fig. 3A). The value of μ_{H} for SnSe-Cl was 30% higher than that of SnSe-Br, even though their m^* values were identical. To clarify the origin of the enhanced μ_{H} , we fit the experimental μ_{H} to the deformation potential model (34) (Fig. 3B). The deformation potential we calculated from the experimental data demonstrated that Cl doping reduced the deformation potential of n-type SnSe crystals enormously—that is, from $\sim 22.4 \text{ eV}$ in SnSe-Br

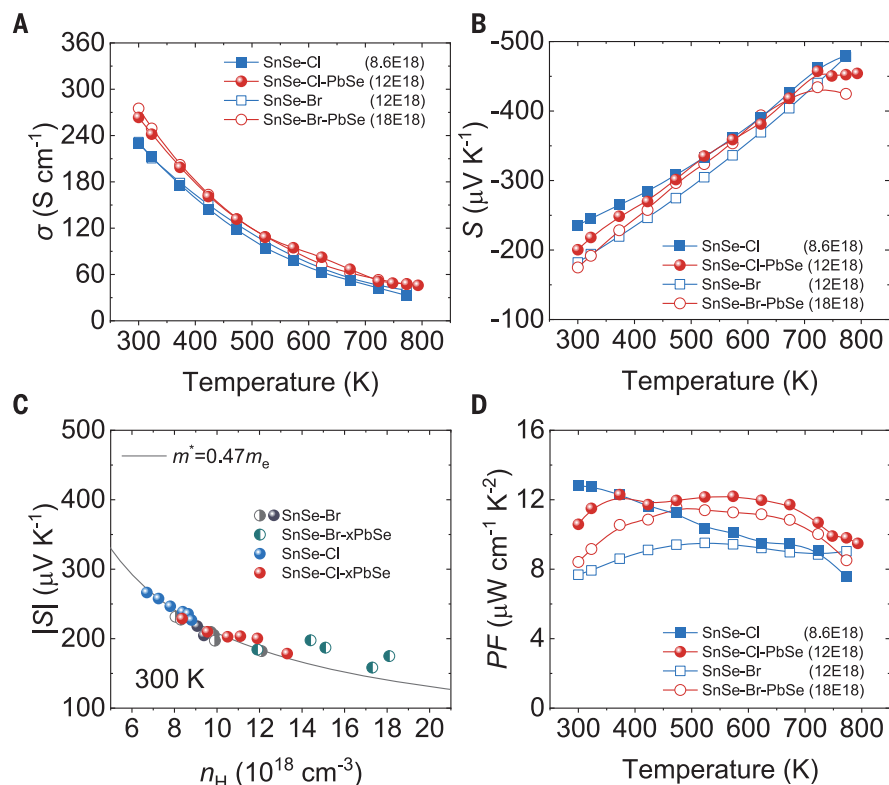


Fig. 2. Electrical transport properties along the out-of-plane direction. (A) Electrical conductivity.

(B) Seebeck coefficient. (C) Seebeck coefficients as a function of carrier concentration at 300 K.

SnSe-Br-xPbSe and SnSe-Cl-xPbSe present Br- or Cl-doped SnSe crystals alloyed with different PbSe amounts ($x = 0$ to 12%) (fig. S7). (D) Power factor. Thermoelectric performance of SnSe-Br/Cl and SnSe-Cl-PbSe samples with different carrier concentrations can be found in figs. S4 to S8. SnSe-Br and SnSe-Br-PbSe data are taken from (23, 33).

to $\sim 17.5 \text{ eV}$ in SnSe-Cl—and was therefore responsible for the improved μ_{H} . The increase in deformation potential after Pb alloying was primarily the result of the enhanced valley degeneracy and alloy scattering potential (32, 35). Nevertheless, the deformation potential decreased with increasing Pb content and reduced to $\sim 17 \text{ eV}$ at 10% Pb alloying, which implies that underlying mechanisms compensated for the detrimental effect of enhanced valley degeneracy and alloy scattering potential.

To illustrate the origin of the reduced deformation potential, we characterized the crystal symmetry evolution in SnSe-Cl, SnSe-Br, and SnSe-Cl-PbSe. The angle θ between the Sn-Se bond and the a axis (Fig. 3C, inset) was selected as an indicator of crystal symmetry (i.e., a lower θ value corresponds to higher crystal symmetry). The high-temperature SR-XRD results revealed that θ was much smaller in SnSe-Cl than in SnSe-Br, and it was further decreased after Pb alloying (Fig. 3C); this can be explained by the introduced strain because of atom substitution. The effective atomic radii were 118 pm (Sn^{2+}), 198 pm (Se^{2-}), 196 pm (Br^-), 181 pm (Cl^-), and 119 pm (Pb^{2+})

(36). Accordingly, Cl^- introduced more prominent strains in the SnSe crystal than Br^- as a result of the more substantial size deviation between Se^{2-} and Cl^- ; this pushed Se atoms toward the adjacent Sn atoms, which reduced θ . However, even though the effective radius of Pb^{2+} is similar to that of Sn^{2+} , the strain became evident as the amount of Pb increased. As a result, both Cl^- and Pb^{2+} substitutes introduced strains to increase crystal symmetry. Because high crystal symmetry implies weak phonon-electron coupling and low deformation potential (37–39), the strain could cause lower deformation potential in SnSe. Beyond the strain, the rising temperature proved to be another cause for the lower deformation potential of SnSe. A distinct two-step continuous phase transition starts from 600 to 800 K in SnSe, wherein the crystal structure evolves from low-symmetry $Pnma$ ($L-Pnma$) to high-symmetry $Pnma$ ($H-Pnma$) and then to the $Cmcm$ phase (33). Consequently, θ decreases with increasing temperature toward 0° , which is responsible for the temperature-dependent μ_{H} deviation in the acoustic phonon scattering model ($\mu_{\text{H}} \propto T^{-3/2}$; Fig. 3D) (33, 40). We also performed density functional theory

(DFT) calculations (figs. S9 to S11) on the basis of the crystal structures of different compositions and temperatures to provide an intuitive interrelationship between the strain- or temperature-induced higher crystal symmetry and the improved μ_H . According to the projected density of states near the conduction band edge and the charge density distribution (34), the out-of-plane charge density is more overlapped with higher crystal symmetry, facilitating the electron transport through the interlayers.

We calculated the weighted mobility ($\mu_w = \mu_H m^{*3/2}$)—the electron mobility weighted by the density of the electronic states (Fig. 3D). Compared with the exponential decline of μ_H , μ_w of all n-type SnSe crystals exhibited a flat decline curve that even increased during the continuous phase transition. Moreover, the μ_w curve upturn was pushed to a lower temperature by Pb alloying because Pb promotes continuous phase transition to a wider temperature range (33). The wide range of high μ_w denoted the enlarged m^* at high temperatures due to band convergence, indicating that crystal symmetry also affects the band degeneracy (23, 33) and contributed to the wide temperature range electrical transport enhancement in SnSe-Cl and SnSe-Cl-PbSe. It is noteworthy that the critical phase tran-

sition temperature is reduced by Pb alloying, leading to the downturn of weighted mobility above 750 K.

SnSe exhibited ultralow κ_{lat} because of its strong anharmonicity. Owing to the layered crystal structure and weak covalent bonding along the a axis, κ_{lat} approached the amorphous limit along the out-of-plane direction at ~ 800 K (23), which can be shifted to lower temperatures by Pb alloying (fig. S7). However, κ_{lat} at low temperatures is still much higher than the amorphous limit because of the weak acoustic phonon scattering. Thus, mass and strain fluctuations induced by alloying still work for further reducing κ_{lat} . To investigate the effect of continuous phase transition on κ_{tot} , we measured C_p of SnSe-Cl-PbSe at different heating rates using differential scanning calorimetry (DSC) and the thermal diffusivity (D) plots near the phase transition temperature using the laser flash method (Fig. 4, A and B, and fig. S12). Notably, we found a pronounced reduction in D and rise in C_p within ~ 50 K near the phase transition temperature that correspond to the phase transition from $H\text{-}Pnma$ to $Cmcm$ (40, 41). This was consistent with other phase change materials, such as Cu_2Se , Cu_2S , Ag_2S , and Ag_2Se , which originate from the critical scattering of phonons and electrons and ΔH during phase transition (42, 43). Notably,

the phase transition from $L\text{-}Pnma$ to $H\text{-}Pnma$ did not exhibit the same behavior (44).

To gain insight into the abnormal thermal transport during the phase transition, we applied the phase transition rate model to correct the measured C_p (34). Generally, κ_{tot} can be calculated according to $\kappa_{\text{tot}} = D\rho C_p$, where ρ is the sample density (45). However, this equation was not applicable to phase change materials because of the abnormally elevated C_p . Therefore, we used the phase transition rate model to obtain the modified κ_{tot} , given as $\kappa_{\text{tot}} = D\rho C_{p,0} \left(1 + \frac{\Delta H}{C_{p,0}} \frac{\partial a}{\partial T} \frac{\partial a}{\partial t}\right)$, where $C_{p,0}$ is the normal heat capacity without the phase transition contribution, t is the time, and a is the molar fraction of the high-temperature phase. Based on the equation, ΔH and the phase transition rate $\frac{\partial a}{\partial t}$ play critical roles in thermal transport during phase transition. We first discussed two limiting conditions: (i) When the phase transition rate is very low ($\frac{\partial a}{\partial t} \rightarrow 0$) or ΔH is very low ($\Delta H \rightarrow 0$), $\kappa_{\text{tot}} = D\rho C_{p,0}$, which indicates that phase transition does not affect the heat transport—the phase transition from $L\text{-}Pnma$ to $H\text{-}Pnma$ fits this situation because of the negligible ΔH at 300 to 723 K (Fig. 4B) (44). (ii) When the phase transition rate is very fast ($\frac{\partial a}{\partial t} \rightarrow \infty$), a is equal to the equivalent a (a_{eq}) and $\kappa_{\text{tot}} = D\rho C_{p,0} \left(1 + \frac{\Delta H}{C_{p,0}} \frac{\partial a_{\text{eq}}}{\partial T}\right) = D\rho C_{p,m}$, where $C_{p,m}$ is the heat capacity measured by DSC. We compared SnSe with other phase change materials and discovered that SnSe exhibited a much lower phase transition rate of $<0.1 \text{ K}^{-1}$ (figs. S12 to S14). To obtain an accurate κ_{tot} during the $H\text{-}Pnma$ -to- $Cmcm$ transition, we modified C_p using the phase transition rate model; the modified C_p exhibited slightly lower values than the average C_p (the values of C_p measured at different heating rates are averaged) (Fig. 4C). As a result, κ_{tot} evaluated by the modified C_p was slightly lower than that evaluated by the average C_p with $\kappa_{\text{tot}} \sim 0.24 \text{ W m}^{-1} \text{ K}^{-1}$ and $\kappa_{\text{lat}} \sim 0.18 \text{ W m}^{-1} \text{ K}^{-1}$ at 748 K (Fig. 4D, inset, and fig. S15). We compared the heat transport properties of SnSe-Cl-PbSe with different calculated C_p values as well, using the Debye model, the Kopp-Neumann model, and the Dulong-Petit model (Fig. 4D, inset, and fig. S16); κ_{tot} revealed similar values at 300 to 723 K with apparent differences at 723 to 748 K, demonstrating the importance of modifying C_p to obtain the real κ_{tot} during phase transition. Figure 4D displays the κ_{tot} values of SnSe-Cl/Br and SnSe-Cl/Br-PbSe. SnSe-Cl exhibited a lower κ_{tot} than SnSe-Br because of the lower n_H and large lattice strains. Moreover, κ_{tot} was further reduced in SnSe-Cl/Br-PbSe because of the mass and strain fluctuations by Pb, particularly at low temperatures. It is noteworthy that low κ_{tot} at high temperatures in SnSe-Cl/Br-PbSe is also derived from the mass and strain fluctuations. The maximum κ_{tot} calculation difference using

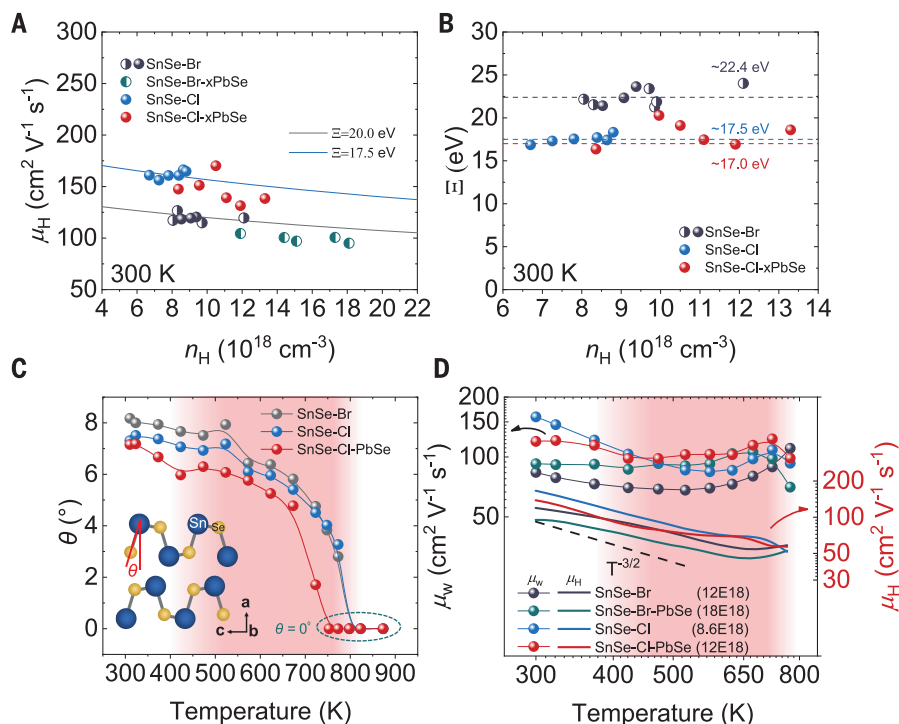


Fig. 3. Promoting carrier mobility. (A) Room-temperature Hall mobility as a function of the carrier concentration. The solid lines represent the single Kane band model with different deformation potentials. (B) Calculated deformation potential for n-type SnSe crystals (34). (C) Angle θ as a function of temperature. The inset is the definition of θ . The red block represents the continuous phase transition of SnSe. (D) Temperature-dependent weighted mobility and Hall mobility. SnSe-Br and SnSe-Br-PbSe data are taken from (23, 33).

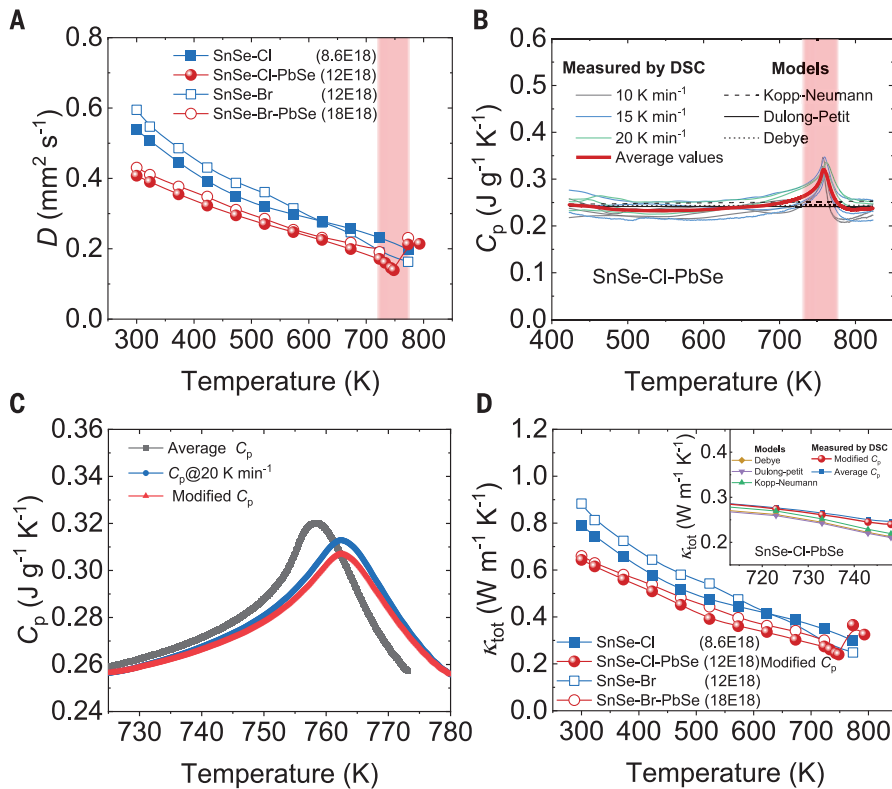


Fig. 4. Thermal transport properties along the out-of-plane direction. (A) Thermal diffusivity. The red block represents the phase transition from H-*Pnma* to *Cmcm*. (B) Heat capacity of SnSe-Cl-PbSe measured at different heating rates using DSC. Different calculated C_p values are presented for comparison, using the Debye model, the Kopp-Neumann model, and the Dulong-Petit model. (C) The comparison between averaged heat capacity of different heating rates, heat capacity measured at 20 K min^{-1} , and modified heat capacity using the phase transition rate model near the phase transition temperature. (D) Total thermal conductivity. Inset displays the total thermal conductivity comparisons derived from different heat capacities. SnSe-Br and SnSe-Br-PbSe data are taken from (23, 33).

modified C_p and average C_p is $<0.01 \text{ W m}^{-1} \text{ K}^{-1}$ (Fig. 4D, inset).

We demonstrated electron and phonon decoupling by facilitating 3D charge transmission and strengthening 2D phonon scattering using Cl and Pb in n-type SnSe to improve μ_H and reduce κ_{lat} . We realized high μ_H by reducing the deformation potential, which was derived from the strain- and temperature-induced high crystal symmetry. Moreover, κ_{lat} was reduced by inducing mass and strain fluctuations through Pb alloying. A phase transition rate model was applied to modify the real κ_{tot} during phase transition. At last, we obtained a Z_{max} of $\sim 4.1 \times 10^{-3} \text{ K}^{-1}$ at 748 K and a high ZT_{ave} of ~ 1.7 at 300 to 773 K in n-type SnSe-Cl-PbSe crystals. The highest performance shows good thermal stability (fig. S17). We measured thermoelectric properties in the in-plane and out-of-plane directions for SnSe-Cl-PbSe as well to indicate the superior out-of-plane thermoelectric performance (fig. S18). These findings mitigate the thermoelectric performance gap between p-type and n-type SnSe crystals and indicate the critical role of

phonon-electron decoupling to achieve high-performance thermoelectrics.

Compared with the substantial progress in thermoelectric materials, the research on thermoelectric modules has progressed slowly (46). The module fabrication using state-of-the-art materials has been the most critical task for broad commercial applications at the present stage. Future research should focus more on the systematic basic research on the engineering issues, such as module structure, contact layer, interface stability, etc. Specifically, the low mechanical strength is another challenge for layered materials. Therefore, increasing mechanical strength through manipulating weak chemical bonds between layers or designing thermoelectric film modules using their advanced out-of-plane transports would be promising areas for future work.

REFERENCES AND NOTES

1. T. R. Wei, C. F. Wu, F. Li, J. F. Li, *J. Mater. Chem.* **4**, 304–320 (2018).
2. G. Tan, L. D. Zhao, M. G. Kanatzidis, *Chem. Rev.* **116**, 12123–12149 (2016).
3. W. Zhao *et al.*, *Nature* **549**, 247–251 (2017).
4. B. C. Qin, D. Y. Wang, L. D. Zhao, *InfoMat* **3**, 755–789 (2021).
5. W. S. Liu *et al.*, *Mater. Today Phys.* **1**, 50–60 (2017).

6. X. Shi, L. Chen, *Nat. Mater.* **15**, 691–692 (2016).
7. J. Yang *et al.*, *NPJ Comput. Mater.* **2**, 15015 (2016).
8. J. Xin *et al.*, *NPJ Quantum Mater.* **3**, 9 (2018).
9. J. P. Heremans *et al.*, *Science* **321**, 554–557 (2008).
10. Y. Pei *et al.*, *Nature* **473**, 66–69 (2011).
11. X. Tang, Z. Li, W. Liu, Q. Zhang, C. Uher, *Interdiscip. Mater.* **1**, 88–115 (2022).
12. B. Jiang *et al.*, *Science* **371**, 830–834 (2021).
13. K. Biswas *et al.*, *Nature* **489**, 414–418 (2012).
14. W. He *et al.*, *Science* **365**, 1418–1424 (2019).
15. L. D. Zhao *et al.*, *Nature* **508**, 373–377 (2014).
16. S. Roychowdhury *et al.*, *Science* **371**, 722–727 (2021).
17. J. Mao *et al.*, *Science* **365**, 495–498 (2019).
18. Y. Xiao, L. D. Zhao, *Science* **367**, 1196–1197 (2020).
19. C. Chang, G. J. Tan, J. Q. He, M. G. Kanatzidis, L. D. Zhao, *Chem. Mater.* **30**, 7355–7367 (2018).
20. Z. G. Chen, X. L. Shi, L. D. Zhao, J. Zou, *Prog. Mater. Sci.* **97**, 283–346 (2018).
21. L. D. Zhao *et al.*, *Science* **351**, 141–144 (2016).
22. B. Qin *et al.*, *Science* **373**, 556–561 (2021).
23. C. Chang *et al.*, *Science* **360**, 778–783 (2018).
24. L. S. Mao *et al.*, *Energy Environ. Sci.* **13**, 616–621 (2020).
25. L.-D. Zhao, S. Wang, Y. Xiao, *Acta Metall. Sin.* **57**, 1171–1183 (2021).
26. G. J. Snyder *et al.*, *Adv. Mater.* **32**, e2001537 (2020).
27. H. Wang, Y. Pei, A. D. LaLonde, G. J. Snyder, *Proc. Natl. Acad. Sci. U.S.A.* **109**, 9705–9709 (2012).
28. C. Herring, E. Vogt, *Phys. Rev.* **101**, 944–961 (1956).
29. J. Bardeen, W. Shockley, *Phys. Rev.* **80**, 72–80 (1950).
30. M. V. Fischetti, S. E. Laux, *J. Appl. Phys.* **80**, 2234–2252 (1996).
31. H. Xie *et al.*, *Adv. Funct. Mater.* **23**, 5123–5130 (2013).
32. X. H. Liu *et al.*, *Adv. Energy Mater.* **3**, 1238–1244 (2013).
33. C. Chang *et al.*, *Adv. Energy Mater.* **9**, 1901334 (2019).
34. Materials and methods are available as supplementary materials.
35. H. Wang *et al.*, *Mater. Adv.* **3**, 734–755 (2022).
36. R. D. Shannon, *Acta Cryst.* **A32**, 751–767 (1976).
37. J. Ma, R. Yang, H. Chen, *Nat. Commun.* **12**, 2314 (2021).
38. J. Zhou *et al.*, *Nat. Commun.* **9**, 1721 (2018).
39. B. Qin *et al.*, *J. Am. Chem. Soc.* **141**, 1141–1149 (2019).
40. A. Dewandre *et al.*, *Phys. Rev. Lett.* **117**, 276601 (2016).
41. K. Kutorasinski, B. Wiendlocha, S. Kaprzyk, J. Tobola, *Phys. Rev. B* **91**, 205201 (2015).
42. H. Chen *et al.*, *Adv. Mater.* **31**, e1806518 (2019).
43. M. T. Agne, P. W. Voorhees, G. J. Snyder, *Adv. Mater.* **31**, e1902980 (2019).
44. C. Zhou *et al.*, *Nat. Mater.* **20**, 1378–1384 (2021).
45. D. Zhao, X. Qian, X. Gu, S. A. Jajja, R. Yang, *J. Electron. Packag.* **138**, 040802 (2016).
46. Q. Yan, M. G. Kanatzidis, *Nat. Mater.* 10.1038/s41563-021-01109-w (2021).

ACKNOWLEDGMENTS

We thank BL14BI (Shanghai Synchrotron Radiation Facility) for the SR-XRD experiments. **Funding:** This work was supported by the Basic Science Center Project of the National Natural Science Foundation of China (51788104), the National Key Research and Development Program of China (2018YFA0702100), the National Science Fund for Distinguished Young Scholars (51925101), the 111 Project (B17002), the Lise Meitner Project (M2889-N), and the National Key Research and Development Program of China (2018YFB0703600). This work is also supported by the National Postdoctoral Program for Innovative Talents (BX20200028). L.-D.Z. is thankful for the high-performance computing resources at Beihang University. **Author contributions:** L.S., C.C., and L.-D.Z. synthesized the samples, designed and carried out the experiments, analyzed the results, and wrote the paper. D.W. conducted the theoretical calculations, analyzed the results, and wrote the paper. S.W. carried out the deformation potential. B.Q. and Y.W. carried out the Hall measurements. Y.Q. and Y.J. carried out the DSC measurements. L.S., B.Q., and Y.W. carried out the Rietveld refinements. All authors conceived the experiments, analyzed the results, and coedited the manuscript. **Competing interests:** The authors declare no competing interests. **Data and materials availability:** All data are available in the main text and the supplementary materials.

SUPPLEMENTARY MATERIALS

science.org/doi/10.1126/science.abn897
Materials and Methods
Figs. S1 to S18
Tables S1 to S8
References (47–55)

30 December 2021; accepted 23 February 2022
10.1126/science.abn897

MEMBRANES

Hydrocarbon ladder polymers with ultrahigh permselectivity for membrane gas separations

Holden W. H. Lai^{1†}, Francesco M. Benedetti^{2†}, Jun Myun Ahn^{1‡}, Ashley M. Robinson¹, Yingge Wang³, Ingo Pinnau³, Zachary P. Smith^{2*}, Yan Xia^{1*}

Membranes have the potential to substantially reduce energy consumption of industrial chemical separations, but their implementation has been limited owing to a performance upper bound—the trade-off between permeability and selectivity. Although recent developments of highly permeable polymer membranes have advanced the upper bounds for various gas pairs, these polymers typically exhibit limited selectivity. We report a class of hydrocarbon ladder polymers that can achieve both high selectivity and high permeability in membrane separations for many industrially relevant gas mixtures. Additionally, their corresponding films exhibit desirable mechanical and thermal properties. Tuning of the ladder polymer backbone configuration was found to have a profound effect on separation performance and aging behavior.

Industrial chemical separations account for 15% of the world's energy consumption (1). Membrane processes can be up to 10 times as energy efficient as traditional separation methods such as distillation and absorption (1). However, a major limitation for membrane-based gas separations has been the well-known trade-off between permeability and selectivity of membrane materials, resulting in performance upper bounds (2). Commercial membranes usually have moder-

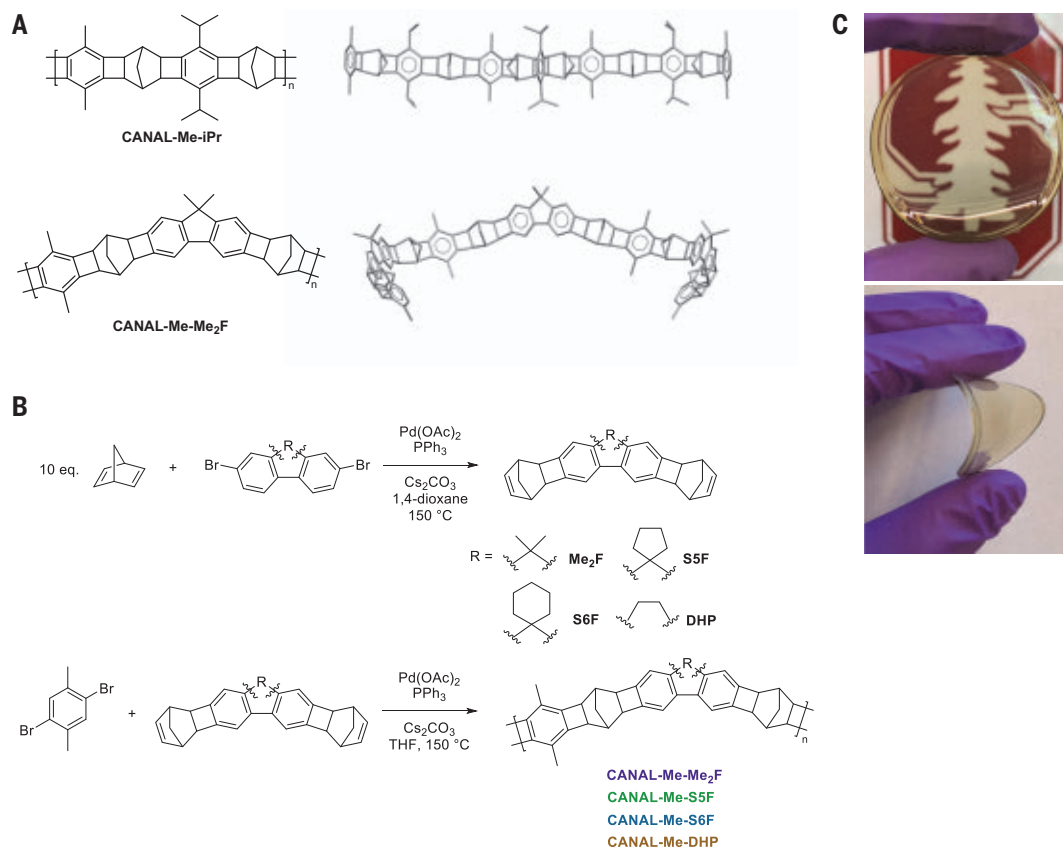
ate selectivity but low permeability. Solution-processable polymers of intrinsic microporosity (PIMs) have emerged as attractive membrane materials. The rigid and contorted PIM backbones lead to frustrated chain packing in the solid state, resulting in abundant fractional free volume and, thus, ultrahigh permeability relative to traditional polymers (3–5). PIMs define the upper bounds for nearly all gas separations (6, 7). Despite these promising recent advances, it remains a challenge to design PIMs

with high selectivity, which is essential for the implementation of membranes in industrially relevant applications. For example, CO₂/CH₄ selectivity >40 and H₂/CH₄ selectivity >50 are needed for natural gas processing and hydrogen recovery, respectively, to meet process specifications (8). Moreover, experimental mixed-gas CO₂/CH₄ separation performance for PIM membranes is far below the pure-gas upper bound limit that is based on calculated ideal selectivities (8). To design polymer membranes for natural gas and biogas upgrading, as well as other gas and vapor separations, it is essential to evaluate membrane performance through mixed-gas permeation experiments at pressures relevant to real processes.

We developed a family of microporous ladder polymers with rigid backbones of fused norbornyl benzocyclobutene repeat units via

Fig. 1. Molecular structures and films of CANAL ladder polymers.

(A) (Left) Actual and (right) simulated (molecular mechanics) structures of a ribbon-like 2D ladder polymer, CANAL-Me-iPr (top), and a 3D ladder polymer, CANAL-Me-Me₂F (bottom). Me, methyl; iPr, isopropyl. **(B)** Synthesis of CANAL-fluorene and CANAL-dihydrophenanthrene monomers (top) and polymers (bottom). Ac, acetyl; Ph, phenyl; THF, tetrahydrofuran. **(C)** Photos of a 50-μm CANAL-Me-Me₂F film.



¹Department of Chemistry, Stanford University, Stanford, CA 94305, USA. ²Department of Chemical Engineering, Massachusetts Institute of Technology, Cambridge, MA 02139, USA. ³Advanced Membranes and Porous Materials Center, Chemical Engineering Program, Division of Physical Sciences and Engineering, King Abdullah University of Science and Technology (KAUST), Thuwal 23955-6900, Kingdom of Saudi Arabia.

*Corresponding author. Email: zpsmith@mit.edu (Z.P.S.); yanx@stanford.edu (Y.X.)

†Present address: Osmoses Inc., 501 Massachusetts Avenue, Cambridge, MA 02139, USA.

‡Present address: Vertex Pharmaceuticals Incorporated, 50 Northern Avenue, Boston, MA 02210, USA.

catalytic arene-norbornene annulation (CANAL) polymerization from readily available chemicals (9–11). These hydrocarbon polymers have glass-transition temperatures that exceed their thermal decomposition temperatures (>400°C). The original CANAL polymers made from the polymerization of norbornadiene and *p*-dibromobenzene derivatives have a ribbon-like ladder geometry with approximately two-dimensional (2D) contortions (Fig. 1A, top). Films of these microporous polymers exhibited high permeability, but their selectivity was low for gas separation applications (11). By tuning the backbone configuration, we discovered a series of 3D-contorted CANAL ladder polymers (Fig. 1A, bottom) that form mechanically robust films with a combination of ultrahigh selectivity and permeability. These 3D-contorted CANAL polymers were synthesized with 2,7-dibromofluorenes or 2,7-dibromo-9,10-dihydrophenanthrene and norbornadiene as building blocks, yielding an unusual polymer configuration that led to high selectivity and permeability in several gas separations.

One distinct advantage of CANAL chemistry is that many aromatic bromides can be used as monomer building blocks. We envisioned that introducing fluorene or dihydrophenanthrene units would confer additional backbone contortions to CANAL ladder polymers, thus further frustrating chain packing and potentially modulating the polymer microporosity. We synthesized such CANAL polymers via a two-step procedure. The 2,7-dibromofluorene derivatives were first reacted with excess norbornadiene (5 equiv relative to aryl bromide) in the presence of a palladium catalyst to yield ladder dinorbornenes **Me₂F**, **S5F**, **S6F**, and **DHP**, which then underwent efficient and clean CANAL polymerization with *p*-dibromo-*p*-xylene to form ladder polymers CANAL-Me-Me₂F, CANAL-Me-S5F, CANAL-Me-S6F, and CANAL-Me-DHP (Fig. 1B) in high molecular weights (67 to 170 kDa), as determined by gel permeation chromatography light-scattering analysis (fig. S1). These polymers exhibited high surface areas (870 to 1190 m² g⁻¹) and high thermal stability ($T_{d,5\%}$ > 450°C) (table S1).

Mechanically robust films (50 to 60 μm thick) of all of these polymers can be easily prepared by solution casting from chloroform (movie S1). After we pretreated the films to remove residual casting solvent and erase processing history using conditions common for PIMs (heating in vacuo at 120°C for 24 hours, followed by soaking in methanol, and then air drying), we performed pure-gas permeation experiments using gases in this order: H₂, CH₄, N₂, O₂, and CO₂ ($T = 35^\circ\text{C}$, $P = 1$ bar). Fresh films of CANAL-Me-Me₂F exhibited high permeabilities but only moderate selectivities (table S2). Surprisingly, upon aging, separation performance of CANAL-

Me-Me₂F improved markedly. Physical aging is commonly observed for PIMs and is a process that reduces excess free volume as the polymer chains densify into more compact packing (12). Aging of PIMs typically leads to greatly decreased permeability and moderately increased selectivity, often following the upper bound trade-off relationships or slightly improving their performance relative to the upper bound (13). By contrast, aging of 3D CANAL polymers improved performance for several industrially relevant gas pairs—including H₂/CH₄, CO₂/CH₄ (Fig. 2, A and B), H₂/N₂, H₂/CO₂, and O₂/N₂ (figs. S4 and S5 and table S2)—by boosting selectivity.

For CO₂/CH₄ separation, CANAL-Me-Me₂F offers twice the selectivity and 100 times the permeability of cellulose acetate, a widely used commercial membrane material (14). Compared with another commercial membrane

material, polysulfone (14), CANAL-Me-Me₂F is two orders of magnitude more permeable and three times as selective for H₂/CH₄ separation. With H₂ permeability >2000 barrer and H₂/CH₄ selectivity of 185, the H₂/CH₄ performance of aged CANAL-Me-Me₂F exceeds that of other PIMs (Fig. 2A), which typically have H₂/CH₄ selectivity <50. Aged CANAL-Me-Me₂F also exhibited excellent CO₂/CH₄ selectivity of ~46 and high CO₂ permeability of ~600 barrer (Fig. 2B).

Other CANAL-fluorene polymers with cyclic substituents, CANAL-Me-S5F and CANAL-Me-S6F, and CANAL-Me-DHP all showed ultrahigh performance upon aging, similar to that of CANAL-Me-Me₂F (Fig. 2 and fig. S4). This finding suggests that the unusual aging behavior is general among 3D CANAL polymers. Compared with CANAL-fluorene polymers, CANAL-Me-DHP became even more selective,

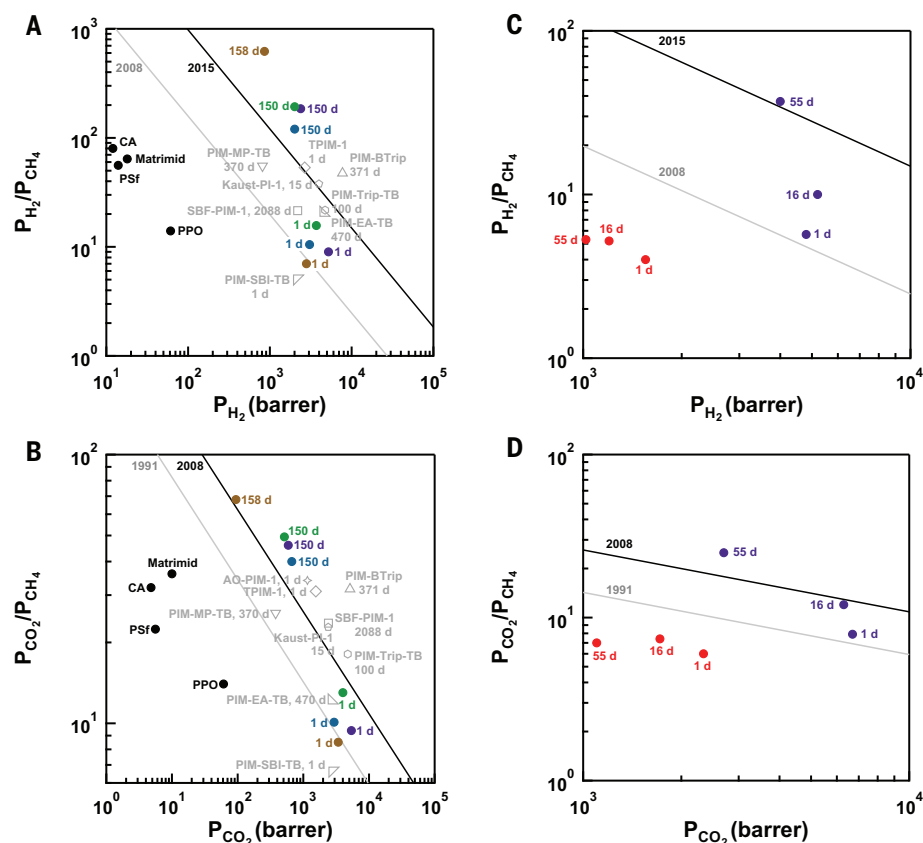


Fig. 2. Pure-gas permeation properties of various CANAL polymers. Pure-gas permeation properties of 50- to 60-μm-thick CANAL-Me-Me₂F (purple), CANAL-Me-S5F (green), CANAL-Me-S6F (blue), and CANAL-Me-DHP (brown) are shown relative to the (A) H₂/CH₄ and (B) CO₂/CH₄ upper bounds. CANAL films plotted in (A) and (B) were heated at 120°C under vacuum for 24 hours, soaked in liquid methanol for 24 hours, and then air dried for 24 hours. State-of-the-art PIMs (open symbols, duration of aging noted in days; see fig. S12 for structures) (3–7, 20–25) and commercial membrane materials [filled black symbols: cellulose acetate (CA), polysulfone (PSf), polyphenylene oxide (PPO)] (14) are plotted for comparison. Pure-gas permeation properties of 110- to 116-μm-thick CANAL-Me-Me₂F (purple) and CANAL-Me-iPr (red) are shown relative to the (C) H₂/CH₄ and (D) CO₂/CH₄ upper bounds. CANAL films plotted in (C) and (D) were heated at 120°C under vacuum for 24 hours. All CANAL films were tested at 35°C and 1 bar. P, permeability.

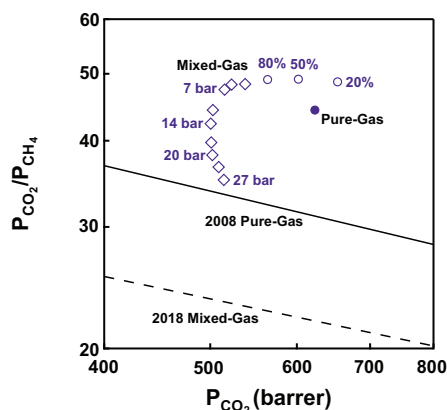


Fig. 3. Mixed-gas permeation properties of CANAL-Me-Me₂F at 35°C (50 μm thick, aged 190 days). Pure-gas ($P = 1$ bar, filled circle), variable-composition CO₂/CH₄ mixed-gas (total $P = 2$ bar, 20, 50, and 80% CO₂, open circles), and variable-pressure 50/50 CO₂/CH₄ mixed-gas (total $P = 3$ to 27 bar, open diamonds) permeation results relative to the 2008 pure-gas (2) and 2018 mixed-gas (8) upper bounds.

reaching CO₂/CH₄ and H₂/CH₄ selectivities of 68 and 621, respectively, while maintaining high CO₂ and H₂ permeabilities of 94 and 860 barrer, respectively, after 158 days of aging. The H₂/CH₄ selectivity of CANAL-Me-DHP also exceeds that of non-solution-processable thermally rearranged polymers (15) and graphene (16). CANAL-Me-DHP also has much higher selectivity for H₂/N₂, H₂/CO₂, and O₂/N₂ than other PIMs (fig. S4).

We did not observe the same aging trend and enhanced performance for our previously reported CANAL polymers with similar hydrocarbon structures but a 2D geometry, such as CANAL-Me-iPr, which showed little or no gain in selectivity and decreased permeability upon aging (Fig. 2, C and D). This further suggests that the effect of ladder-chain configurations is critical for the observed behavior and performance. The substantially different aging profiles of 2D and 3D CANAL polymers prompted us to investigate the origin of improved selectivities for CANAL-Me-Me₂F. We determined diffusion (D) and solubility (S) coefficients according to the solution-diffusion model ($P = DS$) (17), which revealed similar gas-transport behavior for the fresh CANAL-Me-Me₂F, CANAL-Me-iPr samples (table S3), and other PIMs (18). As CANAL-Me-Me₂F and CANAL-Me-iPr aged, solubility coefficients remained relatively constant. However, in contrast to the behavior observed in CANAL-Me-iPr, diffusion coefficients of larger gases in CANAL-Me-Me₂F, such as N₂ and CH₄, decreased significantly more than those of smaller gases, such as CO₂ and O₂ (fig. S7A). For example, after 55 days of aging, the diffusion coefficient of CH₄ decreased

~90%, whereas that of O₂ decreased ~60% (table S3). The constant solubility coefficients during aging suggest that the total free volume of polymers remained relatively stable. However, the large decrease in diffusion coefficients for larger gases suggests that the connections between free-volume elements, or “bottlenecks,” are narrowing as aging occurs to restrict transport of larger gases (i.e., gases larger than 3.5 Å; e.g., N₂ and CH₄ investigated in this study) without substantially affecting the transport of smaller gases (smaller than 3.5 Å; e.g., O₂, CO₂, and H₂ investigated in this study), thus leading to enhanced size selectivity over time. These results are further supported through Brandt model analysis by comparing activation energies of diffusion as a function of gas diameters squared, demonstrating that aged CANAL-Me-Me₂F has a narrower distribution of interchain spacing than other aged high-performance PIMs and the pre-aged CANAL-Me-Me₂F sample (fig. S7B and table S8). By contrast, for CANAL-Me-iPr, permeabilities for all gases decreased by roughly the same relative extent, leading to small changes in selectivity (Fig. 2, C and D). Thus, our results suggest that 3D backbone contortions of CANAL polymers are essential to generate the exceptionally high selectivity that we observed.

We evaluated the CO₂/CH₄ mixed-gas permeation of CANAL-Me-Me₂F with 20, 50, and 80% CO₂ at 2 bar of total pressure (Fig. 3, open circles). For all three compositions, the selectivity remained at 49, surpassing that of the pure-gas, likely as a result of the role of competitive sorption (19). We then evaluated the mixed-gas permeation properties of CANAL-Me-Me₂F in 50/50 CO₂/CH₄ mixtures with increasing pressure. The CO₂/CH₄ mixed-gas selectivity remains >35 even at 14 bar of CO₂ partial pressure, placing the mixed-gas performance of CANAL-Me-Me₂F far above the 2018 mixed-gas upper bound (8). Similarly, the CO₂/CH₄ mixed-gas performance of CANAL-Me-DHP also exceeds the 2018 mixed-gas upper bound (figs. S9 and S10).

On the basis of the observed contrasting aging behavior and separation performance, we speculate that different hydrocarbon ladder configurations can profoundly affect the chain packing and the distribution and connectivity of free-volume elements. Although gas adsorption isotherm and x-ray scattering experiments are commonly used to characterize the porosity of microporous materials, these techniques do not capture the distribution and connectivity of the smallest free-volume elements, which are believed to account for the diffusion bottleneck. It remains a challenge to experimentally and computationally probe the off-equilibrium packing of rigid contorted polymers. Nevertheless, our observations suggest new opportunities to

selectively control transport bottlenecks via tuning the molecular design of membrane polymers for many energy-intensive chemical separations.

REFERENCES AND NOTES

- D. S. Sholl, R. P. Lively, *Nature* **532**, 435–437 (2016).
- L. M. Robeson, *J. Membr. Sci.* **320**, 390–400 (2008).
- C. G. Bezzu et al., *Adv. Mater.* **24**, 5930–5933 (2012).
- M. Carta et al., *Science* **339**, 303–307 (2013).
- B. S. Ghanem, R. Swaidan, X. Ma, E. Litwiller, I. Pinnau, *Adv. Mater.* **26**, 6696–6700 (2014).
- R. Swaidan, B. Ghanem, I. Pinnau, *ACS Macro Lett.* **4**, 947–951 (2015).
- B. Comesaña-Gándara et al., *Energy Environ. Sci.* **12**, 2733–2740 (2019).
- Y. Wang et al., *Mater. Today Nano* **3**, 69–95 (2018).
- S. Liu, Z. Jin, Y. C. Teo, Y. Xia, *J. Am. Chem. Soc.* **136**, 17434–17437 (2014).
- H. W. H. Lai, Y. C. Teo, Y. Xia, *ACS Macro Lett.* **6**, 1357–1361 (2017).
- H. W. H. Lai et al., *Macromolecules* **52**, 6294–6302 (2019).
- R. Swaidan, B. Ghanem, E. Litwiller, I. Pinnau, *Macromolecules* **48**, 6553–6561 (2015).
- Z.-X. Low, P. M. Budd, N. B. McKeown, D. A. Patterson, *Chem. Rev.* **118**, 5871–5911 (2018).
- D. F. Sanders et al., *Polymer* **54**, 4729–4761 (2013).
- H. B. Park et al., *Science* **318**, 254–258 (2007).
- H. W. Kim et al., *Science* **342**, 91–95 (2013).
- J. G. Wijmans, R. W. Baker, *J. Membr. Sci.* **107**, 1–21 (1995).
- A. Fuoco et al., *J. Mater. Chem. A* **7**, 20121–20126 (2019).
- E. Ricci et al., *J. Membr. Sci.* **612**, 118374 (2020).
- R. Williams et al., *J. Mater. Chem. A* **6**, 5661–5667 (2018).
- C. G. Bezzu et al., *J. Mater. Chem. A* **6**, 10507–10514 (2018).
- M. Carta et al., *Adv. Mater.* **26**, 3526–3531 (2014).
- R. Swaidan, B. S. Ghanem, E. Litwiller, I. Pinnau, *J. Membr. Sci.* **457**, 95–102 (2014).
- N. Du et al., *Nat. Mater.* **10**, 372–375 (2011).
- H. A. Patel, C. T. Yavuz, *Chem. Commun.* **48**, 9989–9991 (2012).

ACKNOWLEDGMENTS

Funding: Y.X. acknowledges the Stanford Natural Gas Initiative for seed funding and the Sloan Research Foundation for a Sloan Research Fellowship. Z.P.S. and F.M.B. acknowledge support from the US Department of Energy, Office of Science, Office of Basic Energy Sciences, Separation Science program (DE-SC0019087). H.W.H.L. was supported by NSF-GRFP (DGE-156518). This work made use of the Shared Experimental Facilities supported in part by the MRSEC Program of the National Science Foundation under award DMR-1419807. I.P. was supported by KAUST baseline funding (BAS/1/1323-01-01). **Author contributions:** H.W.H.L. and Y.X. conceived the design of polymers; F.M.B. and Z.P.S. designed the gas permeation study; H.W.H.L., J.M.A., and A.M.R. performed synthesis, structural characterization, and pure-gas permeation and aging tests; F.M.B. performed pure, mixed gas permeation, and aging tests; H.W.H.L. and F.M.B. analyzed data and prepared images; Y.W. and I.P. validated mixed-gas permeation results; and H.W.H.L., F.M.B., Z.P.S., and Y.X. wrote the paper. **Competing interests:** H.W.H.L., F.M.B., Z.P.S., and Y.X. are inventors on a patent application (WO/2021/101659) related to this work. H.W.H.L., F.M.B., and Z.P.S. are cofounders, board members, and officers for Osmoses Inc., and they have equity holdings related to the materials in this work. **Data and materials availability:** All data are available in the manuscript or the supplementary materials.

SUPPLEMENTARY MATERIALS

science.org/doi/10.1126/science.abl7163
Materials and Methods
Figs. S1 to S24
Tables S1 to S11
References (26–36)
Movie S1

6 August 2021; accepted 24 February 2022
10.1126/science.abl7163

INORGANIC CHEMISTRY

Side-on coordination of diphosphorus to a mononuclear iron center

Shuai Wang¹, Jeffrey D. Sears², Curtis E. Moore³, Arnold L. Rheingold¹, Michael L. Niedig², Joshua S. Figueroa^{1*}

The diagonal relationship in the periodic table between phosphorus and carbon has set an expectation that the triple-bonded diatomic diphosphorus molecule (P_2) should more closely mimic the attributes of acetylene ($HC\equiv CH$) rather than its group 15 congener dinitrogen (N_2). Although acetylene has well-documented coordination chemistry with mononuclear transition metals, coordination complexes that feature P_2 bound to a single metal center have remained elusive. We report the isolation and x-ray crystallographic characterization of a mononuclear iron complex featuring P_2 coordination in a side-on, η^2 -binding mode. An analogous η^2 -bound bis-timethylsilylacetylene iron complex is reported for comparison. Nuclear magnetic resonance, infrared, and Mössbauer spectroscopic analysis—in conjunction with density functional theory calculations—demonstrate that η^2 - P_2 and η^2 -acetylene ligands exert a similar electronic demand on mononuclear iron centers but exhibit different reactivity profiles.

In main group chemistry, the diagonal relationship between certain second- and third-period elements of the periodic table has long provided a conceptual framework for rationalizing anomalous trends in chemical reactivity (1, 2). The reactivity and structural patterns of most elements are dictated by their valence shell electron configuration, which is conserved within a periodic group. However, for cases in which the diagonal relationship holds, trends in the chemical reactivity of one element can more closely parallel those of an element of an adjacent group and neighboring period, where electronegativity and frontier orbital energies find greater convergence (2). For molecular systems, an iconic diagonal relationship has long been recognized to exist between carbon and phosphorus, especially in cases where element-element multiple bonding is present (3). In the most fundamental manifestation of element-element multiple bonding, the chemical and electronic structural properties of the free, triple-bonded diphosphorus molecule (P_2) have been shown, both experimentally and theoretically, to more closely mimic those of acetylene ($HC\equiv CH$) rather than its group 15 congener dinitrogen (N_2) (4–8). Similar to triple-bonded acetylene, the reactivity of diphosphorus is dominated by high-energy π bonds, which lie above the corresponding σ -bonding interaction (Fig. 1A) (6, 7). By contrast, the π -bonding interactions of dinitrogen fall below the energy of the σ -bond, which is inherently low in energy on account of the

greater electronegativity of nitrogen relative to carbon and phosphorus (Fig. 1A) (6, 7).

Despite this diagonal relationship, diphosphorus—unlike acetylene—is a highly unstable and reactive molecular species. When generated in free form, diphosphorus is a fleeting species that either rapidly polymerizes (9, 10) or reacts with substrate molecules present in the medium through both π bonds (5, 11–13). The origin of this instability lies in the relatively weak nature of the triple bond in diphosphorus [$D_e(P\equiv P) = 117$ kcal/mol; D_e represents the triple bond dissociation energy] (14), which is substantially weaker than that of acetylene [$D_e(HC\equiv CH) = 230$ kcal/mol] or dinitrogen [$D_e(N\equiv N) = 226$ kcal/mol] (14, 15). Correspondingly, the gap between the highest occupied molecular orbital (HOMO) and lowest unoccupied molecular orbital (LUMO) of diphosphorus is substantially smaller than that of either N_2 or acetylene, thereby signifying a less stable molecular system (Fig. 1A). For decades, one successful strategy for stabilization of reactive π -bonded polyphosphorus species has been complexation to a single transition metal center (16). Indeed, cyclic polyphosphorus aromatic species that mimic the conjugated π systems of the cyclopropenium cation [i.e., (*cyclo*- C_3H_3)⁺], cyclobutadienylium dianion [i.e., (*cyclo*- C_4H_4)²⁺] and cyclopentadienyl monoanion [i.e., (*cyclo*- C_5H_5)⁻] have all been isolated as adducts to a single metal center (Fig. 1B) (16). These cyclic polyphosphorus compounds are among the most prominent manifestations of the diagonal relationship between phosphorus and carbon and have been extensively studied in the context of aromaticity within inorganic systems (17, 18). However, coordination compounds that feature the binding of P_2 to a single metal, where a P-P π bond remains intact and does not benefit from aromatic stabilization, have proved to be elusive targets (11, 19). This is despite theoretical predictions

that P_2 can bind effectively in a side-on configuration (20), analogous to acetylene and other alkynes, which have an extensive documented mononuclear coordination chemistry (21, 22). In addition, phosphalkynes (i.e., $P\equiv CR$, where R denotes an organic substituent)—which possess a direct P-C triple bond and also illustrate the carbon-phosphorus diagonal relationship—have long been established to bind mononuclear transition metals in a side-on configuration (23). Here, we provide synthetic, x-ray crystallographic, and spectroscopic details on an isolable mononuclear iron complex featuring a side-on-bound P_2 molecule. Key to the preparation of this compound is an alternative synthetic strategy that circumvents the intermediacy of free diphosphorus and allows for P-P multiple bond formation within a kinetically stabilizing steric environment.

Multiple synthetic routes have been established for the formation of multinuclear diphosphorus complexes (24–27). Most common among these is the reductive cleavage of the tetrahedral P_4 molecule (i.e., white phosphorus) by low-valent transition metal complexes or the photolytic fragmentation of P_4 in the presence of metal-based acceptor compounds (24, 25). In such reactions, mononuclear P_2 complexes have been proposed as the key unobserved intermediates before aggregation (28). Over the past several years, well-defined reagents have been developed—most prominently by Cummins and colleagues (11, 12)—to install P_2 units on transition metal centers by the release of diphosphorus equivalents in solution. In reactions using these reagents, mononuclear transition metal P_2 complexes have also been proposed as intermediates, but these rapidly dimerize or are intercepted by unsaturated organic substrates to furnish products in which both P-P π bonds are cleaved (11, 12, 19). A less common method for generating multinuclear P_2 complexes is the reaction between a metal-based nucleophile and common phosphorus-based electrophiles. This was the procedure employed by Markó and colleagues in 1973 to produce the first multinuclear P_2 complex, $(\mu_2-\eta^2:\eta^2-P_2)Co_2(CO)_6$, from the nucleophilic carbonylmetallate salt $Na[Co(CO)_4]$ and PCl_3 (29). However, the infrequent application of this metal-nucleophile and phosphorus-electrophile route stems from the ill-defined nature of the P-P bond formation step. We hypothesized that P-P bond formation in this system may occur by direct electrophilic attack by PCl_3 on metal organophosphide intermediates (i.e., M- PCl_2). Moreover, we reasoned that this strategy could provide a mononuclear P_2 complex if a protective coordination platform was employed in conjunction with kinetically labile leaving groups on the phosphorus atoms. Accordingly, we targeted the reaction between the meta-terphenyl isocyanide complex, $K_2[Fe(CO)_2(CNAr^{Dipp2})_2]$ (K_2 [1];

¹Department of Chemistry and Biochemistry, University of California, San Diego, 9500 Gilman Drive, Mail Code 0358, La Jolla, CA, 92093-0358, USA. ²Department of Chemistry, University of Rochester, Rochester, NY 14627, USA.

³Department of Chemistry, The Ohio State University, 88 West 18th Avenue, Columbus, OH 43210, USA.

*Corresponding author. Email: jsfig@ucsd.edu

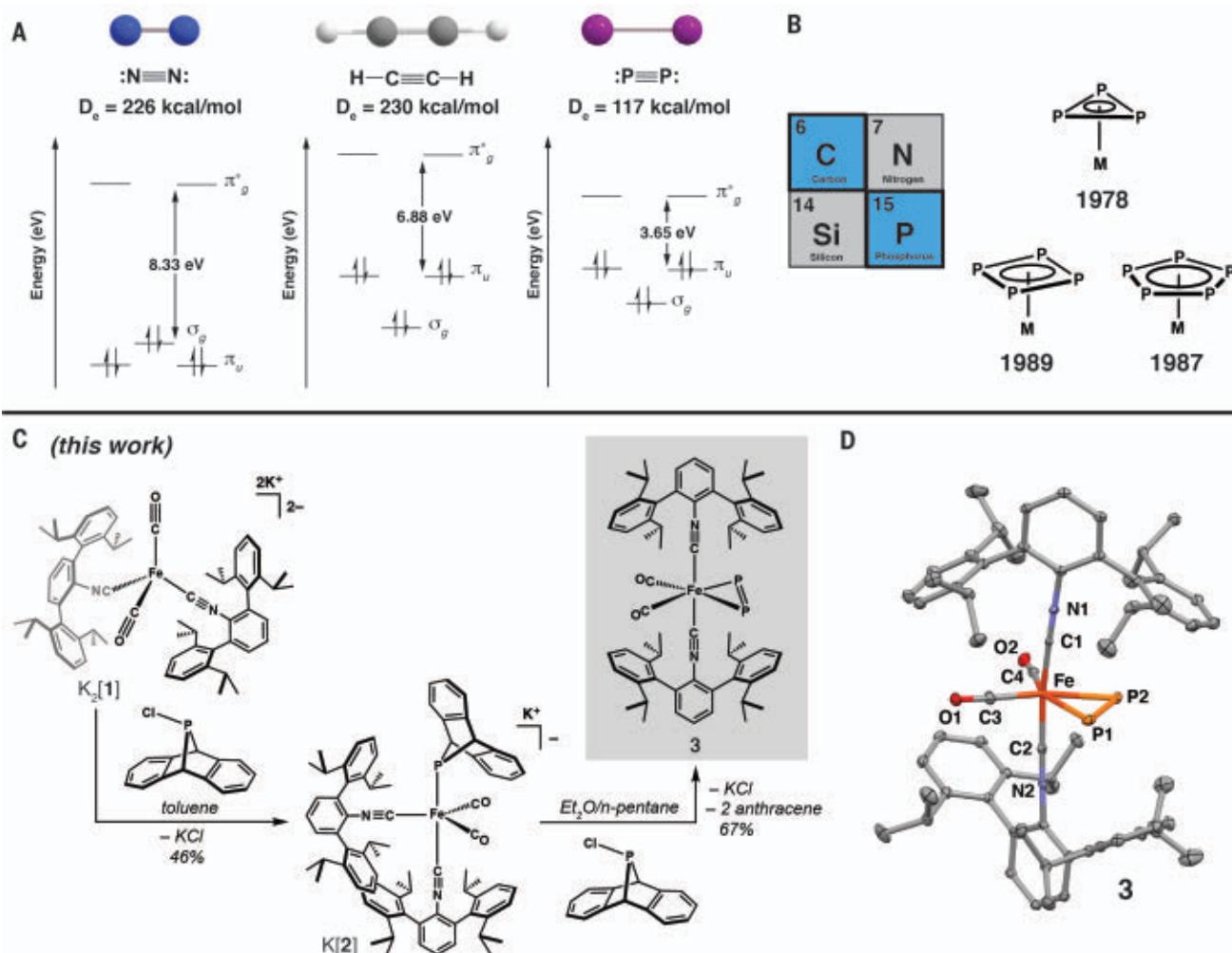


Fig. 1. The diagonal relationship between phosphorus and carbon.

(A) Partial molecular orbital diagrams for dinitrogen (N_2), acetylene ($\text{HC}\equiv\text{CH}$), and diphosphorus (P_2) showing the relative energetic ordering of the frontier σ - and π -symmetry orbitals of the triple bonds. Molecular orbital energy gaps are derived from density functional theory calculations at the BP86/def2-TZVP level. (B) Schematic representation and date of discovery of transition-metal

(M)-bound polyphosphorus aromatic ligands that mimic carbon-based cyclic aromatic molecular species according to the diagonal relationship between phosphorus and carbon. (C) Schematic representation of the synthetic route to the mononuclear iron η^2 -diphosphorus complex **3**. Et, ethyl, CH_2CH_3 . (D) X-ray crystal structure of the mononuclear iron η^2 -diphosphorus complex **3**. Hydrogen atoms have been omitted for clarity.

$\text{Ar}^{\text{Dipp}^2} = 2,6\text{-}(2,6\text{-}(i\text{-Pr})_2\text{C}_6\text{H}_3)_2\text{C}_6\text{H}_3$; $i\text{-Pr}$ = iso-propyl; Fig. 1C (**30**) and the anthracendyl-substituted chlorophosphine, $\text{ClP}(\text{anth})$ (anth = 9,10-anthracendyl; Fig. 1C). Complex $\text{K}_2[1]$ features a nucleophilic $\text{Fe}(\text{-II})$ center in a sterically encumbered environment, whereas the electrophilic $\text{ClP}(\text{anth})$ scaffold is highly susceptible to carbon-phosphorus bond homolysis under mild conditions and can therefore serve as a source of phosphorus atoms for diphosphorus formation (**31**).

Addition of 1.0 equivalents of $\text{ClP}(\text{anth})$ to $\text{K}_2[1]$ in cold toluene solution (-100°C) proceeds with the loss of 1.0 equivalent of potassium chloride (KCl) to yield the salt $\text{K}[\text{Fe}(\text{P}(\text{anth}))(\text{CO})_2(\text{CNAr}^{\text{Dipp}^2})_2]$ (**K[2]**; Fig. 1C), which contains an intact anthracendyl-substituted phosphanyl ligand as determined by single-crystal x-ray diffraction (fig. S15).

Complex **K[2]** persists at room temperature in benzene- d_6 solution for up to 5 days without noticeable decomposition. However, when **K[2]** is treated with a second equivalent of $\text{ClP}(\text{anth})$ in a 3:1 diethyl ether/ n -pentane mixture at low temperature (-100°C ; Fig. 1C), the rapid precipitation of a bright yellow solid is observed. Extraction of this solid into toluene, followed by crystallization at -40°C and structural analysis by means of x-ray crystallography, revealed it to be the mononuclear, side-on-bound diphosphorus complex ($\eta^2\text{-P}_2$) $\text{Fe}(\text{CO})_2(\text{CNAr}^{\text{Dipp}^2})_2$ (**3**; Fig. 1D), thereby demonstrating that the diatomic P_2 molecule can be constructed by successive electrophilic additions to a metal-based nucleophile.

To understand the mechanistic steps leading to P-P bond formation in this system,

K[2] was treated with the diorganochlorophosphines ClPPh_2 (Ph, phenyl, C_6H_5) and $\text{ClP}(i\text{-Pr})_2$, both of which are phosphorus-based electrophiles that do not readily undergo P-C bond homolysis. These reactions proceeded cleanly at -100°C in diethyl ether solution to eliminate KCl and produce, as determined by x-ray crystallography, the neutral phosphanylphosphine complexes $\text{Fe}(\kappa^1\text{-P}(\text{anth})\text{PPh}_2)(\text{CO})_2(\text{CNAr}^{\text{Dipp}^2})_2$ (**4** ^{PPh_2}) and $\text{Fe}(\kappa^1\text{-P}(\text{anth})\text{P}(i\text{-Pr})_2)(\text{CO})_2(\text{CNAr}^{\text{Dipp}^2})_2$ (**4** ^{$\text{P}(i\text{-Pr})_2$}), in which new P-P single bonds are established (Fig. 2A). Presumably, the encumbering steric environment of complex **K[2]** disfavors reaction products where a second electrophilic substrate is directly added to the iron center. However, complexes **4** ^{PPh_2} and **4** ^{$\text{P}(i\text{-Pr})_2$} are both thermally stable at room temperature in benzene- d_6 solution as intermittently assayed

by ^1H nuclear magnetic resonance (NMR) spectroscopy over the course of 3 days. Accordingly, a reasonable mechanistic pathway to the mononuclear diphosphorus complex **3** is through the putative intermediate $\text{Fe}(\kappa^1\text{-P}(\text{anth})\text{P}(\text{anth}))(\text{CO})_2(\text{CNAr}^{\text{Dipp}2})_2$ (**4**^{P(anth)-Int}; Fig. 2B), containing a κ^1 -bound phosphanylphosphine ligand with two anthracendiyl substituents. Anthracene extrusion from the distal P(anth) group relative to the iron center in **4**^{P(anth)-Int} can then afford the phosphanylphosphinidene intermediate (32), $\text{Fe}(\eta^2\text{-P}=\text{P}(\text{anth}))(\text{CO})_2(\text{CNAr}^{\text{Dipp}2})_2$ (**5**-Int; Fig. 2B), from which loss of a second equivalent of anthracene generates the diphosphorus ligand. In support of this mechanistic scenario is the isolation of the borane-substituted phosphine complex $\text{Fe}(\kappa^1\text{P}(\text{anth})\text{B}(9\text{-BBN}))(\text{CO})_2(\text{CNAr}^{\text{Dipp}2})_2$ (**4**^{BBN}; Fig. 1A), through the reaction between **K[2]** and iodo-9-BBN (9-BBN = 9-borabicyclo[3.3.1]nonane). The 9-BBN fragment has a steric profile similar to that of a P(anthracendiyl) unit but is not known to undergo carbon-boron bond homolysis under ambient conditions. Most notably, complex **4**^{BBN} is also thermally stable at room temperature for at least 3 days in benzene-*d*₆ solution. This thermal stability strongly indicates that ejection of the distal anthracendiyl unit in **4**^{P(anth)-Int} is a crucial step leading to diphosphorus complex **3** after initial P-P bond-formation through nucleophile-electrophile coupling.

The solid-state molecular structure and spectroscopic signatures of complex **3** are consistent with its formulation as a mononuclear diphosphorus complex possessing phosphorus-phosphorus multiple bonding interactions. Inspection of the solid-state packing diagram for **3** reveals that each $(\eta^2\text{-P}_2)\text{Fe}$ -containing molecule is a discrete monomeric species, with the closest distance between the P₂ units and any neighboring iron center being 10.6(3) Å (fig. S18; number in parentheses represents estimated standard deviation). Complex **3** crystallizes with two crystallographically independent molecules in the unit cell, which give rise to statistically indistinguishable P-P bond distances of 1.987(3) Å and 1.989(3) Å. The average P-P bond distance for **3** [1.988(1) Å] is elongated relative to that experimentally determined for free P₂ [$d(\text{P}-\text{P}) = 1.8934$ Å] (14). However, it is shorter than the average P=P double bond distance of structurally characterized organodiphosphene compounds [i.e., $\text{RP}=\text{PR}$; $d(\text{P}-\text{P}) = 2.035(\pm 0.018)$ Å] as well as the average P-P bond distance in structurally characterized, dinuclear transition-metal diphosphorus complexes [i.e., $(\mu_2\text{-P}_2)\text{M}_2$ and $(\mu_2\text{-}\eta^2\text{-}\eta^2\text{-P}_2)\text{M}_2$; $d(\text{P}-\text{P}) = 2.103(\pm 0.045)$ Å] (33). It is also substantially contracted relative to the P-P single bond distance in the tetrahedral P₄ molecule [$d(\text{P}-\text{P}) = 2.21(1)$ Å] (34). Accordingly, these latter comparisons reflect that

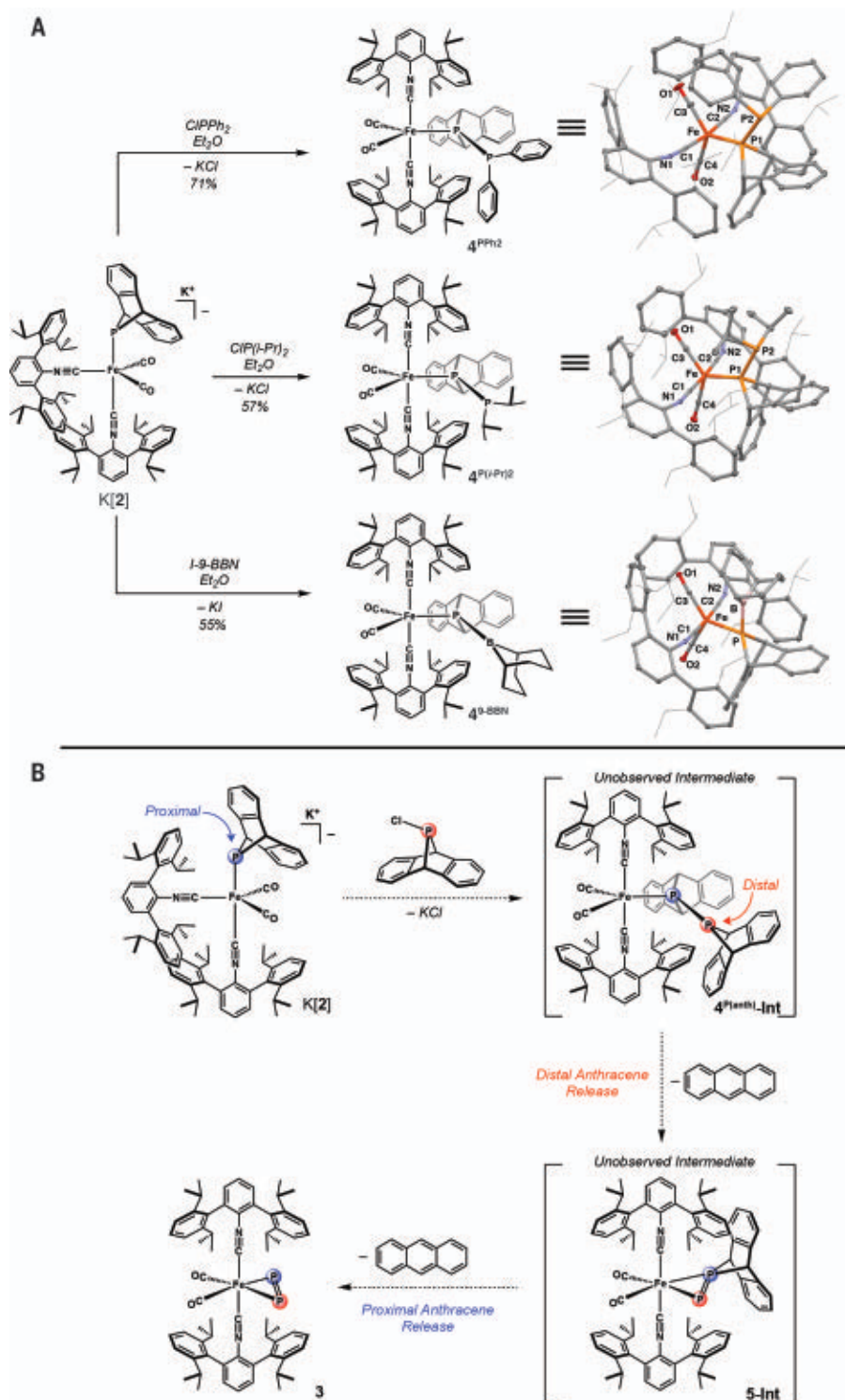


Fig. 2. Mechanistic interrogation of diphosphorus formation on a mononuclear iron center. (A) Schematic representation of the synthetic route to the heteroatom-substituted phosphine complexes **4**^{PPh₂}, **4**^{P(i-Pr)₂} and **4**^{BBN}, which demonstrate that the phosphorus atom in the 9,10-anthracendiylphosphanyl salt **K[2]** serves as the ultimate site of electrophilic addition. X-ray crystallographic structures of **4**^{PPh₂}, **4**^{P(i-Pr)₂} and **4**^{BBN} are shown to the right. For all structures, the iso-propyl groups of the $\text{CNAr}^{\text{Dipp}2}$ ligands are depicted as wireframe for clarity. (B) Proposed mechanism for the formation of the mononuclear $\eta^2\text{-P}_2$ complex **3** through the intermediacy of the unobserved species **4**^{P(anth)-Int} and **5**-Int. Initial anthracene release from the distal position in the phosphanyl-phosphine intermediate **4**^{P(anth)-Int} is proposed to provide the 9,10-anthracendiyl phosphanylphosphinidene intermediate **5**-Int. Anthracene release from **5**-Int provides mononuclear $\eta^2\text{-P}_2$ complex **3**.

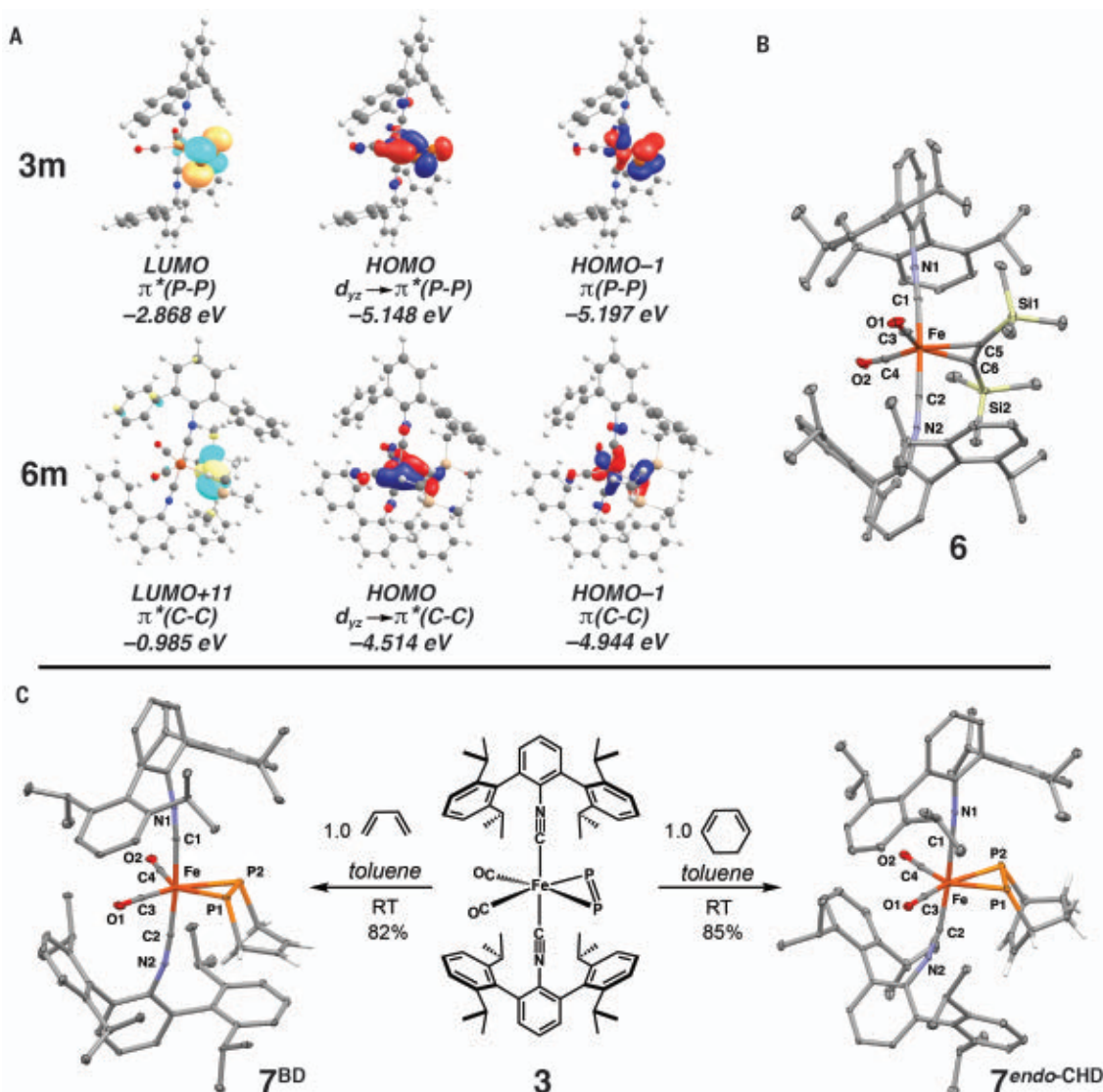


Fig. 3. Electronic structure and reactivity of mononuclear η^2 -acetylene and η^2 -diphosphorus complexes. (A) Density functional theory-calculated molecular orbitals for the model complexes **3m** and **6m** comparing the electronic structure attributes of the π/π^* orbital manifold of the η^2 - P_2 and η^2 -bis-trimethylsilylacetylene (BTMSA) ligands, respectively. (B) X-ray crystal structure of the mononuclear iron BTMSA complex **6**. Hydrogen atoms have been omitted

for clarity. (C) Reactivity of complex **3** with 1,3-butadiene (BD) and 1,3-cyclohexadiene (CHD) to generate the diphospha-Diels-Alder adducts **7^{BD}** and **7^{endo-CHD}** as represented by x-ray crystallographic structures. The hydrogen atoms of the cyclic diphosphene ligands in the structures of **7^{BD}** and **7^{endo-CHD}** have been included to indicate the regiochemical outcome of the diphospha-Diels-Alder reaction. All other hydrogen atoms have been omitted for clarity. RT, room temperature.

considerable phosphorus-phosphorus multiple bonding is retained upon coordination of the P_2 to a single iron center. Moreover, the ^{31}P NMR spectroscopic features of **3** are also consistent with the presence of multiple bonding character. In benzene- d_6 solution, **3** gives rise to a single downfield resonance centered at $\delta = 434.4$ parts per million (ppm; δ , chemical shift) (fig. S6), which is within the range expected for electronically unsaturated phosphorus nuclei. The ^{31}P NMR chemical shift of complex **3** can be further compared to those measured experimentally for P_4 ($\delta = -540$ ppm) (35) and calculated for free P_2 by means of den-

sity functional theory ($\delta = 689.3 \pm 45.4$ ppm) (36–38). Although the ^{31}P NMR chemical shift of **3** more closely matches free P_2 rather than the electronically saturated P_4 molecule, the greater shielding of the resonance exhibited by **3** relative to free P_2 is indicative of an increased energetic separation between the magnetically coupled phosphorus-based π -bonding and π^* -antibonding orbitals upon coordination to a single metal center. Accordingly, this spectroscopic feature of the $(\eta^2-P_2)\text{Fe}$ interaction in **3** is consistent with the Dewar-Chatt-Duncanson bonding model (39), wherein σ -donation from the P_2 ligand to iron energet-

ically stabilizes one P-P π bond, whereas π backdonation from iron results in energetic destabilization of the P-P π^* molecular orbital relative to that found in free P_2 .

Density functional theory calculations provide additional support for the presence of iron-to- P_2 π -backdonation in complex **3**, as well as retention of P-P π bonding. Analysis of the molecular orbitals calculated for the model complex $(\eta^2-P_2)\text{Fe}(\text{CO})_2(\text{CNAr}^{\text{Ph}2})_2$ (**3m**; $\text{Ar}^{\text{Ph}2} = 2,6-(\text{C}_6\text{H}_5)_2\text{C}_6\text{H}_3$) revealed a HOMO consistent with a π -backbonding interaction from iron to the η^2 - P_2 unit in the direction perpendicular to the axially-disposed isocyanide

ligands (Fig. 3A). Correspondingly, the calculated HOMO-1 comprised an unperturbed P-P π bond in the direction parallel to the isocyanide ligands (Fig. 3A). Natural bond orbital (NBO) calculations on **3m** resulted in a Wiberg bond index (WBI) of 2.182 for the η^2 -P₂ ligand. Although this value is less than that calculated for the canonical triple bond in free P₂ [3.000] (20), it indicates that the primary orbital interactions between iron and the η^2 -P₂ in **3** involve only one P-P π bond. Vibrational frequency calculations on model **3m** also indicated that the π -bonding manifold of the η^2 -P₂ ligand is weakened—but not eliminated—upon coordination to a single iron center. These calculations on **3m** predicted a low-intensity ν_{PP} stretching band of 668 cm⁻¹ (fig. S27), which is red-shifted relative to that measured for free P₂ (ν_{PP} = 781 cm⁻¹) (14) and is in accord with electronic occupation of one P-P π^* orbital through π -backdonation. Notably, the solid-state infrared spectrum of complex **3** features a low-intensity band centered at 674 cm⁻¹ that is consistent with the ν_{PP} stretch calculated for **3m** (fig. S12). This assignment is further corroborated by comparison to the infrared spectrum of the tricarbonyl complex Fe(CO)₃(CNAr^{Dipp})₂ (**5**), which presents a similar spectral fingerprint pattern as that of complex **3**, but does not feature this low-intensity band (fig. S12).

To gain additional insight into the properties and electronic influence of the η^2 -P₂ ligand in complex **3**, the η^2 -alkyne complex (η^2 -BTMSA)Fe(CO)₂(CNAr^{Dipp})₂ (**6**; BTMSA = bis-trimethylsilylacetylene) was prepared for comparison and characterized by x-ray crystallography (Fig. 3B). In the solid state, complex **6** is isostructural to **3** and features an η^2 -C,C-bound BTMSA ligand, consistent with the qualitative electronic analogy between alkynes and diphosphorus. However, Mössbauer spectroscopic measurements on complexes **3** and **6** revealed nearly identical isomer shifts (δ = 0.03 and 0.04 mms⁻¹, respectively), thereby providing a quantitative assessment that η^2 -alkyne and η^2 -P₂ ligands exert a similar electronic demand on a mononuclear iron center (figs. S13 and S14). By contrast, the Mössbauer quadrupole splitting parameters (ΔE_Q) for complexes **3** (0.97 mms⁻¹) and **6** (1.38 mms⁻¹) are dissimilar, which is attributed to electric-field effects originating from the noncoordinated, phosphorus-based lone pairs of the η^2 -P₂ ligand of complex **3**, as well as potential contributions from the larger covalent radius of phosphorus relative to carbon in the η^2 -P₂ and η^2 -BTMSA ligands, respectively (40).

Although P₂ and BTMSA exhibit similar binding properties to a mononuclear iron center, their reactivity profiles as coordinated ligands are substantially disparate. Analysis of the LUMO calculated for model **3m** revealed that it exclusively constitutes a P-P π^* orbital

in the direction perpendicular to the (η^2 -P₂)Fe bonding vector (Fig. 3A). By contrast, the corresponding C-C π^* orbital calculated for the model complex (η^2 -C,C-BTMSA)Fe(CO)₂(CNAr^{Ph})₂ (**6m**) is noticeably higher in energy (LUMO +1; Fig. 3A), thereby suggesting that the electrophilic character of the alkyne ligand in **6** will be substantially diminished relative to the P₂ ligand in **3**. Moreover, the quantitative energetic differences between the intact π -bonding and the corresponding π^* -antibonding orbitals calculated for **3m** and **6m** parallel those for free P₂ and acetylene (Figs. 1A and 3A). Consistent with this notion is the finding that complex **6** fails to react with the diene nucleophiles 1,3-butadiene (BD) and 1,3-cyclohexadiene (CHD) at room temperature in toluene solution. However, complex **3** reacts readily with these substrates under identical conditions to yield the corresponding diphosphadiene Diels-Alder adducts **7^{BD}** and **7^{endo-CHD}**, respectively, in which phosphorus-carbon single bonds are established (Fig. 3C). Crystallographic characterization of **7^{BD}** and **7^{endo-CHD}** confirmed that the diphosphorus units in these Diels-Alder adducts remain coordinated to the iron center and possess P-P bond distances [d (P-P) = 2.123(1) Å and 2.1118(10) Å for **7^{BD}** and **7^{endo-CHD}**, respectively] which are elongated relative to that in **3** in a manner consistent with cleavage of the remaining P-P π bond (Fig. 3C).

The diagonal relationship between phosphorus and carbon has long provided a conceptual expectation for the coordination chemistry of the triple-bonded diphosphorus molecule to be analogous to acetylene. The work presented here experimentally affirms this relationship and provides a synthetic strategy to access mononuclear complexes of diphosphorus in laboratory settings. It is anticipated that this coordination mode, in which the π -bonding framework of P₂ is partially maintained, may further enable the development of selective phosphorus-atom transfer reactions to organic molecules.

REFERENCES AND NOTES

- N. N. Greenwood, A. Earnshaw, *Chemistry of the Elements* (Butterworth-Heinemann, ed. 2, 1997).
- G. Rayner-Canham, *Found. Chem.* **13**, 121–129 (2011).
- K. Dillon, F. Mathey, J. Nixon, *Phosphorus: The Carbon Copy: From Organophosphorus to Phospho-Organic Chemistry* (Wiley, 1998).
- N. A. Piro, C. C. Cummins, *J. Am. Chem. Soc.* **130**, 9524–9535 (2008).
- D. Tofan, C. C. Cummins, *Angew. Chem. Int. Ed.* **49**, 7516–7518 (2010).
- K. I. Goldberg, D. M. Hoffman, R. Hoffmann, *Inorg. Chem.* **21**, 3863–3868 (1982).
- W. Kutzelnigg, *Angew. Chem. Int. Ed.* **23**, 272–295 (1984).
- L. T. Xu, T. H. Dunning Jr., *J. Chem. Theory Comput.* **11**, 2496–2507 (2015).
- H. W. Melville, S. C. Gray, *Trans. Faraday Soc.* **32**, 271–285 (1936).
- D. P. Stevenson, D. M. Yost, *J. Chem. Phys.* **9**, 403–408 (1941).
- N. A. Piro, J. S. Figueroa, J. T. McKellar, C. C. Cummins, *Science* **313**, 1276–1279 (2006).
- A. Velian *et al.*, *J. Am. Chem. Soc.* **136**, 13586–13589 (2014).

- D. Rottschäfer *et al.*, *Chemistry* **25**, 8127–8134 (2019).
- K. P. Huber, G. Herzberg, *Constants of Diatomic Molecules*, vol. IV of *Molecular Spectra and Molecular Structure* (Van Nostrand Reinhold, 1979).
- S. W. Benson, *J. Chem. Educ.* **42**, 502 (1965).
- E. Peresyphkina, A. Virovets, M. Scheer, *Coord. Chem. Rev.* **446**, 213995 (2021).
- I. A. Popov, A. I. Boldyrev, in *The Chemical Bond*, G. Frenking, S. Shaik, Eds. (Elsevier, 2014), pp. 421–444.
- F. Kraus, J. C. Aschenbrenner, N. Korber, *Angew. Chem. Int. Ed.* **42**, 4030–4033 (2003).
- A. Velian, C. C. Cummins, *Chem. Sci.* **3**, 1003–1006 (2012).
- C. Esterhuysen, G. Frenking, *Chemistry* **9**, 3518–3529 (2003).
- J. Chatt, G. A. Rowe, A. A. Williams, *Proc. Chem. Soc.* 208 (1957).
- J. L. Templeton, in *Advances in Organometallic Chemistry*, F. G. A. Stone, R. West, Eds. (Academic Press, 1989), vol. 29, pp. 1–100.
- J. F. Nixon, *Coord. Chem. Rev.* **145**, 201–258 (1995).
- B. M. Cossairt, N. A. Piro, C. C. Cummins, *Chem. Rev.* **110**, 4164–4177 (2010).
- M. Caporali, L. Gonsalvi, A. Rossin, M. Peruzzini, *Chem. Rev.* **110**, 4178–4235 (2010).
- L. Liu *et al.*, *Chem. Sci.* **7**, 2335–2341 (2016).
- J. Sun *et al.*, *Chem* **7**, 1952–1962 (2021).
- M. E. Barr, B. R. Adams, R. R. Weller, L. F. Dahl, *J. Am. Chem. Soc.* **113**, 3052–3060 (1991).
- A. Vizi-Orosz, G. Pályi, L. Markó, *J. Organomet. Chem.* **60**, C25–C26 (1973).
- A. E. Carpenter *et al.*, *Inorg. Chem.* **54**, 2936–2944 (2015).
- W. J. Transue *et al.*, *J. Am. Chem. Soc.* **139**, 10822–10831 (2017).
- J. Olkowska-Oetzel, J. P. Kikies, *Appl. Organomet. Chem.* **17**, 28–35 (2003).
- C. S. Database, (CSD), version 2021.2 (Cambridge Crystallographic Data Center, 2021).
- L. R. Maxwell, S. B. Hendricks, V. M. Mosley, *J. Chem. Phys.* **3**, 699–709 (1935).
- K. A. Mandla, C. E. Moore, A. L. Rheingold, J. S. Figueroa, *Angew. Chem. Int. Ed.* **58**, 1779–1783 (2019).
- P. Lazzarretti, J. A. Tossell, *J. Phys. Chem.* **91**, 800–804 (1987).
- A. Dransfeld, D. B. Chesnut, *Chem. Phys.* **234**, 69–78 (1998).
- A. Antušek, M. Jaszurki, M. Olejniczak, *Comput. Theor. Chem.* **970**, 54–60 (2011).
- J. Chatt, L. A. Duncanson, *J. Chem. Soc.* 2939–2947 (1953).
- P. Güttich, E. Bill, A. X. Trautwein, *Mössbauer Spectroscopy and Transition Metal Chemistry: Fundamentals and Applications* (Springer, 2011).

ACKNOWLEDGMENTS

Funding: This work was supported by the US National Science Foundation through grants CHE-1802646 (to J.S.F.) and CHE-1954480 (to M.L.N.), as well as the US National Institutes of Health through grant RO1GM11480 (to M.L.N.). **Author contributions:** S.W. carried out the synthetic work, analytical characterization, and computational studies. J.D.S. and M.L.N. performed the Mössbauer spectroscopy studies. S.W., C.E.M., and A.L.R. carried out the crystallographic studies. J.S.F. assisted with data analysis and directed the research. S.W. and J.S.F. wrote the manuscript, with input from all authors. **Competing interests:** The authors declare no competing interests. **Data and materials availability:** Crystallographic data for compounds **K[2]**, **3**, **4^{Ph}**, **4^{(i-Pr)2}**, **4^{BBN}**, **5**, **6**, **7^{BD}**, and **7^{endo-CHD}** are available free of charge from the Cambridge Crystallographic Data Centre under references CCDC-2103243, CCDC-2103244, CCDC-2103245, CCDC-2103246, CCDC-2103247, CCDC-2103248, CCDC-2103249, CCDC-2103250, and CCDC-2103251, respectively. Additional spectroscopic, crystallographic, and computational data are included in the supplementary materials.

SUPPLEMENTARY MATERIALS

science.org/doi/10.1126/science.abn7100
Materials and Methods
Figs. S1 to S30
Tables S1 to S6
References (41–61)

14 December 2021; accepted 23 February 2022
10.1126/science.abn7100

VALLEYTRONICS

Tunable and giant valley-selective Hall effect in gapped bilayer graphene

Jianbo Yin^{1,2,*†}, Cheng Tan^{3†}, David Barcons-Ruiz¹, Iacopo Torre¹, Kenji Watanabe⁴, Takashi Taniguchi⁴, Justin C. W. Song⁵, James Hone³, Frank H. L. Koppens^{1,6,*}

Berry curvature is analogous to magnetic field but in momentum space and is commonly present in materials with nontrivial quantum geometry. It endows Bloch electrons with transverse anomalous velocities to produce Hall-like currents even in the absence of a magnetic field. We report the direct observation of in situ tunable valley-selective Hall effect (VSHE), where inversion symmetry, and thus the geometric phase of electrons, is controllable by an out-of-plane electric field. We use high-quality bilayer graphene with an intrinsic and tunable bandgap, illuminated by circularly polarized midinfrared light, and confirm that the observed Hall voltage arises from an optically induced valley population. Compared with molybdenum disulfide (MoS₂), we find orders of magnitude larger VSHE, attributed to the inverse scaling of the Berry curvature with bandgap. By monitoring the valley-selective Hall conductivity, we study the Berry curvature's evolution with bandgap. This in situ manipulation of VSHE paves the way for topological and quantum geometric optoelectronic devices, such as more robust switches and detectors.

In 1984, Berry proved that a quantum wave function acquires a geometric phase of $2N\pi$ (N as integer) after an adiabatic evolution along a loop in parameter space (*1*).

This geometric phase was expressed as a surface integral of a vector field, coined as Berry curvature. Globally, the integral of Berry curvature over the full parameter space, representing the Chern number, defines the nature of specific topological states. Locally, Berry curvature $\Omega(\mathbf{k})$ behaves as an effective intrinsic field, analogous to magnetic field, but acting in momentum space. Berry curvature distorts the conventional semiclassical trajectories of Bloch electrons in crystals to endow them with an anomalous velocity perpendicular to an applied electric field \mathbf{E} (*2–6*):

$$\mathbf{v}(\mathbf{k}) = \frac{\partial \epsilon(\mathbf{k})}{\hbar \partial \mathbf{k}} + \frac{q}{\hbar} \mathbf{E} \times \Omega(\mathbf{k}) \quad (1)$$

where \mathbf{v} , \mathbf{k} , ϵ , \mathbf{E} , q , and \hbar are electron velocity, wave vector, band energy, electric field, carrier charge, and reduced Planck's constant, respectively.

Two-dimensional Dirac materials such as graphene and transition metal dichalcogenides (TMDs) are a particularly attractive platform for realizing a host of new topological and quantum geometrical responses (*7*). For instance, low-dissipation valley currents were inferred by measuring nonlocal signals in graphene–boron nitride (BN) superlattices and molyb-

denum disulfide (MoS₂) (*8–11*); under strong laser irradiation, graphene can exhibit a Floquet-driven anomalous Hall phase (*12*). No less notable, however, is gapped bilayer graphene (GBG), which can host enormous Berry curvature density at its band edges (Fig. 1B), which have been predicted to produce a giant anomalous (or valley-selective) Hall effect (*13*). Berry curvature in many materials is often thought to be fixed by its crystal configuration; by contrast, Berry curvature in bilayer graphene can be tailored externally by tuning the interlayer potential, providing a versatile knob to study Berry curvature–driven quantum geometric phenomena. For example, nonlocal valley currents were reported in GBG (*14, 15*), bilayer graphene–BN superlattice (*16*), and twisted double-bilayer graphene (*17*), respectively. However, nonlocal resistance fingerprints have also been predicted to originate from a spatially nonuniform gap profile (*11, 18*), and recent scanning gate imaging experiments found that nonlocal transport signals in graphene can also arise because of charge accumulation at the edges and therefore may not necessarily have a bulk valley Hall effect origin (*19*). In contrast to the nonlocal measurements, direct Hall measurements by optical pumping can quantify the expected giant Hall conductivity in GBG and trace the evolution of Berry curvature with gap and energy. Unlike in TMDs (*20–22*), direct observations of light-induced valley-selective Hall effect (VSHE) and its associated Berry curvature distribution have not been reported in gapped graphene-based systems.

In this work, we directly probe the tunable VSHE in bilayer graphene with variable bandgap E_g from 0 to 0.125 eV by valley-polarizing carriers with circularly polarized infrared light. The concept is shown in Fig. 1A. First, we use top and bottom gates to apply displacement

fields D_T and D_B , as further explained in the materials and methods (*23, 24*). The average of these two fields $\bar{D} = (D_B + D_T)/2$ adds energy bias between the two layers of bilayer graphene, which breaks inversion symmetry and controls E_g as well as the E_g -dependent Berry curvature, as shown in Fig. 1B (*13*). The displacement difference $\delta D = D_B - D_T$ controls the Fermi level E_F . Second, we selectively excite carriers in the K (or K') valley with a right (or left) circularly polarized midinfrared laser (*25–29*). This valley circular dichroism arises directly from the opposite orbital moments of electrons in valleys K and K' when inversion symmetry is broken, enabling circularly polarized light to preferentially induce interband transitions in either K or K' valleys; see also a golden rule calculation in supplementary texts 1 and 7. When we subject the valley-polarized photocarriers to an electric field \mathbf{E} from source-drain bias V_b , the anomalous velocity due to the Berry curvature Ω induces a Hall voltage, as described by Eq. 1. We note that the valley imbalance is essential to observing a Hall voltage: Otherwise, equal valley currents from the two valleys will cancel each other out, because they are driven by opposite Ω (*30*). Third, by independently tuning \bar{D} and δD (fig. S1), we can quantify the expected giant valley-selective Hall conductivity σ_H and study its dependence on E_g and E_F , respectively. Therefore, our measurement can directly probe anomalous (geometric) currents in nontrivial quantum geometric materials with small bandgaps.

A typical Hall device is shown in Fig. 1C and consists of ultraclean hexagonal BN (hBN)-encapsulated bilayer graphene, with monolayer (or few-layer) graphene as the semitransparent top and bottom gates. The device design is optimized for probing the Hall voltage induced by optical illumination of the bulk of the device. The active area of the device is square shaped, with graphite contacts placed at a relatively large distance to avoid spurious photovoltage generation at the contacts. The device is mounted in an optical cryostat (device temperature 33 K) with a focused infrared light source (spot size of $\sim 25 \mu\text{m}$), which can be scanned over the device surface while monitoring longitudinal (along \mathbf{E} and noted by xx) and transverse (perpendicular to \mathbf{E} and noted by yy) voltages. The photoinduced anomalous (or valley selective) Hall voltage V_H is the transverse voltage difference between left and right circularly polarized illuminations $V_H = V_{yy}(\ominus) - V_{yy}(\oplus)$, which is probed by a lock-in amplifier, while the polarization chirality is modulated by a photoelastic modulator at ~ 50 kHz (fig. S2 and materials and methods). To confirm the origin of V_H , we also modulate the laser intensity (on and off) and measure the photocurrent $\Delta I_{xx} = I_{xx}(\text{on}) - I_{xx}(\text{off})$ at the longitudinal terminals, as well as

¹ICFO–Institut de Ciències Fotòniques, The Barcelona Institute of Science and Technology, Castelldefels (Barcelona), Spain.

²Beijing Graphene Institute, Beijing, China. ³Department of Mechanical Engineering, Columbia University, New York, NY 10027, USA. ⁴National Institute for Materials Science, Tsukuba, Japan.

⁵Division of Physics and Applied Physics, Nanyang Technological University, 637371 Singapore, Singapore. ⁶CREA–Institució Catalana de Recerca i Estudis Avançats, Barcelona, Spain.

*Corresponding author. Email: jiyin@icfo.net (J.Y.); frank.koppens@icfo.eu (F.H.L.K.)

†These authors contributed equally to this work.

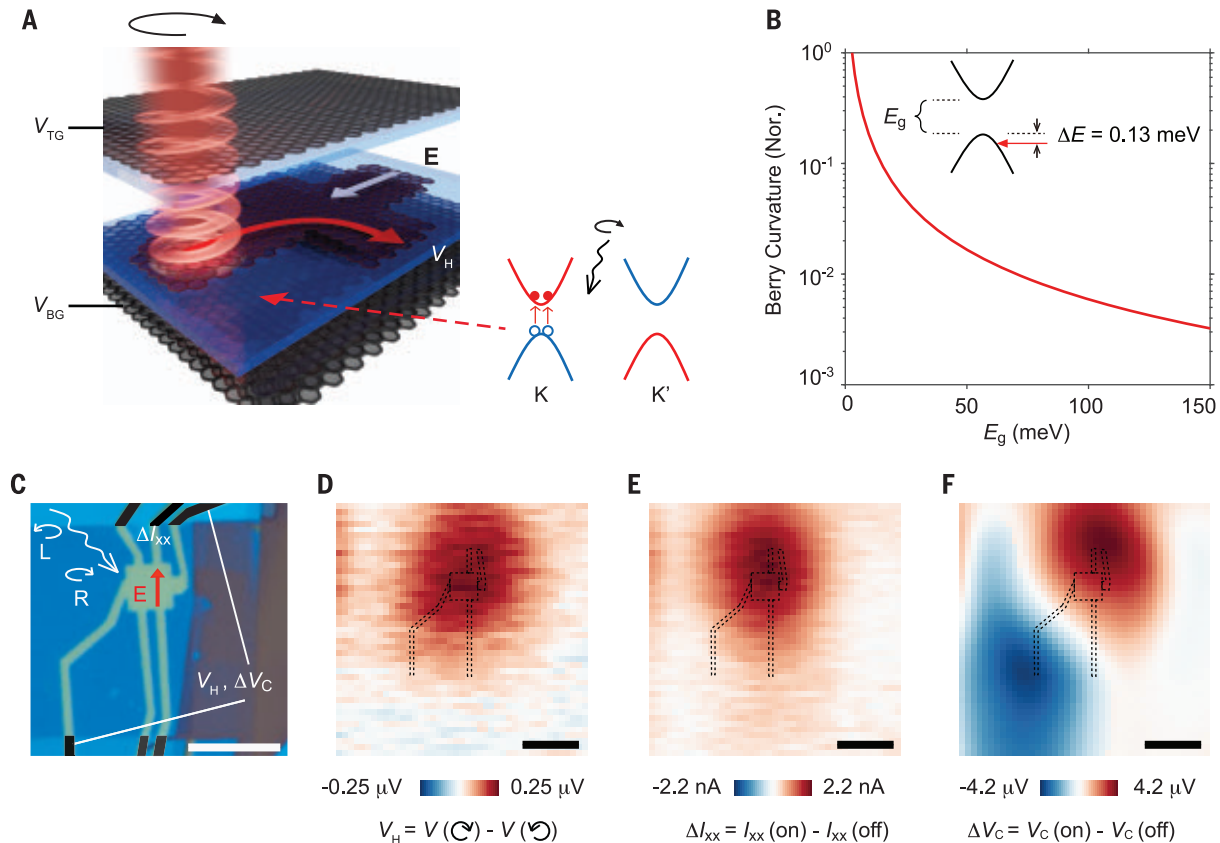


Fig. 1. Valley-selective Hall effect in GBG driven by tunable Berry curvature.

(A) Schematic illustration of a valley-selective Hall measurement. Photocarriers at one valley are selectively excited by circularly polarized light. These photocarriers are driven by the in-plane electric field \mathbf{E} and Berry curvature $\mathbf{\Omega}$, leading to a photoinduced anomalous Hall voltage. The blue and red colors of the illustrative band structure indicate polarities of the Berry curvature. (B) Fast evolution of $\mathbf{\Omega}$ with the gap size of GBG. The curve is based on eq. S16 and describes $\mathbf{\Omega}$ values at bands with $\Delta E = 0.13$ meV away from band extremum. It is normalized by the value at $E_g = 3$ meV. Note that $\mathbf{\Omega}$ vanishes at zero gap. (C) Optical image of a bilayer graphene device. To reduce photovoltage at the

bilayer graphene–electrode junction, all the electrodes are made of graphite, as indicated by the artificial black color. All of the device region shown in the figure overlaps with both top and bottom gates. L, left; R, right. (D to F) Spatial distributions of V_H , ΔI_{xx} , and ΔV_C , recorded by scanning device under a focused infrared laser with $h\nu$ of 123.7 meV, P of $2.2 \mu\text{W} \mu\text{m}^{-2}$, and a beam diameter of about $25 \mu\text{m}$. V_H is collected as indicated by contacts at the furthest distance from the device bulk while the chirality of the circularly polarized light is modulated at 50 kHz. ΔI_{xx} and ΔV_C are collected with a light intensity modulation at 177 Hz. $E_g = 35$ meV, $V_b = 50$ mV, and $n_0 = 0$. Dashed lines indicate device positions. Scale bars indicate $10 \mu\text{m}$.

the transverse photovoltage $\Delta V_C = V_C(\text{on}) - V_C(\text{off})$ between the transverse terminals. The spatial distributions of V_H , ΔI_{xx} , and ΔV_C are shown in Fig. 1, D to F. The monopolar spatial features of both V_H and ΔI_{xx} indicate that these signals arise from the bulk of the device; this contrasts with the bipolar spatial features of ΔV_C that we attribute to local built-in fields at graphene–electrode contacts.

Data establishing the high quality and intrinsic bandgap of the device are presented in Fig. 2A, in which resistivity ρ_{xx} is recorded as a function of \bar{D} and $\delta\bar{D}$ (see line traces in fig. S4). Here, we use $\delta\bar{D} \cdot \epsilon_0 e^{-1}$ (ϵ_0 and e are vacuum permittivity and elementary charge, respectively) to quantify Fermi level sweeping as it equalizes to the gate-injected free-carrier density n_0 at $\bar{D} = 0$. However, at $\bar{D} \neq 0$, the value of $\delta\bar{D} \cdot \epsilon_0 e^{-1}$ is larger than n_0 because the Fermi level needs to move across the bandgap to induce free carriers. The \bar{D} -dependent high-

resistivity plateau when the Fermi level is inside the gap is shown in Fig. 2A, and an instrument-limited value of 10^7 ohms at $\bar{D} > 0.8 \text{ V nm}^{-1}$ has been reached. This high resistivity rules out other conductive channels [e.g., hopping or a topological conductive channel (32)] and confirms the existence of an intrinsic gap. The relation between E_g and \bar{D} is further extracted from temperature-dependent resistance measurements, as shown in Fig. 2B, fig. S5, and supplementary text 2. The Arrhenius plot in fig. S5E shows thermally activated band conduction for the full temperature T range from 37 to 230 K, demonstrating that the device quality overcomes earlier-reported challenges in gapped Dirac materials that are related to impurity-mediated conduction (14, 20). The high quality is also echoed by the high E_g -dependent mobility μ that exceeds $100,000 \text{ cm}^2 \text{ V}^{-1} \text{ s}^{-1}$ at $T < 30 \text{ K}$ (fig. S6 and supplementary text 3); a comprehensive device characteriza-

tion that includes van der Pauw measurements can be found in supplementary texts 2, 3, and 9.

The effect of infrared optical illumination is first studied by probing multiple exciton peaks, visible in the E_g -dependent photocurrent curves displayed in Fig. 2C. For increasing gap size, multiple exciton states resonate with incident photons, giving rise to enhanced interband absorption and photocurrent peaks (32). The exciton states, as indicated by the left dashed line, are further labeled by black crosses in Fig. 2B. The optical excitation of photocarriers manifests as a typical photoconductivity feature under source-drain bias V_b as indicated by the blue arrow in the I_{xx} - V_b curve (Fig. 2D). Photoconductivity is an essential precondition for the VSHE, which clearly differs from the photovoltaic, photothermoelectric, and bolometric effects observed in monolayer and bilayer graphene (33).

In the photoconductive regime, which is central for the study in this work, the ΔI_{xx} and V_H are measured simultaneously as a function of E_g and E_F by tuning \bar{D} and δD independently (Fig. 2, E and F, and their linecuts in fig. S7; photon energy $h\nu = 122.9$ meV, and laser intensity $P = 1.4 \mu\text{W} \mu\text{m}^{-2}$). The dashed triangular zone indicates the region with the Fermi level inside the gap before applying V_b and illumination on the device, where ΔI_{xx} shows a relative uniform distribution until E_g approaches $h\nu$ and triggers resonant absorption at $E_g \sim 120$ meV, depicted by the blue arrow in Fig. 2E and fig. S8. We note that the abrupt decline of ΔI_{xx} outside the triangular zone is mainly caused by a dramatic decrease of V_b (fig. S9).

In contrast to the observation of one resonant peak in ΔI_{xx} , V_H shows two peaks (indicated by two arrows in Fig. 2F). Besides one at $E_g \sim 120$ meV, an additional peak at $E_g \sim 10$ meV is formed by a rapid rise of V_H when E_g increases from zero and a decline of V_H when E_g increases beyond 10 meV. Qualitatively, these features are expected from the inversion symmetry-breaking requirement of the VSHE and the fast decline of Berry curvature with increasing E_g , as shown in Fig. 1B. A more quantitative analysis will follow later in the text. Another prominent feature is the presence of V_H outside the dashed triangular zone, such as the area around coordinate $(\delta D \cdot \epsilon_0 e^{-1}, E_g) = (-1 \times 10^{11} \text{ cm}^{-2},$

20 meV), as indicated by a white arrow. This will be further discussed later in the text as well.

The VSHE has key fingerprints that arise from its dependence on in-plane electric field \mathbf{E} and Berry curvature $\mathbf{\Omega}$ (Eq. 1). The first is a linear V_H - V_b relation, as shown in Fig. 3A, when the laser is positioned in the middle of the device. Spatial scans are shown in fig. S10 and reveal opposite signs of V_H for $V_b = \pm 40$ mV. The second fingerprint is the dependence of V_H on $\mathbf{\Omega}$, which is controlled by selectively exciting the K or K' valley. Experimentally, we change the chirality modulation (bottom arrows in Fig. 3B and fig. S2) to exchange the initially excited valley, which causes a flip of

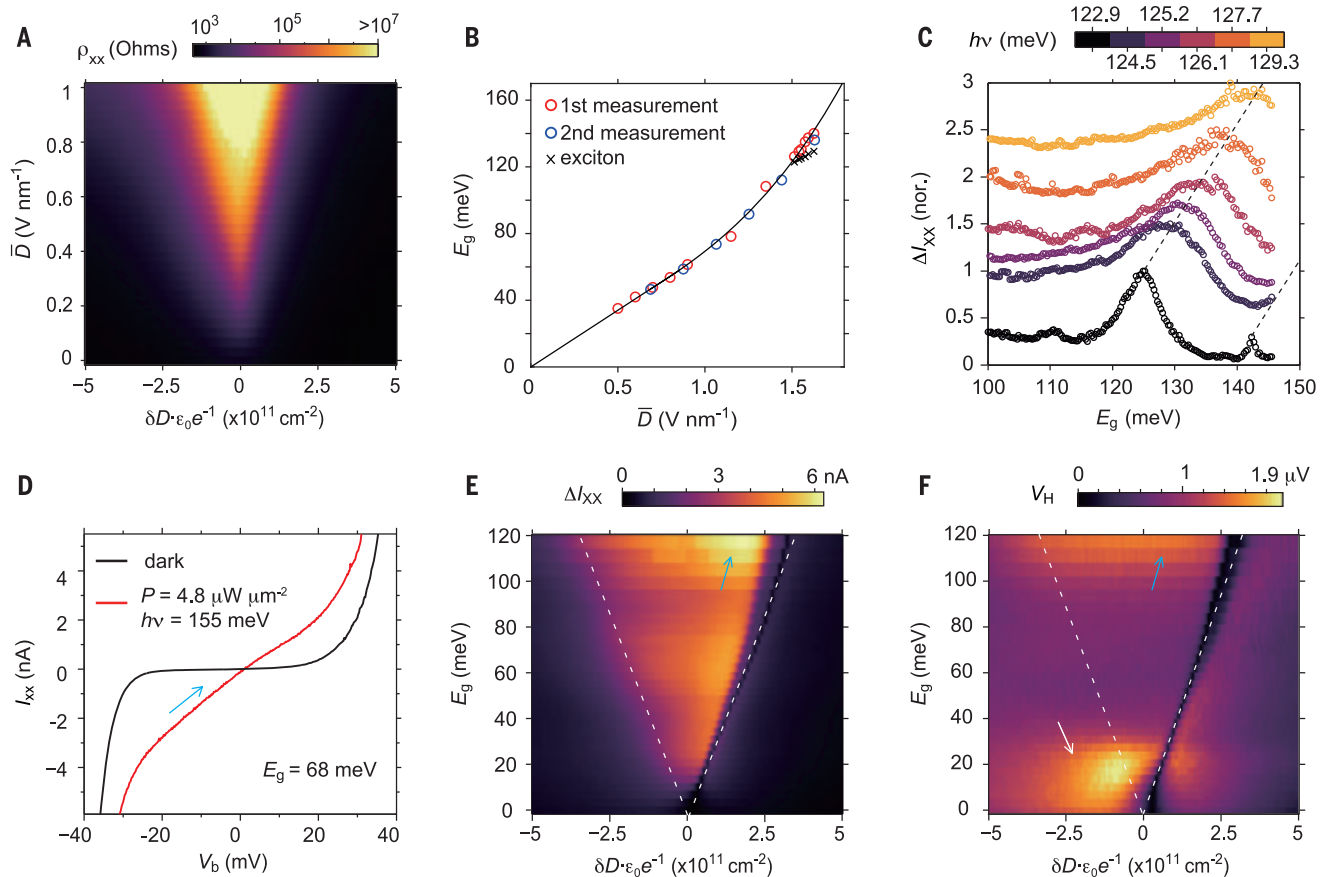


Fig. 2. Exciton states and gap-dependent V_H . (A) Two-dimensional map of the ρ_{xx} of GBG with respect to the average (\bar{D}) and difference (δD) of the top and bottom displacement fields. \bar{D} and δD control E_g and charge carrier density (and E_F), respectively. At $\bar{D} = 0$, $\delta D \cdot \epsilon_0 e^{-1}$ is equal to the gate-induced free-carrier density. $V_b = 1$ mV. (B) E_g of GBG at different \bar{D} . Red and blue circles indicate data from different measurements. Each point is extracted from a series of temperature-dependent transport measurements (fig. S5). Black crosses indicate exciton peaks, as shown by the left dashed line in (C). (C) Normalized ΔI_{xx} of GBG excited by different infrared photons, with $V_b = 0$ and the Fermi level inside the gap. Photocurrent peaks arise from excitonic resonances, which are assigned to two excited states of excitons, as indicated by the dashed lines. The energy values along the left line are labeled as black crosses in (B). Incident laser P increases linearly from 0.16 to $2.6 \mu\text{W} \mu\text{m}^{-2}$ with $h\nu$ increasing from 122.9 to

129.3 meV, as indicated by the color scale. The curves are shifted for clarity. (D) Current-bias (I_{xx} - V_b) curve of GBG in the dark and under illumination ($h\nu = 155.0$ meV, $P = 4.8 \mu\text{W} \mu\text{m}^{-2}$) with $E_g = 68$ meV and the Fermi level inside the gap before applying V_b and illumination. Slope increase (blue arrow) is a typical photoconductive feature. (E and F) ΔI_{xx} and V_H with respect to E_g and δD ($h\nu = 122.9$ meV, $P = 1.4 \mu\text{W} \mu\text{m}^{-2}$). The ΔI_{xx} and V_H are collected by modulating light intensity and chirality of circularly polarized light, respectively. Two dashed lines indicate the insulating region that is due to the presence of a band gap. Blue arrows indicate ΔI_{xx} and V_H peaks that are due to absorption resonance. The white arrow shows an additional V_H peak and the presence of V_H outside the gap. The V_b introduces hole doping and results in a resistance maximum around the right dashed line, along which ΔI_{xx} and hence V_H decreases (see supplementary text 5). V_b increases from 1 to 89 mV with E_g (fig. S9A).

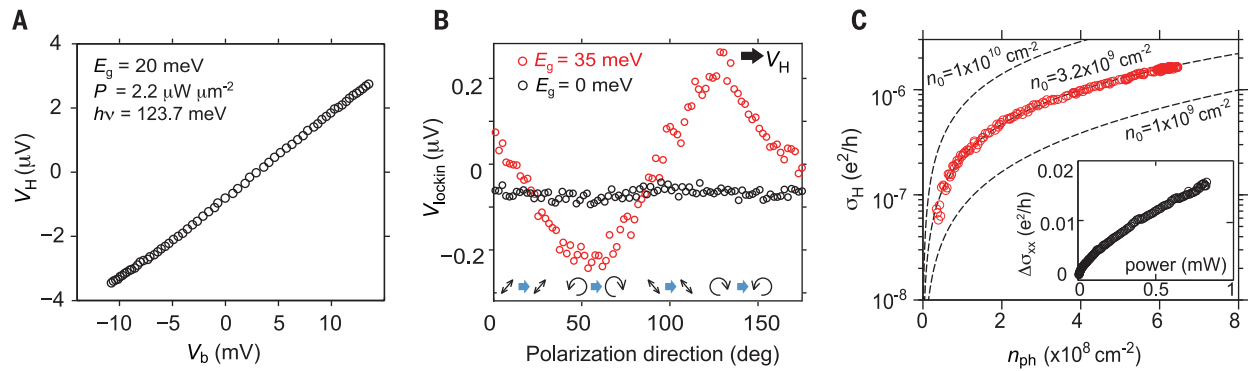


Fig. 3. Fingerprints of VSHE in GBG. (A) Linear dependence of V_H on V_b . The inset shows E_g , P , and $h\nu$. The Fermi level is inside the gap before applying V_b and illumination on the device. (B) Lock-in amplifier signal V_{lockin} measured as a function of the polarization direction of light incident on the photoelastic modulator. Rotation of the polarization changes the chirality-modulation sequence from left-right to right-left (bottom arrows; see also fig. S2). This exchanges the initially excited valley (e.g., from K with Ω to K' with $-\Omega$) and therefore flips V_H (indicated by the black arrow; see red circles with E_g at 35 meV). By contrast, linear-linear modulations at 5° and 95° do not generate valley imbalance and V_H . The same device without displacement field (thus without gap and measurable Ω) shows a featureless curve, as presented by black circles. The shift here is

due to a measurement circuit instead of the device response (see materials and methods). Laser parameters are $P \sim 0.26 \mu\text{W} \mu\text{m}^{-2}$ and $h\nu = 123.7 \text{ meV}$. (C) Fast growth of photoinduced σ_H with n_{ph} . The unit of σ_H is e^2/h , where h is Planck's constant. Experimental results with $E_g = 122 \text{ meV}$, $P = 1.4 \mu\text{W} \mu\text{m}^{-2}$, $h\nu = 122.9 \text{ meV}$, and $V_b = 70 \text{ mV}$ are shown by circles, which agree well with theoretical estimates of σ_H with fitting parameter (initial carrier density) $n_0 = 3.2 \times 10^9 \text{ cm}^{-2}$, as shown by the middle dashed line. Theoretical σ_H with $n_0 = 1 \times 10^9 \text{ cm}^{-2}$ and $1 \times 10^{10} \text{ cm}^{-2}$ are also shown. These three dashed lines show strong correlation between σ_H and n_0 . n_{ph} is obtained by dividing $\Delta\sigma_{xx}$ (inset) by mobility and elementary charge. For dashed theoretical lines, we treated all photocarriers as being in a single valley consistent with absorption resonance (fig. S11C)

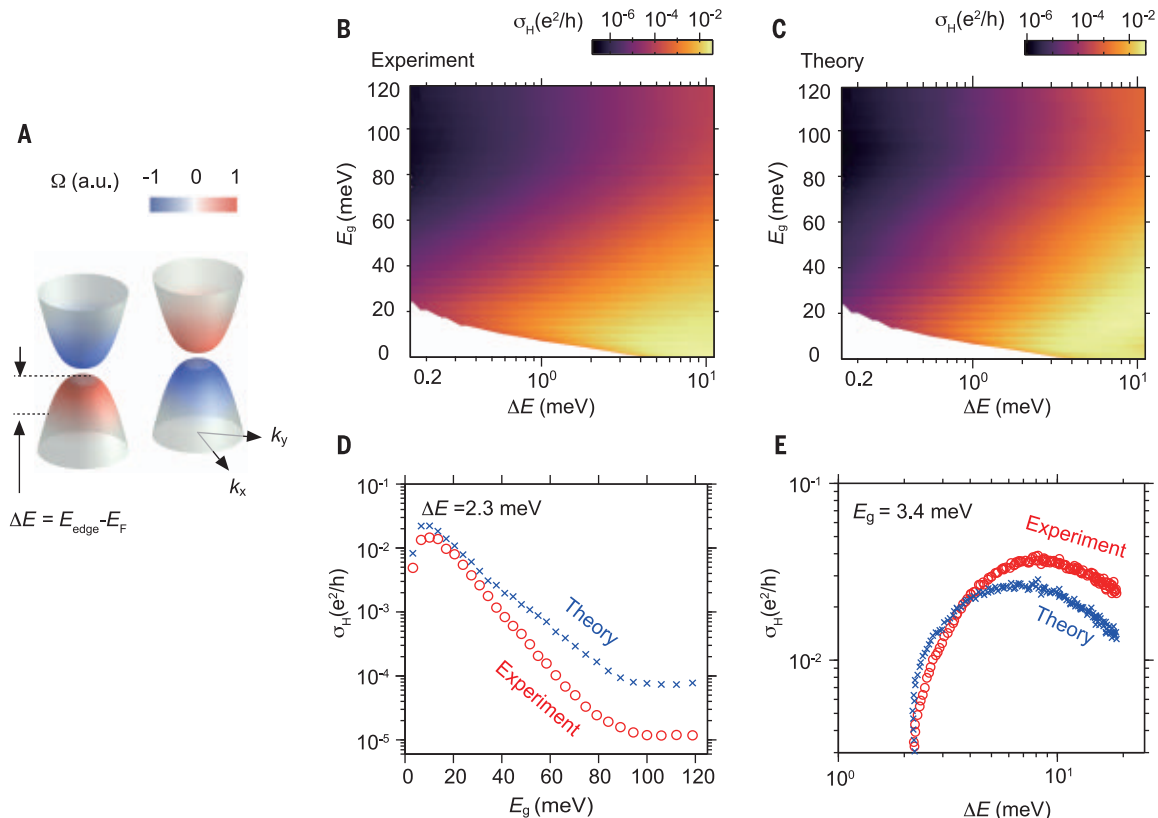


Fig. 4. Evolution of σ_H . (A) Illustrative Berry curvature distribution in GBG. a.u., arbitrary units. (B) Experimental dependence of σ_H with ΔE and E_g . The data at the lower-left corner are not accessible because of finite carrier density at low E_g induced by the bias doping effect. $h\nu = 122.9 \text{ meV}$, and $P = 1.4 \mu\text{W} \mu\text{m}^{-2}$. (C) Theoretical estimate of intrinsic photoinduced σ_H

with E_g and ΔE . Here, n_{ph} was estimated using the measured longitudinal photoconductivity and device mobility; see also supplementary materials for discussion. (D) Vertical line traces of (B) as circles and (C) as crosses, showing an abrupt decrease of σ_H with E_g . $\Delta E = 2.3 \text{ meV}$. (E) Horizontal line traces of (B) and (C), showing nonmonotonic ΔE -dependent σ_H . $E_g = 3.4 \text{ meV}$.

V_H polarity (red circles in Fig. 3B and spatial scans in fig. S3). In a control measurement with inversion symmetry preserved, that is, $\bar{D} = 0$, V_H only shows small and featureless signals (black circles in Fig. 3B; see materials and methods for more discussion), consistent with the fact that the absence of a bandgap erases the Berry curvature.

Next, we present a more quantitative analysis of the photoinduced valley-selective Hall conductivity σ_H , because we can vary several parameters in situ such as photocarrier density n_{ph} , Fermi level E_F , and the bandgap E_g . Here, $\sigma_H \approx \sigma_{xx}^* V_H / V_{xx}$ [(20) and supplementary text 4], with the following measured parameters under illumination: V_H , longitudinal conductivity σ_{xx} , and longitudinal voltage V_{xx} . With this, we can study the dependence of σ_H on n_{ph} , with n_{ph} obtained from the measured longitudinal photoconductivity $\Delta\sigma_{xx} = n_{ph} e \mu$ (see inset of Fig. 3C and supplementary text 6). We find a nonlinear increase of σ_H with n_{ph} (Fig. 3C). The initial fast rise agrees with theoretical predictions [(13) and supplementary text 8] and shows a sensitive valley-selective Hall response with n_{ph} . The data also show that σ_H can be tuned by several orders of magnitude by changing the light intensity within $1.4 \mu\text{W } \mu\text{m}^{-2}$. Theoretical estimates (dashed lines) in Fig. 3C reveal that σ_H is very sensitive to E_F or gate-induced carrier density n_0 . This will be discussed later in the text.

A full parameter dependence of σ_H can be obtained by tuning E_g (via \bar{D}) and the carrier density (via δD). As illustrated in Fig. 4A, the carrier density is proportional to $\Delta E = |E_F - E_{edge}|$, where E_{edge} represents band edges of conduction or valence bands (supplementary text 5). In Fig. 4B, we focus on hole doping with $\Delta E = E_{edge} - E_F$ and plot the experimental σ_H versus E_g and ΔE . Our experimental data are consistent with simple theoretical estimates of intrinsic valley-selective Hall conductivity (13), as presented in Fig. 4C and supplementary text 8. The agreement is notable given that no adjustable fitting parameters and only experiment-based n_{ph} , n_0 , and E_g values are used in the theoretical estimate (fig. S11).

Notably, the measured σ_H in Fig. 4B reaches large values of $0.04 e^2/h$, where h is Planck's constant, despite very weak illuminating power ($P = 1.4 \mu\text{W } \mu\text{m}^{-2}$; $h\nu = 122.9 \text{ meV}$). This value is four orders of magnitude higher than that measured for MoS_2 at the same laser intensity (20). The large σ_H magnitudes arise from the giant values of Berry curvature that can be found in Dirac materials with very narrow gaps such as GBG (13). Indeed, when E_g is increased, we find that σ_H rapidly diminishes (see Fig. 4B and its line trace as red circles in Fig. 4D) by more than three orders of magnitude. This E_g -induced giant tunability of σ_H , consistent with that expected from intrinsic valley-selective

Hall conductivity (13), highlights the extreme sensitivity of Berry curvature-induced optoelectronics to gate-controlled E_g (see also Fig. 1B).

Another prominent feature we observed is a nonmonotonic dependence of σ_H on ΔE , as shown by the red circles in Fig. 4E (a horizontal line trace of Fig. 4B). Here, we vary ΔE but use a small, fixed value of E_g . We find that σ_H first increases by more than an order of magnitude, peaking at $\Delta E \approx 9 \text{ meV}$, and then decreases. This dependence is consistent with theoretical estimates of σ_H based on the extracted experiment-based n_{ph} and n_0 , as shown by blue crosses in Fig. 4E (line trace of Fig. 4C). A similar nonmonotonic dependence can also be found in σ_H versus E_g (red circles in Fig. 4D), displaying a peak at $E_g \approx 10 \text{ meV}$; this qualitative trend is also similarly mirrored by the intrinsic valley-selective Hall conductivity (blue crosses in Fig. 4D).

The agreement between experiment and intrinsic valley-selective Hall conductivity (13) can enable tracking of the quantum geometric properties of bilayer graphene. Even as the simple theoretical (intrinsic) estimates produce the same trends as the observed Hall conductivity, there exist some quantitative discrepancies; see, for example, Fig. 4, B to D. Indeed, other mechanisms such as skew scattering and side jumps may also be present (4, 34). Including these, in addition to other band structure effects such as trigonal warping (35), may provide improved quantitative agreement with the observed σ_H .

The giant ($0.04 e^2/h$ at $P = 1.4 \mu\text{W } \mu\text{m}^{-2}$ and $h\nu = 122.9 \text{ meV}$) and highly (gate) tunable σ_H response in our GBG devices contrasts sharply with that of the small σ_H found in other Dirac materials (e.g., MoS_2) (20). This makes GBG a promising platform for realizing a new “quantum geometric photodetector” in the infrared and terahertz spectral range. Such a detector can use large longitudinal voltage bias to enhance the Hall photocurrent but at the same time suffers nearly zero dark current at transverse Hall contacts, exhibiting a high signal-to-noise ratio.

REFERENCES AND NOTES

- M. V. Berry, *Proc. R. Soc. London Ser. A* **392**, 45–57 (1984).
- D. Xiao, M.-C. Chang, Q. Niu, *Rev. Mod. Phys.* **82**, 1959–2007 (2010).
- R. Karplius, J. M. Luttinger, *Phys. Rev.* **95**, 1154–1160 (1954).
- N. Nagaosa, J. Sinova, S. Onoda, A. H. MacDonald, N. P. Ong, *Rev. Mod. Phys.* **82**, 1539–1592 (2010).
- In addition to intrinsic processes, anomalous Hall effect may also be caused by extrinsic processes such as side jump and skew scattering.
- M. C. Chang, Q. Niu, *Phys. Rev. Lett.* **75**, 1348–1351 (1995).
- J. C. W. Song, P. Samutpraphoot, L. S. Levitov, *Proc. Natl. Acad. Sci. U.S.A.* **112**, 10879–10883 (2015).
- R. V. Gorbachev et al., *Science* **346**, 448–451 (2014).
- K. Komatsu et al., *Sci. Adv.* **4**, eaaq0194 (2018).
- Z. Wu et al., *Nat. Commun.* **10**, 611 (2019).

- T. Aktor, J. H. Garcia, S. Roche, A.-P. Jauho, S. R. Power, *Phys. Rev. B* **103**, 115406 (2021).
- J. W. McIver et al., *Nat. Phys.* **16**, 38–41 (2020).
- J. C. W. Song, M. A. Kats, *Nano Lett.* **16**, 7346–7351 (2016).
- Y. Shimazaki et al., *Nat. Phys.* **11**, 1032–1036 (2015).
- M. Sui et al., *Nat. Phys.* **11**, 1027–1031 (2015).
- K. Endo et al., *Appl. Phys. Lett.* **114**, 243105 (2019).
- S. Sinha et al., *Nat. Commun.* **11**, 5548 (2020).
- S. Roche, S. R. Power, B. K. Nikolic, J. H. Garcia, A.-P. Jauho, *J. Phys. Mater.* **5**, 021001 (2022).
- A. Aharon-Steinberg et al., *Nature* **593**, 528–534 (2021).
- K. F. Mak, K. L. McGill, J. Park, P. L. McEuen, *Science* **344**, 1489–1492 (2014).
- M. Onga, Y. Zhang, T. Ideue, Y. Iwasa, *Nat. Mater.* **16**, 1193–1197 (2017).
- N. Ubrig et al., *Nano Lett.* **17**, 5719–5725 (2017).
- Y. Zhang et al., *Nature* **459**, 820–823 (2009).
- J. B. Oostinga, H. B. Heersche, X. Liu, A. F. Morpurgo, L. M. K. Vandersypen, *Nat. Mater.* **7**, 151–157 (2008).
- W. Yao, D. Xiao, Q. Niu, *Phys. Rev. B* **77**, 235406 (2008).
- H. Zeng, J. Dai, W. Yao, D. Xiao, X. Cui, *Nat. Nanotechnol.* **7**, 490–493 (2012).
- K. F. Mak, K. He, J. Shan, T. F. Heinz, *Nat. Nanotechnol.* **7**, 494–498 (2012).
- T. Cao et al., *Nat. Commun.* **3**, 887 (2012).
- A. M. Jones et al., *Nat. Nanotechnol.* **8**, 634–638 (2013).
- D. Xiao, W. Yao, Q. Niu, *Phys. Rev. Lett.* **99**, 236809 (2007).
- L. Ju et al., *Nature* **520**, 650–655 (2015).
- L. Ju et al., *Science* **358**, 907–910 (2017).
- N. M. Gabor et al., *Science* **334**, 648–652 (2011).
- T. Ando, *J. Phys. Soc. Jpn.* **84**, 114705 (2015).
- S. Slizovskiy, E. McCann, M. Koshino, V. I. Fal'ko, *Commun. Phys.* **2**, 164 (2019).

ACKNOWLEDGMENTS

We thank M. Massicotte, A. Woessner, and F. Vialla for fruitful discussions and M. Ceccanti for helping design Fig. 1A. **Funding:** This work is supported by European Union's Horizon 2020 Research and Innovation Programme under grant agreement ref. 881603 (Graphene Flagship Core Project 3) (F.H.L.K.); European Research Council (ERC) TOPONANOP under grant agreement ref. 726001 (F.H.L.K.); the government of Spain [PID2019-106875GB-I00; FJC2018-037098-I; Severo Ochoa CEX2019-000910-S (MCIN/AEI/10.13039/501100011033)] (F.H.L.K.); Fundació Cellex, Fundació Mir-Puig (F.H.L.K.); Generalitat de Catalunya (CERCA, AGAUR, SGR 1656) (F.H.L.K.); European Union's Horizon 2020 Programme under the Marie Skłodowska-Curie grant agreements VHPHC ref. 747927 (J.Y.); National Natural Science Foundation of China (grant refs. 52072043 and T2188101) (J.Y.); National Key R&D Program of China under grant ref. 2020YFA0308900 (J.Y.); National Science Foundation program for Emerging Frontiers in Research and Innovation (EFRI-1741660) (C.T. and J.H.); the Ministry of Education Singapore, under its MOE ACRF Tier 3 Award MOE2018-T3-1-002 (J.C.W.S.); and a Nanyang Technological University start-up grant (NTU-SUG) (J.C.W.S.). **Author contributions:** F.H.L.K. and J.Y. conceived the idea and designed the experiments; J.Y. performed experiments and analysis of the results; D.B.-R. assisted in bandgap measurement and analysis; J.Y. and J.C.W.S. performed the theoretical analysis together; C.T. and J.H. fabricated the devices, with K.W. and T.T. providing hBN crystals; I.T. performed numerical simulation for electrical transport analysis; F.H.L.K. supervised the project; and J.Y., F.H.L.K., and J.C.W.S. wrote the manuscript with contributions from J.H. and C.T. **Competing interests:** The authors declare that they have no competing interests. **Data and materials availability:** All data are available in the main text or the supplementary materials.

SUPPLEMENTARY MATERIALS

science.org/doi/10.1126/science.abl4266
Materials and Methods
Supplementary Text
Figs. S1 to S12
References (36–39)

17 August 2021; accepted 23 February 2022
10.1126/science.abl4266

QUANTUM OPTICS

Compressibility and the equation of state of an optical quantum gas in a box

Erik Busley, Leon Espert Miranda, Andreas Redmann, Christian Kurtscheid, Kirankumar Karkihalli Umesh, Frank Vewinger, Martin Weitz, Julian Schmitt*

The compressibility of a medium, quantifying its response to mechanical perturbations, is a fundamental property determined by the equation of state. For gases of material particles, studies of the mechanical response are well established, in fields from classical thermodynamics to cold atomic quantum gases. We demonstrate a measurement of the compressibility of a two-dimensional quantum gas of light in a box potential and obtain the equation of state for the optical medium. The experiment was carried out in a nanostructured dye-filled optical microcavity. We observed signatures of Bose-Einstein condensation at high phase-space densities in the finite-size system. Upon entering the quantum degenerate regime, the measured density response to an external force sharply increases, hinting at the peculiar prediction of an infinite compressibility of the deeply degenerate Bose gas.

Quantum gases of atoms, exciton-polaritons, and photons provide a test bed for many-body physics under both in- and out-of-equilibrium settings (1–3). Experimental control over dimensionality, potential energy landscapes, or the coupling to reservoirs offers wide possibilities to explore different phases of matter. For cold atomic gases, thermodynamic susceptibilities and transport properties have been extracted from density measurements (4–9) and have proven to be direct manifestations of the equation of state (EOS). In general, the EOS of a material—for example, its pressure-volume relation—describes both the thermodynamic state of a system under a given set of physical conditions as well as its response to perturbations as mechanical compression. Experimental investigations of the EOS in quantum gases constitute a tool for the characterization of phases and the identification of phase transitions, enabling important tests of physical models in a wide range of systems, from the ideal gas to superfluids and the interior of stars.

Quantum gases of light have so far been experimentally realized in low-dimensional settings, mostly two-dimensional (2D) systems (3).

Institut für Angewandte Physik, Universität Bonn, Wegelerstraße 8, 53115 Bonn, Germany.
*Corresponding author. Email: schmitt@iap.uni-bonn.de

Thermalized photon gases with nonvanishing chemical potential μ as well as Bose-Einstein condensation (BEC) have been demonstrated in dye-filled optical microcavities at harmonic confinement (10–12), including measurements of density-insensitive thermodynamic quantities (13). By contrast, the isothermal compressibility $\kappa_T = n^{-2}(\partial n/\partial \mu)_T$ at temperature T depends on the (local) particle density n in the gas; for a systematic study, it thus is desirable to avoid spatially inhomogeneous density distributions inherent to harmonically trapped gases and instead prepare uniform samples, in which applying a spatially uniform force directly allows one to compress the gas and probe κ_T .

BEC does not occur in the infinite 2D homogeneous Bose gas given that thermal fluctuations at finite temperatures destroy long-range order (14). Although interactions nevertheless stabilize a superfluid through the Berezinskii-Kosterlitz-Thouless (BKT) mechanism, the infinite 2D ideal gas is doomed to remain quantum degenerate without forming a condensate. For a finite-sized homogeneous gas in a box, however, condensation is expected to be possible if the correlation length exceeds the system size at large phase-space densities (15). In ultracold atoms, the crossover between saturation-driven BEC and interaction-driven BKT superfluidity has been investigated in 2D harmonically

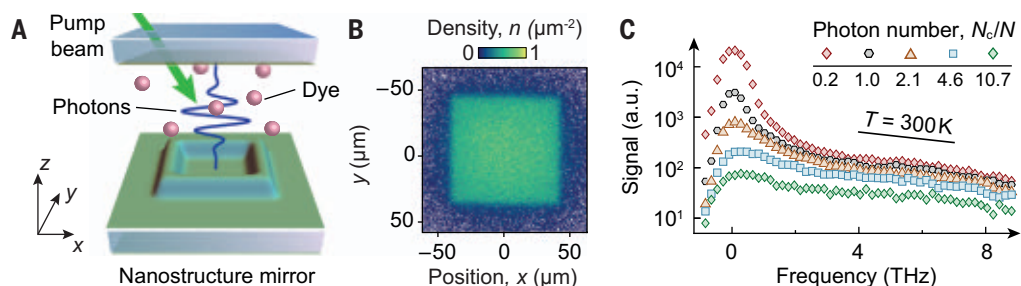
trapped Bose gases by tuning the interactions using a Feshbach resonance (16), whereas studies of homogeneous gases in box potentials have focused on the interacting regime (17–19). In uniform gases of exciton-polaritons (20), on the other hand, the observation of BEC is hampered by reservoir-induced interactions and nonequilibrium effects. Up to now, the compressibility and the EOS have not been determined for optical quantum gases.

We examined a 2D quantum gas of photons in a box potential. In the finite-size homogeneous system, we observed BEC, as evidenced from the measured position and momentum distributions. In subsequent experiments, a mechanical force was exerted onto the photon gas prepared in a regime around the phase transition. By studying the density response to minute forces, we measured both the bulk isothermal compressibility and the EOS of the optical quantum gas.

Our homogeneous 2D photon gases were prepared in a nanostructured optical microcavity filled with a liquid dye solution (Fig. 1A) (21). The photons in the short cavity with mirror spacing on the order of the optical wavelength form a 2D gas of particles with an effective mass m , which are described by their transverse momentum $k = \sqrt{k_x^2 + k_y^2}$.

To spatially confine the unbound plane-wave states of a 2D homogeneous system, we implemented a box potential of size L as a container for the photons. The box potential was realized by using a nanostructuring technique (21, 22), which imprints a position-dependent static surface elevation onto one of the cavity mirrors. The locally reduced cavity length results in a repulsive potential. Thermalization of the photon gas to room temperature was achieved with absorption and reemission processes on the dye molecules (10). An exemplary density distribution of a trapped gas is shown in Fig. 1B, recorded by imaging the cavity emission, and optical frequency spectra over the trapped range $V_0/\hbar \sim 2\pi \times 9$ THz above the cavity low-frequency cutoff $\nu_c = mc^2/(2\pi\hbar)$ are given in Fig. 1C, where \hbar is the reduced Planck's constant and c is the speed of light, for different total particle numbers N . All

Fig. 1. Trapping a homogeneous 2D photon gas. (A) A spatially structured microcavity filled with dye molecules confines and thermalizes the uniform photon gas. The locally elevated surface of one of the cavity mirrors realizes a repulsive box potential. (B) Example surface density of a uniform photon gas in a square box with $L = 80 \mu\text{m}$. (C) Spectral distributions of the cavity emission exhibit an exponential decay that is consistent with $T \approx 300$ K, indicating a thermal equilibrium photon gas. The population in the low-frequency modes is enhanced as N_c/N approaches unity.



spectra show an exponential decay of the population in the high-frequency states that is consistent with $k_B/(2\pi\hbar) \times 300$ K, with Boltzmann's constant k_B , which we attribute as evidence for the gas to be thermalized. Moreover, the population in the lowest-lying states was enhanced as we increased N beyond a critical value N_c , which signals the emergence of a low-entropy phase.

We explored the quantum degenerate behavior in the finite-size homogeneous system. Surface densities in the box for different N are shown in Fig. 2A. Below the critical photon number N_c , the bulk density is uniform as for a normal gas, whereas above N_c , we observed a macroscopic occupation of the ground state

$|\psi_{1,1}(x, y)|^2 = 4L^{-2} \cos^2(\pi x/L) \cos^2(\pi y/L)$, with $|x|, |y| \leq L/2$; the qualitative change is evident from the line profiles. The corresponding momentum distributions below N_c in Fig. 2A resemble a Maxwell-Boltzmann distribution $f(k) \propto \exp(-k^2/\sigma_k^2)$, with $\sigma_k = \sqrt{2mk_B T}/\hbar$; for our data, $\sigma_k = 2.4(1) \mu\text{m}^{-1}$ gives $T = 295(33)$ K (where numbers in parentheses indicate errors calculated from the uncertainties of the fit parameters). Upon increasing the photon number, the population at small k is enhanced and ultimately dominated by a strongly occupied ground state at $k = 0$, the condensate. For large k , we observed signatures of both microscope aperture and finite trap depth (21). A closer inspection in x and k space (Fig. 2A, inset)

Fig. 2. Bose-Einstein condensation of photons in a box.

(A) (Top) Density distributions, (middle) line profiles, and (bottom) momentum-space distributions (k_0 denotes the trap limit, k_{NA} denotes the imaging limit) as N is increased beyond $N_c = 3.5(4) \times 10^3$. Below N_c , the flat-top density and Gaussian k space distribution resemble a thermal gas in the normal phase. Above N_c , the ground state becomes massively populated and deforms the cloud, which is more directly observed in momentum space.

(B) Normalized central spatial density versus N , starting from $n_0 L^2/N = 1$ in the normal phase and approaching the expected value of 4 when the ground state dominates [symbols are as in (A)].

(C) N_c and (inset) $\mathcal{D}_c = N_c(\lambda/L)^2$, extracted from data as in (B), exhibit the predicted scaling (line) with the box size.

$\mathcal{D}_c = N_c(\lambda/L)^2$, extracted from data as in (B), exhibit the predicted scaling (line) with the box size.

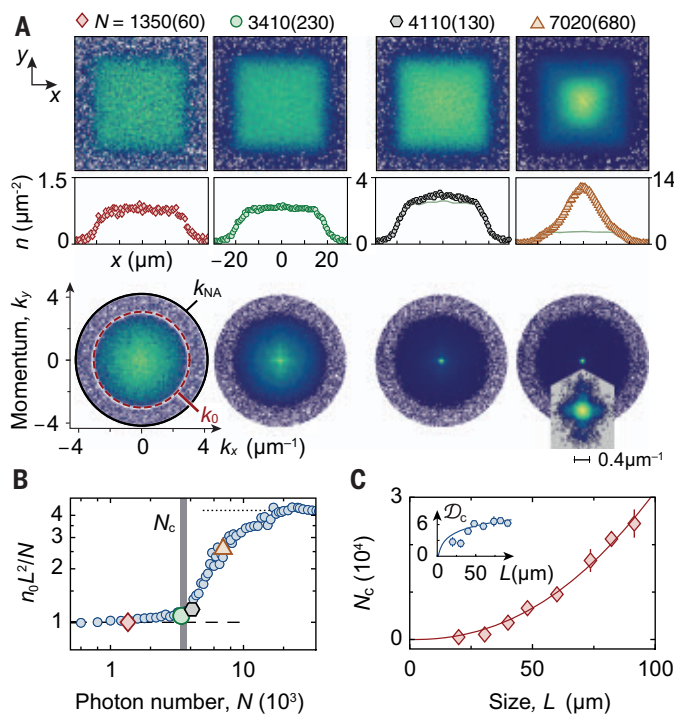
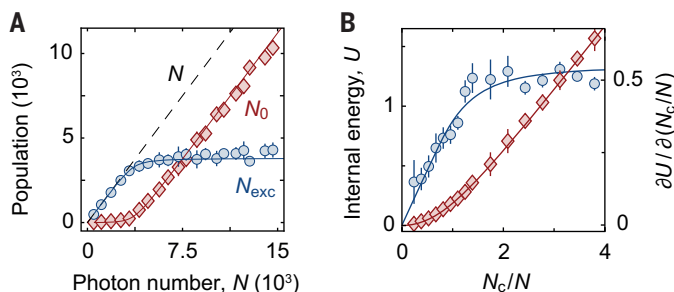


Fig. 3. Saturation and caloric properties.

(A) Population in the ground (red) and excited states (blue). N_0 and N_{exc} , respectively, extracted from k space distributions (as in Fig. 2A, bottom) versus photon number N . At large N , the visible saturation of the normal part N_{exc} indicates that the phase transition is BEC-like.

(B) Normalized internal energy (red), showing a crossover from quadratic (condensed gas, $N_c/N < 1$) to linear (normal, $N_c/N \gg 1$) scaling, and the derivative (blue), which reflects the specific heat per particle, versus N_c/N . In the normal phase, the latter reaches a value near 0.5, which is understood from the finite trap depth V_0 , and is below the value of 1 expected for $V_0 \rightarrow \infty$. Solid lines are finite-size theory.



confirms that the ground state is Heisenberg-limited with an uncertainty product $\Delta x \Delta k = 0.7(1)$, which is in agreement with theory $\Delta x \Delta k = \sqrt{\pi^2/12 - 1/2} \sim 0.6$.

To quantify the transition point, we studied the normalized spatial central density $n_0 L^2/N$ as a function of the particle number. The transition at $N_c = 3.5(4) \times 10^3$ is shown in Fig. 2B; the limiting cases $n_0 L^2/N = 1$ for small N and $n_0 L^2/N = 4$ for large N are well understood to arise from the uniform normal gas and inhomogeneous condensate density with N/L^2 and $4N/L^2$, respectively, at the center. The critical particle number scales with the predicted $N_c \propto (L/\lambda)^2 \log(L/\lambda)$ (Fig. 2C), where $\lambda = 2\sqrt{\pi}/\sigma_k \sim 1.47 \mu\text{m}$ denotes the thermal wavelength. The logarithmic scaling of the critical phase-space density \mathcal{D}_c shown in Fig. 2C, inset, is understood from the dependence of the coherence length reaching the system size (15, 21). At the largest investigated box sizes, we have $\mathcal{D}_c = N_c(\lambda/L)^2 = 6.3(8)$. For interacting 2D gases characterized by an interaction strength \tilde{g} and realized in ultracold atoms (6, 7, 15–17, 19), the BKT phase transition to a superfluid usually occurs before BEC; for example, for homogeneous gases, $\mathcal{D}_{c,BKT} = \log(380/\tilde{g}) \sim 6.5$ for $\tilde{g} = 0.6$ (19). Quite distinctly, for photon gases in dye microcavities, self-interactions with $\tilde{g} \approx 10^{-6}$ (23) imply a much larger $\mathcal{D}_{c,BKT} \geq 20$, and accordingly, both phases are expected to be well separated.

We identified the BEC-like nature of the phase transition by extracting the ground and excited state populations N_0 and N_{exc} , respectively, from the momentum space distributions as a function of the total particle number N . The visible saturation of the normal part is shown in Fig. 3A, which indicates that interaction effects are very small (24); in particular, the saturation gives evidence that in our homogeneous finite-size system, BEC is prevalent instead of BKT. This interpretation is supported by the deduced caloric properties of the gas (Fig. 3B), which closely follow the ideal Bose gas prediction. For the internal energy $U = \langle E \rangle N_c/N^2 k_B T$, where $\langle E \rangle$ denotes the average transverse energy, we observed a crossover from a quadratic to a linear scaling in the condensed and normal phase, respectively, as a function of N_c/N . Correspondingly, its derivative $\partial U/\partial(N_c/N)$ is a smooth function, highlighting that the heat capacities in the normal and condensed phases are linked without any discontinuities (8, 13). In the normal-gas phase, each particle can accommodate only $\approx 0.5 k_B T$ of thermal energy, as well understood from the finite trap depth (21).

To determine the isothermal compressibility $\kappa_T = n^{-2}(\partial n/\partial \mu)_T$ of the optical quantum gas, we exerted a force onto the photons by tilting one of the cavity mirrors, which superimposes a linear potential $U(x) = U_0 x/L$ to the box, and measured the density response.

The displaced center of mass $\langle x \rangle$ (Fig. 4A, y axis) is shown in Fig. 4A as a function of the tilt U_0 . In local density approximation (LDA), with chemical potential $\mu(x) = \mu_0 - U(x)$, the center of mass to first order relates to the compressibility, following $\langle x \rangle/L = -\kappa_T n U_0/12$ (5, 21, 25). For small U_0 , the data in Fig. 4A confirms the linear behavior and shows an enhancement of the density response when going from the normal to the condensed phase. The visible saturation for large U_0 is caused by the finite box size, which limits the displacement.

The compressibility is shown in Fig. 4B, extracted from a linear fit of the region near $U_0 = 0$ (Fig. 4A), along with theory for the infinite and finite system. Below the critical density for condensation $N_c/L^2 \sim 2.6 \mu\text{m}^{-2}$, the photon distribution is spatially homogeneous, as visible in Fig. 2, A and B. For these densities, LDA can be applied (25) to extract κ_T by using data with small tilts ($U_0 \lesssim \mu$), even in the case of very small interactions (21). In the condensed phase, however, the LDA ceases to be valid, and the corresponding region in Fig. 4B is shaded in gray. Within the region of validity, the compressibility compares well with theory. At densities $n \gtrsim 1 \mu\text{m}^{-2}$, we observed a

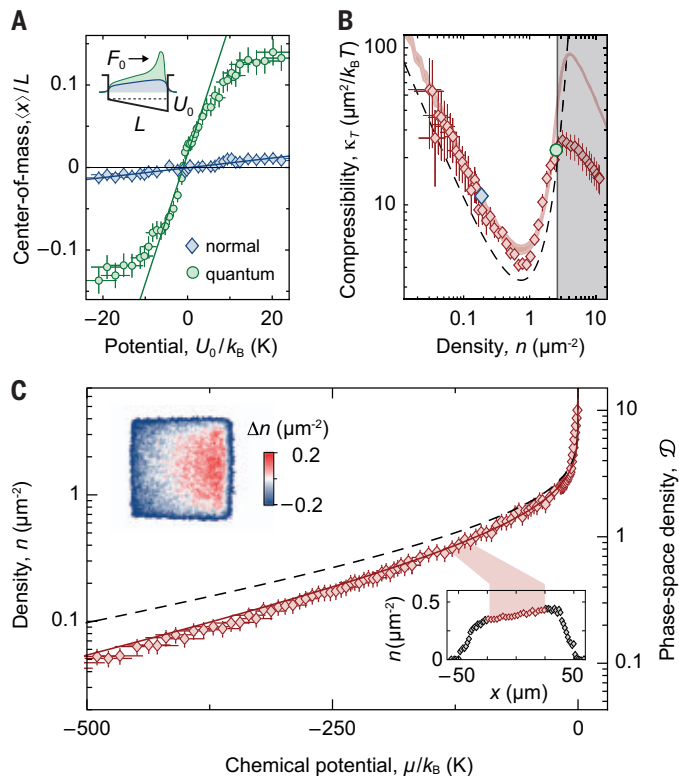
sharp increase of the compressibility; the onset is in good agreement with the prediction for an infinite noninteracting system (Fig. 4B, dashed line) (21). The corresponding function $\kappa_T = [\exp(n\lambda^2) - 1]/(k_B T n^2 \lambda^2)$ exhibits a minimum at $n \approx 1.59/\lambda^2 \sim 0.74 \mu\text{m}^{-2}$, which is close to the measured value of $0.79(5) \mu\text{m}^{-2}$. It is well understood that as the thermal wave packets spatially overlap, the classically expected decrease in compressibility with density (it is harder to compress a dense gas than a dilute one) is replaced with a compressibility increase that stems from the quantum-statistical occupation of low-lying energy levels, reducing the energy cost for compression as compared with that of the classical gas case. In the extreme high-density limit of an infinite-size deeply degenerate gas, bosons can be added to the system at essentially vanishing energy cost, meaning that $(\partial\mu/\partial n)_T$ gradually approaches zero as $\mu \rightarrow 0$, so that the compressibility takes arbitrarily large values.

Last, we studied the EOS $n = f(\mu, T)$ of the photon gas. The variation of the density n as a function of the chemical potential μ is shown in Fig. 4C, as determined from combining recorded density profiles of the gas in a tilted box at different N ; an exemplary density pro-

file from the unperturbed case and the corresponding line profile $n(x)$ are given in Fig. 4C, insets. As above, the conversion from position to chemical potential relies on the potential gradient $U_0/L \approx k_B 0.6 \text{ K } \mu\text{m}^{-1}$, which acts as a calibrated differential energy scale $d\mu = U_0/L dx$. Our data exhibit a larger slope than the EOS of the infinite 2D Bose gas, $n(\mu) = -\lambda^{-2} \log[1 - \exp(\mu/k_B T)]$ (Fig. 4C, dashed line) owing to the finite trap depth, as we confirmed with numerical calculations (21). Except for the condensed regime, in which LDA is invalid, our method reliably extracts the EOS of a quantum gas of light.

We have demonstrated a measurement of the compressibility of an optical quantum gas and determined its EOS. The experiment was carried out by using a 2D photon gas inside a box potential, both below and above the phase transition to a BEC. Compression of optical gases may have direct consequences for thermodynamic machines with light as a work medium (26). An additional perspective is the exploration of sound (17–20). The required dynamic manipulation of optical quantum gases is feasible through, for example, electro-optic trap modulation or spatiotemporally resolved pumping of the dye reservoir (27). Beyond ideal gas theory, a nonvanishing healing length can be achieved by either adding Kerr media or exploiting the weakly dissipative nature of photon condensates (28). The demonstrated homogeneous quantum gas of light in a box opens new possibilities for studies of universal phenomena in two dimensions, including critical behavior (29) and the nonequilibrium Kardar-Parisi-Zhang phase (30).

Fig. 4. Compressibility and EOS. (A) A linear potential realizes a force $F_0 = U_0/L$ that (inset) compresses the photon gas. Depending on its normal (blue) or quantum degenerate (green) state, the gas shows a different center-of-mass response, fitted in the linear response region (lines). (B) The compressibility κ_T decreases with density $n = N/L^2$, until above $n \sim 0.8 \mu\text{m}^{-2}$ quantum degeneracy sets in and the Bose gas becomes highly compressible as a consequence of the gradually vanishing energy cost to increase the density. At $n \gtrsim 2.6 \mu\text{m}^{-2}$ (shaded region), the κ_T extraction ceases to be valid; this range of validity has been confirmed numerically (21). For comparison, we show finite-size theory (red line; shading indicates uncertainty in V_0 , which causes the vertical shift), where the kink at large densities is due to the finite box size, and the prediction for the infinite 2D Bose gas (dashed line). (C) From the density profiles, we extracted the EOS by combining data for different local chemical potentials (21). (Insets) Exemplary density deviation Δn from the case with $U_0 = 0$ and line profile. Lines show theory for finite-depth box (solid line) and infinite-system (dashed line).



REFERENCES AND NOTES

1. I. Bloch, J. Dalibard, W. Zwerger, *Rev. Mod. Phys.* **80**, 885–964 (2008).
2. S. Diehl *et al.*, *Nat. Phys.* **4**, 878–883 (2008).
3. I. Carusotto, C. Ciuti, *Rev. Mod. Phys.* **85**, 299–366 (2013).
4. N. Navon, S. Nascimbène, F. Chevy, C. Salomon, *Science* **328**, 729–732 (2010).
5. T. L. Ho, Q. Zhou, *Nat. Phys.* **6**, 131–134 (2010).
6. T. Yefsah, R. Desbuquois, L. Chomaz, K. J. Günter, J. Dalibard, *Phys. Rev. Lett.* **107**, 130401 (2011).
7. C. L. Hung, X. Zhang, N. Gemelke, C. Chin, *Nature* **470**, 236–239 (2011).
8. M. J. H. Ku, A. T. Sommer, L. W. Cheuk, M. W. Zwierlein, *Science* **335**, 563–567 (2012).
9. C. Mordini *et al.*, *Phys. Rev. Lett.* **125**, 150404 (2020).
10. J. Klaers, J. Schmitt, F. Vewinger, M. Weitz, *Nature* **468**, 545–548 (2010).
11. J. Marelic, R. A. Nyman, *Phys. Rev. A* **91**, 033813 (2015).
12. S. Greveling, K. L. Perrier, D. van Oosten, *Phys. Rev. A* **98**, 013810 (2018).
13. T. Damm *et al.*, *Nat. Commun.* **7**, 11340 (2016).
14. N. D. Mermin, H. Wagner, *Phys. Rev. Lett.* **17**, 1133–1136 (1966).
15. Z. Hadzibabic, J. Dalibard, *Riv. Nuovo Cim.* **34**, 389–434 (2011).
16. R. J. Fletcher *et al.*, *Phys. Rev. Lett.* **114**, 255302 (2015).
17. J. L. Ville *et al.*, *Phys. Rev. Lett.* **121**, 145301 (2018).
18. M. Bohlen *et al.*, *Phys. Rev. Lett.* **124**, 240403 (2020).
19. P. Christodoulou *et al.*, *Nature* **594**, 191–194 (2021).
20. E. Estrecho *et al.*, *Phys. Rev. Lett.* **126**, 075301 (2021).
21. Materials and methods are available as supplementary materials.
22. C. Kurtscheid *et al.*, *EPL* **130**, 54001 (2020).
23. D. Dung *et al.*, *Nat. Photonics* **11**, 565–569 (2017).

24. N. Tammuz *et al.*, *Phys. Rev. Lett.* **106**, 230401 (2011).
 25. L. Pitaevskii, S. Stringari, *Bose-Einstein Condensation and Superfluidity* (Oxford Univ. Press, 2016).
 26. A. Ghosh, V. Mukherjee, W. Niedenzu, G. Kurizki, *Eur. Phys. J. Spec. Top.* **227**, 2043–2051 (2019).
 27. J. Schmitt *et al.*, *Phys. Rev. A* **92**, 011602 (2015).
 28. V. N. Gladilin, M. Wouters, *Phys. Rev. Lett.* **125**, 215301 (2020).
 29. P. Comaron *et al.*, *Phys. Rev. Lett.* **121**, 095302 (2018).
 30. A. Zamora, L. M. Sieberer, K. Dunnett, S. Diehl, M. H. Szymańska, *Phys. Rev. X* **7**, 041006 (2017).
 31. E. Busley *et al.*, Zenodo (2021); doi:10.5281/zenodo.5775757.

ACKNOWLEDGMENTS

We thank F. König, C. Wahl, and D. Dung for experimental assistance and D. Luitz, P. Christodoulou, Z. Hadzibabic, and R. Lopes for fruitful discussions. **Funding:** This work was supported by the DFG within SFB/TR 185 (277625399) and the Cluster of Excellence ML4Q (EXC 2004/1–390534769) and by the EU within the Quantum Flagship project PhoQuS (820392). J.S. acknowledges support from an ML4Q Independence grant. **Author contributions:** Conceived and designed the experiments and analyzed the data: E.B., L.E.M., and J.S. Contributed materials and analysis tools: E.B., L.E.M., A.R., C.K., K.K.U., M.W., and J.S. Performed the experiments: E.B. and L.E.M. Wrote the paper: F.V., M.W., and J.S. **Competing**

interests: The authors declare that they have no competing interests. **Data and materials availability:** The data described in the manuscript are available in the Zenodo database (31).

SUPPLEMENTARY MATERIALS

science.org/doi/10.1126/science.abm2543
 Supplementary Text
 Figs. S1 to S6
 References (32–36)

3 September 2021; accepted 20 December 2021
 10.1126/science.abm2543

CORONAVIRUS

Rapid increase in Omicron infections in England during December 2021: REACT-1 study

Paul Elliott^{1,2,3,4,5,6,*}, Barbara Bodinier^{1,2,†}, Oliver Eales^{1,7,†}, Haowei Wang^{1,7}, David Haw^{1,7}, Joshua Elliott^{3,8}, Matthew Whitaker^{1,2}, Jakob Jonnerby^{1,9}, David Tang^{1,2}, Caroline E. Walters^{1,7}, Christina Atchison^{1,3}, Peter J. Diggle^{5,10}, Andrew J. Page¹¹, Alexander J. Trotter¹¹, Deborah Ashby¹, Wendy Barclay⁸, Graham Taylor⁸, Helen Ward^{1,3,4,7}, Ara Darzi^{3,4,12}, Graham S. Cooke^{3,4,8}, Marc Chadeau-Hyam^{1,2,†}, Christl A. Donnelly^{1,7,13,*†}

The unprecedented rise in severe acute respiratory syndrome coronavirus 2 (SARS-CoV-2) infections during December 2021 was concurrent with rapid spread of the Omicron variant in England and globally. We analyzed the prevalence of SARS-CoV-2 and its dynamics in England from the end of November to mid-December 2021 among almost 100,000 participants in the REACT-1 study. Prevalence was high with rapid growth nationally and particularly in London during December 2021, with an increasing proportion of infections due to Omicron. We observed large decreases in swab positivity among mostly vaccinated older children (12 to 17 years) relative to unvaccinated younger children (5 to 11 years), and in adults who received a third (booster) vaccine dose versus two doses. Our results reinforce the importance of vaccination and booster campaigns, although additional measures have been needed to control the rapid growth of the Omicron variant.

Since its identification in November 2021, the Omicron variant of severe acute respiratory syndrome coronavirus 2 (SARS-CoV-2) has spread rapidly across the world, driven by its ability to cause more breakthrough infections among vaccinated individuals than other variants, likely as a result of genetic mutations within its viral spike protein (*S*). Furthermore, vaccine-induced

protection against the Delta variant (and its sublineages) was already found to be waning (2).

The Real-time Assessment of Community Transmission-1 (REACT-1) study (3–5) has been tracking the spread of the SARS-CoV-2 virus in England approximately monthly since May 2020 as England's first wave of infections declined. REACT-1 charted the complete replacement of Alpha by Delta from round 12 (21 May to 7 June 2021) to round 13 (24 June to 12 July 2021) (5). With round 16 (23 November to 14 December 2021) data, we document Omicron's early spread in England.

The SARS-CoV-2 vaccination program in England evolved quickly. In September 2021, in addition to the vaccinations offered to those 16 years of age and over, children aged 12 to 15 years were offered one dose of vaccine. By 12 December 2021, the opportunity to schedule third (booster) doses had been extended to all adults (aged 18 years and over) with heightened efforts to deliver booster doses as quickly as possible. At the same time, the rollout of the vaccination program to children aged 12 to 17 years was accelerated, with second doses becoming available to 12- to 15-year-olds as well as 16- and 17-year-olds (6).

Here, we document the early detection of Omicron in England using the community-based REACT-1 study to avoid the biases arising in case incidence data, including those due to test-seeking behavior and limited testing capacity (4). We compare SARS-CoV-2 swab positivity in round 16 to that in previous rounds.

In round 16 (23 November to 14 December 2021), 803,864 randomly selected individuals aged 5 years and over in England were invited to participate. Of these, 129,534 (16.1%) registered and 97,089 (12.1%) provided a self-administered throat and nasal swab with a valid RT-PCR (reverse transcription polymerase chain reaction) test result, including 661 samples (12 positives) obtained from 15 to 17 December 2021 (see supplementary materials and fig. S1). A total of 1192 positive swabs were detected, yielding an overall weighted prevalence of 1.41% (95% credible interval: 1.33%, 1.51%), the third highest value observed since the start of data collection in REACT-1 (from 1 May 2020) (table S1).

A P-spline model fit to all REACT-1 data revealed increasing weighted prevalence during round 16 starting around 1 December 2021 (Fig. 1A). We estimated a reproduction number $R = 1.09$ (95% credible interval: 1.04, 1.14) for the whole of round 16 based on an exponential model for the daily weighted prevalence, assuming a gamma-distributed generation time with a mean of 4.6 days and standard deviation of 3.1 days (7). Considering only data from December, the estimate of R was 1.19 (95% credible interval: 1.10, 1.28) (Table 1). We also found an increase in weighted prevalence in those aged 18 to 54 years, with $R = 1.16$ (95% credible interval: 1.10, 1.23) for the whole of round 16 and $R = 1.29$ (95% credible interval: 1.16, 1.42) for December only (Table 1), consistent with the P-spline model (Fig. 1B).

We found strong evidence of increasing weighted prevalence in London, which had the highest weighted prevalence nationally at 1.84% (95% credible interval: 1.59%, 2.12%) compared with 1.23% (95% credible interval: 1.03%, 1.47%) in round 15 (Fig. 2A and table S2). For London, we estimated an R of 1.29 (95% credible interval: 1.19, 1.40) for the whole of round 16, and 1.43 (95% credible interval: 1.24, 1.63) during December only (Table 1).

¹School of Public Health, Imperial College London, London, UK. ²MRC Centre for Environment and Health, School of Public Health, Imperial College London, London, UK.

³Imperial College Healthcare NHS Trust, London, UK.

⁴National Institute for Health Research Imperial Biomedical Research Centre, London, UK. ⁵Health Data Research (HDR) UK, Imperial College London, London, UK.

⁶UK Dementia Research Institute, Imperial College London, London, UK.

⁷MRC Centre for Global Infectious Disease Analysis and Jameel Institute, Imperial College London, London, UK.

⁸Department of Infectious Disease, Imperial College London, London, UK.

⁹National Heart and Lung Institute, Imperial College Healthcare NHS Trust, London, UK.

¹⁰CHICAS, Lancaster Medical School, Lancaster University, Lancaster, UK.

¹¹Quadram Institute, Norwich, UK. ¹²Institute of Global Health Innovation, Imperial College London, London, UK.

¹³Department of Statistics, University of Oxford, Oxford, UK.

*Corresponding author. Email: p.elliott@imperial.ac.uk (P.E.); c.donnelly@imperial.ac.uk (C.A.D.)

†These authors contributed equally to this work.

‡These authors contributed equally to this work.

Region-specific daily estimates of weighted prevalence confirmed a steep increase in London from 0.80% (95% credible interval: 0.36%, 1.75%) on 26 November 2021 to 6.06% (95% credible interval: 4.06%, 9.00%) on 14 December 2021 (Fig. 2B). A slower increase was observed in daily weighted prevalence in the South East, which reached 5.75% (95% credible interval: 2.60%, 12.22%) by 15 December. At the lower-tier local authority (LTLA) level, eight of the 10 highest smoothed estimates of prevalence over the whole of round 16 were in London (Lambeth, Kensington and Chelsea, Hammersmith and Fulham, Southwark, Islington, Westminster, Wandsworth, Camden), with estimates among these eight LTLAs ranging from 2.15% to 1.94%; the remaining two were in the South West (Cornwall, Plymouth), with estimates of 1.94% and 1.81%, respectively (Fig. 2C).

Of the 1192 positive swabs collected during round 16, 770 lineages were determined via viral genome sequencing with at least 50% coverage (Fig. 3, A to D, and table S3), of which 56 (7.3%) were the Omicron variant and all others were Delta or Delta sub-lineages. The

first swab testing positive for Omicron in REACT-1 was obtained on 3 December 2021 in London (Fig. 3B and table S4). Subsequent ($N = 19$) cases from 7 to 12 December 2021 were detected mainly in London and southern parts of England (Fig. 3C) and, from 13 to 17 December 2021, an additional 36 Omicron infections were detected, primarily in London (Fig. 3D).

Daily estimates of the proportion of Omicron (versus Delta and Delta sub-lineages) rapidly increased from 6 December onward (Fig. 3E). Smoothed estimates indicated that the proportion of Omicron infections exceeded 75% by 17 December 2021. We estimate a daily increase of 61.7% (95% credible interval: 46.2%, 82.7%) in the odds of Omicron infection (versus Delta and Delta sub-lineages), conditional on swab positivity. Assuming constant dynamics of Omicron's (and Delta's) transmission, we estimate 8.7 (95% credible interval: 5.4, 15.5) days for Omicron to increase from 10% to 90% of all daily infections, about 3.5 times faster than the estimated 31.4 (95% credible interval: 22.0, 43.9) days taken for Delta to grow from 10% to 90% against Alpha (5).

On the basis of the 56 Omicron variants detected out of 378 positives sequenced for swabs obtained from 1 to 17 December 2021, we estimate a prevalence of swab positivity for Omicron in England of 3700 (95% confidence interval: 700, 20,900) between 1 and 6 December, 142,200 (95% confidence interval: 93,200, 210,000) between 7 and 12 December, and 664,800 (95% confidence interval: 518,300, 803,600) between 13 and 14 December, assuming 100% sensitivity and with a weighted prevalence of 1.32%, 1.58%, and 2.14%, respectively.

Of the 56 participants with Omicron infection confirmed by sequencing, 54 (96.4%) were adults aged 18 to 54 years, for whom we found a steep increase in prevalence during round 16. The two other participants with Omicron infection were aged 65 to 74 years. Most of the participants testing Omicron-positive lived in London ($N = 30$, 53.7%), where there was the fastest increase in prevalence nationally during round 16. We found a difference in mean cycle threshold (Ct) values for the N-gene with mean 27.51 for Omicron compared to 25.62 for Delta-positive swabs

Table 1. Growth rates (per day), reproduction numbers, and doubling/halving times (in days) from exponential model fits on data from round 16 (23 November to 14 December 2021). Data include $N = 661$ samples (12 positives) obtained from 15 to 17 December 2021. Doubling/halving time estimates are shown only when the 95% credible intervals for R exclude 1.

	Growth rate (per day)	R	Probability $R > 1$	Doubling (+) / halving (-) time (in days)
<i>Round 16</i>				
All positives	0.019 (0.010, 0.029)	1.09 (1.04, 1.14)	>0.99	36.1 (71.7, 24.1)
Age				
Aged 17 and under	-0.019 (-0.035, -0.004)	0.91 (0.84, 0.98)	0.01	-35.7 (-19.6, *)
Aged 18 to 54	0.034 (0.021, 0.047)	1.16 (1.10, 1.23)	>0.99	20.3 (33.6, 14.6)
Aged 55 and over	0.005 (-0.022, 0.032)	1.02 (0.90, 1.15)	0.64	
Region				
East Midlands	0.010 (-0.020, 0.040)	1.05 (0.91, 1.19)	0.75	
West Midlands	0.019 (-0.017, 0.054)	1.09 (0.93, 1.26)	0.86	
East of England	0.013 (-0.019, 0.043)	1.06 (0.92, 1.21)	0.79	
London	0.060 (0.040, 0.080)	1.29 (1.19, 1.40)	>0.99	11.6 (17.5, 8.7)
North West	0.001 (-0.032, 0.034)	1.00 (0.86, 1.16)	0.52	
North East	-0.018 (-0.078, 0.038)	0.92 (0.68, 1.18)	0.27	
South East	0.022 (0.000, 0.044)	1.10 (1.00, 1.21)	0.97	
South West	-0.005 (-0.035, 0.024)	0.98 (0.85, 1.11)	0.38	
Yorkshire and The Humber	-0.022 (-0.056, 0.012)	0.90 (0.76, 1.06)	0.10	
<i>Round 16 (December only)</i>				
All positives	0.039 (0.021, 0.057)	1.19 (1.10, 1.28)	>0.99	17.8 (32.9, 12.2)
Age				
Aged 17 and under	-0.014 (-0.045, 0.017)	0.94 (0.80, 1.08)	0.19	
Aged 18 to 54	0.058 (0.034, 0.083)	1.29 (1.16, 1.42)	>0.99	11.9 (20.2, 8.4)
Aged 55 and over	0.011 (-0.044, 0.063)	1.05 (0.81, 1.31)	0.65	
Region				
East Midlands	0.047 (-0.009, 0.101)	1.23 (0.96, 1.52)	0.95	
West Midlands	-0.018 (-0.084, 0.045)	0.92 (0.65, 1.22)	0.29	
East of England	0.032 (-0.028, 0.090)	1.15 (0.88, 1.46)	0.86	
London	0.085 (0.050, 0.120)	1.43 (1.24, 1.63)	>0.99	8.2 (14.0, 5.8)
North West	-0.004 (-0.070, 0.058)	0.98 (0.71, 1.29)	0.46	
North East	0.067 (-0.051, 0.186)	1.34 (0.78, 2.05)	0.87	
South East	0.047 (0.007, 0.087)	1.23 (1.03, 1.44)	0.99	14.6 (*, 7.9)
South West	-0.027 (-0.089, 0.032)	0.88 (0.64, 1.15)	0.19	
Yorkshire and The Humber	-0.004 (-0.072, 0.062)	0.98 (0.70, 1.30)	0.46	

*Doubling/halving time had an estimated magnitude greater than 50 days and so represented approximately constant prevalence.

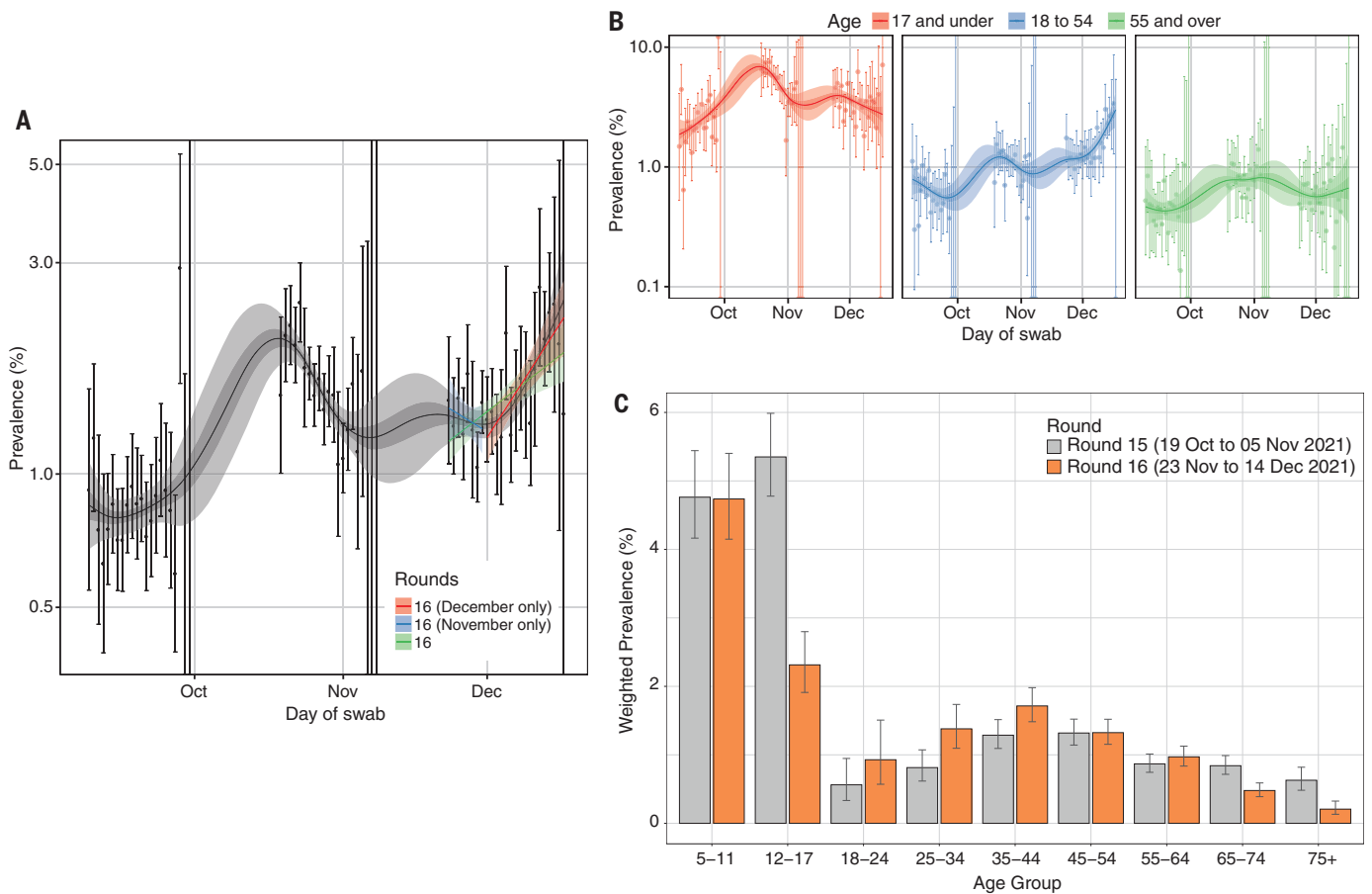


Fig. 1. Dynamics of the prevalence of SARS-CoV-2 swab positivity in England. (A) Comparison of exponential model fits to round 16 overall (green), round 16 from 23 to 30 November (blue), and round 16 from 1 December onward (red) in addition to a P-spline model fit to all rounds of REACT-1 (black, shown here only for rounds 14, 15, and 16). Shaded green, blue, and red regions show the 95% posterior credible interval for the exponential models, and the shaded gray region shows 50% (dark gray) and 95% (light gray) posterior credible intervals for the P-spline model. Results

are presented for each day (x axis) of sampling for rounds 14, 15, and 16; the prevalence of swab positivity is shown (y axis) on a log scale. Weighted observations (black dots) and 95% credible intervals (vertical lines) are also shown. (B) P-spline models for those aged 17 years and under (red), 18 to 54 years (blue), and 55 years and over (green). (C) Weighted prevalence of swab positivity by age group for rounds 15 and 16. Bars show the prevalence point estimates (gray for round 15 and orange for round 16); vertical lines represent the 95% credible intervals.

($P = 0.015$), but no difference in mean Ct values for the E-gene (table S5).

The highest weighted prevalence in round 16 by age was observed among 5- to 11-year-olds, who in December 2021 were not eligible for vaccination. Prevalence was 4.74% (95% credible interval: 4.15%, 5.40%), which was similar to that observed in round 15 at 4.76% (95% credible interval: 4.16%, 5.44%) (Fig. 1C and table S2). Of the 97,089 individuals included in round 16, 84,185 (86.7%) gave consent for linkage to their vaccination data. On the basis of the linked data, 76.6% of participants aged 12 to 17 years in round 16 had received one or two vaccine doses more than 14 days prior to swabbing (fig. S2). Between rounds 15 and 16, weighted prevalence fell in this group from 5.35% (95% credible interval: 4.78%, 5.99%) to 2.31% (95% credible interval: 1.91%, 2.80%).

The linked vaccination data also indicate that in round 16, 91.2% of participants aged

65 to 74 years had received a booster vaccine dose more than 14 days prior to swabbing, as had 96.8% of those aged 75 years and over (fig. S2). Reflecting the high uptake of the booster vaccine at these ages, we observed a fall in swab positivity by 40% in those aged 65 to 74 years [from 0.84% (95% credible interval: 0.72%, 0.99%) in round 15 to 0.48% (95% credible interval: 0.39%, 0.59%) in round 16] and by two-thirds in those aged 75 years and over [from 0.63% (95% credible interval: 0.48%, 0.82%) to 0.21% (95% credible interval: 0.13%, 0.32%)] (table S2).

Weighted prevalence in round 16 was higher in larger households including five people [2.73% (95% credible interval: 2.25%, 3.32%)] and six or more people [2.65% (95% credible interval: 2.00%, 3.50%)], compared to 0.88% (95% credible interval: 0.72%, 1.09%) in single-person households. In households with one or more children, weighted prevalence was 2.43% (95% credible interval: 2.23%, 2.65%) compared

to 0.85% (0.76%, 0.95%) in households without children; it was 8.00% (95% credible interval: 7.25%, 8.82%) among people who had been in contact with a confirmed COVID-19 case versus 0.81% (95% credible interval: 0.73%, 0.89%) for those without such contact; and it was 6.96% (95% credible interval: 6.32%, 7.67%) among people reporting classic COVID-19 symptoms in the month prior to swabbing versus 0.62% (95% credible interval: 0.55%, 0.70%) in those without symptoms (table S6).

In England, the first Omicron infection was recorded on 27 November 2021 (8) and it quickly became the dominant variant, with 76% of samples processed via TaqPath laboratories having S gene target failure (SGTF, an indicator of Omicron) as of 21 December 2021 (9). On the basis of these data, estimates of the regional doubling time for Omicron in England during December 2021 ranged from 1.6 to 2.5 days; London had the highest regional proportion of SGTF at 90.2%, followed by the East of

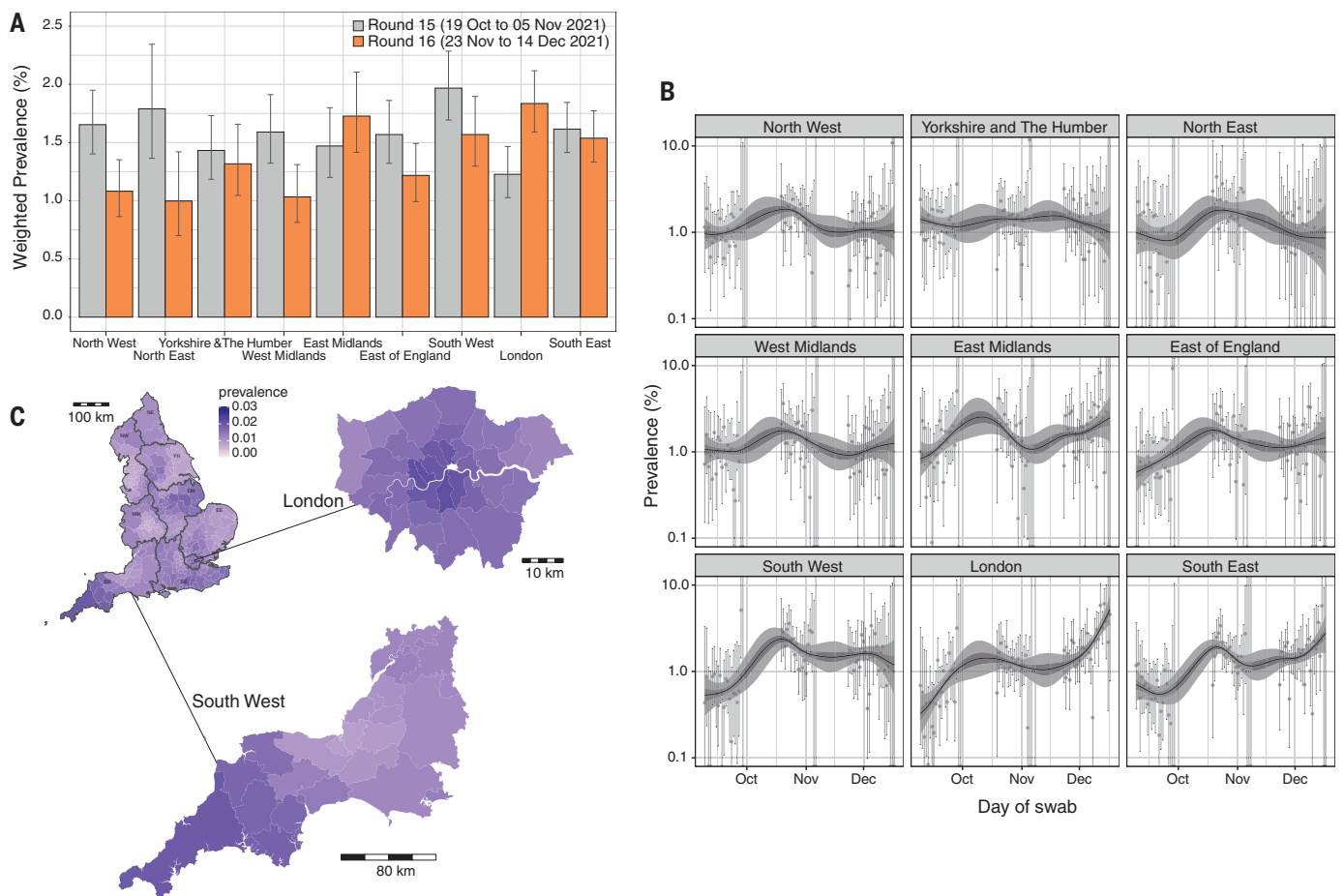


Fig. 2. Spatiotemporal distribution of SARS-CoV-2 prevalence in England.

(A) Weighted prevalence of swab positivity by region for round 15 and round 16. Bars represent prevalence point estimates (gray for round 15 and orange for round 16); vertical lines are the corresponding 95% credible intervals. (B) P-spline models fit to all rounds of REACT-1 for each of the nine regions separately, shown here only for the period of rounds 14, 15, and 16. Shaded regions show 50% (dark shade) and 95% (light shade) posterior credible interval for the P-spline models.

(C) Neighborhood smoothed average prevalence by lower-tier local authority area for round 16. Neighborhood prevalence was calculated from nearest neighbors (the median number of neighbors within 30 km in the study). Average neighborhood prevalence is displayed for individual lower-tier local authorities for the whole of England and for South West and London. Regions: NE = North East, NW = North West, YH = Yorkshire and The Humber, EM = East Midlands, WM = West Midlands, EE = East of England, L = London, SE = South East, SW = South West.

England at 80.0% (9). At the same time, the vaccine rollout in England was accelerating both among children at ages 12 years and over and in the booster program among adults.

Against this backdrop, we observed a mixed picture in round 16, characterized by (i) falling prevalence of swab positivity in children aged 12 to 17 years, where high levels of vaccination had been taking place; (ii) high and constant prevalence in children aged 5 to 11 years, who in December 2021 were ineligible for vaccination; (iii) falling prevalence among older people (65 years and over), who had largely had booster vaccinations; and (iv) since around 1 December 2021, rapidly rising prevalence nationally and especially in London and the South of England, coincident with the rapid rise of Omicron.

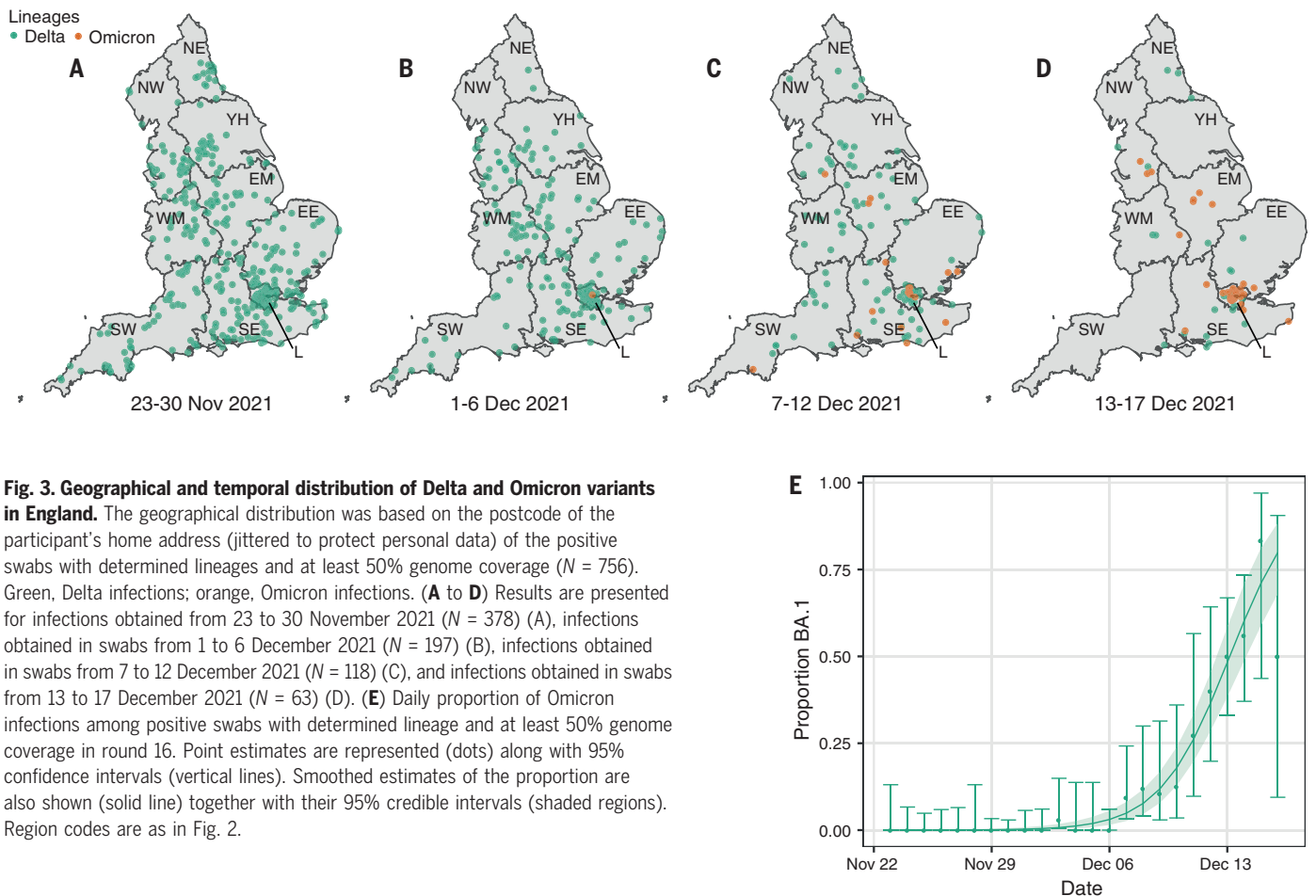
In our data, 56 Omicron infections were detected through 17 December 2021 as the Omicron epidemic became firmly established

in England. This coincided with a rapidly rising proportion of Omicron relative to Delta infections, which reflected both the rapid growth of Omicron and the replacement of Delta by Omicron (9). Household transmission from an Omicron index case is reportedly three times that of Delta (10), which may help to explain its transmission advantage. In addition, Omicron may have greater escape than immunity conferred by vaccination than Delta; the antibody titer required for neutralization of Omicron is estimated to be 20 to 40 times that for Delta (11). Nonetheless, in vitro studies indicate that individuals receiving a booster dose of mRNA vaccine have increased neutralization of the Omicron variant (1, 12).

Our results and the Coronavirus Infection Survey (CIS) data in England (13) suggest that Omicron infections in the first half of December 2021 predominated among young adults for whom hospitalization rates are much

lower than in older people, potentially biasing comparisons of variant severity despite attempts to correct for this statistically (14). Although Omicron appears less severe than Delta (14), a reduced risk of hospitalization could be rapidly offset by the observed exponential growth, which could then spill over into more vulnerable populations.

We estimate that the prevalence of swab positivity in England reached more than 600,000 between 13 and 17 December 2021. Estimates from the UK Health Security Agency indicate that there were 69,147 confirmed Omicron cases and 137,148 SGTF cases in the national testing data to 21 December 2021 (15). However, these figures are likely underestimates, because they depend on people presenting for testing, and unlike community-based studies such as REACT-1 and CIS, they do not include asymptomatic cases. Community-based surveillance studies can be critical in



providing situational awareness and estimates of infection prevalence that are not biased by access to testing (4). Monitoring of hospitalizations data is also important. For example, during the period 12 to 21 December 2021, COVID-19 hospitalizations rose more than 50% in London (16)—a pattern not observed in areas with lower prevalence of Omicron.

Our findings in children aged 12 to 17 years, among whom the vaccination program had been accelerated, are encouraging. Since round 15 (19 October to 5 November 2021), we saw prevalence in this group fall by more than half, while it remained unchanged among children aged 5 to 11 years who had not been vaccinated. This strongly suggests that even a single dose of vaccine was effective against infection in children aged 12 to 17 years, although this was predominantly against Delta; indeed, we did not detect any Omicron infections through sequencing of positive swabs in children, despite them having the highest prevalence of infections overall. Our findings are similarly encouraging among older people (ages 65 years and over) among whom prevalence fell substantially, although again these results mostly applied to Delta infections.

Our study has limitations. Our response rate was 12.1% (i.e., returned and valid tests relative to invitations), which, despite weighted correction of our prevalence estimates (17), could have introduced bias into our estimates. Although all PCR-positive samples were sent for sequencing, reliable sequence data (at least 50% genome coverage) were obtained on ~60% of samples. We estimated R according to a generation time distribution estimated for Delta (7); to the extent that Omicron may have a shorter generation time (7), we may have overestimated R during the latter part of round 16. However, our estimates of doubling time and probability that R exceeded 1 were unaffected. With Omicron being first observed in our data halfway through round 16, we had only 2 weeks of data collection to monitor the spread of Omicron versus Delta. The small number of sequenced Omicron cases precluded us from estimating Omicron-specific vaccine effectiveness directly.

We have documented the rapid rise of Omicron infections in England during December 2021. We found evidence for the effectiveness of vaccination in adolescents and of booster vaccinations in older adults, although this was predominantly against Delta. Thus, further data

are needed to assess how well booster vaccines protect against Omicron. Moreover, given that vaccines may take up to 2 weeks to have their full protective effect (18), vaccination alone may be insufficient to control the spread of Omicron, at least over the short term. Additional measures beyond vaccination have been needed to prevent health services in England and other countries (19, 20) from being overwhelmed.

REFERENCES AND NOTES

1. F. Schmidt *et al.*, *bioRxiv* 21267646 (2021).
2. E. G. Levin *et al.*, *N. Engl. J. Med.* **385**, e84 (2021).
3. S. Riley *et al.*, *Wellcome Open Res.* **5**, 200 (2020).
4. S. Riley *et al.*, *Science* **372**, 990–995 (2021).
5. P. Elliott *et al.*, *Science* **374**, eabl9551 (2021).
6. "NHS opens bookings for 12-15s to get second COVID jab" (NHS England, 2021); www.england.nhs.uk/2021/12/nhs-opens-bookings-for-12-15s-to-get-second-covid-jab/.
7. S. Abbott, K. Sherratt, M. Gerstung, S. Funk, *bioRxiv* 22268920 (2022).
8. Department of Health and Social Care, "First UK cases of Omicron variant identified" (2021); www.gov.uk/government/news/first-uk-cases-of-omicron-variant-identified.
9. UK Health Security Agency, "Omicron daily overview: 21 December 2021" (UK Health Security Agency); https://assets.publishing.service.gov.uk/government/uploads/system/uploads/attachment_data/file/1043098/20211221_OS_Daily_Omicron_Overview.pdf.

10. "SARS-CoV-2 variants of concern and variants under investigation in England: Technical Briefing 32" (UK Health Security Agency); https://assets.publishing.service.gov.uk/government/uploads/system/uploads/attachment_data/file/1042688/RA_Technical_Briefing_32_DRAFT_17_December_2021_2021_12_17.pdf.
11. "SARS-CoV-2 variants of concern and variants under investigation in England: Technical Briefing 31" (UK Health Security Agency); https://assets.publishing.service.gov.uk/government/uploads/system/uploads/attachment_data/file/1042367/technical_briefing-31-10-december-2021.pdf.
12. N. A. Doria-Rose *et al.*, *bioRxiv* 21267805 (2021).
13. "Coronavirus (COVID-19) Infection Survey, early analysis of characteristics associated with the Omicron variant among Covid-19 infections, UK: 21 December 2021"; www.ons.gov.uk/news/statementsandletters/coronaviruscovid19infectionsurveyearlyanalysisofcharacteristicsassociatedwiththemicronvariantamongcovid19infectionsuk20december2021.
14. N. Ferguson, "Report 50: Effectiveness of SARS-CoV-2 vaccines in England in 2021: a whole population survival analysis" (Imperial College London, 2021).
15. "Omicron daily overview: 22 December 2021" (UK Health Security Agency); https://assets.publishing.service.gov.uk/government/uploads/system/uploads/attachment_data/file/1043466/20211222_OS_Daily_Omicron_Overview.pdf.
16. UK Coronavirus Data Dashboard (London); <https://coronavirus.data.gov.uk/details/healthcare?areaType=nhsRegion&areaName=London>.
17. T. Sharot, "Weighting survey results" (1986); www.redresearch.com/wp/wp-content/uploads/2016/01/Weighting-Survey-Results.pdf.
18. N. Andrews *et al.*, *bioRxiv* 21266341 (2021).
19. Prime Minister's Office, "Prime Minister confirms move to Plan B in England" (2021); www.gov.uk/government/news/prime-minister-confirms-move-to-plan-b-in-england.
20. M. van Algemene Zaken, "Slowing the spread of the Omicron variant: lockdown in the Netherlands" (2021); www.government.nl/latest/news/2021/12/18/slowing-the-spread-of-the-omicron-variant-lockdown-in-the-netherlands.
21. doi:10.5281/zenodo.5574472.
22. "Publish with data from GISAID"; www.gisaid.org/help/publish-with-data-from-gisaid/.

ACKNOWLEDGMENTS

We thank key collaborators on this work—Ipsos MORI: K. Beaver, S. Clemens, G. Welch, N. Gilby, K. Ward, G. Pantelidou, and K. Pickering; Institute of Global Health Innovation at Imperial College London: G. Fontana, J. Alford; School of Public Health, Imperial College London: E. Johnson, R. Elliott, G. Blakoe; Quadram Institute, Norwich, UK: N.-F. Alikhan; North West London Pathology and Public Health England (now UKHSA) for help in calibration of the laboratory analyses; the Patient Experience Research Centre at Imperial College London and the REACT Public Advisory Panel; NHS Digital for access to the NHS register; and the Department of Health and Social Care for logistic support. **Funding:** The study was funded by the Department of Health and Social Care in England. The funders had no role in the design and conduct of the study; collection, management, analysis, and interpretation of the data; and preparation, review, or approval of this manuscript. P.E. is Director of the Medical Research Council (MRC) Centre for Environment and Health (MR/L01341X/1, MR/S019669/1). P.E. acknowledges support from Health Data Research UK (HDR UK); the National Institute for Health Research (NIHR) Imperial Biomedical Research Centre; NIHR Health Protection Research Units in Chemical and Radiation Threats and Hazards, and Environmental Exposures and Health; the British Heart Foundation Centre for Research Excellence at Imperial College London (RE/18/4/34215); and the UK Dementia Research Institute at Imperial College London (MC_PC_17114). A.J.P. acknowledges the support of the Biotechnology and Biological Sciences Research Council (BB/R012504/1). B.B. is supported by an MRC PhD Studentship from the MRC Centre for Environment and Health. H.Ward acknowledges support from an NIHR Senior Investigator Award, the Wellcome Trust (205456/Z/16/Z), and the NIHR Applied Research Collaboration (ARC) North West London. J.E. is an NIHR academic clinical fellow in infectious diseases. G.C. is supported by an NIHR Professorship. M.C.-H. and B.B. acknowledge support from Cancer Research UK, Population Research Committee Project grant "Mechanomics" (grant 22184 to M.C.-H.). M.C.-H. and M.W. acknowledge support from the H2020-EXPANSE project (Horizon 2020 grant 874627). C.A.D. acknowledges support from

the MRC Centre for Global Infectious Disease Analysis, the NIHR Health Protection Research Unit in Emerging and Zoonotic Infections and the NIHR-funded Vaccine Efficacy Evaluation for Priority Emerging Diseases (PR-OD-1017-20007). **Author contributions:** Conceptualization: P.E., C.A., P.J.D., D.A., W.B., H. Ward, A.D., G.S.C., M.C.-H., C.A.D.; methodology: P.E., B.B., O.E., H.Wang, D.H., C.E.W., P.J.D., D.A., M.C.-H., C.A.D.; software: B.B., O.E., H.Wang, D.H., J.J., D.T., C.E.W., M.C.-H.; validation: O.E., H.Wang, G.T.; formal analysis: B.B., O.E., H.Wang, D.H., J.J., D.T., A.J.P., M.C.-H.; investigation: P.E., A.J.T., M.C.-H.; resources: P.E., A.J.P.; data curation: B.B., O.E., H.Wang, D.H., M.W., D.T., A.J.P.; writing—original draft: P.E., J.E., G.S.C., M.C.-H., C.A.D.; writing—review and editing: P.E., O.E., D.H., J.E., C.E.W., C.A., P.J.D., A.J.T., D.A., W.B., G.T., H. Ward, G.S.C., M.C.-H., C.A.D.; visualization: B.B., O.E., H.Wang, M.C.-H.; supervision: P.E., C.A., D.A., W.B., H. Ward, A.D., G.S.C., M.C.-H., C.A.D.; project administration: P.E., C.A., W.B., H. Ward, G.S.C., M.C.-H., C.A.D.; funding acquisition: P.E., C.A., D.A., W.B., H. Ward, A.D., G.S.C., C.A.D. All authors revised the manuscript for important intellectual content and approved the submission of the manuscript. P.E., M.C.-H., C.A.D. had full access to the data and take responsibility for the integrity of the data and the accuracy of the data analysis and for the decision to submit for publication. **Competing interests:** A.D. is chairman of the Health Security and Pre-emptive Medicine Initiative, Flagship Pioneering UK plc, and has no conflict of interest to declare. M.C.-H. holds shares in the O-MOSE company. Consulting activities conducted by the company are independent of the present work and M.C.-H. has no conflict of interest to declare. All other authors have no competing interests to declare. **Data and materials availability:** Access to REACT-1 individual-level data is restricted to protect participants' anonymity. Summary statistics, descriptive tables, and code

from the current REACT-1 study are available at <https://github.com/mrc-ide/reactid1>. REACT-1 study materials are available for each round at www.imperial.ac.uk/medicine/research-and-impact/groups/react-study/. Sequence read data are available without restriction from the European Nucleotide Archive at www.ebi.ac.uk/ena/browser/view/PRJEB37886, and consensus genome sequences are available from GISAID (22). We obtained research ethics approval from the South Central-Berkshire B Research Ethics Committee (IRAS ID: 283787). A Public Advisory Panel provides input into the design, conduct, and dissemination of the REACT research program. This work is licensed under a Creative Commons Attribution 4.0 International (CC BY 4.0) license, which permits unrestricted use, distribution, and reproduction in any medium, provided the original work is properly cited. To view a copy of this license, visit <https://creativecommons.org/licenses/by/4.0/>. This license does not apply to figures/photos/artwork or other content included in the article that is credited to a third party; obtain authorization from the rights holder before using such material.

SUPPLEMENTARY MATERIALS

science.org/doi/10.1126/science.abn8347
Materials and Methods
Figs. S1 and S2
Tables S1 to S6
References (23–31)

24 December 2021; accepted 2 February 2022
Published online 8 February 2022
10.1126/science.abn8347

BIOMATERIALS

Topological supramolecular network enabled high-conductivity, stretchable organic bioelectronics

Yuanwen Jiang^{1†}, Zhitao Zhang^{1†}, Yi-Xuan Wang^{1,2*†}, Deling Li^{3,4†}, Charles-Théophile Coen¹, Ernie Hwaun⁵, Gan Chen⁶, Hung-Chin Wu¹, Donglai Zhong¹, Simiao Niu¹, Weichen Wang⁶, Aref Saberi¹, Jian-Cheng Lai^{1,7}, Yilei Wu¹, Yang Wang⁶, Artem A. Trotsyuk^{8,9}, Kang Yong Loh¹⁰, Chien-Chung Shih¹, Wenhui Xu⁶, Kui Liang¹¹, Kailiang Zhang¹¹, Yihong Bai², Gurupranav Gurusankar¹, Wenping Hu², Wang Jia⁴, Zhen Cheng³, Reinhold H. Dauskardt⁶, Geoffrey C. Gurtner⁹, Jeffrey B.-H. Tok¹, Karl Deisseroth^{8,12,13}, Ivan Soltesz⁵, Zhenan Bao^{1*}

Intrinsically stretchable bioelectronic devices based on soft and conducting organic materials have been regarded as the ideal interface for seamless and biocompatible integration with the human body. A remaining challenge is to combine high mechanical robustness with good electrical conduction, especially when patterned at small feature sizes. We develop a molecular engineering strategy based on a topological supramolecular network, which allows for the decoupling of competing effects from multiple molecular building blocks to meet complex requirements. We obtained simultaneously high conductivity and crack-onset strain in a physiological environment, with direct photopatternability down to the cellular scale. We further collected stable electromyography signals on soft and malleable octopus and performed localized neuromodulation down to single-nucleus precision for controlling organ-specific activities through the delicate brainstem.

Implantable and wearable bioelectronic systems are essential in biomedical applications, including multimodal monitoring of physiological signals for disease diagnosis (1, 2), programmable modulation of neural or cardiac activities for therapeutics (3, 4), restoration of lost sensorimotor functions for prosthetics (5, 6), and augmented reality (7). However, many of these existing devices experience performance degradation, and sometimes failure, when operating in a dynamic-moving tissue environment (8). This

stems primarily from the mechanical mismatches between electronics and biological systems (e.g., modulus and stretchability), which inevitably lead to interfacial delamination, fibrotic encapsulation, and/or gradual tissue scarring (9).

To maintain effective electrical signal exchanges across bioelectrode interfaces, efforts have been made to render rigid electronics and inorganic materials compliant to soft biological tissues (10, 11). Meanwhile, intrinsically stretchable organic electronics are fast

emerging as a promising candidate with several specific advantages (12). First, they do not suffer from the inherent trade-off between overall

system stretchability and device density for rigid materials. Therefore, high-resolution mapping and intervention can be realized with conformal biointerfaces (13) (Fig. 1A). Second, the high volumetric capacitance of conducting polymers (CPs) can reduce the electrode-tissue interfacial impedance, especially at physiologically relevant frequency ranges (<10 kHz), which allows high recording fidelity and efficient stimulation charge injection (14, 15). However, electrical conductivities of existing stretchable CPs are too low once they are microfabricated into bioelectronic devices. As a result, rigid metal interconnects are still required, which greatly diminishes the advantages of soft CPs (12).

Here, we describe a rationally designed topological supramolecular network to simultaneously enable three important advancements in bioelectronics. These advancements are (i) biocompatible and stretchable CPs with high conductivity, (ii) direct photopatternability down to cellular-level feature sizes, and (iii) high stretchability maintained after microfabrication with no crack formation under 100%

strain (Fig. 1, B and C), all of which are essential for low-impedance and seamless biointegration (Fig. 1, D to G).

Poly(3,4-ethylenedioxythiophene):polystyrene sulfonate (PEDOT:PSS) is among the highest performing and most investigated CPs for bioelectronic devices (12, 14, 16). Although ionic and molecular additives can improve its conductivity and stretchability (17), after solvent treatment or immersion in aqueous biological environments, the performance of existing PEDOT:PSS films typically drops substantially because the non-cross-linked additives are washed away (18). To overcome these challenges, we designed a cross-linkable supramolecular additive based on a polyrotaxane (PR) structure. Our key hypothesis was that incorporating topology into molecular design might decouple competing effects using multiple molecular building blocks to meet complex requirements (19). We chose mechanically interlocked structures because they have large conformational freedom from the mobile junctions (20, 21). Therefore, by using a single supramolecular cross-linker with tailored chemistry

¹Department of Chemical Engineering, Stanford University, Stanford, CA 94305, USA. ²Tianjin Key Laboratory of Molecular Optoelectronic Sciences, Department of Chemistry, School of Science, Tianjin University, Tianjin 300072, China. ³Department of Radiology, Molecular Imaging Program at Stanford (MIPS), Stanford University, Stanford, CA 94305, USA. ⁴Department of Neurosurgery, Beijing Tiantan Hospital, Beijing Neurosurgical Institute, Capital Medical University, Beijing 100070, China. ⁵Department of Neurosurgery, Stanford University, Stanford, CA 94305, USA. ⁶Department of Materials Science and Engineering, Stanford University, Stanford, CA 94305, USA. ⁷State Key Laboratory of Coordination Chemistry, School of Chemistry and Chemical Engineering, Nanjing University, Nanjing 210093, China. ⁸Department of Bioengineering, Stanford University, Stanford, CA 94305, USA. ⁹Department of Surgery, Stanford University, Stanford, CA 94305, USA. ¹⁰Department of Chemistry, Stanford Chemistry, Engineering & Medicine for Human Health (ChEM-H), Stanford University, Stanford, CA 94305, USA. ¹¹BOE Technology Center, BOE Technology Group Co., Ltd., Beijing 100176, China. ¹²Department of Psychiatry and Behavioral Sciences, Stanford University, Stanford, CA 94305, USA. ¹³Howard Hughes Medical Institute, Stanford University, Stanford, CA 94305, USA. *Corresponding author. Email: zbao@stanford.edu (Z.B.); yx_wang@tju.edu.cn (Y.-X.W.) †These authors contributed equally to this work.

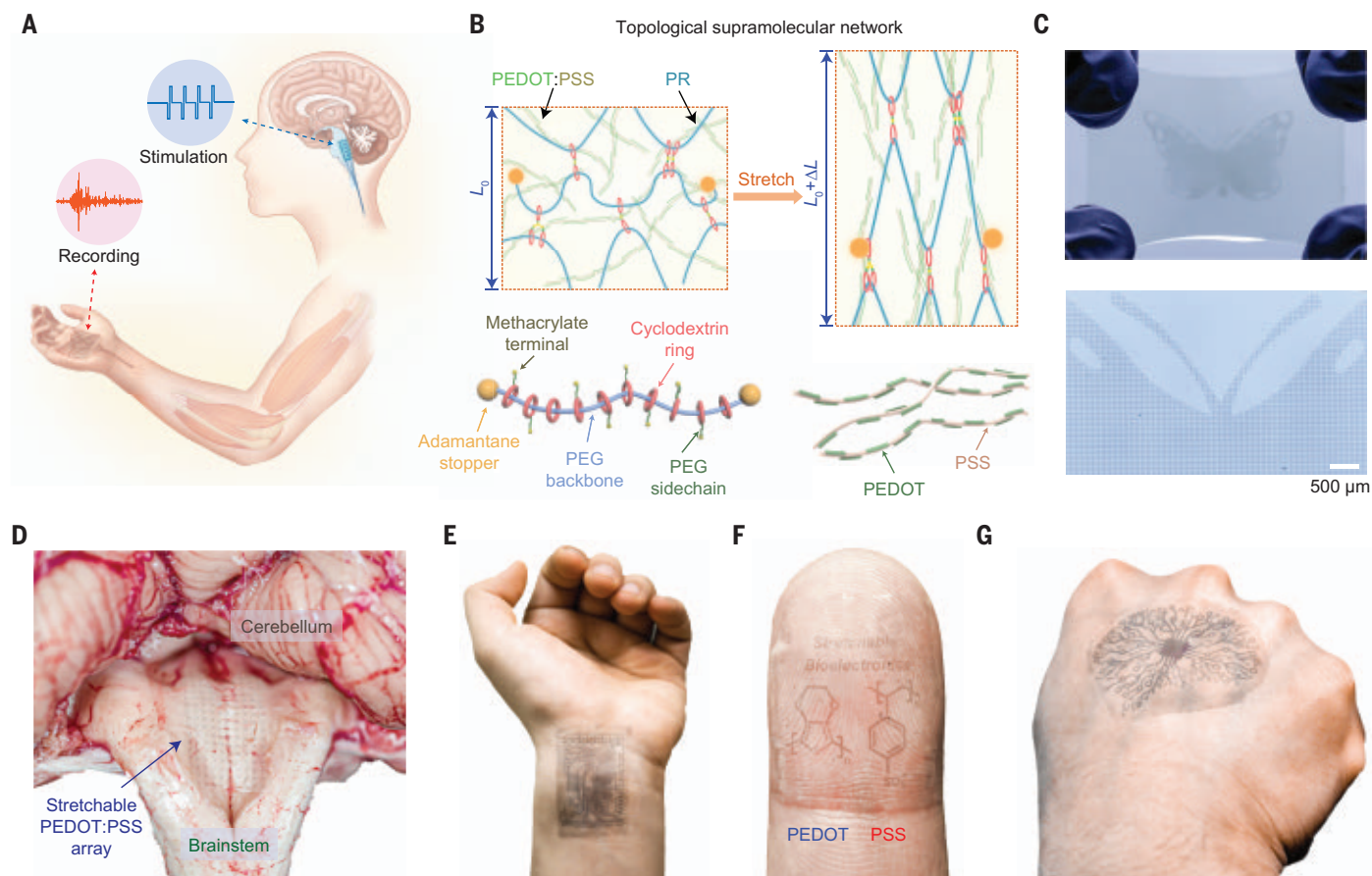


Fig. 1. Intrinsically stretchable organic electronics for multimodal and conformal biointerfaces. (A) A stretchable multielectrode array can form seamless interfaces with multiple organs for bidirectional interrogations with high precision. (B) Schematic diagram illustrating the intrinsically stretchable topological supramolecular network with the key molecular building blocks of

PR monomers. L , length of film. (C) The topological supramolecular network allows direct photopatterning of a large-area, high-density stretchable electrode array. (D to G) Photographic images showing the conformal interface between stretchable PEDOT:PSS devices and underlying tissues, including the brainstem (D), the wrist (E), the finger (F), and the back of the hand (G).

and topology, we could achieve all desirable properties in one CP system (Fig. 1B).

Our PR, which we call TopoE, is composed of a polyethylene glycol (PEG) backbone and sliding cyclodextrins (CDs) functionalized with PEG methacrylate (PEGMA) side chains to induce high conductivity, stretchability, and photopatternability (Fig. 2, A and B; synthesis and characterizations are available in figs. S1 to S9 and table S1). Although PEG has been known to induce the aggregation of PEDOT to enhance conductivity (22), its tendency to crystallize would lead to phase separation and poor stretchability. We hypothesized that the sliding CD units may prevent the crystallization of PEG and provide better stretchability.

We first investigated two control samples with PEG diacrylate (PEGDA) blended into PEDOT:PSS for covalent cross-linking. PEGDA-10k was chosen to mimic a PR backbone, whereas PEGDA-575 was chosen for the PR side chain (see materials and methods). In both cases, crack formations were slightly delayed from ~5% to ~50 or 30% strain, respectively (Fig. 2C and fig. S11). Further analyses using atomic force microscopy (AFM) and grazing incidence x-ray diffraction (GIXD) spectroscopy revealed that the films were inhomogeneous and suffered severe micro-phase separations, likely as a result of the crystallization of PEG (figs. S12 to S14). For PEG-ylated cyclodextrin (CD-PEGMA), its

poor solubility in water prevented uniform blending with PEDOT:PSS such that the final crack-onset strain was measured to be only ~30%. Similarly for PR-MA without any PEG side chains, it also could not dissolve well in water to enable good blending with PEDOT:PSS (Fig. 2D and fig. S11).

However, PR-PEGMA was found to have the right balance between molecular topology and chemical polarity. It has good solubility in water as a result of the PEG-based backbone and side chains yet low crystallinity because of the bulky CD rings (fig. S14). As a result, the photo-cross-linked TopoE film with PR-PEGMA/PEDOT:PSS was uniform and can be stretched up to 150% strain. The

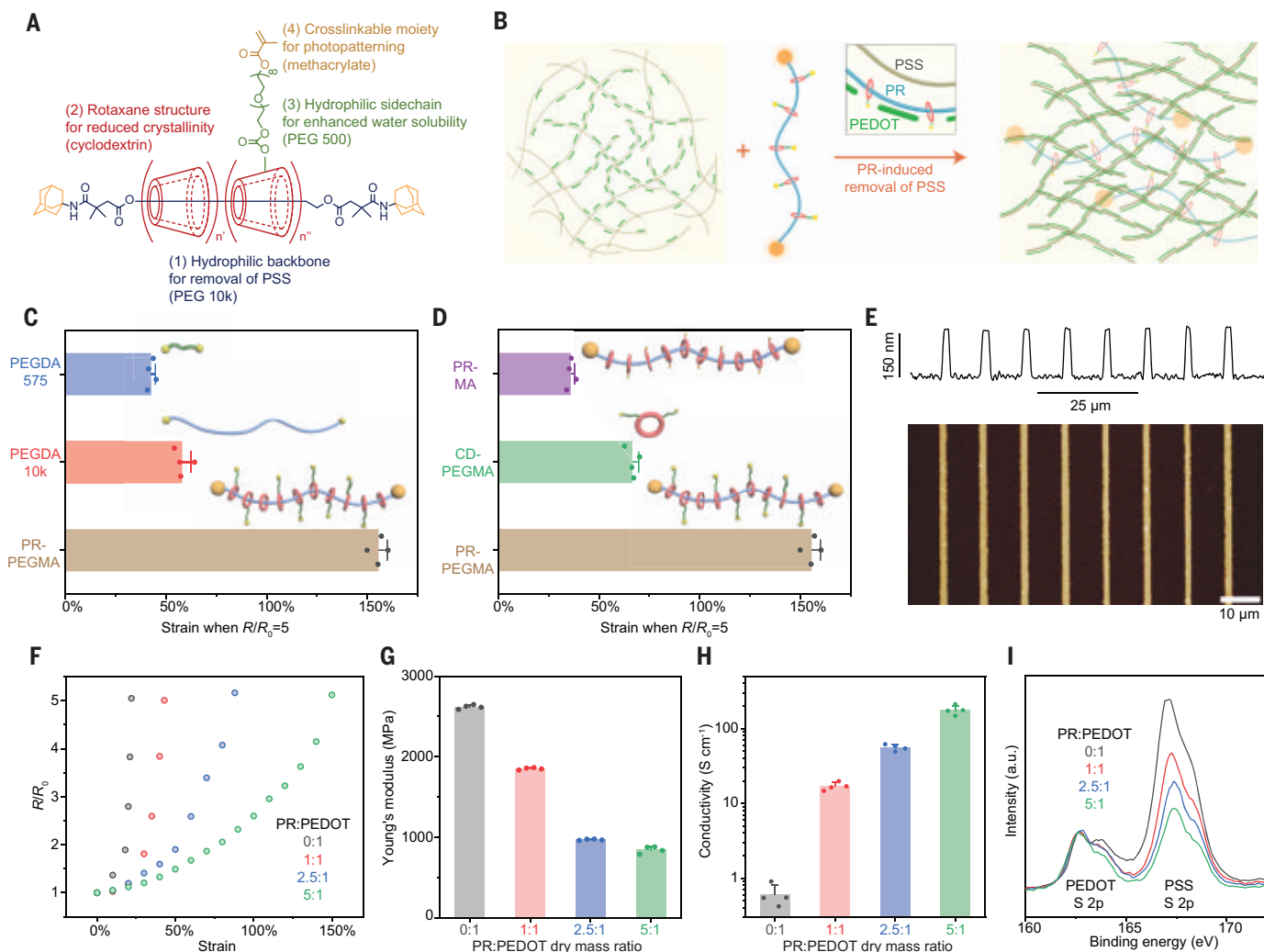


Fig. 2. PR-based topological network enables simultaneously enhanced conductivity, stretchability, and photopatternability of PEDOT:PSS.

(A) Chemical structure of PR-PEGMA and individual roles of each building block. (B) Schematic diagram illustrating the interaction between PR and PEDOT:PSS for enhanced conductivity. (C and D) Stretching tests showing that the PR-blended PEDOT:PSS film could substantially enhance stretchability compared with other control samples. Films were deposited on styrene-ethylene-butylene-styrene (SEBS) elastomers with thicknesses of ~200 nm. R , resistance. (E) AFM height image and corresponding surface profile of a photopatterned

TopoE array with 2- μ m width. (F) Resistance change as a function of strain for TopoE films with different PR over PEDOT:PSS dry mass weight ratios. All films in (F) to (I) were UV cross-linked after blending followed by washing in water and blow drying. (G) Statistical comparison of Young's moduli measured by nanoindentation for different TopoE films indicating that PR can reduce the overall film stiffness. (H) Four-point probe measurements showing enhanced film conductivity with higher PR content. (I) XPS profiles indicating reduced PSS content as the PR over PEDOT:PSS dry mass ratio increases in the film. a.u., arbitrary units.

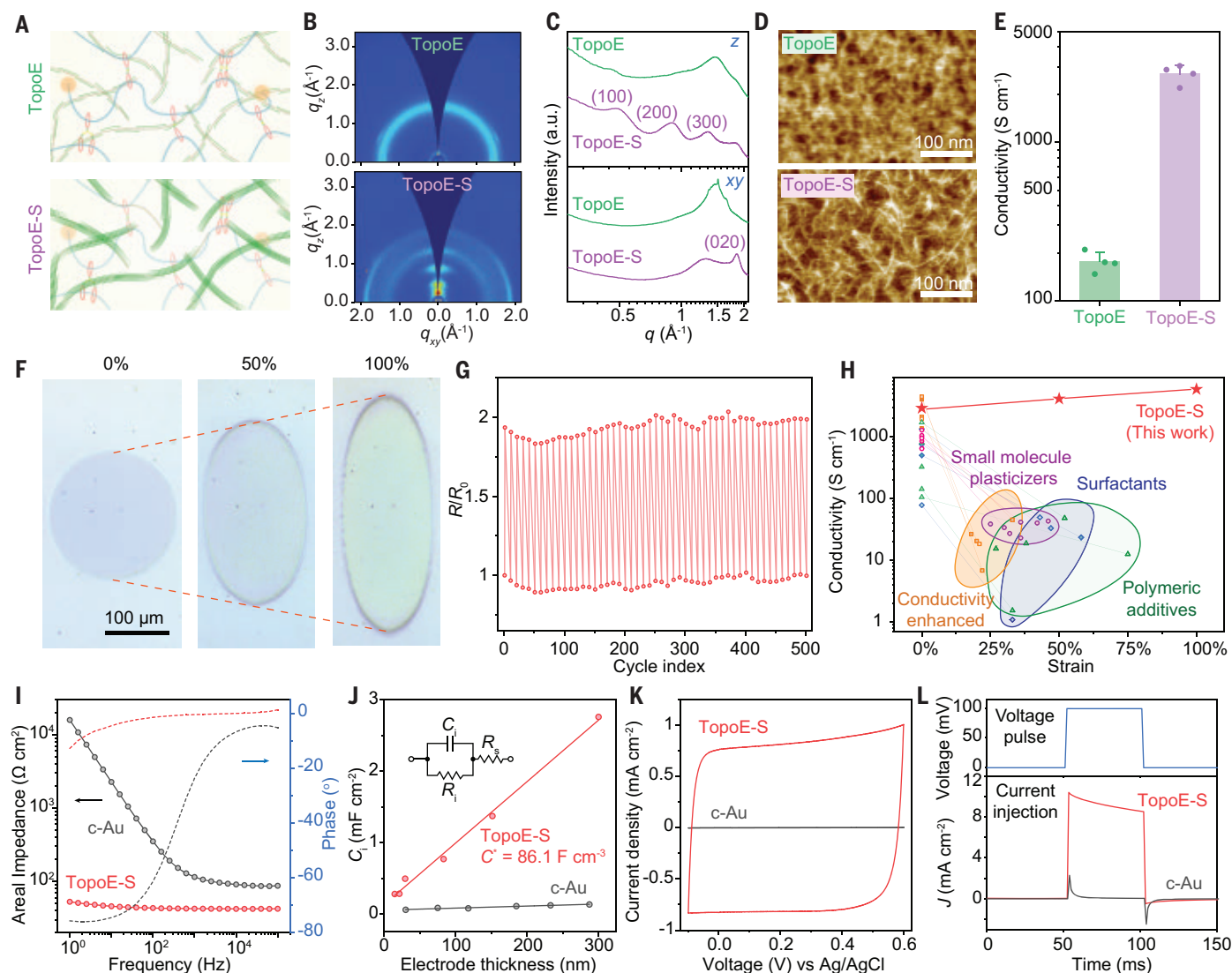


Fig. 3. Fully cross-linked topological network can afford posttreatment toward record-high conductivity and stretchability. (A) Schematic diagram illustrating the change of crystallinity by acid treatment. (B and C) Two-dimensional (2D) spectra (B) and 1D profile (C) of GIXD spectra collected from TopoE and TopoE-S. (D) AFM phase images showing the morphological changes of TopoE and TopoE-S. (E) Electrical measurement showing enhanced conductivity after acid treatment for TopoE-S. (F) Optical microscopy images showing the shape evolution of a TopoE-S pattern during stretching without inducing any cracks. (G) Cyclic stretching test between 0 and 100% strain showing reversible resistance changes of TopoE-S. (H) Conductivity over strain

plots showing high conductivity under strain for TopoE-S versus literature-reported PEDOT:PSS after water soaking. All previously reported methods suffer from severe conductivity degradation from soaking and/or from strain (detailed data and references are in fig. S31). (I) Electrochemical impedance spectroscopy measurements showing the reduced impedance per unit area of TopoE-S compared with c-Au. (J) Interfacial capacitance per unit area from TopoE-S and Au as a function of electrode thickness. (K) Cyclic voltammograms showing the enhanced charge storage capacity per unit area of TopoE-S over c-Au. (L) Current measurements after transient voltage pulses showing better charge injection per unit area of TopoE-S compared with that of c-Au.

number of side chains on each PR-PEGMA molecule was also found to be important, with eight PEGMA chains being the optimal condition with the best stretchability (fig. S15). We also investigated other common multiarm PEGDA derivatives and observed that only our PR pulley topology was effective in enhancing the stretchability of PEDOT:PSS (fig. S16). The TopoE film can be directly photopatterned down to 2 μm (Fig. 2E and fig. S17), and the cross-linked film after development maintained high stretchability (fig. S18). With these

developments, we chose PR-PEGMA₈ (abbreviated as PR) for all future characterizations and fabrications.

As the PR content increased, higher stretchability (Fig. 2F and fig. S19) and lower Young's moduli were obtained (Fig. 2G). Notably, a higher PR content also led to a better PEDOT:PSS conductivity with an enhancement of over two orders of magnitude compared with pristine PEDOT:PSS (Fig. 2H). X-ray photoelectron spectroscopy (XPS) revealed a decreasing trend of the remaining PSS/PEDOT ratio as the PR-

PEGMA content increased, which indicated that a large portion of insulating PSS was removed after blending and water development (Fig. 2I). Ultraviolet (UV)-visible and Raman spectroscopy also confirmed that less PSS remained in the TopoE film (fig. S20). With PR, its polar PEG chains replaced a portion of PSS in interacting with PEDOT, which led to the enhanced aggregation of PEDOT (22) (Fig. 2B and fig. S21). In addition to increased PEDOT content, AFM phase images of the blended films further revealed that the microscale morphology of

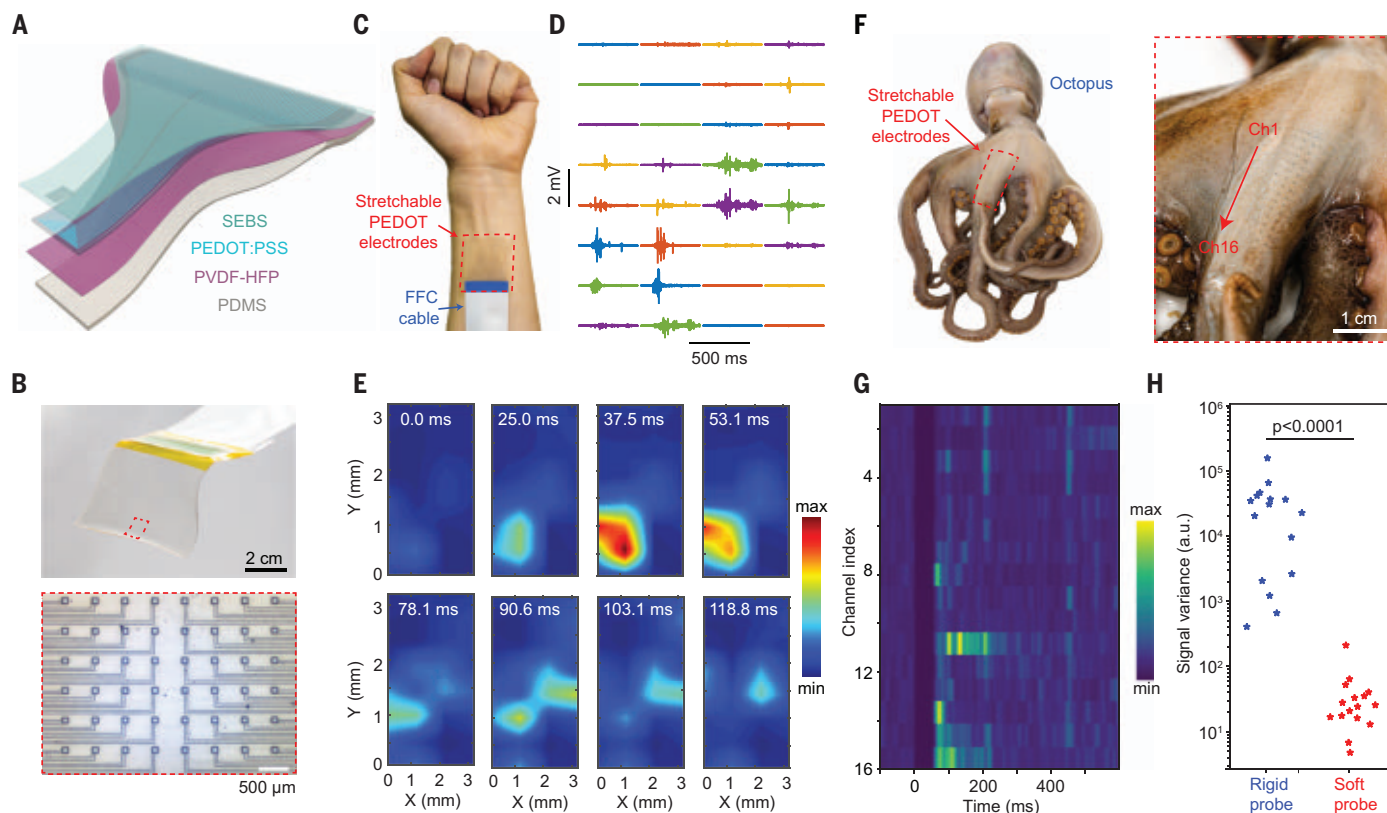


Fig. 4. Soft and stretchable electrode array allows stable electrophysiological monitoring of deformable tissues. (A) Exploded view of the multilayered stacks for the stretchable electrode array. (B) Photograph of an as-fabricated device (top) and an optical microscope image of the active site with 100- μm electrode width (bottom) used for (D) and (E). (C) Photograph of the sEMG measurement setup including a tissue-conforming stretchable electrode array and a flexible flat cable (FFC) for input-output communications. (D) Representative EMG recording traces

during a fist gesture with distinct spatiotemporal dynamics of individual channels. (E) Temporal evolution of EMG activity across different channels corresponding to the raw traces in (D) while making a fist. (F) Photographic images of a stretchable electrode array attached to an octopus arm, with an electrode width of 500 μm . (G) Peristimulus time histogram of evoked EMG activities of the octopus during muscle twitching. (H) Comparison of the signal variance during the resting state recorded by a rigid probe made on polyimide versus a soft and stretchable TopoE-S probe.

PEDOT gradually evolved from grain-like particles to percolated microwebs, which was favorable for enhanced charge transport, especially under strain (figs. S22 and S23).

We confirmed that the topological network could survive the sulfuric acid-dipping process to further improve conductivity (Fig. 3A) using XPS depth profiling investigation (fig. S24). We also used GIXD spectroscopy to track the change of PEDOT crystallization (Fig. 3, B and C). The neat TopoE film showed a scattering profile with a weak (100) diffraction peak, corresponding to the PEDOT lamellar packing. The acid-treated film, termed TopoE-S, showed high-order diffraction peaks with strong intensities, whereas the (100) peak shifted to a larger q value, which suggests denser lamellar packing and longer-range order (23). The π - π (020) peak also emerged in the in-plane direction, indicating longer-range order for π - π stackings between PEDOT backbones (24). In addition to the increased PEDOT crystallinity, AFM phase images showed that the PEDOT morphology became interconnected fibers after acid treat-

ment (Fig. 3D). With both these changes, a film conductivity up to $\sim 2700 \text{ S cm}^{-1}$ was obtained for TopoE-S, which is one order of magnitude of enhancement compared with that of TopoE and three orders of magnitude of enhancement compared with that of pristine PEDOT:PSS (Fig. 3E and fig. S25). The TopoE-S film also had high optical transmittance in the visible range as a transparent conductor (fig. S26).

The photopatterned circular structure of TopoE-S could be stretched to an elliptical shape at 100% strain while remaining intact without observable cracks (Fig. 3F and figs. S27 and S28). AFM phase images and corresponding fast Fourier transform (FFT) spectrograms of the TopoE-S film under strain showed that the PEDOT microfibrils became aligned along the stretching direction and returned to isotropic orientations when strain was released (fig. S29). GIXD spectra confirmed the retention of the PEDOT crystallization in directions both parallel and perpendicular to the strained axis (fig. S30). Finally, cyclic stretching tests between 0 and 100% strain for the TopoE-S film showed

reversible resistance changes for at least 500 cycles (Fig. 3G). For bioelectronics applications, the PEDOT:PSS electrode needs to be immersed in the aqueous physiological environment. Previously reported PEDOT:PSS systems with conductivity-enhancement treatment (23), small molecule plasticizers (17), surfactant blending (25), or polymeric additives (26) all suffered from substantial drops of conductivities upon stretching after immersion (Fig. 3H and fig. S31). By contrast, TopoE-S was able to maintain its high performance at $\sim 2700 \text{ S cm}^{-1}$ initial conductivity and $\sim 6000 \text{ S cm}^{-1}$ at 100% strain with chain alignments (Fig. 3H and figs. S29 and S31).

The electrochemical impedance of TopoE-S measured in phosphate-buffered saline (PBS) solution was found to be lower than that of stretchable cracked Au (c-Au) in all frequency ranges (Fig. 3I). c-Au electrodes are among the best stretchable electrodes for bioelectronics (27). Their high-frequency unit-area impedance is determined by Au thickness and feature size, which are constrained by crack size. Their

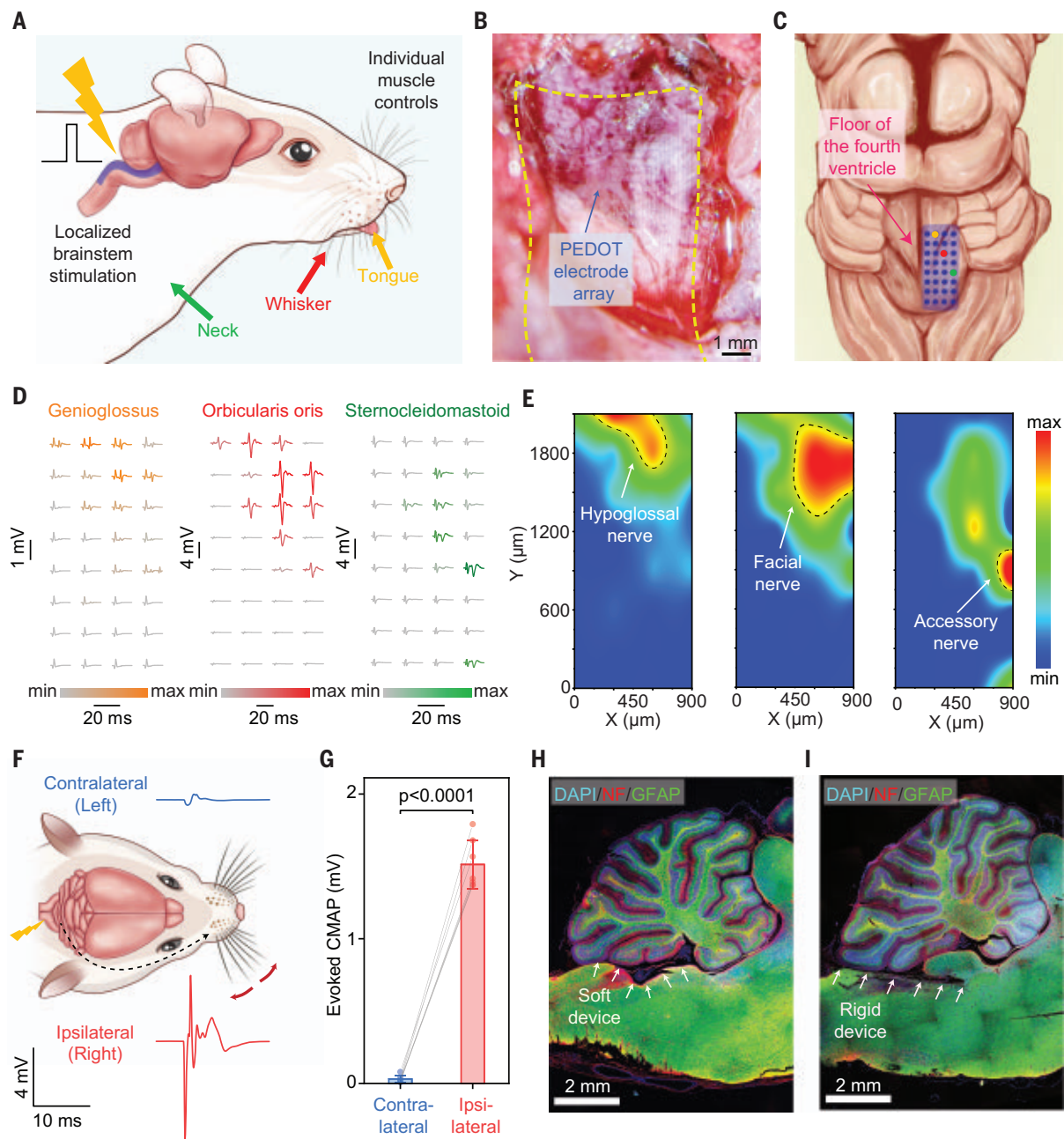


Fig. 5. Stretchable high-density array allows localized neuromodulation for precise control of individual muscle activities. (A) Schematic diagram illustrating the application of the stretchable electrode array for precise neuromodulation through localized brainstem stimulation. (B) Microscopic image of a stretchable electrode array conforming to the curved floor of the fourth ventricle with 50- μm electrode width. (C) Schematic illustration of a multi-electrode array placed on the right side of the brainstem. (D) Evoked muscle activities recorded at the tongue (left), whisker (middle), and neck (right) after electrical stimulation at the brainstem. (E) Activation maps based on the muscle activities depicting the

spatial distribution of different nuclei (marked by dashed lines) in the brainstem with downstream connections to the hypoglossal nerve (left), facial nerve (middle), and accessory nerve (right). (F) Schematic diagram and representative data traces showing the side specificity of the brainstem stimulation. (G) Statistical analyses showing the preferred activation of ipsilateral targets. CMAP, compound muscle action potential. (H and I) Immunohistological staining of a brain slice after the insertion of the soft and stretchable electrode array (H) and a rigid device (I) along the floor of the fourth ventricle between the brainstem and the cerebellum. DAPI, 4',6'-diamidino-2-phenylindole; NF, neurofilament; GFAP, glial fibrillary acidic protein.

low-frequency unit-area impedance is several orders of magnitude higher than that of Topo-E-S because the effective interfacial capacitance for Topo-E-S is much larger than that of c-Au (24) (Fig. 3J). Such a large interfacial capacitance is also responsible for high charge-

storage capacity (Fig. 3K) and efficient charge injection (Fig. 3L), which are both important for low-voltage electrical stimulation (18). Topo-E-S also maintains the electronic-ionic dual conduction from PEDOT:PSS (figs. S32 and S33). The high electrical conductivity is essential

for Topo-E-S to outperform c-Au at all frequency ranges (fig. S34). If the electrical conductivity of PEDOT is lower than $\sim 300 \text{ S cm}^{-1}$, the reduced impedance of PEDOT versus c-Au is only expected in the low-frequency regime. The impedance value of the Topo-E-S electrode

remained stable in PBS for at least 1 month (fig. S35). When the TopoE-S electrode was at 100% strain, its impedance only showed a slight increase because of the electrode geometry change, without inducing any cracks (fig. S36).

We developed a fabrication process for high-density stretchable electrode arrays by optimizing the chemical orthogonality and surface energy of each elastomeric layer (Fig. 4, A and B, and figs. S10 and S37). The as-fabricated stretchable TopoE-S array has a narrow distribution for both the impedance amplitude and the phase angle (fig. S38). Because the entire electrode array (as thin as 20 μm) is made of soft and elastic materials, it can be conformably attached onto human skin (Fig. 4C). This allows for high-density surface electromyography (sEMG) recording even on moving muscles. The typical interelectrode distance for sEMG devices is ~ 5 mm or larger because the high impedance of rigid electrodes and poor skin contact do not allow reliable recording at smaller sizes (28). Because of the low impedance of PEDOT:PSS and the low modulus of the entire electrode array, we reduced the interelectrode distance down to 500 μm with electrode widths of 100 μm while still being able to capture high-fidelity sEMG signals (Fig. 4B). The low unit-area impedance enabled our stretchable electrode array to resolve sEMG propagation dynamics with high spatial resolution (Fig. 4, D and E). Besides recording dynamic information, the integrated EMG signals over time were also distinct enough to differentiate other hand gestures in a highly reproducible manner (figs. S39 to S44).

We can also measure sEMG signals from soft-bodied creatures, such as an octopus, whose muscles can undergo much larger deformations than those of a human (Fig. 4F). We observed that upon electrical stimulation of the octopus arm, our stretchable sEMG array could consistently record the muscle activity dynamics with good signal-to-noise ratio (Fig. 4G, figs. S45 to S47, and movies S1 and S2). By contrast, a rigid probe made of PEDOT:PSS on polyimide was observed to slip along the muscle surface owing to its inability to follow the tissue contour, which resulted in extremely noisy signals—i.e., a low signal-to-noise ratio (Fig. 4H, figs. S48 and S49, and table S2).

Finally, stretchable bioelectronics made with rigid inorganic materials require special structural designs at compromised device densities, whereas TopoE-S can be directly patterned to high-density stretchable arrays (fig. S50), which allows for bioelectronic applications at intricate locations with high precision. In this regard, the brainstem would be a perfect testbed for several reasons (Fig. 5A, fig. S51, and table S3): It is naturally curved and will experience substantial strains from movement of the cervical spine (10, 29). It serves as the central hub for

motor controls of almost all facial and neck motions through 10 pairs of cranial nerves (30). It also regulates cardiac and respiratory functions.

We first showed that our stretchable electrode array, when placed on the floor of the fourth ventricle of a rat, could follow the underlying curvature to form intimate contact (Fig. 5B and fig. S51). Upon implantation, we delivered current pulses to individual electrodes to stimulate the tongue, whisker, and neck separately while EMG and motion signals at those locations were simultaneously recorded to confirm the organ-specific stimulations (Fig. 5C). After scanning the entire array with a 300- μm interelectrode distance and a 50- μm electrode width, we observed distinct muscle electrophysiological signals and movements elicited by each electrode (Fig. 5D, figs. S52 to S54, and movies S3 to S5). By normalizing the EMG amplitudes, we were able to construct three high-resolution activation maps that correlated with individual nuclei for hypoglossal, facial, and accessory nerves that innervated the genioglossus for the tongue, the orbicularis oris for the whisker, and the sternocleidomastoid for the neck, respectively (30) (Fig. 5E and fig. S55). Aside from independent controls of different muscle groups, high-resolution stimulation through the stretchable electrode array showed strong side specificity. Only the muscles on the same side (i.e., ipsilateral) of the electrode would be selectively stimulated, in accordance with the functional organization of corresponding cranial nerves (30) (Fig. 5, F and G, and figs. S55 and S56). The amplitude of the evoked muscle signal could also be modulated by the intensity of the input stimulus (fig. S57). Finally, immunohistological analysis indicated that our electrode array did not induce observable tissue damages or inflammatory responses when placed between the cerebellum and the brainstem, whereas rigid plastic probes supported on polyimide substrates caused severe damage by cutting into the soft brainstem—possibly as a result of frequent neck movements—shortly after implantation (Fig. 5, H and I, and figs. S58 to S60). In conclusion, by introducing a rationally designed topological supramolecular network, we achieved a CP with simultaneously high conductivity, stretchability, and photopatternability and demonstrated bioelectronic applications for a soft-bodied octopus and the fragile rat brainstem.

REFERENCES AND NOTES

1. S.-K. Kang *et al.*, *Nature* **530**, 71–76 (2016).
2. J. Viventi *et al.*, *Nat. Neurosci.* **14**, 1599–1605 (2011).
3. K. Mathieson *et al.*, *Nat. Photonics* **6**, 391–397 (2012).
4. Y. S. Choi *et al.*, *Nat. Biotechnol.* **39**, 1228–1238 (2021).
5. M. Capogrosso *et al.*, *Nature* **539**, 284–288 (2016).
6. F. B. Wagner *et al.*, *Nature* **563**, 65–71 (2018).
7. X. Yu *et al.*, *Nature* **575**, 473–479 (2019).
8. J. C. Barrese *et al.*, *J. Neural Eng.* **10**, 066014 (2013).

9. J. W. Salatino, K. A. Ludwig, T. D. Y. Kozai, E. K. Purcell, *Nat. Biomed. Eng.* **1**, 862–877 (2017).
10. S. P. Lacour, G. Courtine, J. Guck, *Nat. Rev. Mater.* **1**, 16063 (2016).
11. E. Song, J. Li, S. M. Won, W. Bai, J. A. Rogers, *Nat. Mater.* **19**, 590–603 (2020).
12. T. Someya, Z. Bao, G. G. Malliaras, *Nature* **540**, 379–385 (2016).
13. S. Wang *et al.*, *Nature* **555**, 83–88 (2018).
14. B. D. Paulsen, K. Tybrandt, E. Stavrinidou, J. Rivnay, *Nat. Mater.* **19**, 13–26 (2020).
15. H. Yuk, B. Lu, X. Zhao, *Chem. Soc. Rev.* **48**, 1642–1667 (2019).
16. D. Khodagholy *et al.*, *Nat. Neurosci.* **18**, 310–315 (2015).
17. Y. Wang *et al.*, *Sci. Adv.* **3**, e1602076 (2017).
18. Y. Liu *et al.*, *Nat. Biomed. Eng.* **3**, 58–68 (2019).
19. Y. Gu *et al.*, *Nature* **560**, 65–69 (2018).
20. H. Gotoh *et al.*, *Sci. Adv.* **4**, eaat7629 (2018).
21. Y. Okumura, K. Ito, *Adv. Mater.* **13**, 485–487 (2001).
22. D. Alemu Mengistie, P.-C. Wang, C.-W. Chu, *J. Mater. Chem. A* **1**, 9907–9915 (2013).
23. N. Kim *et al.*, *Adv. Mater.* **26**, 2268–2272, 2109 (2014).
24. S. M. Kim *et al.*, *Nat. Commun.* **9**, 3858 (2018).
25. S. Savagatrup *et al.*, *Adv. Funct. Mater.* **25**, 427–436 (2015).
26. C. L. Choong *et al.*, *Adv. Mater.* **26**, 3451–3458 (2014).
27. N. Matsuhsa *et al.*, *Adv. Electron. Mater.* **5**, 1900347 (2019).
28. B. Afsharipour, S. Soedirdjo, R. Merletti, *Biomed. Signal Process. Control* **49**, 298–307 (2019).
29. N. Vachicouras *et al.*, *Sci. Transl. Med.* **11**, eaax9487 (2019).
30. D. E. Haines, *Neuroanatomy: An Atlas of Structures, Sections, and Systems* (Lippincott Williams & Wilkins, ed. 8, 2011).
31. E. Hwaun, ernie7334066/EMG-analysis; publication, *Zenodo* (2022); <https://doi.org/10.5281/zenodo.6236224>.

ACKNOWLEDGMENTS

We thank K. Sun, D. Liu, and J. Tang for technical support. We thank Agfa-Gevaert N.V. for providing PEDOT:PSS, the Asahi Kasei Corporation for providing SEBS, and the Daikin Corporation for providing poly(vinylidene fluoride)-co-hexafluoropropylene (PVDF-HFP). **Funding:** This work was partly supported by BOE Technology Group Co., Ltd., and the Stanford Wu Tsai Neurosciences Institute Big Idea project on Brain Organogenesis. Part of this work was performed at the Stanford Nano Shared Facilities (SNSF), supported by the National Science Foundation under award ECCS-1542152. The GXD measurements were performed at Beamline 11-3 of the Stanford Synchrotron Radiation Light (SSRL) source, supported by the Director, Office of Science, Office of Basic Energy Sciences of the US Department of Energy under contract no. DE-AC02-76SF00515. E.H. and I.S. acknowledge support from an ONR MURI grant (N0014-19-1-2373) and a Wu Tsai Neurosciences Institute Interdisciplinary Scholarship Award on the octopus-related work. D.L. acknowledges support from the National Natural Science Foundation of China Projects (81971668). Y.-X.W. acknowledges financial support from the China Scholarship Council (201806255002) for visiting scholar funding. **Author contributions:** Y.J. and Z.B. conceived the project. Y.J., Y.-X.W., and Z.B. designed the materials. Y.J. and Y.-X.W. carried out the synthesis. Y.J., Z.Z., Y.-X.W., C.-T.C., D.Z., G.C., H.-C.W., S.N., W.W., A.S., J.-C.L., Y.Wu, Y.Wa., A.A.T., K.Y.L., C.-C.S., W.X., K.L., K.Z., Y.B., and G.G. performed testing and characterizations. Y.J., E.H., and I.S. designed and performed the octopus-related experiments. Y.J. and D.L. carried out the brainstem-related experiments. Y.J., Z.Z., Y.-X.W., J.B.-H.T., and Z.B. wrote the paper and incorporated comments and edits from all authors. **Competing interests:** Stanford University has filed patent applications related to this technology. The patent application numbers are 63/139,666 and 62/845,463. The authors declare no other competing interests. **Data and materials availability:** All data are available in the main text or the supplementary materials. The code used to analyze the EMG signals is available in a GitHub repository (<https://github.com/ernie7334066/EMG-analysis>) and Zenodo (31).

SUPPLEMENTARY MATERIALS

science.org/doi/10.1126/science.abj7564
Materials and Methods
Figs. S1 to S60
Tables S1 to S3
References (32–68)
Movies S1 to S5

31 May 2021; accepted 24 February 2022
10.1126/science.abj7564

PIEZOELECTRICS

Relaxor ferroelectric polymer exhibits ultrahigh electromechanical coupling at low electric field

Xin Chen^{1†}, Hancheng Qin^{2†}, Xiaoshi Qian³, Wenyi Zhu⁴, Bo Li⁵, Bing Zhang², Wenchang Lu², Ruipeng Li⁶, Shihai Zhang⁵, Lei Zhu⁷, Fabrice Domingues Dos Santos⁸, J. Bernholc², Q. M. Zhang^{1,4*}

Electromechanical (EM) coupling—the conversion of energy between electric and mechanical forms—in ferroelectrics has been used for a broad range of applications. Ferroelectric polymers have weak EM coupling that severely limits their usefulness for applications. We introduced a small amount of fluorinated alkyne (FA) monomers (<2 mol %) in relaxor ferroelectric poly(vinylidene fluoride-trifluoroethylene-chlorofluoroethylene) (PVDF-TrFE-CFE) terpolymer that markedly enhances the polarization change with strong EM coupling while suppressing other polarization changes that do not contribute to it. Under a low-dc bias field of 40 megavolts per meter, the relaxor tetrapolymer has an EM coupling factor (k_{33}) of 88% and a piezoelectric coefficient (d_{33}) >1000 picometers per volt. These values make this solution-processed polymer competitive with ceramic oxide piezoelectrics, with the potential for use in distinct applications.

Ferroelectric materials have been widely used in electromechanical (EM) energy conversion such as energy harvesting, acoustic transducers for imaging, fault detection, ship navigation, and sensors and artificial muscles in robots (1, 2). Owing to their high pliability, easy fabrication into complicated shapes, light weight, and low cost, ferroelectric polymers are attractive for these applications (2–5). However, the low EM performance of polymers, compared with their inorganic counterparts, severely limits their usefulness in these applications. For example, the EM coupling factor (k_{33}) of 23% and piezoelectric coefficient (d_{33}) of –35 pm/V of poly(vinylidene difluoride) (PVDF)-based ferroelectric polymers, which have the most attract-

ive performance of ferroelectric polymers in the market, are much smaller than $k_{33} > 70\%$ and $d_{33} > 700$ pm/V of the widely used ferroelectric ceramic $\text{Pb}(\text{ZrTi})\text{O}_3$ (PZT) (1, 3–6). In the past several decades, various efforts have been devoted to improving the EM performance of ferroelectric polymers, with limited success (3, 4, 7, 8). For example, Ohigashi and colleagues developed P(VDF-TrFE) (TrFE: trifluoroethylene) single crystals that raised k_{33} to 33% and d_{33} to –40 pm/V (7). More recently, by exploiting the morphotropic phase boundary (MPB) effect in P(VDF-TrFE) copolymers, Liu *et al.* reported a d_{33} of –65 pm/V and $k_{33} < 27\%$ for copolymer compositions near the MPB (8).

In ferroelectrics, the piezoelectric effect from the normal ferroelectrics and the electrostrict-

tive effect from the relaxor ferroelectrics have been investigated and used for EM applications (1, 4, 6, 9–11). Biasing dc electric fields in relaxor ferroelectrics generate piezoelectric states whose EM response can be tuned by varying the dc bias field (see schematic in fig. S1). Relaxor ferroelectric polymers have been developed in the past, and they exhibited relatively high EM responses at high fields such as $k_{33} > 50\%$ at 120 MV/m (4, 12–14). However, high fields prohibit their application in practical devices owing to easy electric breakdown and failure. For the reliable operation of PVDF polymer-based dielectric devices, the applied field should be lower than 60 MV/m (15, 16). We report relaxor ferroelectric P(VDF-TrFE-CFE-FA) (CFE: chlorofluoroethylene, FA: fluorinated alkynes) tetrapolymers that generate large electrostriction at low electric fields. Under a low-dc bias field of 40 MV/m, the tetrapolymer exhibits a k_{33} of 88% and d_{33} of –1050 pm/V.

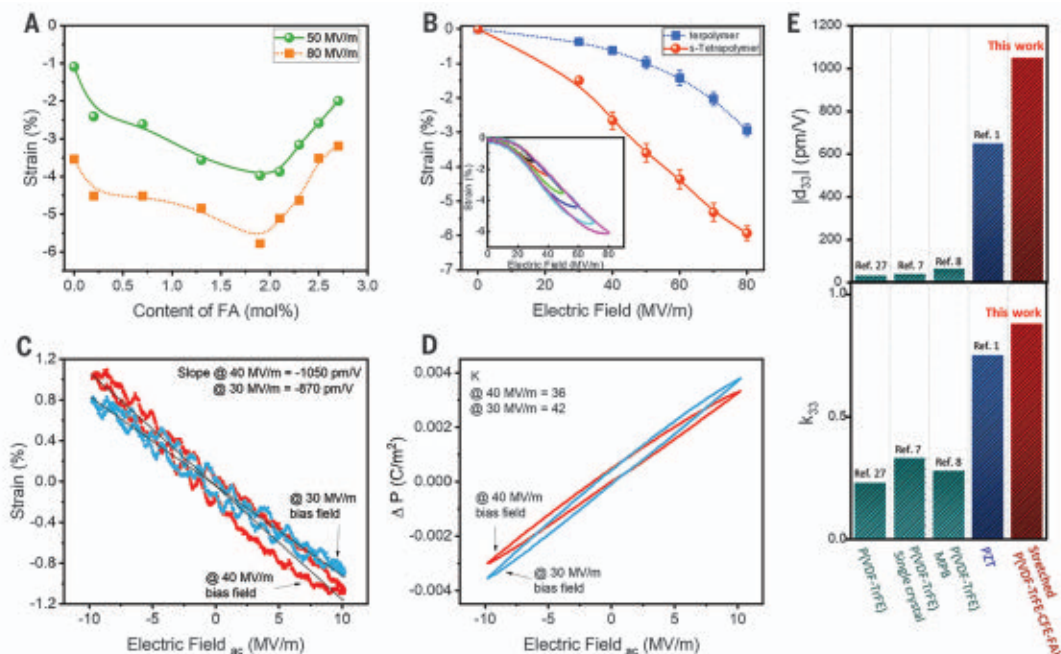
¹Department of Materials Science and Engineering, Materials Research Institute, The Pennsylvania State University, University Park, PA 16802, USA. ²Department of Physics, North Carolina State University, Raleigh, NC 27695-7518, USA. ³Interdisciplinary Research Centre for Metamaterials and Intelligent Systems, State Key Laboratory of Mechanical System and Vibration, and MOE Key Laboratory for Power Machinery and Engineering, School of Mechanical Engineering, Shanghai Jiao Tong University, Shanghai, China. ⁴School of Electrical Engineering and Computer Science, Materials Research Institute, The Pennsylvania State University, University Park, PA 16802, USA. ⁵PolyK Technologies, State College, PA 16801, USA. ⁶National Synchrotron Light Source II, Brookhaven National Laboratory, Upton, NY 11973, USA. ⁷Department of Macromolecular Science and Engineering, Case Western Reserve University, Cleveland, OH 44106-7202, USA. ⁸Arkema-Piezotech, 92700 Colombes, France.

*Corresponding author. Email: qxz1@psu.edu

†These authors contributed equally to this work.

Fig. 1. Electromechanical properties of P(VDF-TrFE-CFE-FA) relaxor polymers.

(A) Thickness strain S_3 of P(VDF-TrFE-CFE-FA) with different FA contents at 50 and 80 MV/m unipolar fields at 1 Hz. (B) Thickness strain of terpolymer and 1.9% stretched tetrapolymer at 1-Hz unipolar field versus electric field. In (A) and (B), the curves serve as a guide to the eye. (C) Strain and (D) polarization at 1-Hz ac field under 30- and 40-MV/m bias fields. (E) Comparison of d_{33} and k_{33} of commercial P(VDF-TrFE) copolymer, copolymer single crystal, and copolymer at MPB, $\text{Pb}(\text{ZrTi})\text{O}_3$ (PZT) piezoceramic, and the relaxor P(VDF-TrFE-CFE-FA) tetrapolymer under 40-MV/m dc bias.



Phenomenologically, the EM responses of ferroelectric materials can be considered as arising from the electrostriction, e.g., the strain S is proportional to the square of the polarization P (4, 9, 10),

$$S_3 = Q_{33}P^2 \quad (1)$$

where S_3 is the thickness strain and Q_{33} is the electrostriction coefficient. For piezoelectric coefficient \bar{d}_{33} ($= \Delta S_3/\Delta E$), $d_{33} = 2 Q_{33} P_b \Delta P/\Delta E$ ($\Delta P/\Delta E = \epsilon_{33}$), and the associated electro-mechanical coupling factor k_{33} is

$$k_{33} = d_{33} \sqrt{Y/\epsilon_{33}} = 2Q_{33}P_b \sqrt{Y\epsilon_{33}} \quad (2)$$

where P_b is the bias polarization, Y is the elastic modulus, and ϵ_{33} is the dielectric permittivity at constant stress (17). $\epsilon_{33} = K \epsilon_0$, where K is the dielectric constant at constant stress and $\epsilon_0 = 8.85 \times 10^{-12}$ F/m is the vacuum permittivity. In most ferroelectrics, the polarization P can arise from many different processes. In inorganic ferroelectrics, P originates from single ferroelectric domains and domain wall motions (6, 18). In polymers such as PVDF-based ferroelectric semicrystalline polymers, in addition to the P from the crystalline phase, additional polarization contributions arise from the amorphous phase and crystalline-amorphous interfaces (3, 19, 20). These different polarization processes will contribute to the EM response differently; they will have different Q values in Eq. 1. For example, in P(VDF-TrFE) ferroelectric polymers, the polarization switch is primarily through successive 60° domain wall motions (3, 21, 22). Owing to the pseudo-hexagonal symmetry of the unit cell, these domain wall motions will not generate high strain. The $|Q_{33}|$ of P(VDF-TrFE) ferroelectric copolymers is usually $<3 \text{ m}^4/\text{C}^2$, resulting in low k_{33} and d_{33} (21, 23). Hence, in developing PVDF-based ferroelectric polymers for generating large EM responses, a critical step is to develop a strategy to raise Q_{33} and ϵ_{33} substantially while maintaining the large polarization or also even enhancing P in the polymers.

We selected the P(VDF-TrFE-CFE) relaxor terpolymer on the basis of these considerations. The relaxor terpolymer exhibits a high dielectric constant K over a broad temperature range ($K > 50$) near room temperature, much higher than that for P(VDF-TrFE) copolymers and other PVDF-based polymers. In functional ferroelectric materials, a small amount of defects and/or dopants can profoundly affect material performance (1, 3, 4, 6, 18). In ferroelectric P(VDF-TrFE) copolymers, copolymerizing with CFEs that are bulkier than both VDF and TrFE monomers (see fig. S2A for size) and hence expand the interchain spacing as random defects converts all-trans bonds into trans-gauche bonds (see fig. S2B for conformations in the PVDF polymers) and

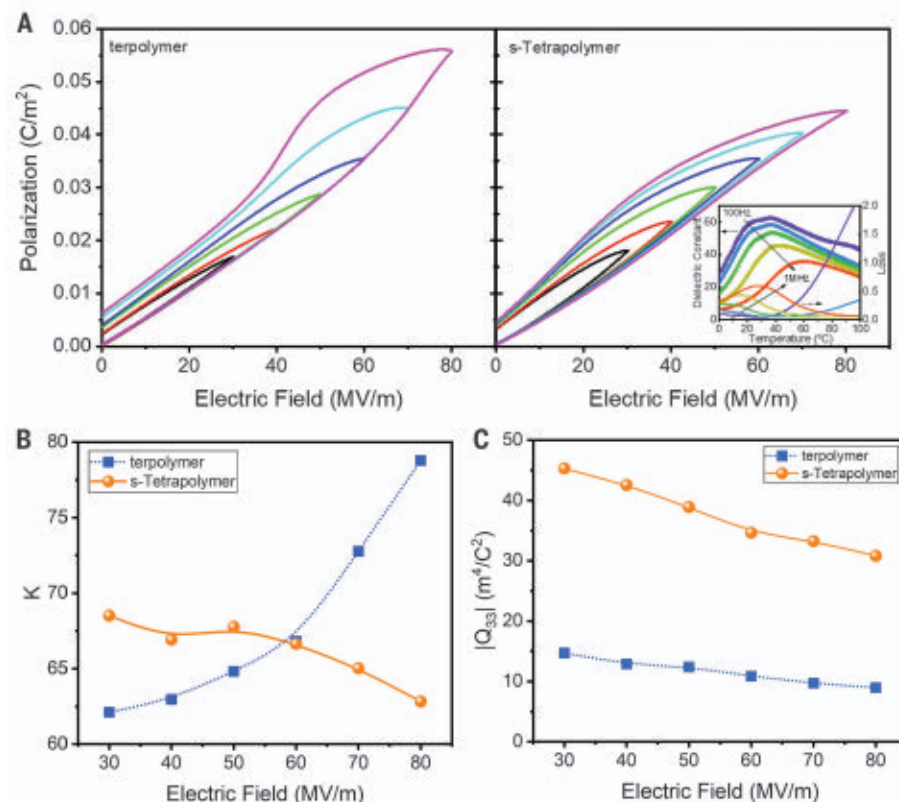


Fig. 2. Polarization data and electrostriction coefficients of P(VDF-TrFE-CFE-FA) relaxor polymers.

(A) Polarization versus electric field measurement at 1 Hz for terpolymer and s-tetrapolymer. (Inset) Dielectric properties versus temperature for s-tetrapolymer. (B) Effective dielectric constant versus electric field for terpolymer and s-tetrapolymer. (C) Electrostriction coefficient $|Q_{33}|$ versus applied electric field for stretched tetrapolymer compared with the terpolymer. In (B) and (C), the curves serve as a guide to the eye.

transforms a ferroelectric into a relaxor ferroelectric at P(VDF-TrFE) compositions $<70/30$ VDF/TrFE mol % (4, 24). As shown by Yang *et al.* (25), CFEs, owing to their bulkier size, are excluded from the crystallites and thus do not prevent the transition of the terpolymer from relaxor to ferroelectric phase at high electric fields.

We investigated FA monomer units, which have a smaller size than VDF and TrFE (fig. S2A), as random defects to modify P(VDF-TrFE-CFE) 63/29.7/7.3 mol % terpolymer, with the VDF/TrFE ratio of 68/32 mol %. Earlier studies showed that a minimum of 7 mol % CFE is required to completely convert ferroelectric P(VDF-TrFE) into relaxor ferroelectric (4, 24). We hypothesize that such smaller-size defects can be at least partially included in the crystalline phase and thus can be effective in controlling the polarization responses in the relaxor polymer. Such FA monomer units can be introduced easily in P(VDF-TrFE-CFE) by dehydrochlorination of CFEs in the terpolymer (fig. S3). We synthesized and characterized P(VDF-TrFE-CFE-FA) tetrapolymers with different FA contents. The tetrapolymer with

the 63/29.7/5.4/1.9 composition displays the highest electroactuation (Fig. 1A). In electroactive polymers, mechanical stretching of polymer films will align the polymer chains and generate morphology changes that can profoundly affect the electroactive responses of the polymers (3). For PVDF-based ferroelectric polymers, electromechanical responses perpendicular and parallel to polymer chains have opposite signs, and thus in polymer films with randomly oriented chains, the combination of these competing effects will lower the electromechanical responses. We uniaxially stretched the tetrapolymer film with 1.9 mol % FA to more than seven times stretching ratio. We determined the thickness strain (S_3) as a function of the applied field (unipolar field) for the stretched tetrapolymer P(VDF-TrFE-CFE-FA) 63/29.7/5.4/1.9 mol % (s-tetrapolymer) at fields below 80 MV/m. The S_3 is -3.5% at 50 MV/m compared with -1% of the terpolymer, a marked enhancement (Fig. 1B). We obtained the strain-applied electric field loops of s-tetrapolymer along with strain loops of terpolymer and unstretched terpolymer (Fig. 1B, inset, and fig. S4, A and B). The general rule

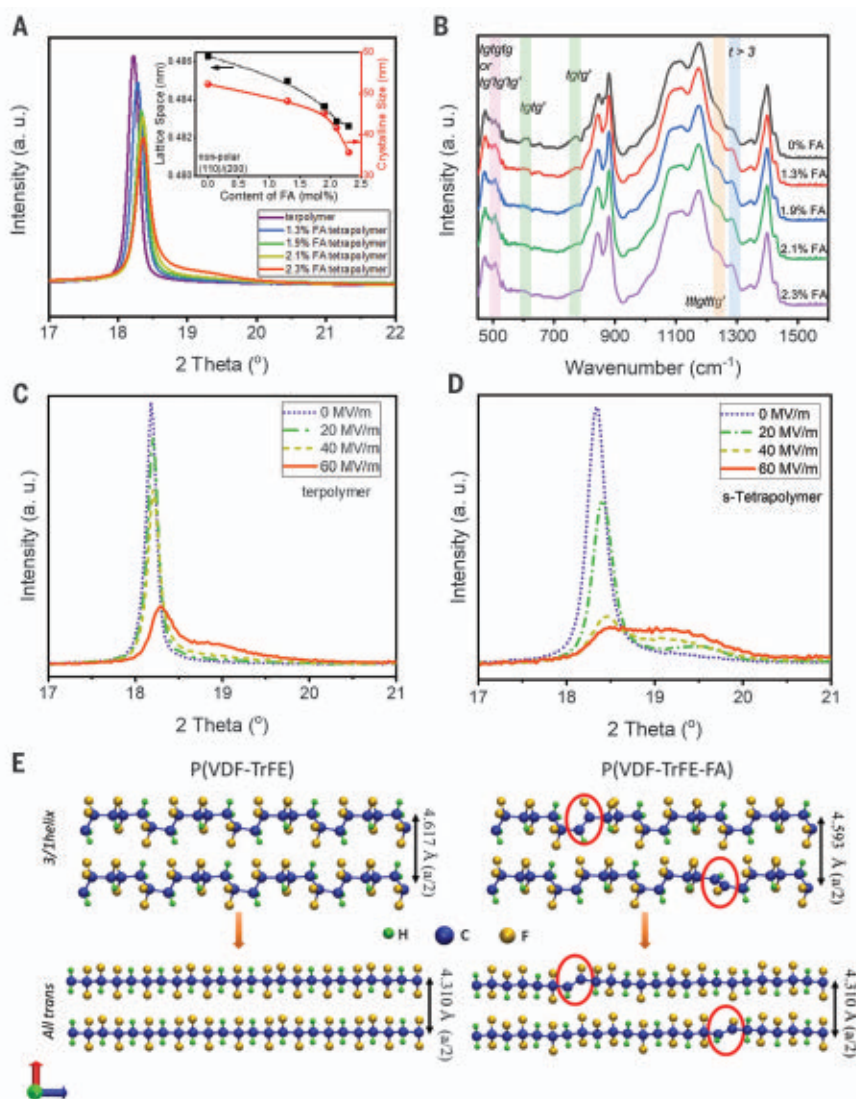


Fig. 3. Structural analysis of P(VDF-TrFE-CFE-FA) relaxor polymers. (A) X-ray diffraction patterns of tetrapolymers with various contents of FA (x-ray wavelength is 0.154 nm). The inset presents the lattice spacing and crystalline size of the (200/110) diffraction peaks versus FA content deduced from XRD data. (B) FT-IR spectra for tetrapolymers with various contents of FA. XRD patterns under different electric fields for (C) terpolymer and (D) s-tetrapolymer. (E) DFT calculations on crystal structures of 3/1 helix and all trans (tttt) for P(VDF-TrFE) and P(VDF-TrFE-FA); detailed parameters in table S2.

for dielectric devices such as polymer actuators and capacitors is that the fields should be lower than 20% of the dielectric breakdown strength. We therefore focused on the compositions with high responses below 60 MV/m.

In addition to the electrostriction, Maxwell stress may also generate large electromechanical responses in polymers (4, 26). For isotropic polymers, the thickness strain S_M from Maxwell stress is

$$S_M = -\frac{1}{2} \epsilon (1 + 2 \sigma) E^2 / Y \quad (3)$$

where σ is the Poisson's ratio and E is the applied electric field. We treat unstretched

tetrapolymer as isotropic and take $\sigma \sim 0.3$ for PVDF-based polymers. At 50 MV/m, the tetrapolymer has $\epsilon = 67 \epsilon_0$, yielding a S_M of -0.53% , about 15% of the observed actuation strain (Fig. 1B and fig. S4B). We approximate the actuation strain in the tetrapolymer as occurring from electrostriction.

A dc bias field is often used in electrostrictive materials to induce a piezoelectric state and piezoelectric response (4, 9–11). We characterized the electroactuation under low dc bias fields, 30 and 40 MV/m, with an ac field amplitude of 10 MV/m. We show the strains and polarizations under the two dc biases for the s-tetrapolymer film (Fig. 1, C and D) and the

unstretched tetrapolymer (fig. S4, C to F) from which $d_{33} (= S/E_{AC})$ and $\epsilon_{33} (= K\epsilon_0 = \Delta P/E_{AC})$ at dc-biased states are obtained (Table 1). We measured the elastic modulus, Y , of unstretched tetrapolymer films as 0.224 GPa using dynamic mechanical analysis (DMA). We deduced k_{33} from $d_{33}\sqrt{Y/\epsilon_{33}}$ at dc-biased states for the tetrapolymer films (Table 1), using $Y = 0.224$ GPa for both the unstretched and s-tetrapolymer films. We found high EM performance of P(VDF-TrFE-CFE-FA) s-tetrapolymers, with a k_{33} of 88% and d_{33} of -1050 pm/V even at low electric fields (<50 MV/m), which exceed the benchmark piezoceramic PZT, as shown in Fig. 1E and table S1 (1, 6–8, 27).

We measured the dielectric properties versus temperature at different frequencies for s-tetrapolymer (Fig. 2A, inset) and terpolymer (fig. S5A) (13). We did not find much change in the dielectric dispersion for s-tetrapolymer associated with the relaxor response, whose broad dielectric peak temperature shifts progressively toward lower temperature with frequency (11–13), but there is an additional, broad dielectric peak around 40°C that does not move much with frequency. Differential scanning calorimetry data (fig. S6) also show a weak transition peak at $\sim 40^\circ\text{C}$. This suggests a diffused ferroelectric transition in the s-tetrapolymer.

We obtained the polarization response under unipolar and bipolar electric fields for the polymers studied, along with the dielectric properties of the tetrapolymer (Fig. 2A and fig. S5, B, C, and E). In relaxor ferroelectrics, a critical field, E_c , exists above which the relaxor transitions to a ferroelectric phase (28). The large increase in the polarization and polarization hysteresis in the P - E data of terpolymer (Fig. 2A) indicate a transition to ferroelectric at fields around 60 MV/m (25), whereas there is no such transition for the s-tetrapolymer at the experimental fields. To make a quantitative comparison, we plotted the P/E ratio as a function of the applied field [$K = P/(\epsilon_0 E)$] for the terpolymer and s-tetrapolymer (Fig. 2B). The terpolymer has a lower K and hence lower polarization values than those of the s-tetrapolymer at fields below 60 MV/m. Above 60 MV/m, the field-induced transition to the ferroelectric phase raises the polarization, polarization hysteresis, and K above those of the s-tetrapolymers. That is, the FA defects in the s-tetrapolymer lower the local polarization switch barriers, which results in a higher polarization response at fields below 60 MV/m. At higher fields, the FA defects also prevent the transition of the relaxor to the ferroelectric phase. All these are desirable for generating high EM coupling.

From the electroactuation strains (Fig. 1B) and polarizations (Fig. 2A), we deduced Q_{33} for the s-tetrapolymer from Eq. 1 at different

Table 1. EM performance for the tetrapolymer at bias fields. Electromechanical and dielectric properties of P(VDF-TrFE-CFE-FA) 63/29.7/5.4/1.9 at dc-biased states.

dc bias	d_{33} (pm/V)	K	k_{33}
30 MV/m (tetrapolymer)	-747	40	59%
30 MV/m (s-tetrapolymer)	-890	42	69%
40 MV/m (tetrapolymer)	-858	34	74%
40 MV/m (s-tetrapolymer)	-1050	36	88%

electric fields (Fig. 2C). We also calculated Q_{33} for the terpolymer for comparison. From the elastic and dielectric properties, it is deduced from Eq. 3 that Maxwell stress generates more than 50% of our observed electroactuation for the terpolymer, and hence the true Q_{33} is only about half that value. Thus, the s-tetrapolymer has more than a four times improvement in Q_{33} . This demonstrates that in PVDF-based ferroelectric polymers, most of the polarization changes do not contribute much to the EM performance, thus yielding a low EM coupling factor and small d_{33} (Fig. 1E and table S1). In the ferroelectric phase, polarization rotations generate very little electromechanical response. The exceptionally large $|Q_{33}|$ in the relaxor tetrapolymer indicates that FA defects effectively suppress the polarization responses that do not contribute appreciably to the electromechanical response. We also deduce Q_{33} from $d_{33} = 2Q_{33}P_b\Delta P/\Delta E$ for the s-tetrapolymer films at the two dc bias fields (Fig. 1, C and D). Q_{33} of s-tetrapolymer films in the dc-biased state can reach more than $60 \text{ m}^4/\text{C}^2$, whereas the dielectric constant K (~ 40) is lower than that at zero-bias field (Fig. 2, A and B).

We examined the polymers' molecular and mesoscopic structures related to the large EM coupling in the tetrapolymers. Our x-ray diffraction (XRD) data show the (110/200) reflection of tetrapolymers shifting to higher angles and broadening with FA content (Fig. 3A). These features are indicative of a reduced interchain spacing and reduced coherent crystallization region (from ~ 51 to 45 nm) by converting CFE to FA in the relaxor polymers. When comparing the s-tetrapolymer to unstretched tetrapolymer with 1.9 mol % FA (fig. S7), we found no change in the peak position but a large reduction of the coherent crystalline size (from ~ 45 to 36 nm). The results suggest that stretching increases the inclusion of FAs in the crystalline phase, generating defect structures that reduce the coherent-scattering crystalline region of the XRD peak. A comparison of Fourier transform infrared (FT-IR) spectra of terpolymer and tetrapolymers (Fig. 3B) reveals that converting

CFE into FA causes an increase in the all-trans bonds and a reduction of 3/1 helix bonds (responsible for the relaxor) and TGTG' bonds (fig. S8) (29, 30). These observations are consistent with the reduced interchain spacing (Fig. 3A). The small-angle x-ray scattering (SAXS) spectra of tetrapolymer (1.9 mol % FA) and terpolymer show a slight reduction of lamellar spacing from terpolymer ($\sim 49.3 \text{ nm}$) to tetrapolymer ($\sim 40.6 \text{ nm}$) (fig. S9). In contrast to CFEs, which are bulkier than VDF/TrFE and are excluded from the crystalline phase, FAs are at least partially included in the crystalline regions and, as a result, generate a large EM response.

Different applied fields can affect the XRD (110/200) peak, as shown in Fig. 3, C to D, and fig. S10. We found little change in the XRD peak at electric fields $\leq 40 \text{ MV/m}$ for the terpolymer, consistent with the low actuation strain at these fields. By contrast, the s-tetrapolymer film exhibits a broad peak at 19.5° even at 20 MV/m , in addition to the original peak at $\sim 18.4^\circ$. This indicates an induced polarization transition that reduces the interchain spacing in the s-tetrapolymer at ultralow fields. The original (110/200) peak broadens with the applied field, showing a decrease in the coherent crystallization region from $\sim 36 \text{ nm}$ at zero electric field to $\sim 23 \text{ nm}$ at 40 MV/m . Our XRD results indicate that converting CFEs to FAs at 1.9 mol % substantially reduces the barriers for switching from non-polar (or less polar) bonds to polar bonds locally in the crystalline phase, generating large EM actuations at low electric fields, consistent with the electroactuation results (Fig. 1).

We performed density functional theory (DFT) calculations to determine the local lattice parameters and probe local structure changes due to FA bonds in the polymer (Fig. 3E and table S2). We also performed a DFT calculation of polarization and strain of the ferroelectric phase of P(VDF-TrFE), in which the polarization response is mainly from dipole reorientation under electric fields (fig. S11). Although the polarization rotation can generate a large polarization change, the electroactuation strain is small (1.1%), causing $|Q_{33}| <$

$3 \text{ m}^4/\text{C}^2$. In a large DFT unit cell, the P(VDF-TrFE) 3/1 helix structure has a lower energy than the polar all-trans structure, both with and without FA defects (table S2). Also, the 3/1 helix has a much smaller polarization than the all-trans. Therefore, as the electric field increases, the all-trans structure becomes energetically more favorable because of the $-\mathbf{E}\cdot\mathbf{P}$ term. The transformation from the helix to the all-trans phase results in substantial negative strain (table S2), in agreement with our experimental observations. We obtained our DFT results for crystalline bulk structures and thin films, but the relaxor polymers that we studied experimentally consisted of small crystalline domains embedded in an amorphous matrix. Nevertheless, our calculations confirmed the observed preference for a low-polarization structure. Prior studies of phase transformations in PVDF show that chain transformations in PVDF-structure polymers proceed in a concerted fashion (31), in which nearby monomers rotate nearly simultaneously, thereby lowering the transformation barriers. The FA monomers are smaller and thereby present fewer steric constraints for chain transformation. They also partially decouple segments between two FA defects from adjacent segments, allowing for easier segment transformation.

The polarization changes in ferroelectric P(VDF-TrFE) polymers can originate from different processes. Some show strong EM coupling, such as molecular conformation changes between TG (3/1 helix, TGTG', and T_3GT_3G') and all-trans bonds, whereas others do not contribute substantially to EM coupling, e.g., polarization reorientations between different crystal directions. Introducing a small amount of FA monomers in relaxor ferroelectric P(VDF-TrFE-CFE) polymers can markedly enhance the polarization changes between TG and all-trans bonds at low electric fields while suppressing the polarization reorientations. P(VDF-TrFE-CFE-FA) tetrapolymer with 1.9 mol % FA generates a higher polarization change at fields below 50 MV/m , leading to large electroactuation. For example, the s-tetrapolymer has an electrostriction coefficient $|Q_{33}|$ larger than $40 \text{ m}^4/\text{C}^2$, about four times that in P(VDF-TrFE-CFE) relaxor polymer. Under a low-dc bias field of 40 MV/m , the s-tetrapolymer exhibits a k_{33} of 88% and d_{33} of -1050 pm/V , which makes them attractive for practical applications such as energy harvesting, sensors and actuators in soft robots and wearable devices, and transducers for imaging.

REFERENCES AND NOTES

1. K. Uchino, *Ferroelectric Devices* (CRC Press, 2018).
2. Y. Wu et al., *Sci. Robot.* **4**, aax1594 (2019).
3. H. S. Nalwa, Ed., *Ferroelectric Polymers* (Dekker, 1995).
4. Y. Bar-Cohen, Ed., in *Electroactive Polymer (EAP) Actuators as Artificial Muscles: Reality, Potential, and Challenges* (SPIE Optical Engineering, 2004), chapter 4.

- A. J. Lovinger, *Science* **220**, 1115–1121 (1983).
- B. Jaffe, W. R. Cook Jr., H. Jaffe, *Piezoelectric Ceramics* (Academic Press, 1971).
- K. Omote, H. Ohigashi, K. Koga, *J. Appl. Phys.* **81**, 2760–2769 (1997).
- Y. Liu *et al.*, *Nature* **562**, 96–100 (2018).
- F. Li, L. Jin, Z. Xu, S. Zhang, *Appl. Phys. Rev.* **1**, 011103 (2014).
- D. Damjanovic, R. E. Newnham, *J. Intell. Mater. Syst. Struct.* **3**, 190–208 (1992).
- L. E. Cross, *Ferroelectrics* **76**, 241–267 (1987).
- Q. M. Zhang, V. Bharti, X. Zhao, *Science* **280**, 2101–2104 (1998).
- F. Xia *et al.*, *Adv. Mater.* **14**, 1574–1577 (2002).
- Z. Zhang, X. Wang, S. Tan, Q. Wang, *J. Mater. Chem. A Mater. Energy Sustain.* **7**, 5201–5208 (2019).
- X. Chen *et al.*, *Appl. Phys. Lett.* **113**, 113902 (2018).
- R. Ma *et al.*, *Science* **357**, 1130–1134 (2017).
- IEEE Standard on Piezoelectricity (ANSI/IEEE Standard 176-1987, 1988).
- D. Damjanovic, *Rep. Prog. Phys.* **61**, 1267–1324 (1998).
- R. G. Kepler, R. A. Anderson, R. R. Lagasse, *Phys. Rev. Lett.* **48**, 1274–1277 (1982).
- T. Wongwirat *et al.*, *Macromolecules* **53**, 10942–10954 (2020).
- T. Furukawa, N. Seo, *Jpn. J. Appl. Phys.* **29** (4R), 675–680 (1990).
- I. L. Guy, J. Unsworth, *Appl. Phys. Lett.* **52**, 532–534 (1988).
- I. Katsouras *et al.*, *Nat. Mater.* **15**, 78–84 (2016).
- R. J. Klein, F. Xia, Q. M. Zhang, F. Bauer, *J. Appl. Phys.* **97**, 094105 (2005).
- L. Yang *et al.*, *Polymer* **54**, 1709–1728 (2013).
- R. Peirine, R. Kornbluh, Q. Pei, J. Joseph, *Science* **287**, 836–839 (2000).
- H. Wang, Q. M. Zhang, L. E. Cross, A. O. Sykes, *J. Appl. Phys.* **74**, 3394–3398 (1993).
- V. Bobnar, Z. Kutnjak, R. Pirc, A. Levstik, *Europhys. Lett.* **48**, 326–331 (1999) (Europhysics Letters).
- Y. Liu *et al.*, *Nat. Mater.* **19**, 1169–1174 (2020).
- A. J. Lovinger, G. T. Davis, T. Furukawa, M. G. Broadhurst, *Macromolecules* **15**, 323–328 (1982).
- V. Ranjan, M. B. Nardelli, J. Bernholc, *Phys. Rev. Lett.* **108**, 087802 (2012).

ACKNOWLEDGMENTS

We thank Z. Han for assistance in NMR measurement of tetrapolymers and Z. Zhu and G. Rui for SAXS data analysis.

Funding: This research is supported by the US Office of Naval Research under award no. N00014-19-1-2028 at Penn State (X.C., W.Z. and Q.M.Z.) and by N00014-19-1-2033 at NCSU (H.Q., B.Z., W.L., and J.B.). L.Z. acknowledges financial support from the National Science Foundation (DMR-2103196). X.Q. acknowledges financial support from National Natural Science Foundation of China (52076127). The calculations were performed at Oak Ridge Leadership Computing Facility, supported by DOE contract DE-AC05-00OR22725. The SAXS used the 11-BM CMS beamline of National Synchrotron Light Source II (NSLS-II), Brookhaven National Laboratory (BNL), a US DOE User Facility operated by BNL under contract DE-SC0012704. **Author contributions:** Q.M.Z. directed the research; X.C., B.L., and W.Z. conducted experiments (except NMR and SAXS); H.Q., B.Z., W.L., and J.B. performed and analyzed DFT calculations; R.L. and L.Z. performed SAXS; X.C. and Q.M.Z. performed experimental data analyses; and all authors participated in discussions. Q.M.Z., J.B., and X.C. prepared the manuscript with input from all authors. **Competing interests:** Q.M.Z. and X.C. have filed a provisional patent at Penn State (US Application No. 63/197,275). Otherwise, the authors declare no competing interests. **Data and materials availability:** All data are available in the main text or supplementary materials.

SUPPLEMENTARY MATERIALS

science.org/doi/10.1126/science.abn0936
Materials and Methods
Supplementary Text
Figs. S1 to S13
Tables S1 to S4
References (32–37)

2 November 2021; accepted 8 February 2022
10.1126/science.abn0936

NANOMATERIALS

Self-assembly of nanocrystals into strongly electronically coupled all-inorganic supercrystals

Igor Coropceanu^{1†}, Eric M. Janke^{1†}, Joshua Portner^{1†}, Danny Haubold^{1,2}, Trung Dac Nguyen³, Avishek Das⁴, Christian P. N. Tanner⁴, James K. Utterback⁴, Samuel W. Teitelbaum⁵, Margaret H. Hudson¹, Nivedina A. Sarma¹, Alex M. Hinkle¹, Christopher J. Tassone⁶, Alexander Eychmüller², David T. Limmer^{4,7,8}, Monica Olvera de la Cruz^{3,9}, Naomi S. Ginsberg^{4,8,10,11}, Dmitri V. Talapin^{1,12*}

Colloidal nanocrystals of metals, semiconductors, and other functional materials can self-assemble into long-range ordered crystalline and quasicrystalline phases, but insulating organic surface ligands prevent the development of collective electronic states in ordered nanocrystal assemblies. We reversibly self-assembled colloidal nanocrystals of gold, platinum, nickel, lead sulfide, and lead selenide with conductive inorganic ligands into supercrystals exhibiting optical and electronic properties consistent with strong electronic coupling between the constituent nanocrystals. The phase behavior of charge-stabilized nanocrystals can be rationalized and navigated with phase diagrams computed for particles interacting through short-range attractive potentials. By finely tuning interparticle interactions, the assembly was directed either through one-step nucleation or nonclassical two-step nucleation pathways. In the latter case, the nucleation was preceded by the formation of two metastable colloidal fluids.

Self-assembly of nanocrystals (NCs) into long-range ordered arrays can enable bottom-up design of hierarchically organized functional and multifunctional materials (1, 2). A large body of work has identified conditions for the assembly of colloidal NCs into face-centered cubic (fcc) and body-centered cubic (bcc) solids (3, 4), multicomponent binary and ternary NC superlattices (5–8), and quasicrystalline structures (9, 10). These approaches used NCs with surfaces functionalized by long hydrocarbon chains or surface-tethered DNA strands that supported colloidal stability but also separated NCs with electrically insulating barriers at least 1 to 2 nm in thickness (fig. S1). These barriers lead to poor electronic conductivity of ordered NC assemblies and constrain their prospects for practical applications. Some collective effects can develop through distant coupling of plasmonic excitations (11) or mag-

netic dipoles (12), but free electron movement is needed to develop conduction bands. The combination of translational symmetry and strong electronic coupling holds the promise of enabling a general platform for the construction of new functional materials from the available library of NCs.

Strong coupling between NCs can be achieved by using very compact (typically inorganic) surface ligands. For example, thin films of CdSe NCs capped with In₂Se₄²⁻ surface ligands can develop band-like electronic transport (13). These ligands add charge to the NC surface, and NCs act as electrostatically stabilized colloids in polar solvents. However, NCs with such ligands fail to form ordered superstructures because the van der Waals attractive forces arising between touching NCs are too strong and arrest the system as a gel or glass (14). An alternative approach to building strongly electronically coupled NC solids is to remove the native insulating organic ligands after assembly (15, 16), which sometimes results in the oriented attachment of NCs (16–18). However, irreversible oriented attachment cannot produce large, ordered supercrystalline (SC) domains because structural defects accumulate. This problem is inherent to any assembly process that lacks a self-healing pathway enabled by microreversibility (19, 20).

We describe a new class of all-inorganic SC materials that combine long-range order with strong electronic coupling. As building blocks, we used NCs (metals such as Au, Pt, and Ni or semiconductors such as PbS and PbSe) capped with small and conductive metal chalcogenide complex (MCC) ligands (such as Sn₂S₆⁴⁻, Sn₂Se₆⁴⁻, In₂Se₄²⁻, AsS₄³⁻, and Cu₆S₄²⁻) that we have previously described (21). Through controlled flocculation using multivalent salts, these NCs assembled into fcc and hexagonal

¹Department of Chemistry, James Franck Institute, and Pritzker School of Molecular Engineering, University of Chicago, Chicago, IL 60637, USA. ²Physical Chemistry, Technische Universität Dresden, Dresden, Germany. ³Department of Chemical and Biological Engineering, Northwestern University, Evanston, IL 60208, USA. ⁴Department of Chemistry, University of California, Berkeley, CA 94720, USA. ⁵Department of Physics and Beus CXFEL Labs, Biodesign Institute, Arizona State University, Tempe, AZ 85287, USA. ⁶Stanford Synchrotron Radiation Lightsource, SLAC National Accelerator Laboratory, Menlo Park, CA 94025, USA. ⁷Chemical Sciences Division and Materials Sciences Division, Lawrence Berkeley National Laboratory, Berkeley, CA 94720, USA. ⁸Kavli Energy NanoSciences Institute, University of California, Berkeley, CA 94720, USA.

⁹Department of Materials Science and Engineering, Department of Chemistry, and Department of Physics and Astronomy, Northwestern University, Evanston, IL 60208, USA. ¹⁰Department of Physics, University of California, Berkeley, CA 94720, USA.

¹¹Materials Sciences Division, Molecular Biophysics and Integrated Biomedical Division, Lawrence Berkeley National Laboratory, Berkeley, CA 94720, USA. ¹²Center for Nanoscale Materials, Argonne National Laboratory, Argonne, IL 60517, USA.

*Corresponding author. Email: dvtalapin@uchicago.edu

†These authors contributed equally to this work.

close-packed SCs, as well as other structures with more complex symmetry (Fig. 1 and figs. S2 and S3). Alkali metals, NH_4^+ , or N_2H_5^+ served as cations for charge balance.

Faceted three-dimensional SCs of 5-nm Au NCs capped by $\text{Sn}_2\text{S}_6^{4-}$ ions (Fig. 1, A and B) showed micrometer-size domains containing $\sim 10^8$ NCs. The MCC ions remained in the superlattice (fig. S4) and separated the Au NCs by ~ 0.3 nm (fig. S5). The small- and wide-angle x-ray scattering (SAXS and WAXS, respectively) patterns of macroscopic samples showed two sets of fcc reflections: from the atomic planes inside individual NCs at the momentum transfers $q > 1 \text{ \AA}^{-1}$ and from the SC planes at $q < 1 \text{ \AA}^{-1}$ (Fig. 1, C and D). These structures formed spontaneously upon addition of $\text{K}_4\text{Sn}_2\text{S}_6$ to a concentrated (~ 100 mg/ml) colloidal solution of Au NCs with $\text{Sn}_2\text{S}_6^{4-}$ surface ligands in polar solvents *N*-methylformamide (NMF) or hydrazine (see supplementary materials section 1). The addition of 1:1 electrolytes such as NaCl precipitated amorphous aggregates (fig. S6) typical for irreversible binding of NCs, as had been seen with many previous studies of electrostatically stabilized NC colloids (14). An additional observation was that NCs of materials with high dielectric constant (ϵ_{NC}) such as metals ($\epsilon_{\text{NC}} \rightarrow \infty$), PbS ($\epsilon_{\text{NC}} = 170$), and PbSe ($\epsilon_{\text{NC}} = 220$) readily formed SCs, whereas any NCs with $\epsilon_{\text{NC}} < 20$ (CdSe, InAs, and Fe_2O_3) formed gels or glasses (figs. S7 to S21).

These observations suggest possible connections among SC formation, ionic charge, and ϵ_{NC} . An understanding of the phase behavior (formation of SCs versus disordered glass or gel structures) begins with the knowledge of the interaction potentials between particles. However, the exact form of pair potentials for colloidal NCs < 10 nm is generally not known and cannot be easily extracted from available experimental data (22). Derjaguin-Landau-Verwey-Overbeek (DLVO) theory (23) can serve as the minimal framework accounting for three major components: van der Waals (vdW) attraction, electrostatic repulsion, and an additional steep short-range repulsion at hard contact of NC cores (see supplementary materials section 2.1). For a broad range of input parameters, such as surface charge and Hamaker constant, the competition between vdW attraction and electrostatic repulsion results in a narrow (< 1 nm width) potential well with depth larger than $5 k_{\text{B}}T$, where k_{B} is the Boltzmann constant and T is temperature (Fig. 2A).

Computational studies on model colloids have shown that it is not only the depth but also the range of pair potentials that plays a critical role in the formation of crystalline phases versus glasses or gels (24, 25). As a rule, attractive potentials with a range of $< 20\%$ of the particle diameter and a depth of 3 to $4 k_{\text{B}}T$ are most favorable for crystal nucleation and

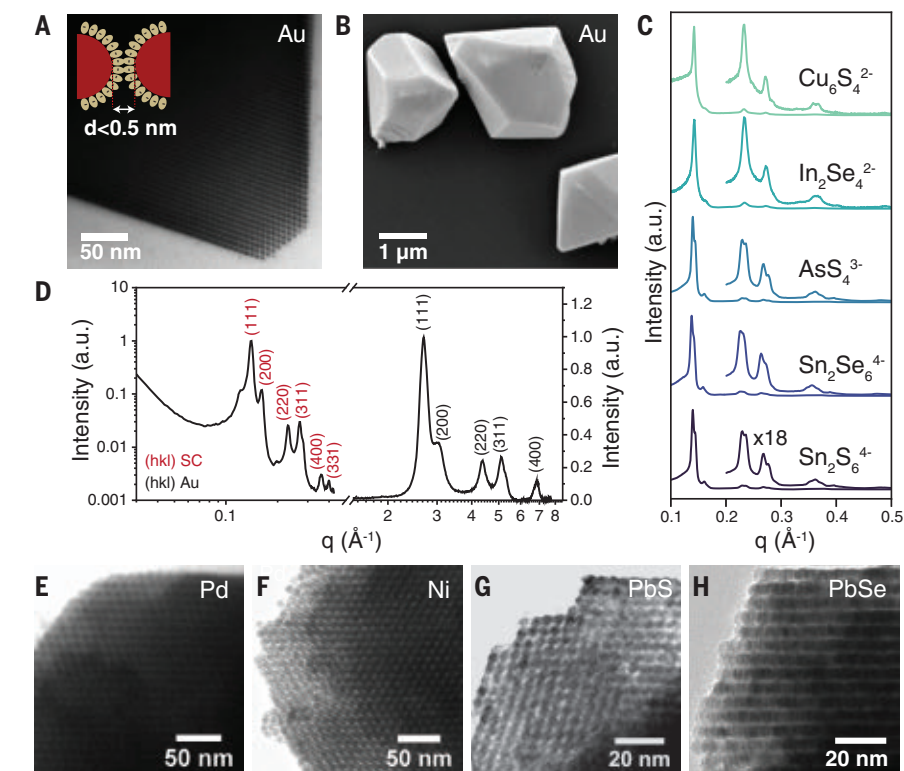


Fig. 1. Compositional diversity of all-inorganic NC assemblies. (A) TEM and (B) scanning electron microscopy (SEM) images of supercrystals assembled from 3.8-nm Au NCs with $(\text{N}_2\text{H}_5)_4\text{Sn}_2\text{S}_6$ surface ligands. (C) SAXS patterns for self-assembly of a population of 5-nm Au NCs with different MCC ligands, yielding crystalline superlattices in each case. Inset: vertically magnified view of the SAXS pattern after the 111 peak. (D) SAXS and WAXS patterns of supercrystals assembled from Au NCs with $(\text{N}_2\text{H}_5)_4\text{Sn}_2\text{S}_6$ ligands showing fcc crystalline order at both the supercrystal and atomic length scales. Data have been normalized to the 111 peaks. (E to H) TEM micrographs of different all-inorganic NC assemblies showing ordered domains of 9 nm Pd, 9 nm Ni, 5 nm PbS, and 6 nm PbSe NCs with MCC ligands, respectively.

growth, whereas the exact shape of the potential is less important (25, 26). For a 5-nm-diameter Au NC, this would correspond to an extremely short, subnanometer range of attraction. At this length scale, continuum theories such as DLVO can provide only approximate guidance (27), whereas accurate atomistic simulations are impeded by the large size of the system.

According to the Noro-Frenkel extended law of corresponding states, the equilibrium phase diagram of different systems with short-range attraction can be represented by particles interacting in square-well potentials (Fig. 2C, inset) with depth u_0 and width $2\lambda R$, where R is the particle radius (26). For $\lambda < 0.2$, regardless of the exact well shape, the phase diagram consists of two equilibrium phases, a colloidal fluid and a solid, with a “hidden” binodal curve separating two metastable fluid phases (Fig. 2B) (24, 28). Haxton *et al.* modeled the dynamics of a colloidal fluid as function of u_0 and λ (Fig. 2C) and mapped regions with high probability to form crystals (regions I and II), metastable fluids with a prohibitively slow nucleation rate (region III), kinetically

frozen metastable gels (region IV), and a stable liquid phase (region V).

Although the exact parameters of NC pair potentials may be difficult to access, the appearance, evolution, and final state of NC colloid offer insights into its location within the phase diagram. In our experiments, the formation of SCs was often preceded by separation of NC colloid into dense and dilute fluid phases (Fig. 3A; see supplementary materials section 2.2). Such behavior was reported for polymethylmethacrylate (PMMA) spheres (29) and globular proteins (30) but not for inorganic NCs. For Au NCs, optical studies showed that the dense fluid was highly metastable and converted into SCs within seconds, but for PbS NCs, the dilute and dense fluid phases, both with no long-range order, could coexist for many hours, followed by the slow formation of fcc SCs from the dense fluid phase. The dense fluid phase exhibited a short-range structure factor (fig. S22) resulting from interparticle correlations at high concentration, similar to previous reports of large PMMA spheres (31). Such triple-phase coexistence of two metastable colloidal fluids and SCs confirmed the

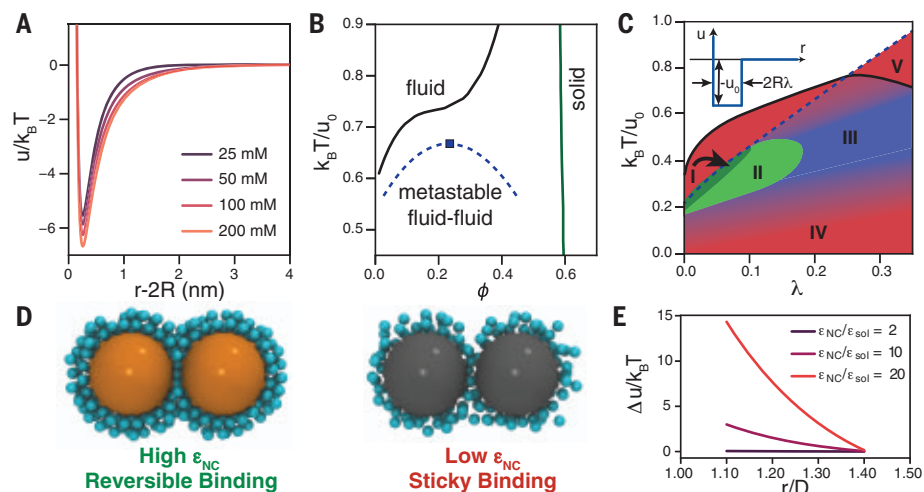


Fig. 2. Modeling interactions and phase equilibria of charge-stabilized colloidal nanocrystals.

(A) Estimated pair potential for 4.5-nm Au NCs in the presence of different concentrations of 1:3 electrolyte. (B) Phase diagram for a colloid with a square-well attractive potential with $\lambda = 0.18$. Solid square shows the metastable fluid-fluid critical point. Data were taken from references (25) and (28). (C) Probability of supercrystal nucleation represented by color gradients (green indicates high; blue, intermediate; and red, low) as a function of u_0 and λ of a square-well potential for a colloid with volume fraction of $\phi = 0.1$. The diagram highlights regions corresponding to (I) one-step nucleation, (II) two-step nucleation, (III) coexistence of two metastable fluids with a slow nucleation rate, (IV) gel formation, and (V) a thermodynamically stable colloidal fluid. The dashed blue curve is the metastable fluid-fluid binodal curve, and the solid black curve is the thermodynamic boundary for stability of an fcc crystal. Inset: a square-well potential determined by the depth (u_0) and range of the attraction (λ). Data were taken from reference (25). (D) Qualitative difference in interactions of NCs with high ($\epsilon_{\text{NC}} = 200$) and low ($\epsilon_{\text{NC}} = 10$) dielectric constant, with multivalent ions resulting in reversible and sticky NC binding, respectively. (E) Computed repulsive component of the interparticle potential at varying dielectric contrast $\epsilon_{\text{NC}}/\epsilon_{\text{sol}}$, where ϵ_{sol} is solvent dielectric constant. The repulsive interaction increases for NCs with high polarizability.

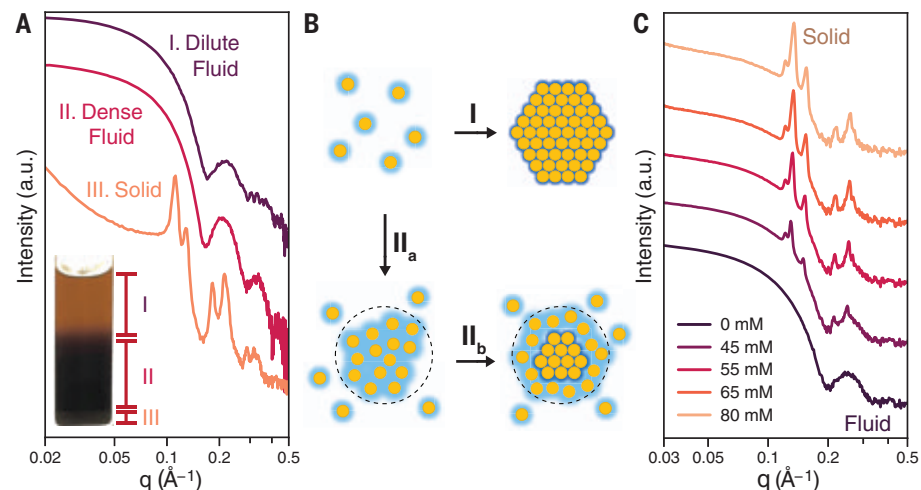


Fig. 3. Triple-phase coexistence and nucleation in charge-stabilized NC colloids. (A) Homogeneous colloidal solutions of 5.5-nm PbS NCs capped with $\text{Sn}_2\text{S}_6^{4-}$ ligands in NMF spontaneously form three phases upon addition of acetonitrile. SAXS data show three separate phases of dilute fluid, dense fluid, and fcc solid supercrystals. Inset: photograph of 5.5-nm PbS NC colloid showing the coexistence of three phases. (B) Schematic representation of one-step nucleation (I) and two-step nucleation (II_a and II_b) of supercrystals; phase separation precedes crystallization in the latter case. (C) In situ SAXS data for one-step nucleation of 4.6-nm Au NCs capped with $(\text{N}_2\text{H}_5)_4\text{Sn}_2\text{S}_6$ and flocculated by gently increasing the $(\text{N}_2\text{H}_5)_4\text{Sn}_2\text{S}_6$ concentration.

presence of a fluid-fluid binodal curve and further supported that our charge-stabilized NC colloids followed the predictions for spheres with short-range attractive potentials.

The formation of SCs required the use of multivalent anionic ligands on the NC surface and as a flocculant (co-ions) to induce self-assembly. By contrast, the addition of NaCl or another 1:1 electrolyte resulted in gelation for all studied conditions, which is characteristic of region III shown in Fig. 2C and also agrees with the potentials shown in Fig. 2A, the attractive well of $\sim 6 k_B T$ being too deep for reversible binding and crystallization at experimentally accessible time scales (25, 32). Multivalent counterions can also promote the crystallization of NCs in polar solvents (33). The observation that NC assembly required the addition of a salt containing multivalent ions could not be explained by DLVO. Generally, concentrated and multivalent electrolytes showed strong ion-ion correlations. Ion correlations under confinement resulted in an additional attractive force (34), but for the multivalent co-ions used in this study, the effect was small (35). However, we show here that co-ion valency can have a prevalent effect on the effective two-body potentials for NCs with high polarizability and correspondingly large ϵ_{NC} .

Our molecular dynamics (MD) simulations, as well as direct chemical analysis data (fig. S23), showed that multivalent ions formed a dense layer near the NC surface for metallic NCs ($\epsilon_{\text{NC}} \rightarrow \infty$), whereas typical dielectric NCs ($\epsilon_{\text{NC}} < 20$) had only loosely associated counterions with the NC surface (Fig. 2D). The radial density profiles of the anions revealed that as ϵ_{NC} increased, the anions accumulated near the NC surface beyond one full monolayer (fig. S24). The driving force resulted from the dielectric mismatch between the NCs and the surrounding medium (36). This mismatch induced polarization, which created an attraction between the anions and the image charges inside the NCs (37). As the anion valency was decreased, the surface-induced charges were reduced, which led to loose packing of the condensed anions (fig. S25).

MD simulations of two NCs surrounded by multivalent anions revealed an additional force exerted on each NC as a function of their center-to-center distance (see supplementary materials section 2.3). This force was purely repulsive at short range (Fig. 2E), reduced the depth of the attractive well, and enabled the microreversibility of NC binding necessary for nucleation and growth of long-range ordered SCs. Our simulation of NC colloids further corroborated this hypothesis, showing that when the attractive well was deep ($\sim 6 k_B T$), the particles were arrested into gel-like structures, similar to experimentally observed structures for NCs with $\epsilon_{\text{NC}} < 20$. However, when the

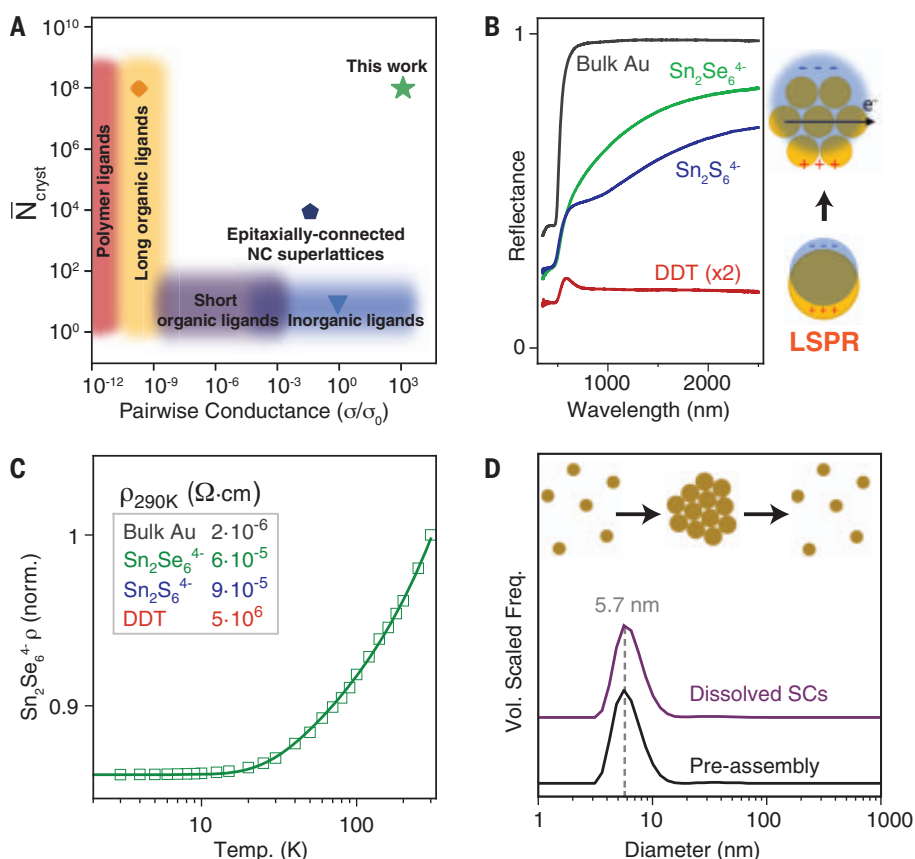


Fig. 4. Strong coupling and reversibility in all-inorganic NC superlattices. (A) Order-coupling diagram for existing NC solids. As a measure of electronic coupling in different ordered and disordered structures, we used the interparticle conductance ($\sigma^* = \sigma/\sigma_0$) normalized by the conductance quantum ($\sigma_0 = 2e^2/h$), where e is the electron charge and h is Planck's constant. As a measure of the ordering, we took the average number of particles in a crystalline domain. The data points indicated are as follows: red diamond, superlattices of DDT-capped Ag NCs (47); light blue inverted triangle, film of inorganically capped HgTe NCs (48); and dark blue pentagon, epitaxially connected PbSe superlattice by oriented attachment (17). Green star indicates data from the present work. (B) Left: reflectance data of 5-nm Au NCs capped with MCC and DDT ligands compared with bulk Au. Right: schematic for delocalization of LSPR in strongly coupled NC arrays. (C) Temperature-dependent resistivity data for supercrystals assembled from 5-nm Au NCs with $\text{Sn}_2\text{Se}_6^{4-}$ ligands. Inset: ρ at 290 K for bulk Au and Au NCs with three different ligands. (D) Dynamic light-scattering data showing that colloidal NCs can be assembled into SCs and then redissolved to recover the original colloidal solution.

attraction strength was moderate (~ 3 to $4 k_B T$), the coexistence of a metastable high-density liquid and crystal was present (fig. S26), closely resembling the behavior of metal semiconductor NCs with large ϵ_{NC} .

The metastable binodal curve in the colloidal phase diagram includes a fluid-fluid critical point (Fig. 2B). ten Wolde and Frenkel suggested that critical density fluctuations in the vicinity of this critical point lower the activation barrier for crystal nucleation (24). The SC nucleation can proceed along two different pathways (Figs. 2C, regions I and II, and 3B) (24, 25). In a narrow window of parameters very close to the binodal curve, classical one-step nucleation (region I) is predicted to be the main pathway to a crystalline state. Indeed, in situ SAXS studies showed that a gen-

tle increase of $(\text{N}_2\text{H}_5)_4\text{Sn}_2\text{S}_6$ concentration in hydrazine up to ~ 50 mM induced a rapid nucleation of 4.6 nm Au NCs into SCs, which grew at the expense of the free colloid (Fig. 3C and fig. S27).

A qualitatively different pathway was observed after the rapid addition of 100 to 125 mM $(\text{N}_2\text{H}_5)_4\text{Sn}_2\text{S}_6$ to a colloid of similarly sized Au NCs. Instead of direct nucleation of SCs, the colloidal solution divided into two fractions with different density (figs. S28 and S29). The dense phase initially showed no long-range order and resembled aggregated NCs but ultimately converted into SCs. This showed that the dense phase was not an arrested state but rather a dynamically evolving intermediate preceding SC formation, with transmission electron microscopy (TEM) studies further

suggesting that crystallization occurs within the matrix of disordered NCs (figs. S30 to S33). In the case of 5.5-nm PbS NCs in NMF flocculated with K_3AsS_4 in the presence of acetonitrile (Fig. 3A and fig. S34), SC nucleation was preceded by a separation of the homogeneous colloid into droplets of dilute and dense fluids according to the binodal separation of two fluids in Fig. 2B, and the nucleation occurred within the metastable dense fluid phase. Such a pathway is reminiscent of the nonclassical two-step nucleation, which is rather common for globular proteins (38, 39).

In many previous studies, NC films with strong electronic coupling and high electron mobility showed no long-range order, whereas long-range-ordered two- and three-dimensional SCs typically used insulating organic ligands. The resulting “order versus coupling” tradeoff (Fig. 4A; see supplementary materials section 2.4) is detrimental for the applications of colloidal NCs in optoelectronic devices. For the all-inorganic SCs described in this work, compared with SCs with traditional organic surfactants, the smaller interparticle spacing in all-inorganic SCs and the semiconducting nature of MCC ligands enabled much stronger electronic coupling between neighboring NCs while maintaining the high NC order and low strain previously observed only for SCs containing soft, deformable organic ligands (fig. S35).

The optical reflectance spectra measured for Au SCs with different surface ligands showed the crossing from weakly coupled localized surface plasmon resonance (LSPR) in the arrays of Au NCs with 1-dodecanethiol (DDT) ligands into the strong coupling regime for SCs assembled from Au NCs with $\text{Sn}_2\text{S}_6^{4-}$ ions approaching that of bulk metals (Fig. 4B and fig. S36). For Au NCs assembled with more conductive and polarizable $\text{Sn}_2\text{Se}_6^{4-}$ ions, the transition to metallic reflectance was even more complete, with higher reflectance overall and no sign of a residual LSPR component.

Measurements of direct current transport further supported assignment of metallic character to Au NC solids with MCC ligands (Fig. 4C). Resistivity decreased monotonically from 300 down to 3 K with no evidence of thermally activated transport between localized states that would manifest as increasing resistivity in the low-temperature limit. Instead, the temperature-dependent resistivity data were well described by the Boltzmann transport theory, as for typical metallic solids. A Bloch–Grüneisen model fit (40) successfully captures the phenomenology of the R versus T relation and is plotted as a solid line through the discrete data points (fig. S37). Between 300 and 3 K, the resistivity of the sample dropped by a factor of 0.86, yielding a residual resistivity ratio (RRR) $\rho_{300\text{K}}/\rho_{4\text{K}} = 1.16$. Such values of RRR are commonly measured from metallic alloys (41, 42) and degenerately doped crystalline

semiconductors (43). Magnitudes of 290 K resistivities (Fig. 4C, inset) of $\text{Sn}_2\text{Se}_6^{4-}$ -capped Au solids without any thermal annealing are within a factor of 30 of evaporated bulk Au films (Fig. 4A, star symbol). These values were measured over “polysupercrystalline” films and contained resistivity contribution from grain boundary scattering.

Surface-ligand-dependent transport in Au NC solids has been of interest for studies of the transition between insulating and metallic behavior (44). For NC films with short organic ligands, an applied compression can induce electron delocalization (45). Au NC films with inorganic thiocyanate ligands also show metallic-type direct current resistivity (46). However, previously studied metallic NC solids shared the common trait that particles were rendered insoluble by the chemical or heat treatments that improve conductivity. This loss of solubility made it difficult to rule out partial sintering of NCs along the current percolation path.

Our SCs dissolved completely into their individual NC building blocks when placed into pure NMF or hydrazine (figs. S38 and S39). Dynamic light-scattering measurements (Fig. 4D) confirmed that the colloidal particles recovered from redissolved SCs after low-temperature electronic measurements were indeed individual Au NCs, so the metallic transport that we observed did not result from NC necking or sintering. We observed the metallic character of our assemblies with no thermal annealing and with infilling materials (glassy SnS_2 or SnSe_2) that did not have conduction bands aligned to the Fermi level of Au. Strong electronic coupling between neighboring NC units was achieved through a combination of the short interparticle distance and greater polarizability with a lower tunneling barrier afforded by the inorganic infill compared with that of analogous organic ligands.

REFERENCES AND NOTES

1. D. Vanmaekelbergh, *Nano Today* **6**, 419–437 (2011).
2. M. A. Boles, M. Engel, D. V. Talapin, *Chem. Rev.* **116**, 11220–11289 (2016).
3. C. B. Murray, C. R. Kagan, M. G. Bawendi, *Annu. Rev. Mater. Sci.* **30**, 545–610 (2000).

4. A. Fortini, E. Sanz, M. Dijkstra, *Phys. Rev. E Stat. Nonlin. Soft Matter Phys.* **78**, 041402 (2008).
5. E. V. Shevchenko, D. V. Talapin, N. A. Kotov, S. O'Brien, C. B. Murray, *Nature* **439**, 55–59 (2006).
6. M. A. Boles, D. V. Talapin, *J. Am. Chem. Soc.* **137**, 4494–4502 (2015).
7. T. Paik, B. T. Diroll, C. R. Kagan, C. B. Murray, *J. Am. Chem. Soc.* **137**, 6662–6669 (2015).
8. R. J. Macfarlane *et al.*, *Science* **334**, 204–208 (2011).
9. D. V. Talapin *et al.*, *Nature* **461**, 964–967 (2009).
10. X. Ye *et al.*, *Nat. Mater.* **16**, 214–219 (2017).
11. N. S. Mueller *et al.*, *Nature* **583**, 780–784 (2020).
12. J. Chen *et al.*, *Nano Lett.* **10**, 5103–5108 (2010).
13. J.-S. Lee, M. V. Kovalenko, J. Huang, D. S. Chung, D. V. Talapin, *Nat. Nanotechnol.* **6**, 348–352 (2011).
14. M. Y. Lin *et al.*, *Nature* **339**, 360–362 (1989).
15. G. H. Carey *et al.*, *MRS Commun.* **3**, 83–90 (2013).
16. M. P. Boneschanscher *et al.*, *Science* **344**, 1377–1380 (2014).
17. A. Abelson *et al.*, *Nat. Mater.* **19**, 49–55 (2020).
18. K. Whitham *et al.*, *Nat. Mater.* **15**, 557–563 (2016).
19. D. M. Balazs *et al.*, *ACS Nano* **9**, 11951–11959 (2015).
20. M. C. Weidman, K. G. Yager, W. A. Tisdale, *Chem. Mater.* **27**, 474–482 (2015).
21. M. V. Kovalenko, M. Scheele, D. V. Talapin, *Science* **324**, 1417–1420 (2009).
22. A. E. Saunders, B. A. Korgel, *J. Phys. Chem. B* **108**, 16732–16738 (2004).
23. J. N. Israelachvili, *Intermolecular and Surface Forces* (Elsevier, 1985).
24. P. R. ten Wolde, D. Frenkel, *Science* **277**, 1975–1978 (1997).
25. T. K. Haxton, L. O. Hedges, S. Whitelam, *Soft Matter* **11**, 9307–9320 (2015).
26. M. G. Noro, D. Frenkel, *J. Chem. Phys.* **113**, 2941–2944 (2000).
27. N. Kallay, S. Zilac, *J. Colloid Interface Sci.* **253**, 70–76 (2002).
28. H. Liu, S. Garde, S. Kumar, *J. Chem. Phys.* **123**, 174505 (2005).
29. W. C. K. Poon *et al.*, *Phys. Rev. Lett.* **83**, 1239–1242 (1999).
30. M. Muschol, F. Rosenberger, *J. Chem. Phys.* **107**, 1953–1962 (1997).
31. P. N. Pusey, W. van Megen, *Nature* **320**, 340–342 (1986).
32. D. Klotska, R. L. Jack, *Soft Matter* **7**, 6294–6303 (2011).
33. T. Bian *et al.*, *Nat. Chem.* **13**, 940–949 (2021).
34. J. W. Zwanikken, M. Olvera de la Cruz, *Proc. Natl. Acad. Sci. U.S.A.* **110**, 5301–5308 (2013).
35. Y. Jing, V. Jadhao, J. W. Zwanikken, M. Olvera de la Cruz, *J. Chem. Phys.* **143**, 194508 (2015).
36. R. M. Malossi, M. Girotto, A. P. Dos Santos, Y. Levin, *J. Chem. Phys.* **153**, 044121 (2020).
37. G. I. Guerrero García, M. Olvera de la Cruz, *J. Phys. Chem. B* **118**, 8854–8862 (2014).
38. O. Gliko *et al.*, *J. Am. Chem. Soc.* **127**, 3433–3438 (2005).
39. A. Sauter *et al.*, *Faraday Discuss.* **179**, 41–58 (2015).
40. J. Chelikowsky, *Quantum Theory of Real Materials* (Springer, 1996).
41. A. F. Clark, G. E. Childs, G. H. Wallace, *Cryogenics* **10**, 295–305 (1970).
42. J. Bardeen, *J. Appl. Phys.* **11**, 88–111 (1940).
43. C. Yamanouchi, K. Mizuguchi, W. Sasaki, *J. Phys. Soc. Jpn.* **22**, 859–864 (1967).
44. A. Zabet-Khosousi, A.-A. Dhirani, *Chem. Rev.* **108**, 4072–4124 (2008).
45. S. Henrichs, C. P. Collier, R. J. Saykally, Y. R. Shen, J. R. Heath, *J. Am. Chem. Soc.* **122**, 4077–4083 (2000).
46. J.-H. Choi *et al.*, *Science* **352**, 205–208 (2016).
47. Y. Yu, D. Yu, B. Sadigh, C. A. Orme, *Nat. Commun.* **9**, 4211 (2018).
48. X. Lan *et al.*, *Nat. Mater.* **19**, 323–329 (2020).

ACKNOWLEDGMENTS

We thank J. Ondry (University of Chicago) for many stimulating discussions and for critical reading of the manuscript. **Funding:** Self-assembly experiments, in situ x-ray scattering studies, and associated data interpretations were supported by the Office of Basic Energy Sciences (BES), US Department of Energy (DOE) (award no. DE-SC0019375). Nanomaterials synthesis and surface functionalization studies were supported by the Advanced Materials for Energy-Water Systems (AMEWS) Center, an Energy Frontier Research Center funded by the DOE, Office of Science, BES. Modeling and simulations of pair potentials were supported by the Midwest Integrated Center for Computational Materials (MICCOM) as part of the Computational Materials Sciences Program funded by the DOE, Office of Science, BES, Materials Sciences and Engineering Division (award no. 5J-30161-0010A). Spectroscopic and charge transport studies were supported by the Department of Defense Air Force Office of Scientific Research (grant no. FA9550-18-1-0099). D.H. and A.E. were supported by the Deutsche Forschungsgemeinschaft (award no. DFG1401/02). M.H. was supported by the University of Chicago Materials Research Science and Engineering Center, which is funded by the National Science Foundation (NSF) (award no. DMR-2011854). The work used resources of the Center for Nanoscale Materials, a U.S. DOE (DOE) Office of Science User Facility operated for the DOE Office of Science by Argonne National Laboratory (contract no. DE-AC02-06CH11357). Use of the Stanford Synchrotron Radiation Lightsource, SLAC National Accelerator Laboratory, is supported by the DOE, Office of Science, Office of Basic Energy Sciences (contract no. DE-AC02-76SF00515). C.P.N.T. was supported by the NSF (Graduate Research Fellowship no. DGE1106400). J.K.U. was supported by an Arnold O. Beckman Postdoctoral Fellowship in Chemical Sciences from the Arnold and Mabel Beckman Foundation. N.S.G. and D.V.T. were supported by an Alfred P. Sloan Research Fellowship, a David and Lucile Packard Foundation Fellowship for Science and Engineering, and a Camille and Henry Dreyfus Teacher-Scholar Awards. M.-O.C. thanks the Sherman Fairchild Foundation for computational support. **Author contributions:** I.C., E.M.J., and J.P. performed and designed the experiments, analyzed data, and cowrote the paper. D.H. participated in the early stage of the project under supervision by A.E. M.H.H., N.A.S., and A.M.H. synthesized nanocrystals and participated in data analysis; T.D.N. and A.D. performed simulations under supervision from M.-O.C. and D.T.L., respectively. J.K.U., S.W.T., and N.S.G. designed and performed beamtime synchrotron studies. D.V.T. conceived and designed experiments and simulations, analyzed data, cowrote the paper, and supervised the project. All authors discussed the results and commented on the manuscript. **Competing interests:** The authors declare no competing interests. **Data and materials availability:** All data needed to evaluate the conclusions in the study are present in the main text or the supplementary materials. Samples can be provided by the authors upon reasonable request under a materials transfer agreement with the university.

SUPPLEMENTARY MATERIALS

science.org/doi/10.1126/science.abm6753
Materials and Methods
Supplementary Text
Figs. S1 to S39
References (49–82)

5 October 2021; accepted 24 February 2022
10.1126/science.abm6753



myIDP:
A career plan customized for you, by you.

For your career in science, there's only one **Science**

Features in myIDP include:

- Exercises to help you examine your skills, interests, and values.
- A list of 20 scientific career paths with a prediction of which ones best fit your skills and interests.

 Visit the website and start planning today!
myIDP.sciencecareers.org

ScienceCareers In partnership with:     



Shenzhen Institute of Advanced Technology
Chinese Academy of Sciences




Established in partnership between the Chinese Academy of Sciences and the Shenzhen Municipal Government, the Shenzhen Institute of Advanced Technology (SIAT) is a newly-created university with an objective to become the world's preeminent institute for emerging science and engineering programs. SIAT is equipped with state-of-art teaching and research facilities and is dedicated to cultivating international, visionary, and interdisciplinary talents while delivering research support to pursue innovation-driven development.

SIAT is located in Shenzhen, also known as the "Silicon Valley of China," a modern, clean, and green city, well-known for its stunning architecture, vibrant economy, and its status as a leading global technology hub. SIAT is seeking applications for faculty positions of all ranks in the following academic programs: Computer Science and Engineering, Bioinformatics, Robotics, Life Sciences, Material Science and Engineering, Bio-medical Engineering, Pharmaceutical Sciences, Synthetic Biology, Neurosciences, etc. SIAT seeks individuals with a strong record of scholarship who possess the ability to develop and lead high-quality teaching and research programs. SIAT offers a comprehensive benefits package and is committed to faculty success throughout the academic career trajectory, providing support for ambitious and world-class research projects and innovative, interactive teaching methods.

Further information:
<https://www.siat-sz.edu.cn/>

JOB FOCUS: CANCER



**UNIVERSITY OF CALIFORNIA, IRVINE
CANCER RESEARCH INSTITUTE**


Postdoctoral positions are available both immediately and with a delayed start date in UC Irvine cancer cell biology laboratories using collaborative, interdisciplinary approaches.

UC Irvine is located near the California coast, mid-way between Los Angeles and San Diego and is home to the NCI-designated Chao Family Comprehensive Cancer Center offering a cutting-edge, but highly collegial, research environment.

American citizens and permanent residents are eligible for positions on the Interdisciplinary Cancer Biology NCI-supported T32 training grant which offers increased opportunities for mentoring and career development. UC Irvine is committed to providing both resources and a workplace climate that will expand the participation of underrepresented groups in STEM.

Recruitment stipends are available for applicants with a strong record of and commitment to activities promoting diversity, equity, and inclusion in the sciences. Postdocs at UCI are also eligible to apply for the UC Presidential Postdoctoral Fellowship Program (<https://ppfp.ucop.edu/info/about-ppfp/index.html>) which offers enhanced opportunities to obtain tenure track positions at all UC campuses; workshops are offered to facilitate these applications.

Information on UC Irvine cancer research laboratories can be found at: <https://cancerresearch.uci.edu/training/> and <https://cancerresearch.uci.edu/>. Interested applicants should contact possible mentors directly or send a CV and cover letter to CRI Director David Fruman (dfroman@uci.edu) or Co-Director Aimee Edinger (aedinger@uci.edu) for more information or help identifying appropriate mentors.



**FACULTY IN CANCER IMMUNOLOGY
AND IMMUNOTHERAPEUTICS**

The Houston Methodist Cancer Center invites applications for a **faculty position** within our Cancer Immunology and Immunotherapeutics Program. We seek an NCI-funded, accomplished researcher, eligible for rank of **Assistant, Associate or Full Professor**, working towards the development of the next generation of immunotherapies with a solid tumor focus.

Candidates must have an MD, MD/PhD, or PhD degree with established expertise in a targeted field of research, e.g. cancer vaccines, cell and gene therapy, and the tumor immune microenvironment, a track record of sustained and ongoing funded research program, and an outstanding record of collaborative cancer research-related activities.

The Houston Methodist Cancer Center attracts top talent from across the nation and provides competitive start-up packages with a strong commitment to programmatic development, and recruitment of future faculty. Faculty members will benefit from highly collaborative research environment, state of the art research building, infrastructure, and core services; these research facilities are housed adjacent to multi-disciplinary inpatient and outpatient cancer related clinical areas providing the opportunity for translational research. Primary appointment will be in the Houston Methodist Academic Institute, with a potential appointment at Weill Cornell Medical College upon additional approval.

To apply, please include the following with your application, and send via email to: CancerCenterRecruitment@houstonmethodist.org

- Cover Letter highlighting accomplishments and research interests
- Curriculum Vitae with funding and publication list
- A list of three references

Who's the top employer for 2021?



Science Careers' annual survey reveals the top companies in biotech & pharma voted on by *Science* readers.

Read the article and employer profiles at sciencecareers.org/topemployers

What's Your Next Career Move?

From networking to mentoring to evaluating your skills, find answers to your career questions on *Science Careers*

To view the complete collection, visit ScienceCareers.org/booklets



ScienceCareers

FROM THE JOURNAL SCIENCE 

By Astrid C. H. Jaeger

No shame in my pain

At the beginning of my second year as a Ph.D. student, I started to spend hours each month curled in the fetal position on the floor, unable to leave the house, let alone work. I thought the stabbing pelvic pain and alarming blood loss were just part of having a period, to be handled with painkillers and an extra-large menstruation cup. As the months passed, the pain and cramps became constant, interfering with my days, my Ph.D., my life. The doctor said it was just stress, but I was at the end physically and emotionally. When I took sick time I felt I was failing as a Ph.D. student, and I tried to make up for the missed hours by working extra in the evenings and on weekends. Yet because of the stigma around many women's health issues, I was too embarrassed to tell my colleagues what I was going through.

When people asked how I was doing, I put on my best smile and told them I was OK, just tired. I worried that if I complained they might see me as too sensitive. But I was desperate to find an answer.

After three doctor's visits within 2 months, I saw a specialist. A lengthy investigation of my uterus by 3D ultrasound revealed lesions and a mandarin-size ovarian cyst—signs of endometriosis, a chronic disorder in which tissue that typically lines the uterus grows outside it. The disease, which strikes one in 10 people who menstruate, causes extreme pain and often results in infertility. I was relieved the pain finally had a name and that, more than a year after the symptoms began, I had a diagnosis. But there is no cure, and the root of the disease is unknown.

I couldn't control what was going on inside my body, so I started to focus on what I could control—including sharing my story with colleagues, despite the stigma. I wanted them to know why I had not been around as much, and I hoped being open about my experience might help others going through anything similar. So, during a coffee break, I gathered all my courage and opened up to my colleagues about the pain and how being ill interfered with my work. Telling my story led to an entire conversation about everyone's period problems, including laughing about our most embarrassing experiences. It felt good to be understood.

I also felt the need to tell my supervisor. I was afraid he would be disappointed with me or even question whether I should continue as a Ph.D. student, and I spent many sleepless nights working out how to approach the conversation. To my relief, when we finally met, he was very



“I thought the stabbing pelvic pain and alarming blood loss were just part of having a period.”

understanding. We talked about my health and how it affects my quality of life and my work. We adjusted my schedule, and he told me I could ask our lab technician to help with my experiments and delegate some analyses to student assistants and interns.

Unburdening myself to my colleagues, and the support I received in return, helped me regain my motivation. I felt ready to beat the pain. Four months after getting diagnosed, I had a small surgery to remove a cyst. I changed my diet and started hormone therapy to halt the growth of the disease—though that treatment comes with its own side effects. I also learned how to manage the pain with pelvic floor physiotherapy, herbal medications, and acupuncture instead of massive loads of painkill-

ers. I still experience 1 or 2 days of pain every month—not as severe as before, but enough that I need to use sick leave and do not forget my disease.

For many years, endometriosis was known as the “career woman’s disease.” It was believed to afflict women who put off marriage and pregnancy to pursue their careers. But it is not our career paths that shape our disease; it is the disease that disrupts our careers. Endometriosis is just one of many women’s health issues that are too often stigmatized or ignored—often with dire consequences for our health and well-being, not to mention our careers. But being open and seeking help can open the way back into work and life. ■

Astrid C. H. Jaeger is a Ph.D. candidate at ETH Zürich. Send your career story to SciCareerEditor@aaas.org.





Share Your Robotics Research with the World.

Shaping the future of robotics with high impact research!

As a multidisciplinary online-only journal, *Science Robotics* publishes original, peer-reviewed, research articles that advance the field of robotics. The journal provides a central forum for communication of new ideas, general principles, and original developments in research and applications of robotics for all environments.

Submit your research today. Learn more at: science.org/journal/scirobotics

 Twitter: @SciRobotics

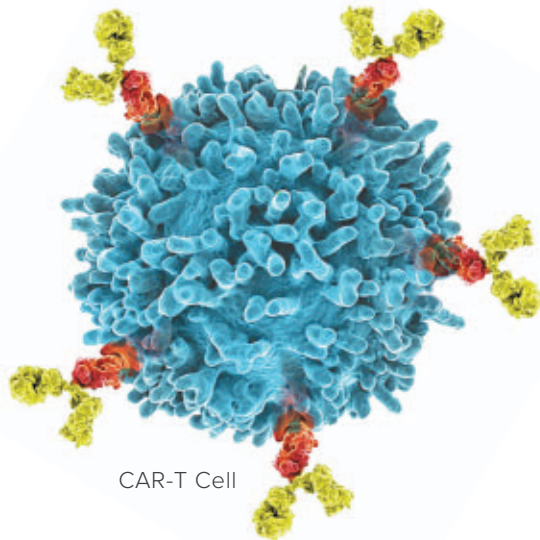
 Facebook: @ScienceRobotics

Science Robotics

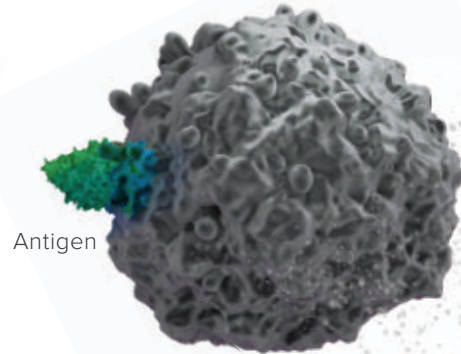
 AAAS

CAR-T Products & Engineering

Innovating Chimeric Antigen Receptors for Research & Development



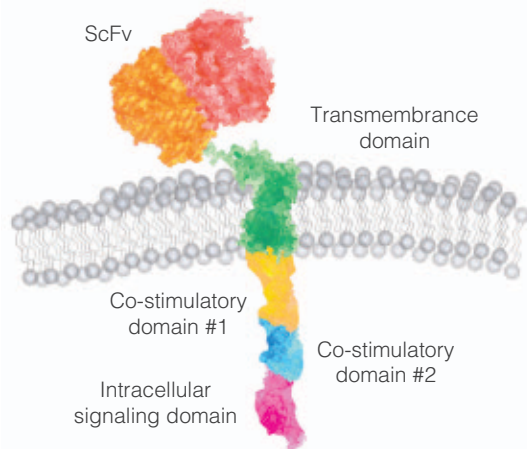
CAR-T Cell



Antigen

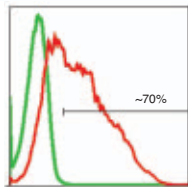
Tumor Cell

Current CAR-T Products



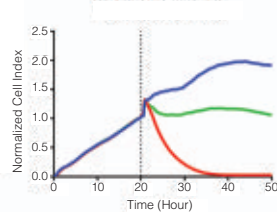
- alpha Fetaprotein
- B7H4
- BCMA
- c-Met
- CD19
- CD19 + CD22
- CD20
- CD22
- CD24
- CD33
- CD37
- CD38
- CD4
- CD47
- CD70
- CD123
- CD133
- CD138
- CD147
- CEA
- CLDN 18.2
- CS1
- EGFR
- EpCAM
- EphA2
- Folate receptor alpha chain
- GPC3
- Her2
- MCAM
- Mock Control
- MSLN
- NGFR
- PDL-1
- PSMA
- ROR1
- VEGFR2

CAR Expression



— Target cells alone — T cells — CAR-T cells

Cytotoxicity Assay



Custom design, development, and manufacturing services available.

ProMab Biotechnologies offers over 60 types of off-the-shelf CAR-T cells and target cells ready to use for cell therapy research applications. In addition to ready-to-use products, ProMab offers comprehensive pre-clinical platform for custom CAR engineering in different immune cell subsets. With many different options for gene delivery and large scale production, learn more about how ProMab can help accelerate cell therapy research.

All products are for research use only

Discover more | www.promab.com



📍 2600 Hilltop Dr, Building B, Suite C320, Richmond, CA 94806
 📞 1.866.339.0871 | ✉ info@promab.com

